

Assessment of Seismic Analysis Methodologies for Deeply Embedded Nuclear Power Plant Structures

Brookhaven National Laboratory

**U.S. Nuclear Regulatory Commission
Office of Nuclear Regulatory Research
Washington, DC 20555-0001**



NUREG/CR-6896
BNL-NUREG-75410-2006

Assessment of Seismic Analysis Methodologies for Deeply Embedded Nuclear Power Plant Structures

Manuscript Completed: February 2006
Date Published: February 2006

Prepared by
J. Xu¹, C. Miller¹, C. Costantino¹, and C. Hofmayer¹
H.L. Graves²

¹Brookhaven National Laboratory
Upton, NY 11973-5000

H.L. Graves, NRC Program Manager

Prepared for
²Division of Engineering Technology
Office of Nuclear Regulatory Research
U.S. Nuclear Regulatory Commission
Washington, DC 20555-0001
NRC Job Code Y6718



ABSTRACT

To support the review of preliminary applications for new reactor designs, the Nuclear Regulatory Commission's (NRC) Office of Nuclear Regulatory Research has sponsored a research program at Brookhaven National Laboratory (BNL) on deeply embedded and/or buried (DEB) structures. BNL investigated the extent to which procedures acceptable for shallow embedments are also adequate for deeper embedments. The overall objective of this research was to investigate the applicability of existing NRC review guidance, seismic design practice, and soil-structure interaction (SSI) computer codes to DEB structures, and to identify areas for improvement.

This report includes (1) review and evaluation of existing seismic design practice, (2) assessment of simplified vs. detailed SSI in-structure response spectrum analysis of DEB structures, (3) assessment of methods for computing seismic-induced earth pressures on DEB structures, and (4) development of criteria for benchmark problems, which could be used to validate code for computing seismic responses of DEB nuclear power plant structures. BNL's review included the existing standards, tests, and practices that have been used in the design and analysis of DEB structures, including NRC seismic analysis guidelines as outlined in the Standard Review Plan. Computer codes, especially the program entitled "A System for the Analysis of Soil-Structure Interaction," were reviewed for applicability to the SSI analyses for DEB structures. Criteria for a set of benchmark problems were developed, and two sets of benchmark problems were completed which include pertinent attributes pertaining to DEB nuclear power plant structures.

FOREWORD

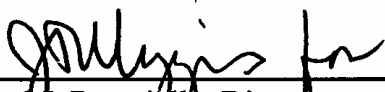
Over the past three decades, extensive research has been performed to study the phenomenon of soil-structure interaction (SSI) and its impact on seismic response, especially for nuclear power plant (NPP) structures. To date, this research has considerably advanced the understanding of the interacting mechanisms associated with SSI, led to the development of analytical methodologies and computer programs for seismic response, and provided much needed field data from real earthquake events.

Established computer codes used for SSI analysis in the nuclear industry have primarily been developed for current light-water reactors, and applied to coupled SSI models in which the structures are founded at or near the ground surface with shallow embedment. However, several “new generation” NPP designs, i.e. the pebble bed modular reactor and the high temperature gas-cooled reactor designs, have proposed deeply embedded or buried (DEB) structural configurations. For two of these new designs submitted to U.S. Nuclear Regulatory Commission (NRC) for preliminary review, the entire reactor building and a significant portion of the steam generator building are either partially or completely embedded below the ground surface.

Because current seismic analysis methodologies have been developed for shallow embedded structures, existing regulatory guidance, codes, and standards (e.g., ASCE-4, “Seismic Analyses of Safety-Related Nuclear Structures”) suggest that simple formulations may be used to model the embedment effect when the depth of embedment is less than 30 percent of its foundation equivalent-radius. Therefore, to support the review of preliminary applications for new reactor designs, the NRC has sponsored a research program, under which Brookhaven National Laboratory (BNL) investigated the extent to which procedures acceptable for shallow embedments are also adequate for deeper embedments. The overall objective of this research is to investigate the applicability of existing NRC review guidance, seismic design practice, and SSI computer codes to DEB structures, and to identify areas for improvement.

This report includes (1) review and evaluation of existing seismic design practice, (2) assessment of simplified vs. detailed methodologies for SSI in-structure response spectrum analysis of DEB structures, (3) assessment of methodologies for computing seismic-induced earth pressures on DEB structures, and (4) development of criteria for benchmark problems, which could be used to validate code for computing seismic responses of DEB NPP structures.

Based on the results of this study, the NRC concluded that existing linear SSI methodologies, including both simplified and detailed approaches can be extended, to varying extents, to DEB structures and produce acceptable SSI response calculations, provided that the SSI response induced by the ground motion is very much within the linear regime or the non-linear effect is not expected to control the SSI response parameters. Furthermore, strong ground motion response data from additional tests or earthquake recordings could prove useful in validating the pertinent modeling assumptions for SSI response analysis of DEB NPP structures.



Carl J. Paperiello, Director
Office of Nuclear Regulatory Research
U.S. Nuclear Regulatory Commission

TABLE OF CONTENTS

	<u>Page No.</u>
Abstract	iii
Foreword.....	v
Table of Contents	vii
List of Figures	xi
Executive Summary	xxvii
Acknowledgments	xxxii
1.0 INTRODUCTION	1
1.1 Background.....	1
1.2 Scope and Objectives.....	1
1.3 Report Organization	3
2.0 EXISTING SEISMIC ANALYSIS AND DESIGN PRACTICE.....	4
2.1 Literature Review of Seismic Analysis and Design Practice for DEB Structures.....	4
2.1.1 Impact of SSI Effects on DEB Structures	5
2.1.2 Seismic Induced Dynamic Pressure on DEB Structures	7
2.1.3 State-of-the-art Analysis Methods for Seismic Response Calculations of DEB Structures	10
2.1.4 Examples of Practical Applications Using Established Approaches to DEB Structures.....	12
2.2 Review of Guidance Documents	16
2.2.1 ASCE 4-98 (Seismic Analysis of Safety-Related Nuclear Structures and Commentary).....	16
2.2.2 U.S. NRC Standard Review Plan (SRP)	17
2.2.3 U.S. DOE Guidelines for Buried Waste Tanks	18
2.2.4 Japanese Guidelines	19
2.3 Review of Computer Programs	20
2.3.1 Codes Based on Continuum Models	20
2.3.2 Codes Based on Discrete Models.....	21
2.4 Review of Existing Recorded Data	22
2.5 Potential Issues Related to SSI Effects for DEB Structures and Planned Studies	24

TABLE OF CONTENTS

	<u>Page No.</u>
3.0 ASSESSMENT OF SIMPLIFIED VS. DETAILED METHODOLOGIES FOR SSI ANALYSIS OF DEB STRUCTURES	29
3.1 Approach	29
3.1.1 Description of Facility	29
3.1.2 Simplified Model Using the CARES Program	31
3.1.3 Detailed Model Using SASSI Program	33
3.2 Embedment Effect on Kinematic Response of DEB Structures	33
3.2.1 SASSI Analysis of DEB Structures Subject to Incident Waves	34
3.2.2 SASSI vs. CARES Analyses of DEB Structures Subject to Vertical Incident Shear Waves	35
3.3 Embedment Effect on SSI Response of DEB Structures	36
3.4 Assessment of Analysis Methodologies for Computing SSI Response of DEB Structures	37
4.0 ASSESSMENT OF METHODOLOGIES FOR COMPUTING SEISMIC INDUCED EARTH PRESSURES ON DEB STRUCTURES	87
4.1 Approach	87
4.1.1 SASSI Model	87
4.1.2 LS-DYNA Model	88
4.2 SASSI Analysis of Embedment Effect on Seismic Induced Earth Pressures for DEB Structures	90
4.2.1 SASSI Analysis for the 11.5 m Depth of Burial	90
4.2.2 SASSI Analysis for the 23 m Depth of Burial	92
4.2.3 SASSI Analysis for the 34.5 m Depth of Burial	93
4.2.4 SASSI Analysis for the 46 m Depth of Burial	95
4.2.5 SASSI Assessment of the Depth of Burial Effect	96
4.3 LS-DYNA Analysis of Seismic Induced Earth Pressures and Comparisons With SASSI Results	97
4.3.1 LS-DYNA Free Field Analysis	97
4.3.2 Comparison of LS-DYNA and SASSI Analyses for the 11.5 m Depth of Burial	98
4.3.3 Comparison of LS-DYNA and SASSI Analyses for the 23 m Depth of Burial	100

4.3.4	Comparison of LS-DYNA and SASSI Analyses for the 34.5 m Depth of Burial	102
4.3.5	Comparison of LS-DYNA and SASSI Analyses for the 46 m Depth of Burial	104
4.3.6	LS-DYNA Assessment of the Depth of Burial Effect	106
4.4	Assessment of the Effect of Soil-Structure Interface Modeling on Seismic Response Characteristics of DEB Structures.....	107
4.4.1	Assessment of the Effect of Soil-Structure Interface Modeling for the 11.5 m Depth of Burial Using LS-DYNA	107
4.4.2	Assessment of the Effect of Soil-Structure Interface Modeling for the 23 m Depth of Burial Using LS-DYNA.....	110
4.4.3	Assessment of the Effect of Soil-Structure Interface Modeling for the 34.5 m Depth of Burial Using LS-DYNA	112
4.4.4	Assessment of the Effect of Soil-Structure Interface Modeling for the 46 m Depth of Burial Using LS-DYNA.....	115
4.4.5	Frequency Domain Assessment of the Interface Modeling Effect on DEB SSI Response.....	117
4.4.6	Estimation of Non-linear Effects at the Soil-Structure Interface from the SASSI Results for the 23 m Depth of Burial	118
4.5	Assessment of Nonlinear Material Effect on Seismic Response of DEB Structures	119
5.0	DEVELOPMENT OF BENCHMARK PROBLEMS	260
5.1	Criteria Used to Select Benchmark Problems	260
5.2	Problem Characteristics.....	260
5.2.1	Cylindrical Structure.....	261
5.2.2	Square Box Type Structure.....	262
6.0	CONCLUSIONS AND RECOMMENDATIONS	265
7.0	REFERENCES	273

List of Figures

<u>Figure No.</u>		<u>Page No.</u>
3.1.1-1	Sketch of Typical Advanced Reactor Containment Structure.....	39
3.1.1-2	Sketch of Analysis Model for Methodologies Assessments	40
3.1.1-3	Site Soil Profiles Used for SSI Analyses.....	41
3.1.1-4	5% Damping Response Spectrum of Rock Outcrop Motion.....	41
3.1.1-5	Rock Outcrop Accelerogram.....	42
3.1.1-6	Free Field Response Spectra for Soil Column A.....	42
3.1.1-7	Free Field Response Spectra for Soil Column B.....	43
3.1.1-8	Free Field Response Spectra for Soil Column C.....	43
3.1.2-1	CARES SSI Model.....	44
3.1.3-1	SASSI Structural Model.....	44
3.2.1-1	Translational Spectra for Soil Column A at the Basement Center of SASSI Kinematic Model with 11.5m Embedment for Various Incident SH-Waves.....	45
3.2.1-2	Translational Spectra for Soil Column A at the Surface Center of SASSI Kinematic Model with 11.5m Embedment for Various Incident SH-Waves..	45
3.2.1-3	Translational Spectra for Soil Column A at the Basemat Center of SASSI Kinematic Model with 46m Embedment for Various Incident SH-Waves.....	46
3.2.1-4	Translational Spectra for Soil Column A at the Surface Center of SASSI Kinematic Model with 46m Embedment for Various Incident SH-Waves.....	46
3.2.1-5	Torsional Spectra for Soil Column A at the Surface Center of SASSI Kinematic Model with 11.5m Embedment for Various Incident SH-Waves..	47
3.2.1-6	Torsional Spectra for Soil Column A at the Surface Center of SASSI Kinematic Model with 46m Embedment for Various Incident SH-Waves.....	47
3.2.1-7	Translational Spectra for Soil Column A at the Basemat Center of SASSI Kinematic Model with 11.5m Embedment for Various Incident SV-Waves.....	48
3.2.1-8	Translational Spectra for Soil Column A at the Surface Center of SASSI Kinematic Model with 11.5m Embedment for Various Incident SV-Waves.....	48
3.2.1-9	Translational Spectra for Soil Column A at the Basemat Center of SASSI Kinematic Model with 46m Embedment for Various Incident SV-Waves.....	49
3.2.1-10	Translational Spectra for Soil Column A at the Surface Center of SASSI Kinematic Model with 46m Embedment for Various Incident SV-Waves.....	49
3.2.1-11	Translational Spectra for Soil Column B at the Basemat Center of SASSI Kinematic Model with 11.5m Embedment for Various Incident SH-Waves.....	50
3.2.1-12	Translational Spectra for Soil Column B at the Surface Center of SASSI Kinematic Model with 11.5m Embedment for Various Incident SH-Waves.....	50
3.2.1-13	Translational Spectra for Soil Column B at the Basemat Center of SASSI Kinematic Model with 46m Embedment for Various Incident SH-Waves.....	51

3.2.1-14	Translational Spectra for Soil Column B at the Surface Center of SASSI Kinematic Model with 46m Embedment for Various Incident SH-Waves.....	51
3.2.1-15	Torsional Spectra for Soil Column B at the Surface Center of SASSI Kinematic Model with 11.5m Embedment for Various Incident SH-Waves.....	52
3.2.1-16	Torsional Spectra for Soil Column B at the Surface Center of SASSI Kinematic Model with 46m Embedment for Various Incident SH-Waves.....	52
3.2.1-17	Translational Spectra for Soil Column B at the Basemat Center of SASSI Kinematic Model with 11.5m Embedment for Various Incident SV-Waves.....	53
3.2.1-18	Translational Spectra for Soil Column B at the Surface Center of SASSI Kinematic Model with 11.5m Embedment for Various Incident SV-Waves.....	53
3.2.1-19	Translational Spectra for Soil Column B at the Basemat Center of SASSI Kinematic Model with 46m Embedment for Various Incident SV-Waves.....	54
3.2.1-20	Translational Spectra for Soil Column B at the Surface Center of SASSI Kinematic Model with 46m Embedment for Various Incident SV-Waves.....	54
3.2.1-21	Translational Spectra for Soil Column C at the Basemat Center of SASSI Kinematic Model with 11.5m Embedment for Various Incident SH-Waves.....	55
3.2.1-22	Translational Spectra for Soil Column C at the Surface Center of SASSI Kinematic Model with 11.5m Embedment for Various Incident SH-Waves.....	55
3.2.1-23	Translational Spectra for Soil Column C at the Basemat Center of SASSI Kinematic Model with 23m Embedment for Various Incident SH-Waves.....	56
3.2.1-24	Translational Spectra for Soil Column C at the Surface Center of SASSI Kinematic Model with 23m Embedment for Various Incident SH-Waves.....	56
3.2.1-25	Translational Spectra for Soil Column C at the Basemat Center of SASSI Kinematic Model with 34.5m Embedment for Various Incident SH-Waves.....	57
3.2.1-26	Translational Spectra for Soil Column C at the Surface Center of SASSI Kinematic Model with 34.5m Embedment for Various Incident SH-Waves.....	57
3.2.1-27	Translational Spectra for Soil Column C at the Basemat Center of SASSI Kinematic Model with 46m Embedment for Various Incident SH-Waves.....	58
3.2.1-28	Translational Spectra for Soil Column C at the Surface Center of SASSI Kinematic Model with 46m Embedment for Various Incident SH-Waves.....	58
3.2.1-29	Torsional Spectra for Soil Column C at the Surface Center of SASSI Kinematic Model with 11.5m Embedment for Various Incident SH-Waves.....	59
3.2.1-30	Torsional Spectra for Soil Column C at the Surface Center of SASSI Kinematic Model with 23m Embedment for Various Incident SH-Waves.....	59

3.2.1-31	Torsional Spectra for Soil Column C at the Surface Center of SASSI Kinematic Model with 34.5m Embedment for Various Incident SH-Waves.....	60
3.2.1-32	Torsional Spectra for Soil Column C at the Surface Center of SASSI Kinematic Model with 46m Embedment for Various Incident SH-Waves.....	60
3.2.1-33	Translational Spectra for Soil Column C at the Basement Center of SASSI Kinematic Model with 11.5m Embedment for Various Incident SV-Waves.....	61
3.2.1-34	Translational Spectra for Soil Column C at the Surface Center of SASSI Kinematic Model with 11.5m Embedment for Various Incident SV-Waves.....	61
3.2.1-35	Translational Spectra for Soil Column C at the Basement Center of SASSI Kinematic Model with 23m Embedment for Various Incident SV-Waves.....	62
3.2.1-36	Translational Spectra for Soil Column C at the Surface Center of SASSI Kinematic Model with 23m Embedment for Various Incident SV-Waves.....	62
3.2.1-37	Translational Spectra for Soil Column C at the Basement Center of SASSI Kinematic Model with 34.5m Embedment for Various Incident SV-Waves.....	63
3.2.1-38	Translational Spectra for Soil Column C at the Surface Center of SASSI Kinematic Model with 34.5m Embedment for Various Incident SV-Waves.....	63
3.2.1-39	Translational Spectra for Soil Column C at the Basement Center of SASSI Kinematic Model with 46m Embedment for Various Incident SV-Waves.....	64
3.2.1-40	Translational Spectra for Soil Column C at the Surface Center of SASSI Kinematic Model with 46m Embedment for Various Incident SV-Waves.....	64
3.2.2-1	Comparison of Responses Spectra for Soil Column A at the Basemat Center of Kinematic Model with 11.5m Embedment	65
3.2.2-2	Comparison of Responses Spectra for Soil Column A at the Surface Center of Kinematic Model with 11.5m Embedment	65
3.2.2-3	Comparison of Responses Spectra for Soil Column A at the Basemat Center of Kinematic Model with 46m Embedment	66
3.2.2-4	Comparison of Responses Spectra for Soil Column A at the Surface Center of Kinematic Model with 46m Embedment	66
3.2.2-5	Comparison of Responses Spectra for Soil Column B at the Basemat Center of Kinematic Model with 11.5m Embedment	67
3.2.2-6	Comparison of Responses Spectra for Soil Column B at the Surface Center of Kinematic Model with 11.5m Embedment	67
3.2.2-7	Comparison of Responses Spectra for Soil Column B at the Basemat Center of Kinematic Model with 46m Embedment	68
3.2.2-8	Comparison of Responses Spectra for Soil Column B at the Surface Center of Kinematic Model with 46m Embedment	68
3.2.2-9	Comparison of Responses Spectra for Soil Column C at the Basemat Center of Kinematic Model with 11.5m Embedment	69
3.2.2-10	Comparison of Responses Spectra for Soil Column C at the Surface Center of Kinematic Model with 11.5m Embedment	69

3.2.2-11	Comparison of Responses Spectra for Soil Column C at the Basemat Center of Kinematic Model with 23m Embedment	70
3.2.2-12	Comparison of Responses Spectra for Soil Column C at the Surface Center of Kinematic Model with 23m Embedment	70
3.2.2-13	Comparison of Responses Spectra for Soil Column C at the Basemat Center of Kinematic Model with 34.5m Embedment	71
3.2.2-14	Comparison of Responses Spectra for Soil Column C at the Surface Center of Kinematic Model with 34.5m Embedment	71
3.2.2-15	Comparison of Responses Spectra for Soil Column C at the Basemat Center of Kinematic Model with 46m Embedment	72
3.2.2-16	Comparison of Responses Spectra for Soil Column C at the Surface Center of Kinematic Model with 46m Embedment	72
3.3-1	Comparison of Response Spectra for Soil Column A at the Basemat Center of SSI Model with 11.5m Embedment	73
3.3-2	Comparison of Response Spectra for Soil Column A at the Roof Center of SSI Model with 11.5m Embedment	73
3.3-3	Comparison of Response Spectra for Soil Column A at the Basemat Center of SSI Model with 46m Embedment	74
3.3-4	Comparison of Response Spectra for Soil Column A at the Roof Center of SSI Model with 46m Embedment	74
3.3-5	Comparison of Response Spectra for Soil Column B at the Basemat Center of SSI Model with 11.5m Embedment	75
3.3-6	Comparison of Response Spectra for Soil Column B at the Roof Center of SSI Model with 11.5m Embedment	75
3.3-7	Comparison of Response Spectra for Soil Column B at the Basemat Center of SSI Model with 46m Embedment	76
3.3-8	Comparison of Response Spectra for Soil Column B at the Roof Center of SSI Model with 46m Embedment	76
3.3-9	Comparison of Response Spectra for Soil Column C at the Basemat Center of SSI Model with 11.5m Embedment	77
3.3-10	Comparison of Response Spectra for Soil Column C at the Roof Center of SSI Model with 11.5m Embedment	77
3.3-11	Comparison of Response Spectra for Soil Column C at the Basemat Center of SSI Model with 23m Embedment	78
3.3-12	Comparison of Response Spectra for Soil Column C at the Roof Center of SSI Model with 23m Embedment	78
3.3-13	Comparison of Response Spectra for Soil Column C at the Basemat Center of SSI Model with 34.5m Embedment	79
3.3-14	Comparison of Response Spectra for Soil Column C at the Roof Center of SSI Model with 34.5m Embedment	79
3.3-15	Comparison of Response Spectra for Soil Column C at the Basemat Center of SSI Model with 46m Embedment	80
3.3-16	Comparison of Response Spectra for Soil Column C at the Roof Center of SSI Model with 46m Embedment	80
3.4-1	Performance Evaluation Based on Primary Spectral Peak Differences of Kinematic Analyses for Soil Columns A and B.....	81
3.4-2	Performance Evaluation Based on Primary Spectral Peak Differences of SSI Analyses for Soil Columns A and B	81
3.4-3	Performance Evaluation Based on Primary Spectral Peak Differences of Kinematic and SSI Analyses for Soil Columns C.....	82

3.4-4	Performance Evaluation Based on Frequency Dependent Area Differences of Kinematic Analyses for Soil Columns A	82
3.4-5	Performance Evaluation Based on Frequency Dependent Area Differences of Kinematic Analyses for Soil Columns B	83
3.4-6	Performance Evaluation Based on Frequency Dependent Area Differences of Kinematic Analyses for Soil Columns C	83
3.4-7	Performance Evaluation Based on Frequency Dependent Area Differences of SSI Analyses for Soil Columns A	84
3.4-8	Performance Evaluation Based on Frequency Dependent Area Differences of SSI Analyses for Soil Columns B	84
3.4-9	Performance Evaluation Based on Frequency Dependent Area Differences of SSI Analyses for Soil Columns C	85
3.4-10	Comparison of Response Spectra for Soil Column A at the Roof Center of SSI Model with 11.5m Embedment. Reduced Damping.....	85
3.4-11	Comparison of Response Spectra for Soil Column C at the Roof Center of SSI Model with 11.5m Embedment. Reduced Damping.....	86
4.1.2-1	LS-DYNA Model for the 11.5 m Embedment.	123
4.1.2-2	Zoom-in View of the Structure and Surrounding Soil in LS-DYNA Model for the 11.5 m Embedment.....	123
4.1.2-3	LS-DYNA Model for the 23 m Embedment.	124
4.1.2-4	Zoom-in View of the Structure and Surrounding Soil in LS-DYNA Model for the 23 m Embedment.	124
4.1.2-5	LS-DYNA Model for the 34.5 m Embedment.	125
4.1.2-6	Zoom-in View of the Structure and Surrounding Soil in LS-DYNA Model for the 34.5 m Embedment.....	125
4.1.2-7	LS-DYNA Model for the 46 m Embedment.	126
4.1.2-8	Zoom-in View of the Structure and Surrounding Soil in LS-DYNA Model for the 46 m Embedment.	126
4.2.1-1	Normal Pressure on the Head-on Soil Element near the Ground Surface Computed from the 11.5 m DOB SASSI Model.....	127
4.2.1-2	Circumferential Distribution of Normal Pressure Computed from the 11.5 m DOB SASSI Model.	127
4.2.1-3	Circumferential Distribution of Tangential Shears Computed from the 11.5 m DOB SASSI Model.	128
4.2.1-4	Circumferential Distribution of Vertical Shears Computed from the 11.5 m DOB SASSI Model.	128
4.2.1-5	Vertical Distributions of Soil Pressure Computed from the 11.5 m DOB SASSI Model.	129
4.2.1-6	Lateral Wall Displacements Computed from the 11.5 m DOB SASSI Model.	130
4.2.1-7	Lateral Wall Shear Displacements Computed from the 11.5 m DOB SASSI Model.....	130
4.2.1-8	Structural Acceleration at 8.99 Seconds Computed from the 11.5 m DOB SASSI Model.	131
4.2.1-9	Variation of Shear over DOB at 8.99 Seconds Computed from the 11.5 m DOB SASSI Model.	131
4.2.1-10	Variation of Moment over DOB at 8.99 Seconds Computed from the 11.5 m DOB SASSI Model	132

4.2.2-1	Normal Pressure on the Head-on Soil Element near the Mid-height of Structural Wall Computed from the 23 m DOB SASSI Model.....	132
4.2.2-2	Vertical Distribution of Soil pressure Computed from the 23 m DOB SASSI Model.	133
4.2.2-3	Lateral Wall Displacements Computed from the 23 m DOB SASSI Model.	134
4.2.2-4	Lateral Wall Shear Displacements Computed from the 23 m DOB SASSI Model.....	134
4.2.2-5	Structural Acceleration at 10.85 Seconds Computed from the 23 m DOB SASSI Model.	135
4.2.2-6	Variation of Shear over DOB at 10.85 Seconds Computed from the 23 m DOB SASSI Model.	135
4.2.2-7	Variation of Moment over DOB at 10.85 Seconds Computed from the 23 m DOB SASSI Model.	136
4.2.3-1	Normal Pressure on the Head-on Soil Element near the Mid-height of Structural Wall Computed from the 34.5 m DOB SASSI Model.	136
4.2.3-2	Vertical Distribution of Soil pressure Computed from the 34.5 m DOB SASSI Model.	137
4.2.3-3	Lateral Wall Displacements Computed from the 34.5 m DOB SASSI Model.....	138
4.2.3-4	Lateral Wall Shear Displacements Computed from the 34.5 m DOB SASSI Model.....	138
4.2.3-5	Structural Acceleration at 10.845 Seconds Computed from the 34.5 m DOB SASSI Model.	139
4.2.3-6	Variation of Shear over DOB at 10.845 Seconds Computed from the 34.5 m DOB SASSI Model.....	139
4.2.3-7	Variation of Moment over DOB at 10.845 Seconds Computed from the 34.5 m DOB SASSI Model.	140
4.2.4-1	Normal Pressure on the Head-on Soil Element near the Mid-height of Structural Wall Computed from the 46 m DOB SASSI Model.	141
4.2.4-2	Circumferential Distribution of Normal Pressure Computed from the 46 m DOB SASSI Model.	141
4.2.4-3	Circumferential Distribution of Tangential Shear Computed from the 46 m DOB SASSI Model.....	142
4.2.4-4	Circumferential Distribution of Vertical Shear Computed from the 46 m DOB SASSI Model.	142
4.2.4-5	Vertical Distribution of Soil pressure Computed from the 46 m DOB SASSI Model.	143
4.2.4-6	Lateral Wall Displacements Computed from the 46 m DOB SASSI Model.	144
4.2.4-7	Lateral Wall Shear Displacements Computed from the 46 m DOB SASSI Model.....	144
4.2.4-8	Structural Acceleration at 11.005 Seconds Computed from the 46 m DOB SASSI Model.	145
4.2.4-9	Variation of Shear over DOB at 11.005 Seconds Computed from the 46 m DOB SASSI Model.	145

4.2.4-10	Variation of Moment over DOB at 11.005 Seconds Computed from the 46 m DOB SASSI Model.	146
4.2.5-1	Comparison of Vertical Distributions of Normal Pressure Computed from the SASSI Models.	147
4.2.5-2	Comparison of Vertical Distributions of Tangential Shears Computed from the SASSI Models.	148
4.2.5-3	Comparison of Vertical Distributions of Vertical Shears Computed from the SASSI Models.	149
4.3.1-1	LS-DYNA Free Field Model.	150
4.3.1-2	Comparison of Free Field Surface Spectra.	150
4.3.2-1	Nodes of Soil Elements on the Interface for the 11.5 m LS-DYNA Model. ...	151
4.3.2-2	Nodes of the Structure on the Interface for the 11.5 m LS-DYNA Model. ...	151
4.3.2-3	Soil Elements on the Interface for the 11.5 m LS-DYNA Model.	152
4.3.2-4	Comparison of Response Spectra at the Base for 11.5 m Embedment.	152
4.3.2-5	Comparison of Response Spectra at the Roof for the 11.5 m Embedment. ...	153
4.3.2-6	Soil Pressure in the Head-on Soil Element near the Ground Surface for the 11.5 m Embedment.	153
4.3.2-7	Soil Pressure in the Head-on Soil Element near the Mid-Height of Structure Wall for the 11.5 m Embedment.	154
4.3.2-8	Circumferential Distribution of Vertical Shear Computed from Tied LS-DYNA Model without Gravity Load for the 11.5 m Embedment at 9 Seconds.	154
4.3.2-9	Circumferential Distribution of Tangential Shear Computed from Tied LS-DYNA Model without Gravity Load for the 11.5 m Embedment at 9 Seconds.	155
4.3.2-10	Circumferential Distribution of Normal Pressure Computed from Tied LS-DYNA Model without Gravity Load for the 11.5 m Embedment at 9 Seconds.	155
4.3.2-11	Vertical Distribution of Head-on Soil Stresses Computed from Tied LS-DYNA Model without Gravity Load for the 11.5 m Embedment at 9 Seconds.	156
4.3.2-12	Lateral Embedded Wall Displacements Computed from Tied LS-DYNA Model without Gravity Load for the 11.5 m Embedment at 9 Seconds.	157
4.3.2-13	Lateral Wall Shear Displacements Computed from Tied LS-DYNA Model without Gravity Load for the 11.5 m Embedment at 9 Seconds.	158
4.3.2-14	Fourier Spectra of Soil Pressure Computed at the Head-on Soil Element near Mid-Height Embedded Wall for 11.5 m DOB LD-DYNA model.	158
4.3.3-1	Nodes of Soil Elements on the Interface for the 23 m LS-DYNA Model.	159
4.3.3-2	Nodes of the Structure on the Interface for the 23 m LS-DYNA Model.	159
4.3.3-3	Soil Elements on the Interface for the 23 m LS-DYNA Model.	160
4.3.3-4	Comparison of Response Spectra at the Base for 23 m Embedment.	160
4.3.3-5	Comparison of Response Spectra at the Roof for the 23 m Embedment.	161
4.3.3-6	Normal Pressure in the Head-on Soil Element near the Ground Surface for the 23 m Embedment.	161
4.3.3-7	Normal Pressure in the Head-on Soil Element near the Mid-Height of Structure Wall for the 23 m Embedment.	162
4.3.3-8	Circumferential Distribution of Vertical Shear Computed from Tied LS-DYNA Model without Gravity Load for the 23 m Embedment at 12.6 Seconds.	162

4.3.3-9	Circumferential Distribution of Tangential Shear Computed from Tied LS-DYNA Model without Gravity Load for the 23 m Embedment at 12.6 Seconds	163
4.3.3-10	Circumferential Distribution of Normal Pressure Computed from Tied LS-DYNA Model without Gravity Load for the 23 m Embedment at 12.6 Seconds.....	163
4.3.3-11	Vertical Distribution of Head-on Soil Stresses Computed from Tied LS-DYNA Model without Gravity Load for the 23 m Embedment at 11 Seconds.....	164
4.3.3-12	Lateral Embedded Wall Displacements Computed from Tied LS-DYNA Model without Gravity Load for the 23 m Embedment at 11 Seconds.....	165
4.3.3-13	Lateral Wall Shear Displacements Computed from Tied LS-DYNA Model without Gravity Load for the 23 m Embedment at 11 Seconds.	165
4.3.3-14	Fourier Spectra of Soil Pressure Computed at the Head-on Soil Element near Mid-Height Embedded Wall for 23 m DOB LD-DYNA model.	166
4.3.4-1	Nodes of Soil Elements on the Interface for the 34.5 m LS-DYNA Model..	166
4.3.4-2	Nodes of the Structure on the Interface for the 34.5 m LS-DYNA Model. ...	167
4.3.4-3	Soil Elements on the Interface for the 34.5 m LS-DYNA Model.	167
4.3.4-4	Comparison of Response Spectra at the Base for 34.5 m Embedment.	168
4.3.4-5	Comparison of Response Spectra at the Roof for the 34.5 m Embedment. ...	168
4.3.4-6	Soil Pressure in the Head-on Soil Element near the Ground Surface for the 34.5 m Embedment.	169
4.3.4-7	Soil Pressure in the Head-on Soil Element near the Mid-Height of Structure Wall for the 34.5 m Embedment.....	169
4.3.4-8	Circumferential Distribution of Vertical Shear Computed from Tied LS-DYNA Model without Gravity Load for the 34.5 m Embedment at 10.86 Seconds.....	170
4.3.4-9	Circumferential Distribution of Tangential Shear Computed from Tied LS-DYNA Model without Gravity Load for the 34.5 m Embedment at 10.86 Seconds.....	170
4.3.4-10	Circumferential Distribution of Normal Pressure Computed from Tied LS-DYNA Model without Gravity Load for the 34.5 m Embedment at 10.86 Seconds.....	171
4.3.4-11	Vertical Distribution of Head-on Soil Stresses Computed from Tied LS-DYNA Model without Gravity Load for the 34.5 m Embedment at 7.11 Seconds.....	172
4.3.4-12	Lateral Embedded Wall Displacements Computed from Tied LS-DYNA Model without Gravity Load for the 34.5 m Embedment at 12.03 Seconds.	173
4.3.4-13	Lateral Wall Shear Displacements Computed from Tied LS-DYNA Model without Gravity Load for the 34.5 m Embedment at 12.03 Seconds.	173
4.3.4-14	Fourier Spectra of Soil Pressure Computed at the Head-on Soil Element near Mid-Height Embedded Wall for 34.5 m DOB LD-DYNA model.	174
4.3.5-1	Nodes of Soil Elements on the Interface for the 46 m LS-DYNA Model.....	174
4.3.5-2	Nodes of the Structure on the Interface for the 46 m LS-DYNA Model.	175
4.3.5-3	Soil Elements on the Interface for the 46 m LS-DYNA Model.	175
4.3.5-4	Comparison of Response Spectra at the Base for 46 m Embedment.	176
4.3.5-5	Comparison of Response Spectra at the Roof for the 46 m Embedment.	176
4.3.5-6	Normal Pressure in the Head-on Soil Element near the Ground Surface for the 46 m Embedment.	177
4.3.5-7	Normal Pressure in the Head-on Soil Element near the Mid-Height of Structure Wall for the 46 m Embedment.....	177

4.3.5-8	Circumferential Distribution of Vertical Shear at 10.3702 sec When Head-on Mid-Height S_{rr} Reaches Peak for Tied LS-DYNA Model Without Gravity Load for the 46 m Embedment.....	178
4.3.5-9	Circumferential Distribution of Tangential Shear at 10.3702 sec When Head-on Mid-Height S_{rr} Reaches Peak for Tied LS-DYNA Model without Gravity Load for the 46 m Embedment.	178
4.3.5-10	Circumferential Distribution of Normal Pressure at 10.3702 sec When Head-on Mid-Height S_{rr} Reaches Peak for Tied LS-DYNA Model without Gravity Load for the 46 m Embedment.	179
4.3.5-11	Vertical Distribution of Pressures When Head-on Surface S_{rr} Reaches Peak for Tied LS-DYNA Model without Gravity Load for the 46 m Embedment.....	180
4.3.5-12	Lateral Embedded Wall Displacements Computed from Tied LS-DYNA Model without Gravity Load for the 46 m Embedment.	181
4.3.5-13	Lateral Wall Shear Displacements Computed from Tied LS-DYNA Model without Gravity Load for the 46 m Embedment.	181
4.3.5-14	Fourier Spectra of Soil Pressure Computed at the Head-on Soil Element near Mid-Height Embedded Wall for the 46 m DOB LD-DYNA model.	182
4.3.6-1	Comparison of Vertical Distributions of Normal Pressures Computed from Tied LS-DYNA Model for Various DOBs at Their Respective Surface Peak Times.	183
4.3.6-2	Comparison of Vertical Distributions of Tangential Shears Computed from Tied LS-DYNA Model for Various DOBs at Their Respective Surface Peak Times.	184
4.3.6-3	Comparison of Vertical Distributions of Vertical Shears Computed from Tied LS-DYNA Model for Various DOBs at Their Respective Surface Peak Times.	185
4.4.1-1	Relative Lateral Displacement of Structural Wall and Surrounding Soil at the Interface near ground Surface ($\theta=0$) from the 11.5 m DOB Contact Interface Model.	186
4.4.1-2	Vertical Distribution of Lateral Displacements of Structural Wall and Surrounding Soil at the Interface ($\theta=0$) from the 11.5 m DOB Contact Interface Model at 10.56 Seconds.....	186
4.4.1-3	Comparison of Lateral Wall Shear Displacements Computed from the 11.5 m DOB Contact and Tied Interface Models at 10.56 Seconds.....	187
4.4.1-4	Vertical Displacements of Structural Foundation Relative to the Base Soil Computed from the 11.5 m DOB Contact Interface Model at $\theta = 0$	187
4.4.1-5	Vertical Displacements of Structural Foundation Relative to the Base Soil Computed from the 11.5 m DOB Contact Interface Model at $\theta = 180$. .	188
4.4.1-6	Comparison of Response Spectra at the Base for the 11.5 m DOB with various LS-DYNA models.	188
4.4.1-7	Comparison of Response Spectra at the Roof for the 11.5 m DOB with various LS-DYNA models.	189
4.4.1-8	Comparison of Normal Pressure on the Head-on Soil Element near the Ground Surface Computed from the 11.5 m DOB Contact and Tied Interface Models.	189
4.4.1-9	Comparison of Normal Pressure on the Head-on Soil Element near the Mid-height of Structural Wall Computed from the 11.5 m DOB Contact and Tied Interface Models.....	190

4.4.1-10	Comparison of Circumferential Distributions of Vertical Shear Computed from the 11.5 m DOB Contact and Tied Interface Models at Respective Mid-Height Peak S_{rr} Times.	190
4.4.1-11	Comparison of Circumferential Distributions of Normal Pressures Computed from the 11.5 m DOB Contact and Tied Interface Models at Respective Mid-Height Peak S_{rr} Times.	191
4.4.1-12	Comparison of Circumferential Distributions of Tangential Shear Pressures Computed from the 11.5 m DOB Contact and Tied Interface Models at Respective Mid-Height Peak S_{rr} Times.	191
4.4.1-13	Comparison of Vertical Distributions of Normal Pressures Computed from the 11.5 m DOB Contact and Tied Interface Models at Respective Surface Peak S_{rr} Times.	192
4.4.1-14	Comparison of Vertical Distributions of Tangential Shear Computed from the 11.5 m DOB Contact and Tied Interface Models at Respective Surface Peak S_{rr} Times.	193
4.4.1-15	Comparison of Vertical Distributions of Vertical Shear Computed from the 11.5 m DOB Contact and Tied Interface Models at Respective Surface Peak S_{rr} Times.	194
4.4.1-16	Vertical Distributions of Soil Stresses Computed from the 11.5 m DOB Tied Interface Model at Surface Peak S_{rr} Times.	195
4.4.1-17	Vertical Distributions of Soil Stresses Computed from the 11.5 m DOB Contact Interface Model at Surface Peak S_{rr} Times.	196
4.4.2-1	Relative Lateral Displacement of Structural Wall and Surrounding Soil at the Interface near ground Surface ($\theta=0$) from the 23 m DOB Contact Interface Model.	197
4.4.2-2	Vertical Distribution of Lateral Displacements of Structural Wall and Surrounding Soil at the Interface ($\theta=0$) from the 23 m DOB Contact Interface Model at 11.03 Seconds.	197
4.4.2-3	Comparison of Lateral Wall Shear Displacements Computed from the 23 m DOB Contact and Tied Interface Models at 11.03 Seconds.	198
4.4.2-4	Vertical Displacements of Structural Foundation Relative to the Base Soil Computed from the 23 m DOB Contact Interface Model at $\theta = 0$	198
4.4.2-5	Vertical Displacements of Structural Foundation Relative to the Base Soil Computed from the 23 m DOB Contact Interface Model at $\theta = 180$	199
4.4.2-6	Comparison of Response Spectra at the Base for the 23 m DOB with various LS-DYNA models.	199
4.4.2-7	Comparison of Response Spectra at the Roof for the 23 m DOB with various LS-DYNA models.	200
4.4.2-8	Comparison of Normal Pressure on the Head-on Soil Element near the Ground Surface Computed from the 23 m DOB Contact and Tied Interface Models.	200
4.4.2-9	Comparison of Normal Pressure on the Head-on Soil Element near the Mid-height of Structural Wall Computed from the 23 m DOB Contact and Tied Interface Models.	201
4.4.2-10	Comparison of Circumferential Distributions of Vertical Shear Computed from the 23 m DOB Contact and Tied Interface Models at Respective Mid-Height Peak S_{rr} Times.	201
4.4.2-11	Comparison of Circumferential Distributions of Normal Pressures Computed from the 23 m DOB Contact and Tied Interface Models at Respective Mid-Height Peak S_{rr} Times.	202

4.4.2-12	Comparison of Circumferential Distributions of Tangential Shear Computed from the 23 m DOB Contact and Tied Interface Models at Respective Mid-Height Peak S_{rr} Times.	202
4.4.2-13	Comparison of Vertical Distributions of Normal Pressures Computed from the 23 m DOB Contact and Tied Interface Models at Respective Surface Peak S_{rr} Times	203
4.4.2-14	Comparison of Vertical Distributions of Tangential Shear Computed from the 23 m DOB Contact and Tied Interface Models at Respective Surface Peak S_{rr} Times.....	204
4.4.2-15	Comparison of Vertical Distributions of Vertical Shear Computed from the 23 m DOB Contact and Tied Interface Models at Respective Surface Peak S_{rr} Times.	205
4.4.2-16	Vertical Distributions of Soil Stress Computed from the 23 m DOB Tied Interface Model at Surface Peak S_{rr} Time.	206
4.4.2-17	Vertical Distributions of Soil Stresses Computed from the 23 m DOB Contact Interface Models at Surface Peak S_{rr} Time.	207
4.4.3-1	Relative Lateral Displacement of Structural Wall and Surrounding Soil at the Interface near ground Surface ($\theta=0$) from the 34.5 m DOB Contact Interface Model.	208
4.4.3-2	Vertical Distribution of Lateral Displacements of Structural Wall and Surrounding Soil at the Interface ($\theta=0$) from the 34.5 m DOB Contact Interface Model at 11 Seconds.....	208
4.4.3-3	Comparison of Lateral Wall Shear Displacements Computed from the 34.5 m DOB Contact and Tied Interface Models at 11 Seconds.....	209
4.4.3-4	Vertical Displacements of Structural Foundation Relative to the Base Soil Computed from the 34.5 m DOB Contact Interface Model at $\theta = 0$	209
4.4.3-5	Vertical Displacements of Structural Foundation Relative to the Base Soil Computed from the 34.5 m DOB Contact Interface Model at $\theta = 180$. .	210
4.4.3-6	Comparison of Response Spectra at the Base for the 34.5 m DOB with various LS-DYNA models.	210
4.4.3-7	Comparison of Response Spectra at the Roof for the 34.5 m DOB Computed with various LS-DYNA models.	211
4.4.3-8	Comparison of Normal Pressure on the Head-on Soil Element near the Ground Surface Computed from the 23 m DOB Contact and Tied Interface Models.....	211
4.4.3-9	Comparison of Normal Pressure on the Head-on Soil Element near the Mid-height of Structural Wall Computed from the 34.5 m DOB Contact and Tied Interface Models.....	212
4.4.3-10	Comparison of Circumferential Distributions of Vertical Shear Computed from the 34.5 m DOB Contact and Tied Interface Models at Respective Mid-Height Peak S_{rr} Times.	212
4.4.3-11	Comparison of Circumferential Distributions of Normal Pressures Computed from the 34.5 m DOB Contact and Tied Interface Models at Respective Mid-Height Peak S_{rr} Times.	213
4.4.3-12	Comparison of Circumferential Distributions of Tangential Shear Computed from the 34.5 m DOB Contact and Tied Interface Models at Respective Mid-Height Peak S_{rr} Times.	213
4.4.3-13	Comparison of Vertical Distributions of Normal Pressures Computed from the 34.5 m DOB Contact and Tied Interface Models at Respective Surface Peak S_{rr} Times.	214

4.4.3-14	Comparison of Vertical Distributions of Tangential Shear Computed from the 34.5 m DOB Contact and Tied Interface Models at Respective Surface Peak S_{rr} Times.....	215
4.4.3-15	Comparison of Vertical Distributions of Vertical Shear Computed from the 34.5 m DOB Contact and Tied Interface Models at Respective Surface Peak S_{rr} Times.....	216
4.4.3-16	Vertical Distributions of Soil Stress Computed from the 34.5 m DOB Tied Interface Model at Surface Peak S_{rr} Time.....	217
4.4.3-17	Vertical Distributions of Soil Stresses Computed from the 34.5 m DOB Contact Interface Model at Surface Peak S_{rr} Time.....	218
4.4.4-1	Relative Lateral Displacement of Structural Wall and Surrounding Soil at the Interface near ground Surface ($\theta=0$) from the 46 m DOB Contact Interface Model.....	219
4.4.4-2	Vertical Distribution of Lateral Displacements of Structural Wall and Surrounding Soil at the Interface ($\theta=0$) from the 46 m DOB Contact Interface Model.....	219
4.4.4-3	Comparison of Lateral Wall Shear Displacements Computed from the 46 m DOB Contact and Tied Interface Models.....	220
4.4.4-4	Vertical Displacements of Structural Foundation Relative to the Base Soil Computed from the 46 m DOB Contact Interface Model at $\theta = 0$	220
4.4.4-5	Vertical Displacements of Structural Foundation Relative to the Base Soil Computed from the 46 m DOB Contact Interface Model at $\theta = 180$	221
4.4.4-6	Comparison of Response Spectra at the Base for the 46 m DOB.....	221
4.4.4-7	Comparison of Response Spectra at the Roof for the 46 m DOB.....	222
4.4.4-8	Comparison of Normal Pressure on the Head-on Soil Element near the Ground Surface Computed from the 46 m DOB Contact and Tied Interface Models.....	222
4.4.4-9	Comparison of Normal Pressure on the Head-on Soil Element near the Mid-height of Structural Wall Computed from the 46 m DOB Contact and Tied Interface Models.....	223
4.4.4-10	Comparison of Circumferential Distributions of Vertical Shear Computed from the 46 m DOB Contact and Tied Interface Models at Respective Mid-Height Peak S_{rr} Times.....	223
4.4.4-11	Comparison of Circumferential Distributions of Normal Pressures Computed from the 46 m DOB Contact and Tied Interface Models at Respective Mid-Height Peak S_{rr} Times.....	224
4.4.4-12	Comparison of Circumferential Distributions of Tangential Shear Computed from the 46 m DOB Contact and Tied Interface Models at Respective Mid-Height Peak S_{rr} Times.....	224
4.4.4-13	Comparison of Vertical Distributions of Normal Pressures Computed from the 46 m DOB Contact and Tied Interface Models at Respective Surface Peak S_{rr} Times.....	225
4.4.4-14	Comparison of Vertical Distributions of Tangential Shear Computed from the 46 m DOB Contact and Tied Interface Models at Respective Surface Peak S_{rr} Times.....	226
4.4.4-15	Comparison of Vertical Distributions of Vertical Shear Computed from the 46 m DOB Contact and Tied Interface Models at Respective Surface Peak S_{rr} Times.....	227

4.4.4-16	Comparison of Vertical Distributions of Soil Stresses Computed from the 46 m Tied Interface Models at Surface Peak S_{tr} Times.....	228
4.4.4-17	Comparison of Vertical Distributions of Soil Stresses Computed from the 46 m DOB Contact Interface Model at Surface Peak S_{tr} Time.	229
4.4.5-1	Smoothed Fourier Spectra of Soil Pressure in the Head-on Soil Element near the Mid-Height Wall Section for DOB = 11.5 m.	230
4.4.5-2	Smoothed Fourier Spectra of Soil Pressure in the Head-on Soil Element near the Mid-Height Wall Section for DOB = 23 m.	230
4.4.5-3	Smoothed Fourier Spectra of Soil Pressure in the Head-on Soil Element near the Mid-Height Wall Section for DOB = 34.5 m.	231
4.4.5-4	Smoothed Fourier Spectra of Soil Pressure in the Head-on Soil Element near the Mid-Height Wall Section for DOB = 46 m.	231
4.4.5-5	Smoothed Fourier Spectra of Von-Mises Effective Stress in the Head-on Structural Shell Element near the Ground Surface for DOB = 11.5 m.	232
4.4.5-6	Smoothed Fourier Spectra of Von-Mises Effective Stress in the 5 th Head-on Structural Shell Element from the Base for DOB = 23 m.	232
4.4.5-7	Smoothed Fourier Spectra of Von-Mises Effective Stress in the 5 th Head-on Structural Shell Element from the Base for DOB = 34.5 m.	233
4.4.5-8	Smoothed Fourier Spectra of Von-Mises Effective Stress in the 5 th Head-on Structural Shell Element from the Base for DOB = 46 m.	233
4.4.6-1	Normal Pressure (+Comp) for the 23 m DOB SASSI Model at Depth = 1 m.....	234
4.4.6-2	Normal Pressure (+Comp) for the 23 m DOB SASSI Model at Depth = 5 m.....	234
4.4.6-3	Normal Pressure (+Comp) for the 23 m DOB SASSI Model at Depth = 11 m.....	235
4.4.6-4	Head-on Friction Coefficient for the 23 m DOB SASSI Model at Depth = 1 m.....	235
4.4.6-5	Head-on Friction Coefficient for the 23 m DOB SASSI Model at Depth = 5 m.....	236
4.4.6-6	Head-on Friction Coefficient for the 23 m DOB SASSI Model at Depth = 11 m.....	236
4.4.6-7	Side-on Friction Coefficient for the 23 m DOB SASSI Model at Depth = 1 m.....	237
4.4.6-8	Side-on Friction Coefficient for the 23 m DOB SASSI Model at Depth = 5 m.....	237
4.4.6-9	Side-on Friction Coefficient for the 23 m DOB SASSI Model at Depth = 11 m.....	238
4.5-1	Relative Lateral Displacement of Structural Wall and Surrounding Soil at the Interface near ground Surface ($\theta=0$) from the 23 m DOB Contact Interface Model using Coulomb Soil.....	238
4.5-2	Vertical Distribution of Lateral Displacement of Structural Wall and Surrounding Soil at the Interface near ground Surface ($\theta=0$) from the 23 m DOB Contact Interface Model using Coulomb Soil at 7.95 Seconds.....	239
4.5-3	Vertical Displacement of Structural Foundation Relative to Base Soil Computed from the 23 m DOB Contact Interface Model using Coulomb Soil at $\theta = 0$	239
4.5-4	Vertical Displacement of Structural Foundation Relative to Base Soil Computed from the 23 m DOB Contact Interface Model using Coulomb Soil at $\theta = 180$	240

4.5-5	Effect of Soil Material Models on the Contact Interface LS-DYNA Response Spectra (5% Damping) at Structural Base with Butterworth Low-Pass High Cut Filter ($f_{\text{cutoff}} = 20$ Hz).	240
4.5-6	Effect of Soil Material Models on the Contact Interface LS-DYNA Response Spectra (5% Damping) at Structural Roof.	241
4.5-7	Effect of Soil Material Models on the Tied Interface LS-DYNA Response Spectra (5% Damping) at Structural Base with Butterworth Low-Pass High Cut Filter ($f_{\text{cutoff}} = 20$ Hz).	241
4.5-8	Effect of Soil Material Models on the Tied Interface LS-DYNA Response Spectra (5% Damping) at Structural Roof.	242
4.5-9	Effect of Soil Material Models on Normal Pressure in the Head-on Soil Element near Ground Surface Computed from 23 m DOB Contact Interface Model	242
4.5-10	Effect of Soil Material Models on Normal Pressure in the Head-on Soil Element near Mid-Wall Height Computed from 23 m DOB Contact Interface Model	243
4.5-11	Effect of Soil Material Models on Normal Pressure in the Head-on Soil Element near Ground Surface Computed from 23 m DOB Tied Interface Model.	243
4.5-12	Effect of Soil Material Models on Normal Pressure in the Head-on Soil Element near Mid-Wall Height Computed from 23 m DOB Tied Interface Model	244
4.5-13	Fourier Spectra of Normal Pressure in the Head-on Soil Element near Mid-Wall Height Computed from 23 m DOB Contact Interface Model.	244
4.5-14	Fourier Spectra of Normal Pressure in the Head-on Soil Element near Mid-Wall Height Computed from 23 m DOB Tied Interface Model.....	245
4.5-15	Effect of Soil Material Models on Circumferential Distribution of Normal Pressure Computed from the 23 m DOB Contact Interface LS-DYNA Model at Respective Mid-Height Peak S_{rr} Times.	245
4.5-16	Effect of Soil Material Models on Circumferential Distribution of Tangential Shear Computed from the 23 m DOB Contact Interface LS-DYNA Model at Respective Mid-Height Peak S_{rr} Times.	246
4.5-17	Effect of Soil Material Models on Circumferential Distribution of Vertical Shear Computed from the 23 m DOB Contact Interface LS-DYNA Model at Respective Mid-Height Peak S_{rr} Times.	246
4.5-18	Effect of Soil Material Models on Circumferential Distribution of Normal Pressure Computed from the 23 m DOB Tied Interface LS-DYNA Model at Respective Mid-Height Peak S_{rr} Times	247
4.5-19	Effect of Soil Material Models on Circumferential Distribution of Vertical Shear Computed from the 23 m DOB Tied Interface LS-DYNA Model at Respective Mid-Height Peak S_{rr} Times.	247
4.5-20	Effect of Soil Material Models on Circumferential Distribution of Tangential Shear Computed from the 23 m DOB Tied Interface LS-DYNA Model at Respective Mid-Height Peak S_{rr} Times.	248
4.5-21	Effect of Soil Material Models on Vertical Distribution of Normal Pressure Computed from the 23 m DOB Contact Interface LS-DYNA Model at Respective Ground Surface Peak S_{rr} Times.....	249
4.5-22	Effect of Soil Material Models on Vertical Distribution of Tangential Shear Computed from the 23 m DOB Contact Interface LS-DYNA Model at Respective Ground Surface Peak S_{rr} Times.	250

4.5-23	Effect of Soil Material Models on Vertical Distribution of Vertical Shear Computed from the 23 m DOB Contact Interface LS-DYNA Model at Respective Ground Surface Peak S_{rr} Times.	251
4.5-24	Effect of Soil Material Models on Vertical Distribution of Normal Pressure Computed from the 23 m DOB Tied Interface LS-DYNA Model at Respective Ground Surface Peak S_{rr} Times.	252
4.5-25	Effect of Soil Material Models on Vertical Distribution of Tangential Shear Computed from the 23 m DOB Tied Interface LS-DYNA Model at Respective Ground Surface Peak S_{rr} Times.	253
4.5-26	Effect of Soil Material Models on Vertical Distribution of Vertical Shear Computed from the 23 m DOB Tied Interface LS-DYNA Model at Respective Ground Surface Peak S_{rr} Times.	254
4.5-27	Vertical Distribution of Soil Stresses in the Head-on Soil Element near Ground Surface Computed using Elastic Soil Model from the 23 m DOB Contact Interface LS-DYNA Model at Respective Ground Surface Peak S_{rr} Times.	255
4.5-28	Vertical Distribution of Soil Stresses in the Head-on Soil Element near Ground Surface Computed using Coulomb Soil Model from the 23 m DOB Contact Interface LS-DYNA Model at Respective Ground Surface Peak S_{rr} Times.	256
4.5-29	Vertical Distribution of Soil Stresses in the Head-on Soil Element near Ground Surface Computed using Coulomb Soil Model from the 23 m DOB Tied Interface LS-DYNA Model at Respective Ground Surface Peak S_{rr} Times.	257
4.5-30	Vertical Distribution of Soil Stresses in the Head-on Soil Element near Ground Surface Computed using Elastic Soil Model from the 23 m DOB Tied Interface LS-DYNA Model at Respective Ground Surface Peak S_{rr} Times.	258
4.5-31	Fourier Spectra of Von-Mises Effective Stress in the 5 th Head-on Structural Wall Shell Element Computed from 23 m DOB Contact Interface Model.	259
4.5-32	Fourier Spectra of Von-Mises Effective Stress in the 5 th Head-on Structural Wall Shell Element Computed from 23 m DOB Tied Interface Model.	259
5.2-1	Sketch of Cylindrical Benchmark Model.	263
5.2-2	Sketch of Square Benchmark Model.	264

EXECUTIVE SUMMARY

The Office of Nuclear Regulatory Research (RES), which has broad responsibilities to plan and direct research programs and standards development for nuclear safety in the design, qualification, construction, inspection, and testing of current and advanced nuclear reactors, is sponsoring a research program to develop a technical basis to support the safety evaluation of deeply embedded and/or buried (DEB) structures proposed for advanced reactor designs. For two of the new reactor designs submitted to the NRC for preliminary review [NRC RES, 2002, General Atomics, 1996], the entire reactor building and a significant portion of the steam generator building are either partially or completely embedded below grade. Therefore, it is important from a regulatory standpoint that, practical aspects of existing methods and computer programs need to be evaluated to determine their applicability and adequacy in capturing the seismic behavior of DEB nuclear power plant (NPP) structures. Brookhaven National Laboratory (BNL) under JCN Y-6718 is performing this research program. The overall objective of this research is to investigate the applicability of existing seismic design practice and SSI computer codes to DEB structures and to make recommendations for any modifications, if necessary.

Specifically, in this program, a study is performed to investigate the extent to which existing standards, tests, and practices have been applied to the seismic design and analysis of DEB structures and to identify important issues which may potentially impact the seismic response of DEB structures. Effort is then made in this program to both qualitatively and quantitatively evaluate the impact of the identified issues on various analytical methods commonly utilized in practice for the seismic response analysis and design of NPP structures.

This report consists of four major elements: 1) Review and evaluation of existing seismic design practice, 2) Assessment of simplified vs. detailed methodologies for SSI in-structure response spectrum analysis of DEB structures, 3) Assessment of methodologies for computing seismic induced earth pressures on DEB structures, and 4) Development of the criteria for benchmark problems which could be used for validating computer programs for computing seismic responses of DEB NPP structures.

Several specific areas where uncertainty may have a potential impact on the analytical methods for the seismic response of deeply embedded facilities are identified and are discussed in the report. The major uncertainties found are: 1) the effect of deep embedment on the relative significance of kinematic interaction; 2) the extent to which non vertically propagating shear waves may be more important for deeply embedded structures than for those with shallow embedment depth; 3) the impact of deep embedment on the accuracy of side wall impedance functions calculated with standard methods; 4) the effect of nonlinear effects (separation of wall and soil, and soil material properties) on wall pressure calculations.

The term kinematic interaction refers to the modification of the free-field seismic waves by the geometry of the embedded portion of a structure and therefore is independent of the inertial properties of the structure. The term inertial interaction is associated with the dynamic response of the coupled structure-foundation system, which is governed by the inertial properties of the structure and foundation impedance functions.

The above uncertainties provide the bases for the subjects of the study that is summarized in Sections 3 and 4 of this report. In Section 3, a containment structure for the conceptual design of a typical advanced reactor was considered. The "Computer Analyses for Rapid Evaluation of Structures" (CARES) and "A System for the Analysis of Soil-Structure Interaction" SASSI programs were used which are representative of simplified and detailed analysis methods,

respectively. Analyses were performed using both codes on the containment structure with various embedment conditions (25%, 50%, 75% and 100% of the structural height) to address the embedment effect on SSI characteristics (both kinematic and inertial interaction) and the non-vertical wave propagation problem, as well as the methodologies to address them in terms of in-structure response spectrum calculations. Comparisons of basemat and roof response spectra are made to evaluate differences between the simplified and detailed analytical methods. Solutions are computed for three soil columns: a soft uniform column, a hard uniform column, and a variable stiffness column typical of a granular material. Based on the analyses performed for three soil profiles, both kinematic interaction and SSI analyses were performed for assessing the performance of simplified vs. detailed methods for computing in-structure response spectra.

Two performance rating indexes were defined to evaluate relative performance of the simplified vs. detailed analysis methods. One index uses relative peak spectral acceleration and the other utilizes the frequency dependent relative spectral area differences. Both indexes were computed for the kinematic and SSI analyses results, and it is concluded that: 1) when the peak rating indexes are used and assuming that a 10 % under prediction is considered to be acceptable, the CARES kinematic interaction results are acceptable for embedment to radius (E/R) ratios less than 2 and 3.5 for the soft and hard uniform soil columns, respectively. When SSI spectra are considered, the CARES results are never acceptable for the soft uniform soil column and are acceptable for E/R less than 2 for the hard uniform soil column. For the indexes with the variable soil column, CARES results are acceptable for E/R less than 2.5 for the kinematic spectra and for E/R less than 1.3 for the SSI spectra; 2) when the rating indexes based on spectral areas are used, assuming again that the 10% difference is used as acceptance criteria, the CARES results are: not acceptable for the soft uniform soil column, acceptable for E/R less than 2.1 for the hard uniform column, and acceptable for E/R less than 2.2 for the variable soil column.

The assessment of methodologies for computing seismic induced earth pressures on DEB structures is conducted using the SASSI and LS-DYNA codes. Due to the phenomenological change of SSI from primarily an inertial interaction effect for shallow embedded structures to predominantly a kinematic interaction effect for DEB structures, seismic induced wall pressures and their effects on the stresses induced in the embedded walls may become embedment dependent. In Section 4, the SASSI and LS-DYNA programs are first used for an assessment of the linear methodologies to investigate various important embedment effects on seismic induced pressures. The linear analysis results have indicated that although the LS-DYNA and SASSI utilize different approaches to SSI, both programs have computed comparable estimates of soil induced wall pressures for the structure with the depths of burial ranging from shallow to fully buried configurations.

In order to develop insights into the interface modeling effect on the seismic response parameters, the analysis results of the LS-DYNA analysis with the contact wall/soil interface model are compared with a similar LS-DYNA analysis with the tied soil/structure interface model.

Based on the comparisons of the analysis results between the tied interface and the contact interface models, which use the linear elastic model for soil, it is concluded that the separation effect at the structural wall and soil interface on the seismic response parameters is important. However, the largest amount of separation of the wall/soil interface is seen for the 11.5m depth of burial (DOB) case (15.4 mm) and is gradually reduced as the DOB increases. The computed shear displacement is several magnitudes smaller than the computed total displacement, which implies that the structure mainly experiences rigid body movement. The shear displacement computed with the contact interface models appear to be reduced compared to that computed with the tied interface models. The structural base experiences up lifting from the supporting soil. However, the

amount of base uplift reduces as DOB increases. For the fully buried configuration, no base uplift was observed. The in-structure response spectra are affected by the separation effect, including both peak amplification and peak shift to lower frequencies compared to the results computed with the tied interface model; the peak shift is more pronounced for shallow DOB cases. Furthermore, the soil/wall separation effect was also confirmed using the SASSI linear analysis for the 23m DOB case (Section 4.4.6). In this case, the SASSI results indicate that separation occurs at the interface between the wall and the soil from the ground surface to 11m in depth.

Based on the results documented in this report, it can be concluded that the linear SSI methodologies, including both simplified and detailed approaches, can be extended to DEB structures and produce acceptable SSI response calculations, provided that the SSI response induced by the ground motion is very much within the linear regime or the non-linear effect is not anticipated to control the SSI response parameters. Since there are as yet no general criteria that enable an analyst to predict a priori when nonlinear effects will become significant for a particular problem, it is recommended that the results of the linear calculations be examined in enough detail to evaluate the potential for such effects. For example, peak stresses and stress ratios (shear/pressure) at critical locations along the building wall-soil interface can be determined from the linear calculation to estimate if separation and/or shear sliding may potentially occur. Similarly, stresses under the toe of the foundation slabs can be examined to estimate if stress ratios are high enough to potentially lead to local failure levels.

For the case of strong ground motions, the non-linear effect is expected to have a strong impact on the SSI response calculations. For DEB structures, this study has shown significant uncertainties exist in the aspects of the interface modeling and soil material modeling. In this case, it was noted that the SSI response calculation is sensitive to the modeling assumptions made for the soil/structure interface and application of a particular material model for the soil. These modeling assumptions can only be validated through correlations with field or laboratory measured seismic response data, which unfortunately are scarce, especially for moderate to strong earthquake events.

Additional strong ground motion response data are needed from tests and/or earthquake recordings to validate the pertinent modeling assumptions made for SSI response analysis of DEB NPP structures. Recognizing that it is difficult to obtain such data, it is recommended that additional analytic studies be performed using the available nonlinear codes to try to determine which parameters of the structure-soil system are controlling SSI responses. For example, for the case of a linear structure and soil system, the parameters controlling separation and sliding along building-soil interfaces can be determined as a function of ground motion level. Once these controlling parameters are determined, the impact of nonlinear soil behavior on these relationships can be evaluated, using constitutive soil models considered appropriate for typical soil types. This process can lead to a scheme that a reviewer can use to ascertain when nonlinear behavior may be important.

ACKNOWLEDGMENTS

This report was prepared as part of a research program sponsored by the Office of Nuclear Regulatory Research of the U.S. Nuclear Regulatory Commission. The authors would like to express their gratitude to Mr. Herman Graves, NRC Project Manager, for the technical and administrative support he has provided in performing this study.

A Peer Review Panel was established to review the work performed at BNL and to provide technical guidance for the program. The members of the Panel consist of: Dr. Syed A. Ali, Mr. Goutam Bagchi, Dr. Farhang Ostadan, and Professor Jose Roesset. The authors would like to express their appreciation for the participation of the Panel members and thank them for their valuable comments on the research and recommendations for the program direction.

A special acknowledgement is made to Dr. Charles A. Miller who, for the past three decades, has made significant contributions to many NRC research programs and in particular this study. Dr. Miller passed away shortly before the completion of this project. Dr. Miller was an exceptional engineer and teacher, with keen insights and engineering capabilities. He will be surely missed by his colleagues from BNL, NRC, and the entire earthquake engineering community at large.

The authors also express special thanks to Ms. Susan Signorelli for her secretarial help in the preparation of this report.

1. INTRODUCTION

1.1 Background

Over the past three decades or so, extensive research has been performed to study the phenomenon of soil-structure interaction (SSI), and its impact on seismic response of structures, especially for nuclear power plant (NPP) structures. To date, considerable advancement has been made in better understanding the interacting mechanisms associated with SSI [Roesset, 1989], developing analysis methodologies and computer programs for seismic response calculations which incorporate SSI effects, and obtaining much needed field test data from real earthquake events. However, established SSI analysis computer codes used in the nuclear industry have been primarily developed for the current generation of Light Water Reactors (LWRs) and applied to coupled soil-structure models where the structures are founded at or near the ground surface with shallow embedment (Note that the criteria contained in Section 3.3.4.2.4 of ASCE 4 suggest that simple formulations may be used to model embedment effect when the depth of embedment is less than 30 percent of the foundation radius).

Influenced by many beneficial considerations such as easy access for refueling, reduction of seismic effects, missile protection and improved site visual activities, several advanced reactor designs have proposed to bury or partially bury reactor structures as one of the major features of their designs [NRC RES, 2002, General Atomics, 1996]. The event of the September 11 malevolent attacks on the World Trade Center should also provide a crucial impetus to addressing potential issues related to the safety and safeguard of nuclear power plant structures against similar assaults in the future. Locating safety related structures, systems and components (SSC) below grade could be an effective option to address these issues. Hence, from the regulatory point of view, potential seismic issues pertaining to deeply embedded and/or buried (DEB) structures should be addressed. Issues relating to kinematic interaction and seismic induced earth pressure effects may be more important for DEB structures during seismic events than for nuclear plants founded at or near the ground surface. Furthermore, the methods and computer programs established primarily for the assessment of SSI effects for the current generation of reactors need to be assessed in the light of the DEB NPP structures to determine their applicability and adequacy in capturing the seismic behavior of this class of structures.

1.2 Scope and Objectives

The Office of Nuclear Regulatory Research (RES), which has broad responsibilities to plan and direct research programs and standards development for nuclear safety in the design, qualification, construction, inspection, and testing of current and advanced nuclear reactors, is sponsoring a research program to develop a technical basis to support the safety evaluation of DEB structures proposed for advanced reactor designs. For two of the new reactor designs submitted to the NRC for preliminary review [NRC RES, 2002, General Atomics, 1996], the entire reactor building and a significant portion of the steam generator building are to be partially or completely embedded below grade. Therefore, it is imperative that from a regulatory standpoint, all practical aspects of existing methods and computer programs need to be evaluated to determine their applicability and adequacy in capturing the seismic behavior of DEB NPP structures. Brookhaven National Laboratory (BNL) under JCN Y-6718 is charged to conduct this research program. The overall objective of this research is to investigate the

applicability of existing seismic design practice and SSI computer codes to DEB structures and to make recommendations for any modifications, if necessary.

Specifically, in this program, a study is performed to investigate the extent to which existing standards, tests, and practices can be applied to the seismic design and analysis of DEB structures and to identify important issues which may potentially impact the seismic response of DEB structures. Effort is then made in this program to both qualitatively and quantitatively evaluate the impact of these issues on various analytical methods commonly utilized in practice for the seismic response analysis and design of NPP structures. With respect to the seismic induced passive earth pressure, special attention is paid to determining whether it is appropriate to designate the passive earth pressure as the sole parameter for the seismic design of embedded walls when the structure is deeply embedded. Based on the results of the study for the embedment effect on analytical methods, the criteria for benchmark problems with the characteristics important to capturing the seismic response of DEB NPP structures are defined. These benchmark problems are aimed at determining the accuracy and adequacy of an analysis methodology or a computer program to be used for the seismic response analysis of DEB NPP structures.

The approach for investigating the extent to which existing standards, tests, and practices that have been applied to the seismic design and analysis of DEB structures is to review and survey the open literature, codes and standards, as well as projects sponsored by the U.S. Government. Research performed by foreign R&D organizations and regulators is also reviewed for applicability and to determine gaps where additional research is needed. This report provides the results of BNL's review and evaluation of existing practices for SSI analyses. The scope of this activity includes the review of existing standards, tests, and practices that have been used in the design and analysis of DEB structures. The computer codes, especially the program entitled "A System for the Analysis of Soil-Structure Interaction," (SASSI) were reviewed pertaining to their applicability to the SSI analyses for DEB structures. This report also includes BNL's evaluation of NRC seismic analysis guidelines as outlined in the Standard Review Plan (SRP) in light of proposed advanced reactor design features.

Based on BNL's review of the existing technologies for SSI analyses, gaps that may exist in knowledge and potential issues that may require better understanding are identified and discussed, and analyses are performed to evaluate the impact of the embedment related issues on various analytical methods commonly applied for the seismic response analysis and design of NPP structures. As discussed before with respect to the seismic induced passive earth pressure, special effort is made to evaluate the appropriateness of using the passive earth pressure as the sole design parameter for embedded walls when the structure is deeply embedded. Based on the results of the study, this report defines the criteria for a series of benchmark problems with the characteristics important to the seismic response of DEB NPP structures. These benchmark problems, when analyzed and verified with test data, could be used to verify the accuracy and adequacy of an analysis methodology or a computer program to be used for the seismic response analysis of DEB NPP structures.

It is expected that the findings and recommendations from this program are to be used either to confirm the applicability of existing criteria or to develop new acceptance criteria, if necessary, for guidance to NRC staff for seismic evaluations of DEB NPP structures.

1.3 Report Organization

This report is organized in five sections. Following this introduction, Section 2 provides a retrospective review of the literature with respect to both analytical and experimental treatment of the seismic response analyses of DEB structures. It also includes a review of the relevant codes, standards, and regulatory guidelines to determine their applicability and limitations in the seismic design and analyses for DEB structures. Based on BNL's review of the existing technologies for SSI analyses, gaps that may exist in knowledge and potential issues that may require better understanding are identified and discussed.

Based on the potential issues identified in Section 2, analyses are performed to investigate their effects on the seismic response of NPP structures which are deeply embedded, and to evaluate various analytical methods commonly used by the nuclear industry with respect to whether the aspect of the SSI response associated with the embedment can be adequately captured. The methods and results of these analyses are discussed in Sections 3 and 4.

Section 3 provides an assessment of simplified vs. detailed methodologies for the SSI analysis of DEB structures. A simplified method for seismic analyses is usually referred to as the lumped mass beam representation of a structure connected to the supporting soils via the so called SSI coefficients (or foundation impedance functions), while detailed analyses are related to finite element solutions to the SSI problems such as sub-structuring or hybrid methods. For SSI response in terms of response spectra, the CARES and SASSI2000 computer programs are used to represent the simplified and detailed methods, respectively. A description of these programs is provided in Section 3. Also provided in Section 3 are the analysis results of a DEB structure for a range of embedment depths with respect to the kinematic interaction effect, the inclined wave effect, and full SSI response analysis.

Section 4 provides an assessment of methodologies for computing seismic induced earth pressures on DEB structures. Phenomenologically speaking, when a structure is shallow embedded, its seismic response is primarily induced as a result of the inertial interaction. As the depth of embedment of the structure is increased, the effect of the inertial interaction is reduced and the kinematic interaction contributes more to the seismic response. As the structure is fully embedded in the ground, the kinematic interaction is believed to be primarily responsible for its seismic response. In Section 4, the effect of the depth of embedment is examined to determine qualitatively and quantitatively how the seismic induced earth pressure is impacted by the inertial and kinematic interaction phenomena.

Based on the results of the assessments performed in Sections 3 and 4, the criteria for a series of benchmark problems with the characteristics important to the seismic response of DEB NPP structures are defined in Section 5. The benchmark problems, when analyzed and verified with test data, could be used to verify the accuracy and adequacy of an analysis methodology or a computer program to be used for the seismic response analysis of DEB NPP structures.

Finally, conclusions and recommendations are provided in Section 6.

2.0 EXISTING SEISMIC ANALYSIS AND DESIGN PRACTICE

In this section, a review and evaluation of existing seismic analysis and design practice for DEB structures are described. This review consists of a retrospective look at the literature with respect to both analytical and experimental treatment of the seismic response analyses of DEB structures. The relevant computer codes, standards, and regulatory guidelines are also reviewed to determine the extent of their applicability to performing seismic design and analyses of DEB structures. Limitations of the various methods are discussed. The insights gleaned from the literature review are used to identify methods, data and computer programs which are capable of addressing SSI effects associated with seismic response analyses of DEB structures, and to identify knowledge gaps and potential issues that may require further investigation.

The open literature survey of methods, analyses and pertinent SSI considerations for DEB structures is provided in Section 2.1. Section 2.2 reviews the available codes and standards, as well as regulatory guidance documents. The review and evaluation focus on their applicability to address the importance of the SSI effects in the seismic design and analyses for DEB structures. Relevant computer programs are reviewed and evaluated in Section 2.3. Section 2.4 provides a review of existing recorded data including both free field and structural responses. Finally, potential issues related to SSI effects for DEB structures are identified and discussed in Section 2.5.

2.1 Literature Review of Seismic Analysis and Design Practice for DEB Structures

The DEB structures considered in this survey consist of massive, stiff structures such as large-scale waste storage tanks [Chen, 1975, Uldrich, 1991, Wang, 1995, Houston, 1999], underground nuclear shelters [Baron, 1960, ASCE Manual, 1961], and nuclear power reactor buildings [Masao, 1979, Prato, 1998, Celebi, 1979]. Evaluation of the seismic response and the design of these types of structures require a detailed consideration of SSI effects (kinematic and inertial interactions), and the prediction of dynamic earth pressures which include nonlinear effects developed between structures and surrounding soils when subjected to a strong seismic motion.

Considerable progress has been made over the years in addressing these issues, although much of the work has been focused on surface or near surface facilities. The development of methods that could capture all of the dynamic interaction effects for deeply embedded facilities remains a challenge to the research community. The main focus of this section is to review the open literature pertaining to the treatment of SSI effects and the analysis methods used for the dynamic analysis of DEB structures subjected to seismic loads. Experimental verification of the accuracy of different analytical techniques is also an important issue for this program.

The literature review includes a search for existing recorded data for the DEB structures; the review and evaluation of that data are discussed in Section 2.4. In addition to the DEB structures being reviewed in this study, it should be recognized that there are other buried structures developed as part of our nation's civil infrastructure such as railroad and subway tunnels, underground lifeline systems for water, gas, sewerage, electric and telecommunications, as well as buried piping in nuclear power plants. Treatments of this group of structures subjected to seismic motions have been studied extensively, and their dynamic analyses may be performed using well-established methods [Kuesel, 1969, Newmark, 1971, Okamoto, 1980, Agrawal, 1983, Wang, 1977, Stamos, 1995, Ostadan, 2001]. Therefore no further discussion is provided in this

report with regard to this group of structures, since this study focuses on massive, reinforced concrete structures typically encountered in NPPs (e.g., containments).

2.1.1 Impact of SSI Effects on DEB Structures

Consideration of the SSI phenomenon is usually broken down into kinematic interaction and inertial interaction effects. Kinematic interaction refers to the modification of the free-field seismic waves by the geometry of the embedded portion of a structure and therefore is independent of the inertial properties of the structure, while inertial interaction is associated with the dynamic response of the coupled structure-foundation system which is governed by the inertial properties of the structure and foundation impedance functions. This subsection takes a retrospective look at the literature for computing and assessing SSI effects, especially the impact of embedment.

Foundation impedance functions (often referred to as dynamic stiffness functions) can be obtained by solving a mixed boundary value problem with displacements prescribed at the contact area between the foundation and the soil and tractions vanishing at the soil surface. Since this problem is very difficult to solve mathematically, boundary integral solutions are available mostly for surface founded and very simple geometries such as circular, rectangular and strip footings [Kausel, 1974, 1975, 1976, Luco, 1971, 1972, Wong, 1978]. When an embedded foundation or a buried structure with wall flexibility is considered, an exact solution to the mixed boundary value problem becomes impractical; solutions for the impedance functions need to resort to either approximate formulas [Pais, 1985, Dominguez, 1978] or finite element methods [Day, 1977, Lysmer, 1999]. The impedance functions of rigid cylindrical and rectangular foundations were computed by Pais and Kausel [Pais, 1985] for various depths of embedment. Their study observed that impedance functions tend to increase with the depth of embedment. Another discussion by Roesset [Roesset, 1995] indicated that the main effect of inertial interactions are the modification of the frequency of the structure due to added flexibility of the foundation and a change in effective damping of the system attributed to radiation damping. The importance of these effects depends on the relative stiffness of the structure with respect to soil. As the embedment increases, foundation impedance functions tend to increase, therefore, resulting in a decrease in the inertial interaction effect due to the increase in the SSI frequency and the effective damping. Depending on the characteristics of seismic motions and the fixed-base structural frequencies, an SSI frequency increase may or may not be helpful in reducing the seismic response; however, an increase in effective damping is always beneficial in amplitude reduction. Typical interaction impedance functions were derived by Pais and Kausel [Pais, 1985] for an embedded rigid cylinder with various E/R (embedment/radius) ratios, and in terms of the real and imaginary parts of the impedance functions for horizontal and rocking response. The real part corresponds to the stiffness component while the imaginary component corresponds to the damping component. As shown by Pais and Kausel, both components are greatly affected by the depth of embedment (E/R ratio) shown on the vertical axis.

Kinematic interaction effects are associated with modification of the free-field motions due to the structural rigidity of an embedded foundation or structure. When a train of seismic waves propagates in an obliquely incident direction in the free field, the induced ground motion varies spatially at any instant of time. Since a typical embedded foundation or structure tends to be much stiffer than the surrounding soils, when subjected to a train of seismic waves traversed in an oblique direction, it cannot accommodate such spatial variability of the ground motion. Instead, the embedded structure tends to maintain its geometry and force the surrounding soils to move with it, which leads to modification of the free-field motion (averaging out the spatially variable motions). It is clear that the kinematic interaction is influenced by the size and rigidity, as well as

the depth of embedment of a structure. Because of the nature of the problem, the exact solution for the kinematic interaction effect is very complex and difficult to attain. For the analytical solutions available in literature, only simple geometries were actually considered, namely, circular, rectangular and strip footings; in most cases, an assumption of rigid foundation was used [Aspel, 1976, Wong, 1974, Iguchi, 1982]. In contrast, numerical methods such as finite element and boundary element methods can be more suitable for investigating the kinematic interaction effect [Day, 1977, Roesset, 1995, Romanel, 1993, Murakami, 1987]. This is especially true for deeply embedded structures when wall flexibility is included in the modeling. In these cases numerical approaches clearly exhibit advantages over the analytical solutions [Lysmer, 1999] for computing kinematic interaction effects for a variety of geometries.

Pais and Kausel [Pais, 1985] performed a detailed investigation of the effects of embedment and inclined SH waves on the kinematic interaction for circular and rectangular foundations. In their study, an approximate formula by Iguchi [Iguchi, 1982], treating the kinematic interaction for embedded rigid foundations of arbitrary shape, was utilized to obtain the kinematic interaction response functions for foundations where the depth of embedment was varied from 0 times to two times the foundation radius. The structures considered in the study are comprised of cylindrical and rectangular rigid, massless foundations embedded in an elastic half-space and subjected to obliquely incident SH waves. Transfer functions between the free-field motion at the surface and the motions of the foundation in terms of translation, rocking and torsion were computed for various depths of embedment and a range of the arriving angles of the incident waves.

Their study found that in general, the transfer functions are significantly affected by the foundation embedment for the SH waves that propagate at steep angles, while for shallow SH waves, the transfer functions are little influenced by the depth of embedment. The embedment usually results in reduction in translational and torsional responses while inducing significant rocking motion, especially for vertically propagating SH waves. For waves arriving at intermediate angles, the rocking transfer functions approach those for waves propagating vertically as the depth of embedment is increased. However, the study found that the maximum value of the rocking is not sensitive to the depth of embedment. Furthermore, their study revealed a shift of the major peak in the transfer function to a lower frequency for the case of the deeper embedment, indicating a stronger kinematic interaction effect. In addition, the maximum torsion is, in general, induced by shallow waves. These observations with respect to the embedment effects, however, were arrived at based on elastic half-space and SH waves. In reality, soils are usually layered with different properties for each layer and earthquake motions may be propagated with a combination of a variety of different body waves (P, SV, SH) and surface waves (Rayleigh and Love). Further study that encompasses more realistic soil conditions (e.g., layering effect) and other wave patterns needs to be performed to establish an understanding of the kinematic effects that may be unique to these situations.

For practical applications, the seismic response in terms of response spectrum is a more meaningful representation of the facilities' response. To demonstrate the embedment effect on the seismic response of a structure, Pais and Kausel employed a stochastic response analysis for a simple 1-D structure based on the work by Kiureghian [Kiureghian, 1981]. The structure employed consists of a single mass attached to a rigid, mass-less embedded foundation. The seismic response of the simple system was computed using an approximate formula by Kiureghian [Kiureghian, 1981] based on random vibration theory and Vanmarcke's distribution for the first-crossing problem [Vanmarcke, 1975]. Response spectra were computed for three mass locations considering only kinematic interaction. The resulting horizontal response spectra thus obtained for different depths of embedment were plotted together with the spectrum of the free-field input motion. A number of typical results for steep waves were provided in the study; the

results for the rest of the cases can be found in Reference [Pais, 1985]. Comparisons of response spectra versus depth of burial reveal that the embedment usually reduces substantially the maximum response of the structure, except for tall structures, in which case the response spectrum can increase as a result of the kinematic interaction. It is apparent that considering the kinematic effect is beneficial for computing the seismic response of DEB structures. However, the extent to which the kinematic interaction is affected by the depth of embedment is not clearly demonstrated by the data presented in their report and therefore may require further investigation.

The effect of embedment on the dynamic response of DEB structures subjected to various seismic waves was also investigated by a number of other authors [Roesset, 1995, Morray, 1975, Dominguez, 1975, Aviles, 1998]. Findings from these studies showed that the embedment effect, as well as the angle of incidence of the traveling wave effect, on the dynamic behavior of an embedded rigid foundation are consistent with the observations made by Pais and Kausel [Pais, 1985].

Roesset also extended his investigation to include the flexibility of the sidewalls [Roesset, 1995], using vertically propagating shear waves. An embedded cylindrical foundation similar to the one employed by Pais and Kausel [Pais, 1985] was used, assuming elastic sidewalls with the properties of concrete while still maintaining a rigid base. Transfer functions were computed for horizontal translation and rocking vibrations. The transfer function for the horizontal translation is expressed as the ratio of the horizontal translation at the base center to the free-field motion at the surface, while the transfer function for rocking is calculated as the ratio of the rotation of the base multiplied by the base radius to the free-field motion at the surface. Roesset studied the transfer functions vs. frequency (f) for elastic sidewalls and rigid sidewalls, which revealed that the effect of sidewall flexibility on the horizontal translation is negligible, while the rocking was reduced by about 20% when the sidewall flexibility is considered. In addition, a study by Younan [Younan, 1997] was performed utilizing an approximate method to examine the response to horizontal ground shaking of flexible walls retaining a uniform, linear, viscoelastic stratum of constant thickness and semi-infinite extent in the horizontal direction.

It should be noted that most of the analytical studies were based on the assumption that perfect bond exists between the structure and the surrounding soils. The actual conditions of the backfill soils are much more complex, and slippage and separation between the structure and the soil as well as base uplifting could take place during a seismic motion. These nonlinear effects could also influence the rocking response.

2.1.2 Seismic Induced Dynamic Pressure on DEB Structures

Much of the past research effort investigating the effect of seismic induced pressures was primarily focused on earth retaining wall structures. Standard evaluation procedures have been established such as ASCE 4-98 [ASCE 4-98, 1998] which requires either an elastic solution or use of the Mononobe-Okabe (M-O) method [Okabe, 1926, Mononobe, 1929] for the calculation of the seismic induced pressures on earth retaining wall structures. The M-O method is a pseudo static approach based on the Coulomb wedge theory which considers the limit state of soil supported by the retaining wall. Recognizing that the spatial distribution of the pressure could not be determined by the M-O method, a number of studies were conducted to investigate the distribution characteristics of the seismic pressures on retaining wall structures. Two examples are: (1) the work done by Wood [Wood, 1975] using the finite element method attempted to characterize the dynamic pressure distribution against a fixed structure where the soil is considered as a uniform elastic material, and (2) the study by Nadim and Whitman [Nadim,

1983], and improved subsequently by Siddharthan and Norris [Siddharthan, 1991], to investigate the nonlinear effects induced by potential failures at the soil-wall interface on the distribution of the seismic pressures. In addition, simplified approaches were developed [Scott, 1973, Ortigosa, 1991, Veletsos, 1992, 1993, 1994, Richards, 1999] to characterize the seismic induced pressure distribution on retaining structures. Furthermore, the work by Ostadan and White [Ostadan, 1998] provided an insightful discussion on practical approaches to computing seismic soil pressure in design.

Extensive experimental work was also performed to confirm and complement the analyses or evaluation methods for the dynamic seismic pressure effect on retaining structures [Ichihara, 1973, 1977, Sherif, 1982, Kawamura, 1987, Ishibashi, 1987]. Findings from these experiments provided laboratory measurements of the thrust and distribution of the lateral earth pressure as it varies with the ground acceleration, the angle of wall friction, the magnitude of wall movement, etc. The ultimate active thrusts measured in the experiments were reasonably close to those calculated by the M-O method and the measured distribution of the dynamic pressure differs in most cases from the hydrostatic case.

No significant U.S. studies could be found in the literature dealing with seismic pressure effects on typical DEB NPP structures. The lack of research investment in this area in the U. S. may be due to the fact that most of the current generation NPPs do not have deeply embedded or buried containment structures. However, in Japan, because of frequent seismic activities, typical NPP reactor buildings tend to be deeply embedded in soil, and consequently significant research effort has been focused on understanding phenomena associated with seismic induced pressure loads and developing the assessment capability for the seismic pressure effects on the embedded portion of a deeply embedded NPP reactor building.

Although the M-O method is still commonly used in the evaluation of the dynamic earth pressure acting on the underground walls of deeply embedded NPP reactor buildings [Nukui, 1989], research activities (both analyses and experiments) have been conducted to focus on issues related to the seismic pressure effects which are unique to deeply embedded NPP reactor structures. Field experiments were conducted in Japan for assessing the adequacy of analysis techniques for the seismic pressure effects on deeply embedded NPP structures. In a paper by Narikawa [Narikawa, 1989], a field experiment was described which involved a 1/15 scale reinforced concrete (RC) model of a NPP reactor building. According to the paper, many earthquakes have been recorded since the earth pressure gauges were installed in December 1984; the maximum ground surface acceleration recorded for these earthquakes ranges from 16 gal to 120 gal [$1 \text{ gal} = 10^{-2} \text{ m/sec}^2$]. To evaluate the validity and adequacy of analytical techniques for predicting the seismic induced earth pressures, a 2-D model and a 3-D model, respectively, using the finite element (FE) method, were developed for the experiment. The FE analysis using the analytical models was performed to predict the seismic induced earth pressure on the reactor model for an earthquake event recorded off Fukushima Prefecture on April 7, 1987 (Magnitude 6.6). As reported in the paper, the analysis results in terms of maximum seismic induced earth pressure were compared with the corresponding recorded response. The comparisons showed that the analytical prediction using the 3-D model compares fairly well with the recorded data, although the relative differences may require further examination because of certain under-predictions of the 3-D analysis shown in the plots. On the other hand, the 2-D model prediction did not capture the pressure distribution as exhibited by the recordings. This is mainly due to the 3-D nature of the wave propagation which could not be adequately simulated with a 2-D model.

In addition, there are other field observation data of actual earthquakes in Japan such as those reported by Onimaru [Onimaru, 1995] and Hirota [Hirota, 1992] for the seismic induced earth

pressure on underground walls of embedded NPP structures. Large-scale shaking table tests were performed in Japan such as the one reported by Ohtomo [Ohtomo, 2001] for an underground reinforced concrete duct-type NPP structure. These experimental programs conducted in Japan could be used to evaluate and verify the applicability and adequacy of the analytical methods and computer programs with respect to DEB NPP structures. Furthermore, the shaking table tests [Ohtomo, 2001] also permit the study of many non-linear phenomena associated with a DEB NPP structure subjected to large magnitude earthquakes, such as material non-linearity, geometric non-linearity (slippage and gaps developed at the structure-soil interface [Weidlinger, 1991] and their impact on the SSI response and dynamic pressure distributions.

Parallel to the experimental and analytical activities described above, effort was also made in Japan to develop simplified, practical methods to account for the seismic induced pressure effects on DEB type NPP structures. The following briefly describes a simplified method proposed by Nukui [Nukui, 1989] for calculating the seismic induced dynamic pressure distribution for a massive, rigid DEB structure. The base of the structure is considered either founded on or embedded in the bedrock, which often is the case for the design of NPP reactor buildings in Japan. The earth pressure induced by earthquakes is assumed to counter the inertial force of the structure. Therefore, two types of dynamic pressures could be defined: 1) loading earth pressure in which the pressure acts in the same direction as the inertial force of the structure, and 2) supporting earth pressure when the pressure is in the opposite direction of the inertial force. A schematic description of the two types of dynamic pressures was provided in the paper. To illustrate the simplistic nature of the method, a brief description of the formulation is provided below.

For loading earth pressure, an approximate formula by Tajimi [Tajimi, 1985] was used:

$$P = \frac{\sqrt{3(1+\nu)}}{4} \rho H^2 \alpha, \quad (1)$$

where

- P : Loading earth pressure in terms of resultant force per unit width
- ν : Poisson's ratio of soil
- ρ : Soil density
- H : Depth of embedment
- α : Acceleration

In the above formula, if a uniform distribution of the earth pressure is assumed along the depth and the maximum ground surface acceleration is used, Eq. (1) is bounded by

$$P_a = 0.6\rho H^2 \alpha_{\max} \quad (2)$$

Where

- P_a : Loading earth pressure
- α_{\max} : Maximum acceleration at ground surface level.

The supporting earth pressure resultant was related to the shear ratio of the surrounding soil and the total inertial force of the structure:

$$P_s = \beta F \quad (3)$$

Where

- P_s : Resultant force of the supporting earth pressure
 β : Shear ratio of the surrounding soil
 F : Total inertial force of the structure.

The total inertial force F is calculated from the maximum acceleration distribution of the structure induced by a seismic input, considering the reduction effect on the acceleration in the embedded portion of the structure when the maximum supporting pressure occurs.

A simple relation was introduced for calculating the shear ratio:

$$\beta = K / [2(1+K)]$$
$$K = \frac{S}{0.06 + 0.15S} \left(\frac{V_{SE}}{V_{SD}} \right)^2, S = H / L \quad (4)$$

where

- L : Width of the embedded portion of the structure
 V_{SE} : Mean shear wave velocity of the surrounding ground
 V_{SD} : Shear wave velocity of the bedrock.

The shear ratio computed using Equation 4 was compared with a static finite element (FE) analysis in which the shear ratio is calculated from the reaction force of the surrounding soil when a static unit loading was applied to the structure at about 1/2 and 2/3 of the height of the structure. Figure 18 shows a plot of shear ratio vs. H/L computed using both FE analysis and the simplified formula (Eq. 4). As seen in the figure, for the range of H/L , the simplified formula exhibits good correlation with FE analysis results.

Furthermore, an assumption of linear distribution was utilized for the supporting earth pressure with the pressure of $1.5P_{sm}$ at the ground surface and $0.5P_{sm}$ at the base of embedment, where P_{sm} is the mean pressure obtained from the supporting pressure resultant given in Eq. (3).

According to the paper [Nukui, 1989], in order to demonstrate the applicability of the simplified method, the dynamic pressure for an embedded reactor building was estimated by both the simplified method and a dynamic FEM analysis. The dynamic pressure results were compared between the simplified method and the FE analysis. The resulting comparison showed that when the surface layer is soft, the loading pressure calculated based on the simplified method is overestimated compared with the FE results. When the surface layer is hard or the structure is embedded in bedrock, close correlation of the supporting pressure was obtained between the simple method and the FE result.

2.1.3 State-of-the-art Analysis Methods for Seismic Response Calculations of DEB Structures

This section provides a brief overview of the state-of-the-art methods for the seismic analyses of DEB structures, with special emphasis on large, massive box-type structures having all their dimensions comparable to NPP containment structures. The seismic behavior of long structures (tunnels, pipelines) has also been studied extensively in the literature. A very informative review of the literature was performed by Stamos [Stamos, 1995] to identify robust methods for seismic analyses of long structures, and therefore it is not repeated in this review.

In a broad sense, the analysis techniques for seismic response calculations of DEB structures may be characterized by the following aspects: 1) continuum vs. discrete formulations, 2) detailed vs. simplified models, 3) direct vs. sub-structuring approaches. Depending on the characteristics of the physical problems to be analyzed, factors such as linear vs. non-linear material, geometric conditions, and time domain vs. frequency domain techniques, may influence the choice of methods for seismic analysis, as compared to the size of models and computational efficiency, thanks to the rapid advance in computer technology.

According to Roesset [Roesset, 1989], the classification of continuum vs. discrete approaches is intended to distinguish between boundary integral equation or boundary element methods (BEM), referred to as continuum models, and finite differences or finite element methods (FEM), referred to as discrete models. Stamos [Stamos, 1995] provided a chronicle of methods developed for both regimes. In between these two extremes, there are other formulations that take advantage of both approaches, such as a hybrid formulation which uses a discrete scheme or finite elements for the near field and boundary elements for the far field. The hybrid method is especially convenient for situations where a structure is deeply embedded and/or buried, or irregular soils are present in close proximity to a structure. For instance, a hybrid formulation by Romanel [Romanel, 1993] assumes discretization by finite elements for the structure and surrounding soils (near field) and couples it with a far-field multi-layer half-space wave propagation solution based on Green's functions. The coupling is enforced by conditions that traction reciprocity between the two regions is satisfied while the displacement continuity across the common interface is enforced in a least-squares sense. However, boundary element methods based on Green's functions are limited to linear problems, while discrete approaches can be utilized to model problems with nonlinear dynamic characteristics, such as material non-linearity and geometric non-linearity. It should be noted that while the continuum approach uses an analytic solution for wave propagations in a half-space, a discrete method (e.g., finite elements) models the half-space with finite domain. Therefore, when the complete soil domain is discretized, caution needs to be taken to impose appropriate boundary conditions at the edges of the finite domain to reproduce the radiation of waves away from the zone of interest, or the boundaries of the finite domain must be placed at a sufficient distance to guarantee that the reflected waves reaching the structure have a negligible amplitude.

With respect to the distinction of detailed vs. simplified approaches, it was intended to differentiate between FEM or BEM models and lumped mass parameter models. For complex soil-structure systems, a detailed approach has the advantage of capturing various effects which simplified methods may not be able to characterize, such as irregular soil zones, seismic induced pressure effect, etc. However, a detailed model of the SSI system requires much greater computational effort than a simplified model. Simplified lumped parameter models typically include lumped-mass parameter systems and the "lattice model". A typical lumped mass parameter model consists of the structure represented by a series of lumped masses and beams, and the SSI effect which is modeled by springs and dashpots often referred to as the SSI coefficients. The SSI coefficients represent the dynamic stiffness of the foundation and are usually derived based on either analytic or semi-analytic solutions to the vibration of a rigid foundation on a half-space which could be either uniform or layered. Depending on the particular formulation to be applied, the dynamic stiffness can be either frequency independent or frequency dependent. The lattice model, which has been frequently used in Japan for seismic SSI analyses [Murakami, 1987], utilizes a system of lumped masses for both the structure and a finite domain of soils with a transmitting boundary [Kuroda, 1981]. Since it is kind of a simplified discrete approach, the kinematic interaction effect is built into the model. For a lumped mass parameter model, the kinematic interaction effect can be incorporated with various schemes such as one proposed by Iguchi for rigid circular or rectangular foundations [Iguchi, 1982], an oscillator

representation of the kinematic interaction by Aviles [Aviles, 1998], or the FEM approach proposed by Kausel [Kausel, 1977].

The distinction between direct and sub-structuring approaches has been discussed by many [Roesset, 1989, Lysmer, 1981] in the literature, and therefore only a brief discussion is provided. The direct approach by definition is the analysis in which the structure and the soil are modeled together and the total solution to the system's seismic response is computed in a single step. In practice, however, it is necessary to determine first the compatible motions and stresses at the boundaries of the soil domain (both lateral and bottom boundaries) that would reproduce the desired earthquake at the free surface of the soil. This procedure is particularly attractive for true nonlinear analyses including the complete SSI effects. A rigorous solution requires, however, a fully 3-D model and an appropriate set of nonlinear constitutive equations, which also increase significantly the computational efforts. In practice, direct solutions are often sought using a 2-D or a pseudo 3-D soil model (a two dimensional slice is taken through the structure) and nonlinear soil behavior is simulated through equivalent linearizations.

In contrast to the direct approach, the sub-structuring approach treats the SSI system as a combination of a series of simpler sub-systems. Solutions for the subsystems are superimposed to obtain the response of the original SSI system. A typical sub-structuring approach divides the SSI problem into several sub-problems including: 1) the site response problem (the free field with no presence of structure), 2) the scattering problem, 3) the impedance problem, and 4) the structural response problem. Certain algorithm manipulations, such as the flexible volume and subtraction methods implemented in SASSI [Lysmer, 1999], can be performed for explicit modeling of the embedment in the free field, in which case, the scattering problem can be avoided. It is noticed that most of the analysis programs based on the sub-structuring approach were developed in the frequency domain. Because of the implicit use of the superposition principle, the sub-structuring approach is limited mainly to linear problems, although it is possible to perform true nonlinear analyses if the solution is formulated in the time domain and the coupling between the sub-structures is carried out in each time step. Nevertheless, because of its clear definition and dissection of the physical problems associated with the SSI phenomenon, the sub-structuring approach enjoys growing popularity among practitioners for seismic analyses.

2.1.4 Examples of Practical Applications Using Established Approaches to DEB Structures

Several analysis examples are presented in this section to demonstrate practical applications using established approaches to DEB structures. These examples were selected based on a search of open literature, and may not necessarily represent the best analyses or methods, but are intended as illustrations of various applicable methods and techniques for seismic analyses of typical DEB structures. To this end, only brief descriptions are provided pertaining to the structural models, analytical treatments and analysis results.

To assist readers who wish to learn more on these analyses, references from which these analyses were obtained are also provided. The examples described below are presented in a chronological order.

A 2-D Seismic Analysis of Large Underground Cylindrical Tank [Chen, 1975]

In this study, a large underground tank was analyzed for its seismic response using a 2-D finite element model. The tank consists of a cylindrical steel tank and its protective concrete shell. The steel tank has an inner diameter of 54 ft and a height of 20 ft, and was used to store radioactive waste. The concrete shell encasing the steel tank has an inner diameter of 60 ft and

overall height of about 36 ft. The shell thickness is about 3 ft and 6 inches. The shell is laterally constrained by five reinforcing steel rings spaced vertically at 8 ft on centerlines, and 3 ft of plain concrete backfills the space between the shell and the ring supports. The tank is buried about 13 ft below the ground surface.

The seismic input was defined at the ground surface using the Regulatory Guide 1.60 [Regulatory Guide 1.60, 1973] spectrum with 2% damping. Convolution analysis was performed using a 1-D propagating shear wave model for the soil column to determine the motion at the base of the soil deposit. The analysis was carried out utilizing SHAKE [Schnabel, 1972] and the modulus degradation curves by Seed and Idriss [Seed, 1970]. The base motion of the soil deposit was then used as input to an SSI finite element model.

The SSI finite element model was developed using the 2-D LUSH code [Lysmer, 1974], which uses the direct approach to solve the SSI response problem in a single step. In order to adapt to the 2-D analysis, an equivalent 2-D model for the waste tank was developed by the concept of dynamic equivalence of two different structures. The dynamic equivalence is established if the two different structures have the same dynamic characteristics such as frequencies, mode shapes, and dynamic responses. In this study, a 3-D axisymmetric finite element model was developed to determine the frequencies and mode shapes of the waste tank. A 2-D LUSH model was then constructed such that the model frequencies and mode shapes of the waste tank were close to those of the 3-D model. The motion input in the form of an acceleration time history was then applied to the base of the LUSH SSI model. The analysis results include acceleration time history responses of the tank and the induced seismic pressure distributions on the tank.

A 2-D Non-Linear Seismic Analysis of a Deeply Embedded NPP Building [Mukherjee, 1978]

A 2-D non-linear finite element model was developed in this analysis to determine the seismic response of a deeply embedded NPP building. The non-linear program ADINA [Mukherjee, 1977] was employed for the analysis which used the direct approach to model the soil-structure system. The structure was modeled with linear elastic finite elements, while the soil from the bedrock to the surface was sub-divided into a number of layers and behaves in a non-linear fashion. The soil properties were determined using a non-linear stress-strain relationship based on the Drucker-Praeger yield criterion.

The seismic input was specified at the bedrock and expressed as an acceleration time history. The analysis results in terms of response spectra were compared with those obtained from a linear SSI analysis. As indicated by the paper, the foundation response spectra determined by the non-linear model shows decreased accelerations in the lower frequency range when compared with the linear analysis results. The study also showed the formation of plastic areas under the foundation slab and the spread of these areas over a period of time.

Study of Embedment Effects of JPDR Reactor Building with Different Analytical Models [Takada, 1987]

The analysis described in this paper was performed for the Japan Power Demonstration Reactor (JPDR), which was the first nuclear power reactor (15,200MW) built in Japan. The JPDR reactor building is a reinforced concrete rigid cylindrical structure, which is 40 meter high, 20 meter in diameter, and weighs about 13,000 tons. One third of the reactor building was embedded in an alluvial deposit.

Before being decommissioned, the JPDR reactor building was used to record the dynamic response of the structure and the surrounding soil to real earthquake events. According to the study, the largest recorded event was used to carry out the analyses.

The recorded seismic responses (both structure and soil) were used to examine various analytical techniques. Six sway-rocking (SR) models and two finite element models were developed to provide analytical estimates of the seismic response of the JPDR reactor building. The analysis results were then compared with the recorded response to assess the effectiveness of their respective analytical techniques.

The SR models assume the structure discretized using a simple lumped mass beam model; but they differ in the representation of SSI effects and input motion. Two types of SSI models were considered in these SR configurations, one with static soil springs and constant damping ratios for sway and rocking, and the other utilized frequency dependent soil springs and dampers. The static soil springs were derived based on typical static half space theory, while the frequency dependent springs were defined based on the dynamic admittance theory [Tajimi, 1968] and the Novak's treatment [Novak, 1977] of embedment effects. Treatment of the input motion varied among different SR models, ranging from applying an outcrop motion directly to the base of the foundation, to an effective input motion that accounted for variation with depth of embedment, to fully considering the kinematic effect due to embedment. The analysis results indicated that the SR model with dynamic SSI soil springs and kinematic effect considered generated better comparisons with the recorded response than the simpler SR models. However, the simpler SR models had a tendency to over estimate the response.

The two finite element models examined include a plane-strain FLUSH model and a 3-D axisymmetric model. Both models were developed using the direct approach. Based on the comparisons with the recorded responses, the 3-D axisymmetric model performed better in capturing the peak and predominant frequency of the soil-structure system than the 2-D model, which is incapable of reproducing the out-plane effect.

A SASSI Analysis of the ICPP High Level Liquid Waste Tanks and Vaults [Uldrich, 1991]

This paper described a seismic analysis of storage vaults located at the Idaho Chemical Processing Plant (ICPP), Idaho National Engineering Laboratory (INEL). These vaults, which have octagonal cross section and consisted of reinforced concrete construction, enclose steel tanks used to store high-level radioactive liquid waste. The vaults are buried about 7ft below ground surface and closely spaced between each other.

A detailed 3-D SASSI model was developed for the seismic response analysis of the vaults. The model included adjacent soils both on the top and sides of the vaults. The seismic input was defined at a rock outcrop and convolution analysis was performed to first generate the motion at the rock/soil interface and then back up to the soil surface in the free field, which was used as input to the SASSI analysis.

The analysis results reported included accelerations and member forces and moments. The variability of soil properties was considered by applying lower and upper bounds for soil properties in the SSI analysis.

A Feasibility Study of Deeply Buried Twin-Type Advanced BWR for Seismic Concerns [Togashi, 1995]

In Japan, the site feasibility requirement requires that the reactor building (R/B) be directly supported by bedrock. To meet this requirement, R/B structures for the current generation NPPs were embedded about 40m below grade. This paper describes a feasibility study for a much more deeply buried twin-type advanced BWR design in Japan. In particular, this study provided an assessment of the seismic behavior of buried R/B structures and a deeply embedded turbine building (T/B).

Both analytical models and experimental models were utilized for the study. The cases studied in the analytical models included a single buried R/B structure, twin adjacent buried R/B structures, a pile supported T/B structure, and a buried R/B adjacent to a T/B configuration. Dynamic experiments were performed for the structural configurations investigated in the analytical models.

The seismic analyses were performed using pseudo 3-D FEM. The analysis results in terms of acceleration, displacement and wall pressure were compared with the results of corresponding experiments. The study concluded that the interaction effect due to close proximity of adjacent structures is important to the seismic response of individual structures.

A Dynamic Model and Response of Rigid Embedded Cylinder [Veletsos, 1994]

This study investigated the dynamic response of deeply embedded vertical cylindrical structures, using an approach which models the soil medium by a series of elastically constrained, rather than unconstrained, thin horizontal layers with a circular hole at the center. The impedances of the constrained layers were then established and used to evaluate the dynamic response of a cylinder embedded in a uniform viscoelastic stratum of constant thickness and infinite extent in the horizontal direction. The cylinder and the surrounding soil stratum were assumed to be supported on a rigid base undergoing a uniform horizontal motion. The effects of both harmonic and earthquake induced ground motions were considered. The response quantities examined in the study included the dynamic force per unit of cylinder height and the corresponding base shear and base moment.

A Parametric Analysis of Kinematic Effect on Underground Vaults [Xu, 1996]

A buried concrete cylindrical vault typical of those found in the Department of Energy's High-Level Waste sites was used in this study to investigate the kinematic interaction effect on the seismic response of buried structures. A 3-D FEM model of the vault was developed using the SASSI code. The kinematic effect was induced by changing the stiffness of the vault and the seismic input was applied at the ground surface. The results in terms of response spectra indicated that the kinematic interaction effect reduces the peak response of a buried structure at high frequencies, while there is no appreciable impact on the response for low frequencies.

A SASSI Analysis of an Embedded Fuel Storage Facility [Houston, 1999]

The analysis described in this paper was associated with a seismic upgrade of the Irradiated Fuel Storage Facility (IFSF) at Idaho National Environment and Engineering Laboratory (INEEL). The facility is founded on a thirty-foot thick soil layer overlying stiff rock. The structure has an irregular foundation that is shallowly embedded at one end and bears near the bedrock at the opposite end. A 3-D SASSI model of the structure was developed for the SSI analysis. Separately, a fixed-base seismic analysis was performed. The comparison of the analyses with/without SSI effect indicated that in this case, neglecting the effects of SSI underestimates the demand in the stiff direction of the building.

A 3-D Seismic Analysis of a Deeply Buried Reactor Building [Yamamoto, 1999]

The analysis described in this paper is an extension to the feasibility study of a deeply buried twin-type advanced BWR in Japan, as discussed previously. The original study [Togashi, 1995] utilized pseudo 3-D FEM models. The current analysis used a detailed 3-D finite element model which explicitly modeled both the R/B and T/B structures as well as the adjacent soils. The 3-D soil-structure model was connected laterally to the free field using viscous boundary conditions.

The 3-D analysis results were compared with earlier pseudo 3-D analysis [Togashi, 1995] and the paper concluded that the 3-D analysis amplified the responses in terms of the pile forces, the seismic pressure on the R/B structures and the relative displacement between the R/B and T/B

structures. However, the paper did not mention whether comparisons were made between the 3-D analysis and the experimental results as discussed in Reference [Togashi, 1995].

2.2 Review of Guidance Documents

Guidance provided related for the design and analysis of buried facilities by the ASCE, USNRC, USDOE, and the Japan Electric Association (JEA) are reviewed and discussed in this section of the report. The following aspects of the seismic response problem are of primary interest to this study:

- Convolution of the free field motion throughout the soil media
- Interaction of the free field motion with the stiffness and mass characteristics of the structure
- Evaluation of soil pressures acting on the structure as a result of seismic effects.

This report focuses on those aspects of the problem that pertain to the deeply embedded characteristic of the structures of interest.

2.2.1 ASCE 4-98 (Seismic Analysis of Safety-Related Nuclear Structures and Commentary)

ASCE 4-98 [ASCE 4-98, 1998] is a consensus document published by the American Society of Civil Engineers and provides guidance on most aspects relating to the analysis of structures subjected to seismic loading. Requirements contained in this document form the basis for many of the criteria contained in the other guidance documents considered here.

It is recommended in Section 3.3.1 of ASCE 4-98 that variation of the seismic motion throughout the free field may be computed based on a vertically propagating shear and compression wave models of the soil. Non-linear soil characteristics can be included by performing an iterative series of elastic analyses where the soil properties are revised based on the magnitude of the strains found from the prior solution. When there is an indication that the vertically wave propagating model is not appropriate, the use of a 5% offset in the structures center of mass from the geometric center of the foundation can be used, together with results obtained using the vertical wave propagation model, to account for the torsional effects that may be introduced by the non vertical propagation of the free field waves. These torsional effects may be more significant for deeply embedded structures than for the structures of interest to ASCE 4 and hence could be of special interest to this study. The propagation of the free field waves is usually based on a linear elastic model of the soil.

Two types of analyses are recommended in ASCE 4 for evaluating the interaction of the free field motion with the structure (SSI). The first SSI method is called the direct method and requires the development of a combined model for the soil and structure. The model usually consists of finite elements and/or boundary elements. Soil boundaries are placed distant enough from the structure so that the structure's response is not overly influenced by reflections from the boundaries. Free field motions, consistent with the anticipated seismic motion at the foundation elevation, are applied at the boundaries. These motions should be consistent with the soil properties, types of waves propagating during the earthquake, and boundary characteristics. There may be a larger uncertainty in generating these motions for the deeply embedded structures of interest here than for the structures discussed in ASCE 4.

The second (SSI method) is called the impedance method and uncouples the free field from the structure. A solution for the motion of a mass-less rigid foundation (kinematic interaction problem) is first found, given the shape of the foundation and the free field motion. A model of the structure is then connected to the free field with impedance functions (inertial interaction problem) and the foundation motion found from the kinematic interaction problem used as input to the impedance functions. Solutions for impedance functions representing the soil above the roof of a totally buried structure are not available and would need to be developed. Also, impedance functions for the soil along the sidewalls of an embedded structure are uncertain and the effect of the uncertainty increases as the depth of burial increases. ASCE suggests that soil near the top of the embedded depth not be connected to the structure, thereby accounting for some separation of the soil from the structure. Further work is required to determine the extent to which sidewall impedance functions currently in use are applicable to deeply embedded structures.

ASCE 4 recommends that elastic solutions be used to determine wall pressures. An elastic model of the soil is attached to an elastic model of the structure and the pressures determined from the interaction forces between the soil and structure are used to define the wall pressures. This solution may not be valid for those cases where the soil tends to separate from the structure. In these cases the soil tends to bridge over the separation areas thereby decreasing the pressure acting on the wall. The extent to which such bridging can occur is limited by the strength of the soil. Non-linear strength models of the soil are required to account for this effect.

The Mononobe–Okabe model is an active soil pressure solution and accounts for the bridging action of the soil and generally results in lower soil pressures than found with elastic models. It should be noted, however, that the development of this bridging action requires sizeable displacements of the wall. It must be determined that the functionality of the wall is not compromised before such solutions can be used. If the separation of the soil from the structure occurs from the soil surface down to some depth, it may be possible that the bridging action of the soil does not reduce the soil pressure. In this case the wall pressures that have been relieved near the surface are transferred down through the soil and may result in higher wall pressures at depth. This case can be considered by uncoupling the soil from the structure near the surface and then using an elastic solution. If this is done the elastic solution leads to conservative results provided an appropriate depth of separation is used.

2.2.2 U.S. NRC Standard Review Plan (SRP)

Seismic analysis sections (e.g., Section 3.7.2: Seismic System Analysis) of the US NRC SRP [NUREG-0800, Rev. 2, 1989] are much less prescriptive than ASCE 4. The SRP generally discusses the characteristics of the problem that need to be considered, but does not usually contain specific information describing the models that should be used. There is no special mention of those facilities which are deeply embedded or buried.

The SRP recommends that the seismic response of structures be determined based on either the direct approach, where simultaneous solutions are obtained for the free field and structure, or a substructure approach, where separate solutions are obtained and then coupled together. It is suggested that non-linear soil properties can be handled by performing iterative solutions with the soil properties for the current iteration based on soil strains found in the prior iteration. In either case, it is required to consider both kinematic and inertial interaction, the potential variation in soil properties, and the potential de-bonding between the soil and structure. Variation of

parameter studies is required to assess the impact of problem uncertainties and when possible the analysis methods are to be qualified by comparison with benchmark problems.

However, the SRP does not contain specific guidance for the calculation of seismic induced soil pressures which is more pertinent to structures that are deeply embedded or buried in the ground. Guidance can be implied in that the same models used to evaluate SSI effects may be applied to compute soil pressures on the exterior walls. The linear elastic models recommended in the SRP for evaluation of SSI effects, however, are known to provide quite conservative estimates of the seismic induced soil pressures. The SRP should include some discussion of different aspects of seismic induced soil pressures and provide recommendations for alternative methods of computing them with models that are less conservative than the linear SSI models.

2.2.3 U.S. DOE Guidelines for Buried Waste Tanks

The US DOE developed guidelines [BNL Report, 1995] that can be used for the analysis and design of buried waste tanks. These tanks are usually completely embedded and often have some soil cover over the top of the tank. The following recommendations contained in the guidelines are of interest to the current study:

- The control point motion should generally be specified at the ground surface. In those cases, however, where a shallow soft surface layer overlies a stiffer soil layer the control point should be specified at the top of the stiffer layer and the input motion given as an equivalent outcrop motion. In either case motions throughout the free field are calculated using standard convolution methods using the vertically propagating shear wave model. The convolution studies are not required when the site is “uniform” (the shear wave velocity of the soil 1 diameter below the foundation is less than 1.5 times the shear wave velocity of the soil above the foundation). In this case, the motion over the depth of embedment can be assumed to be equal to the surface motion. These conclusions were based on the results of parametric studies where properties of the soil column were varied and response spectra derived using these soil columns were compared with response spectra of the input surface motion.
- Soil structure interaction can be done using either the continuum model or the lumped parameter model. It is shown that the neglect of soil structure interaction effects result in less than a 20% error for facilities located in “uniform” soil, having no soil cover, and having embedment depth to radius ratios less than unity. For these same conditions it is found that soil structure interaction effects reduce the load acting on the facility. This conclusion was also based on comparison of response spectra developed using the “uniform soil” description with response spectra for the surface input motion.
- Impedance functions for the lumped parameter method are based on the assumption that the foundation is rigid as compared to the soil it replaces. This condition is found to be satisfied when the shear stiffness of the foundation is at least three times the stiffness of the soil it replaces. It is also recommended that the lumped parameter method be restricted to those cases where the soil cover is less than one half the foundation radius.
- Kinematic interaction is shown to reduce the response of the facility when the depth of embedment to foundation radius ratio is between 0.5 and 1, and the depth of soil cover is less than 0.5 times the foundation radius. It is also shown to be conservative to represent

the motion input to the base and top of the foundation as the free field motion at the respective depths.

- It is recommended that wall pressures be calculated with elastic models with the possibility of reducing the wall pressure so that the soil stresses are limited by the Coulomb-Mohr soil strength model.

2.2.4 Japanese Guidelines

Current earthquake engineering practice for Japanese nuclear power plants is described in JEAG 4601-1987, “Technical Guidelines for Aseismic Design of Nuclear Power Plants,” published by JEA. The USNRC sponsored BNL to translate this document, which consisted of more than 900 pages of technical material, into English [Park, 1994]. Summaries of the information in this guideline are included in References 95 and 96.

JEAG 4601-1987 is a comprehensive handbook for the structural analysis and design of nuclear power plants. It contains chapters dealing with: (a) the selection of earthquake ground motions for a site, (b) procedures to be used to investigate foundation and bedrock conditions, (c) criteria for the evaluation of slope stability and the effects of ground movement on buried piping and structures, and (d) procedures for the analysis and design of structures, equipment and distribution systems (piping, electrical raceways, instrumentation, tubing and HVAC duct).

The document discusses the procedures for the selection of the design basis earthquakes (S1 and S2), including the use of past earthquake and micro tremor records and empirical equations for estimating ground motion intensities. It provides a comprehensive description of the requirements for detailing the site soil conditions. For buried structures conventional methods of analysis as well as more detailed finite element methods are presented, including items such as settlement induced by liquefaction, buoyancy effects and the evaluation of seismic effects on sidewalls. Procedures for the simplified nonlinear analysis of structures are presented, including empirical equations for the evaluation of shear walls and procedures for evaluating foundation uplifting. Methods to perform soil structure interaction analysis are presented, as well as detailed guidelines and formulas for the seismic analysis of equipment and supports.

Guidelines are presented for analytical techniques, limitations, and practical modeling schemes to apply various SSI models for both simplified and detailed approaches. A significant emphasis is placed on reducing the uncertainty associated with complex SSI analyses by standardizing modeling details such the proper sizing of elements and boundary treatments. Simplified approaches include the sway/rocking (SR) model, Kobori’s ground compliance theory, and Tajimi’s vibration admittance theory. Detailed approaches include the multi-degree-of-freedom (MDOF) parallel ground model, the FEM model, the thin-story-element model and the boundary element method (BEM) model. Among the SSI models, the empirical SR model and the MDOF parallel model appear to be highly popular in Japan and detailed descriptions regarding refinement efforts and practical modeling techniques are given in the JEAG 4601 guidelines, including the 1991 Supplement [JEA, 1991].

In JEAG 4601-1987, the MDOF parallel soil model and the FEM soil model are described to account for the effects of embedment. In the 1991 Supplement to JEAG 4601, new improvements in the SR model to account for embedment effects are described together with the determination criteria for the soil region for the MDOF parallel soil and the FEM soil models. JEAG 4601-1987 also describes methods to account for uplifting using nonlinear soil springs.

The 1991 Supplement describes the limitation of contact ratios regarding both the applicability of the analysis model and the linear approximation. The 1991 Supplement also summarizes the evaluation methods for the earth pressure on underground walls based on recorded pressure data and analyses. To evaluate the long-term pressure, the methods to account for excavation, building design and backfill effects are described. For the earth pressure during earthquakes, analysis limitations as well as the simplified evaluation method of earth pressure based on SSI analysis are described.

2.3 Review of Computer Programs

There are two types of computer codes that are generally used to perform seismic analysis. The first type of code uses the continuum method and solves the response of the free field and the structure at the same time. The second type of code uses discrete methods which uncouple the free field from the structure and solves the response problem separately for each. Computer codes based on each of these methods are discussed in this section.

2.3.1 Codes Based on Continuum Models

These models divide the problem into near and far field areas. The near field includes the soil in the immediate area of the foundation and the structure. The soil and structure are generally modeled with finite elements. The far field includes the remaining soil between the near field soil and some arbitrary boundaries. This soil is modeled with finite elements, boundary elements, or finite difference grids. The arbitrary boundaries are placed far enough from the structure so as to minimize the effects of wave reflections from the boundaries and in some cases may incorporate “non reflecting boundaries.” Programs in this category are elastic and their solutions are carried out in either the frequency or time domain. Inelastic effects can be simulated by using iterative solutions with the soil properties used in the current iteration based on soil strains found in the previous solution. The SASSI computer code operates in this manner, and since SASSI is the most used code for SSI analyses in the nuclear industry, it is selected for the current study.

SASSI was developed by Lysmer and his team at U.C. Berkeley [Lysmer, 1981]. Since then the SASSI program has gone through extensive improvement, especially in the past ten years (SASSI 2000, [Lysmer, 1999]). In addition to the sub-structuring methods such as the flexible volume, flexible boundary and rigid boundary methods as in the previous versions, SASSI 2000 implemented a new subtraction method, which has been proven to be quite an efficient algorithm with no compromise for quality for the SSI response calculations. The following paragraphs describe briefly the approach used by SASSI 2000, with special emphasis on the subtraction method. The material used in the following discussion was drawn primarily from the SASSI 2000 theoretical manual [Lysmer, 1999].

The sub-structuring approach divides the SSI problem into several sub-problems including: 1) the site response problem (the free field with no presence of structure), 2) the scattering problem, 3) the impedance problem, and 4) the structural response problem. For the rigid and flexible boundary methods, since the embedment is explicitly modeled in the free field, all four sub-problems are required to be solved. While for the flexible volume and subtraction methods, the scattering problem is not required due to the use of superposition to avoid explicit modeling of the embedment in the free field; although the other three sub-problems still need to be solved. However, the treatment of impedance analysis for the flexible volume and subtraction methods is quite different from the rigid and flexible boundary methods. The impedance is computed for the rigid and flexible boundary methods in the free field with the indentation of the structural embedment. For the flexible volume and subtraction methods, the impedance is calculated in the

free field without the indentation of the structural embedment, therefore significantly simplifying the SSI problem.

In contrast to the impedance treatment for the flexible volume method which computes the impedance at every nodal point within the embedment, the newly implemented subtraction method recognizes that the soil-structure interaction takes place only at the common boundary of the soil and the structure, and formulates the dynamic equations of motion in such a way that the interior nodes of the embedment are eliminated. Therefore, for the subtraction method, the impedance is computed only for the interfacing nodes of the soil and the structure, resulting in significant savings in computing time. In addition, the site response calculation for the subtraction method is performed only for the interaction nodes as opposed to all nodes within the embedment for the flexible volume method. This results in additional savings for the subtraction method. For a more detailed description, the reader is referred to the SASSI 2000 theoretical manual [Lysmer, 1999].

Because of the frequency domain solution algorithm employed by SASSI, which implies application of the principle of superposition, the SASSI code is limited mainly to linear problems. As discussed previously, the SSI phenomena may induce certain non-linear effects such as material non-linearity and geometric non-linearity between a DEB structure and the surrounding soils. For large magnitude earthquake events, these non-linear effects may be significant, and their significance should be assessed using other tools specialized for non-linear problems.

Separation of the foundation walls from the surrounding soil is a non-linear problem that is not well suited for these iterative elastic solutions. LS-DYNA [LSTC, 2001] is a code that operates similarly to SASSI, but is specialized for non-linear problems, including both the material non-linearity and the geometric non-linearity effects. LS-DYNA is a general-purpose transient dynamic finite element program capable of simulating complex real world problems. Its versatility and reliability for modeling a wide spectrum of different physical problems makes it popular in applications such as: crashworthiness, occupant safety, metal forming and cutting, biomedical, blast loading, fluid-structure interaction, and earthquake engineering. LS-DYNA has extensive element and material libraries as well as well-defined interfaces, which are suitable for non-linear dynamic analysis. This code is used in the current program to determine the impact that wall separation and other nonlinear soil properties have on wall/soil interaction and in predictions of wall pressures caused by seismic motions.

2.3.2 Codes Based on Discrete Models

The discrete models attach a finite element model of the structure to the free field with impedance functions representing soil-structure interaction effects. These impedance functions are based on analytic solutions for a basemat resting on an elastic foundation and a cylindrical strip embedded in an elastic media. The solutions are only available for rigid foundations so that the method is restricted to these cases and is not useful to evaluate soil pressures acting on the foundation in those cases where foundation wall flexibility is significant. The free field motion is used as input motion to the impedance functions and may include modifications to the free field motions resulting from kinematic interaction effects.

These solutions are usually carried out in the frequency domain because of the dependence of the impedance functions on frequency. Two computer codes which are based on this methodology are: the Kausel suite of codes and CARES [Xu, et al., 1990 and Miller, et al., 2000]. The Kausel suite of codes [Kausel, 1992] consists of three codes: LAYSOL which treats the convolution of a given control motion over the depth of the free field; SUPERM computes

effective foundation impedance functions and treats the kinematic interaction problem; and EKSSI computes the inertial interaction effects. The CARES code performs the same functions but all are contained within a single computer code. The CARES computer code is used as the representative code for the analyses of discrete models in this program, since it was developed for use by the NRC staff in licensing reviews.

2.4 Review of Existing Recorded Data

In this program, a search was performed to identify existing recorded data for the response of structures and soils to real earthquake events. Experimental data utilizing earthquake simulation techniques such as blasts and shaking table tests were sought. These data are useful in understanding the dynamic behavior of various types of structures undergoing seismic motions. They could also be valuable for verifying and validating analytical techniques for computing the seismic response of a soil-structure system.

For the past two decades or so, comprehensive experimental activities have been undertaken throughout the world. Large-scale field tests were performed to study the seismic behavior of typical NPP containment structures such as the Lotung and Hualien projects. Simulation tests using blasts were achieved in the SIMQUAKE I project. Field tests were also conducted on actual reactor structures where seismometers were installed on the structures and various locations in down-hole arrays, to collect response data to actual earthquake events such as Humbolt Bay and Fukushima. A brief description of some of the recorded data is provided in this section.

At the beginning of this project, it was thought that data sources limited only to free field data could be of use in definition of the free field input motion. At the advice of the Peer Review Panel for the program, it was decided that these data sources would not be of interest since questions concerning the definition of the free field motion would not be included in the study. These potential data sources have therefore been eliminated from this report.

SIMQUAKE I [EPRI, 1981]

SIMQUAKE I was a series of high explosive tests designed to simulate earthquake effects on nuclear power plant models. These test were performed near Albuquerque, NM, during the spring 1977. Two arrays of high explosive were placed in front of the structures to be tested. Each of the arrays was about 200ft wide and 100ft deep. Detonation of the high explosives produces a traveling wave within the soil in front of the arrays simulating an earthquake wave. The generated waves were generally of shorter duration and higher particle velocities than found with actual earthquakes. As an example, the spectra of the SIMQUAKE motion at 60 m from the detonation is very similar to the USNRC Regulatory Guide 1.60 spectra, anchored at 0.75 g, at frequencies greater than 3 cps but falls below the Reg. Guide spectra at lower frequencies.

The test structures were cylindrical and sized to represent 1/48, 1/24, and 1/12 scale models of containments. The largest of the models was 10ft in diameter, 15ft high, and weighed 39 tons. The structures were placed on the surface, embedded 25% of the height, and buried to twice the height.

Ground motions were measured at various ranges and depths with velocity and acceleration gages. The free field readings were taken from the surface down to 62ft and from 25ft in front of the array to 300ft behind the test structures. The test structures are located 120ft and 150ft from the explosive array. Measurements in the structure were made with accelerometers and with pressure gages at the soil-structure interface.

Tests results are available at two different ground motion levels; one with the detonation occurring at the front array and one with the detonation at the back array. The highest input levels resulted in separation at the soil-structure interface for some of the models.

Although the levels of input are sufficiently large so that non-linear separation effects could be evident, it is thought that this test series would not be appropriate for benchmarking due to the much shorter duration and other characteristics of the free field motions which are considered not to be representative of real earthquakes.

Humbolt Bay [Velera, 1977]

The Humbolt Bay Power Plant is located on the California coast southwest of Eureka City. The power plant has three units, two of which are fossil fuel units and the third unit is nuclear. The nuclear unit has been decommissioned. While it was still operating during the 1970s, strong motion instruments were installed in both the structure and the surrounding soils. The June 7, 1975 Ferndale earthquake (magnitude approximately 5.5 on the Richter scale) had its epicenter approximately 15 miles south of the plant site and triggered the strong motion instruments at the Humbolt Bay Power Plant. Although the duration of strong shaking recorded was only approximately 3 to 5 seconds, the baseline-corrected peak accelerations developed in the free field were 0.35g in the transverse and 0.26g in the longitudinal directions, respectively, making these the strongest earthquake motions to which a nuclear power plant had been subjected to at the time.

The design features for the nuclear unit included a buried reactor structure within the Refueling Building, which is of particular interest to this study. The buried reactor structure consisted of a massive concrete caisson embedded to a depth of approximately 85ft (26m) below the ground surface. The various surrounding structures were lightweight structures and were founded at or close to the ground surface. The soils at the site consist of medium-dense to dense sand underlain by stiff clay and then a deep bed of dense sand with some clay. The soil conditions at the plant site were well studied and documented. However, it is believed that no pressure transducers were installed to provide the seismic induced soil pressure data.

Lotung and Hualien [EPRI, 1989, Miller, 2001]

Two test series were conducted in seismically active regions in Taiwan during the mid 1980's to 2000. Both sites are located on the east coast of Taiwan. A quarter-scale model for containment structure was constructed at each site. The test structures were cylindrical in shape, 35ft in diameter, and about 53ft tall. The structure is embedded about 31% of the height. The soil at Lotung is soft having a shear velocity equal to 300 fps, while the soil at Hualien has a shear wave velocity equal to about 1000 fps.

The test structures were instrumented with accelerometers placed on the roof, mid-height, and basemat. Accelerometers were placed at several radial distances from the center on the roof and basemat. The field free instrumentation was placed on the ground surface along three radial lines from the structure. Along each radial line surface instruments were located at 0.5, 1, 2, 3.5, and 5.5 diameters from the center of the model. Accelerometers were also located in three downholes down to depths of 170ft.

The tests conducted at both sites were very similar. Shaker tests were performed both before and after backfill. Five shaker tests were done in each series: EW excitation with shaker on roof,

NS excitation with shaker on roof, EW excitation with shaker on basemat, NS excitation with shaker on basemat, and vertical excitation with shaker on basemat. Data was then collected as earthquakes occurred above a “trigger” level. There are probably data from about 50 earthquakes at each site with the largest free field motion being about 0.15 g.

Additional arrays (SMART I and SMART II) were also placed at each of these sites. These arrays were primarily surface and extended over a rather large area. The surface array data is not too useful for the present study. However, both SMART I and SMART II contain a few 50m to 100m deep vertical arrays which may be useful to complement the Lotung and Hualien data.

About a dozen organizations made predictions of the response to the various earthquakes and then compared the predictions with the measured responses. However, no separation of the wall from the surrounding soils was predicted. This may be due to the fact that the site is fully saturated. It may also be further complicated by the evident anisotropy of the site soil properties.

Fukushima [Miller, 1985]

The Fukushima Nuclear Power station, located in Japan, was subjected to a 7.4 magnitude earthquake in June 1978. The peak ground acceleration at the plant was about 0.1 g. The structure is embedded about 30% of the height into a rather stiff soil.

Free field measurements were taken at depths of: 0, 14 m, 24 m, 35 m, and 50 m below the surface. Measurements were also taken at four elevations in the structure ranging from the basement to near the roof.

The measured data was compared with predictions made with a lumped parameter [Yamamoto, 1999] code and found to agree quite well. However, based on informal discussions with representatives from Japan, it was concluded that this data was not appropriate for investigating the effect of seismic induced soil pressures.

Based on the above discussion, it is concluded that other sources of test data would be needed to assess the effect of seismic induced soil pressures.

2.5 Potential Issues Related to SSI Effects for DEB Structures and Planned Studies

The literature review discussed above uncovered several areas where uncertainties exist in the analytical methods used to evaluate the seismic response of deeply embedded facilities. The major uncertainties found during the review are: the effect of deep embedment on the relative significance of kinematic interaction; the extent to which non vertically propagating shear waves may be more important for deeply embedded structures than for those with shallow embedment depth; the effect of nonlinear effects (separation of wall and soil and soil properties) on wall pressures; and the impact of deep embedment on the accuracy of side wall impedance functions calculated with standard methods, as well as the spatial incoherence issue. These issues and associated key attributes of importance, as well as computational requirements to address them are provided in the following Table.

Table. Summary of Key Issues Important to SSI

Key Issues	Attributes of Importance	Current Computational Ability
Kinematic Interaction (KI)	The purpose is to incorporate the variability in free-field ground motion on SSI response	Automatically incorporated into SASSI, the standard code used to determine linear SSI response. SASSI performs computations in the frequency-domain where variation of KI with frequency can be explicitly evaluated. Incorporated into time-domain computer codes that can track wave passage effects.
Free-Field Seismic Motions	Input seismic motions are typically defined in terms of vertically propagating P, SH or SV motions. SSI response directly influenced by definition of wave type selected for the input motion.	All computer codes typically utilized to address SSI response issues can address issue of free-field input motion characteristics. Issue of treatment of boundary effects must be carefully evaluated for each computer code since results are directly influenced by definition of site boundary conditions.
Wall Pressures and Other Nonlinear Effects	Nonlinear effects have been found to be extremely important in determining SSI responses. These effects can include: (I) nonlinear material constitutive properties and (II) nonlinear stress transfer at soil-structure boundaries. Either or both effects may be important.	The SASSI Code can only treat the linear problem. The impact of nonlinear material models is typically handled in preliminary 1D site response evaluations (SHAKE, CARES). These models have a major impact on input ground motions used for the SSI evaluations. Nonlinear effects can currently only be treated in time-domain codes having this capability (LSDYNA, ABACUS). However, detailed calculations needed to address these effects require extensive run times. The codes require the definition of various input parameters to properly incorporate these effects within the model. These parameters are difficult to determine in the laboratory.
Sidewall Interaction	For the linear problem, sidewall interaction effects are	The SASSI Code can treat this problem correctly for a given

	important to properly couple the free-field kinematic interaction effect into the SSI problem.	free-field configuration and input motion. Simplified SSI codes (e.g., CARES) make use of parameters from a library of solutions available in the literature. Therefore, they require the determination of these effects for a suite of configurations appropriate for the problem under consideration.
Incoherence	The influence of incoherence has a major impact on high frequency (greater than 10 Hz) SSI response of typical critical facilities. This is particularly true on facilities sited in the CEUS on hard rocks.	The codes typically available to evaluate these effects are currently in their developmental stage. In addition, the data used to develop the incoherence parameters is relatively restricted. Formulation of these properties for hard rock sites, for which the effects are most pronounced, is currently lacking.

The following provides detailed discussions of the key issues and their importance to the SSI effect that are related to DEB structures.

a. Kinematic Interaction

The results of kinematic interaction are the response of a rigid, massless foundation to the free field seismic motion. This calculation is done separately with the lumped parameter SSI solutions and the resulting foundation motion is used as input to the inertial interaction problem. In many cases, kinematic interaction effects are neglected since this has been shown to be conservative for shallow depths of burial. The importance of kinematic interaction effects for deeply embedded facilities should be investigated. The kinematic interaction solutions given in Pais and Kausel are used to determine their magnitude for facilities which are deeply embedded. These solutions are benchmarked against results obtained using SASSI before proceeding with this activity.

The soil characteristics, depth of burial, and the angle of the incoming seismic waves are varied for the solutions. Soil models considered include: uniform sites having low shear wave velocities, uniform sites with high shear wave velocities, layered sites (especially with the layering selected so as to introduce relatively large changes in the free field motion over the burial depth), and sites with both large and small depths of burial. The Pais – Kausel models are used for the uniform soil sites and SASSI are used for the other sites. The depth of burial is varied from 30 % of the radius of the foundation to the full diameter. Specific details of the models used for these parametric studies are described in Section 3.

The angle of the incoming seismic waves is varied from vertically propagating to near horizontally propagating. Spectra of the motions including kinematic effects are then compared with spectra of the free field motions (neglecting kinematic interaction) to assess the significance

of the effects. Criteria are then developed defining those ranges where neglect of kinematic interaction is conservative. The degree of conservatism in the solutions is then defined for those ranges where it is found to be conservative.

b. Free Field Seismic Motions

Current criteria recommend that one-dimensional vertically propagating shear wave models be used to evaluate the free field seismic response. If deemed necessary a 5% offset between the foundation mass and geometric center of the foundation may be modeled to account for torsional effects that may arise because of non-vertically propagating seismic wave fields. This has been shown to be adequate for facilities with embedment depths less than 30% of the foundation radius. The objective of this activity is to determine whether this simple criterion is adequate for foundations which are embedded more than 30% of the foundation radius.

Available recorded data are used to examine this question. Simple stick models representing the superstructure are placed on typical NPP foundations. Responses of the stick are then determined, now including inertial interaction effects, for the seismic waves propagating at the various angles. Comparison of these results should indicate the significance of the angle of the seismic waves. If found important, additional solutions are obtained for the same structural model with the center of the stick offset from the geometric center of the foundation. A comparison of these solutions with the solutions found above would then be made to evaluate the extent to which the offset model can compensate for the effects of non-vertically propagating seismic waves.

c. Wall Pressures and Other Non Linear Effects

The current criteria for seismic analysis discuss non-linear effects such as soil property dependence on strain, and separation between the wall and soil. The first is generally treated by iterative elastic solutions as discussed above. This approach has generally been found to be acceptable. The separation of soil and wall is often dismissed as unimportant for the depths of burial of typical facilities of interest. The significance of the separation effects is likely to change as the depth of embedment increases. More importantly, separation effects should be important for an evaluation of wall pressures. The objective of this activity is to investigate the extent to which separation effects may be important for both an evaluation of the overall building responses and the prediction of seismic load induced wall pressures.

The LS-DYNA computer code is a non-linear dynamic code that can model separation effects. This code is used to generate solutions for a range of problems and the results compared with those obtained using the SASSI elastic code. The SASSI models are varied by debonding some of the soil from the wall to determine if this could be used with SASSI to approximate the effects of separation. Solutions with both codes should be obtained for a range of problems where the following parameters are varied: soil properties, geometry of foundation, stiffness of foundation, and magnitude of the seismic input motion.

A primary objective of this activity is to evaluate the distribution of shears introduced by the seismic loading acting on the structure. Relative displacements of various elevations within the structure should also be followed as a check on the shear evaluations.

d. Sidewall Interaction

The lumped parameter SSI model is based on approximate impedance functions accounting for interaction effects along the walls of the foundation. These solutions have been shown to be adequate for foundations with depths of embedment less than 30% of the diameter. Most of the available approximate solutions are also based on problems where the soil on the side of the foundation is uniform. The objective of this task is to determine limitations to the approximate models.

The approximate solutions for the sidewall interaction models should be extended so that they may be used to determine equivalent interaction parameters for sites with soil layering over the depth of embedment and for sites with varying soil properties as one moves radially out from the foundation (such as might occur as a result of construction). Solutions obtained using SASSI should be compared with those obtained with a lumped parameter code (CARES).

e. Incoherence

Current approaches to assessing SSI effects on reactor facilities presume that a single deterministic definition of ground motion is available to describe the site ground motion to which the facility will be subjected. For the case of assumed vertically propagating waves (either direct SV or P waves), this ground motion is considered to be the same at all points at a given elevation (or depth below the ground surface). Any vertical variation in the ground motion is defined by means of one-dimensional site response evaluations. For the case of inclined SV or P waves, the presumption in SSI analysis is that ground motions vary at any one elevation only by a given phase delay, the so-called coherent wave passage effect. The relative time histories, measured from the time of arrival of the wave front, are assumed to be the same at any point in the free-field at the same elevation.

Actual recorded data (for example, Yamazaki, 1992), however, measured at sites where an array of embedded geophones are located across the site, indicate differences in ground motion from point to point. These differences, determined after an average coherent wave passage effect is removed, are found to be random, frequency dependent and increase as distances between points increase (Schneider, 1992, Abrahamson, 1991, and Abrahamson, 1992). On the basis of these characteristics, models of the random incoherence have been developed and incorporated into computer codes typically used to perform soil-structure interaction analyses (Wong, 1980, CLASSI, Lysmer, 1981).

On the basis of this formulation, recent recommendations have been made to incorporate these random ground motion effects into SSI evaluations. The numerical results generated to date indicate that for structures founded on relatively rigid foundations as compared to the free-field soil or rock, the in-structure response spectra decrease with increasing frequency. At frequencies up to 10 hz, the decrease is relatively small (of the order of 10% for average size foundations). At higher frequencies, the in-structure response spectra may be significantly reduced. The implication of this effect for evaluation of plants sited on hard rock in the CEUS is significant, since these spectra can have significant high frequency content. This effect, however, is still not incorporated into design guidance for critical facilities since various aspects of the approach require peer review and evaluation.

3. ASSESSMENT OF SIMPLIFIED VS. DETAILED METHODOLOGIES FOR SSI ANALYSIS OF DEB STRUCTURES

In Section 2.5, several SSI issues were identified which may be important when considering the seismic response of DEB structures and the methodologies used to capture these effects. Two methodologies are usually used to evaluate SSI effects, namely, simplified and detailed methods, respectively.

The simplified method makes required assumptions so that solutions for the free field and the structure are uncoupled. The detailed method treats the response of the free field and the structure as a coupled problem. The CARES computer code is used to represent the simplified approach and the SASSI2000 code is used to represent the detailed approach. This section provides a comparison of response predictions made by both methods. Of course, the prediction made using the detailed methodology is assumed to be the most accurate.

The response comparisons made in this section are in terms of response spectra. Three aspects of the SSI problem are considered in the study: kinematic interaction (the response of the free field with the soil located within the foundation volume removed), inertial interaction (the response of the free field and facility including the inertial effects of the facility mass and stiffness), and soil pressures acting on the facility walls. The first two of these are discussed in this section of the report; the soil pressures are discussed in Section 4. Before these are considered, the general approach is discussed. Finally, conclusions are drawn regarding the relative accuracy of the simplified method as compared with the detailed method.

3.1 Approach

A structure representative of those proposed for the new generation of nuclear power plants is analyzed by both methodologies. The horizontal and rotational responses of the structure are considered. The analyses are performed using several depths of burial and a range of soil conditions typical of what might be found at sites for the new plants. The seismic input to the problem is described with a rock outcrop motion anchored at 0.3 g ZPA.

The CARES code [Miller, 2000] is used to perform the calculations based on the simplified method and the SASSI code [Lysmer, 1999] is used to perform the calculations based on the detailed method. A detailed description of the typical facility is first given. This is then followed with a description of the codes and facility models used in making the calculations for each of these codes.

3.1.1 Description of Facility

The sample problems are selected with several objectives in mind. First, the structural and site conditions should, as much as possible, be representative of the next generation of NPP structures. Second, the problems should be simple enough so that it is feasible to conduct parametric studies within the time and budgetary constraints of the project. Third, the focus of the parametric studies should be on depth of burial effects.

The structural model is derived from the characteristics of a conceptual design for an advanced reactor shown on Figure 3.1.1-1. The cylindrical portion of the facility containing the reactor and the power conversion vessel is selected as the structure to be used in this study. This cylinder is 46 m long and has an outer diameter of 27 m. The actual containment consists of a variable thickness outer shell and several major walls spanning across the containment providing

both flexural rigidity and dividing the space into major areas. This is modeled with a uniform thickness cylindrical shell. The wall thickness (2 m) is selected to match the combined moment of inertia of the actual outer shell and major interior dividing walls. A sketch of the model is shown on Figure 3.1.1-2. The cross sectional area and moment of inertia of the cylindrical shell are 157.1m^2 and $12,272\text{ m}^4$ respectively.

A major parameter varied in the study is the depth of burial of this model. The model is buried to depths (E) equal to 25% (11.5 m), 50% (23 m), 75% (34.5 m), and 100 % (46 m) of the structural height. These depths of burial (DOB) correspond to DOB / radius ratios (E/R) of 0.85, 1.7, 2.55, and 3.4 respectively. Current technology has been limited to DOB at the lowest end of this scale so that the primary objective of the study is to determine whether the application of this technology leads to uncertainties when the DOB increases beyond 25 % of the facility height or 85 % of the facility radius.

The stiffness characteristics of the internal equipment are not included in the model. However, the mass of the equipment is lumped with the mass of the cylindrical shell; the combined weight is 92,202 kN. The weights of the basemat and roof are 40,474 kN and 4,448 kN respectively. The weights have been reduced to some extent from the actual weights to obtain structural frequencies that are likely to be interactive with the SSI frequencies. The frequencies of the above ground cantilever portion of the structure are found to be about 5 cps, 20 cps, and 78 cps for DOB = 11.5 m, 23 m, and 34.5 m respectively.

The following properties are used for the concrete:

- Compressive strength = $27,579\text{ kN/m}^2$
- Poisson's ratio = 0.2
- Damping = 2 % of critical
- Density = 23.2 kN/m^3

Three soil profiles are used in the study: a uniform soft site designated by Soil Column A, a uniform hard site designated by Soil Column B, and a layered site designated by Soil Column C. In each case the soil column is founded on bedrock at a depth of 80 m. The bedrock has a shear wave velocity equal to 2,000 m/s, a density equal to 17.28 kN/m^3 , and a material damping equal to 2 % of critical.

The uniform soft site has a shear wave velocity equal to 250 m/s and the uniform hard site has a shear wave velocity equal to 1,000 m/s. In both cases, the other soil properties are: weight density = 17.28 kN/m^3 , Poisson's ratio = 0.3 and material damping equal to 4 % of critical. The soil shear modulus and damping are not degraded as a function of shear strain in the soil column. In this way the level of the seismic input is not a parameter considered in the variation of parameter studies.

The layered soil column is selected to have a shear wave velocity equal to 250 m/s at the surface and 1,000 m/s at a depth of 80 m. Based on a relation between the low strain soil shear modulus and the confined soil pressure [Seed, et al., 1984], the variation of shear wave velocity between the surface and 80 m depth is determined:

$$V = 250 + 250.78 z^{1/4}$$

The other soil properties are the same as used for the uniform soil columns. A plot of the shear wave velocities for the three soil profiles is shown on Figure 3.1.1-3. The stepped velocity profile shown on Figure 3.1.1-3 is used to represent the variable soil property column for the CARES and SASSI runs.

The following soil column frequencies (defined as: shear wave velocity/4*DOB) are computed:

<u>SOIL COLUMN FREQUENCY (cps)</u>			
DOB (m)	Uniform Soft (Soil Column A)	Uniform Hard (Soil Column B)	Layered (Soil Column C)
11.5	5.4	21.7	13.5
23	2.7	10.9	7.5
34.5	1.8	7.3	5.3
46	1.4	5.4	4.2

The input motion is specified at a rock outcrop and standard convolution procedures for vertically propagating horizontal shear waves are used to compute the free field motions within the soil column. The rock output motion is developed according to the procedures specified in RG 1.165 together with the recent recommendations contained in NUREG/CR-6728. The spectrum, as shown on Figure 3.1.1-4, is used to represent the rock outcrop motion. The development of the outcrop motion begins with the definition of the dominant or characteristic event defined for the site hazard. For this generic study, the characteristic event was defined as a magnitude 7 earthquake located at a distance of 25 kilometers from the site. The peak acceleration associated with this dominant event was selected as 0.3 g. The rock outcrop motion, shown on Figure 3.1.1-5, is developed by modifying a seed motion until it “fits” the spectra shown on Figure 3.1.1-4. Convolution methods are then used to generate equivalent motions over the depth of the variable property soil column. Spectra of these motions are shown on Figures 3.1.1-6, 3.1.1-7 and 3.1.1-8 for soil columns A, B, and C, respectively. It can be seen that the motion at the base of column A is essentially the same as the outcrop motion whereas the motion at the base of the other columns is attenuated from the outcrop motion at the column frequencies (about 3 cps for both columns B and C). The shapes of the spectra are similar for columns B and C, but the column A spectra is quite different.

3.1.2 Simplified Model Using the CARES Program

The CARES Code is based on the simplifying assumptions that the foundation of the structure is rigid and that the free field response may be uncoupled from the structural response. The foundation of the structure is tied to the free field through impedance functions representing soil structure interaction effects. There are several sets of SSI coefficients that can be used in the code and each are based on analytic solutions for the impedance functions which are based on the rigid foundation assumption. The Beredugo – Novak [Beredugo, 1972] model is used for the current study.

Solutions for the free field responses are determined based on a vertically propagating shear wave model. “Average” free field motions (displacements and rotations) are computed at the foundation interface assuming that the foundation is rigid and massless (the kinematic interaction problem). These “average” motions are then used as input to the impedance functions supporting the structure (the inertial interaction problem).

There are several limitations of this approach which make it less reliable than the more rigorous methods such as used for the SASSI Code described in the following section:

- Structural deformations of the foundation are neglected.
- Base impedance functions are derived for the case where a rigid mat rests on the surface of an elastic half-space. The properties of these functions are likely to depend on the depth at which the mat is buried. Unfortunately, general solutions are not available for this case.
- Impedance functions for the sidewall are derived for plane horizontal slices neglecting the interaction between adjacent slices or the effect of depth of burial of the slice.

The first of these limitations is not likely to be significant since most foundations of nuclear plants are rigid. The last two could be significant especially for the larger depths of embedment. An objective of this study is to investigate the extent to which these limitations are significant.

There are three types of analyses that are incorporated into CARES:

- A free field solution is obtained giving the response at a desired location in the free field for a specified motion at any location in the free field. These solutions are based on a vertically propagating, horizontally polarized shear wave model. The soil properties are elastic. Soil property degradation effects may be included in an iterative manner so that the degraded soil properties used for the current solution are based on shear strains found in the previous solution.
- Kinematic interaction solutions, yielding “average” foundation displacements, are found based on the Iguchi [Iguchi, 1982] model. Rigid body displacements (horizontal deformation and rotation) of the foundation are found through “best fits” to the free field displacements determined through the free field portion of the code. Additional displacements are then computed which relieve the foundation surface tractions. The sum of these two solutions represents the kinematic response of the structure.
- Inertial interaction effects are computed by using the kinematic interaction solutions as input to the SSI impedance functions. The structure is modeled with lumped masses and structural elements which can be: 3-D beams, shear walls, or springs. All of the solutions are carried out in the frequency domain and FFT methods used to convert to the time domain when required.

The following specific models are used to apply the CARES code to these analyses. The soil columns are divided into 2.5 m layers and extend to a depth of 80 m (location of bedrock). The soil convolution portion of the code is then used to generate free field time histories at each layer. These time histories are then used as input to the kinematic interaction portion of the code to generate foundation displacement and rotation histories that include the kinematic interaction effects. Response spectra of the surface and basemat motions are then generated and compared with the SASSI kinematic interaction effects as discussed below.

The next step in the solution is to determine the total response of the facility including the inertial interaction effects. The cylindrical structure is modeled as a lumped mass beam as shown

on Figure 3.1.2-1. The 9 lumped masses are equally spaced along the 46 m beam. The masses of the cylinder and internal equipment are equally spaced along the beam. The mass of the roof and basemat are, of course, included in the top and bottom masses respectively. The interaction forces, horizontal shear and moment, are placed at the bottom node and computed from the interaction impedance functions based on the difference between the rigid body horizontal displacement and rotation of the foundation and the horizontal and rotation computed from the kinematic interaction model as discussed above. The impedance functions computed within CARES allow for constant soil properties over the depth of burial and constant (but different) soil properties below the foundation.

To satisfy these requirements average properties are used for each. The soil properties below the foundation are averaged over a depth equal to the diameter of the foundation. The properties of the beam elements above grade are taken as the moment of inertia and shear area of the cylindrical shell as discussed above. The stiffness of the beam elements below grade are increased to account for the support provided by the soil along the sidewall. The beam stiffness and sidewall soil interaction stiffness are considered as parallel elements in this model.

3.1.3 Detailed Model Using SASSI Program

The detailed models for the SSI analysis use the sub-structuring method as implemented in SASSI 2000 developed by Lysmer and his team at U.C. Berkeley (Lysmer, 1999). The SASSI program has gone through extensive improvement in the past ten years. In addition to the sub-structuring methods such as the flexible volume, flexible boundary and rigid boundary methods as in the previous versions, SASSI 2000 implemented a new subtraction method, which the BNL study used to carry out the SSI response calculations.

In the detailed finite element models developed using the SASSI 2000 program, the portion of the structure below the ground surface is modeled with explicit finite elements (e.g., 3-D bricks and shells), while the superstructure above the ground surface is represented with simple lumped masses and 3-D beams. The models are developed for different embedment conditions, ranging from shallow embedment to full burial. A typical SASSI DEB model is shown in Figure 3.1.3-1. Due to the symmetric configuration of the structure, only half of the structure is modeled with the plane $y=0$ as the symmetry plane. As shown in this figure, the basemat is modeled with brick elements and the sidewalls and internals are modeled with shell elements. The base of the superstructure is connected to the sidewalls by rigid links to simulate the rigid diaphragm of the floor expected to exist at grade level. In order to apply the subtraction method as implemented in SASSI 2000, the nodes at the boundary of the excavation need to be identified as the interaction nodes and the volume of the excavated pit is modeled.

Generally speaking, for computing the seismic response, there is no advantage in splitting the motion into components caused by kinematic and inertial interactions. However, for the assessment of the embedment effect, it is important to understand the role that the kinematic interaction plays. To this end, the kinematic interaction response can be easily computed in the SASSI model by assuming nearly rigid stiffness and zero mass for the structure.

3.2 Embedment Effect on Kinematic Response of DEB Structures

Two aspects of this problem are considered. First, the effects of angle of incidence of the seismic wave on the kinematic interaction problem are investigated. Second, the results obtained for the kinematic interaction problem using both the SASSI and CARES computer codes are compared.

3.2.1 SASSI Analysis of DEB Structures Subject to Incident Waves

In this section, the effects of angle of incidence of the seismic waves on the kinematic interaction are investigated. Two types of waves are studied: SH and SV waves. The angle of incidence is measured from the vertical axis to the direction of wave propagation and is specified at the base of the soil column. For uniform soils, the incidence angle remains constant as the wave propagates through the site, while for layered sites such as the soil column C, the initial angle of incidence as specified at the base of the soil column becomes smaller as the wave propagates up towards the ground surface [Wolf, 1985].

In the BNL study, for the SH wave, the incidence effect is analyzed for the range of zero to about 90 degrees and the input ground motion is specified at the ground surface and remain the same for the various incident angles. Since both P and SV reflected waves are associated with SV incidence wave, and a reflected P-wave does not exist for shallow incident SV-wave, a critical angle of incidence exists for the SV-wave. The critical angle of incidence is a function of Poisson ratio of the soil and is determined by the following relation [Wolf, 1985]:

$$\Phi_{cr} = \frac{\pi}{2} - \arctan \sqrt{\frac{1}{1-2\nu}}$$

in which, Φ_{cr} represents the critical angle of incidence and ν is Poisson's ratio. For ν equal to 0.35, Φ_{cr} is equal to 28.7 degrees which is the maximum incidence angle of the SV waves in this study.

SSI analyses, using SASSI, are performed for the three soil conditions, as described in Section 3.1.1, to examine the effect of angle of incidence for various depths of embedment ranging from 25% to 100% of the structural height. The SSI responses of the structure are obtained in terms of the 5% damping response spectra at the basemat center and the surface center of the structure. The spectra are presented in Figures 3.2.1-1 through 3.2.1-10 for the soft uniform soil column, Figures 3.2.1-11 through 3.2.1-20 for the hard uniform soil column, and Figures 3.2.1-21 through 3.2.1-40 for the variable property soil column.

For the soft uniform soil column (Soil Column A), Figures 3.2.1-1 through 3.2.1-4 represent spectral plots for SH-waves with incidence angles from 0 to 90 degrees. As shown in these figures, the incidence angle has no effect on the translational acceleration response spectra for shallow embedded structure. Even for the fully burial case, only a small effect is observed at the major peak response and the vertically incident wave appears to induce the highest peak response.

In addition to the translational motion, an SH-wave also induces torsional motion on the structure. The torsional spectra for various incidence angles are displayed in Figures 3.2.1-5 to 3.2.1-6. Note that SASSI prints out the torsional response in units of radians per second squared divided by the gravitational constant. The same units are used on the spectra, shown on Figures 3.2.1-5 and 3.2.1-6. These spectra show that the torsional response increases as the wave propagates towards the direction parallel to the ground surface. The maximum translational peak acceleration induced due to torsion was also examined. Figure 3.2.1-5 shows that the peak spectral acceleration is about 0.0045rad/s²/g. Using the average radius of the structure which is 12.5m, the maximum translational peak spectral acceleration caused by the torsional response would occur at the edge of the structure and would be equal to 0.05g, which is less than 5% of the corresponding translational peak spectral acceleration shown in Figure 3.2.1-2. Therefore, from a practical standpoint, the torsional response can be neglected.

For the SV-wave, the spectra for various incidence angles up to the critical angle are presented in Figures 3.2.1-7 through 3.2.1-10. Again, these figures show that the spectra are not affected by the angle of incidence when the structure is shallow embedded. However, significant reduction is observed due to the effect of incidence angle for the fully buried case. This is because the structural response is primarily controlled by the kinematic interaction and less effect due to inertial interaction; whereas the seismic response of a shallow embedded structure is dominated by inertial loadings. It is also shown in these figures that a vertically propagated SV-wave generates the highest peak spectral response.

For the hard uniform soil column (Soil Column B), Figures 3.2.1-11 through 3.2.1-14 present the spectra for the SH-wave with various incidence angles, and Figures 3.2.1-17 through 3.2.1-20 for the spectral generated by the SV-wave. As shown in these figures, the incidence angles have practically no effect on the spectral response, which is consistent with the findings of previous SSI studies on stiff sites. For the torsional response as shown in Figures 3.2.1-15 to 3.2.1-16, the higher peak response is associated with the shallower embedded structure and shallower SH-wave, which is consistent with the soft soil column as discussed in the previous paragraph. The same procedure in the previous paragraph is followed to calculate the torsional effect on the major peak spectral acceleration. Figure 3.2.1-12 shows that the major spectral peak appears near 3 Hz and the maximum torsional spectral value near 3 Hz is about 0.0062g, which in turn produces 0.0078g translational spectral acceleration at the edge of the structure. However, compared to the translational spectral peak value shown in Figure 3.2.1-12, the torsion induced translational spectral acceleration is less than 7%. Therefore, in this case, the torsional effect could be ignored.

For the variable property soil column (Soil Column C), the translational response spectra associated with inclined SH-waves are presented in Figures 3.2.1-21 through 3.2.1-28, and the spectra associated with inclined SV-waves are displayed in Figures 3.2.1-33 through 3.2.1-40. These figures indicate negligible effect due to incidence angles, except for the spectra induced by SV-waves. In this case, the spectral amplitude near 20 Hz shows a bump up for the waves propagating near the critical angle of incidence; a similar effect is also observed for the other two soil columns. For the torsional responses induced by the SH-waves, Figures 3.2.1-29 through 3.2.1-32 show the torsional spectra for various burial conditions. As depicted in these figures, the torsional effect increases as embedment of the structure becomes shallower and the incidence angle approaches to 90 degrees. Further, applying the same approach for calculating the torsional induced translational spectral acceleration as for soil columns A and B, it is readily shown that the torsion induced translational response is small and neglecting it can be justified. These observations are consistent with those analyzed for the other two uniform soil columns.

3.2.2 SASSI vs. CARES Analyses of DEB Structures Subject to Vertical Incident Shear Waves

Solutions for the SASSI and CARES models of the facility described in Section 3.1.1 are completed for the kinematic interaction problem. The specific models used for the CARES and SASSI solutions are described in Sections 3.1.2 and 3.1.3, respectively. Solutions are obtained for the 11.5 m and 46 m DOB for the uniform soil columns and for all four DOBs (11.5 m, 23 m, 34.5 m and 46 m) for the variable property soil column. Response spectra are obtained at the surface elevation and at the basemat elevation for each of the solutions. In all cases the spectra are generated for the case of 5 % damping.

The spectra are presented in Figures 3.2.2-1 through 3.2.2-4 for the soft uniform soil column, Figures 3.2.2-5 through 3.2.2-8 for the hard uniform soil column, and 3.2.2-9 through 3.2.2-16 for

the variable property soil column. The free field surface and basemat spectra as appropriate are included for all cases so that the significance of kinematic interaction effects may be evaluated.

Detailed comparisons of the SASSI and CARES spectra are given in Section 3.4 below. Some preliminary comments are given here. For the soft uniform soil column:

- Since the free field spectra are quite different from the kinematic interaction spectra at the surface for frequencies greater than 2 cps, it can be concluded that kinematic interaction effects are important.
- Kinematic interaction effects are much less significant at the basemat elevation and could probably be neglected.

The CARES predictions at both the basemat and the surface are close to the SASSI predictions for the shallow depth of burial. The two predictions for the deeper depth of burial are close at the basemat, but depart somewhat at the surface. At this location the CARES predictions are generally higher than the SASSI predictions.

For the hard uniform soil column:

- Kinematic interaction effects are not significant for the shallow DOB but are significant for the deepest DOB.
- For the deepest DOB, the SASSI kinematic interaction predictions are higher than the CARES predictions at the surface, especially at frequencies greater than 3 cps. The predictions are quite close at the basemat.

For the variable property soil column:

- The SASSI and CARES predictions are very close for the 11.5 m and 23 m DOBs.
- The CARES predictions at the surface are generally lower than the SASSI predictions for the 34.5 m and 46 m DOBs at frequencies greater than about 2 cps.
- The CARES and SASSI predictions are quite close at the basemat, except for the region around 10 cps where the SASSI predictions exceed the CARES predictions.
- In general, kinematic interaction effects are significant for this soil column for all cases.

3.3 Embedment Effect on SSI Response of DEB Structures

The same problems are solved for the inertial interaction problems using both SASSI and CARES. Response spectra are obtained at the roof elevation and at the basemat elevation for each of the solutions. In all cases the spectra are generated for the case of 5 % damping.

The spectra are presented in Figures 3.3-1 through 3.3-4 for the soft uniform soil column, Figures 3.3-5 through 3.3-8 for the hard uniform soil column, and 3.3-9 through 3.3-16 for the variable property soil column.

Detailed comparisons of the SASSI and CARES spectra are given in Section 3.4 below. Some preliminary comments are given here. For the soft uniform soil column:

- The SASSI and CARES predictions are similar for the 11.5 m embedment, except at the roof where the SASSI prediction exceeds the CARES prediction at about 2 cps.

- The SASSI and CARES predictions are quite close at the basemat for the 46 m depth of burial, but the SASSI predictions exceed the CARES predictions at the roof.

For the hard uniform soil column:

- The SASSI and CARES predictions are generally very close for both the shallow and deepest DOBs.

For the variable property soil column:

- The SASSI and CARES predictions are generally very close for the 11.5 m and 23 m DOBs except for the shallower DOB at the roof and at about 6 cps, where the SASSI prediction exceeds the CARES prediction.
- The SASSI and CARES predictions for the two deeper DOBs are somewhat different with the CARES predictions generally exceeding the SASSI predictions. The SASSI predictions exceed the CARES predictions at the basemat at about 10 cps.

3.4 Assessment of Analysis Methodologies for Computing SSI Response of DEB Structures

An assessment of the comparison of SASSI with CARES for the 16 kinematic interaction and 16 SSI spectra, presented in the previous two sections of the report, is made in this section. The following two spectral characteristics are examined to make these assessments:

- The peak spectral accelerations are compared between the CARES and SASSI predictions. The spectral peaks for the two predictions generally lie within the spectral broadening criteria (plus and minus 15%) so that the comparison can be made without consideration of the small frequency differences. It should be noted that the frequency comparisons between CARES and SASSI are quite good. The differences that exist between CARES and SASSI lie in the magnitude of the spectral peaks. The rating index used is defined as $[\text{CARES prediction} - \text{SASSI prediction}] / \text{SASSI prediction}$ or $(P_{\text{CARES}} - P_{\text{SASSI}}) / P_{\text{SASSI}}$. The SASSI prediction is assumed to be the more reliable of the two. The rating index is plotted as a function of depth of burial so that the reliability of CARES may be tested as the depth of burial increases. Of course positive indexes indicate conservative CARES predictions.
- The differences between the areas under the CARES spectra and the SASSI spectra are also compared. The rating index used is defined as $[\text{CARES area} - \text{SASSI area}] / \text{SASSI area}$ or $(A_{\text{CARES}} - A_{\text{SASSI}}) / A_{\text{SASSI}}$. The portion of the spectra where CARES predictions are less than SASSI predictions (negative index) may be offset by portions of the spectra where the opposite is true. To avoid this problem, the positive and negative areas are recorded separately and both are plotted. If desired, a comparison of the net area differences can be determined by algebraically adding the positive and negative areas at a given E/R.

The rating indexes based on peak spectral accelerations are shown on Figures 3.4-1 through 3.4-3. The indexes for the uniform soil columns are shown on Figure 3.4-1 for the kinematic interaction spectra and on Figure 3.4-2 for the SSI interaction spectra. If 10 % under predictions are considered to be tolerable, the CARES kinematic interaction results are acceptable for E/R ratios less than 2 and 3.5 for the soft and hard uniform soil columns, respectively. When SSI

spectra are considered, the CARES results are never acceptable for the soft uniform soil column and are acceptable for all E/R ratios for the hard uniform soil column. The differences for the soft column comparisons are discussed below. The indexes for the variable soil column are shown on Figure 3.4-3. It can be seen that CARES results are acceptable for E/R ratios less than 2.5 for the kinematic spectra and for E/R ratios less than 1.3 for the SSI spectra. The difference between the SSI roof spectra shown on Figure 3.4-3 is also discussed below.

The rating indexes based on kinematic spectral areas are shown on Figures 3.4-4 through 3.4-6 for the soft uniform soil column, the hard uniform soil column, and the variable soil column, respectively. If the 10 % difference is used as acceptance criteria, it can be seen that the CARES results are: acceptable for the soft uniform soil column, acceptable for E/R ratios less than 2 for the hard uniform and variable soil columns. The rating indexes based on SSI spectral areas are shown on Figures 3.4-7 through 3.4-9 for the three soil columns. It can be seen that the CARES results are never acceptable for the soft soil column and are acceptable for the hard uniform and variable soil columns for E/R ratios less than 2.

An examination of the detailed SSI spectra indicate that the CARES and SASSI results agree quite well for E/R ratios less than about 2, except for places where the SASSI spectral peaks exceed the CARES peaks (e.g., Figures 3.3-2 and 3.3-10). Since the frequencies at which the peak accelerations occur agree so well between the CARES and SASSI results, the radiation damping used in the CARES model is examined. The Beredugo – Novak [Beredugo, 1972] SSI model is used to represent the interaction coefficients between the structure and the free field. The sidewall interaction coefficients (both stiffness and damping terms) are derived by considering a horizontal slice of soil interacting with the structure. Wolf [Wolf, 1996] has shown that for the three dimensional problem a cut-off frequency exists below which the radiation damping is zero. This frequency occurs at the soil layer's natural frequency.

A parametric study is therefore performed to examine the extent to which reduction in the radiation damping included in the Beredugo – Novak may bring the spectral peaks predicted with CARES closer to those predicted with SASSI. Figures 3.4-10 and 3.4-11 show comparisons between the CARES and SASSI results when the radiation damping used in CARES is reduced to 70 % of the values contained in the present version of CARES. As may be seen the agreement would be quite good. Of course, a general rule to reduce the radiation damping in CARES to 70 % of the current values would result in conservative CARES predictions at other depths of burial. It is recommended that a study be undertaken to develop a suitable model for handling the radiation damping within CARES.

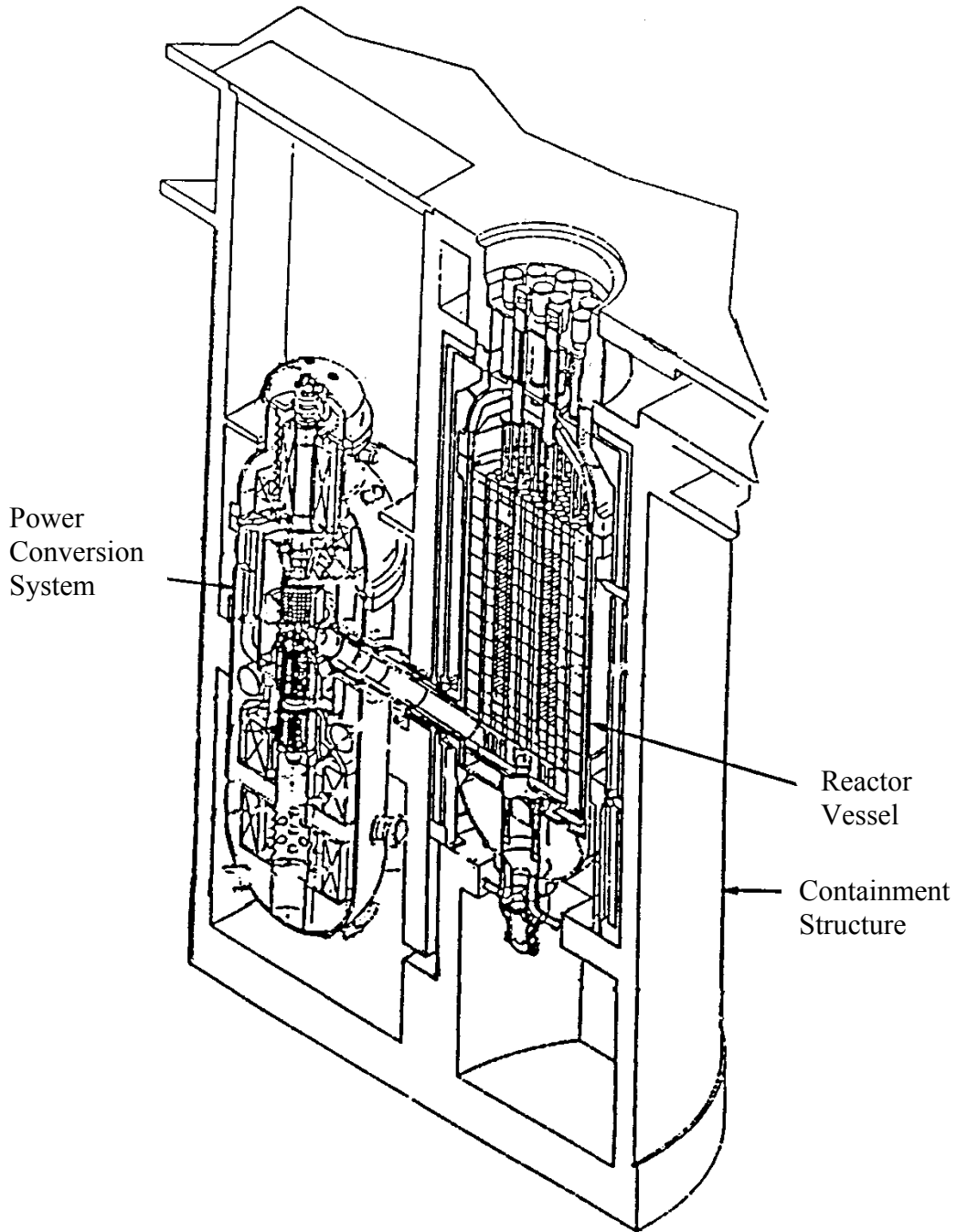
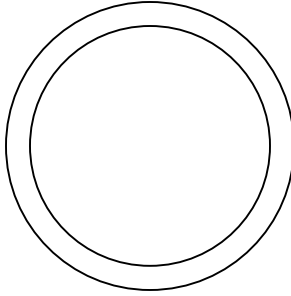
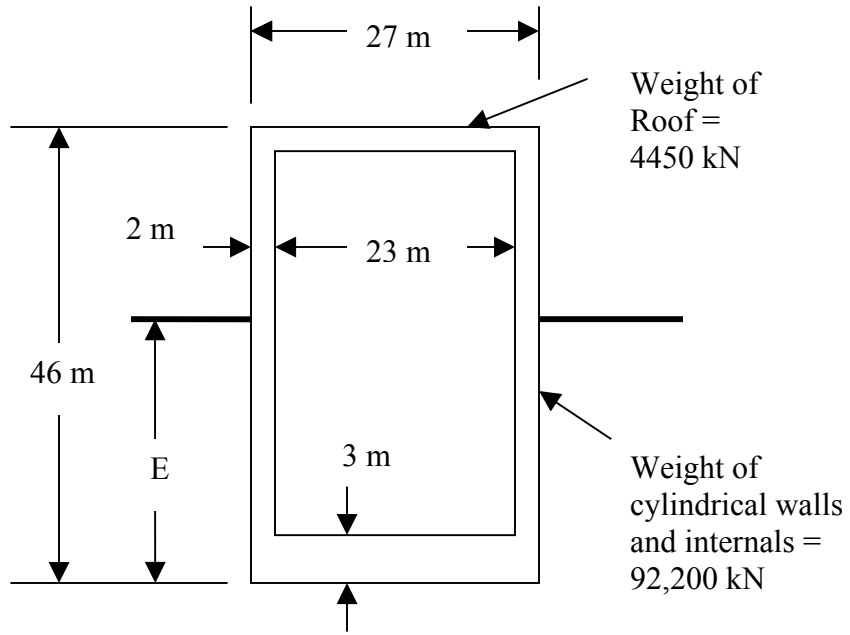


Figure 3.1.1-1 Sketch of Typical Advanced Reactor Containment Structure.



(a) Cross Section



(b) Elevation

Figure 3.1.1-2 Sketch of Analysis Model for Methodologies Assessments

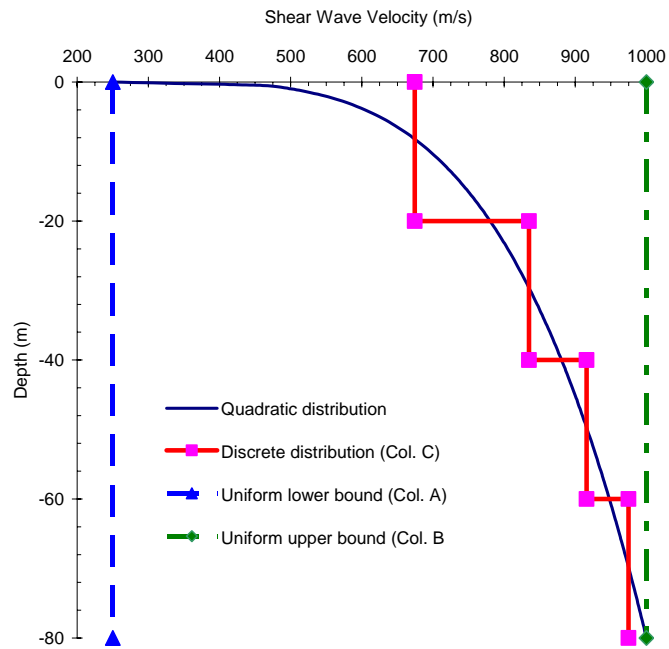


Figure 3.1.1-3 Site Soil Profiles Used for SSI Analyses

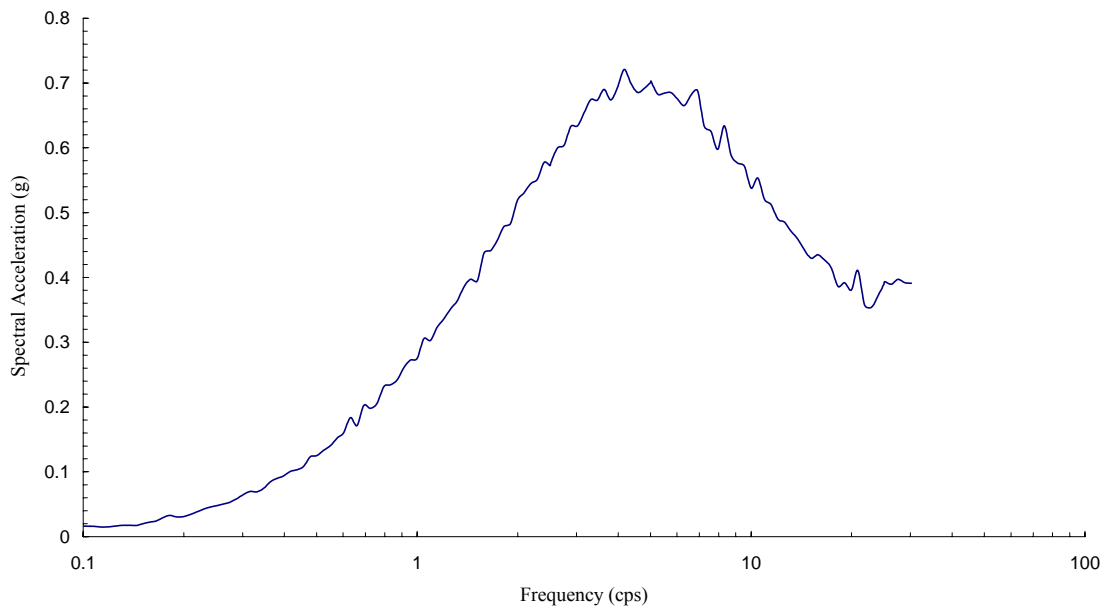


Figure 3.1.1-4 5% Damping Response Spectrum of Rock Outcrop Motion.

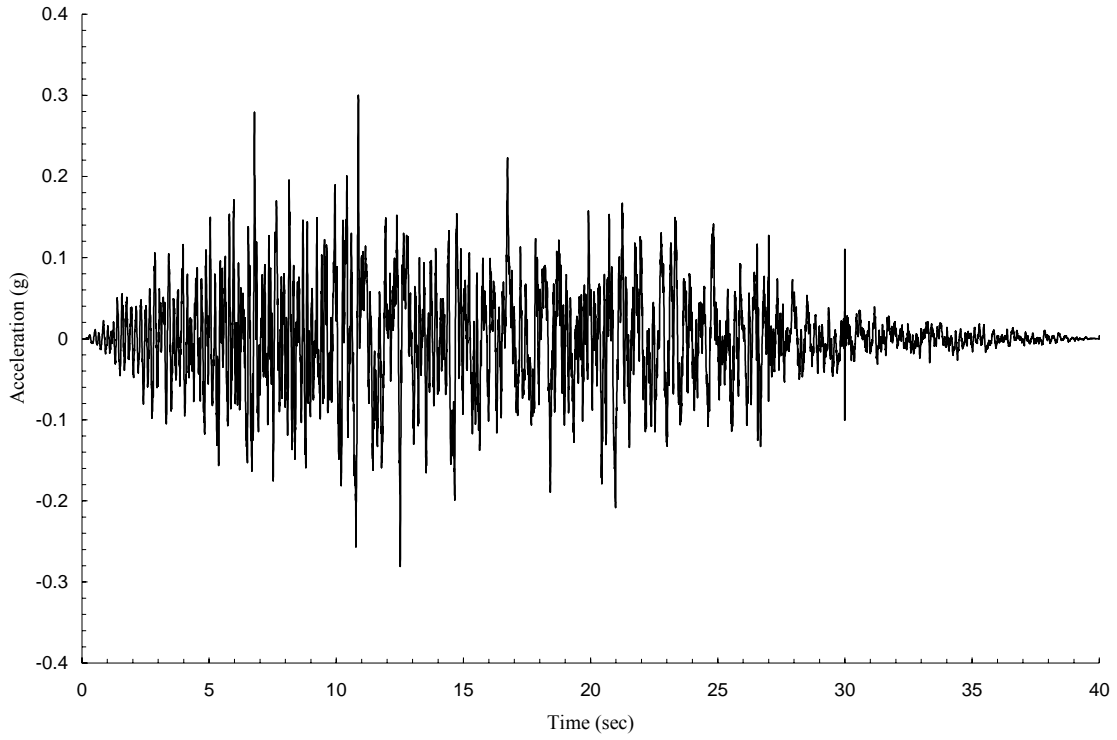


Figure 3.1.1-5 Rock Outcrop Accelerogram.

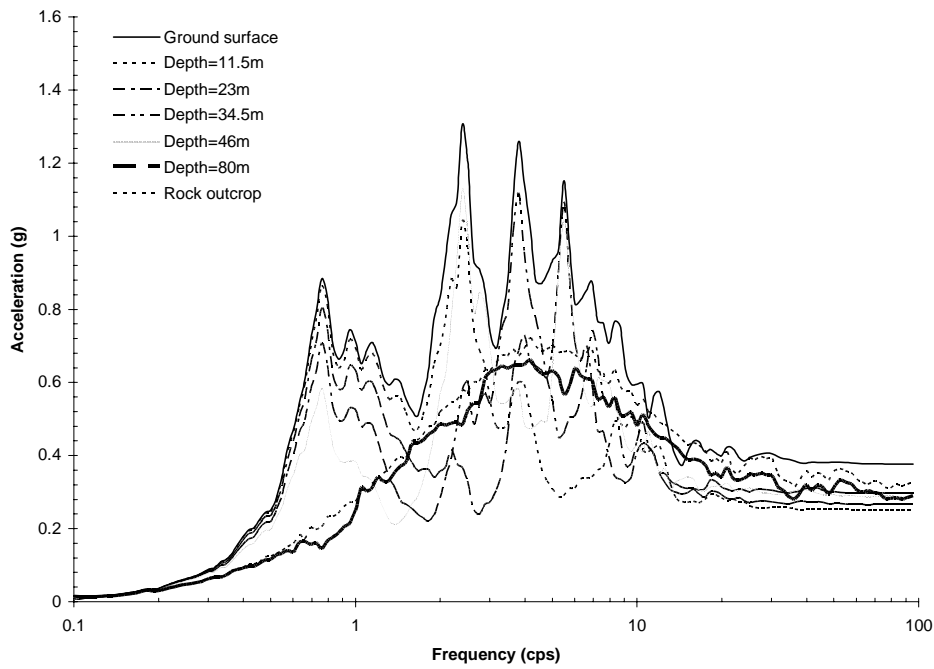


Figure 3.1.1-6 Free Field Response Spectra for Soil Column A

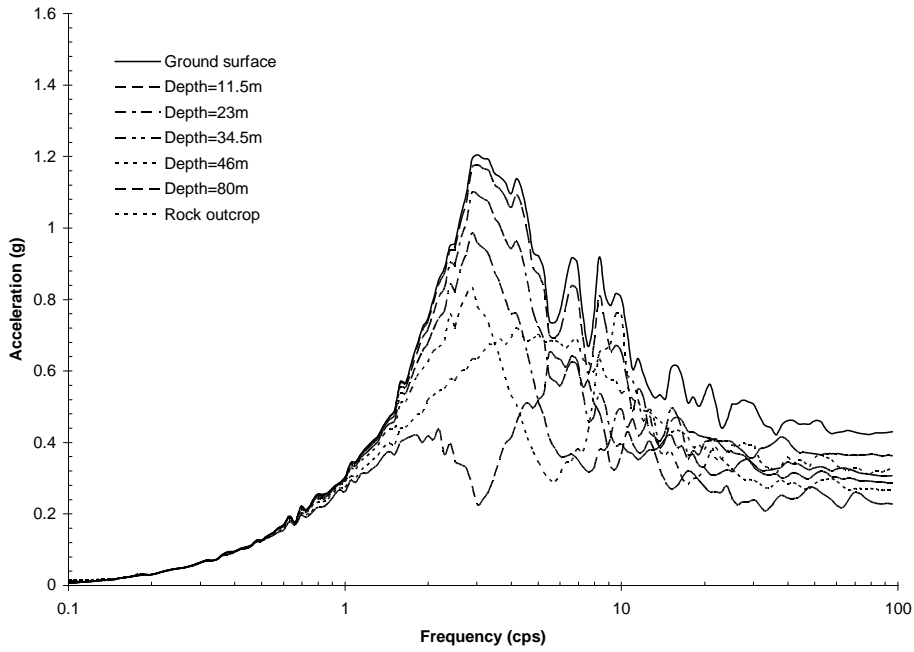


Figure 3.1.1-7 Free Field Response Spectra for Soil Column B

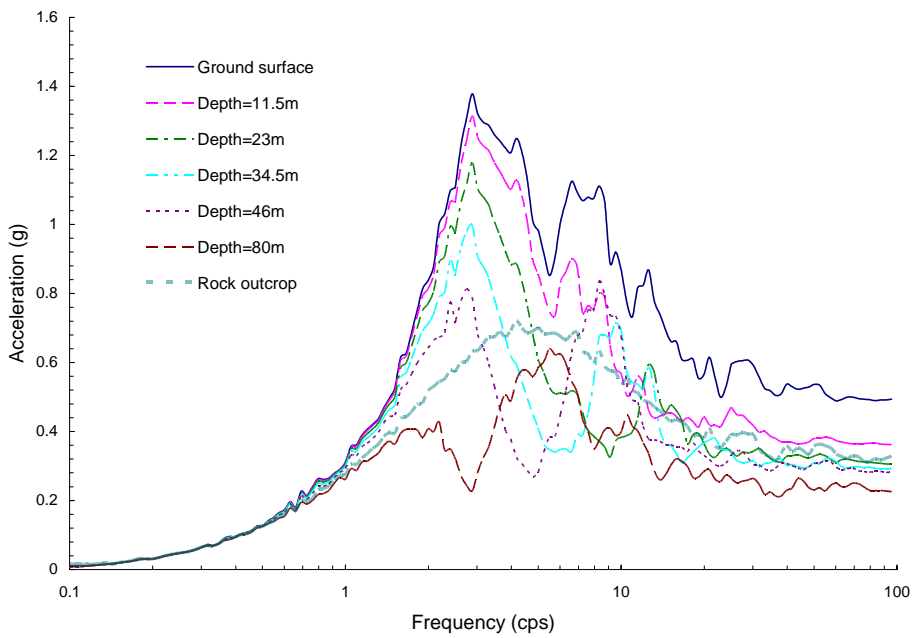


Figure 3.1.1-8 Free Field Response Spectra for Soil Column C.

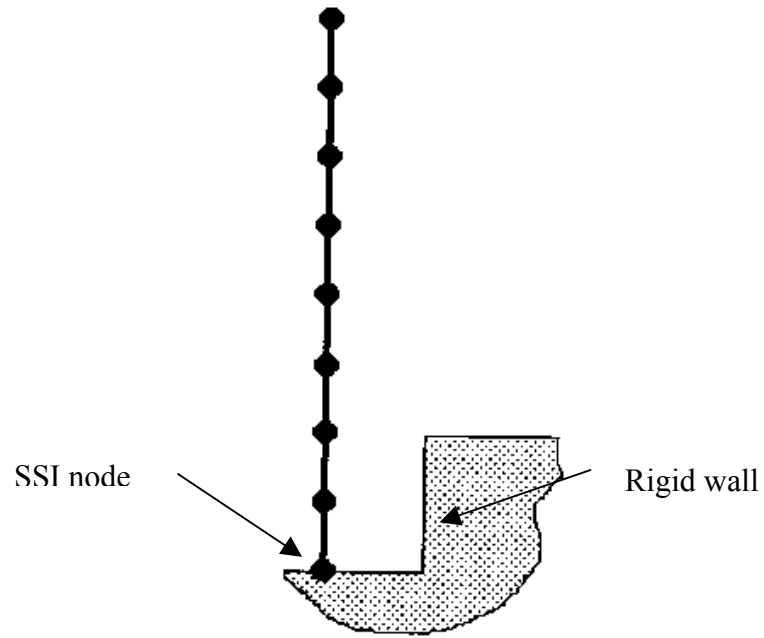


Figure 3.1.2-1 CARES SSI Model.

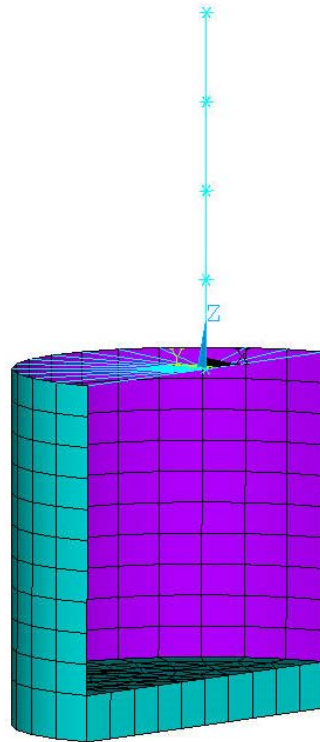


Figure 3.1.3-1 SASSI Structural Model.

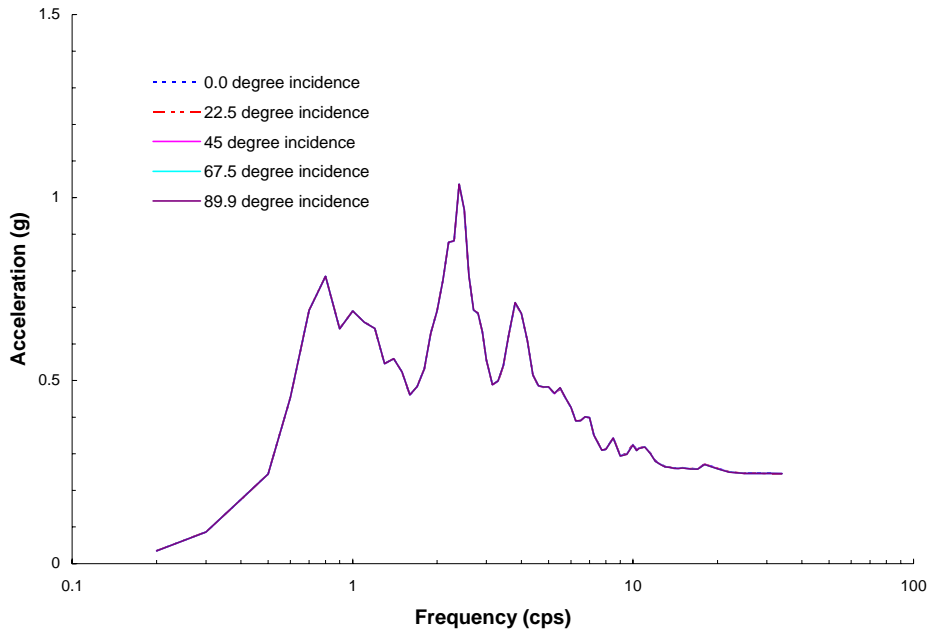


Figure 3.2.1-1 Translational Spectra for Soil Column A at the Basemat Center of SASSI Kinematic Model with 11.5m Embedment for Various Incident SH-Waves.

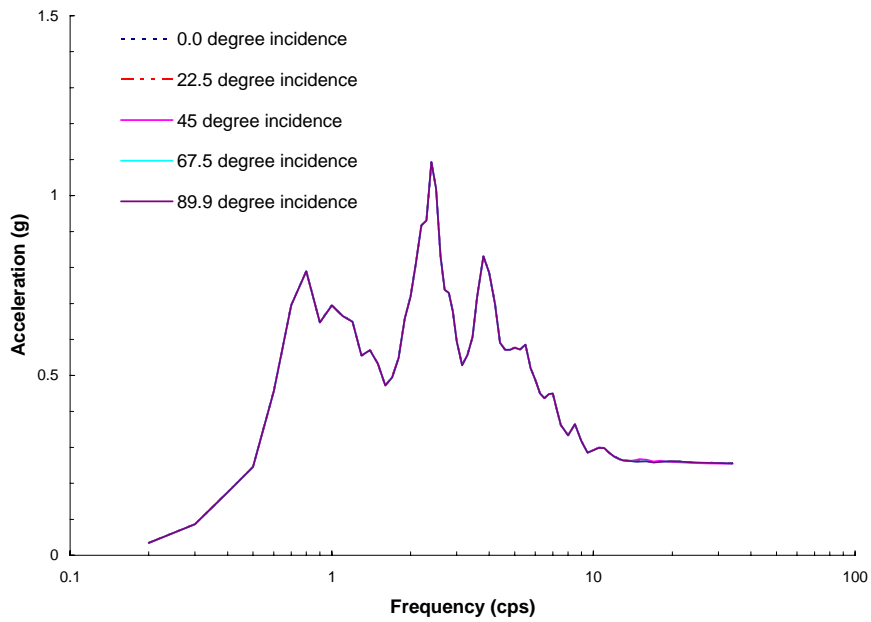


Figure 3.2.1-2 Translational Spectra for Soil Column A at the Surface Center of SASSI Kinematic Model with 11.5m Embedment for Various Incident SH-Waves.

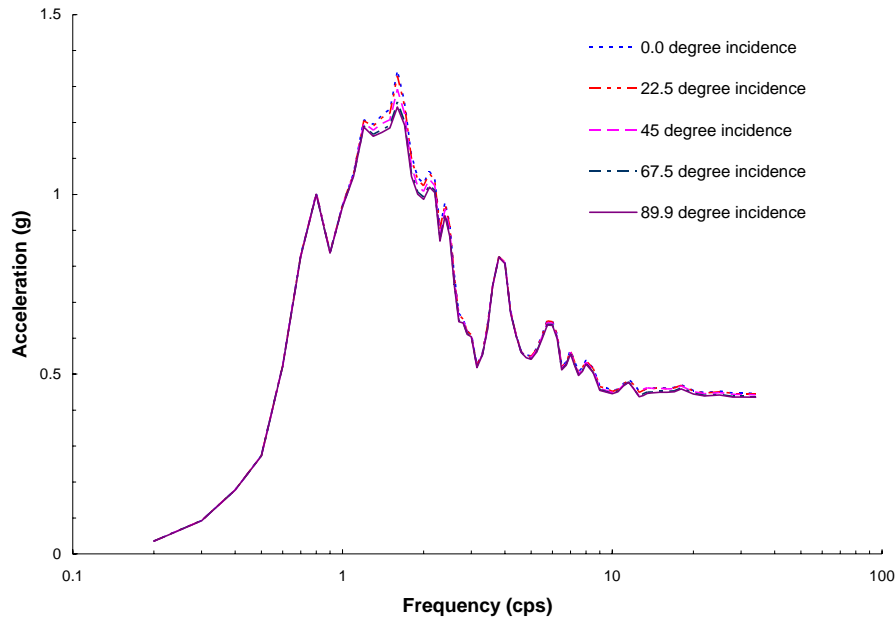


Figure 3.2.1-3 Translational Spectra for Soil Column A at the Basemat Center of SASSI Kinematic Model with 46 m Embedment for Various Incident SH-Waves.

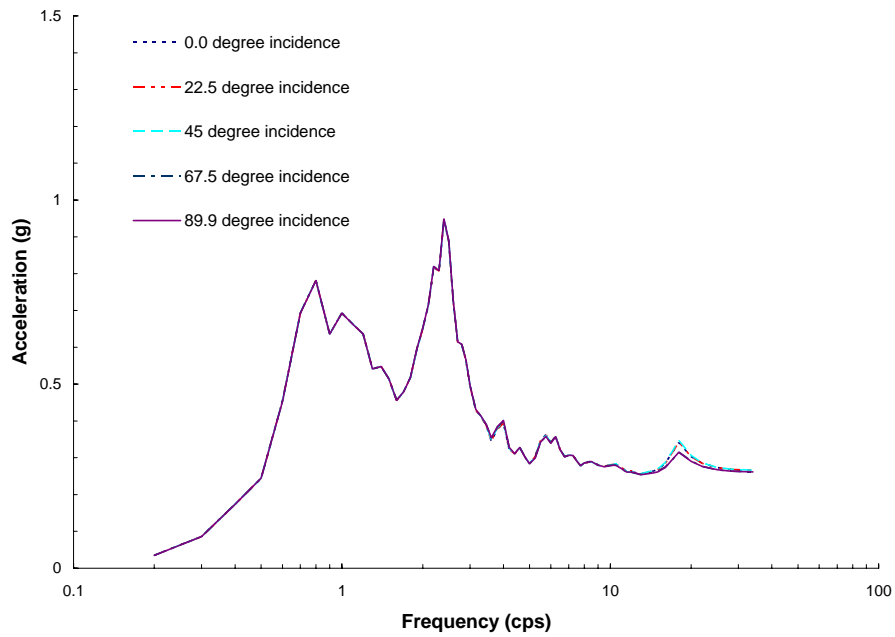


Figure 3.2.1-4 Translational Spectra for Soil Column A at the Surface Center of SASSI Kinematic Model with 46 m Embedment for Various Incident SH-Waves.

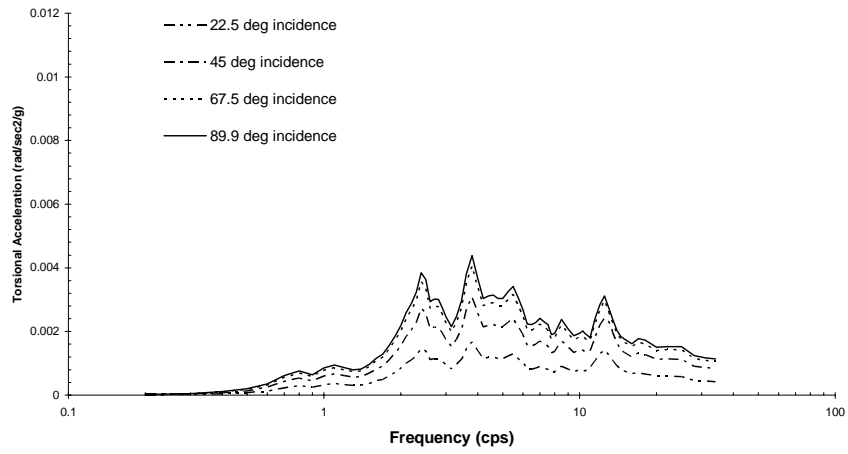


Figure 3.2.1-5 Torsional Spectra for Soil Column A at the Surface Center of SASSI Kinematic Model with 11.5 m Embedment for Various Incident SH-Waves.

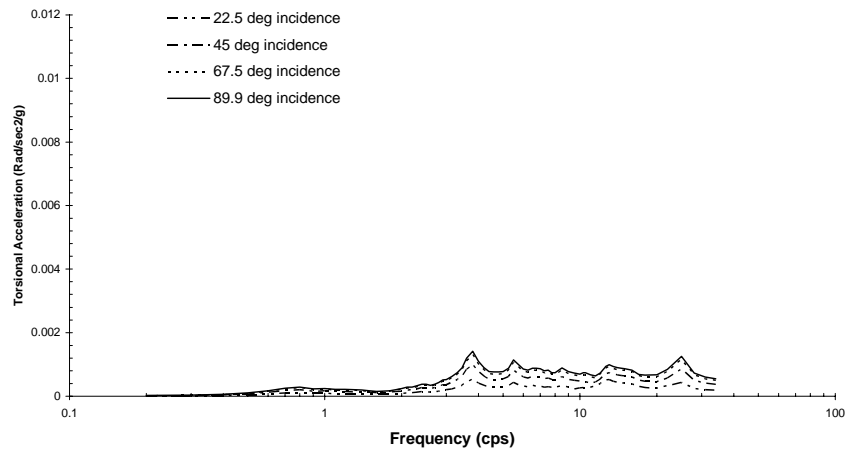


Figure 3.2.1-6 Torsional Spectra for Soil Column A at the Surface Center of SASSI Kinematic Model with 46 m Embedment for Various Incident SH-Waves

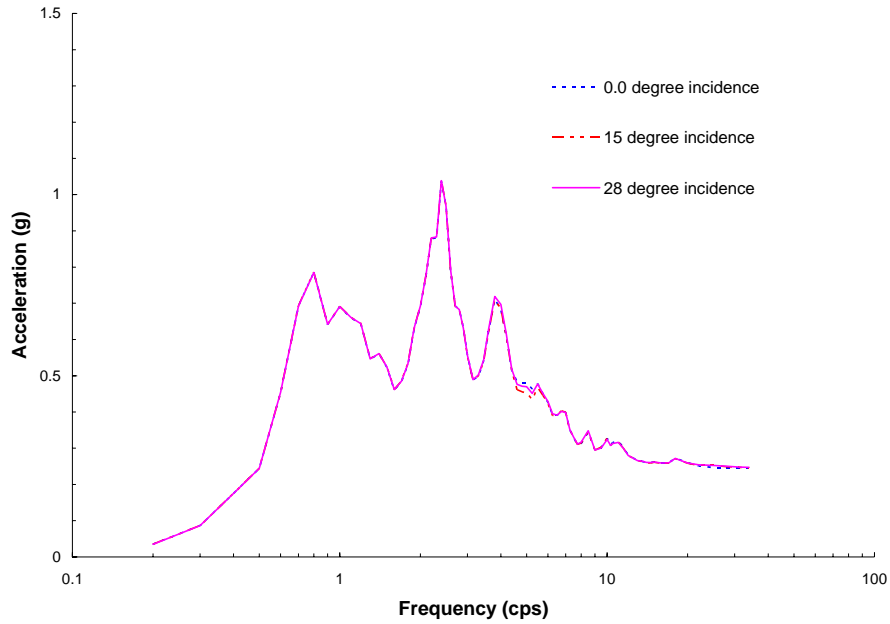


Figure 3.2.1-7 Translational Spectra for Soil Column A at the Basemat Center of SASSI Kinematic Model with 11.5 m Embedment for Various Incident SV-Waves.

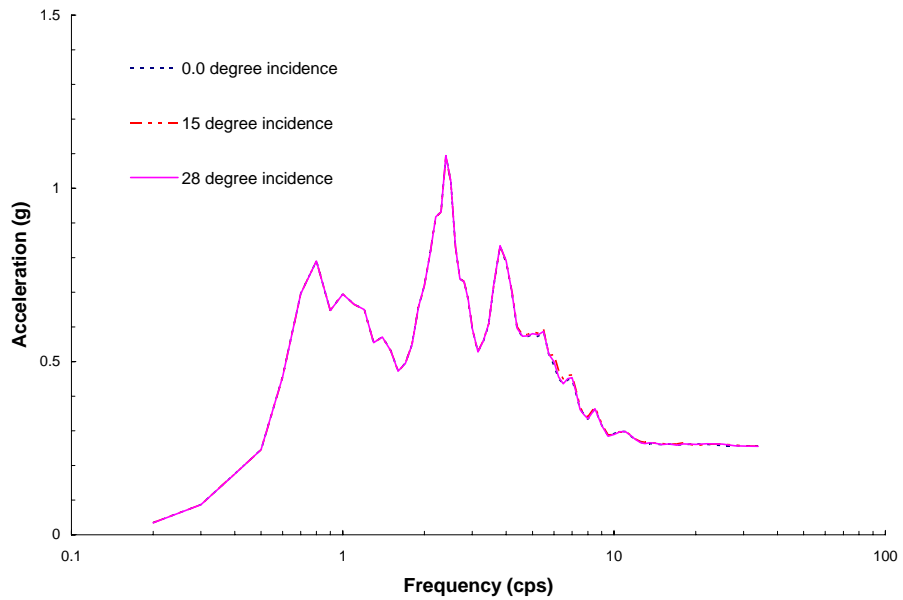


Figure 3.2.1-8 Translational Spectra for Soil Column A at the Surface Center of SASSI Kinematic Model with 11.5 m Embedment for Various Incident SV-Waves.

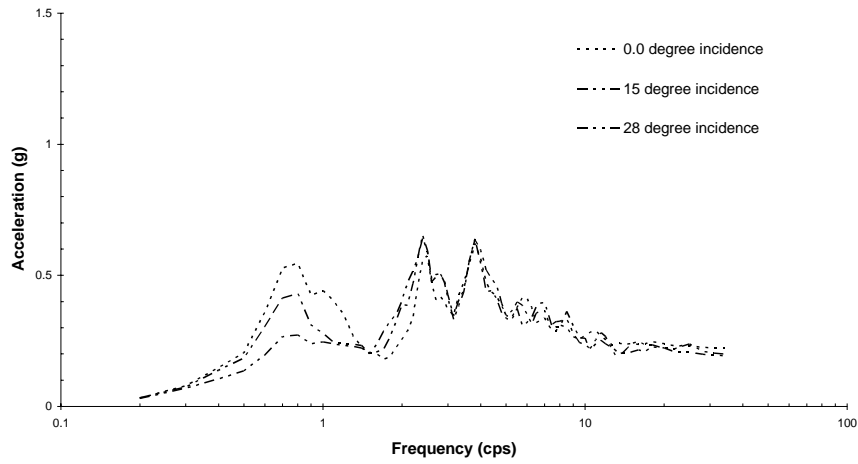


Figure 3.2.1-9 Translational Spectra for Soil Column A at the Basemat Center of SASSI Kinematic Model with 46 m Embedment for Various Incident SV-Waves.

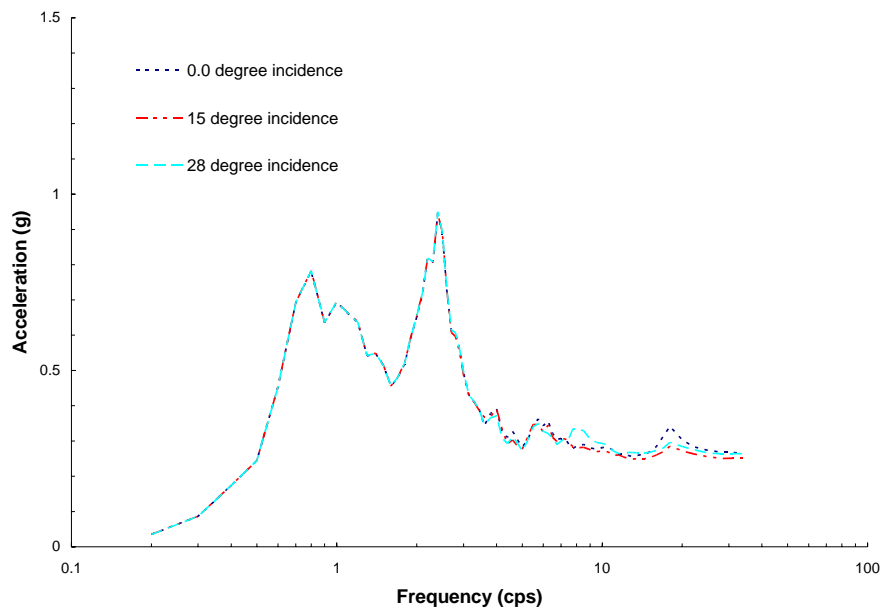


Figure 3.2.1-10 Translational Spectra for Soil Column A at the Surface Center of SASSI Kinematic Model with 46 m Embedment for Various Incident SV-Waves.

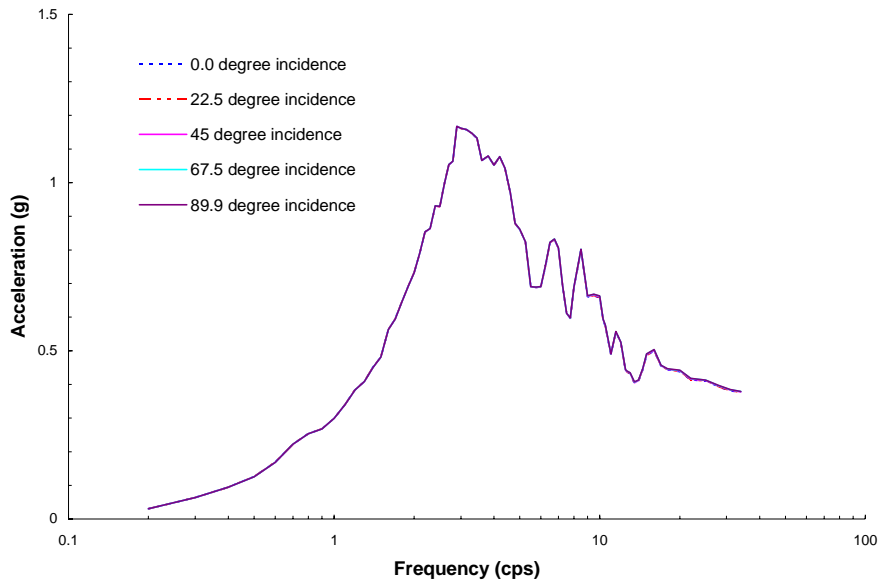


Figure 3.2.1-11 Translational Spectra for Soil Column B at the Basemat Center of SASSI Kinematic Model with 11.5 m Embedment for Various Incident SH-Waves.

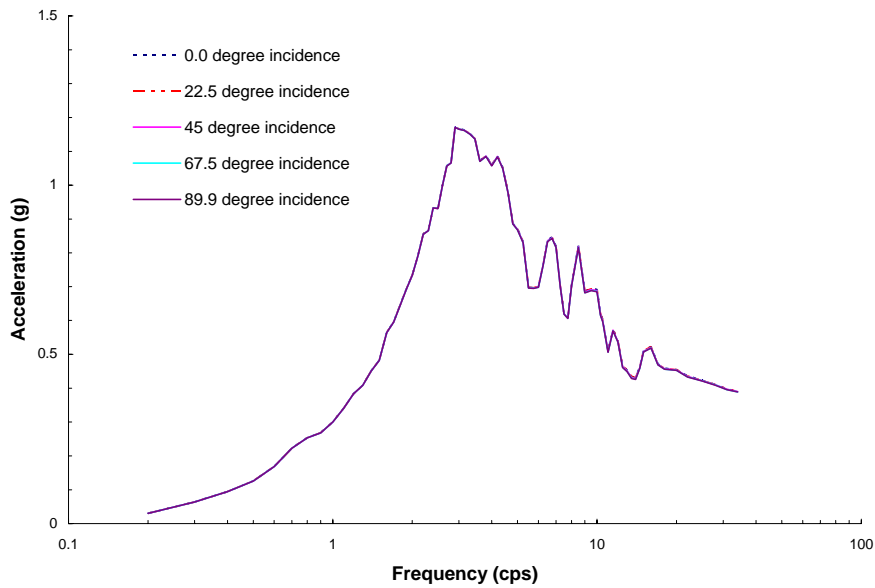


Figure 3.2.1-12 Translational Spectra for Soil Column B at the Surface Center of SASSI Kinematic Model with 11.5 m Embedment for Various Incident SH-Waves.

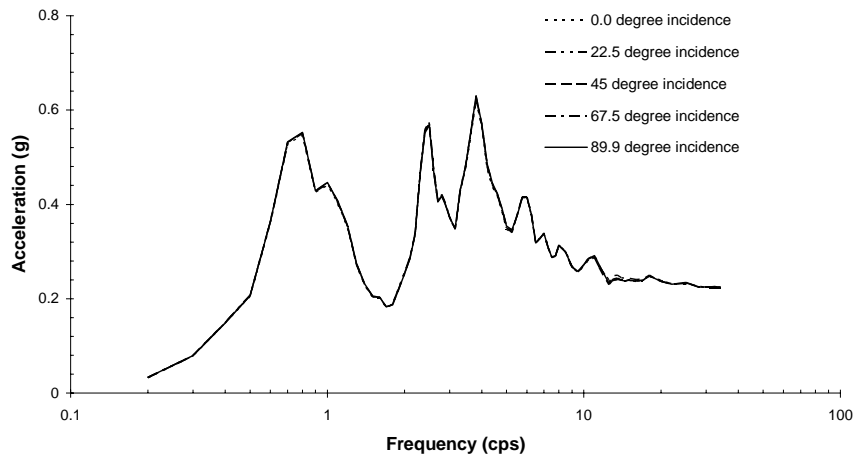


Figure 3.2.1-13 Translational Spectra for Soil Column B at the Basemat Center of SASSI Kinematic Model with 46 m Embedment for Various Incident SH-Waves.

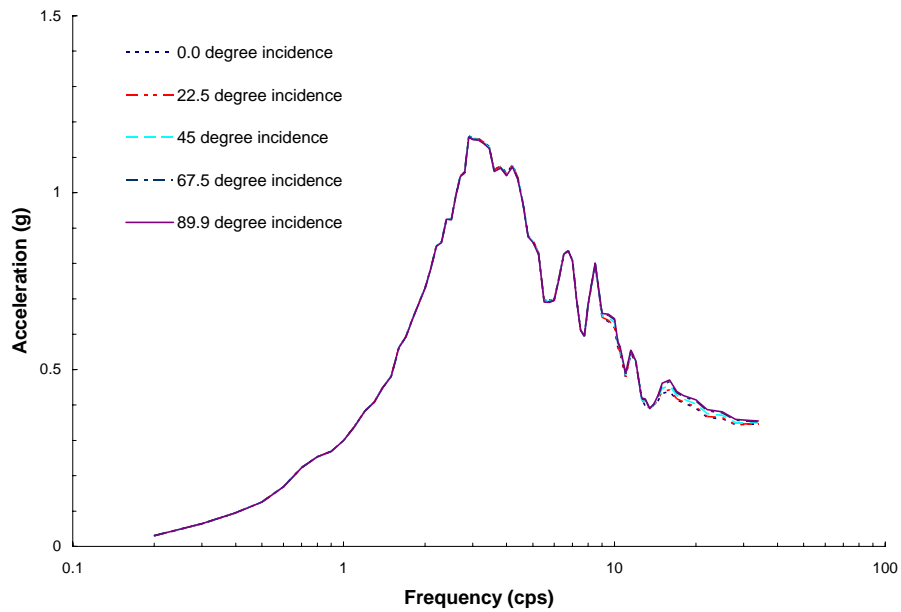


Figure 3.2.1-14 Translational Spectra for Soil Column B at the Surface Center of SASSI Kinematic Model with 46 m Embedment for Various Incident SH-Waves.

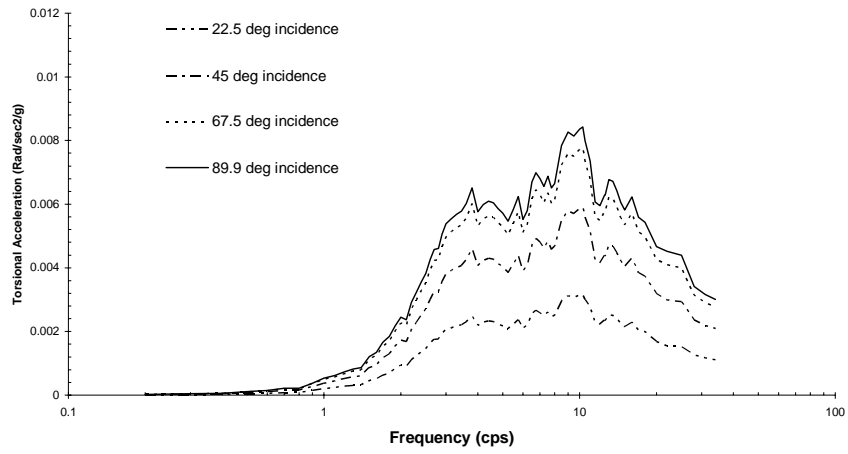


Figure 3.2.1-15 Torsional Spectra for Soil Column B at the Surface Center of SASSI Kinematic Model with 11.5 m Embedment for Various Incident SH-Waves.

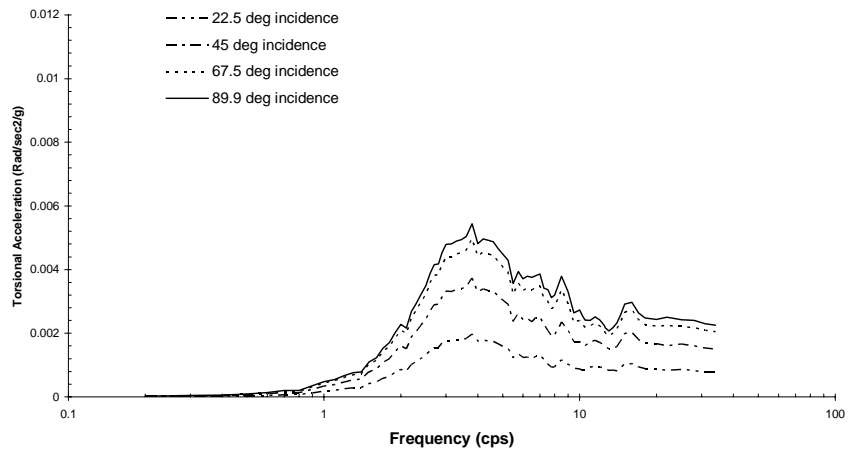


Figure 3.2.1-16 Torsional Spectra for Soil Column B at the Surface Center of SASSI Kinematic Model with 46 m Embedment for Various Incident SH-Waves.

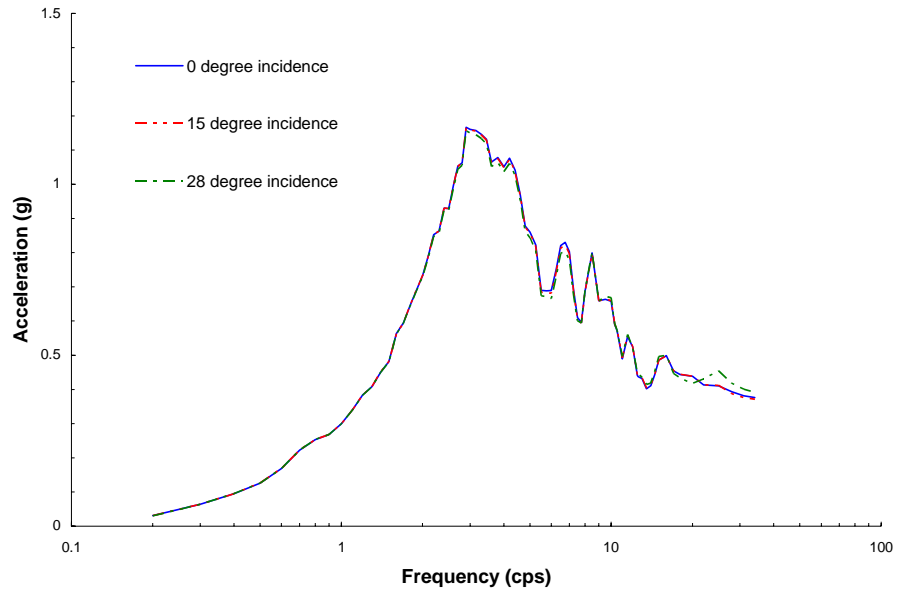


Figure 3.2.1-17 Translational Spectra for Soil Column B at the Basemat Center of SASSI Kinematic Model with 11.5 m Embedment for Various Incident SV-Waves.

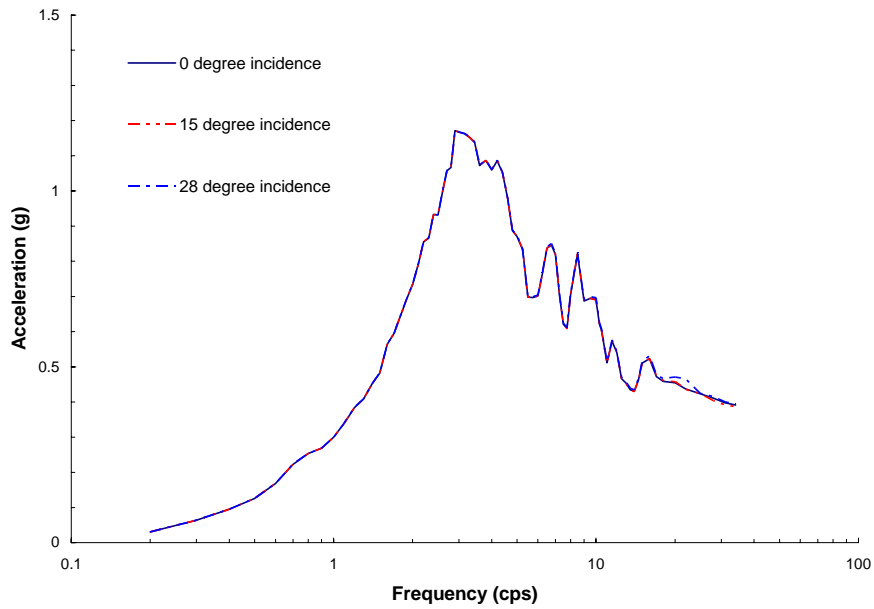


Figure 3.2.1-18 Translational Spectra for Soil Column B at the Surface Center of SASSI Kinematic Model with 11.5 m Embedment for Various Incident SV-Waves.

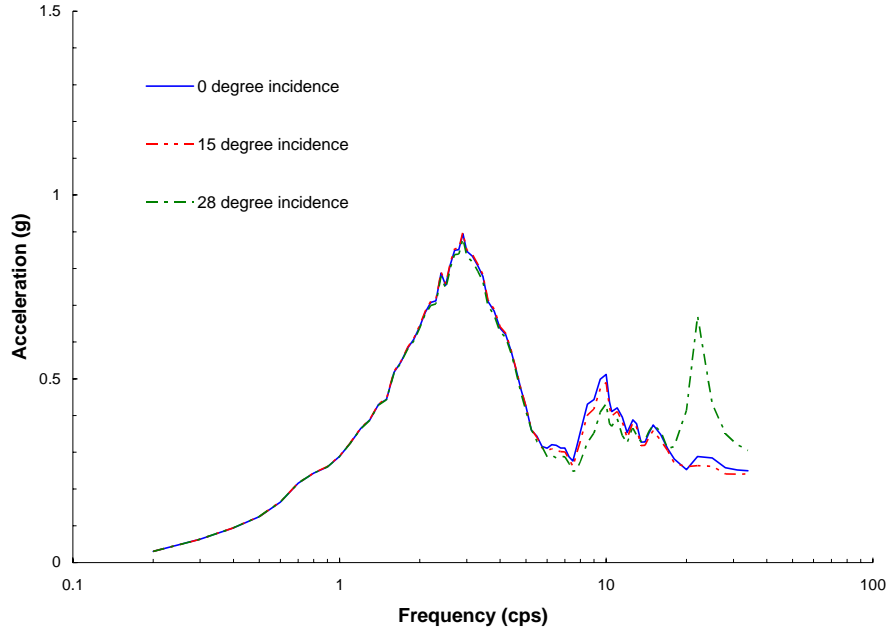


Figure 3.2.1-19 Translational Spectra for Soil Column B at the Basemat Center of SASSI Kinematic Model with 46 m Embedment for Various Incident SV-Waves.

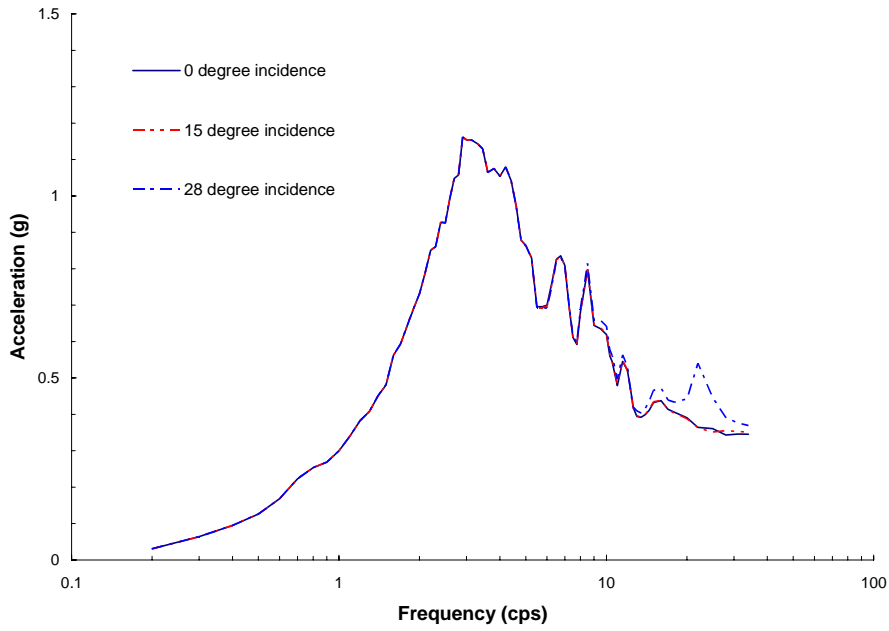


Figure 3.2.1-20 Translational Spectra for Soil Column B at the Surface Center of SASSI Kinematic Model with 46 m Embedment for Various Incident SV-Waves.

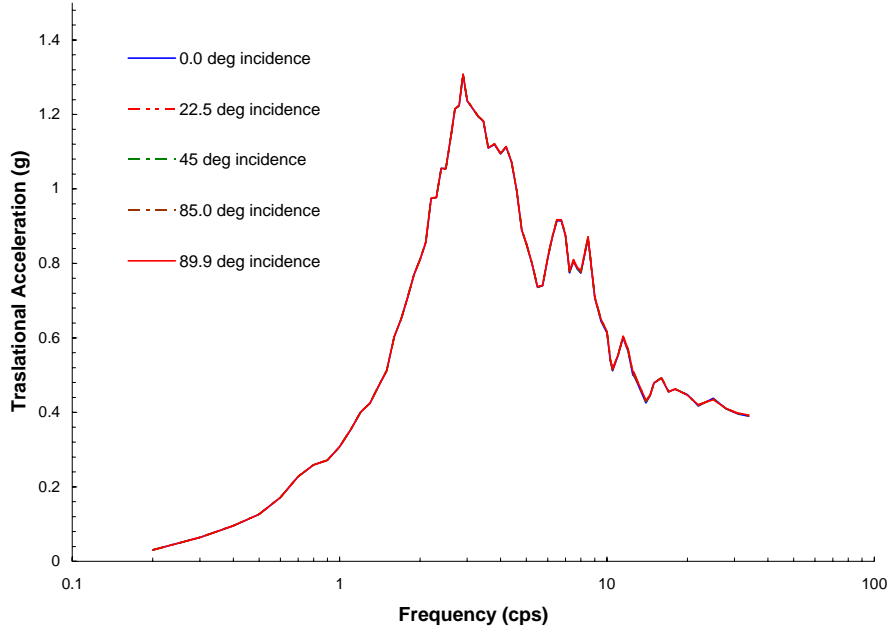


Figure 3.2.1-21 Translational Spectra for Soil Column C at the Basemat Center of SASSI Kinematic Model with 11.5 m Embedment for Various Incident SH-Waves.

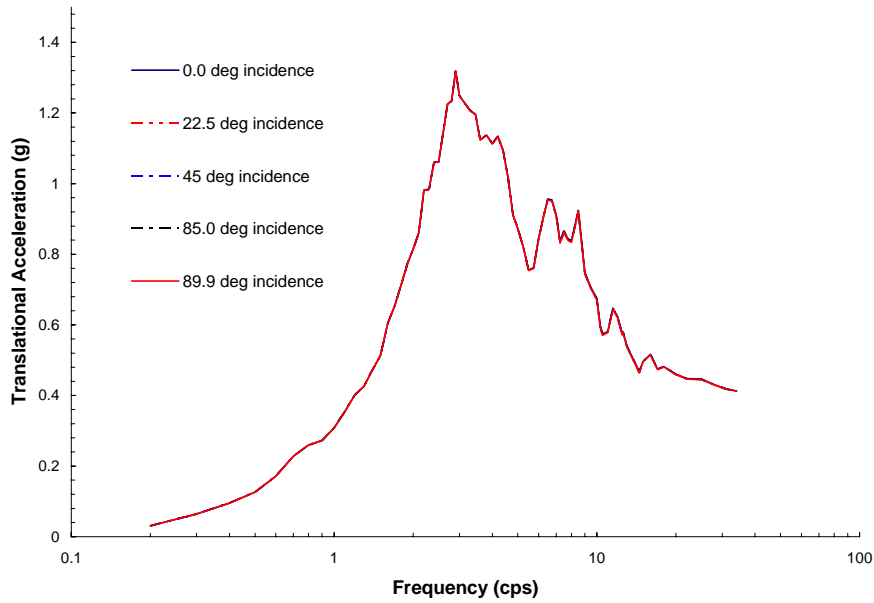


Figure 3.2.1-22 Translational Spectra for Soil Column C at the Surface Center of SASSI Kinematic Model with 11.5 m Embedment for Various Incident SH-Waves.

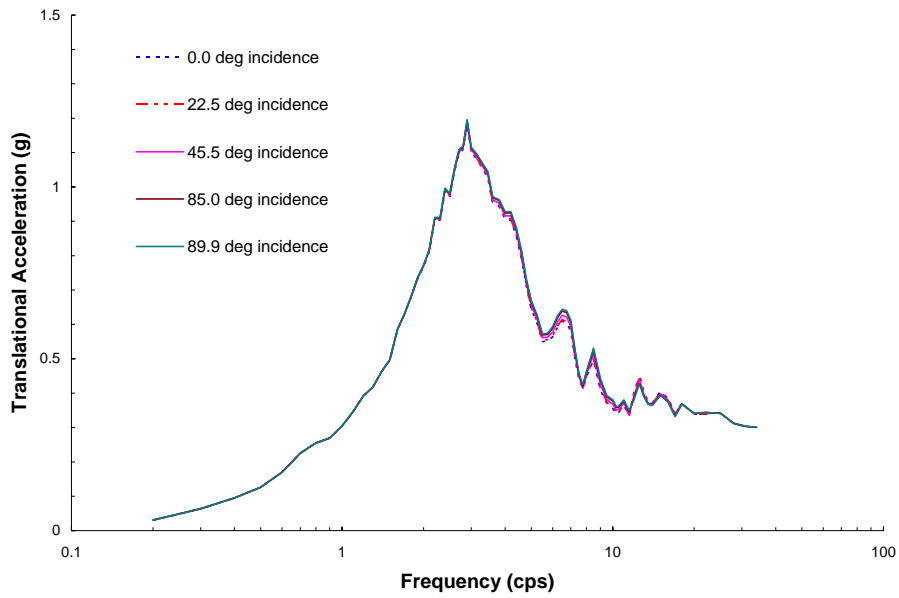


Figure 3.2.1-23 Translational Spectra for Soil Column C at the Basemat Center of SASSI Kinematic Model with 23 m Embedment for Various Incident SH-Waves.

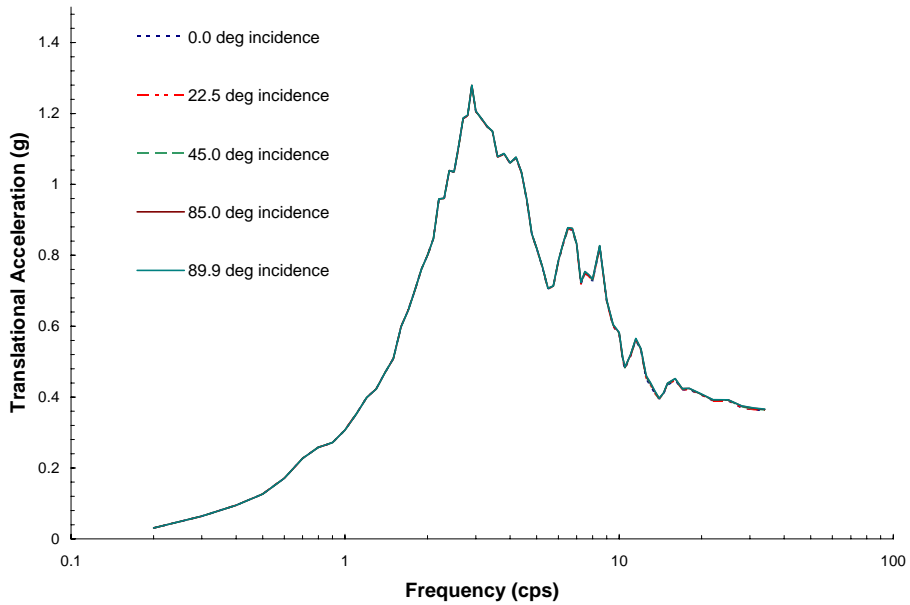


Figure 3.2.1-24 Translational Spectra for Soil Column C at the Surface Center of SASSI Kinematic Model with 23 m Embedment for Various Incident SH-Waves.

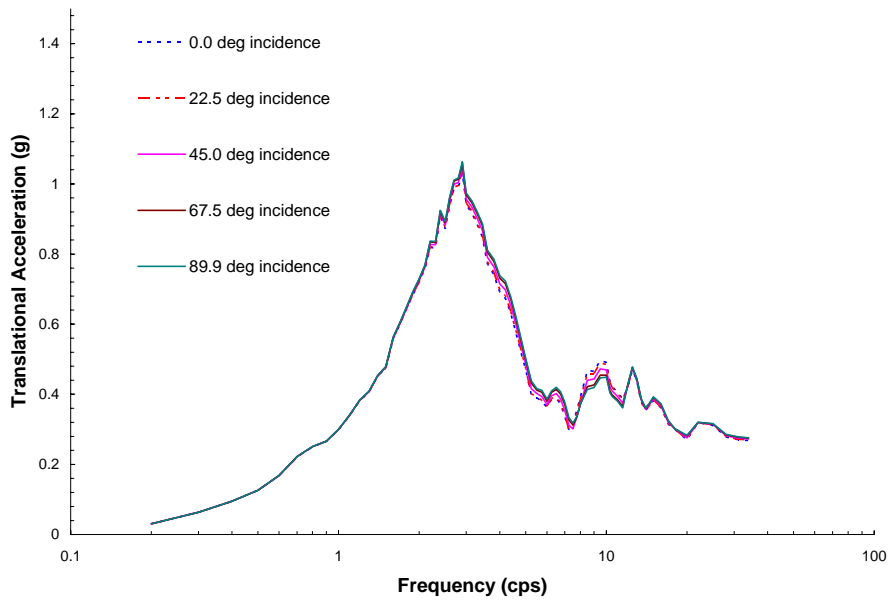


Figure 3.2.1-25 Translational Spectra for Soil Column C at the Basemat Center of SASSI Kinematic Model with 34.5 m Embedment for Various Incident SH-Waves.

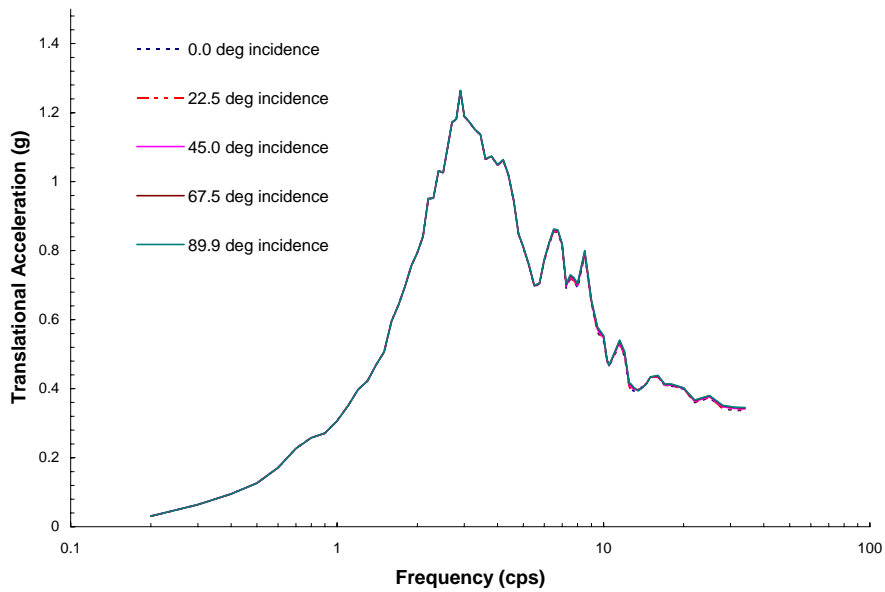


Figure 3.2.1-26 Translational Spectra for Soil Column C at the Surface Center of SASSI Kinematic Model with 34.5 m Embedment for Various Incident SH-Waves.

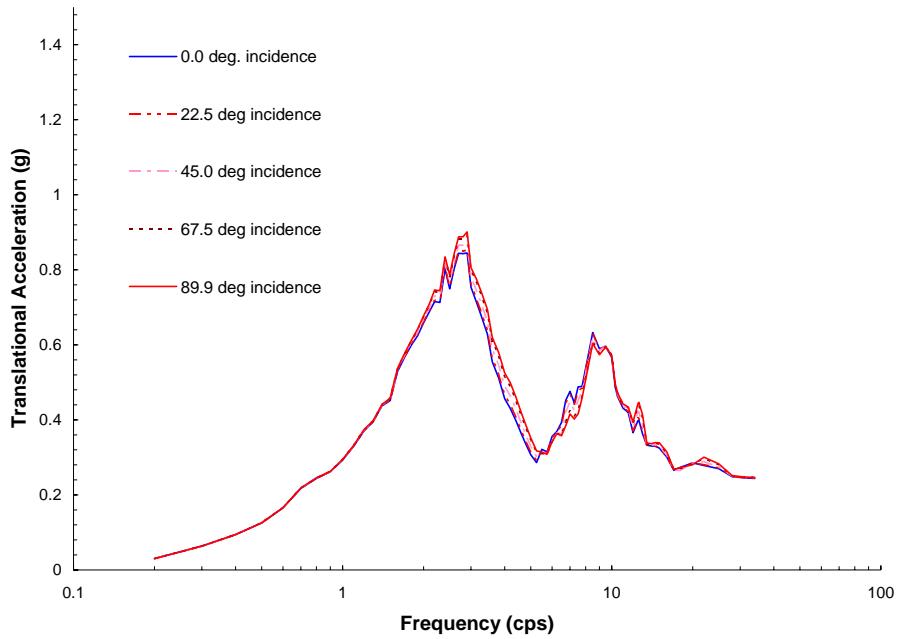


Figure 3.2.1-27 Translational Spectra for Soil Column C at the Basemat Center of SASSI Kinematic Model with 46 m Embedment for Various Incident SH-Waves.

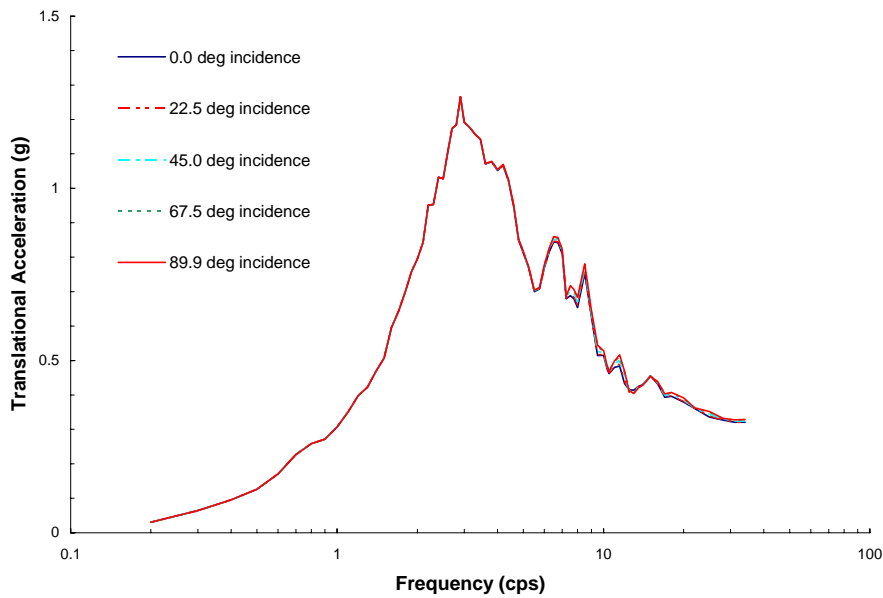


Figure 3.2.1-28 Translational Spectra for Soil Column C at the Surface Center of SASSI Kinematic Model with 46 m Embedment for Various Incident SH-Waves.

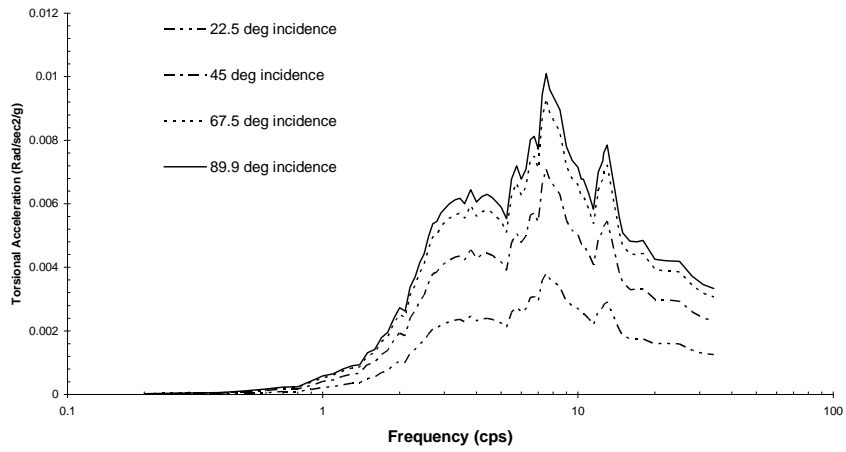


Figure 3.2.1-29 Torsional Spectra for Soil Column C at the Surface Center of SASSI Kinematic Model with 11.5 m Embedment for Various Incident SH-Waves.

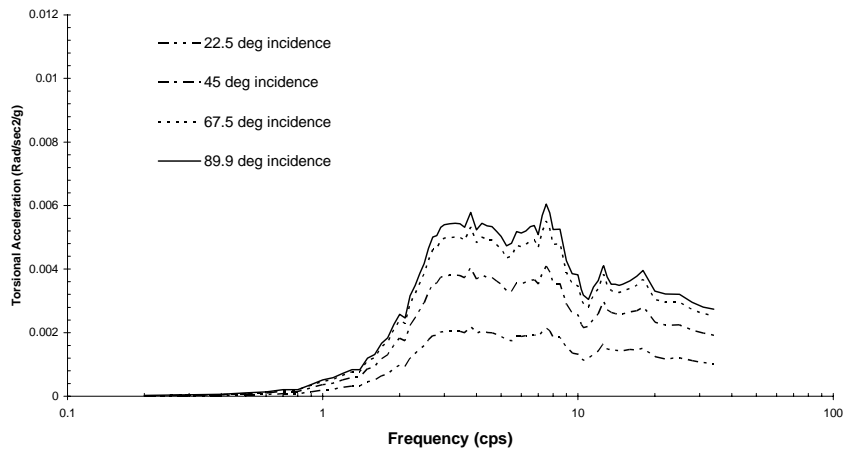


Figure 3.2.1-30 Torsional Spectra for Soil Column C at the Surface Center of SASSI Kinematic Model with 23m Embedment for Various Incident SH-Waves.

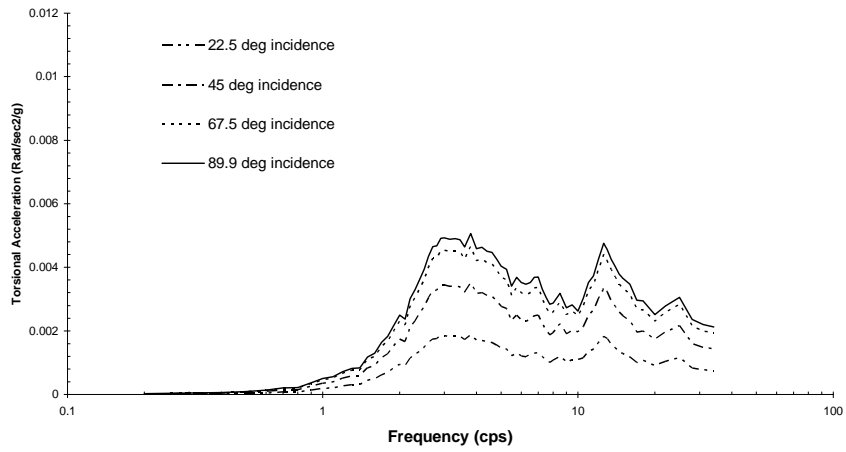


Figure 3.2.1-31 Torsional Spectra for Soil Column C at the Surface Center of SASSI Kinematic Model with 34.5 m Embedment for Various Incident SH-Waves.

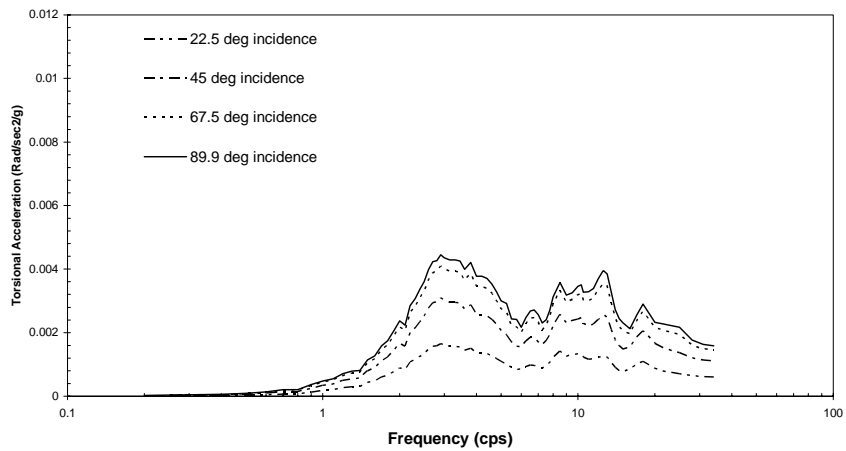


Figure 3.2.1-32 Torsional Spectra for Soil Column C at the Surface Center of SASSI Kinematic Model with 46 m Embedment for Various Incident SH-Waves.

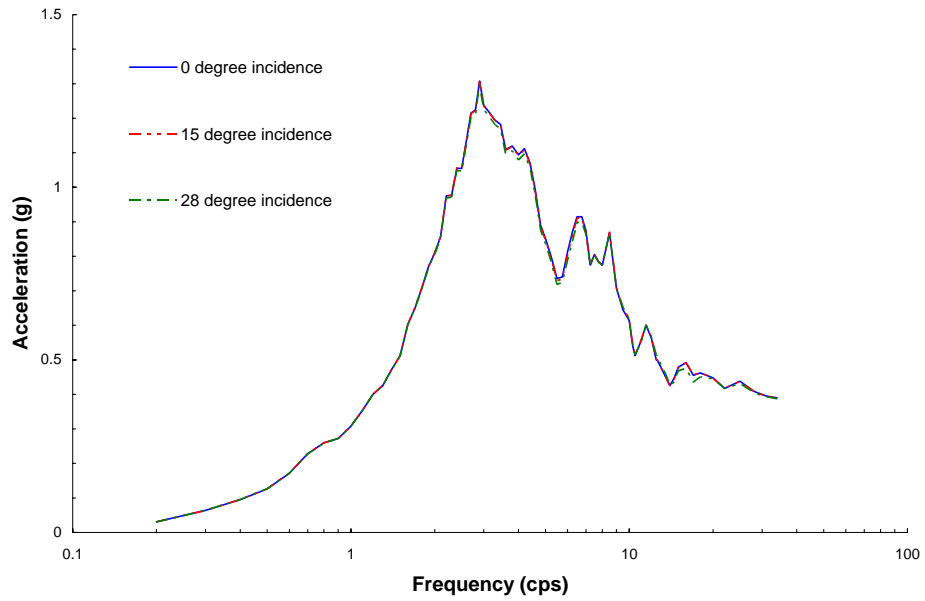


Figure 3.2.1-33 Translational Spectra for Soil Column C at the Basemat Center of SASSI Kinematic Model with 11.5 m Embedment for Various Incident SV-Waves.

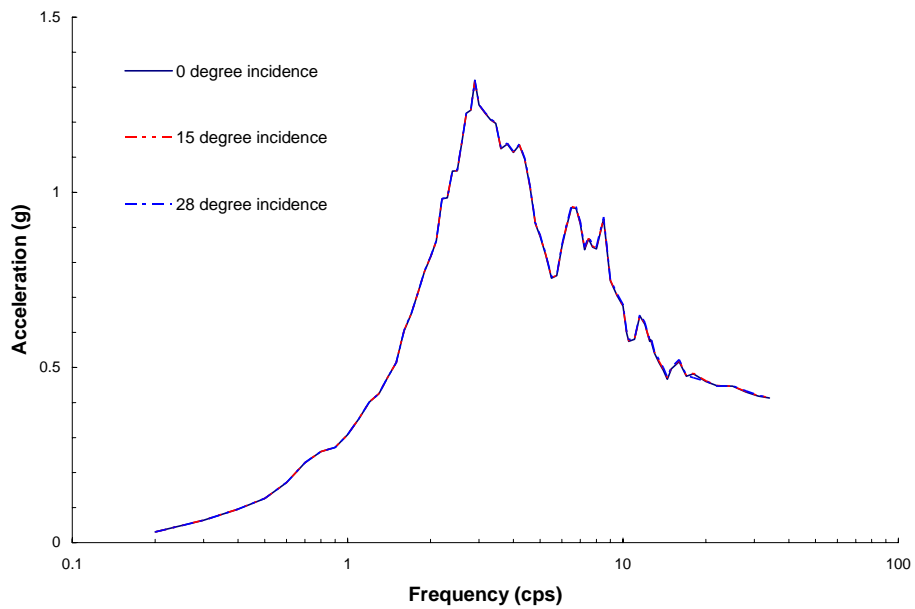


Figure 3.2.1-34 Translational Spectra for Soil Column C at the Surface Center of SASSI Kinematic Model with 11.5m Embedment for Various Incident SV-Waves.

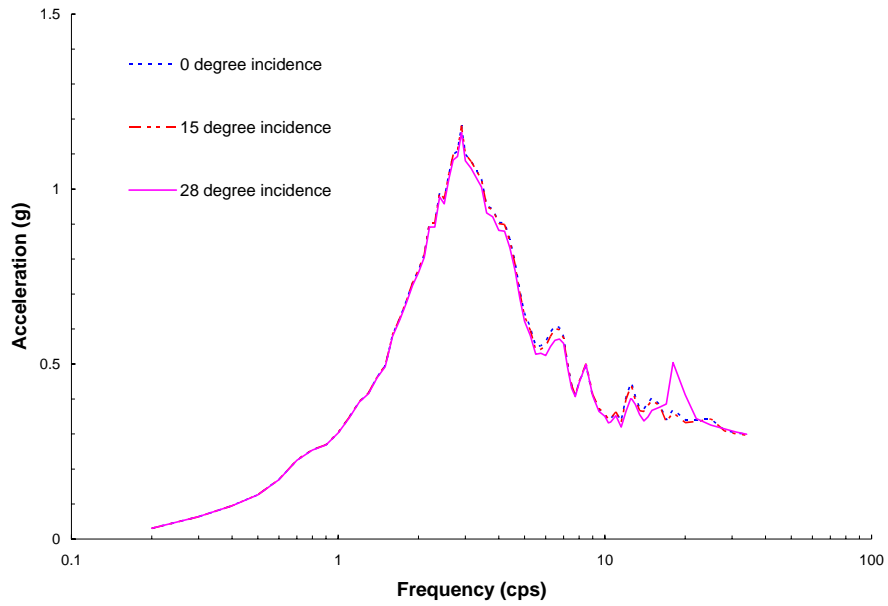


Figure 3.2.1-35 Translational Spectra for Soil Column C at the Basemat Center of SASSI Kinematic Model with 23 m Embedment for Various Incident SV-Waves.

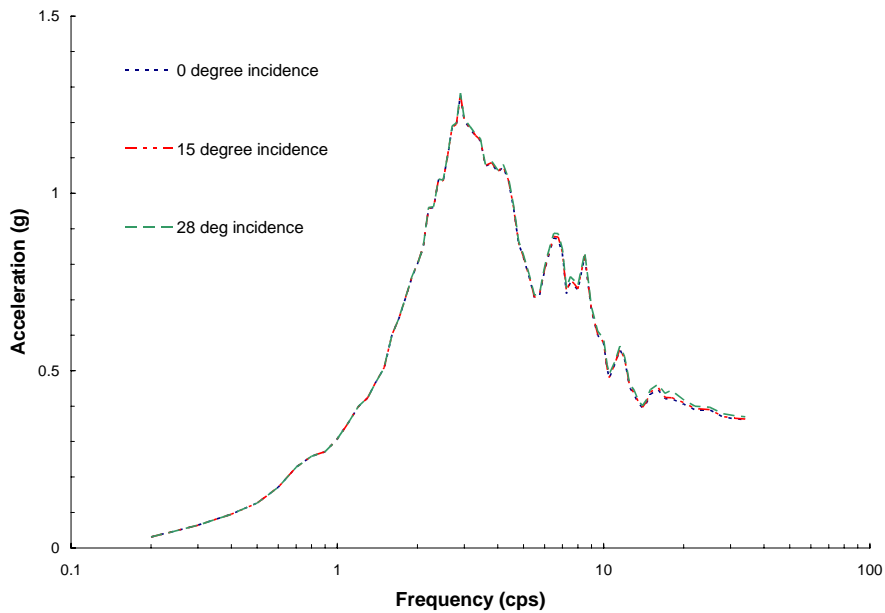


Figure 3.2.1-36 Translational Spectra for Soil Column C at the Surface Center of SASSI Kinematic Model with 23 m Embedment for Various Incident SV-Waves.

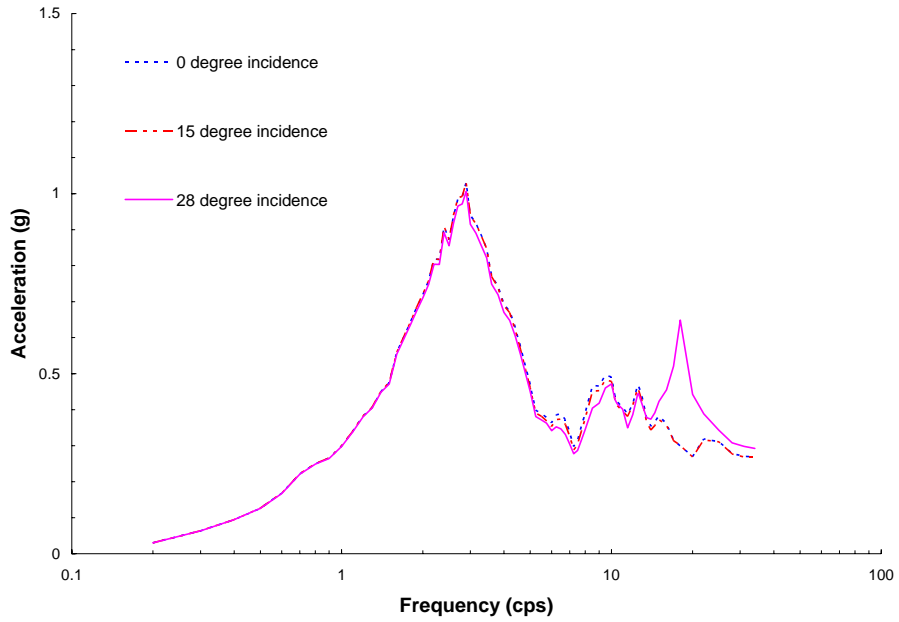


Figure 3.2.1-37 Translational Spectra for Soil Column C at the Basemat Center of SASSI Kinematic Model with 34.5 m Embedment for Various Incident SV-Waves.

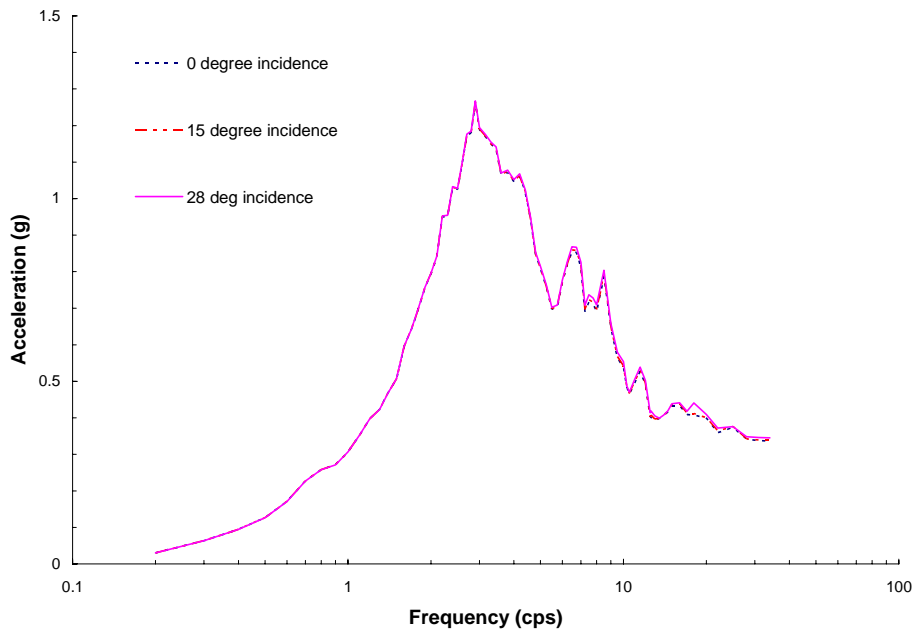


Figure 3.2.1-38 Translational Spectra for Soil Column C at the Surface Center of SASSI Kinematic Model with 34.5 m Embedment for Various Incident SV-Waves.

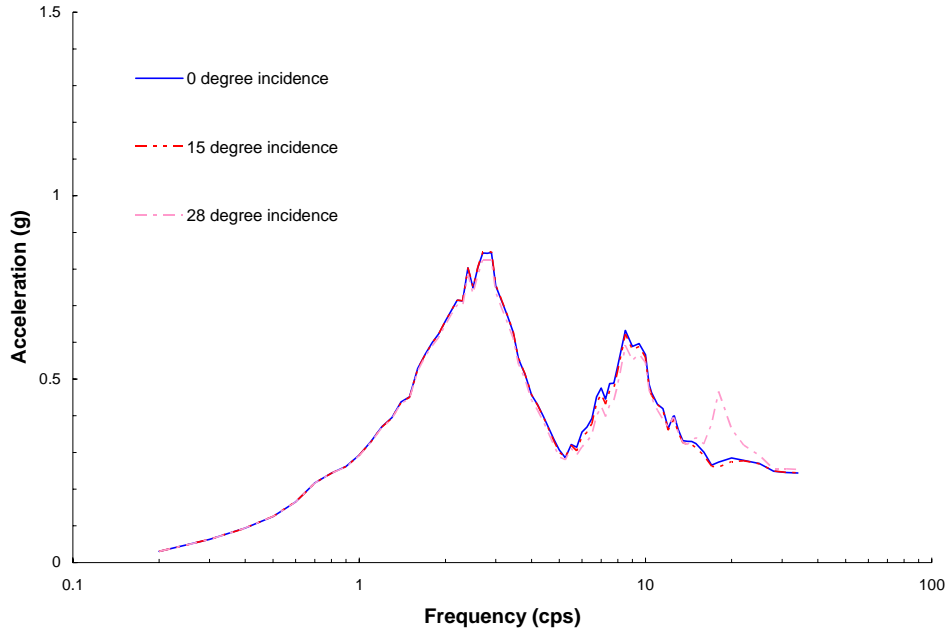


Figure 3.2.1-39 Translational Spectra for Soil Column C at the Basemat Center of SASSI Kinematic Model with 46 m Embedment for Various Incident SV-Waves.

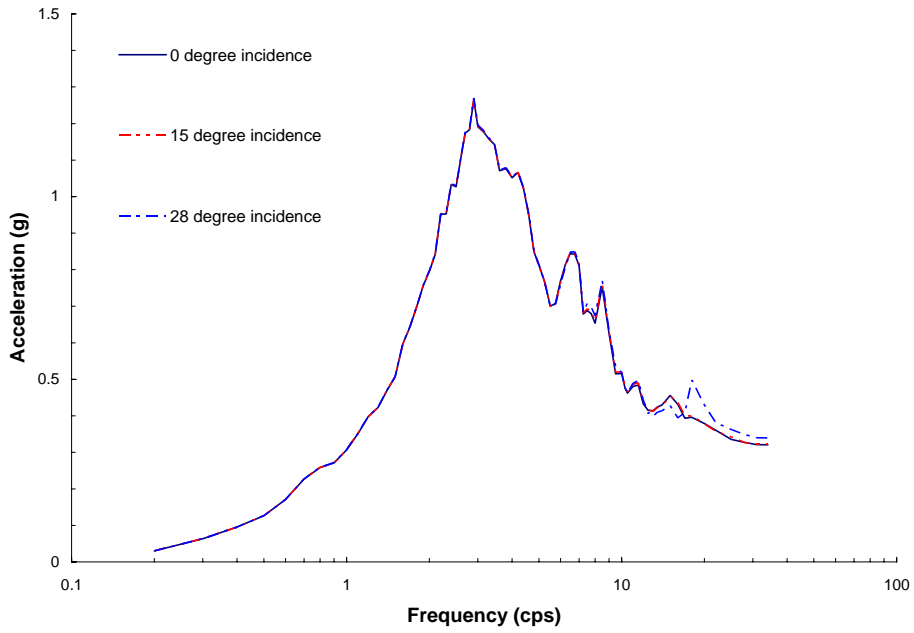


Figure 3.2.1-40 Translational Spectra for Soil Column C at the Surface Center of SASSI Kinematic Model with 46 m Embedment for Various Incident SV-Waves.

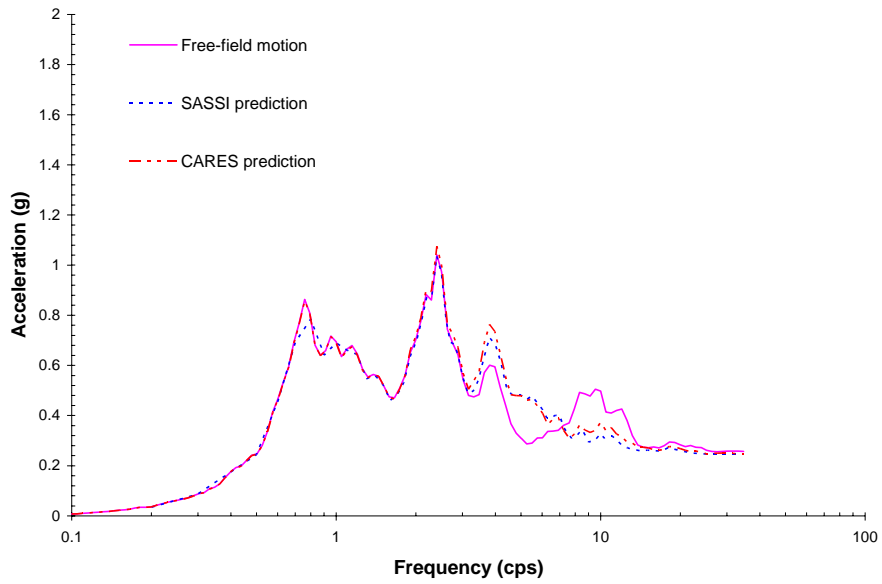


Figure 3.2.2-1 Comparison of Response Spectra for Soil Column A at the Basemat Center of Kinematic Model with 11.5 m Embedment.

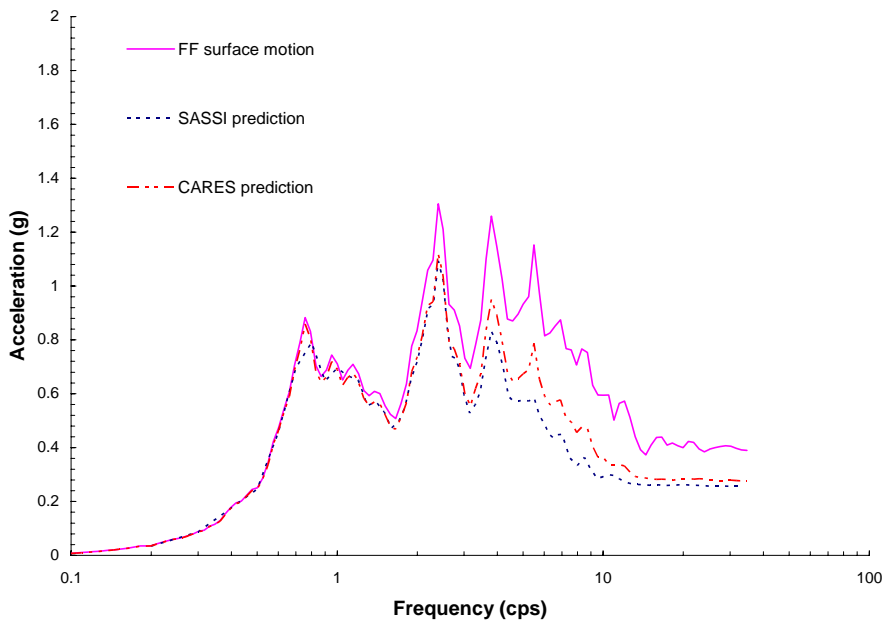


Figure 3.2.2-2 Comparison of Response Spectra for Soil Column A at the Surface Center of Kinematic Model with 11.5 m Embedment.

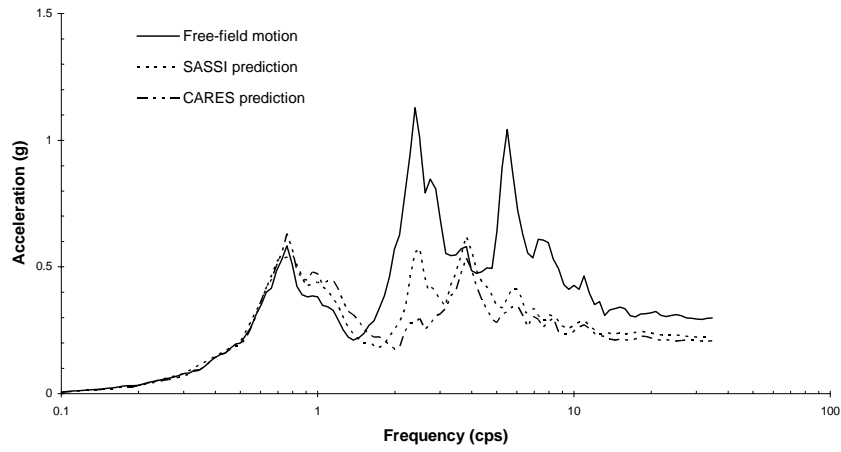


Figure 3.2.2-3 Comparison of Response Spectra for Soil Column A at the Basemat Center of Kinematic Model with 46 m Embedment.

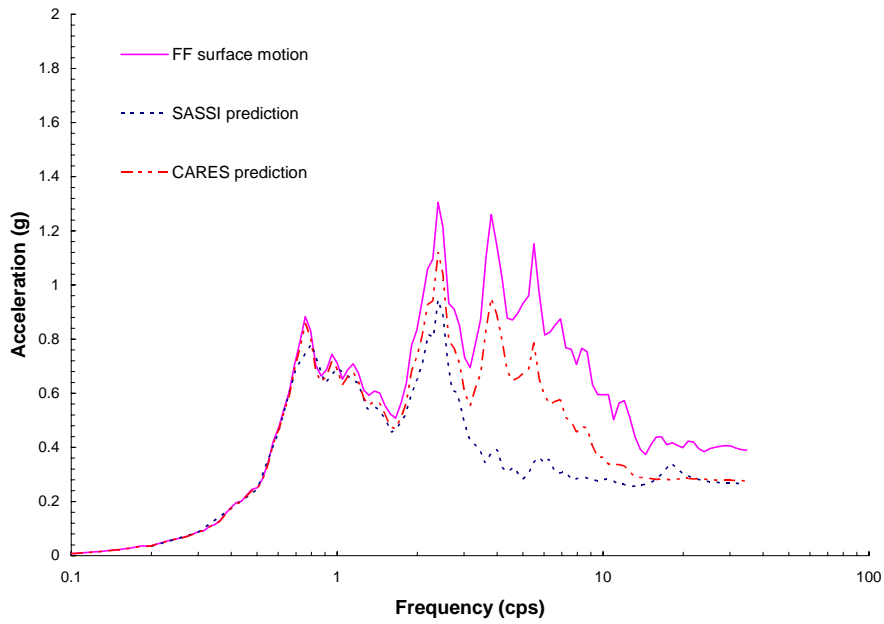


Figure 3.2.2-4 Comparison of Response Spectra for Soil Column A at the Surface Center of Kinematic Model with 46 m Embedment.

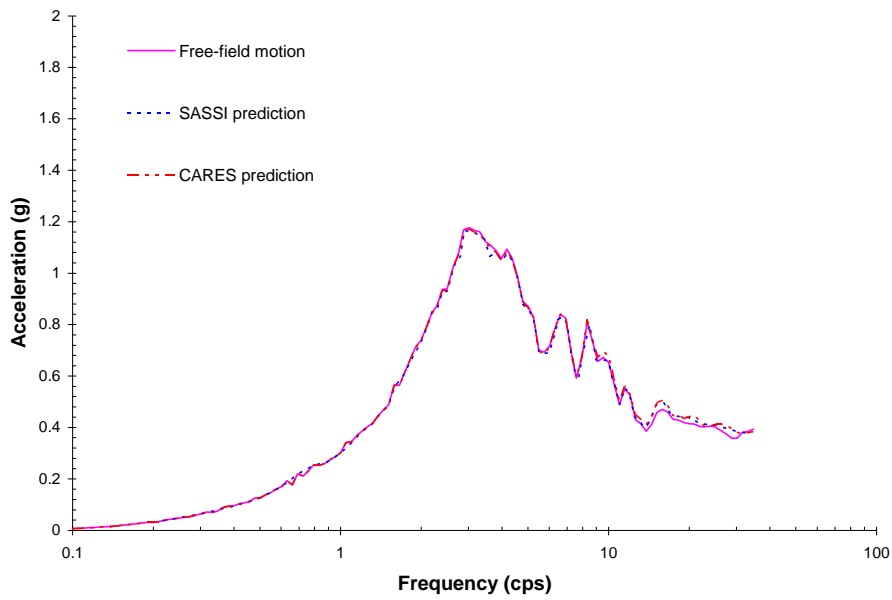


Figure 3.2.2-5 Comparison of Response Spectra for Soil Column B at the Basemat Center of Kinematic Model with 11.5 m Embedment.

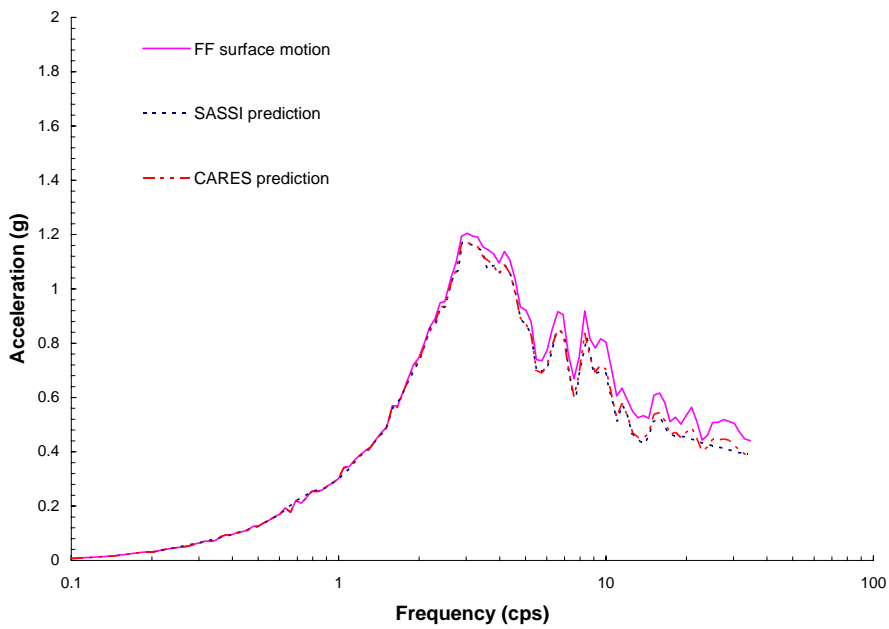


Figure 3.2.2-6 Comparison of Response Spectra for Soil Column B at the Surface Center of Kinematic Model with 11.5 m Embedment.

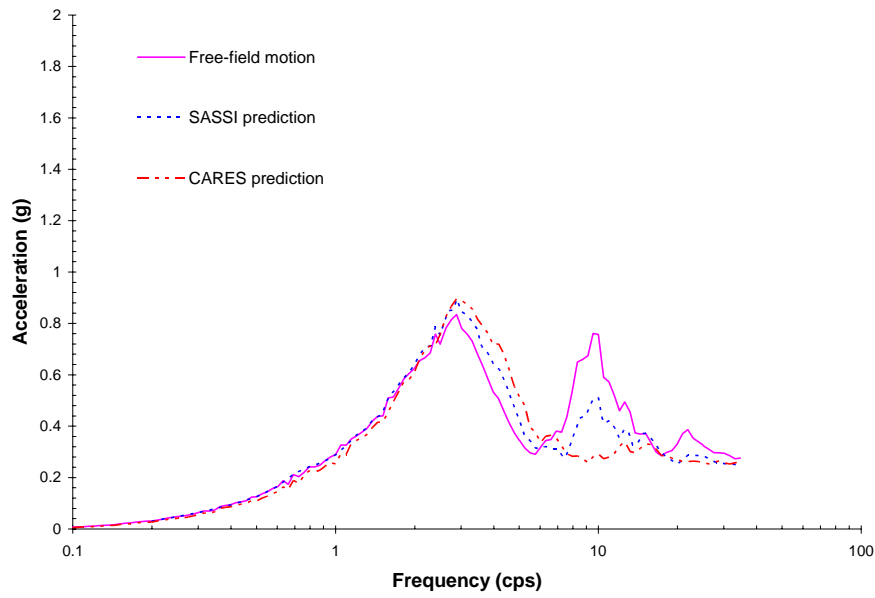


Figure 3.2.2-7 Comparison of Response Spectra for Soil Column B at the Basemat Center of Kinematic Model with 46 m Embedment.

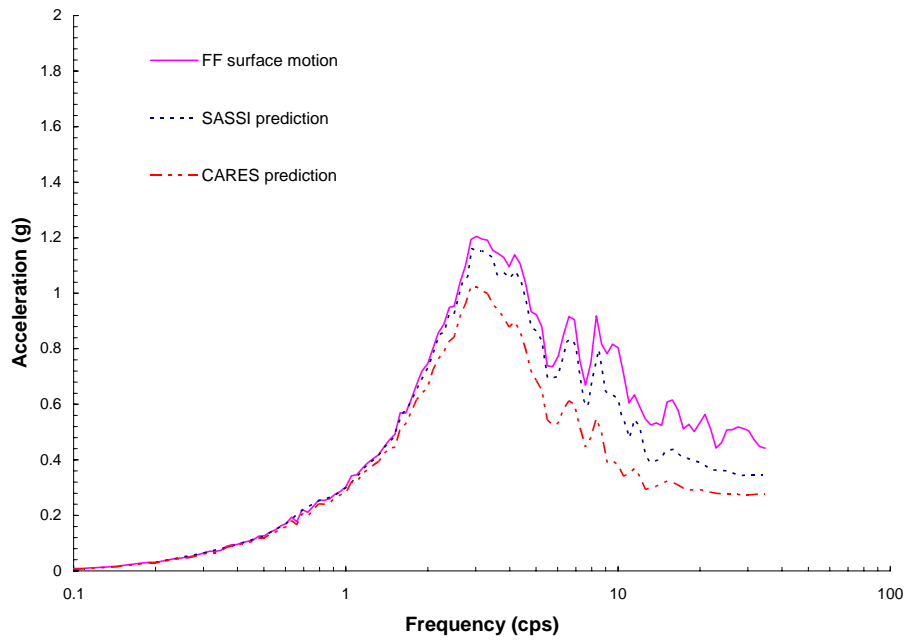


Figure 3.2.2-8 Comparison of Response Spectra for Soil Column B at the Surface Center of Kinematic Model with 46 m Embedment.

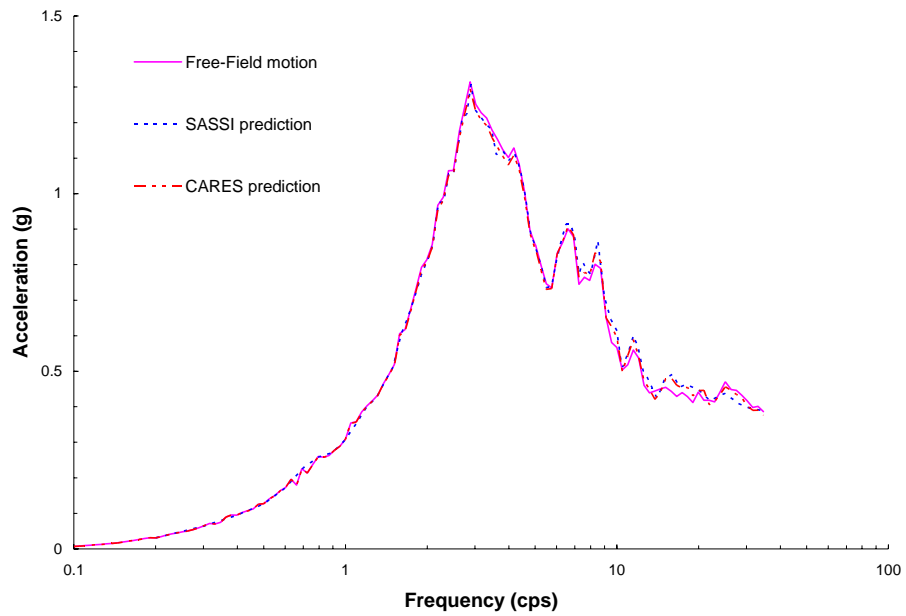


Figure 3.2.2-9 Comparison of Response Spectra for Soil Column C at the Basemat Center of Kinematic Model with 11.5 m Embedment.

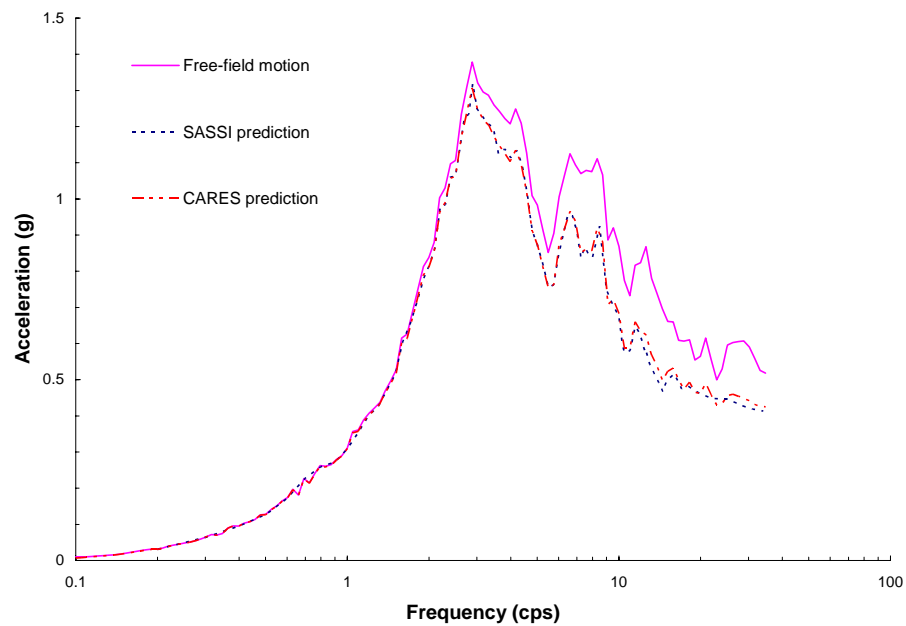


Figure 3.2.2-10 Comparison of Response Spectra for Soil Column C at the Surface Center of Kinematic Model with 11.5 m Embedment.

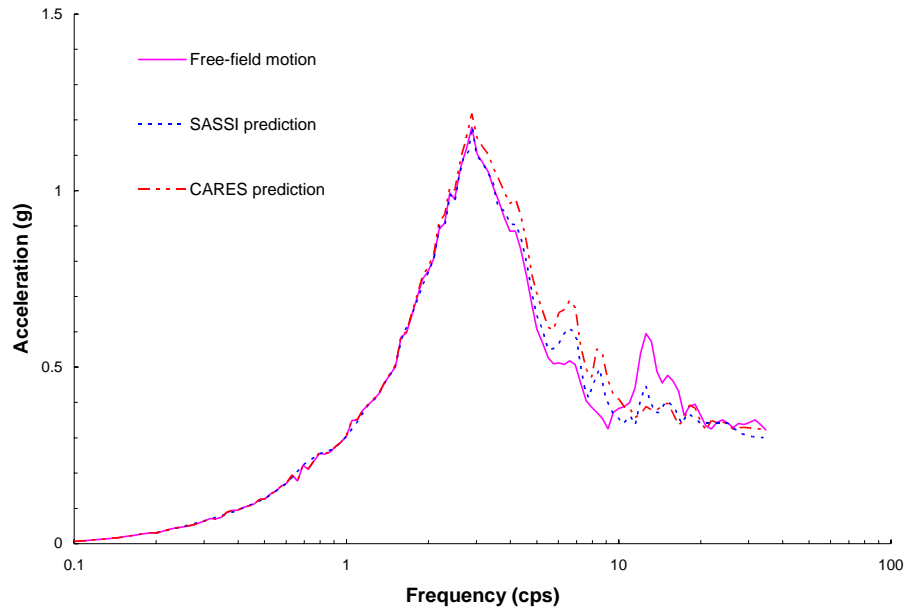


Figure 3.2.2-11 Comparison of Response Spectra for Soil Column C at the Basemat Center of Kinematic Model with 23 m Embedment.

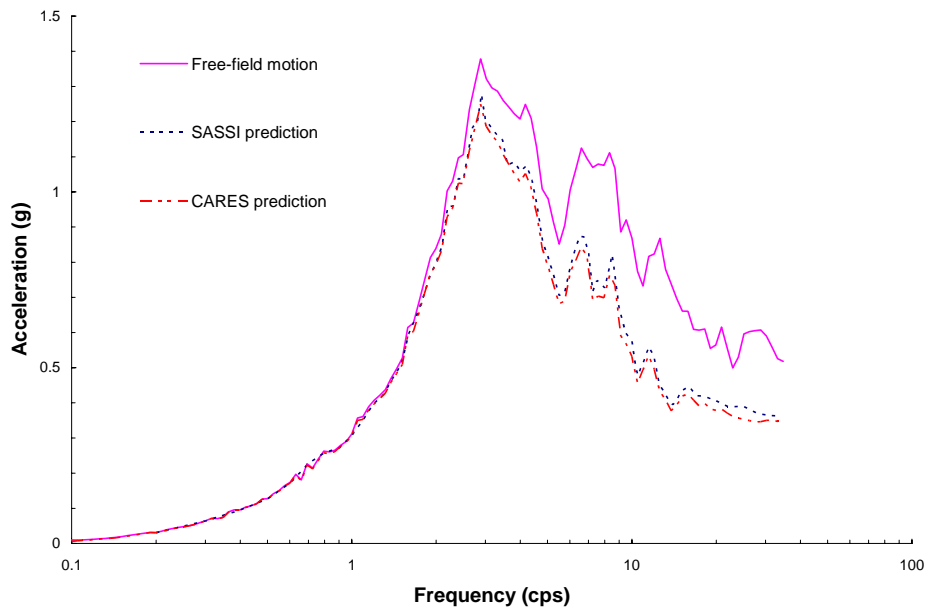


Figure 3.2.2-12 Comparison of Response Spectra for Soil Column C at the Surface Center of Kinematic Model with 23 m Embedment.

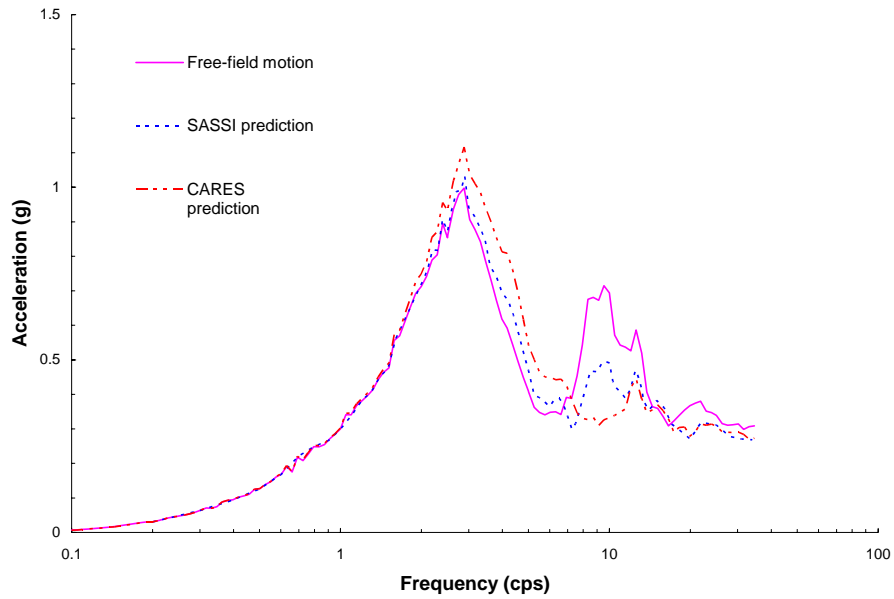


Figure 3.2.2-13 Comparison of Response Spectra for Soil Column C at the Basemat Center of Kinematic Model with 34.5 m Embedment.

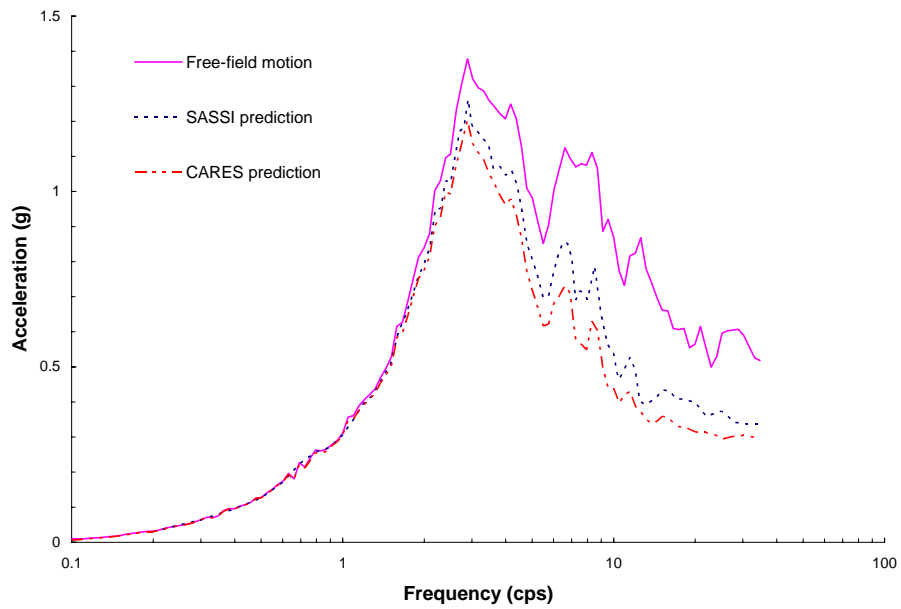


Figure 3.2.2-14 Comparison of Response Spectra for Soil Column C at the Surface Center of Kinematic Model with 34.5 m Embedment.

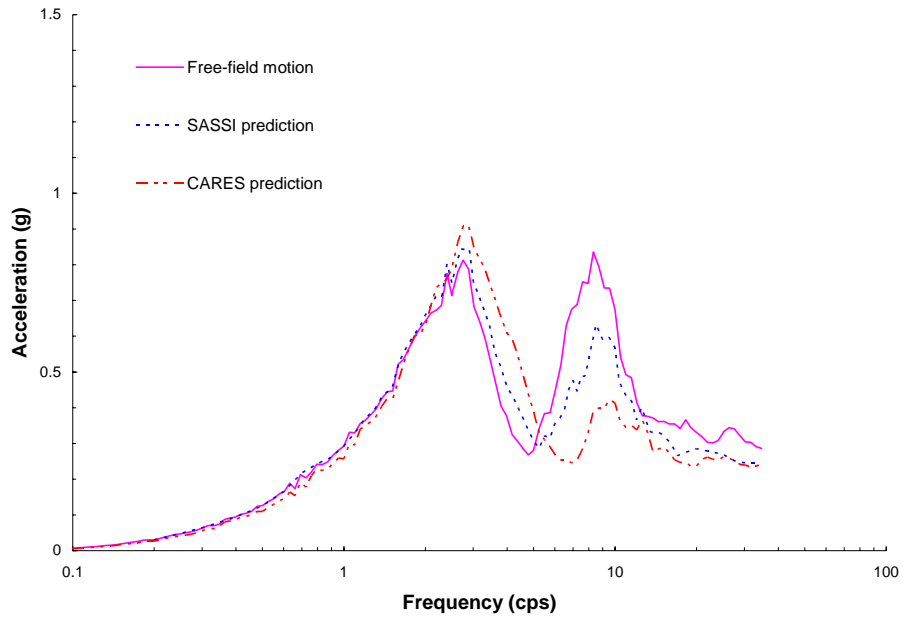


Figure 3.2.2-15 Comparison of Response Spectra for Soil Column C at the Basemat Center of Kinematic Model with 46 m Embedment.

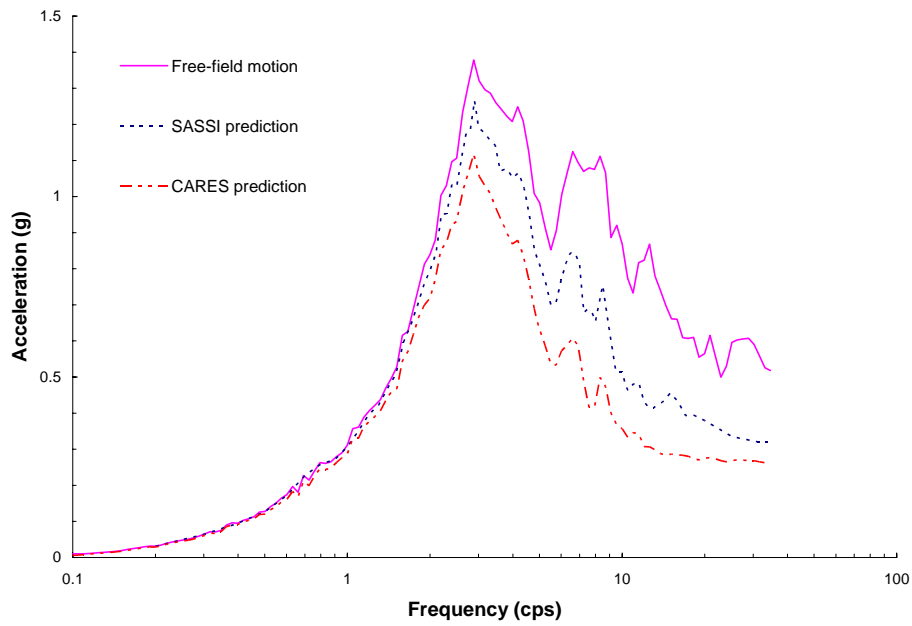


Figure 3.2.2-16 Comparison of Response Spectra for Soil Column C at the Surface Center of Kinematic Model with 46 m Embedment.

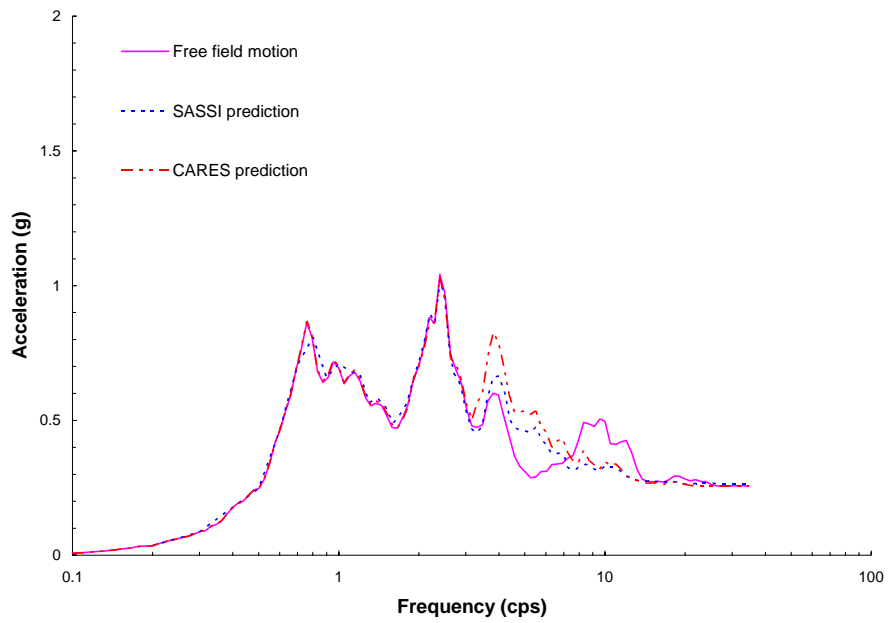


Figure 3.3-1 Comparison of Response Spectra for Soil Column A at the Basemat Center of SSI Model with 11.5 m Embedment.

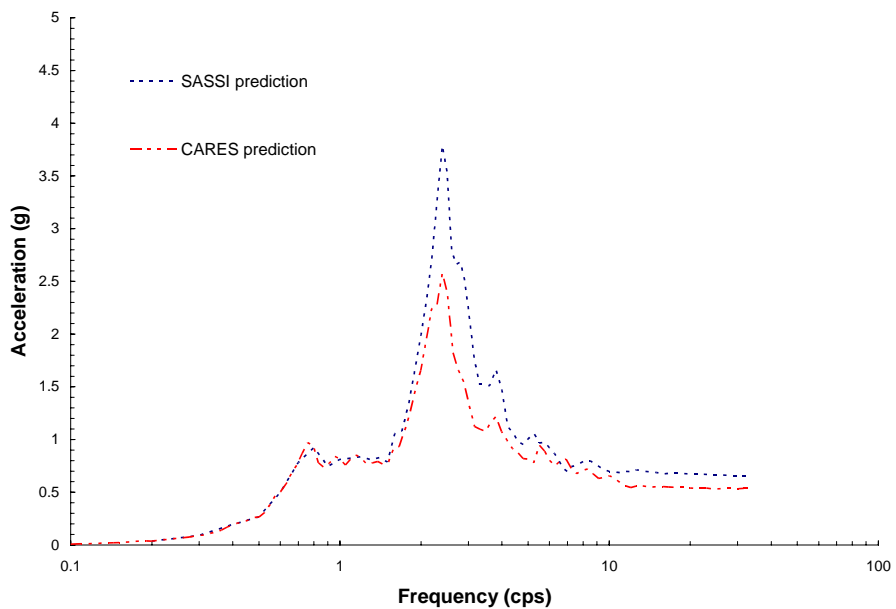


Figure 3.3-2 Comparison of Response Spectra for Soil Column A at the Roof Center of SSI Model with 11.5 m Embedment.

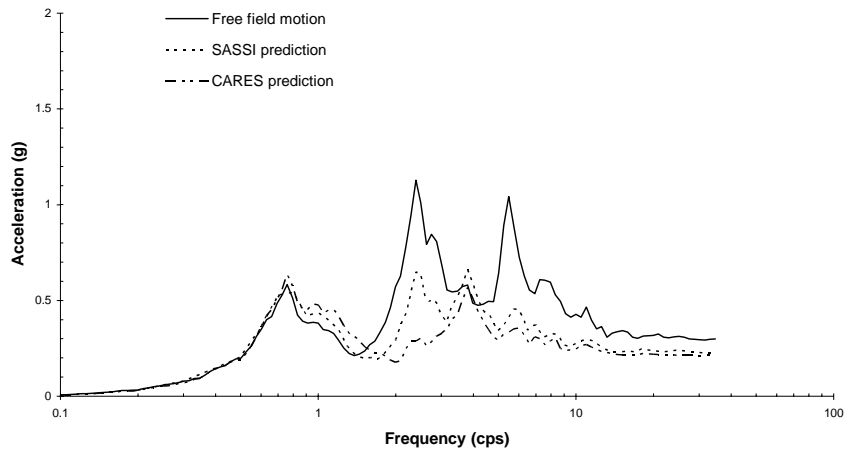


Figure 3.3-3 Comparison of Response Spectra for Soil Column A at the Basemat Center of SSI Model with 46 m Embedment.

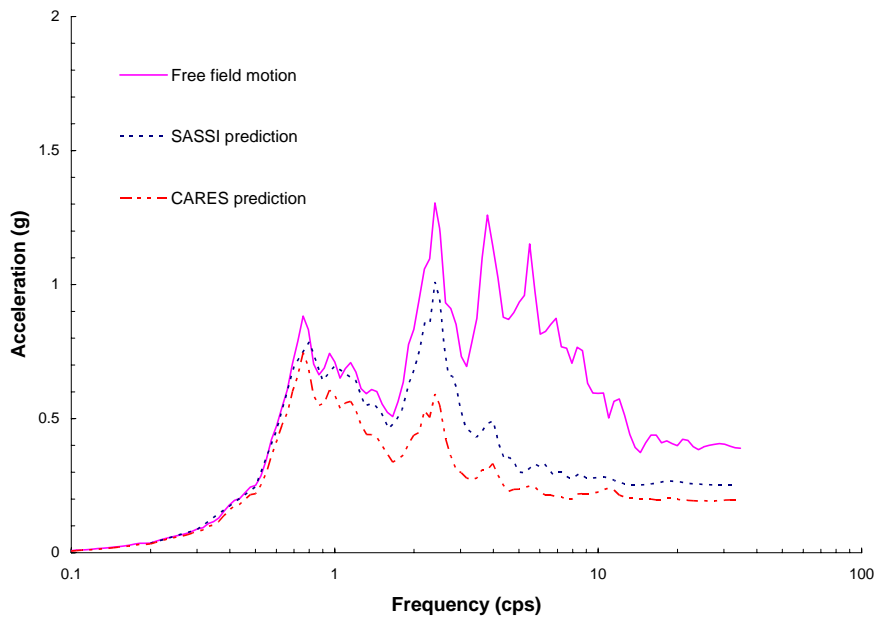


Figure 3.3-4 Comparison of Response Spectra for Soil Column A at the Roof Center of SSI Model with 46 m Embedment.

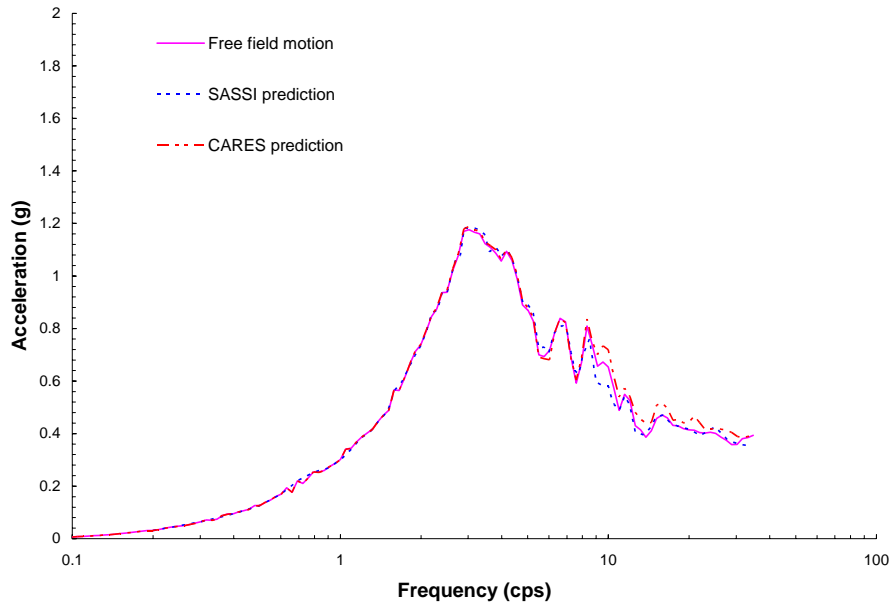


Figure 3.3-5 Comparison of Response Spectra for Soil Column B at the Basemat Center of SSI Model with 11.5 m Embedment.

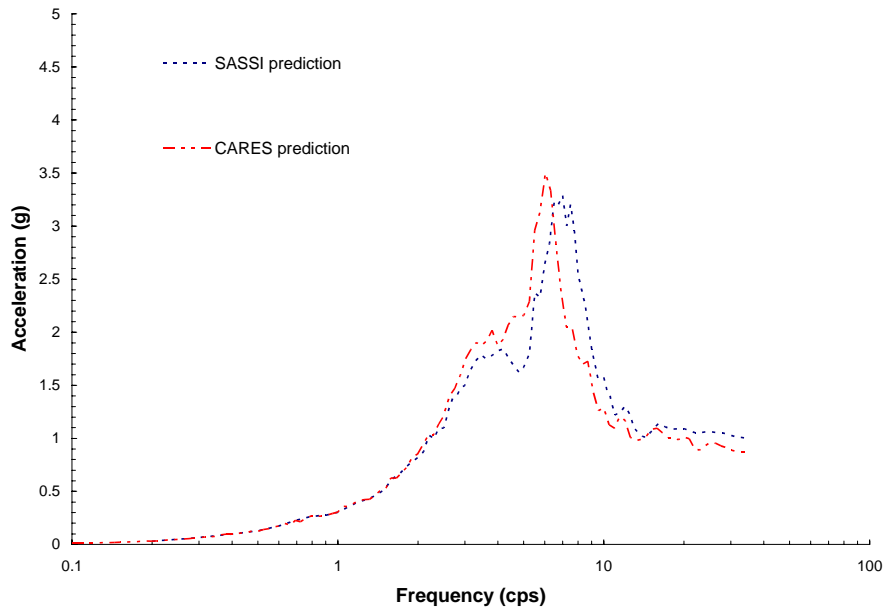


Figure 3.3-6 Comparison of Response Spectra for Soil Column B at the Roof Center of SSI Model with 11.5 m Embedment.

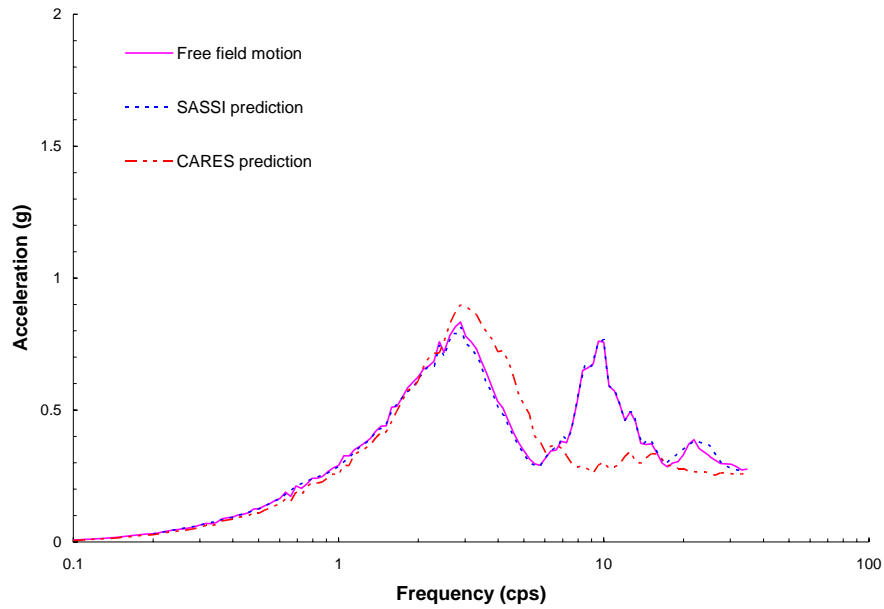


Figure 3.3-7 Comparison of Response Spectra for Soil Column B at the Basemat Center of SSI Model with 46 m Embedment.

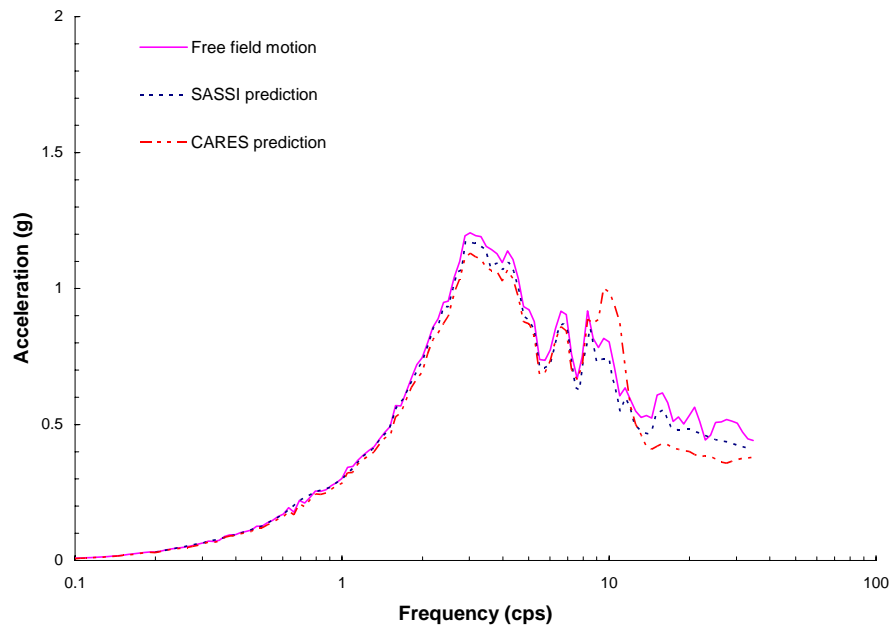


Figure 3.3-8 Comparison of Response Spectra for Soil Column B at the Roof Center of SSI Model with 46 m Embedment.

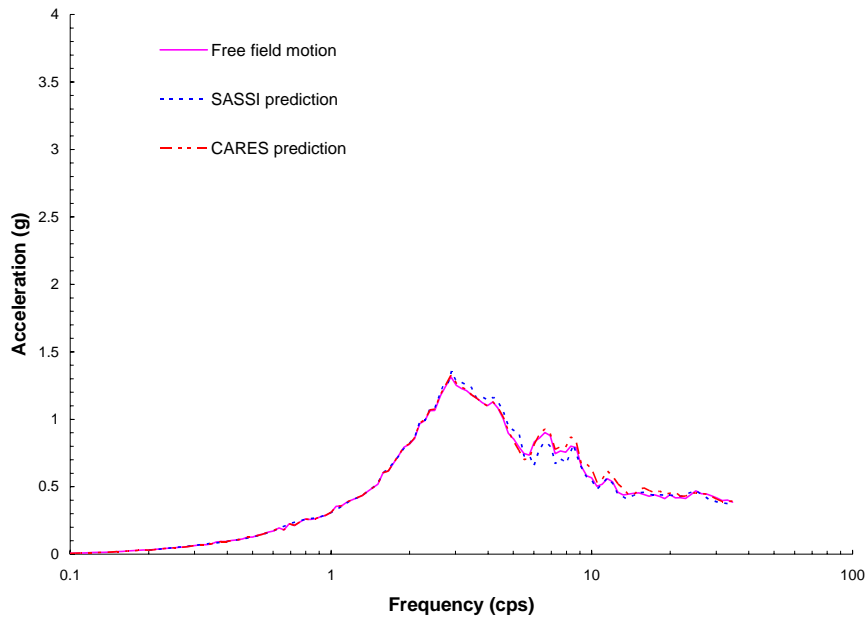


Figure 3.3-9 Comparison of Response Spectra for Soil Column C at the Basemat Center of SSI Model with 11.5 m Embedment.

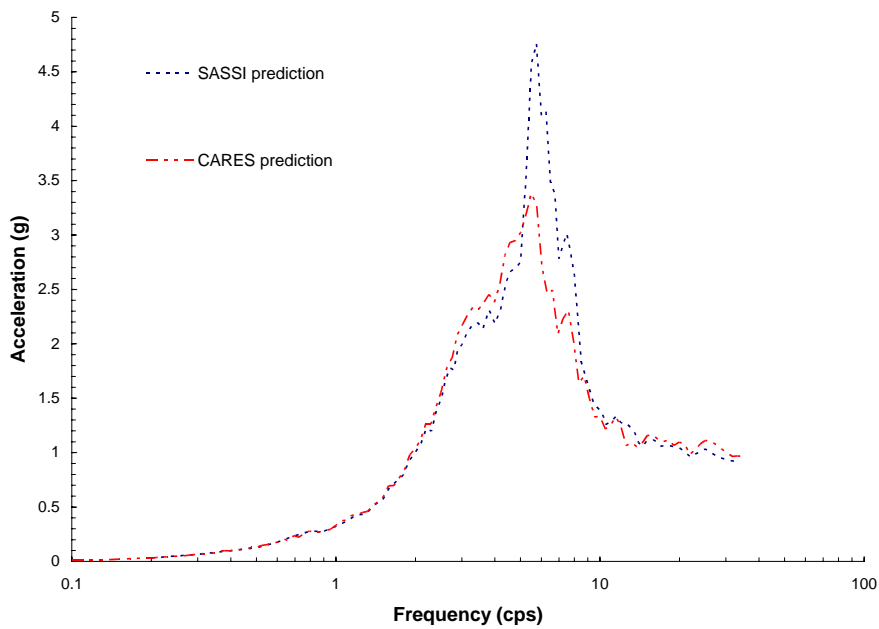


Figure 3.3-10 Comparison of Response Spectra for Soil Column C at the Roof Center of SSI Model with 11.5 m Embedment.

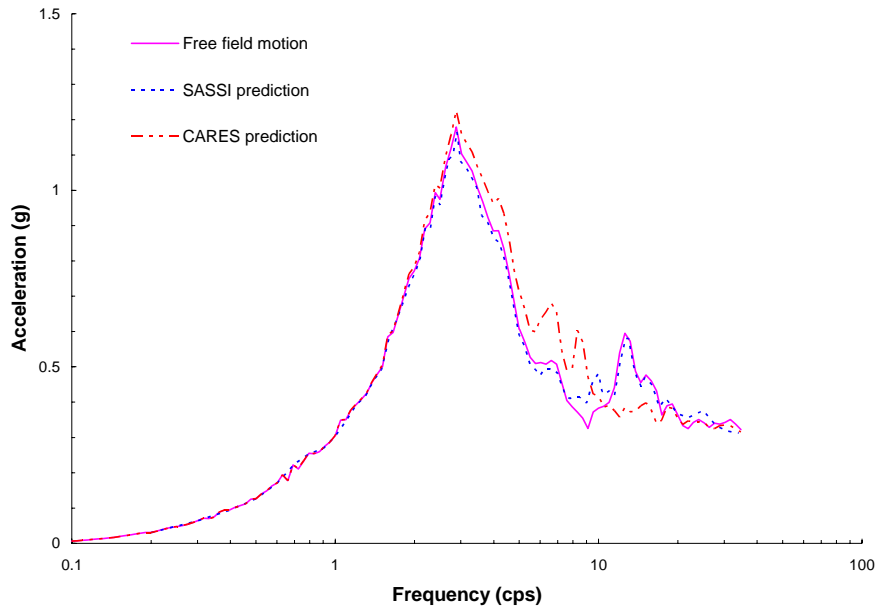


Figure 3.3-11 Comparison of Response Spectra for Soil Column C at the Basemat Center of SSI Model with 23 m Embedment.

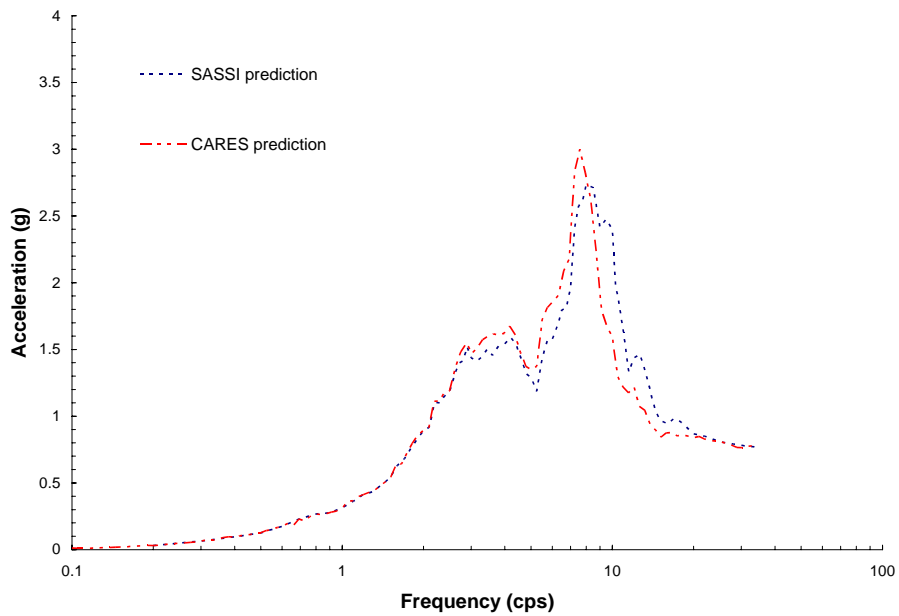


Figure 3.3-12 Comparison of Response Spectra for Soil Column C at the Roof Center of SSI Model with 23 m Embedment.

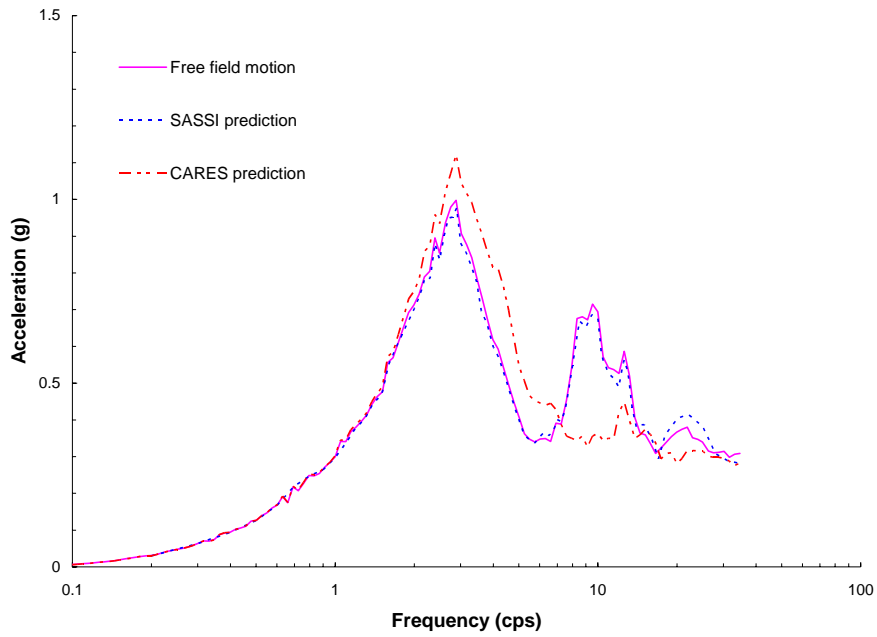


Figure 3.3-13 Comparison of Response Spectra for Soil Column C at the Basemat Center of SSI Model with 34.5 m Embedment.

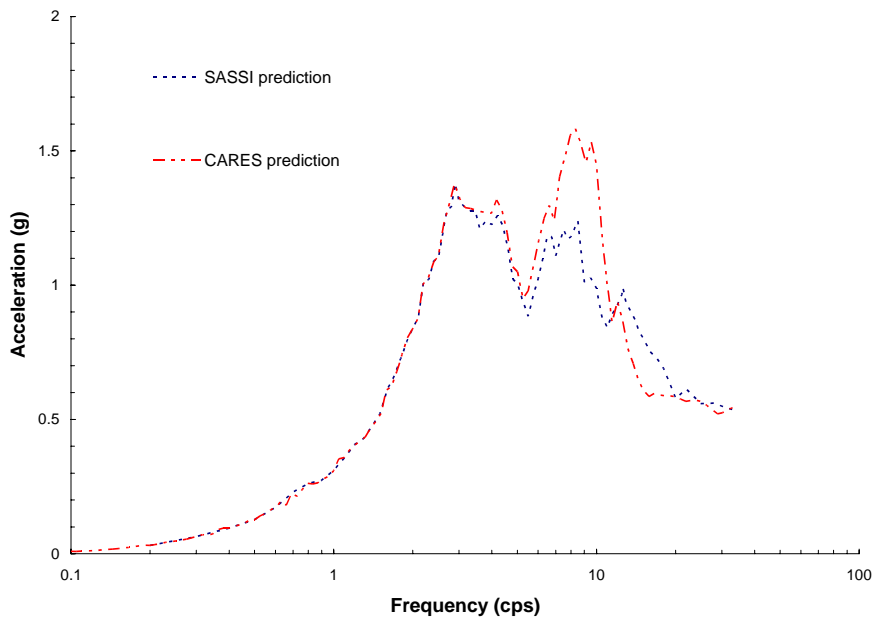


Figure 3.3-14 Comparison of Response Spectra for Soil Column C at the Roof Center of SSI Model with 34.5 m Embedment.

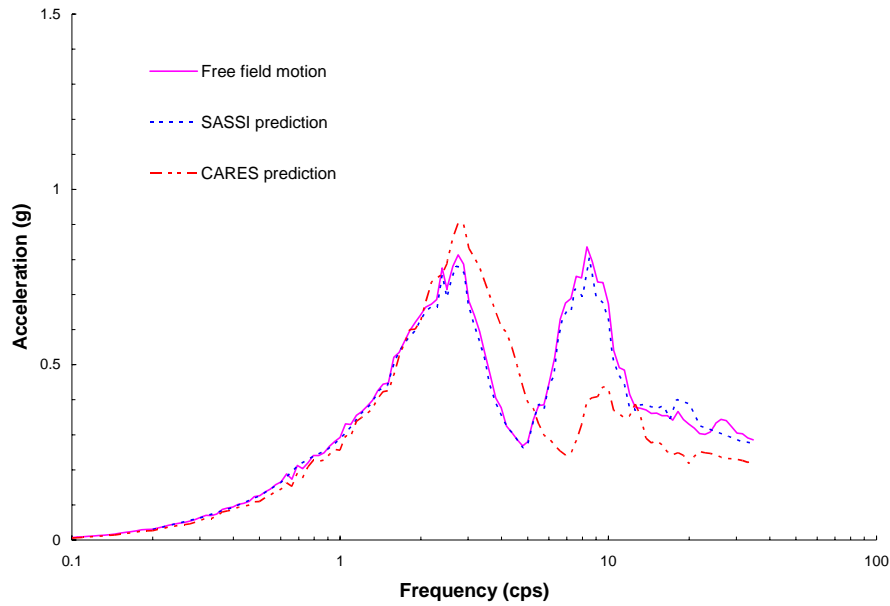


Figure 3.3-15 Comparison of Response Spectra for Soil Column C at the Basemat Center of SSI Model with 46 m Embedment.

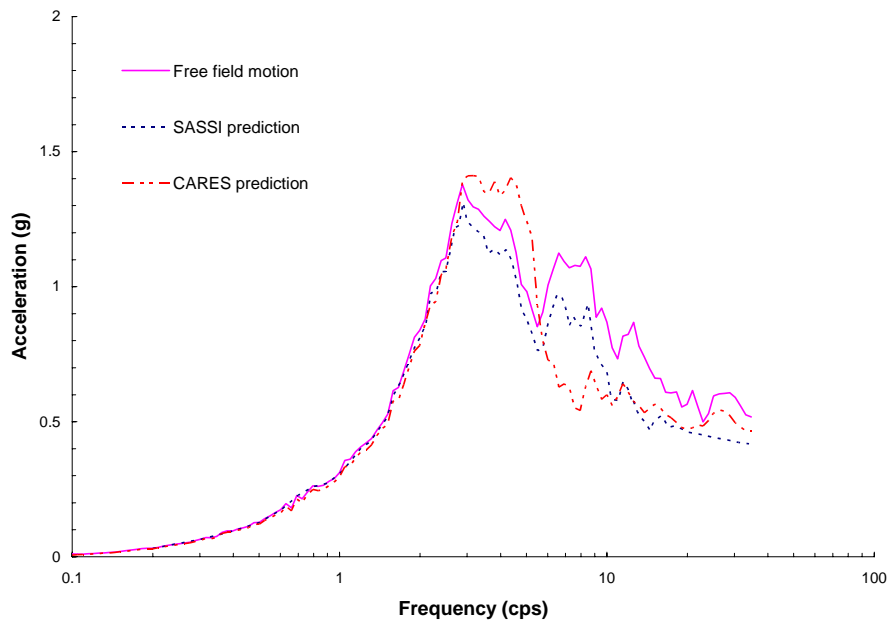


Figure 3.3-16 Comparison of Response Spectra for Soil Column C at the Roof Center of SSI Model with 46 m Embedment.

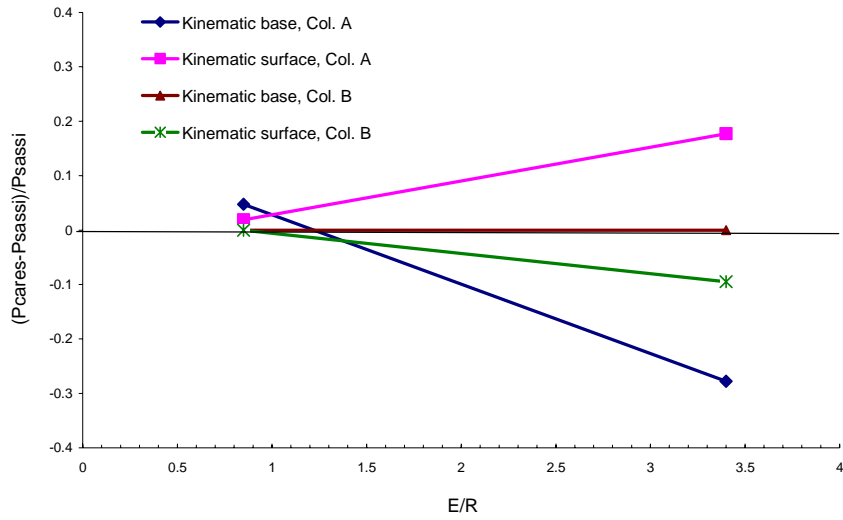


Figure 3.4-1 Performance Evaluation Based on Primary Spectral Peak Differences of Kinematic Analyses for Soil Columns A and B.

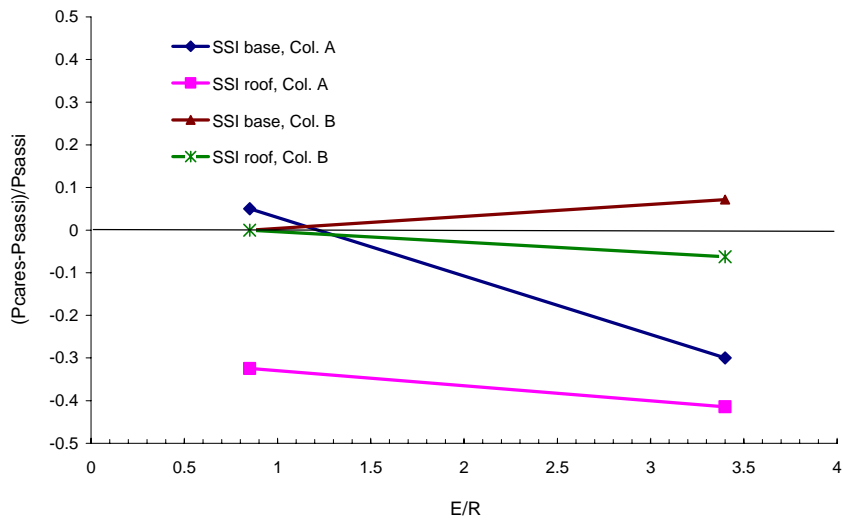


Figure 3.4-2 Performance Evaluation Based on Primary Spectral Peak Differences of SSI Analyses for Soil Columns A and B.

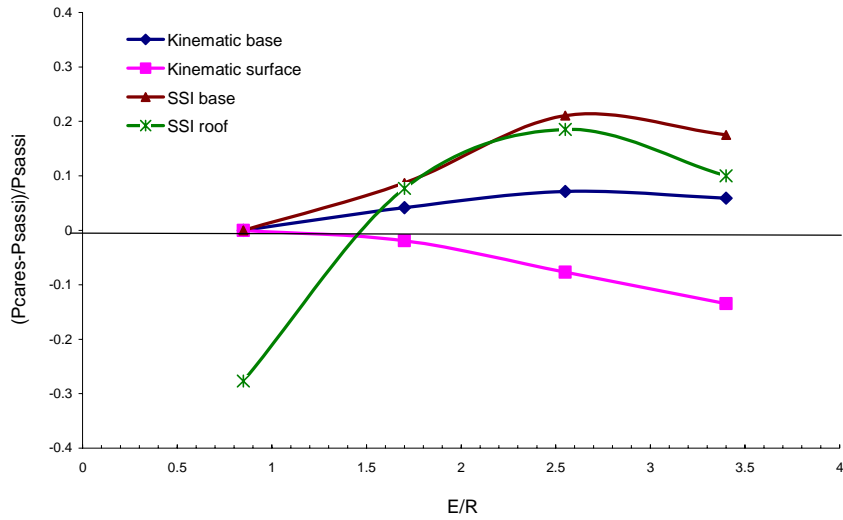


Figure 3.4-3 Performance Evaluation Based on Primary Spectral Peak Differences of Kinematic and SSI Analyses for Soil Column C.

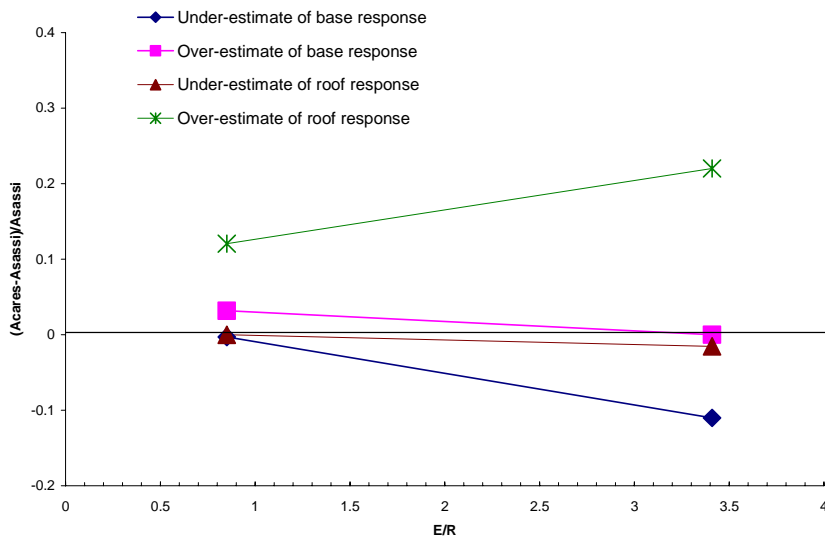


Figure 3.4-4 Performance Evaluation Based on Frequency Dependent Area Differences of Kinematic Analyses for Soil Column A.

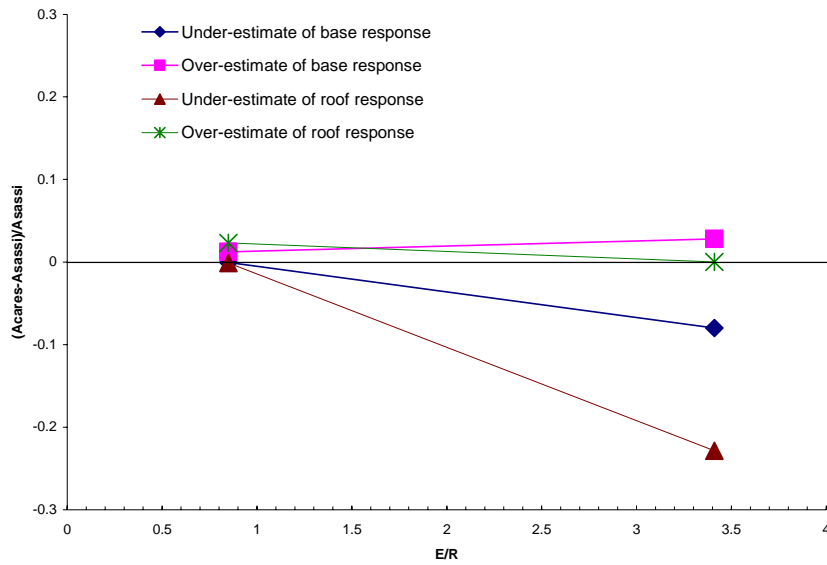


Figure 3.4-5 Performance Evaluation Based on Frequency Dependent Area Differences of Kinematic Analyses for Soil Column B.

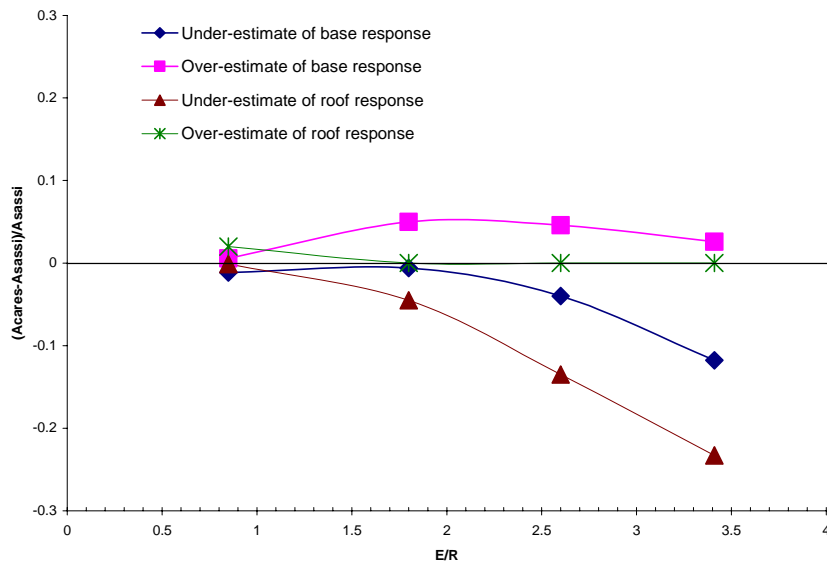


Figure 3.4-6 Performance Evaluation Based on Frequency Dependent Area Differences of Kinematic Analyses for Soil Column C.

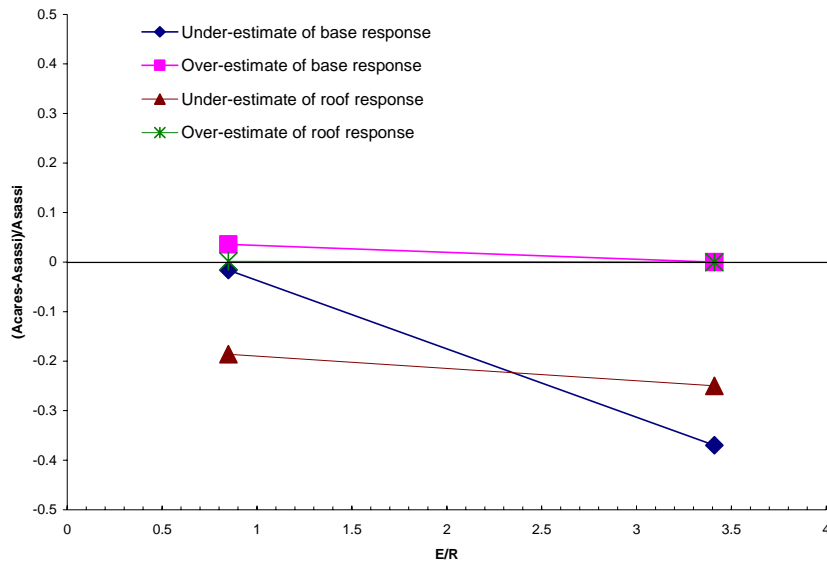


Figure 3.4-7 Performance Evaluation Based on Frequency Dependent Area Differences of SSI Analyses for Soil Column A.

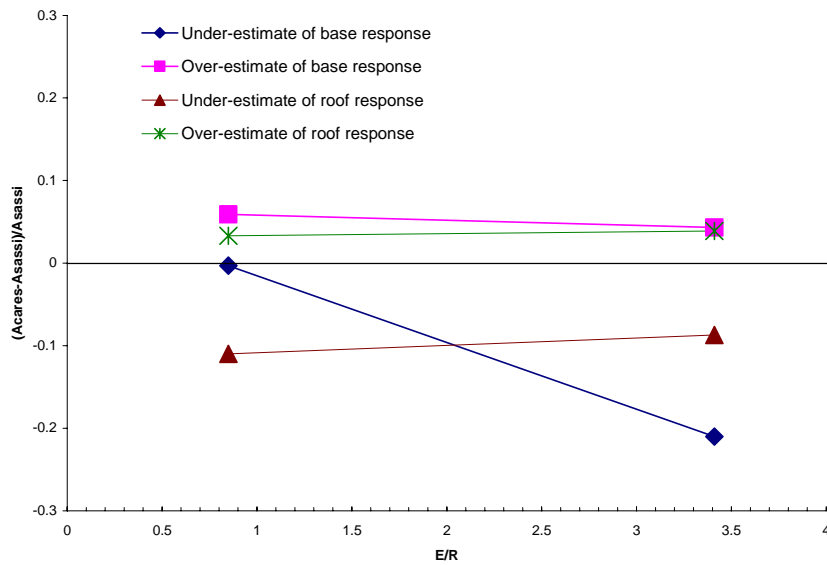


Figure 3.4-8 Performance Evaluation Based on Frequency Dependent Area Differences of SSI Analyses for Soil Column B.

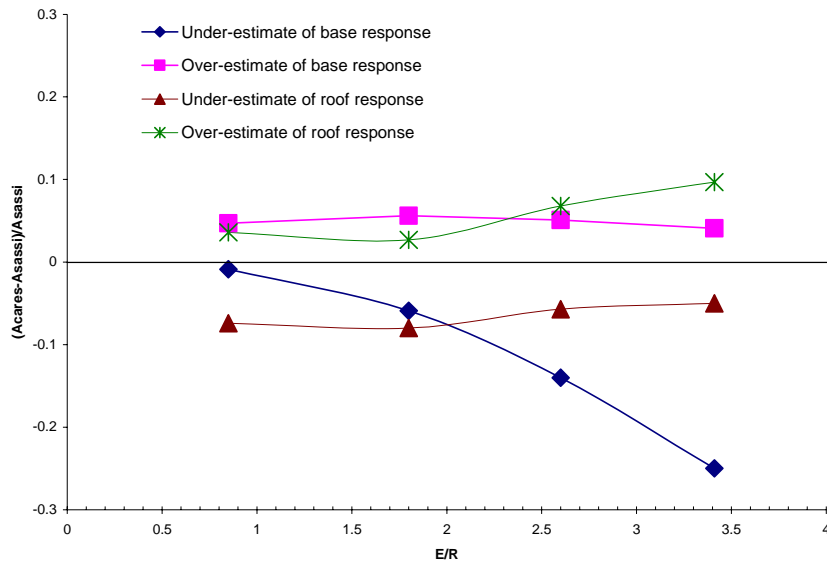


Figure 3.4-9 Performance Evaluation Based on Frequency Dependent Area Differences of SSI Analyses for Soil Column C.

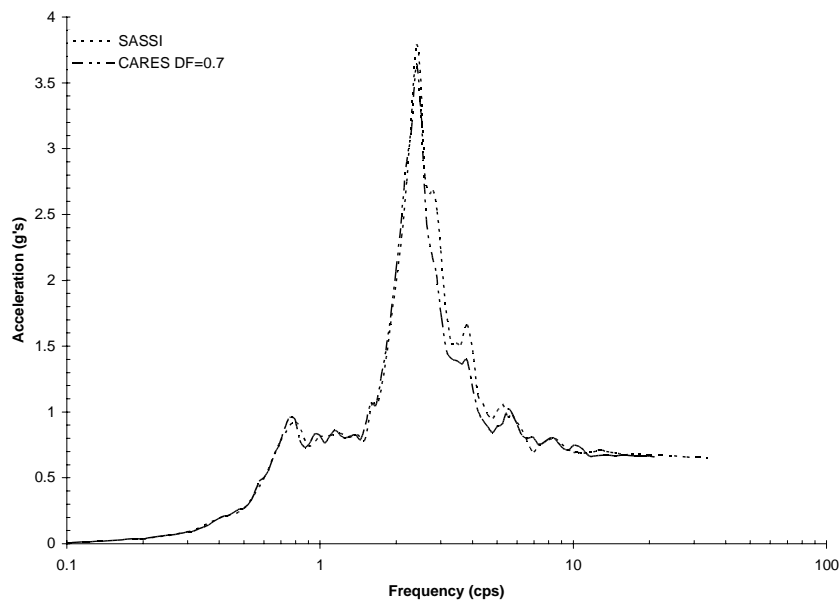


Figure 3.4-10 Comparison of Response Spectra for Soil Column A at the Roof Center of SSI Model with 11.5 m Embedment. Reduced Radiation Damping.

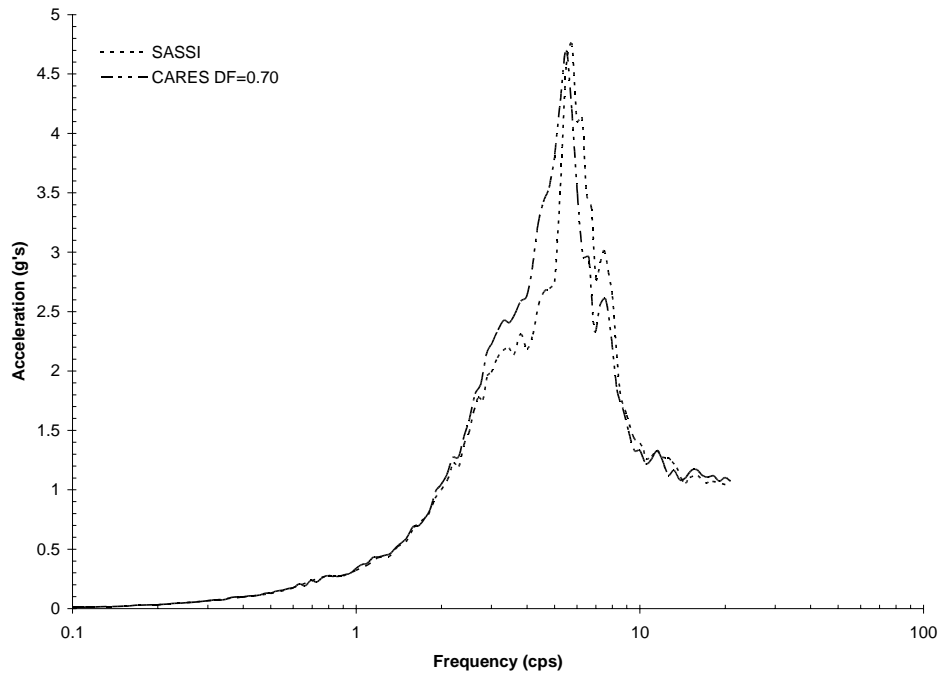


Figure 3.4-11 Comparison of Response Spectra for Soil Column C at the Roof Center of SSI Model with 11.5 m Embedment. Reduced Radiation Damping

4.0 ASSESSMENT OF METHODOLOGIES FOR COMPUTING SEISMIC INDUCED EARTH PRESSURES ON DEB STRUCTURES

As discussed in Section 2.1.2, large uncertainties exist in the manner in which seismic induced earth pressures are now calculated. It is expected that these uncertainties should become more serious as the depth of embedment for the new generation nuclear power plants is increased. Furthermore, from a phenomenological standpoint, the SSI effect changes from the predominantly inertial interaction effect for shallow embedded structures to the principally kinematic interaction effect for deeply embedded or fully buried structures, which in turn may impact the seismic induced earth pressures and the methodologies for their computation. Therefore, this topic has been included in the current study.

The current methodologies generally compute pressures either directly from the stresses in soil elements adjacent to the structural exterior walls or from separate analyses that are derived from “retaining wall” type solutions. The first class of analyses suffers from the fact that nonlinear effects (such as separation of the wall from the soil) cannot be included in the usual linear models used for the seismic analyses. The second class of analyses has the deficiency of relying on a methodology that is separate and largely independent from that used to determine the seismic response of the structure. The current study focuses on the first class of solutions.

4.1 Approach

Soil pressures are evaluated using both a linear code (SASSI) and a nonlinear code (LS-DYNA) in which nonlinear effects such as separation of the wall and soil may be considered. Solutions are obtained for the same structural model as used for the Section 3 variation of parameter studies.

The variable property soil column used for the studies described in Section 3 is used for the soil pressure study. Three components of the wall surface tractions are considered: the radial pressure acting on the wall, the shear in the tangential direction, and the shear in the vertical direction. Each of these components is equated to the corresponding stress in soil finite elements that are adjacent to the wall. It is expected that the soil pressures result from a combination of two effects: the inertial loads on the structure, and the kinematic deformations imposed on the foundation boundary.

It is expected that the inertial loads would be most significant for the shallow depths of burial where relatively large shear and moment inertial loads are transmitted from the superstructure to the foundation. It is also expected that the kinematic effects would be most significant and the inertial effect is gradually reduced for the larger depths of burial. Four depths of burial are considered for the SASSI and LS-DYNA solutions so that changes in the characteristics of the soil pressures may be monitored as the burial depth increases.

4.1.1 SASSI Model

The SASSI model used for this study employs the structure identical to the one described in Section 3.1.2 with the addition of solid soil finite elements placed around the plate elements used to define the cylindrical shell. These elements are used to compute the soil stresses that are then related to the wall pressures. There are two circles of elements added to the previous model; each is 2.5 m thick in the radial direction and follows the circumferential and vertical patterns described in Section 3.1.2.

4.1.2 LS-DYNA Model

The LS-DYNA models are developed to investigate soil pressure effects for the various depths of embedment. A key aspect associated with DEB structures is the interaction effect at the interface between the embedded part of the structure and the surrounding soils. The conventional linear analyses, such as SASSI, typically assume perfect bonding between the structure and the surrounding soils. Therefore, such analyses are incapable of addressing the nonhomogeneous behavior of soils, as well as possible separation effect at the soil-structure interface. As discussed in Section 2.3.1, LS-DYNA is particularly suitable for the finite element (FE) analysis of problems which require modeling structural interfaces and material nonlinearities.

The LS-DYNA models developed in this section fall into the category of continuum models as described in Section 2.3.1. While following the philosophy of the direct method, the LS-DYNA models are developed in the 3-dimensional domain. The soil and structure are modeled with explicit FEs, and the boundaries of the FE soil model are connected with a series of viscous dampers which are to ensure non-reflection of outgoing waves. In LS-DYNA, the approach used by Cohen and Jennings [1983] who in turn credited the method to Lysmer and Kuhlemeyer [1969] was implemented, in which viscous normal and shear stresses are applied to the boundaries in a manner as defined in the following equations:

$$\sigma_{\text{normal}} = -\rho c_d V_{\text{normal}}$$

$$\sigma_{\text{shear}} = -\rho c_s V_{\text{tangential}}$$

where ρ , c_d , and c_s are the material density, material longitudinal and shear wave velocities of the transmitting media. These equations reveal that the magnitude of these stresses at the boundaries is proportional to the particle velocities in the normal, (V_{normal}) and tangential, ($V_{\text{tangential}}$) directions.

The Lysmer's dampers placed on the artificial boundary are effective in reducing unwanted wave reflections if the boundary of the finite element mesh is sufficiently far outward. However, in doing so, the size of the near field finite element mesh is increased significantly and so is the cost of running the dynamic analysis. The exact stress field on the soil boundary of the given problem is a function of frequency dependent dampers and springs. As shown by Wolf [Wolf, 1999], the springs dominate the boundary stress field in low frequencies and near field, and as the frequency and the mesh boundary approaches infinity, the boundary stress field becomes a function of dampers only. Therefore, for a finite mesh of the unbounded soil medium, an improved transmitting boundary can be developed by applying a combination of springs and dampers to the boundary.

Wolf [Wolf, 2000] and Luco [Luco, 2004] have proposed such advanced transmitting boundaries, which can be incorporated in codes that are amenable to source changes. In this study, the soil mesh for the LS-DYNA models is extended sufficiently far outward from the structure to negate the impact of not including the springs in the transmitting boundary. As shown below, both the mesh size and the cost for running the analysis also increase significantly. In addition to the transmitting boundary, a circular boundary is placed on the lateral end of the soil mesh to ensure proper wave propagation near the boundary and to avoid the so called "corner effect" which would occur if a rectangular boundary is imposed on the mesh.

To be consistent with the SASSI models for soil pressure evaluation, four LS-DYNA SSI models are developed which correspond to the depth of burial (DOB) of the structure equal to

25% (11.5m), 50% (23m), 75% (34.5m) and 100% (46m) of the structural height. The 11.5m embedded FE model is shown in Figure 4.1.2-1 and a zoom-in view of the structure with the surrounding soil is depicted in Figure 4.1.2-2. Taking advantage of the structural symmetry, the model includes half of the soil structure system. The origin of the model coordinate system is placed on the symmetry plane at the soil surface with z-axis pointing upward and y-axis extending into the soil normal to the symmetry plane.

The soil FE model, which consists of brick elements, is extended outward 360m from the origin in the horizontal direction and 84m in the vertical direction (-z-axis). The first 80m depth of the soil model represents the overburden soil and a 4m layer of rock is placed beneath the overburden soil such that the transmitting boundary which is attached to the base of the 4m layer of rock assumes the rock property to represent the half-space rock underlain the soil overburden. The seismic input motion is defined as the outcrop motion at 80m below grade and is first converted to the in-column motion at 80m and then is applied to all nodes of the soil mesh at 80m below grade.

The LS-DYNA SSI model for the 11.5m embedment consists of 232,213 nodes and 219,110 elements. As discussed in Section 3.1.3, the typical SASSI approach for SSI analysis is to model the portion of the structure below the ground surface with explicit FEs while the superstructure above ground surface is represented with simple lumped masses and 3-D beams, which is rigidly linked to the below ground portion FEs at the ground surface. As opposed to the SASSI models, in the LS-DYNA models, the entire structure is modeled with explicit FEs, as depicted in Figure 4.1.2-2 in which the structural wall and roof are modeled with shell elements while the basemat is modeled with brick elements. It is noted that the LS-DYNA model mesh is created using Truegrid developed by XYZ Scientific Applications, Inc. [2001].

Following this approach, the LS-DYNA SSI models for the other three DOB cases are similarly developed. Figure 4.1.2-3 shows the LS-DYNA SSI model for the 23m embedment case (50% embedded) and a zoom-in view of the structure with the surrounding soil is provided in Figure 4.1.2-4. The 23m embedment model consists of 267,228 nodes and 253,470 solid and shell elements. The 34.5m embedment (75% embedded) LS-DYNA model is shown in Figures 4.1.2-5 and 4.1.2-6, while Figures 4.1.2-7 and 4.1.2-8 depict the 46m embedment (100% embedded) LS-DYNA model. The 34.5m embedment LS-DYNA model is comprised of 266,775 nodes and 253,010 solid and shell elements, and the 46m embedment LS-DYNA consist of 275,243 nodes and 291,310 solid and shell elements.

In estimating the seismic induced soil pressure, an important consideration and a real challenge in developing the SSI model is how to represent the structure-soil interface as close as possible to the real situation. Since the LS-DYNA SSI models are to be used in this study for 1) comparing with the SASSI analysis results of soil pressure response and 2) investigating the impact of the soil-structure interface modeling on the seismic induced pressure and the structural response, two bonding conditions are considered for representing the structure-soil interface in the LS-DYNA models. One condition considers that the structure and the surrounding soil are perfectly bonded (tied interface) which is done using the LS-DYNA keyword *CONTACT_TIED_SURFACE_TO_SURFACE. The effect of the tied interface is to ensure that soil and the structure move together at the interface, so that nonlinearity due to the soil/structure interface opening does not occur.

The second condition approximates the actual contact surfaces with a prescribed friction coefficient (0.7 is used in this model, which corresponds to 35 degree friction angle) and this is done using the LS-DYNA keyword *CONTACT_AUTOMATIC_SURFACE_TO_SURFACE.

The contact interface permits opening/closing and slipping at the soil/structure interface, which induces the effect of geometrical nonlinearity in the SSI model. The contact interface model is considered more realistic from a theoretical viewpoint. Practically speaking, however, the nonlinearity which associated with the use of the contact interface requires more delicate treatment in developing the SSI model. Any mishandling could potentially trigger other numerical issues that may compromise the analysis result.

For comparing with the SASSI analysis results, the tied interface LS-DYNA models without gravity load are developed, which is essentially a linear analysis. However, the difference between the LS-DYNA and SASSI remains that SASSI is a frequency domain program that employs a closed form solution of wave propagation in far field and a finite element representation for the structure and irregular soils in near field, while LS-DYNA uses an explicit algorithm in time domain which models both soil and structure in explicit finite elements and connects the exterior boundary to a series of transmitting dampers to ensure that the far field is the wave sink not as a wave source.

Since the use of a contact interface introduces geometric nonlinearity, the associated dynamic analysis therefore becomes load path dependent. For this reason, a pre-load of 1G gravity is performed before commencing the seismic analysis in the study of the effect of interface modeling on the seismic induced pressure and structural responses.

4.2 SASSI Analysis of Embedment Effect on Seismic Induced Earth Pressures for DEB Structures

This subsection describes the SASSI analysis results of seismic induced soil pressure response. As discussed above, solutions for the 11.5 m, 23 m, 34.5 m, and the 46 m depths of burial are considered. Results for each of these cases are first presented and they are followed with a comparison of the results for the four cases.

4.2.1 SASSI Analysis for the 11.5 m Depth of Burial

The SASSI problem discussed in Section 3.3 is rerun for the variable soil column and with the additional soil elements outside of the plate elements. Stresses in the layer of soil elements adjacent to the cylinder are then used to compute soil pressures acting on the cylinder. The stresses determined from SASSI are in the Cartesian coordinate system. These are first transposed to a cylindrical coordinate system (θ representing the tangential position on the cylinder, R the radial position in the model, and Z the vertical position in the model.) The radial pressure acting on the cylinder is S_{rr} , the tangential shear is $S_{r\theta}$, and the vertical shear is S_{rz} . These are equaled to the corresponding stresses in the soil elements.

The variation of the radial stress (normal pressure) with time is shown on Figure 4.2.1-1. This is done for the head on element ($\theta = 0$) with the element centered at the mid-height of structural wall. The two highest pressures are found at time equal to 8.99 seconds when the peak stress is 302 kN/m² and at 12.63 seconds when the stress is -287 kN/m². The first peak occurs when the acceleration at the top of the structure reaches its highest value (0.91 g). The peak acceleration at the second peak is only 0.84 g but at this time the accelerations over the buried portion of the structure are higher than at 8.99 seconds (0.35 g versus 0.01 g). Results obtained at 8.99 seconds are used for all of the following discussions.

The pressure distributions over the shell vary with both elevation (z) and angular position (θ), with $\theta = 0$ at the head on location of the shell. The problem is symmetric (both in geometry and loading) about the x axis and the loading is anti-symmetric about the y axis. It is therefore assumed that the pressures vary as either $\cos \theta$ or $\sin \theta$. The variation of the radial pressure at the mid-height of the depth of burial (about 5 m) is assumed to have a cosine variation and the SASSI results (solid line) are compared with a cosine variation as shown on Figure 4.2.1-2. The variation of the tangential shear is assumed to have a sine variation and the SASSI results are compared with the sine variation on Figure 4.2.1-3. The variation of the vertical shear is assumed to have a cosine variation and the SASSI results are compared with the cosine variation on Figure 4.2.1-4. As may be seen, the assumed variations very closely fit the SASSI calculated results.

The variation of these three pressure components with z is shown on Figure 4.2.1-5. The applied shear from the upper cantilever portion of the structure is resisted by the normal pressure and the hoop shear pressure while the bending moment from the cantilever portion of the structure is resisted by all three pressure components. It can be seen (by virtue of its strong variation with z) that the normal pressure component is primarily due to bending with a small shear component. It is interesting to note that the likely soil horizontal pressure due to dead weight of the soil is one half of the column weight so that at a depth of 10 m the horizontal dead weight pressure is about 86 kN/m^2 and it would increase linearly with depth. This would indicate that negative pressures would occur for depths less than about 4 m. One might then expect that separation between the soil and wall would occur above 4 m and that this separation could significantly affect the results.

The foundation displacements at 8.99 seconds are considered next. The SASSI predicted displacements are shown as the plotted points on Figure 4.2.1-6. Of course, these displacements include a rigid body component that does not cause shear in the structural components. A “best fit” line through the predicted displacements is found and shown as the solid line on Figure 4.2.1-6. It can be seen that the major portion of the displacements is due to rigid body motion. The difference between the points and this line are shear displacements and result in shear loads within the structural walls. These are plotted on Figure 4.2.1-7. The relatively small magnitude of these displacements as compared to the total displacements leads to questions of accuracy in the shear displacements (taking differences between two numbers which are large and close together). Small errors in the predictions of the total displacements may result in large errors in the predictions of the shear displacements. It may not be a good idea to use these predicted displacements to calculate shear loads in the structural walls.

As an alternative it may be better to use the applied loads as calculated in SASSI to evaluate the internal shear loads in the structural walls. The loads that must be considered are the inertial loads and the loads resulting from the wall pressures discussed above. The inertial loads result from the accelerations acting on the masses of the structure. A plot of these accelerations at 8.99 seconds is shown on Figure 4.2.1-8. It can be seen that the above grade portion of the structure rotates as a rigid body about the ground surface. The results shown on Figures 4.2.1-6 and 4.2.1-8 indicate that the foundation has reached a maximum negative displacement and the accelerations show that the negative displacements now begin to decrease in absolute magnitude.

These loads are applied to the structure and beam shear variation along the structure is computed and plotted on Figure 4.2.1-9. The solid line represents the shear resulting from the inertial loading. The shear resulting from the radial pressure (S_r) and the tangential shear (S_t) are represented by the small dashed and dot-dashed lines, respectively. The vertical shear makes no contribution to the total shear. It can be seen that the effect of the radial pressure is about 4 times that of the tangential shear. It could be argued that for this shallow depth of burial the tangential

shear could be neglected. The shear load that must be carried by the structure is the sum of the three curves. At the basemat depth (11.5 m), it can be seen that the sum of the soil pressure effect more than equilibrates the shear load due to inertial effects. This load (24,000 kN) is taken out at the basemat. The direction of this basemat shear is verified by the negative displacement shown on Figure 4.2.1-6.

The variation in bending moment along the cylinder caused by the three loads is shown on Figure 4.2.1-10. The same notation is used as discussed above for the loads with the exception that the vertical shear now has an effect and it is shown with the large dashed line on the figure. It can be seen that the vertical shear now carries the major portion of the bending moment with the radial pressure contributing about 80 % of the vertical shear and the hoop shear contributes about 20 % of the vertical shear.

4.2.2 SASSI Analysis for the 23 m Depth of Burial

The same problem as discussed in the previous section is run with SASSI for the 23 m depth of burial. Stresses in the soil elements are retrieved and transformed from the Cartesian coordinate system of the model to a cylindrical coordinate system. The variation of the radial stress (normal pressure) with time is shown on Figure 4.2.2-1. This is done for the head on element ($\theta = 0$) with the element centered at a depth equal to -13 m (about the middle of the cylinder). The two highest pressures are found at time equal to 10.85 seconds when the peak stress is 23.6 kN/m^2 and at 10.95 seconds when the stress is 22 kN/m^2 . The first peak occurs when the accelerations at most of the structural nodes reach their peak values (about 0.3 g). Results obtained at 10.95 seconds are used for all of the following discussions.

The pressure distributions over the shell vary with both elevation (z) and angular position (θ), with $\theta = 0$ at the head on location of the shell. It is assumed that the pressures vary as either $\cos \theta$ or $\sin \theta$ as discussed above. This is verified above for the shallow depth of burial and again for the deepest depth of burial (46 m) and is not verified again for this case.

The variation of these three pressure components with z is shown on Figure 4.2.2-2. The normal pressures can be seen to be rather uniform with a small spike near the surface. This is quite different from the 11.5 m results, where the normal pressure varies strongly with depth. The peak pressures for the 23 m case are much smaller than for the 11.5 m case (45 kN/m^2 as compared to 300 kN/m^2). The tangential shear is now smaller than found for the 11.5 m case and has a smaller variation with depth than might be expected for a beam resting on an elastic foundation. The vertical shear now varies strongly with depth in an almost linear manner indicating that most of the bending moments are carried by this pressure component. The peak values of the vertical shear are about the same as found for the 11.5 m. It is interesting to note that the likely soil horizontal pressure due to dead weight of the soil is one-half of the column weight so that at a depth of 10 m, the horizontal dead weight pressure is about 86 kN/m^2 and it would increase linearly with depth. This would indicate that negative pressures would not occur and separation of soil and structure would not be an issue for seismic inputs with ZPAs less than 0.3 g

The foundation displacements at 10.95 seconds are considered next. The SASSI predicted displacements are shown as the plotted points on Figure 4.2.2-3. Of course, these displacements include a rigid body component that does not cause shear in the structural components. A “best fit” line through the predicted displacements is found and shown as the solid line on Figure 4.2.2-3. It can be seen that the major portion of the displacements is due to rigid body motion. The difference between the points and this line are shear displacements and result in shear loads within the structural walls. These are plotted on Figure 4.2.2-4. The relatively small magnitude of

these displacements, as compared to the total displacements, leads to questions of accuracy in the shear displacements (taking differences between two numbers which are large and close together). Peak shear displacements are found to be on the order of 0.0001 while peak total displacements are 10 times higher. Small errors in the predictions of the total displacements may result in large errors in the predictions of the shear displacements. It may not be a good idea to use these predicted displacements to calculate shear loads in the structural walls.

As an alternative it may be better to use the applied loads as calculated in SASSI to evaluate the internal shear loads in the structural walls. The loads that must be considered are the inertial loads and the loads resulting from the wall pressures discussed above. The inertial loads result from the accelerations acting on the masses of the structure. A plot of these accelerations at 10.95 seconds is shown on Figure 4.2.2-5. It can be seen that peak accelerations are about 0.3 g. This likely indicates that the frequency of the cantilever portion of the structure protruding above grade is too high to be excited by the seismic input. If the frequency of the 23 m cantilever were lower the soil pressure characteristics might be closer to the 11.5 m case where the inertial loading on the cantilever is dominant.

These loads are applied to the structure and shear variation along the structure is computed and plotted on Figure 4.2.2-6. The solid line represents the shear resulting from the inertial loading. The shear resulting from the radial pressure (S_{rr}) and the tangential shear (S_{rt}) are represented by the small dashed and dot-dashed lines, respectively. The vertical shear makes no contribution to the shear. It can be seen that the effect of the radial pressure is about one half that of the tangential shear. It can be seen that the 23 m case is governed primarily by the tangential shear stress as compared to the 11.5 m case which was governed primarily by the normal pressure. The shear load that must be carried by the structure is the sum of the three curves. At the basement depth (23 m) it can be seen that the sum of the soil pressure effects equilibrates to one-half of the inertial shear with the remainder carried through the base SSI shear.

The variation in bending moment along the cylinder caused by the three loads is shown on Figure 4.2.2-7. The same notation is used as discussed above for the loads with the exception that the vertical shear now has an effect and it is shown with the large dashed line on the figure. It can be seen that most of the bending moment induced by the inertial loads is resisted by the vertical shear pressure.

4.2.3 SASSI Analysis for the 34.5 m Depth of Burial

The same problem as discussed in the previous section is run with SASSI for the 34.5 m depth of burial. Stresses in the soil elements are retrieved and transformed from the Cartesian coordinate system of the model to a cylindrical coordinate system. The variation of the radial stress (normal pressure) with time is shown on Figure 4.2.3-1. This is done for the head on element ($\theta = 0$) with the element centered at a depth equal to -17 m (about the middle of the cylinder). The two highest pressures are found at time equal to 10.845 seconds when the peak stress is 18.3 kN/m^2 and at 10.98 seconds when the stress is -16.6 kN/m^2 . The first peak occurs when the accelerations at most of the structural nodes reach their peak values (about 0.3 g). Results obtained at 10.845 seconds are used for all of the following discussions.

The pressure distributions over the shell vary with both elevation (z) and angular position (θ), with $\theta = 0$ at the head on location of the shell. It is assumed that the pressures vary as either $\cos \theta$ or $\sin \theta$ as discussed above. This is verified above for the shallow depth of burial and again for the deepest depth of burial (46 m) and is not verified again for this case.

The variation of the three pressure components with z is shown on Figure 4.2.3-2. The normal pressures can be seen to be rather small with peak values of about 30 kN/m^2 . The tangential shear varies in the same manner as the normal pressure and is slightly larger. The vertical shear is small from the surface to a depth of about 12 m and then varies strongly with depth in an almost linear manner indicating that most of the bending moments are carried by this pressure component. The peak value of the vertical shear is about 160 kN/m^2 . It is interesting to note that the likely soil horizontal pressure due to dead weight of the soil is one-half of the column weight, so that at a depth of 10 m, the horizontal dead weight pressure is about 86 kN/m^2 and it would increase linearly with depth. This would indicate that negative pressures would not occur and separation of soil and structure would not be an issue for seismic inputs with ZPAs less than 0.3 g

The foundation displacements at 10.845 seconds are considered next. The SASSI predicted displacements are shown as the plotted points on Figure 4.2.3-3. Of course, these displacements include a rigid body component that does not cause shear in the structural components. A “best fit” line through the predicted displacements is found and shown as the solid line on Figure 4.2.3-3. It can be seen that the major portion of the displacements is due to rigid body motion. The difference between the points and this line are shear displacements and result in shear loads within the structural walls. These are plotted on Figure 4.2.3-4. The relatively small magnitude of these displacements as compared to the total displacements leads to questions of accuracy in the shear displacements (taking differences between two numbers which are large and close together). Peak shear displacements are found to be on the order of 0.0002, while peak total displacements are 40 times higher. Small errors in the predictions of the total displacements may result in large errors in the predictions of the shear displacements. It may not be a good idea to use these predicted displacements to calculate shear loads in the structural walls.

As an alternative, it may be better to use the applied loads as calculated in SASSI to evaluate the internal shear loads in the structural walls. The loads that must be considered are the inertial loads and the loads resulting from the wall pressures discussed above. The inertial loads result from the accelerations acting on the masses of the structure. A plot of these accelerations at 10.845 seconds is shown on Figure 4.2.3-5. It can be seen that peak accelerations vary between 0.23 g and 0.3 g, with the maximum acceleration occurring at a depth of 20 m. This likely indicates that the frequency of the cantilever portion of the structure protruding above grade is too high to be excited by the seismic input. If the frequency of the 34.5 m cantilever was lower, the soil pressure characteristics might be closer to the 11.5 m case where the inertial loading on the cantilever is dominant.

These loads are applied to the structure and the shear variation along the structure is computed and plotted on Figure 4.2.3-6. The solid line represents the shear resulting from the inertial loading. The shear resulting from the radial pressure (S_r) and the tangential shear (S_t) are represented by the small dashed and dot-dashed lines, respectively. The vertical shear makes no contribution to the total shear. It can be seen that the effect of the radial pressure is slightly smaller than that of the tangential shear. The shear load that must be carried by the structure is the sum of the three curves. At the basemat depth (34.5 m) it can be seen that the sum of the soil pressure effects equilibrates to slightly less than one half of the inertial shear, with the remainder carried through the basemat SSI shear.

The variation in bending moment along the foundation caused by the loads is shown on Figure 4.2.3-7. The same notation is used as discussed above for the loads, with the exception that the vertical shear now has an effect and it is shown with the large dashed line on the figure. Most

of the resisting moment is supplied by the vertical shear. The net moment at the basemat is close to zero.

4.2.4 SASSI Analysis for the 46 m Depth of Burial

The SASSI problem discussed above is rerun for the case of 46 m depth of burial. Stresses in the soil elements are retrieved and transformed from the Cartesian coordinate system of the model to a cylindrical coordinate system. The variation of the radial stress (normal pressure) with time is shown on Figure 4.2.4-1. This is done for the head on element ($\theta = 0$) with the element centered at a depth equal to -21 m (about the middle of the cylinder). The two highest pressures are found at times equal to 8.945 seconds when the peak stress is 11.1 kN/m^2 and at 11.005 seconds when the stress is -12 kN/m^2 . Results obtained at 11.005 seconds are used for all of the following discussions.

The pressure distributions over the shell vary with both elevation (z) and angular position (θ), with $\theta = 0$ at the head on location of the shell. The problem is symmetric (both in geometry and loading) about the x axis and the loading is anti-symmetric about the y axis. It is therefore assumed that the pressures vary as either $\cos \theta$ or $\sin \theta$. The variation of the radial pressure is assumed to have a cosine variation and the SASSI results (solid line) are compared with a cosine variation as shown on Figure 4.2.4-2. The variation of the tangential shear is assumed to have a sine variation and the SASSI results are compared with the sine variation on Figure 4.2.4-3. The variation of the vertical shear is assumed to have a cosine variation and the SASSI results are compared with the cosine variation on Figure 4.2.4-4. As may be seen, the assumed variations very closely fit the SASSI calculated results.

The variation of these three pressure components with z is shown on Figure 4.2.4-5. The radial pressure varies fairly uniformly with depth at about 20 kN/m^2 , except for the increase to 75 kN/m^2 at the base. The tangential shear varies in the same fashion but is slightly larger than the normal pressure. The vertical shear varies almost linearly with depth, reaching a peak value equal to about 175 kN/m^2 at the base. It is interesting to note that the likely soil horizontal pressure due to dead weight of the soil is one half of the column weight so that at a depth of 10 m the horizontal dead weight pressure is about 86 kN/m^2 and it would increase linearly with depth. This would indicate that negative pressures would not occur for this case so that separation does not occur.

The foundation displacements at 11.005 seconds are considered next. The SASSI predicted displacements are shown as the plotted points on Figure 4.2.4-6. Of course, these displacements include a rigid body component that does not cause shear in the structural components. A “best fit” line through the predicted displacements is found and shown as the solid line on Figure 4.2.4-6. It can be seen that the major portion of the displacements is due to rigid body motion. The difference between the points and this line are shear displacements and result in shear loads within the structural walls. These are plotted on Figure 4.2.4-7. The relatively small magnitude of these displacements as compared to the total displacements leads to questions of accuracy in the shear displacements (taking differences between two numbers which are large and close together). Small errors in the predictions of the total displacements may result in large errors in the predictions of the shear displacements. It may not be a good idea to use these predicted displacements to calculate shear loads in the structural walls.

As an alternative, it may be better to use the applied loads as calculated in SASSI to evaluate the internal shear loads in the structural walls. The loads that must be considered are the

inertial loads and the loads resulting from the wall pressures discussed above. The inertial loads result from the accelerations acting on the masses of the structure. A plot of these accelerations at 11.005 seconds is shown on Figure 4.2.4-8. The accelerations vary from 0.14 g to 0.26 g.

These loads are applied to the structure and shear variation along the structure is computed and plotted on Figure 4.2.4-9. The solid line represents the shear resulting from the inertial loading. The shear resulting from the radial pressure (S_{rr}) and the tangential shear (S_{rt}) are represented by the small dashed and dot-dashed lines respectively. The vertical shear makes no contribution to the shear. It can be seen that the effect of the radial pressure is about the same as that of the tangential shear. The shear load that must be carried by the structure is the sum of the three curves.

The variation in bending moment along the foundation caused by the loads is shown on Figure 4.2.4-10. The same notation is used as discussed above for the loads with the exception that the vertical shear now has an effect and it is shown with the large dashed line on the figure. It can be seen that the vertical shear carries the major portion of the bending moment with the radial and tangential shears contributing equal amounts.

4.2.5 SASSI Assessment of the Depth of Burial Effect

The four wall pressure solutions (for depths of burial equal to 11.5 m, 23 m, 34.5m, and 46 m) discussed in the previous sections are compared in this section of the report. The peak radial pressures are found to occur at 8.99 sec, 10.95 sec, 10.845 sec, and 11.005 sec, for DOB equal to 11.5m, 23 m, 34.5 m and 46 m, respectively. The latter three cases occur when the input rock outcrop motion reaches peak values (see Figure 3.1.1-5). The first case is largely driven by the large inertial loads acting on the above grade portion of the structure. The frequency of this portion of the structure is about 12 cps. It is likely that the energy in the input pulse around this frequency is the largest around 9 seconds.

Variation of the radial, tangential, and vertical shears with depth, are shown on Figures 4.2.5-1, 4.2.5-2, and 4.2.5-3, respectively, for all four depths of burial. The depth is normalized with the embedment depth so that all four cases may be compared. It can be seen that the pressure distributions and magnitudes are very similar for the latter three cases, while the 11.5 m DOB results are quite different. Both the radial and tangential shears are almost constant with depth for the three latter cases. The pressure amplitudes are about 25 kN/m². The tangential shear increases to about 55 kN/m² near the base for all three cases. The vertical shear for the three cases varies linearly from zero at the surface to about 160 kN/m² near the base. The 11.5 m DOB case has characteristics which are opposite from the other three cases. The vertical shear is about constant (75 kN/m²) with depth, while the radial and tangential shears vary from zero at the basemat to a large value near the surface (320 kN/m² for the radial pressure and 80 kN/m² for the tangential shear).

The differences between the 11.5 m case and the other deeper depths of burial cases are likely caused by the large inertial loads in the above ground portion of the structure. Peak accelerations in the above ground portion of the structure for the 11.5 m DOB case reach 0.91 g. The peak accelerations for the 23 m, 34.5 m, and 46 m DOBs reach 0.74 g, 0.43 g, and 0.39g, respectively. The 11.5 m case has a much taller structure above grade leading to larger shear and moment loads which are not directly supported by the soil. It would be interesting to conduct a variation of parameter study where the shear and moment loads acting on the foundation portion of the structure are varied.

4.3 LS-DYNA Analysis of Seismic Induced Earth Pressures and Comparisons with SASSI Results

To investigate the characteristics of seismic induced earth pressures as affected by the depth of embedment and to assess the methodologies for computing the seismic induced pressure, the LS-DYNA models with tied interfaces as described in Section 4.1.2 are used to perform a comparative study of the seismic induced pressure analysis with SASSI. In order to make comparisons of the LS-DYNA analysis with the SASSI results, the LS-DYNA models used in this section do not include the effect of the gravity load and again consider the same four DOB cases. As alluded in Section 4.1.2, the seismic input motion to the LS-DYNA models is specified at the base of the soil overburden, which is at 80m below the ground surface. This input motion is generated from a rock outcrop motion as discussed in Section 3.1.1 using the CARES program. It is noted that, in the present analysis, the material nonlinearity is not considered, and linear elastic material is assumed for soil.

4.3.1 LS-DYNA Free Field Analysis

LS-DYNA was developed primarily for impact related simulations and hasn't been extensively used to address seismic issues. Based on the literature search performed during the course of this study, limited published seismic analyses [e.g., Pascal, 2001, Field, 2003] have been found which were performed using LD-DYNA, and none were performed to address the SSI phenomenon. However, LD-DYNA has both explicit and implicit solution algorithms, and with extensive material and interface models, as well as transmitting boundary elements, the program meets all pertinent requirements pertaining to SSI analyses. In this program, a graded approach is taken which allows for comparisons with solutions computed with other codes [CARES, SASSI]. The first step taken is the free field analysis.

Figure 4.3.1-1 shows an LS-DYNA model of the free field soil block which has 231,400 nodes and 218,500 brick elements. Similar to the LD-DYNA SSI models described in Section 4.1.2, the free field model takes advantage of the symmetry condition, and its boundaries are attached to transmitting boundary elements in a manner as described in Section 4.1.2. The input motion in terms of acceleration time history is specified at the base of soil overburden (80m below ground surface), which is computed using CARES from a rock outcrop accelerogram as shown in Figure 3.1.1-5 and Figure 3.1.1-6. An LS-DYNA time domain analysis of the free field model is performed using the explicit algorithm, and the resulting surface response spectrum at 5% damping is compared with the CARES convolution result.

As depicted in Figure 4.3.1-2, the free field surface spectra computed by LS-DYNA and CARES are compared. This figure shows that the LS-DYNA spectrum generally envelopes the CARES spectrum; excellent agreement between LS-DYNA (3-D) and CARES (1-D) results for frequencies below 5 Hz, and above 12 Hz. Since the time domain solution is employed in LS-DYNA using the Rayleigh type of damping, the specified damping in terms of percentage of critical damping is non-uniformly distributed across the frequency band. The Rayleigh damping generally has a bathtub shape defined with two frequencies (in the free field analysis, 4% of critical damping is specified for the two frequencies, 2 and 8 Hz, respectively). Between the two specified frequencies, the computed damping tends to be lower than the prescribed damping value, and for frequencies outside the two specified frequencies, the computed damping is always higher than the assigned damping value. CARES employs the frequency domain time history scheme and uses a constant material damping. Therefore, the difference in the spectral comparison may be attributed to the different damping models used in the two codes.

4.3.2 Comparison of LS-DYNA and SASSI Analyses for the 11.5 m Depth of Burial

In this section, the LS-DYNA model with the tied interface for 11.5 m depth of burial, which corresponds to the 25% embedment case as described in Section 4.1.2, is used to perform the SSI response analysis and compare the analysis results to the SASSI results. The response quantities examined include the SSI response spectra at the base and the roof of the structure, and soil pressure distributions in circumferential and vertical directions. Furthermore, the LS-DYNA estimates of the lateral displacement and shear displacement of the wall are compared with SASSI results. Although it is customary to identify the peak pressure in the time domain for design practice, it is often more effective for comparison purposes to examine the respective quantity in the frequency domain. Therefore, the seismic induced pressure at a selected location is also computed and compared in Fourier spectrum with the respective SASSI result. To be consistent with the SASSI solution, as described before, the 1g gravity load is excluded in the LS-DYNA analysis models.

Figures 4.3.2-1 through 4.3.2-3 show the nodes and elements at the structure-soil interface, which are used to develop the analysis results. The SSI response spectra are computed at the basemat and roof centers of the structure, and are compared with the corresponding SASSI results as presented in Section 3.3. These spectral comparisons are shown in Figure 4.3.2-4 and Figure 4.3.2-5 and indicate that the LS-DYNA spectrum correlates closely to the SASSI result at the base, and envelop the SASSI result at the roof with good agreement in peak frequencies. These spectrum comparisons are also consistent with the comparison of the free field response as discussed previously in Section 4.3.1. The differences seen in the spectral comparisons may be attributed to the different implementations of damping with each program.

To examine the pressure distributions for the LS-DYNA model, stresses in soil elements surrounding the structural wall are first retrieved and transformed from the Cartesian coordinate system of the model to a cylindrical coordinate system. The variations of the radial stresses (normal pressure) with time are then plotted, which are shown in Figures 4.3.2-6 and 4.3.2-7. Figure 4.3.2-6 shows the stress time history for the head-on soil element ($\theta = 0$) near the ground surface (centered at 1m below the ground surface), while Figure 4.3.2-7 presents the stress time history for the head-on soil element near the mid-height of the embedded wall (centered at 5m below the ground surface). The temporal pressure peaks are examined first. As shown in the figures, the first two highest pressure peaks in the soil near the ground surface are 376.8 kN/m^2 and -370 kN/m^2 , and are located at time equal to 9 seconds and 12.6 seconds, respectively. For the head-on soil element near the mid-height of the embedded wall, the first two highest pressure peaks are identified to be 70 kN/m^2 and 62 kN/m^2 , and are located at time equal to 9 seconds and 6 seconds, respectively. Comparing the temporal pressure peaks computed from LS-DYNA with the SASSI result as discussed in Section 4.2.1, the SASSI analysis results for the pressure time history are processed for the head-on soil element near the ground surface (centered at 1 m below the ground surface) and indicate the first two highest pressure peaks as 302 kN/m^2 and -287 kN/m^2 , occurring at time equal to 8.99 seconds and 12.63 seconds, respectively. Given the many differences that exist between the LS-DYNA model and the SASSI model (explicit soil FE with transmitting boundary in LS-DYNA versus continuous, wave propagation formulation for soil in SASSI), the closeness of temporal pressure peak comparison between the two models is extraordinary, especially the temporal locations of these peaks. Other structural modeling differences, which may contribute to peak differences in the comparison, should also be recognized, such as full 3-D FE structure for LS-DYNA model, while SASSI model uses rigid link to connect the superstructure (lumped mass beams) to the buried wall FEs. For discussion purposes, the results obtained at 9 seconds which corresponds to the first pressure peak near the mid-height of the embedded wall are used for discussing the pressure distributions.

The pressure distributions over the structural wall which is modeled with shell elements vary with both elevation (z) and angular position (θ), with $\theta = 0$ at the head-on location of the shell. The problem is symmetric (both in geometry and loading) about the x -axis and the loading is anti-symmetric about the y -axis. The SASSI solution as presented in Section 4.2 has established that the pressures vary in sinusoidal pattern as either $\cos \theta$ or $\sin \theta$, in which the variation of the radial soil pressure and vertical shear soil pressure follow cosine variations and the hoop shear soil pressure tracks a sine variation. This is substantiated by the LS-DYNA model solution. Figures 4.3.2-8 through 4.3.2-10 present the circumferential variation of the soil pressure near the mid-height of the embedded wall. As depicted in Figure 4.3.2-8, the circumferential distribution of the vertical shear (solid line) follows closely with a cosine trendline. Similarly, the circumferential variation of the tangential shear, as plotted in Figure 4.3.2-9, traces with a sine trendline, and the circumferential variation of the pressure is tracked with a cosine trendline as is presented in Figure 4.3.2-10.

Next, the vertical variation of the soil pressure computed with the LS-DYNA model is assessed. The vertical distributions are calculated at the head-on location ($\theta = 0$) for the normal pressure and the vertical shear, and near $\theta = 90$ for the tangential shear. Figure 4.3.2-11 presents the pressure distributions in the vertical direction, which are calculated at time equal to 9 seconds. Comparing the LS-DYNA result with the vertical distribution of the soil pressures computed by SASSI (Figure 4.2.1-5), it is noted that similar predictions are also achieved using both models. The predominant normal head-on pressure near the ground surface also suggests that a strong inertial effect is induced by the rocking of the super-structure and is resisted by the soil pressure on the wall near the ground surface; however, the soil pressure attenuates rapidly towards the foundation.

In order to examine the shear displacements of the embedded wall, the lateral wall displacements at 9 seconds are computed, as shown in Figure 4.3.2-12. The displacements are shown as the points in Figure 4.3.2-12. To separate the rigid body displacement that does not cause shear in the structural components, a “best fit” line through the predicted displacements is found and shown as the solid line in Figure 4.3.2-12. It can be seen that the major portion of the displacements is due to rigid body motion. The difference between the points and the “best fit” line are shear displacements which result in shear loads within the structural walls. Following this approach, the resulting shear displacements are computed as depicted in Figure 4.3.2-13 which is very similar to the SASSI results (Figure 4.2.1-7). The shear displacements calculated by LS-DYNA supports the observation stated earlier based on the SASSI results, that the relatively small magnitude of these displacements as compared to the total displacements leads to questions of accuracy in the calculation of shear displacements (taking differences between two numbers which are large and close together). Therefore, small errors in the predictions of the total displacements may result in large errors in the predictions of the shear displacements.

It is often advantageous and natural to compare earthquake responses in the frequency domain in lieu of the time domain. In this context, the soil pressure time history in the head-on soil element near the mid-height embedded wall is transformed into frequency domain, and the Fourier spectra of the soil pressure are plotted and compared between the LS-DYNA model and the SASSI model. Before making the comparison, both the SASSI and LS-DYNA Fourier spectra for soil pressure time history were calculated and then smoothed with an algorithm which is defined as a triangular window function as below:

$$A_s(f_m) = \frac{1}{\text{SUM}(i)} \sum_{\substack{\text{All } i \\ |f_i - f_m| \leq \Delta f_m / 2}} \alpha_i A_r(f_i) \quad , m=1, M$$

and,

$$\alpha_i = \frac{4}{\Delta f_m} [f_i - (f_m - \Delta f_m / 2)], \quad f_m - \Delta f_m / 2 \leq f_i \leq f_m$$

$$\frac{4}{\Delta f_m} [(f_m + \Delta f_m / 2) - f_i], \quad f_m < f_i \leq f_m + \Delta f_m / 2$$

where,

- Δf_m Width of the applied frequency window
- $A_s(f_m)$ Smoothed Fourier ratios
- $A_r(f_i)$ Fourier ratios of recorded motions.

The width of the frequency window is assumed 0.5 Hz for this study. Figure 4.3.2-14 presents a comparison of the smoothed Fourier spectra of the computed soil pressure between the SASSI and the LS-DYNA models. It shows a close match of the frequency content between the two model results and the higher peak pressure by the LS-DYNA estimate that is consistent with the conclusion arrived from the comparisons in the time domain. Furthermore, the Fourier spectrum comparison has clearly demonstrated the similar frequency characteristics of the SSI response calculated from the two models.

4.3.3 Comparison of LS-DYNA and SASSI Analyses for the 23 m Depth of Burial

Following the same approach as the 11.5 m embedment case, the LS-DYNA analysis results for the 23 m depth of burial, which corresponds to the 50% embedment case, are presented in this section. The LS-DYNA results are then compared with the corresponding SASSI results.

The nodes and elements at the structure-soil interface of the LS-DYNA model that are used to develop the analysis results are shown in Figures 4.3.3-1 through 4.3.3-3. The SSI response spectra are computed at the basemat and roof centers, and are compared with the corresponding SASSI results for the 23 m depth of burial as presented in Section 3.3. These spectral comparisons are shown in Figure 4.3.3-4 and Figure 4.3.3-5. As indicated in these figures, the LS-DYNA spectra mostly correlate with or envelop the SASSI solution, except that near 9 Hz, the LS-DYNA spectrum at the roof dips slightly with respect to the SASSI result. As discussed in the previous section, the modeling differences between the LS-DYNA and SASSI analyses may be attributed to the differences in the response spectral comparison.

To examine the side soil pressure distributions, stresses in the soil elements outside of the structural wall are retrieved and transformed from the Cartesian coordinate system of the model to a cylindrical coordinate system. The variations of the radial stresses (normal pressure) with time are shown on Figures 4.3.3-6 and 4.3.3-7. Figure 4.3.3-6 shows the stress time history for the head-on soil element ($\theta = 0$ and centered at 1m below the ground surface) near the ground surface, while Figure 4.3.3-7 presents the stress time history for the head-on soil element near the mid-height (centered at -13 m below the ground surface) of the embedded wall. As shown in these figures, the first two highest normal pressure peaks in the soil near the ground surface are

identified to be 138.7 kN/m^2 and -137 kN/m^2 , and the pressure peaks are located at time equal to 10.99 seconds and 9.03 seconds, respectively. For the head-on soil element near the mid-height of the embedded wall, the first two highest normal pressure peaks are 19.5 kN/m^2 and 17.8 kN/m^2 , and these pressure peaks are located at time equal to 12.6 seconds and 10.87 seconds, respectively. As discussed in Section 4.2.2, the SASSI analysis results for the 23 m depth of burial are processed for the normal pressure time history in the head-on soil element centered at a depth equal to 13 m below grade. The first two highest normal pressure peaks in the head-on soil element calculated by SASSI are equal to 23.6 kN/m^2 and -22 kN/m^2 , occurring at time equal to 10.85 seconds and 10.95 seconds, respectively. The LS-DYNA pressure peaks in the time domain in the soil element near the mid-wall are slightly lower than the SASSI result, which suggests that the LS-DYNA SSI model for the 23 m embedment is less stiff than the SASSI model. Note that the SASSI model for the super-structure utilizes a lumped mass beam which is rigidly linked to the embedded wall. For discussion purposes, the LS-DYNA results obtained at 10.99 seconds which corresponds to the first normal pressure peak near the mid-height of the embedded wall are used for presenting the pressure distributions.

Similar to the previous section, the pressure distributions over the structural wall which is modeled with shell elements vary with both elevation (z) and angular position (θ), with $\theta = 0$ at the head-on location of the shell. The problem is symmetric (both in geometry and loading) about the x -axis and the loading is anti-symmetric about the y -axis. The soil pressure and vertical and tangential shears in the center of soil elements adjacent to the wall are computed along the circumference of the shell. Figure 4.3.3-8 presents the circumferential distribution of the vertical shear (solid line) calculated by the LS-DYNA analysis and a cosine trendline is also plotted as shown by the dashed line in the figure. It shows that the circumferential distribution of the vertical shear correlates to the cosine trendline, which is similar to the 11.5 m embedment case. The circumferential variation of the tangential shear is plotted in Figure 4.3.3-9, in conjunction with a sine trendline. As depicted in this figure, the tangential shear also correlates the sine trendline in the circumferential direction, especially for the head-on portion ($0 - 90$ degrees). The LS-DYNA calculated tangential shear in the back portion of the shell ($90 - 180$ degrees) appears uneven but varies closely to the sine trendline. Similarly, the circumferential variation of the normal pressure is plotted in Figure 4.3.3-10 with a cosine trendline. As shown in this figure, the soil pressure generally tracks with a cosine trendline, however, not as well as the 11.5 m embedment case.

The vertical distributions of the soil pressure are computed at the time when the surface normal pressure peaks. The locations for calculating the distributions are selected at the head-on location ($\theta = 0$) for the normal pressure and the vertical shear, and near $\theta = 90$ for the tangential shear. Figure 4.3.3-11 presents the vertical direction distributions of the soil pressure, which are calculated at time equal to 10.99 seconds. The LS-DYNA result is then compared with the SASSI estimate of the vertical distribution of the soil pressure (Figure 4.2.2-2). The comparison shows very similar vertical distributions between LS-DYNA and SASSI models, except that the higher magnitude in the LS-DYNA result than the SASSI calculation is observed, and this may be due to the fact that the SASSI solution of the vertical soil pressure distribution is obtained at the time which corresponds to peak normal pressure in the soil element near the mid-height of the wall.

To compute the shear displacements of the embedded wall, the lateral wall displacements at 10.975 seconds are plotted, as shown in Figure 4.3.3-12. The displacements are shown as the points on Figure 4.3.3-12. To separate the rigid body displacement that does not cause shear in the structural components, a “best fit” line through the predicted displacements is found and shown as the solid line in Figure 4.3.3-12. It can be seen that the major portion of the displacements is due to rigid body motion. The difference between the points and the “best fit”

line are shear displacements which result in shear loads within the structural walls. Following this approach, the resulting shear displacements are computed as depicted in Figure 4.3.3-13 which is very similar to the SASSI results (Figure 4.2.2-4). It can be readily observed that the shear displacements computed are several magnitudes smaller than the corresponding total displacements. This observation again supports the earlier statement based on the SASSI results that the relatively small magnitude of these displacements as compared to the total displacements leads to questions of accuracy in the calculation of shear displacements (taking differences between two numbers which are large and close together). Therefore, small errors in the predictions of the total displacements may result in large errors in the predictions of the shear displacements.

To compliment the time domain peak soil pressure comparisons, the frequency domain response characteristics of the soil pressure calculations between the two models are now compared. Following the same procedure for computing Fourier spectra of the pressure response as described in the preceding subsection for the 11.5 m embedment case, Fourier spectra of the soil pressure in the head-on soil element near the mid-height structural wall are computed and compared between LS-DYNA and SASSI models.

As depicted in Figure 4.3.3-14, the Fourier spectra of the soil pressure are compared well between the LS-DYNA and SASSI models for the 23 m embedment case, especially the frequency content which is consistently estimated across the frequency band of engineering interest between the two models.

4.3.4 Comparison of LS-DYNA and SASSI Analyses for the 34.5 m Depth of Burial

This section presents the LS-DYNA analysis results for the 34.5 m depth of burial which corresponds to the 75% embedment case, and comparisons are made between the LS-DYNA results and the corresponding SASSI solutions.

The nodes and elements at the structure-soil interface of the LS-DYNA model that are used to develop the analysis results are shown in Figures 4.3.4-1 through 4.3.4-3. The SSI response spectra are computed at the basemat and roof centers, and are compared with the corresponding SASSI results for the 34.5 m depth of burial as discussed in Section 3.3. These spectral comparisons are shown in Figure 4.3.4-4 and Figure 4.3.4-5. As shown in these figures, the in-structure response spectra calculated by the LS-DYNA model either closely matches or envelops the SASSI solution for frequencies up to 5 Hz, and mostly exceed the SASSI result at the higher frequencies. The high frequency excursions in the LS-DYNA estimated spectra relative to the SASSI result may be attributed to the inadequate refinement of the mesh size of the LS-DYNA model and the difference in the representation of the structure between the LS-DYNA and SASSI models.

To examine the pressure distributions for the 34.5 m depth of burial case, stresses in these soil elements outside of the structural wall are retrieved and transformed from the Cartesian coordinate system of the model to a cylindrical coordinate system. The variations of the radial stresses (normal pressure) with time are shown on Figures 4.3.4-6 and 4.3.4-7. Figure 4.3.4-6 shows the stress time history for the head-on soil element ($\theta = 0$ and centered at 1 m below the ground surface) near the ground surface, while Figure 4.3.4-7 presents the stress time history for the head-on soil element near the mid-height (centered at 17 m below the ground surface) of the embedded wall. As shown in these figures, the first two highest normal pressure peaks in the soil near the ground surface are identified to be -36.47 kN/m^2 and 32.2 kN/m^2 , and the pressure peaks are located at time equal to 7.11 seconds and 10.99 seconds, respectively. For the head-on soil

element near the mid-height of the embedded wall, the first two highest normal pressure peaks are 20.04 kN/m^2 and -19.8 kN/m^2 , and these pressure peaks are located at time equal to 10.86 seconds and 10.5 seconds, respectively. As discussed in Section 4.2.3, the SASSI analysis results for the 34.5 m depth of burial case are presented for the normal pressure time history in the head-on soil element centered at a depth equal to 17 m below grade. The first two highest normal pressure peaks in the head-on soil element calculated by SASSI are equal to 18.3 kN/m^2 and -16.6 kN/m^2 , occurring at time equal to 10.845 seconds and 10.98 seconds, respectively. These peak pressure comparisons between the LS-DYNA and SASSI results show good correlation of peak soil pressure responses estimated by the two programs. The circumferential distribution of the soil pressure is discussed next by comparing the LS-DYNA calculated circumferential distribution of soil pressure with standard sinusoidal functions. For the discussion purpose, the LS-DYNA results obtained at 10.86 seconds which corresponds to the first normal pressure peak near the mid-height of the embedded wall are used for presenting the pressure distributions.

The pressure distributions over the structural wall which is modeled with shell elements are examined for both elevation (z) and angular position (θ), with $\theta = 0$ at the head-on location of the shell. The problem is symmetric (both in geometry and loading) about the x -axis and the loading is anti-symmetric about the y -axis. Figure 4.3.4-8 presents the circumferential distribution of the vertical shear (solid line) calculated by the LS-DYNA analysis and the vertical shear is compared well with a cosine trendline as shown by the dashed line in the figure. The circumferential variation of the tangential shear is plotted in Figure 4.3.4-9, in conjunction with a sine trendline. As depicted in the figure, the tangential shear also traces closely to the sine trendline. The circumferential variation of the normal pressure is presented in Figure 4.3.4-10 and is generally tracked with a cosine trendline, although near the front and the back part of the circumference the LS-DYNA result is off the trendline. This may be caused by an inadequate mesh size refinement of the LS-DYNA model. However, the LS-DYNA results for the 34.5 m embedment case confirm that the sinusoidal variation in the circumference holds true for the soil pressure estimated using the linear elastic assumption without gravity preload.

The vertical distributions of the soil pressure are computed at the time when the surface normal pressure peaks. The locations for calculating the distributions are selected at the head-on location ($\theta = 0$) for the normal pressure and the vertical shear, and near $\theta = 90$ for the tangential shear. Figure 4.3.4-11 presents the vertical pressure distributions calculated at time equal to 7.11 seconds. As depicted in this figure, the normal pressure near the ground surface attenuates rapidly with the depth, which resembles closely to the SASSI result (Figure 4.2.3-6). The vertical shear computed by the LS-DYNA model generally follows a linear distribution in the vertical direction which also holds true for the SASSI estimate for the vertical shear (Figure 4.2.3-6). The tangential shear also compares well between the LS-DYNA and SASSI models. Note that the SASSI pressure results are obtained for the soil element near the mid-height wall location as opposed to the surface location for the LS-DYNA results. Although some small differences may exist between the LS-DYNA and SASSI results, no significant characteristic changes are identified in the solutions computed using the two models.

To compute the shear displacements of the embedded wall, the lateral wall displacements at 12.03 seconds are plotted, as shown in Figure 4.3.4-12. The displacements are shown as the points on Figure 4.3.4-12. To separate the rigid body displacement that does not cause shear in the structural components, a “best fit” line through the predicted displacements is found and shown as the solid line in Figure 4.3.4-12. It can be seen that the major portion of the displacements is due to rigid body motion. The difference between the points and the “best fit” line are shear displacements which result in shear loads within the structural walls. Following this approach, the resulting shear displacements are computed as depicted in Figure 4.3.4-13 which is

very similar to the SASSI results (Figure 4.2.3-4). It can be readily observed that the shear displacements computed are several magnitudes smaller than the corresponding total displacements. This observation again supports the earlier statement based on the SASSI results that the relatively small magnitude of these displacements as compared to the total displacements leads to questions of accuracy in the calculation of shear displacements (taking differences between two numbers which are large and close together). Therefore, small errors in the predictions of the total displacements may result in large errors in the predictions of the shear displacements.

To compliment the time domain peak soil pressure comparisons, the frequency domain response characteristics of the soil pressure calculations between the two models are now compared. Following the same procedure for computing Fourier spectra of the pressure response as described in the preceding subsection for the 11.5 m embedment case, Fourier spectra of the soil pressure in the head-on soil element near the mid-height structural wall are computed and compared between LS-DYNA and SASSI models.

As depicted in Figure 4.3.4-14, the Fourier spectra of the soil pressure for the 34.5 m embedment case are compared well between the LS-DYNA and SASSI models, for both the spectral amplitude and the frequency content. Therefore, the frequency comparison confirms the consistent pressure estimates across the frequency band of engineering interest between the two models.

4.3.5 Comparison of LS-DYNA and SASSI Analyses for the 46 m Depth of Burial

This section discusses the LS-DYNA analysis results for the 46 m depth of burial case which corresponds to the 100% embedment case. Similar to the previous cases, the soil pressure comparisons are made between the LS-DYNA results and the corresponding SASSI solutions.

The nodes and elements at the structure-soil interface of the LS-DYNA model that are used to develop the analysis results are shown in Figures 4.3.5-1 through 4.3.5-3. The SSI response spectra are computed at the basemat and roof centers, and are compared with the corresponding SASSI results for the 46 m depth of burial as discussed in Section 3.3. These spectral comparisons are shown in Figure 4.3.5-4 and Figure 4.3.5-5. The in-structure response spectrum calculated at the roof by the LS-DYNA model either closely matches or envelops the SASSI solution across the frequency band of interest. Some exceedance in the LS-DYNA spectra compared to the SASSI result appears at the higher frequencies. However, the exceedance is relatively small and nonetheless it may be caused by the inadequate mesh size refinement of the LS-DYNA model and the difference in the representation of the structure between the LS-DYNA and SASSI models.

To examine the pressure distributions for the 46 m depth of burial case, stresses in these soil elements outside of the structural wall are retrieved and transformed from the Cartesian coordinate system of the model to a cylindrical coordinate system. The variations of the radial stresses (normal pressure) with time are shown on Figures 4.3.5-6 and 4.3.5-7. Figure 4.3.5-6 shows the stress time history for the head-on soil element ($\theta = 0$ and centered at 1 m below the ground surface) near the ground surface, while Figure 4.3.5-7 presents the stress time history for the head-on soil element near the mid-height (centered at 21 m below the ground surface) of the embedded wall. As shown in these figures, the first two highest normal pressure peaks in the soil near the ground surface are identified to be -19.36 kN/m^2 and 17.15 kN/m^2 , and the pressure peaks are located at time equal to 6.9 seconds and 11.3 seconds, respectively. For the head-on soil element near the mid-height of the embedded wall, the first two highest normal pressure peaks are

18.61 kN/m² and 16.86 kN/m², and these pressure peaks are located at time equal to 10.4 seconds and 11 seconds, respectively. As discussed in Section 4.2.4, the SASSI analysis results for the 46 m depth of burial case are presented for the normal pressure time history in the head-on soil element centered at a depth equal to 21 m below grade. The first two highest normal pressure peaks in the head-on soil element calculated by SASSI are equal to -12 kN/m² and 11.1 kN/m², occurring at time equal to 11.005 seconds and 8.945 seconds, respectively. In this case, higher pressure peaks are predicted by the LS-DYNA model than the SASSI results, but the peak occurrence times predicted by both codes are close. Since the approximate nature of the side transmitting boundary influences the SSI response more for the fully buried LS-DYNA model (explicit FE modeling of the near field soil), the LS-DYNA pressure estimate is expected to be affected compared with the SASSI solution (analytical form of the wave equation is used for the free field response). Therefore, given the above consideration, the pressure peak estimates are considered reasonably close between the two models. The circumferential distribution of the soil pressure is discussed next by comparing the LS-DYNA calculated circumferential distribution of soil pressure with standard sinusoidal functions. For the discussion purpose, the LS-DYNA results obtained at 10.4 seconds which corresponds to the first normal pressure peak near the mid-height of the embedded wall are used for presenting the pressure distributions.

The pressure distributions over the structural wall which is modeled with shell elements are examined for both elevation (z) and angular position (θ), with $\theta = 0$ at the head-on location of the shell. The problem is symmetric (both in geometry and loading) about the x -axis and the loading is anti-symmetric about the y -axis. Figure 4.3.5-8 presents the circumferential distribution of the soil vertical shear (solid line) calculated by the LS-DYNA analysis. The vertical shear correlates well with a cosine trendline as shown by the dashed line in the figure. The circumferential variation of the tangential shear is plotted in Figure 4.3.5-9, in conjunction with a sine trendline. As depicted in this figure, the tangential shear oscillates about the sine trendline and does not closely track the sine trendline compared to the other embedment cases. The circumferential variation of the normal pressure is presented in Figure 4.3.5-10 and is generally tracked with a cosine trendline, although near the front and the back part of the circumference the LS-DYNA result appears to be off the trendline. The unevenness in the LS-DYNA estimate for both tangential shear and normal pressure may be induced by the inadequate mesh size refinement and the approximate nature of the transmitting boundary of the LS-DYNA model.

The vertical distributions of the soil pressure are computed at the time when the surface normal pressure peaks. The locations for computing the vertical distributions are selected at the head-on location ($\theta = 0$) for the normal pressure and the vertical shear, and near $\theta = 90$ degree for the tangential shear. Figure 4.3.5-11 presents the pressure distributions in the vertical direction, which are calculated at time equal to 6.9 seconds corresponding to the peak of the soil pressure at the ground surface. As shown in this figure, the pattern of the vertical distributions calculated using the LS-DYNA model is similar to the SASSI result in that the transmitting mechanism of the soil pressure to the wall is changed from the predominant normal pressure shown in the shallower embedment cases to the vertical shear. This is primarily due to the increasing kinematic interaction effect and the reduced inertial influence for the deep embedment and/or full burial of the structure.

To compute the shear displacements of the embedded wall, the lateral wall displacements at 12.0 seconds are plotted, as shown in Figure 4.3.5-12. The displacements are shown as the points on Figure 4.3.5-12. To separate the rigid body displacement that does not cause shear in the structural components, a “best fit” line through the predicted displacements is found and shown as the solid line in Figure 4.3.5-12. It can be seen that the major portion of the displacements is due to rigid body motion. The difference between the points and the “best fit” line are shear

displacements which result in shear loads within the structural walls. Following this approach, the resulting shear displacements are computed as depicted in Figure 4.3.5-13 which is very similar to the SASSI results (Figure 4.2.4-7). It can be readily observed that the shear displacements computed are several magnitudes smaller than the corresponding total displacements. This observation again supports the earlier statement based on the SASSI results that the relatively small magnitude of these displacements as compared to the total displacements leads to questions of accuracy in the calculation of shear displacements (taking differences between two numbers which are large and close together). Therefore, small errors in the predictions of the total displacements may result in large errors in the predictions of the shear displacements.

Again, to compliment the time domain peak soil pressure comparisons, the frequency domain response characteristics of the soil pressure calculations between the LS-DYNA and SASSI models are now compared for the 46 m embedment case. Following the same procedure for computing Fourier spectra of the pressure response as described in the preceding subsection for the 11.5 m embedment case, Fourier spectra of the soil pressure in the head-on soil element near the mid-height structural wall are computed and compared between LS-DYNA and SASSI models. As depicted in Figure 4.3.5-14, the Fourier spectra of the soil pressure computed for the LS-DYNA 46 m model does not compare well with the corresponding SASSI result in terms of the Fourier amplitude (mostly higher amplitude is predicted by LS-DYNA for frequencies in 3 – 7 Hz). However, the frequency content is matched well between the two models for the frequency band of engineering interest.

4.3.6 LS-DYNA Assessment of the Depth of Burial Effect

The four soil pressure solutions computed by the LS-DYNA models (for depths of burial equal to 11.5 m, 23 m, 34.5m, and 46 m) discussed in the previous sections are compared in this section. The vertical distributions of the normal pressure, the vertical shear and the tangential shear are plotted at the time of the respective peak occurrence of the normal pressure at the ground surface for different depth of burial cases. The peak normal pressures in the head-on soil elements are found to occur at 9 sec, 10.99 sec, 7.11 sec, and 6.9 sec for DOB equal to 11.5m, 23 m, 34.5 m and 46 m, respectively. The normal pressure and vertical shear distributions are calculated at $\theta = 0$ degree (head-on) while the tangential shear distribution is computed at a location near $\theta = 90$ degree.

The variations of the normal pressure, the tangential shear, and the vertical shears with depth are shown on Figures 4.3.6-1, 4.3.6-2, and 4.3.6-3, respectively, for all four depths of burial. The depth is normalized with the embedment depth so that all four cases may be compared on the same scale as a percentage of the respective burial. It can be seen that the normal pressure is reduced rapidly as the depth of burial increases. Even for the shallow embedment case (11.5 m DOB), the normal pressure attenuates quickly with the depth in a close to bilinear fashion. This result is very similar to the SASSI prediction presented in Section 4.2.5. The vertical distributions of the tangential and vertical shear for various depths of burial are also similar between the LS-DYNA and SASSI results. Therefore, the SASSI program is affirmed by the LS-DYNA analysis to be adequate for linear seismic analysis.

From the comparisons of the vertical distributions among various DOBs, an observation can be readily made that the 11.5 m case is largely driven by the large inertial loads acting on the above grade portion of the structure while the kinematic interaction effect is primarily responsible for the deeper DOBs cases. Furthermore, the inertial effect is mostly localized near the ground surface and attenuates rapidly with the depth, while the kinematic effect is usually distributed more evenly along the depth of burial. In terms of the impact on the structure, the inertial effect

appears much more severe than the kinematic effect, especially for massive stiff structures, such as NPP containments. Therefore, the design feature with a deeper depth of burial could significantly reduce the soil pressure and thereby the seismic load on the structure.

However, as the depth of burial becomes a primary feature of the soil-structure system, certain modeling considerations for computing the seismic load, which are less important for the shallow embedded structures, may be necessary for the adequate characterization of the seismic response of DEB structures. These considerations include the soil-structure interface modeling and the effect of material non-linearity in soils. To assess the effect of geometric and material non-linearities, the linear-based analysis may be no longer adequate, and non-linear methodology may need to be applied. In the ensuing sections, the LS-DYNA program is employed to assess the effect of the soil-structure interface modeling, as well as material non-linearity in soils.

4.4 Assessment of the Effect of Soil-Structure Interface Modeling on Seismic Response Characteristics of DEB Structures

In this section, a LS-DYNA analysis is performed to determine how and to what extent to which the modeling of the soil-structure interface impacts the seismic response characteristics of DEB structures. To accomplish this objective, two LS-DYNA interface models are implemented as discussed in Section 4.1.2, one with a tied soil-structure interface condition (no slipping and separation between the structure and soils) and second with a contact soil-structure interface with a prescribed friction coefficient equal to 0.7 (permitting slipping and separations). The friction coefficient of 0.7 corresponds to a 35 degree friction angle which is reasonable for typical soils used as backfills. Another assumption implied in the choice of a 0.7 friction coefficient is that the failure at the soil/wall interface occurs within the soil, given the fact that the construction of concrete structure always induces some roughness on the surface to prevent the soil from slipping off the wall surface. In order to adequately address the interface condition, a 1g gravity load is applied to both models before commencing the transient seismic analysis. Therefore, the LS-DYNA analysis to be performed involves a two-phase process, a non-linear static 1g ramp-up (dynamic relaxation phase in LS-DYNA) followed by the non-linear transient seismic response analysis. The analysis results computed from the two interface models are then compared to develop insights pertaining to the significance of the consideration of interface modeling for SSI analyses of DEB structures.

In the following sub-sections, four depths of burial (DOB) are analyzed, which are 11.5 m, 23 m, 34.5 m and 46 m. For each DOB case, several aspects of response parameters associated with the interface modeling are investigated, which are: 1) separation of the structure-soil wall interface, 2) structural base uplift, 3) soil pressure distributions in vertical and circumferential directions, and 4) in-structure response spectra. In order to concentrate this section on the interface modeling effect, the soil is assumed to be linear elastic. The effect of nonlinearity of the soil property is addressed in Section 4.5.

4.4.1 Assessment of the Effect of Soil-Structure Interface Modeling for the 11.5 m Depth of Burial Using LS-DYNA

In order to assess the effect of the interface modeling on the response characteristics, the relative lateral displacement time history at the structure/soil interface is computed for the LS-DYNA model with the contact interfaces. Figure 4.4.1-1 shows the relative lateral displacement time history which is computed at the nodes of the structure/soil at the interface near the ground surface at $\theta = 0$ (head-on). Since the relative displacements are calculated by subtracting the structural displacement from the adjacent soil displacement, positive displacement implies that

the structure is experiencing a lateral separation effect from the surrounding soil. It is indicated in Figure 4.4.1-1 that frequent separations and closings occur at the interface between the structure and the surrounding soil. The maximum lateral separation is identified at time equal to 10.56 seconds. However, the magnitude of the peak separation is only about 15 mm, which is rather small compared to the size of the structure (27 m in diameter). The vertical distribution of the relative structure/soil displacement corresponding to the peak separation time is computed at $\theta = 0$, as shown in Figure 4.4.1-2. In this figure, the horizontal axis represents the lateral structure/soil displacements and the vertical axis is the depth in the z-direction expressed as a percentage of the foundation embedment ($E = 11.5$ m). The diamond symbols represent the data points for the structure and the data points for the soil are designated by the triangular symbols. As shown in this figure, at the peak separation time, the separation of the wall from the surrounding soil is quite extensive along the depth, even though the peak separation magnitude is very small.

Using the same approach as described in previous sections for computing the shear displacements, the shear displacements of the structural wall from the LS-DYNA model with the contact interface are also calculated at the peak separation time, and these shear displacements are compared with those for the LS-DYNA model with the tied interface computed at the same time. The comparison of the vertical distribution of shear displacements between the two models is presented in Figure 4.4.1-3. It can be seen from Figures 4.4.1-2 and 4.4.1-3 that the structure mainly experiences rigid-body motion and the shear displacements are much smaller than the total displacements calculated from both models.

The base uplifting of the structure induced by the seismic motion, which has been studied extensively in the past [e.g., Miller, 1986], is investigated using the LS-DYNA model with the contact interface. The relative vertical displacement time histories, which are computed at the nodes of the structure/soil at the base of the structure, are examined at $\theta = 0$ ($x = 12.5$ m, head-on) and $\theta = 180$ ($x = -12.5$ m). Figures 4.4.1-4 and 4.4.1-5 show the relative vertical displacement time histories at the structural base. Since the relative vertical displacement time histories are computed by subtracting the soil displacements from the corresponding structural base displacements, positive values in the figures represent separation of the structural base from the supporting soils. Figures 4.4.1-4 and 4.4.1-5 reveal that the structure experiences numerous occurrences of uplifting at the base from the foundation soil, and the peak uplifting occurs at the time when the peak lateral structure/soil separation takes place. However, the magnitude of the separation is comparable to the side wall separation with the soil and is quite small considering the size of the structure.

The effect of the interface modeling and its induced base uplifting and wall separation can be assessed by examining the in-structure response spectra. Figures 4.4.1-6 and 4.4.1-7 present the comparisons of response spectra computed for the basemat and the roof of the structure, respectively. The spectra calculated from three LS-DYNA models are included for the comparison: 1) the tied interface and excluding the 1g gravity load, 2) the tied interface and including the 1g gravity load, and 3) the contact interface and including 1g gravity load. As seen in these comparisons, the spectra at both the basemat and the roof are near identical for the tied interface model with/without the 1g gravity load. Therefore, the 1g gravity preload has no effect on the computation of the in-structure response spectra. However, when the contact interface is included, as the comparisons show, the response spectrum at the base experiences an upward drift in higher frequencies, and at the roof, the spectral peak shift towards lower frequency. The effect on the computed spectra from the contact LS-DYNA model may be caused by the modeling of the interface in that the induced structure-soil separations reduce the stiffness of the SSI system and therefore cause the roof spectrum to shift toward lower frequency, and the impact resulting from the open/close of the interface may be responsible for the upward drift of the base spectrum

in the high frequency region. These observations of the kinematic features of the structure/soil system provide useful insights which could be used to evaluate the effect of the structure-soil interface modeling on the seismic response characteristics of DEB structures.

Next, the effects of the interface modeling on the distribution of the soil pressure are examined for the 11.5 m DOB. The seismic induced pressure is calculated using the LS-DYNA models with both contact and tied interface conditions. For the head-on locations near the ground surface and the mid-height of the structural wall, comparisons of the normal pressure time histories between the contact and tied interface LS-DYNA models are presented in Figures 4.4.1-8 and 4.4.1-9. As depicted in these figures, the normal pressure calculated from the contact interface model exhibits compressive stress only while the tied interface model results in both compressive and tensile stresses similar to the linear models discussed in Section 4.3. It can also be observed in these figures that for the contact interface model, the first two peak normal pressures in the head-on soil element near the ground surface occur at times equal to 10.35 seconds and 10.83 seconds, with the pressure magnitudes equal to -902.86 kN/m^2 and -863.39 kN/m^2 , respectively. For the tied interface model, the first two peak normal pressures in the head-on soil element near the ground surface are calculated to be 378.59 kN/m^2 and 369.6 kN/m^2 , which occur at times equal to 9 seconds and 12.7 seconds, respectively. Besides the one-sided feature of the normal pressure for the contact interface model, the seismic induced pressure amplitudes appear much larger for the contact interface model than for the tied interface model. A similar comparison of the normal pressures is made for the mid-height of the structural wall as shown in Figure 4.4.1-9. For this location, the first two peak normal pressures calculated from the contact interface model are identified to be -309 kN/m^2 and -306 kN/m^2 , which occurred at times equal to 10.3 seconds and 10.9 seconds, while for the tied interface model, the first two peak normal pressures are computed to be -84 kN/m^2 and -74.9 kN/m^2 , at times equal to 6.2 seconds and 9.1 seconds, respectively. It is readily seen that, near the mid-height of the structural wall, the contact interface model induces much higher normal pressure than the tied interface.

To examine the soil pressure distributions in circumferential and vertical directions, the peak occurring time of the normal soil pressure near the mid-height of the structural wall are selected for computing the soil stresses in the circumferential direction, which is, as indicated in Figure 4.4.1-8, 10.3 seconds for the contact interface model and 6.2 seconds for the tied interface model. The circumferential distributions are computed in the soil elements at the structure/soil interface. The vertical distributions are calculated at the peak occurring time of the normal soil pressure near the ground surface (10.35 seconds for the contact interface model and 9 seconds for tied interface model), and are carried out in the head-on soil elements for the normal pressure and the vertical shear and near $\theta = 90$ degrees for the tangential shear. Figures 4.4.1-10 through 4.4.1-12 present the comparisons of the circumferential distributions of the vertical shear, the normal pressure and the tangential shear computed for both contact and tied interface models at their respective peak times. As shown in these comparisons, quite different characteristics of the pressure variation in the circumference are revealed from the comparison between the two interface models. With the contact interface model, the soil pressures are induced only on the supporting side of the structure (from $\theta = 0$ to $\theta = 90$ degrees) and are nearly vanished from $\theta = 90$ to $\theta = 180$ degrees, as opposed to the tied interface model which produces soil pressures on the structure from $\theta = 0$ to $\theta = 180$ degrees in the circumferential direction in either symmetric or anti-symmetric fashions. Furthermore, the pressure peak is much higher resulting from the contact interface model.

With respect to the effect of interface modeling on the vertical distributions of the pressure, Figures 4.4.1-13 through 4.4.1-15 present the comparisons of the vertical distributions of the

normal pressure, the tangential shear and the vertical shear computed with the contact and tied interface models. As shown in these figures, the normal pressure and the vertical shear are much higher in the vertical direction computed from the contact interface model than the tied interface model, while the reverse is observed for the tangential shear. Further, the shape of the vertical distribution of the normal pressure suggests that the inertial load of the super-structure is the driving force for the seismic induced soil pressure for the 11.5 m DOB case. Furthermore, the vertical distributions of the pressure components for the tied interface model are displayed in Figure 4.4.1-16. Figure 4.4.1-17 presents the vertical distributions for the contact interface model. These two figures show similar relative vertical distributions of the soil pressure between the contact and tied interface models. It should be emphasized that for the contact interface model, the shear stress at the contact surface is calculated using the assigned friction coefficient which, in this study, is assigned to a value equal to 0.7. Therefore, the relative comparison between the shear and normal pressure for the contact interface model should be interpreted only in the context of the particular friction coefficient applied.

4.4.2 Assessment of the Effect of Soil-Structure Interface Modeling for the 23 m Depth of Burial Using LS-DYNA

In this subsection, the effect of the interface modeling on the response characteristics for the 23 m DOB is discussed. The relative lateral displacement time history at the structure/soil interface is examined first for the LS-DYNA model with the contact interfaces. Figure 4.4.2-1 shows the relative lateral displacement time history which is computed at the nodes of the structure/soil at the interface near the ground surface at $\theta = 0$ (head-on). Since the relative displacements are calculated by subtracting the structural displacement from the adjacent soil displacement, positive displacement implies that the structure is experiencing a lateral separation effect from the surrounding soil. Figure 4.4.2-1 shows that frequent openings and closings occur at the interface between the structure and the surrounding soil; however, the magnitude of the peak wall/soil separation is quite small (12.2 mm) compared to the size of the structure (27 m diameter with wall thickness equal to 2 m). The peak lateral separation is identified to occur at time equal to 11.03 seconds. The vertical distribution of the relative structure/soil displacement along the wall corresponding to the peak separation time is then computed at $\theta = 0$, which is shown in Figure 4.4.2-2. In this figure, the horizontal axis represents the lateral structure/soil displacements and the vertical axis is the depth in the z-direction expressed as a percentage of the foundation embedment ($E = 23$ m). The diamond symbols represent the data points for the structure and the data points for the soil are designated by the triangular symbols. As shown in this figure, at the peak separation time, the structural wall separation from the surrounding soils is extensive, albeit the size of the peak opening is quite small.

Similar to the comparison of the shear displacements described in the previous section, the shear displacements of the structural wall for the 23 m DOB from the LS-DYNA model with the contact interface are calculated at the peak separation time. These shear displacements are then compared with those from the LS-DYNA model with the tied interface computed at the same instant. The comparison of the vertical distribution of shear displacements between the two models is presented in Figure 4.4.2-3. It can be seen from Figures 4.4.2-2 and 4.4.2-3 that the structure mainly experiences rigid-body motion and the shear displacements are much smaller than the total displacements calculated from both models for the 23 m DOB case, and the impacts resulted from the openings and closings of the structure/soil interface appear to have an effect on the lateral shear displacements.

The base uplifting of the structure induced by the seismic motion is assessed using the LS-DYNA model with the contact interface. Similar to the calculation performed for the 11.5 m

DOB case, the relative vertical displacement time histories are examined at $\theta = 0$ ($x = 12.5$ m, head-on) and $\theta = 180$ ($x = -12.5$ m). Figures 4.4.2-4 and 4.4.2-5 show the relative vertical displacement time histories at the structural base. Since the relative vertical displacement time histories are computed by subtracting the soil displacements from the corresponding structural base displacements, positive values in the figures represent separation of the structural base from the supporting soils. Figures 4.4.2-4 and 4.4.2-5 reveal that the structure experiences some occurrences of uplifting at the base from the foundation soil; however, they are not as frequent as shown in the 11.5 m DOB case. Furthermore, the basemat uplift (the peak vertical separation is equal to 4.6 mm) is much smaller than the peak separation of the side wall (12.2 mm) with the surrounding soil. As compared to the 11.5 DOB case where the peak uplifting occurs at the time when the peak lateral structure/soil separation takes place, for the 23 m DOB case, the peak uplifting also occurs at the peak time of the lateral structure/soil separation.

With respect to the effect of the interface modeling and its induced base uplifting and wall separation on the in-structure response spectra, the response spectra are computed at the center of basemat and the center of the roof of the structure from both the contact and tied interface models. Figures 4.4.2-6 and 4.4.2-7 present the comparisons of response spectra between the two models and also the tied model without the 1g gravity load. As seen in these comparisons, the 1g gravity load has no impact on the spectral computation. However, the effect of the contact interface model is significant. As indicated in these figures, the response spectrum at the base experiences an upward drift in higher frequencies, and at the roof, the spectral peak shift towards lower frequency, and is significantly amplified. The spectral amplification at the roof is also much higher for the 23 m DOB than shown in the 11.5 m DOB case.

Next, the effects of the interface modeling on the distribution of soil pressure are examined for the 23 m DOB. The seismic induced pressure is calculated using the LS-DYNA models with both contact and tied interface conditions. For the head-on locations near the ground surface and the mid-height of the structural wall, the comparisons of normal pressure time histories are provided in Figures 4.4.2-8 and 4.4.2-9. As shown in these figures, the normal pressures calculated from the contact interface model exhibit compressive stress only while for the tied interface model the normal pressure is mostly in tension at the surface which is caused by the 1g gravity load pulling the soil near the ground surface. It should be cautioned that the tensile normal pressure in the soil element near the ground surface is induced by the tied interface modeling when preloaded with the 1g gravity, and does not represent the actual soil behavior in that region.

From the pressure time history plots given in Figures 4.4.2-8 and 4.4.2-9, the peak normal pressures can readily be identified. For the contact interface model, the first two peak normal pressures in the head-on soil element near the ground surface occur at times equal to 10.93 seconds and 14.7 seconds, with the pressure magnitudes equal to -305.43 kN/m^2 and -284.23 kN/m^2 , respectively. For the tied interface model, the first two peak normal pressures in the head-on soil element near the ground surface are calculated to be 237.63 kN/m^2 and 230 kN/m^2 , which occur at times equal to 10.99 seconds and 10.4 seconds, respectively. In addition to the one-sided feature of the normal pressure for the contact interface model, the seismic induced pressure amplitudes for the contact interface model appear much higher than the peak pressure computed with the tied interface model. A similar comparison of the normal pressures is also made for the mid-height of the structural wall as shown in Figure 4.4.2-9. For this location, the first two peak normal pressures calculated from the contact interface model are identified to be -79.78 kN/m^2 and -79.63 kN/m^2 , which are occurred at times equal to 10.94 seconds and 8.43 seconds. For the tied interface model, the first two peak normal pressures are computed to be -64.77 kN/m^2 and -55.49 kN/m^2 , at times equal to 6.9 seconds and 11 seconds, respectively. It is readily seen that

near the mid-height of the structural wall the contact interface model also estimates higher normal pressure than the tied interface model.

To examine the soil pressure distributions in circumferential directions, the occurring time of the peak normal soil pressures near the mid-height of the structural wall are selected, which is, as indicated in Figure 4.4.2-9, 10.94 seconds for the contact interface model and 6.9 seconds for the tied interface model. The circumferential distributions are computed in the soil elements at the structure/soil interface. Figures 4.4.2-10 through 4.4.2-12 present the comparisons of the circumferential distributions of the vertical shear, the normal pressure and the tangential shear computed for both contact and tied interface models. As shown in these comparisons, for the contact interface model, the soil pressures are induced mostly on the supporting side of the structure (from $\theta = 0$ to $\theta = 90$ degrees) and are vanished from $\theta = 90$ to $\theta = 180$ degrees, as opposed to the tied interface model which produces soil pressures on the structure from $\theta = 0$ to $\theta = 180$ degrees in the circumferential direction in either symmetric or anti-symmetric fashions. For the normal pressure, the pressure magnitudes are comparable between the two models. The estimate for the vertical shear is much higher from the tied interface model, while for the tangential shear, the estimate is higher from the contact interface model.

With respect to examining the effect of interface modeling on the vertical distributions of the soil pressure, the occurring time of the peak normal soil pressures near the ground surface are selected, which is, as indicated in Figure 4.4.2-8, 10.93 seconds for the contact interface model and 10.99 seconds for the tied interface model. The vertical distributions are calculated in the head-on soil elements for the normal pressure and vertical shear, and the tangential shear is calculated near $\theta = 90$ degrees. Figures 4.4.2-13 through 4.4.2-15 present the comparisons of the vertical distributions of the normal pressure, the tangential shear and the vertical shear computed with the contact and tied interface models, respectively. As shown in these figures, the vertical distributions in terms of the pressure shape are very similar in the middle portion of the embedment depth between the two interface models, and the response magnitudes are also close between the two models for the tangential shear and the normal pressure. However, near the base and the ground surface, the pressure estimates diverge between the two models. For the vertical shear, the tied interface model provides a much higher estimate than the contact interface model. Therefore, the 23 m DOB results also substantiate the importance of the modeling aspect of the soil/structure interface.

Furthermore, for the vertical distributions of the normal pressure, the vertical and tangential shears for the tied interface model are grouped together and plotted in Figures 4.4.2-16. Figure 4.4.2-17 provides a similar grouping of the vertical distributions for the contact interface model. For the tied interface model, the normal pressure attenuates rapidly from the ground surface to a depth equal about 17% DOB and behaves in a bilinear manner, while shears remain nearly constant along the depth of burial. For the contact interface model, the tangential and vertical shears in the vertical direction are much less than the normal pressure which also behaves closer to a bilinear fashion; however, unlike the tied interface model, the normal pressure computed from the contact interface model does not change sign.

4.4.3 Assessment of the Effect of Soil-Structure Interface Modeling for the 34.5 m Depth of Burial Using LS-DYNA

This section discusses the effect of the interface modeling on the response characteristics for the 34.5 m DOB. The relative lateral displacement time history at the structure/soil interface is examined first for the LS-DYNA model using the contact interfaces. Figure 4.4.3-1 shows the relative lateral displacement time history which is computed at the nodes of the structure/soil at

the interface near the ground surface at $\theta = 0$ (head-on). Since the relative displacements are calculated by subtracting the structural displacement from the adjacent soil displacement, positive displacements imply that the structure is experiencing a lateral separation effect from the surrounding soil. Similar to both the 11.5 m and 23 m DOB cases, Figure 4.4.3-1 shows that frequent openings and closings occur at the interface between the structure and the surrounding soil near the ground surface; however, the peak separation (5.57 mm) is much smaller than the 11.5 m and 23 m DOB cases. The peak lateral opening is identified to occur at time equal to 11 seconds. The vertical distribution of the relative structure/soil displacement corresponding to the peak separation time is then computed at $\theta = 0$, which is shown in Figure 4.4.3-2. In this figure, the horizontal axis represents the lateral structure/soil displacements and the vertical axis is the depth in the z-direction expressed as a percentage of the foundation embedment ($E = 34.5$ m). The diamond symbols represent the data points for the structure and the data points for the soil are designated by the triangular symbols. As shown in this figure, at the peak separation time, the structure is separated from the surrounding soils from the ground surface, but less extensive than the 11.5 m and 23 m DOB cases.

Similar to the comparison of the shear displacements described in the previous sections, the shear displacements of the structural wall for the 34.5 m DOB from the LS-DYNA model with the contact interface are calculated at the peak separation time. These shear displacements are then compared with those computed from the LS-DYNA model with the tied interface. The comparison of the vertical distribution of shear displacements between the two models is presented in Figure 4.4.3-3. It can be seen from Figures 4.4.3-2 and 4.4.3.3 that the structure mainly experiences rigid-body motion and the shear displacements are much smaller than the total displacements calculated from both models. The impacts resulting from the openings and closings of the structure/soil interface appear to have an effect on the vertical distribution of the lateral shear displacements.

The base uplifting of the structure induced by the seismic motion is assessed for the 34 m DOB case using the LS-DYNA model with the contact interface. Similar to the calculation performed for the previous two DOB cases, the relative vertical displacement time histories are examined at $\theta = 0$ ($x = 12.5$ m, head-on) and $\theta = 180$ ($x = -12.5$ m). Figures 4.4.3-4 and 4.4.3-5 show the relative vertical displacement time histories at the structural base. Since the relative vertical displacement time histories are computed by subtracting the soil displacements from the corresponding structural base displacements, positive values in the figures represent separation of the structural base from the supporting soils. Figures 4.4.3-4 and 4.4.3-5 show that the structure experiences negligible separations at the base from the foundation soil with the peak separation equal to 1.8 mm, which is much smaller than the two previous DOB cases.

With respect to the effect of the interface modeling and its induced soil/structure separation on the in-structure response spectra computed with both contact and tied interface models, Figures 4.4.3-6 and 4.4.3-7 present the comparisons of response spectra at the basemat and the roof of the structure computed with the two models and also the tied model without the 1g gravity load. As seen in these comparisons, the 1g gravity load has no impact on the spectral computation. However, the effect of the contact interface model on the response spectra is significant, especially at the roof where the response spectrum is greatly amplified compared to the spectra computed using the tied interface models.

The effects of the interface modeling on the distribution of soil pressures are next assessed for the 34.5 m DOB. The seismic induced pressures are calculated using the LS-DYNA models with both contact and tied interface conditions. For the head-on locations near the ground surface and the mid-height of the structural wall, the comparisons of normal pressure time histories are

provided in Figures 4.4.3-8 and 4.4.3-9. As shown in these figures, the normal pressures calculated from the contact interface model exhibit a compressive characteristic while the tied interface model results in tensile stresses which are due to the tied connection of the soil and the wall at the surface and the pull of the soil by the 1g gravity preload. As mentioned in the previous section, this behavior of the normal pressure computed by the tied interface model is caused by the modeling and is not believed to represent the true soil behavior under seismic motions. It also proves that the pressure estimate is very sensitive to the interface modeling.

From the pressure time history plots given in Figures 4.4.3-8 and 4.4.3-9, the peak normal pressures can readily be identified. For the contact interface model, the first two peak normal pressures in the head-on soil element near the ground surface occur at times equal to 10.63 seconds and 10.9 seconds, with the pressure magnitudes equal to -144.27 kN/m^2 and -130.95 kN/m^2 , respectively. For the tied interface model, the first two peak normal pressures in the head-on soil element near the ground surface are calculated to be 196.96 kN/m^2 and 195 kN/m^2 , which occur at times equal to 10.99 seconds and 12.8 seconds, respectively. The soil pressure estimated using the contact interface model appears to be more realistic and is one-sided as opposed to the pressure computed by the tied interface model, which remains in tension throughout. For the mid-height of the structural wall, the comparison of the normal pressures is shown in Figure 4.4.3-9. For this location, the first two peak normal pressures calculated from the contact interface model are identified to be -68.17 kN/m^2 and -59.45 kN/m^2 , which occurred at times equal to 9 seconds and 11 seconds. For the tied interface model, the first two peak normal pressures are computed to be -93.98 kN/m^2 and -91.33 kN/m^2 , at times equal to 10.5 seconds and 10 seconds, respectively. It is readily seen that, for the 23 m DOB case, the contact interface model computes much less normal pressure than the tied interface model near the mid-height of the structural wall.

To investigate the soil pressure distributions in the circumferential direction, the occurring time of the peak normal soil pressures near the mid-height of the structural wall is selected, which is, as indicated in Figure 4.4.3-9, 9 seconds for the contact interface model and 10.5 seconds for the tied interface model. The circumferential distributions are computed in the soil elements at the structure/soil interface. Figures 4.4.3-10 through 4.4.3-12 present the comparisons of the circumferential distributions of the vertical shear, the normal pressure and the tangential shear computed from both contact and tied interface models. As shown in these comparisons, the soil stresses estimated from the contact interface model are much smaller than those computed from the tied interface model. Furthermore, less variation of the soil stresses in the circumference is observed for the contact interface model than the tied interface model.

With respect to examining the effect of interface modeling on the vertical distributions, the normal pressure and the vertical shear are calculated in the head-on soil elements and the tangential shear is calculated near $\theta = 90$ degrees. Further, the occurring time of the peak normal soil pressures near the ground surface (10.63 seconds for the contact interface model and 10.99 seconds for the tied interface model) is selected for computing the vertical distributions. Figures 4.4.3-13 through 4.4.3-15 present the comparisons of the vertical distributions of the normal pressure, the tangential shear and the vertical shear computed with the contact and tied interface models.

As shown in these figures, the normal pressure comparison between the two models is closer in the mid-section of the embedded wall than near the ground surface and the base of the structure where the tied interface model predicted higher normal pressure than the contact interface model. Similar comparison is also observed for the tangential shear. For the vertical shear, the prediction by the tied interface model is much higher than by the contact interface model.

Lastly, for the vertical distributions of the normal pressure, the vertical and tangential shears computed from the tied interface model are grouped together and plotted in Figures 4.4.3-16. In a similar fashion, Figure 4.4.3-17 shows the grouped vertical distributions for the contact interface model. These grouped comparisons show very distinct characteristics of relative distribution of the soil stresses predicted with each model in that the choice of a soil/wall interface model plays an essential role in determining the distribution of shears. An obvious over estimate of shears by the tied interface model can readily be seen in Figure 4.4.3-16. In this respect, the contact interface model provides a more realistic estimate of shears through the prescribed interface friction coefficient. It is also observed that the inertial interaction effect is much more severe than the kinematic interaction effect in the seismic environment in inducing the pressure on the structure. As the DOB increases, the influence of inertial interaction is gradually reduced and the kinematic interaction effect increases, and these figures have shown consistent decrease in the normal pressure if the effect of the 1g gravity load is removed.

4.4.4 Assessment of the Effect of Soil-Structure Interface Modeling for the 46 m Depth of Burial Using LS-DYNA

This section examines the effect of the interface modeling on the response characteristics for the 46 m DOB, which is the full burial case. The relative lateral displacement time history at the structure/soil interface is evaluated first for the LS-DYNA model with the contact interfaces. Figure 4.4.4-1 displays the relative lateral displacement time history which is computed at the nodes of the structure/soil at the interface near the ground surface at $\theta = 0$ (head-on). Since the relative displacements are computed by subtracting the structural displacement from the adjacent soil displacement, positive displacements imply that the structure is experiencing lateral separation effect from the surrounding soil. Similar to the previous DOB cases, Figure 4.4.4-1 shows that frequent openings and closings occur at the interface between the structure and the surrounding soil near the ground surface; however, the peak separation is very small (1.4 mm). The peak lateral opening is identified to occur at time equal to 11 seconds. The vertical distribution of the relative structure/soil displacement corresponding to the peak separation time is then computed at $\theta = 0$, which is shown in Figure 4.4.4-2. In this figure, the horizontal axis represents the lateral structure/soil displacements and the vertical axis is the depth in the z-direction expressed as a percentage of the foundation embedment ($E = 46$ m). The diamond symbols represent the data points for the structure and the data points for the soil are designated by the triangular symbols. As shown in this figure, at the peak separation time, the structure is separated from the surrounding soils but much less extensive along the depth of burial than other embedment cases as discussed previously.

Similar to the comparison of the shear displacements described in the previous sections, the shear displacements of the structural wall for the 46 m DOB from the LS-DYNA model with the contact interface are calculated at the peak separation time. These shear displacements are then compared with those computed from the LS-DYNA model with the tied interface. The comparison of the vertical distribution of shear displacements between the two models is presented in Figure 4.4.4-3. It can be seen from Figures 4.4.4-2 and 4.4.4-3 that unlike the previous three DOB cases where the structure mainly experiences rigid-body motion and the shear displacements are much smaller than the total displacements calculated from both models, for the 46 m DOB case, the shear displacement constitutes a major part of the total displacement, which further substantiate the thesis that the kinematic interaction effect is the driving seismic response mechanism for DEB structures. Figure 4.4.4-3 also reveals that the shear displacement calculated from the contact interface model is much smaller than that computed using the tied interface model.

The base uplifting of the structure induced by the seismic motion is assessed using the LS-DYNA model with the contact interface. Similar to the calculation performed for the previous DOB cases, the relative vertical displacement time histories are examined at $\theta = 0$ ($x = 12.5$ m, head-on) and $\theta = 180$ ($x = -12.5$ m). Figures 4.4.4-4 and 4.4.4-5 show the relative vertical displacement time histories at the structural base. Since the relative vertical displacement time histories are computed by subtracting the soil displacements from the corresponding structural base displacements, positive values in the figures represent separation of the structural base from the supporting soils. Figures 4.4.4-4 and 4.4.4-5 show that the structure experiences almost no separation at the base from the foundation soil for the 46 m DOB case. Placed in the context of the results for the other DOB cases as discussed in previous sections, an observation can be readily made that a design with more embedment and less superstructure reduces wall/soil separation and foundation uplifting, as well as the normal soil pressure which is mostly induced by the inertial interaction effect.

With respect to the interface modeling effect on the in-structure response spectra, Figures 4.4.4-6 and 4.4.4-7 present the comparisons of response spectra at the basemat and the roof of the structure computed with the two models and also the tied model without the 1g gravity load. As seen in these comparisons, the 1g gravity load has no impact on the spectral computation. However, the interface modeling has pronounced effect on the prediction of the response spectra, especially for high frequency response. As shown in the spectral comparisons, the contact interface model predicts the response spectra which exhibit an upward drift in higher frequencies. The upward spectral drift in higher frequencies is more pronounced for the roof. Consistent with the other DOB cases, the contact interface always introduces some degree of impact effect in the computed structural response spectra.

The effects of the interface modeling on the distribution of soil pressures are next assessed for the 46 m DOB. The seismic induced pressures are calculated using the LS-DYNA models with both contact and tied interface conditions. For the head-on locations near the ground surface and the mid-height of the structural wall, the comparisons of normal pressure time histories are provided in Figures 4.4.4-8 and 4.4.4-9. As shown in these figures, the normal pressures calculated from the contact interface model exhibit compressive stress only while the tied interface model results in tensile normal stress which is induced by the 1g gravity preload pulling the soil near the ground surface. It can be observed in these figures that for the contact interface model, the first two peak normal pressures in the head-on soil element near the ground surface occur at times equal to 10.87 seconds and 12.61 seconds, with the pressure magnitudes equal to -56.58 kN/m^2 and -27.16 kN/m^2 , respectively. For the tied interface model, the normal pressure in the head-on soil element near the ground surface appears consistently in tension and does not exhibit any appreciable peaks. For the mid-height of the structural wall, the comparison of the normal pressures is shown in Figure 4.4.4-9. For this location, the normal pressure time histories computed using both models appear to trend in a similar fashion, oscillating within a narrow band without appreciable pressure peaks. The tied interface model, however, results in consistently higher normal pressure than the contact interface model. For the purpose of discussing the circumference distribution of soil pressure (consistent with other DOB cases), the peak normal pressure in the head-on soil element near the mid-height of the structural wall is identified to be -78.78 kN/m^2 , at 3 seconds.

To investigate the soil pressure distributions in the circumferential direction, the occurring time of the peak normal soil pressure near the mid-height of the structural wall computed from the contact interface model is selected, which is 3 seconds as alluded in the previous paragraph. Since the normal pressure computed from the tied interface model exhibits consistent decline and

no appreciable pressure peaks exist, the circumferential distribution of soil pressure is computed for both models at 3 seconds. Figures 4.4.4-10 through 4.4.4-12 present the comparisons of the circumferential distributions of the vertical shear, the normal pressure and the tangential shear computed for both contact and tied interface models. As shown in these comparisons, the contact interface model consistently provides a much smaller estimate in the vertical shear and the normal pressure than the tied interface model, while for the tangential shear, both models give comparable estimates.

With respect to examining the effect of interface modeling on the vertical distributions, the normal pressure and the vertical shear are calculated in the head-on soil elements and the tangential shear is calculated near $\theta = 90$ degrees. Further, the occurring time (10.87 seconds) of the peak normal soil pressures near the ground surface from the contact interface model is applied to both models for computing the vertical distributions, since no appreciable pressure peaks exist in the normal pressure time history computed from the tied interface model. Figures 4.4.4-13 through 4.4.4-15 present the comparisons of the vertical distributions of the normal pressure, the tangential shear and the vertical shear computed with the contact and tied interface models. As shown in these figures, the vertical distributions for the normal pressure are very close between the contact and tied interface models in the middle portion along the depth of burial, and the tied interface model predicts higher pressure near the ground surface and the base the structure. Further, the pressure varies nearly linear with the depth estimated from both models suggesting that the normal pressures are less influenced by the kinematic effect. The tied interface model also predicts higher tangential and vertical shears than the contact interface model. The vertical shear appears linearly distributed in the vertical direction for the both contact and tied interface models. Similar to the 34.5 m DOB case, it is observed for the 46 m DOB case that the inertial effect diminishes drastically and the kinematic interaction effect is primarily responsible for the soil pressure. Furthermore, when the contact interface model is employed, the vertical distribution of the normal pressure is reduced significantly from the static 1g gravity load (note that the contact model already includes the 1g gravity load) and it leads to an observation that for the 46 m DOB case, considering only the static 1g gravity load may be conservative in computing the normal soil pressure.

The vertical distributions of the pressure components for the tied interface model are grouped together in Figures 4.4.4-16. Figure 4.4.4-17 shows the vertical distributions of the pressure components for the contact interface model. The tangential shear displays very little changes in the vertical direction for both models, while the normal pressure and the vertical shear follow close to a linear distribution in the vertical direction.

4.4.5 Frequency Domain Assessment of the Interface Modeling Effect on DEB SSI Response

To complement the time domain assessment of the interface modeling effect as provided above, this section examines the results computed from different interface models in the frequency domain. Fourier spectra are computed for the normal pressure in the head-on soil element near the mid-height of the structural wall for both the contact and tied interface models. In order to make an objective comparison, these Fourier spectra are then smoothed using a smoothing algorithm as discussed in Section 4.3.2. The smoothed Fourier spectra are compared between the contact and tied interface models.

Figures 4.4.5-1 through 4.4.5-4 present the comparisons of the Fourier spectra for the depth of burial equal to 11.5m, 23m, 34.5m and 46m, respectively. For the tied interface model, the Fourier spectra has one prominent peak located between 5-6 Hz for the 11.5m burial case and the peak shifts towards a much lower frequency (less than 1 Hz) as the depth of burial increases. On

the other hand, the Fourier spectra computed from the contact interface model show the reverse effect with respect to the pressure peak shifting. In this case, the peak pressure for the 11.5m depth of burial is located between 2-3 Hz, and is shifted to between 6-7 Hz when the depth of burial is increased to 34.5m. This reversal of the peak pressure shift is caused by the soil/structure interaction taking place at the interface (open/close and slippage) as a result of placing the contact interface in the SSI model. However, for the 46m embedment case, Fourier spectra predicted using both models trace very closely together for frequencies 4Hz and above, and the tied interface model predicts higher Fourier response in frequencies below 4 Hz.

To further investigate how the peak soil pressure is transmitted into the structural elements, the Von-Mises effective stress in the structural shell element is plotted in terms of Fourier spectra. Figures 4.4.5-5 through 4.4.5-8 present these Fourier spectra computed from both the tied and contact interface models for the four depths of burial cases. These figures indicate that the structural stresses generally follow the same distributions as the soil pressures. However, these comparisons also indicate that the structural stresses induced by the soil pressures are not trivial, even though the structure is fairly rigid.

4.4.6 Estimation of Nonlinear Effects at the Soil Structure Interface from the SASSI Results for the 23 m Depth of Burial

Since the LSDYNA results indicate that nonlinear effects at the soil structure interface are significant, interface pressures computed with SASSI are examined to determine whether they lead to the same conclusion. Results for the 23 m DOB are used for this analysis.

Two types of geometric nonlinear effects are considered: separation of the soil and wall, and slipping of the soil along the wall surface. The first occurs when the normal pressure at the interface becomes negative. Since the seismic induced normal pressure varies as a cosine function, the maximum tendency for separation occurs at either the head on location ($\theta = 0^\circ$) or at the opposite location ($\theta = 180^\circ$) depending on which is a tensile pressure. The net pressure at the interface is computed as the dead load pressure minus the maximum seismic pressure. The dead load pressure is assumed to be equal to one half the weight of the soil column above the point of interest. Time histories of net pressure at depths of 1 m, 5m, and 11 m are shown on Figures 4.4.6-1 through 4.4.6-3 respectively. Negative net pressures indicate tensile normal pressures and therefore separation. As may be seen significant separation occurs at 1 m depth and 5m depths but very little separation occurs at 11 m depth. It should also be noted that separation occurs at many different times so that nonlinear separation effects would be expected to have a significant impact on the seismic response of the facility.

The second type of nonlinear effect considered is slipping of the soil over the wall resulting from the shear stresses (both vertical and tangential shears). The vertical shear varies as a cosine function and has a peak value at the head on point. The tangential shear varies as a sine function and has a peak value at the side on point ($\theta = 90^\circ$). A coefficient of friction required to restrain slipping is computed as the shear pressure divided by the normal pressure. It is assumed that there is a tendency to slip when the coefficient of friction exceeds 0.6. It should be noted that negative friction coefficients are computed when the normal pressure is tensile. In these cases separation occurs and there is no resistance to slippage. Therefore, nonlinear slippage effects are to be expected except when the coefficient of friction varies between 0 and 0.6.

Time histories of the coefficient of friction computed for the vertical shear are shown on Figures 4.4.6-4 through 4.4.6-6 for depths of 1 m, 5 m, and 11 m, respectively. Significant

tendency for slippage due to the vertical shear occurs at the 1 m depth but the tendency decreases significantly at the 5 m depth and is almost gone at the 11 m depth.

Time histories of the coefficient of friction computed for the tangential shear are shown on Figures 4.4.6-7 through 4.4.6-9 for depths of 1 m, 5 m, and 11 m, respectively. Significant tendency for slippage due to the tangential shear occurs at the 1 m depth but the tendency is almost gone for the 5 m and the 11 m depths.

In summary, the soil structure interface pressures computed with the SASSI code indicate that there is a significant tendency for separation and slipping at the interface over the upper one half of the foundation. This would indicate that the SASSI results may not accurately predict the seismic response of the facility when non-linear effects should be considered.

4.5 Assessment of Nonlinear Material Effects on Seismic Response of DEB Structures

The LS-DYNA analyses performed in the previous sections model the soil as a linear elastic material, since the intent there is to investigate the effect of modeling of the soil/wall interfaces. In this section, the effect of the soil material modeling is examined. In geotechnical engineering, soils are typically represented with a Coulomb material model, which is characterized by shear failure of the material. The Coulomb failure model is governed by cohesion and internal friction, and is included in the LS-DYNA material library. To assess the soil material modeling effect, the LS-DYNA model for the 23 m DOB case is modified to incorporate the Coulomb material for the soil. This section presents the results of the LS-DYNA model with the Coulomb soil representation and their comparison with the results predicted using the LS-DYNA model with linear elastic soils.

In order to be consistent with the soil profile used for the previous LS-DYNA analyses, the equation of state governing the pressure vs. volumetric strain relationship is determined using the same elastic properties. Further, to simplify the model, zero cohesion and 0.7 internal friction coefficient for the soil are assumed. The Coulomb soil model so defined is implemented in the LS-DYNA SSI model for the 23 m DOB case for both contact and tied interfaces. The SSI response parameters are computed and compared with the solution of the corresponding LS-DYNA models with linear elastic soil representation, which are discussed below.

The relative lateral displacement time history at the structure/soil interface is examined first. Figure 4.5-1 shows the relative lateral displacement time history which is computed at the nodes of the structure/soil at the interface near the ground surface at $\theta = 0$ (head-on). Since the relative displacements are calculated by subtracting the structural displacement from the adjacent soil displacement, positive displacement implies that the structure is experiencing a lateral separation effect from the surrounding soil. Figure 4.5-1 shows only one occurrence of separation at the soil/wall interface as opposed to the frequent openings and closings predicted by the model with elastic soil (Figure 4.4.2-1). The magnitude of the peak wall/soil separation calculated using the Coulomb soil is quite small (0.15 mm) compared to the peak separation predicted by the elastic soil (12.2 mm).

The vertical distribution of the relative structure/soil displacement along the wall corresponding to the peak separation time is displayed in Figure 4.5-2. In this figure, the horizontal axis represents the lateral structure/soil displacements and the vertical axis is the depth in the z-direction expressed as a percentage of the foundation embedment ($E = 23$ m). The diamond symbols represent the data points for the structure and the data points for the soil are designated by the triangular symbols. As shown in this figure, the soil/wall separation in the

vertical direction is minimal compared the separation predicted by the elastic soil (Figure 4.4.2-2). The significant reduction of the separation effect is due to the use of Coulomb soil model which reduces the impact effect at the soil/wall interface by absorbing the energy through the internal friction. It again demonstrates the sensitive modeling effect of different aspects of the SSI problem, especially for DEB structures.

The base uplifting of the structure estimated using the LS-DYNA model with the Coulomb soil is discussed next. This is carried out by subtracting the soil displacements at the foundation base from the corresponding structural base displacements. Figures 4.5-3 and 4.5-4 present the relative vertical displacement time histories computed at $\theta = 0, 180$, respectively. Positive values in the figures represent separation of the structural base from the supporting soils. These figures indicate that the LS-DYNA model with the Coulomb soil also predicts the base uplifting the extent of which is similar to the one predicted by the LS-DYNA model with the elastic soil (Figures 4.4.2-4 and 4.4.2-5).

To examine the effect of the Coulomb soil model on the in-structure response spectra, the response spectra are computed at the center of basemat and the center of the roof of the structure from both the contact and tied interface LS-DYNA models with the Coulomb soil. Figures 4.5-5 and 4.5-9 present the comparisons of response spectra between the Coulomb soil representation and the elastic soil model. For the contact interface, the response spectrum at the base exhibits unwanted upward drift. To correct it, a Butterworth low-pass and high-cut filter with a cut off frequency equal to 20 Hz is applied to the computed base spectrum to eliminate the high frequency drift. Figures 4.5-5 and 4.5-6 show the spectral comparison for the contact interface solution. These figures indicate that the base spectrum computed with the Coulomb soil is much higher than the elastic soil while the computed roof spectrum appears less sensitive to the soil representation. This observation can also be extended to the tied interface solutions as depicted in Figures 4.5-7 and 4.5-8.

Next, the effects of using the Coulomb material model for the soil in the LS-DYNA SSI model is examined with respect to the distribution of soil pressure. The seismic induced pressure is calculated using the LS-DYNA models with both contact and tied interface conditions. For the head-on locations near the ground surface and the mid-height of the structural wall, the normal pressure is computed using the Coulomb soil for both the contact and tied interface models, and then is compared with the results calculated using the elastic soil. These comparisons of normal pressure time histories are provided in Figures 4.5-9 and 4.5-12. As shown in these figures, the normal pressures calculated from the contact interface model exhibit similar compressive characteristics for both Coulomb and elastic soil models at the ground surface, while near the mid-height of the structural wall, the pressure calculated with the Coulomb soil begins to increase rapidly at 6.8 seconds with respect to the solution computed with the elastic soil model. For the tied interface model, the normal pressure comparison near the mid-height of the structural wall between the Coulomb soil and elastic soil models exhibit a similar trend, while the surface comparison shows that Coulomb soil produces compression only soil stress as opposed to the mostly tension characteristic for the elastic soil solution. The frequency content of the normal pressure is examined by computing the corresponding Fourier spectrum near the mid-height of the structural wall, which is shown in Figure 4.5-13 for the contact interface model, and in Figure 4.5-14 for the tied interface model. These figures show that the significant upward drift in the low frequencies is attributed to the increase in the normal pressure calculated using the Coulomb soil model. As discussed in Section 4.1.2, the low frequency drift is primarily due to the approximate nature of the Lysmer transmitting boundary effect, and it appears to impact the prediction of the soil pressure more for the Coulomb soil model.

The pressure time history plots given in Figures 4.5-9 and 4.5-12 are also used to identify the seismic induced peak normal pressures calculated with the Coulomb soil. For the contact interface model, the first two peak normal pressures in the head-on soil element near the ground surface occur at times equal to 14.93 seconds and 11.08 seconds, with the pressure magnitudes equal to -247.73 kN/m^2 and -241.7 kN/m^2 , respectively. These compare to the first two peak normal pressures equal to -305.43 kN/m^2 and -284.23 kN/m^2 calculated using the elastic soil. For the tied interface model, the first two peak normal pressures in the head-on soil element near the ground surface are calculated with the Coulomb soil to be -306.1 kN/m^2 and 281.3 kN/m^2 , which occur at times equal to 11 seconds and 7.3 seconds, respectively. These compare to the peak pressures calculated using the elastic soil equal to 237.63 kN/m^2 and 230 kN/m^2 . For the mid-height of the structural wall, the first two peak soil pressures calculated from the contact interface model are identified to be -194.87 kN/m^2 and -182.98 kN/m^2 , when using the Coulomb soil, compared to -79.78 kN/m^2 and -79.63 kN/m^2 computed with the elastic soil. As discussed above, the Lysmer transmitting boundary is responsible for this increase in the soil pressure using the Coulomb soil model. For the tied interface model, the first two peak normal pressures near the mid-height of the structural wall are computed to be -184.1 kN/m^2 and -183.4 kN/m^2 for the Coulomb soil model compared to -64.77 kN/m^2 and -55.49 kN/m^2 computed using the elastic soil.

To examine the Coulomb material model effect on the soil pressure distributions in circumferential directions, the occurring time of the peak normal soil pressures near the mid-height of the structural wall are selected. This time is indicated in Figure 4.5-1 as 11.1 seconds for the contact interface model and about the same time for the tied interface model as shown in Figure 4.5-12. The circumferential distributions are then computed in the soil elements at the structure/soil interface. Figures 4.5-15 through 4.5-17 present the comparisons of the circumferential distributions of the vertical shear, the normal pressure and the tangential shear between the Coulomb and elastic soils for the contact interface model. As shown in these comparisons, the Coulomb soil model predicts much higher normal pressure than the elastic soil model, while the predictions for the tangential and vertical shears are close between the two soil models. The circumferential variations predicted by the Coulomb soil appear less smooth than the ones computed with the elastic soil model. For the tied interface model, the circumferential distributions of soil pressures are compared between the Coulomb and elastic soil models, which are exhibited in Figures 4.5-18 through 4.5-20. Again, in this case, the Coulomb soil model predicts much higher normal pressure than the one computed using the elastic soil model. Further, the prediction for the vertical shear is comparable between the two soil models while the Coulomb soil model predicts less tangential shear than the elastic soil model. In addition, the Coulomb soil model with the tied interface computes much smoother soil stresses in the circumference than with the contact interface model, which suggests that the impact effect at the soil/wall interface surely plays a role in the calculation of pressure distributions.

With respect to examining the effect of the Coulomb soil model on the vertical distributions of the soil pressure, the occurring time of the peak normal soil pressures near the ground surface are selected, which is, as indicated in Figure 4.5-9, 14.93 seconds for the contact interface model and 11.04 seconds for the tied interface model as shown in Figure 4.5-11. The vertical distributions are then calculated in the head-on soil elements for the normal pressure and vertical shear, and the tangential shear is calculated at near $\theta = 90$ degrees. Figures 4.5-21 through 4.4.2-21 present the results of the vertical distributions of the normal pressure, the tangential shear and the vertical shear computed with the contact and tied interface models, respectively. Also presented in these figures are the corresponding results calculated with the elastic soil model. As shown in these figures, for the contact interface results, the Coulomb soil model effect on the vertical distributions for the tangential and vertical shears is less than for the normal pressure distribution in the vertical direction in that the Coulomb soil model predicts substantially higher

normal pressure than the elastic soil model. These figures also indicate sizeable impact due to the use of the Coulomb soil model on the vertical distributions for the tied interface results, compared with the elastic soil solution.

Furthermore, the vertical distributions of the normal pressure, the vertical and tangential shears for the Coulomb soil and elastic models are grouped together and plotted in Figures 4.5-27 through 4.5-30. These figures show that the Coulomb soil model induces larger normal pressure than the elastic soil model, while the effect of the Coulomb soil on the shears is either negligible or shows a reduction of magnitude.

Finally, to demonstrate the stresses induced in the structural wall due to the soil pressure, Fourier spectra for the Von-Mises effective stress is computed for the head-on wall location in the 5th shell element from the basemat, and plotted in Figure 4.5-31 for the contact interface model and Figure 4.5-32 for the tied interface model. These figures show that even though the Coulomb soil model predicted higher normal pressure, the induced structural stresses are actually close to or lower than that computed with the elastic soil model. This is because the higher pressure computed by the Coulomb soil model is mostly due to the drift on low frequencies (Figures 4.5-13 and 4.5-14), which are much lower than the natural frequency of the structure. If the low frequency drift of the normal pressure is filtered, the frequency characteristics of the normal pressure and the corresponding structural stresses are very similar (Figure 4.5-13 vs. Figure 4.5-31). Implied in these comparisons also is that shears in the soil in the vicinity of the structure have much less impact on the structural stresses than the soil normal pressure, which means that DEB features are beneficial in reducing seismic demand on the structure.

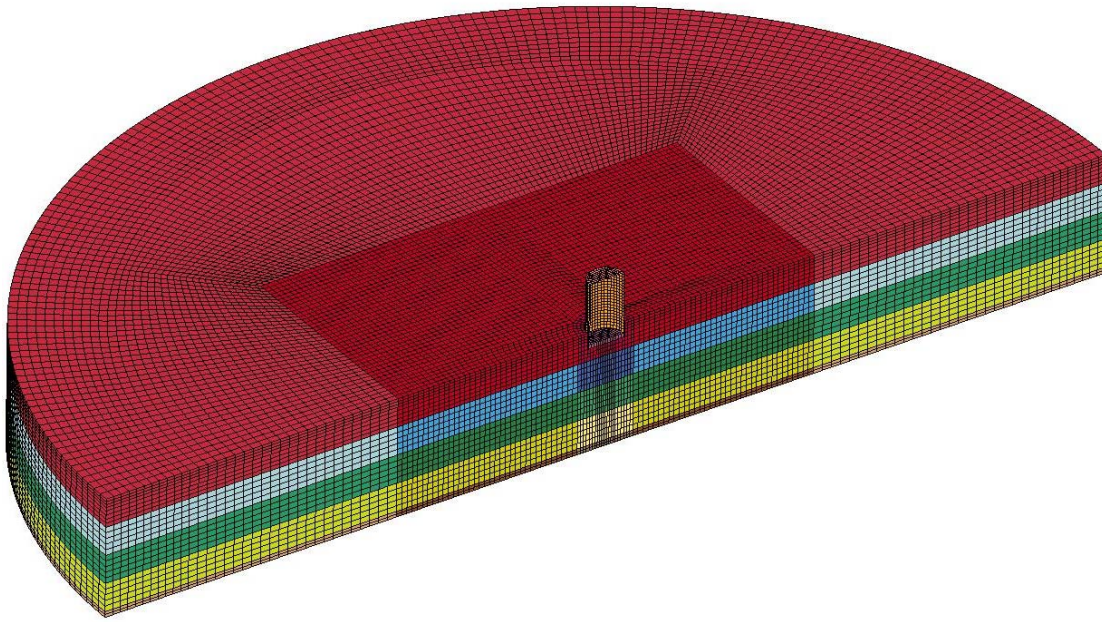


Figure 4.1.2-1 LS-DYNA Model for the 11.5 m Embedment.

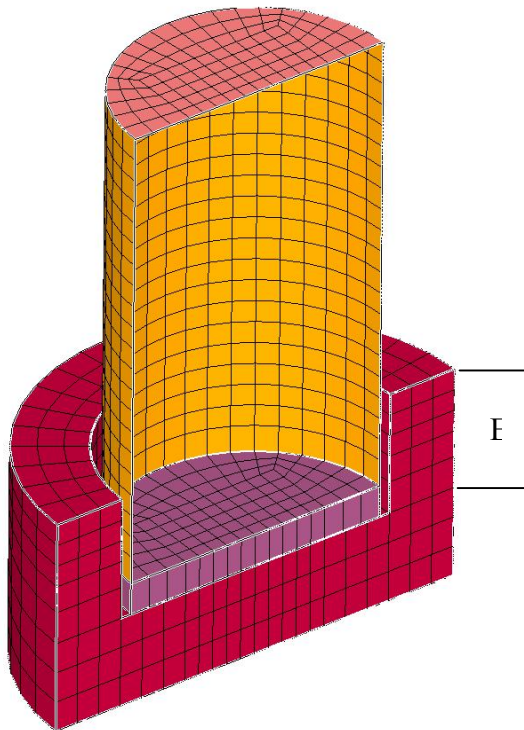


Figure 4.1.2-2 Zoom-in View of the Structure and Surrounding Soil in LS-DYNA Model for the 11.5 m Embedment.

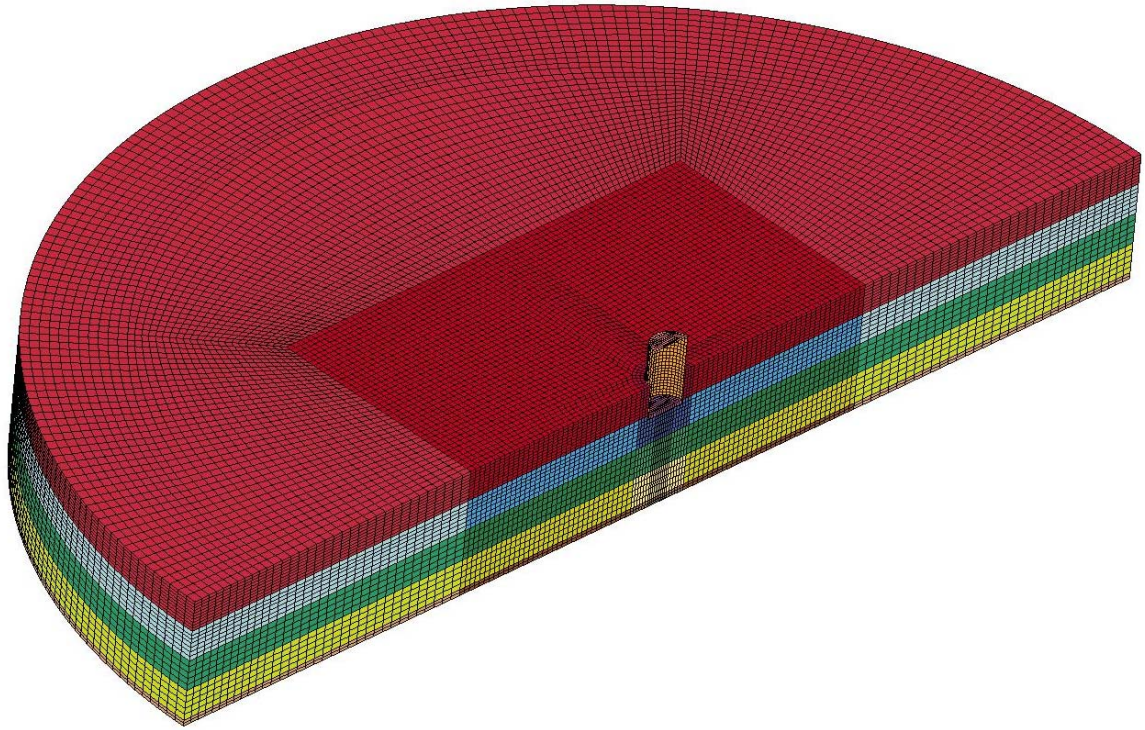


Figure 4.1.2-3 LS-DYNA Model for the 23 m Embedment.

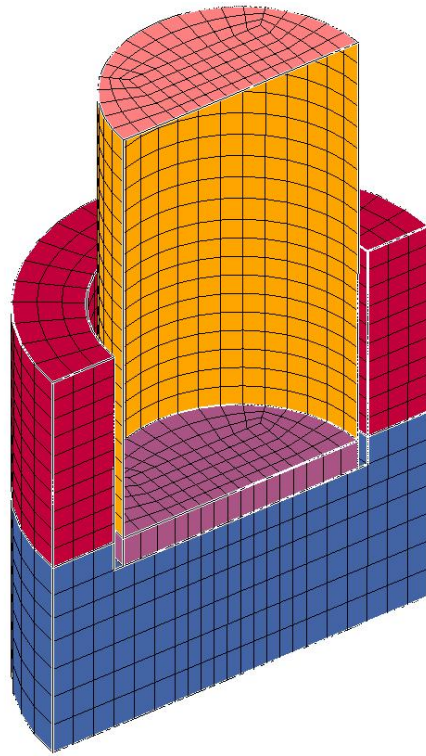


Figure 4.1.2-4 Zoom-in View of the Structure and Surrounding Soil in LS-DYNA Model for the 23 m Embedment.

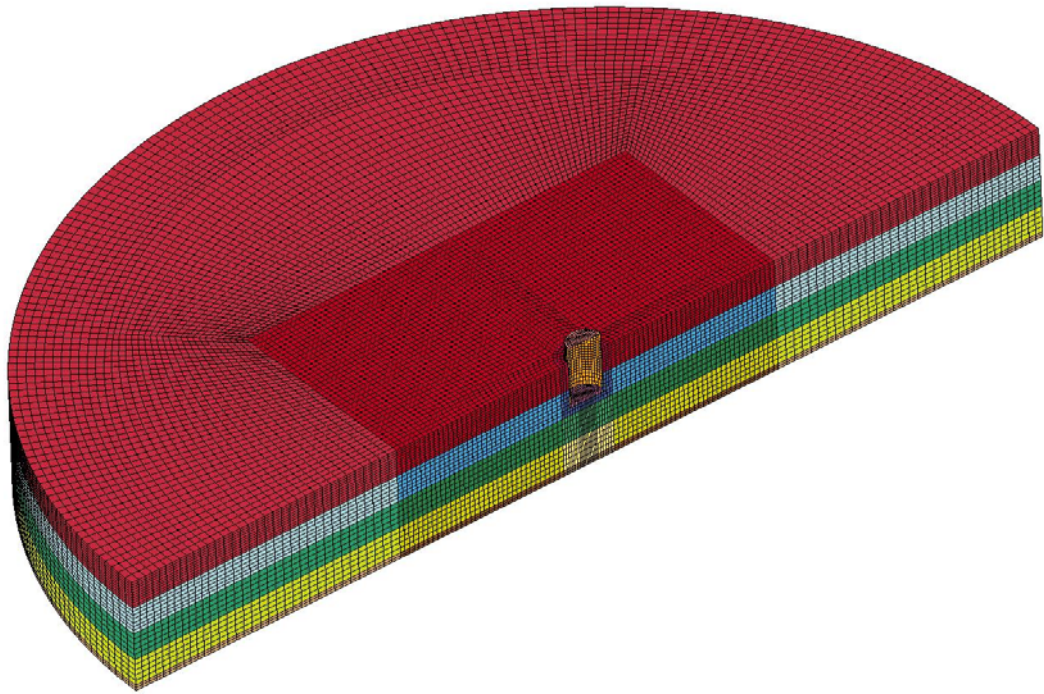


Figure 4.1.2-5 LS-DYNA Model for the 34.5 m Embedment.

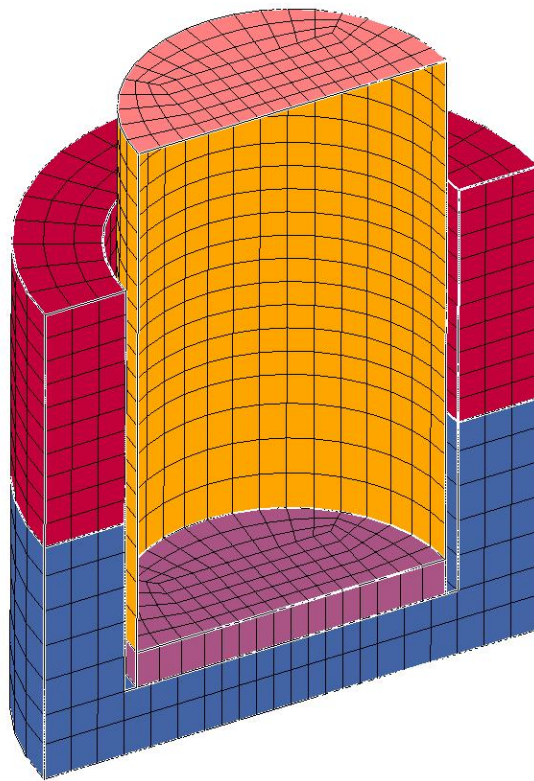


Figure 4.1.2-6 Zoom-in View of the Structure and Surrounding Soil in LS-DYNA Model for the 34.5 m Embedment.

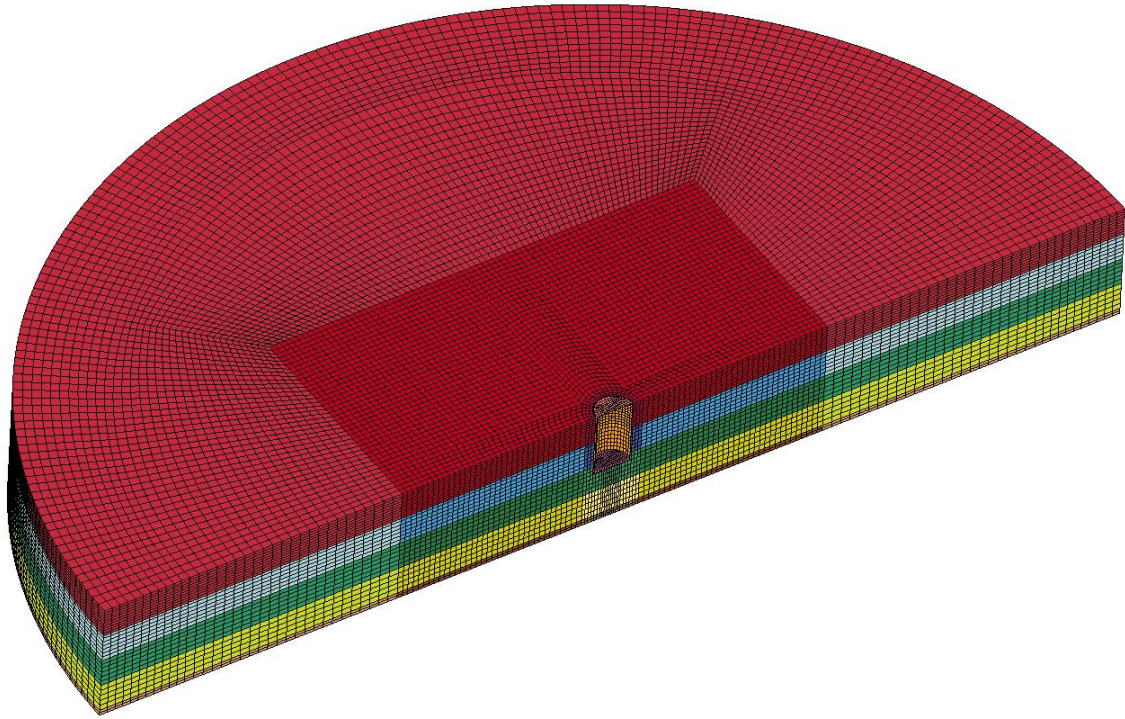


Figure 4.1.2-7 LS-DYNA Model for the 46 m Embedment.

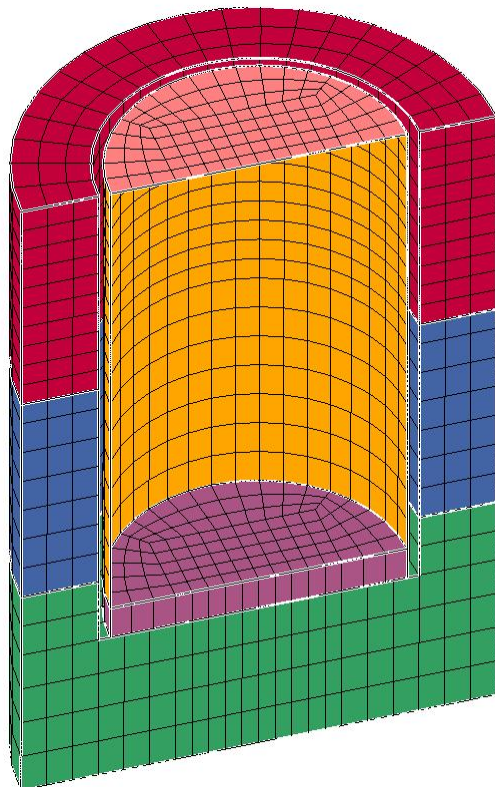


Figure 4.1.2-8 Zoom-in View of the Structure and Surrounding Soil in LS-DYNA Model for the 46 m Embedment.

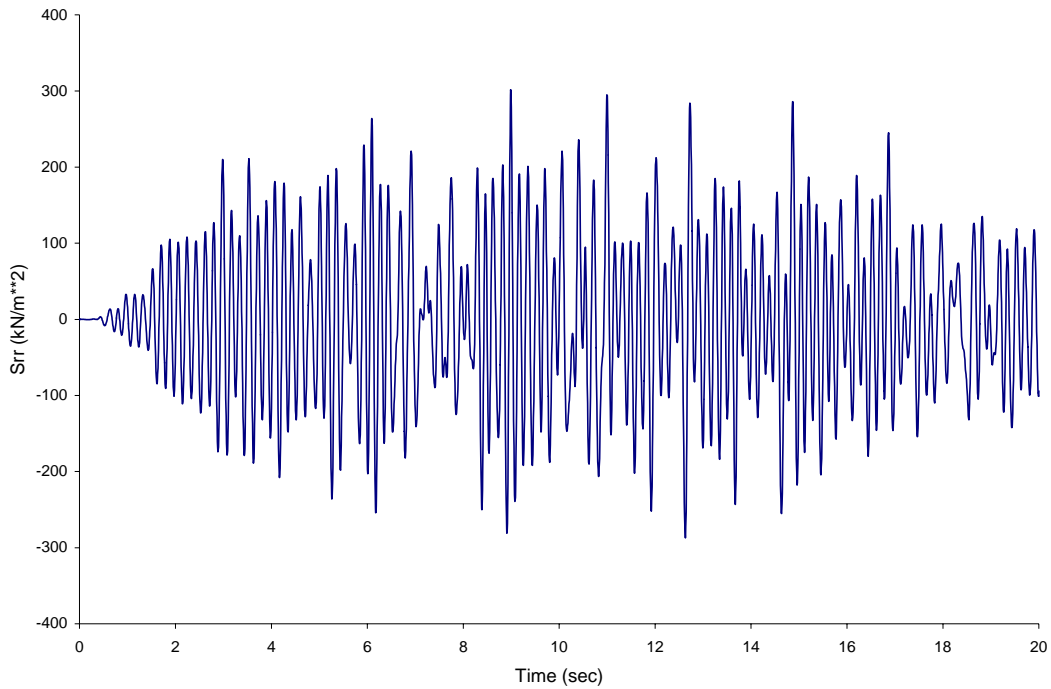


Figure 4.2.1-1 Normal Pressure on the Head-on Soil Element near the Ground Surface Computed from the 11.5 m DOB SASSI Model.

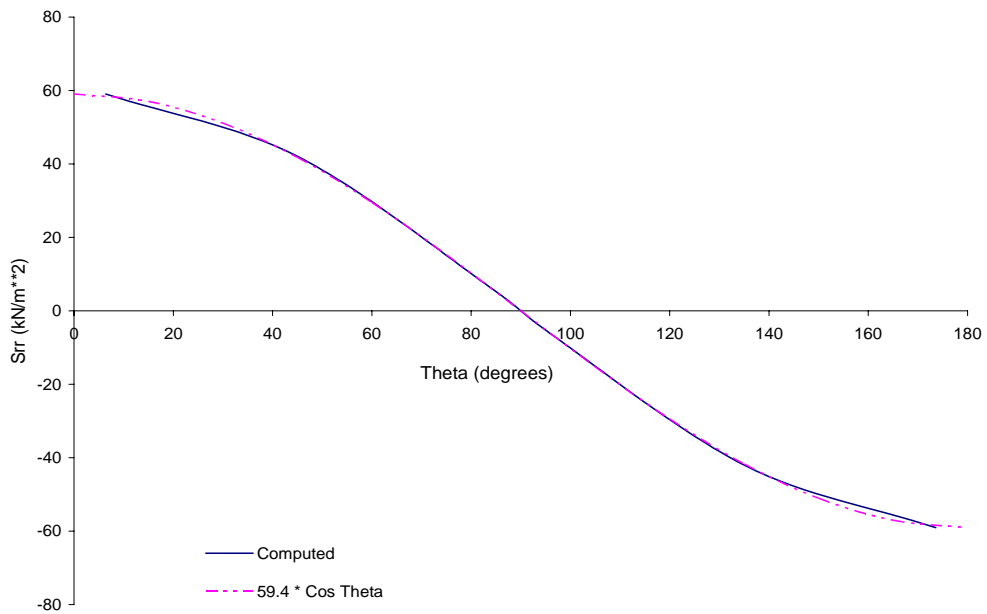


Figure 4.2.1-2 Circumferential Distribution of Normal Pressure Computed from the 11.5 m DOB SASSI Model.

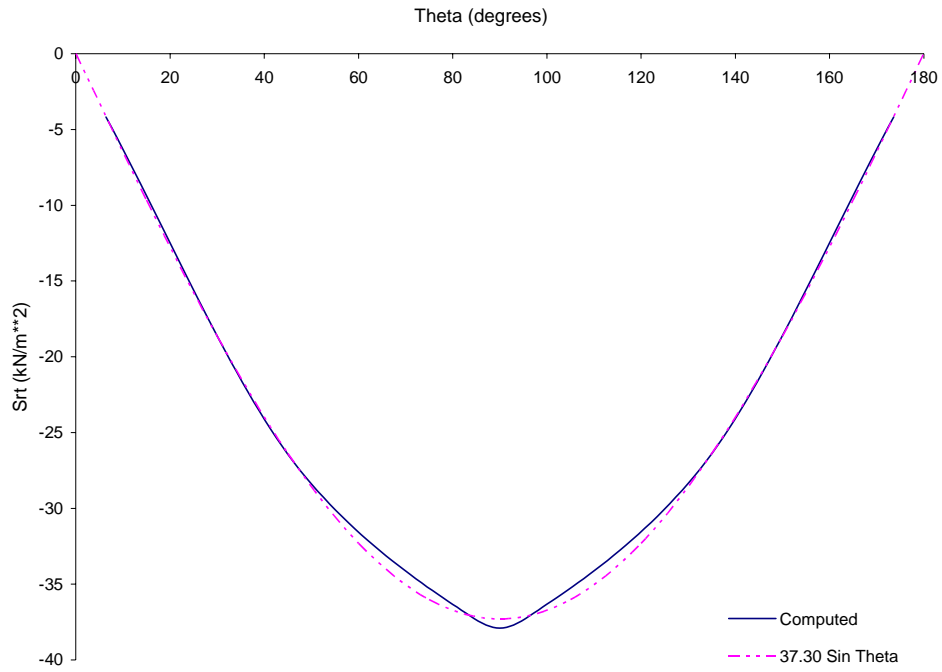


Figure 4.2.1-3 Circumferential Distribution of Tangential shears Computed from the 11.5 m DOB SASSI Model.

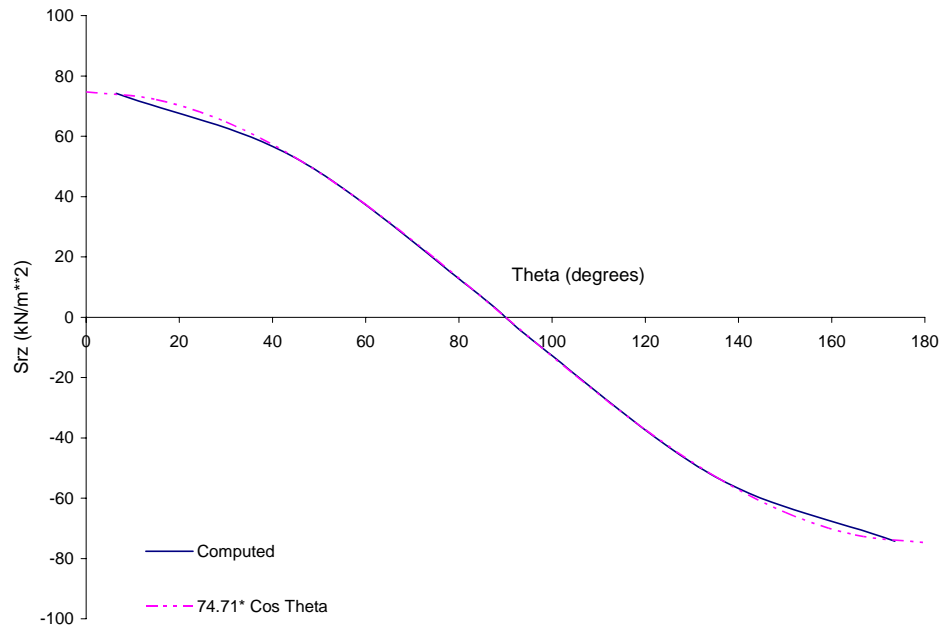


Figure 4.2.1-4 Circumferential Distribution of Vertical shears Computed from the 11.5 m DOB SASSI Model.

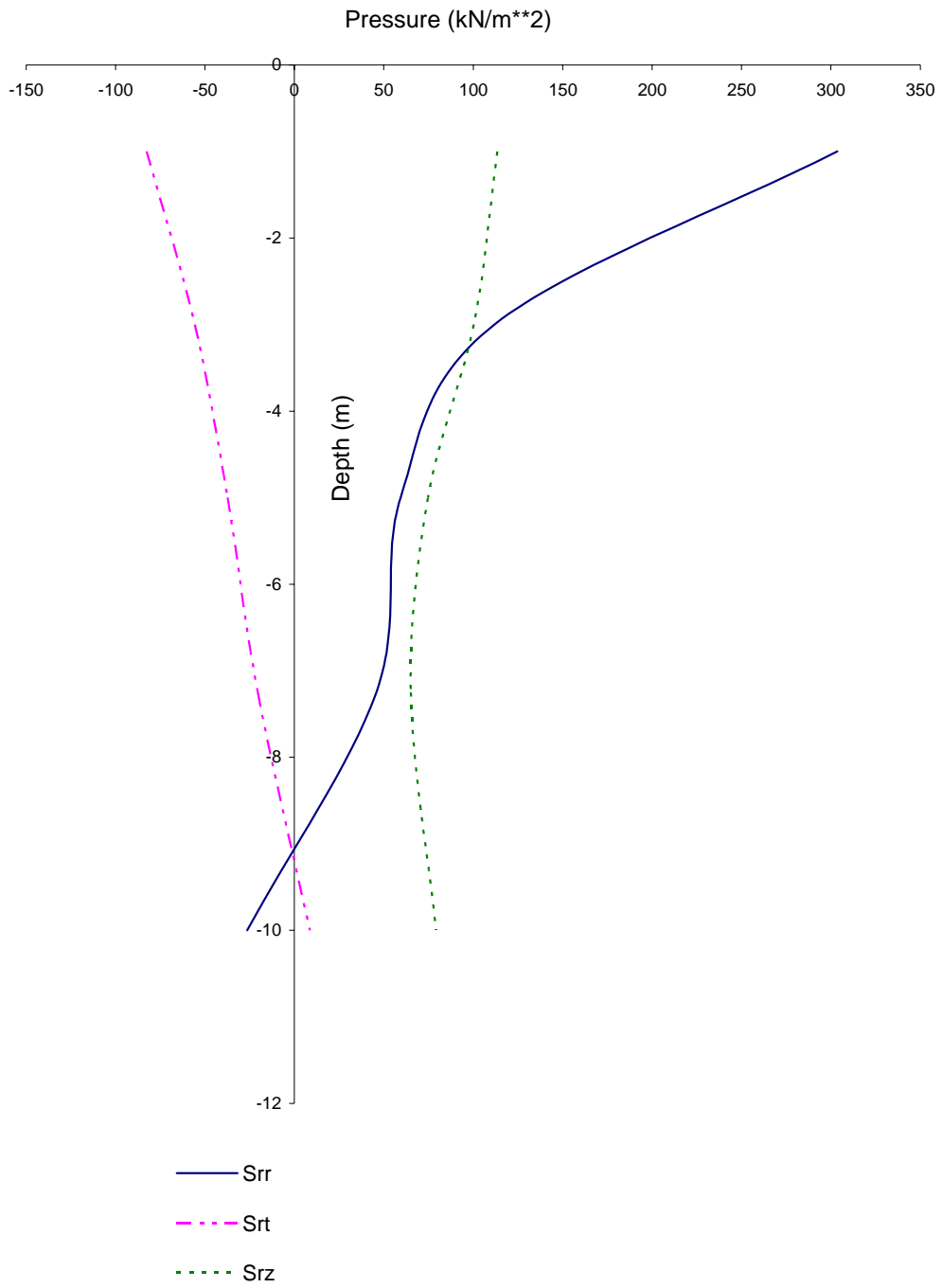


Figure 4.2.1-5 Vertical Distributions of Soil Pressure Computed from the 11.5 m DOB SASSI Model.

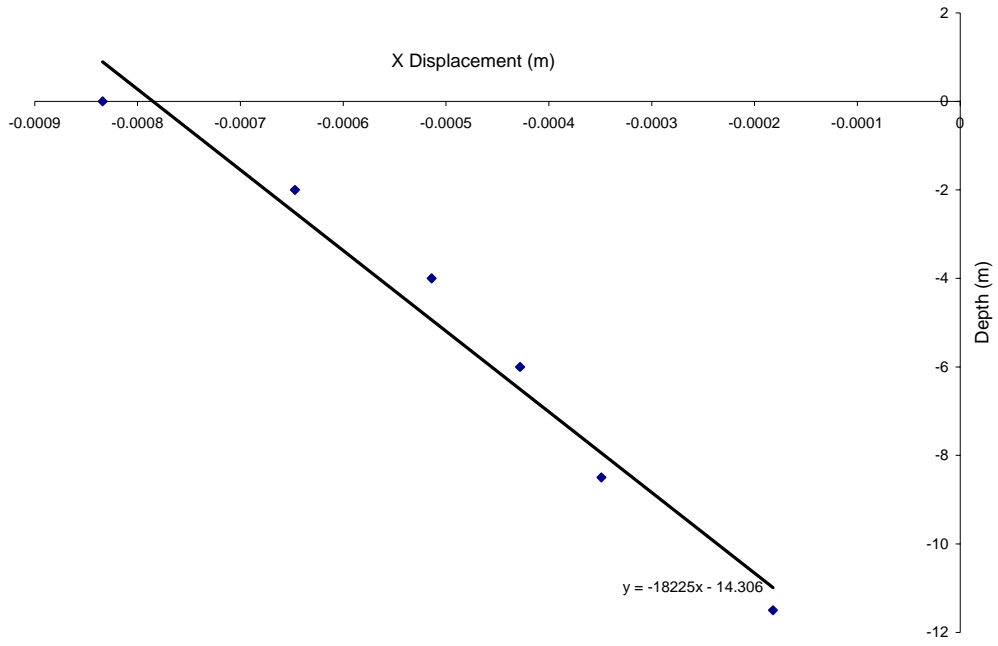


Figure 4.2.1-6 Lateral Wall Displacements Computed from the 11.5 m DOB SASSI Model.

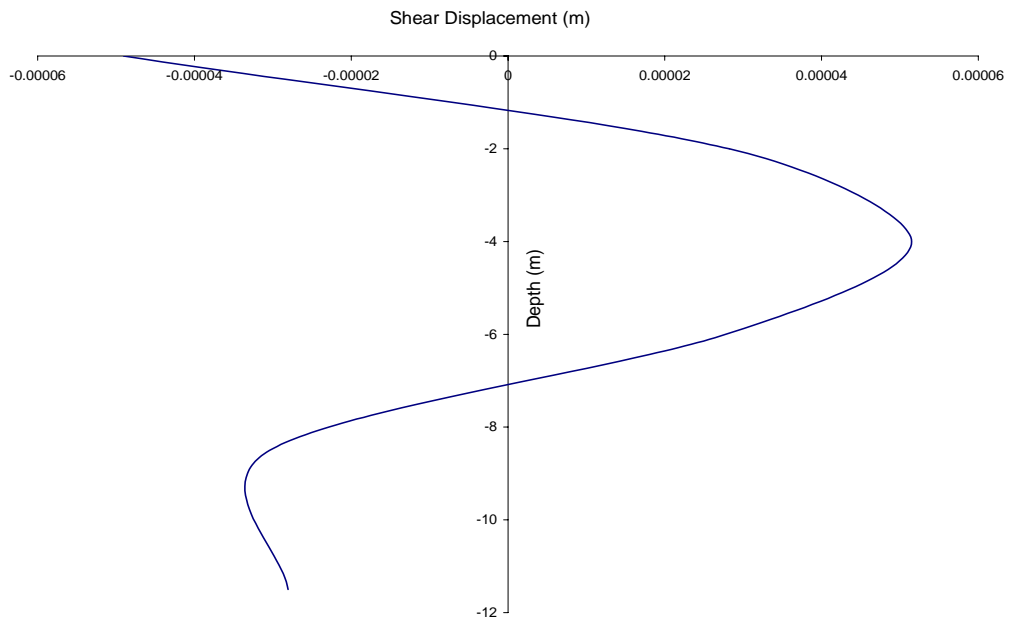


Figure 4.2.1-7 Lateral Wall Shear Displacements Computed from the 11.5 m DOB SASSI Model.

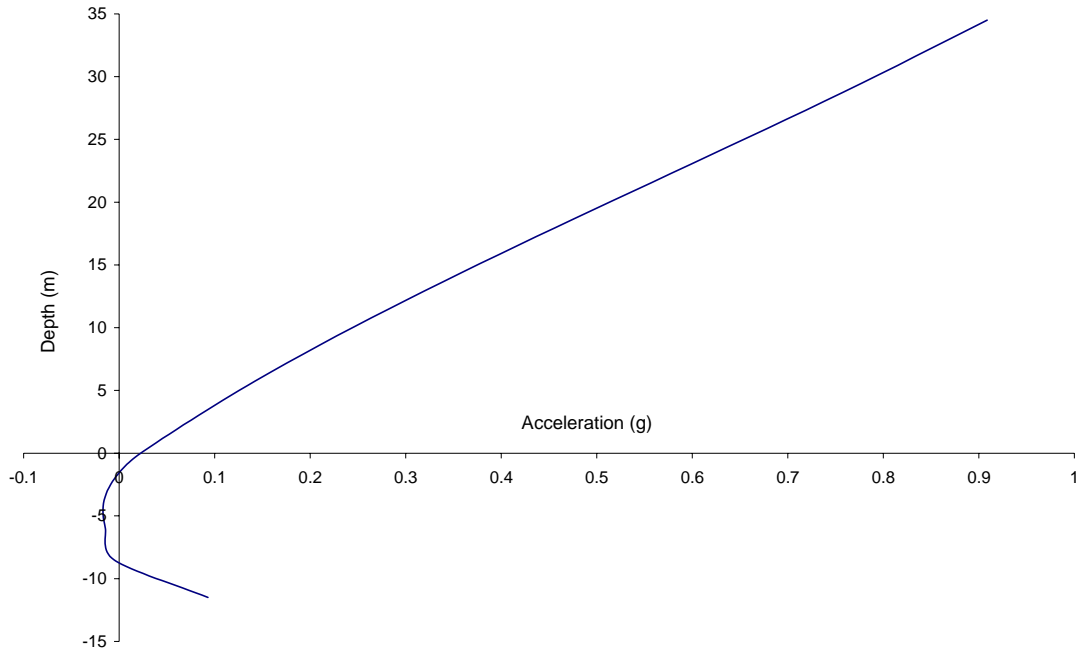


Figure 4.2.1-8 Structural Acceleration at 8.99 Seconds Computed from the 11.5 m DOB SASSI Model.

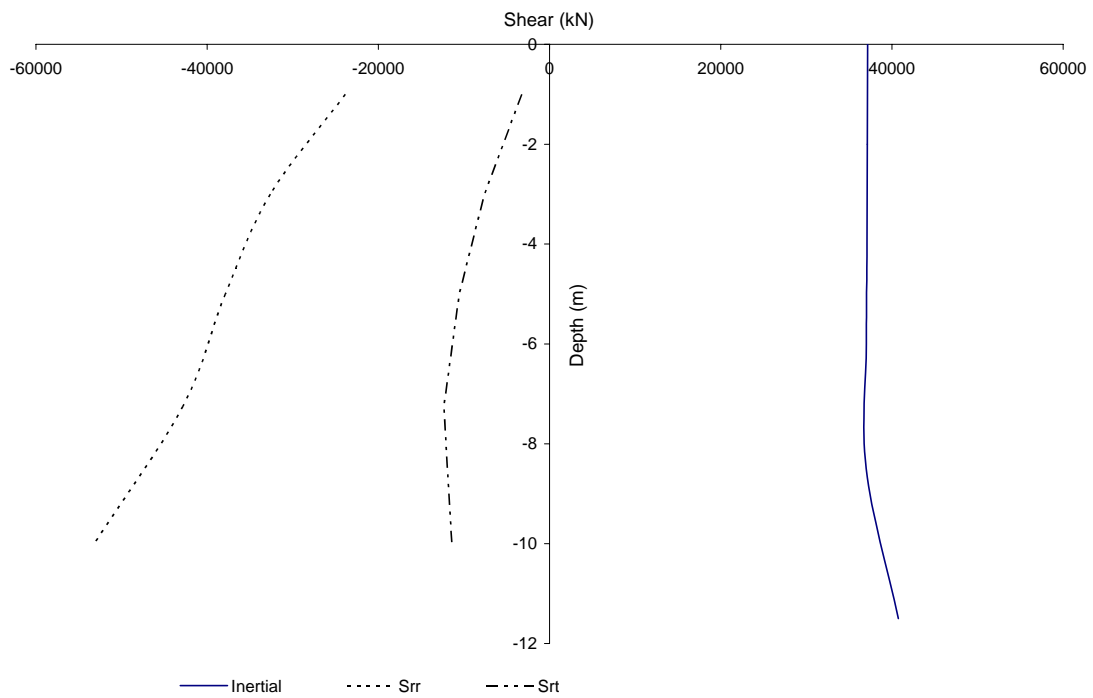


Figure 4.2.1-9 Variation of Shear over DOB at 8.99 Seconds Computed from the 11.5 m DOB SASSI Model.

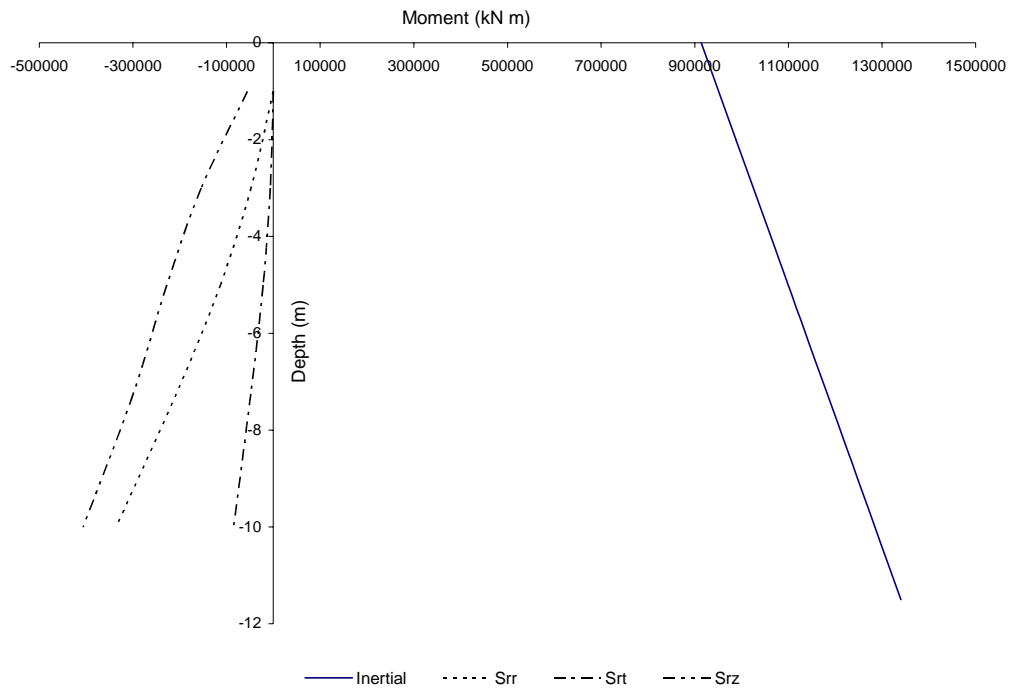


Figure 4.2.1-10 Variation of Moment over DOB at 8.99 Seconds Computed from the 11.5 m DOB SASSI Model.

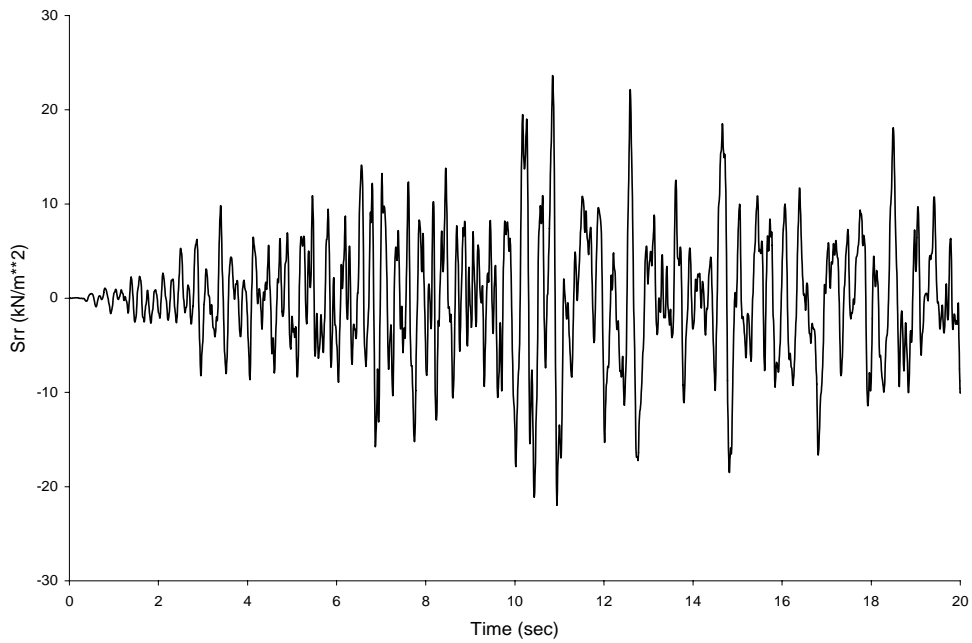


Figure 4.2.2-1 Normal Pressure on the Head-on Soil Element near the Mid-height of Structural Wall Computed from the 23 m DOB SASSI Model.

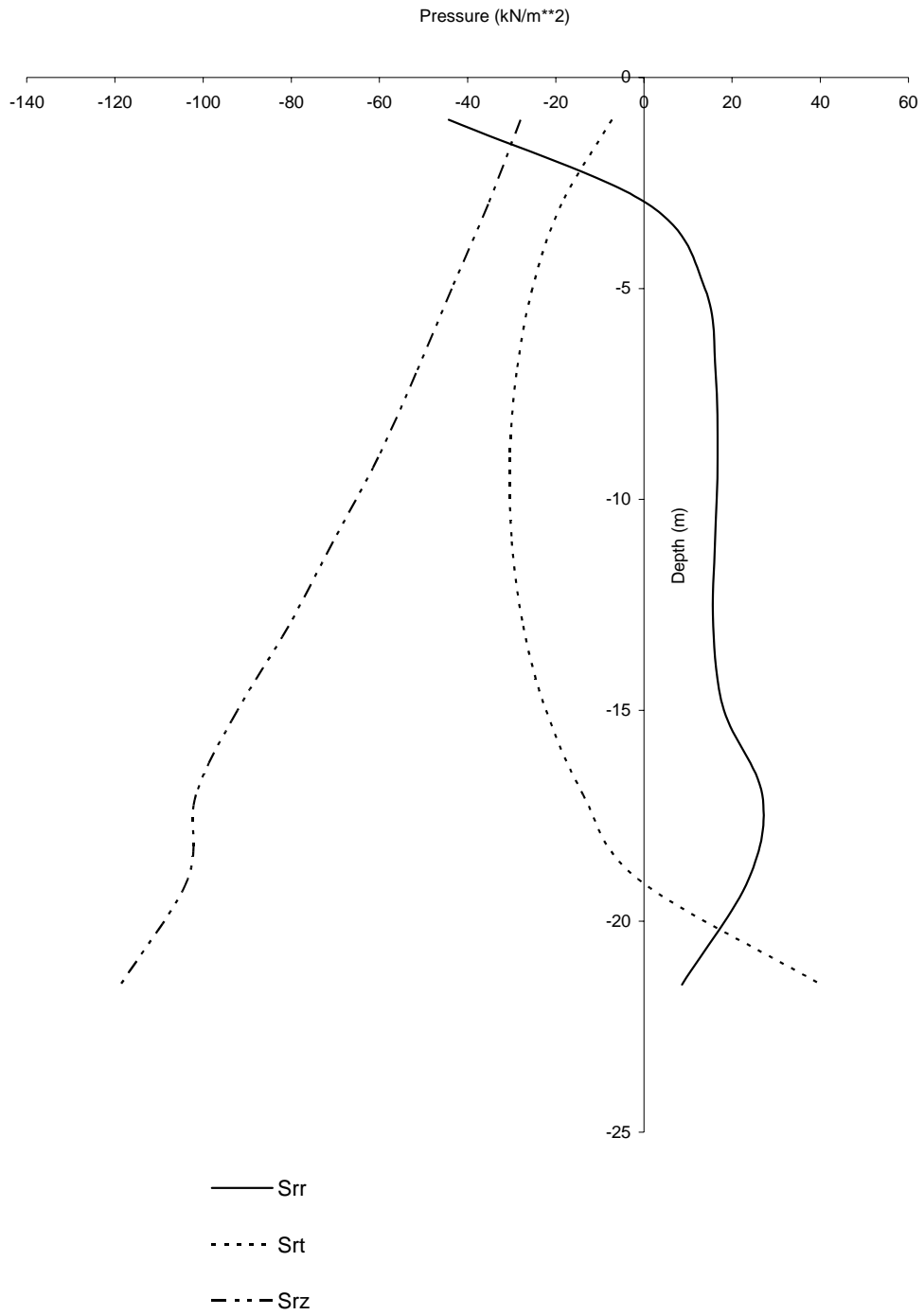


Figure 4.2.2-2 Vertical Distributions of Soil Pressure Computed from the 23 m DOB SASSI Model.

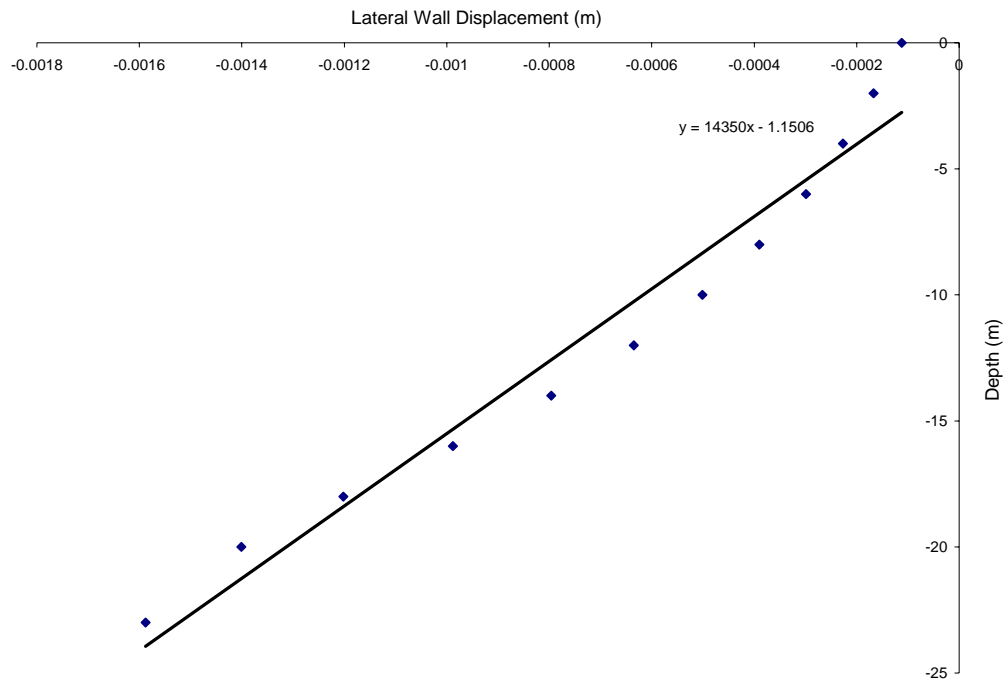


Figure 4.2.2-3 Lateral Wall Displacements Computed from the 23 m DOB SASSI Model.

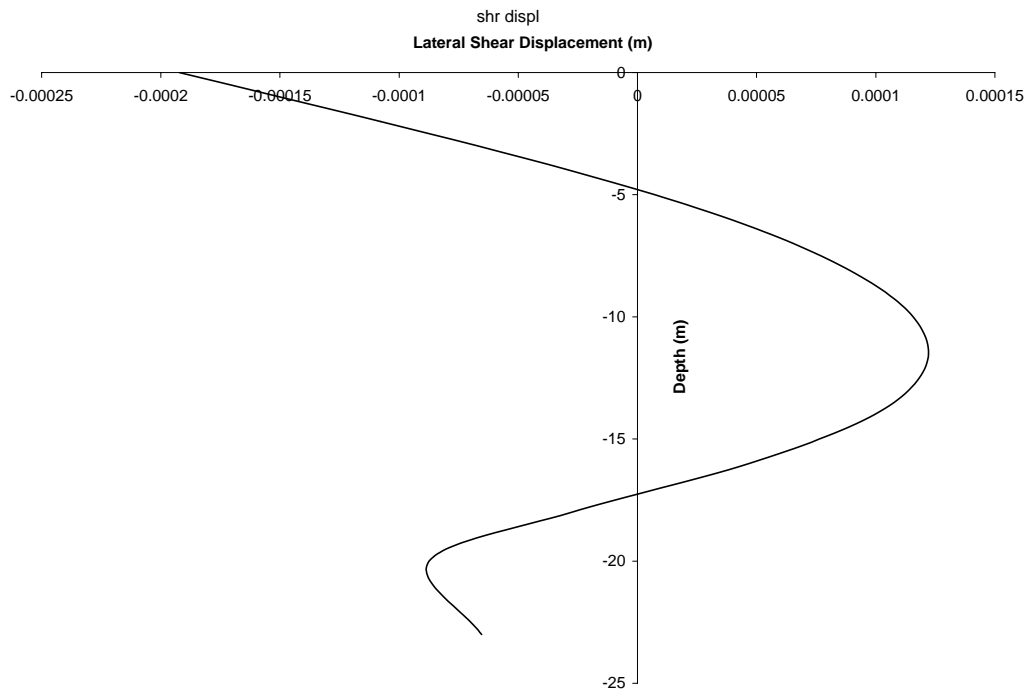


Figure 4.2.2-4 Lateral Wall Shear Displacements Computed from the 23 m DOB SASSI Model.

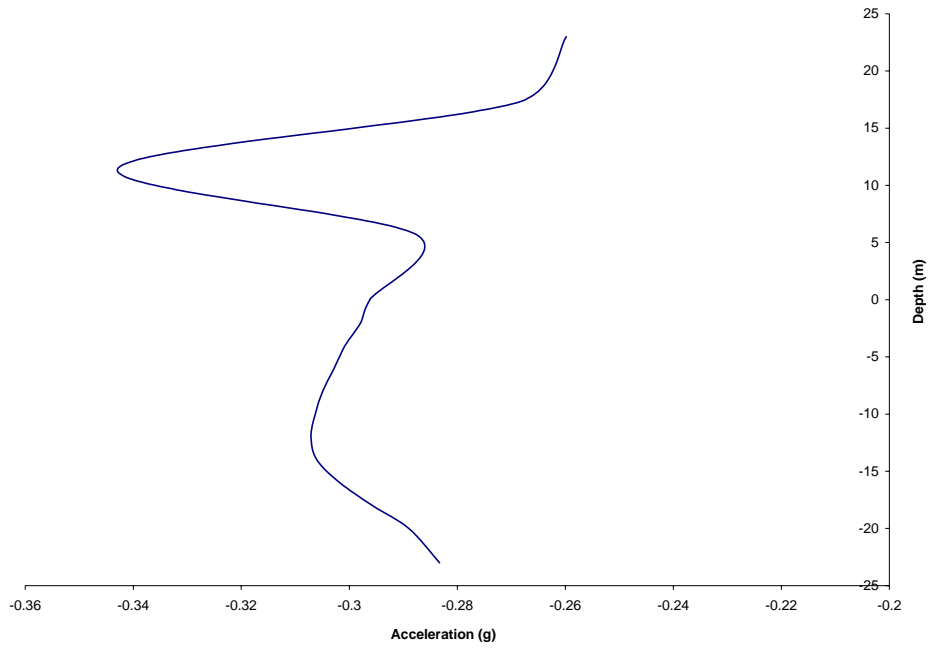


Figure 4.2.2-5 Structural Acceleration at 10.85 Seconds Computed from the 23 m DOB SASSI Model.

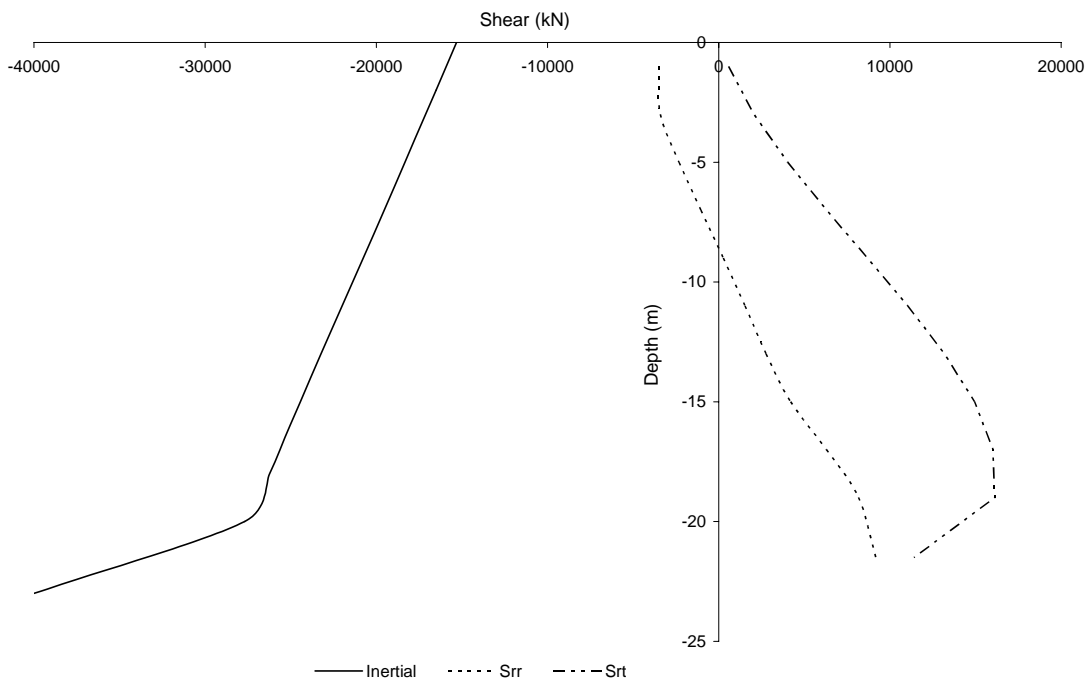


Figure 4.2.2-6 Variation of Shear over DOB at 10.85 Seconds Computed from the 23 m DOB SASSI Model.

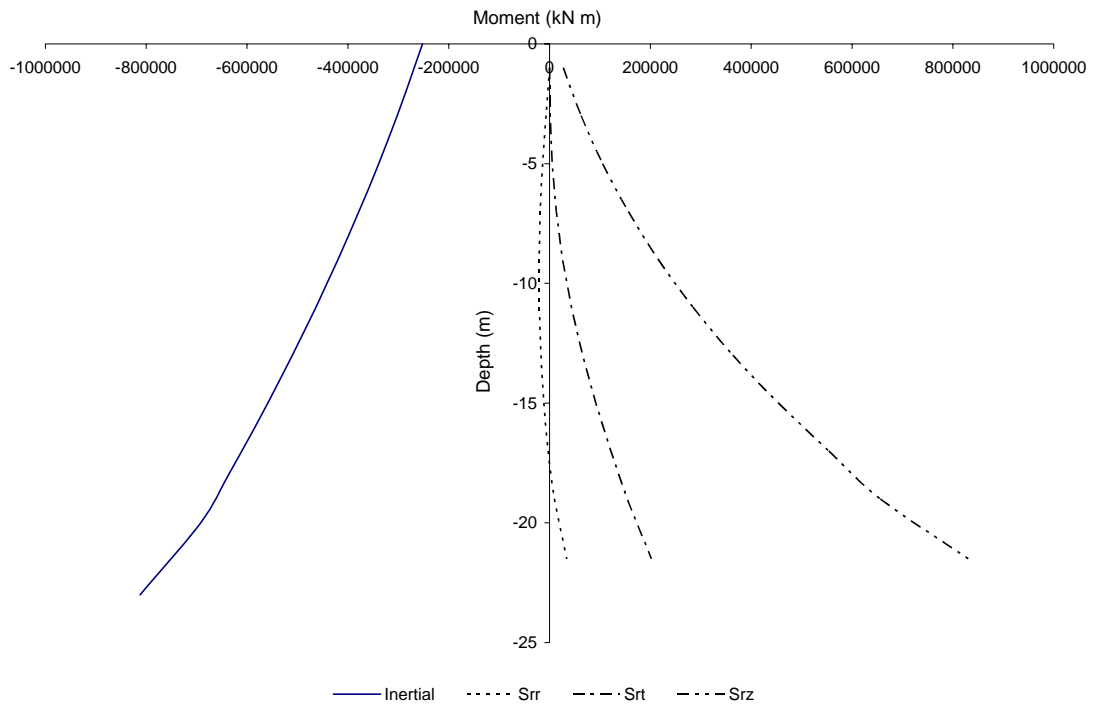


Figure 4.2.2-7 Variation of Moment over DOB at 10.85 Seconds Computed from the 23 m DOB SASSI Model.

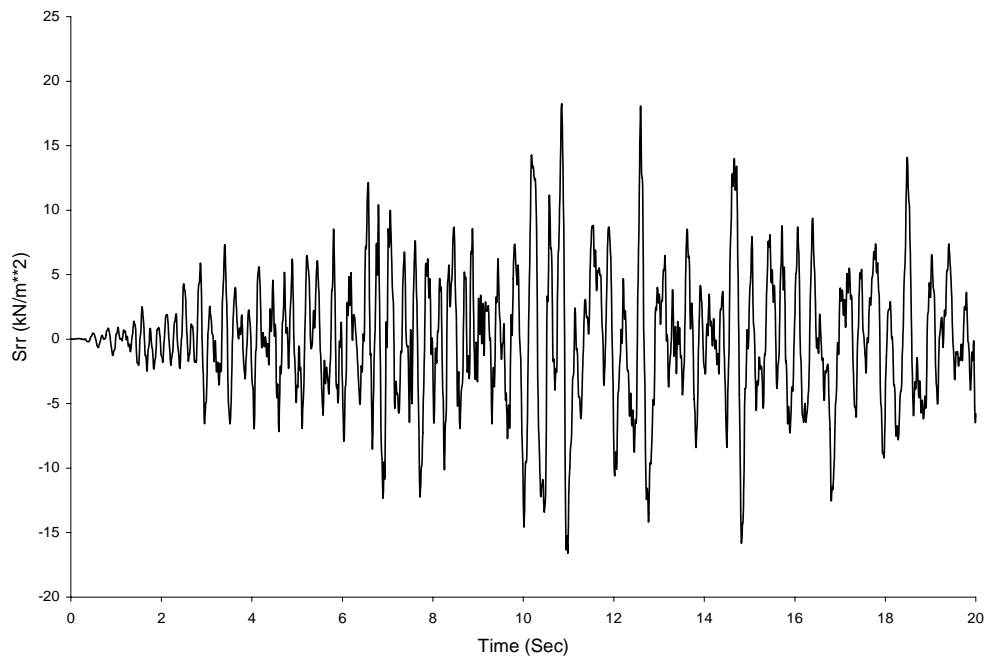


Figure 4.2.3-1 Normal Pressure on the Head-on Soil Element near the Mid-height of Structural Wall Computed from the 34.5 m DOB SASSI Model.

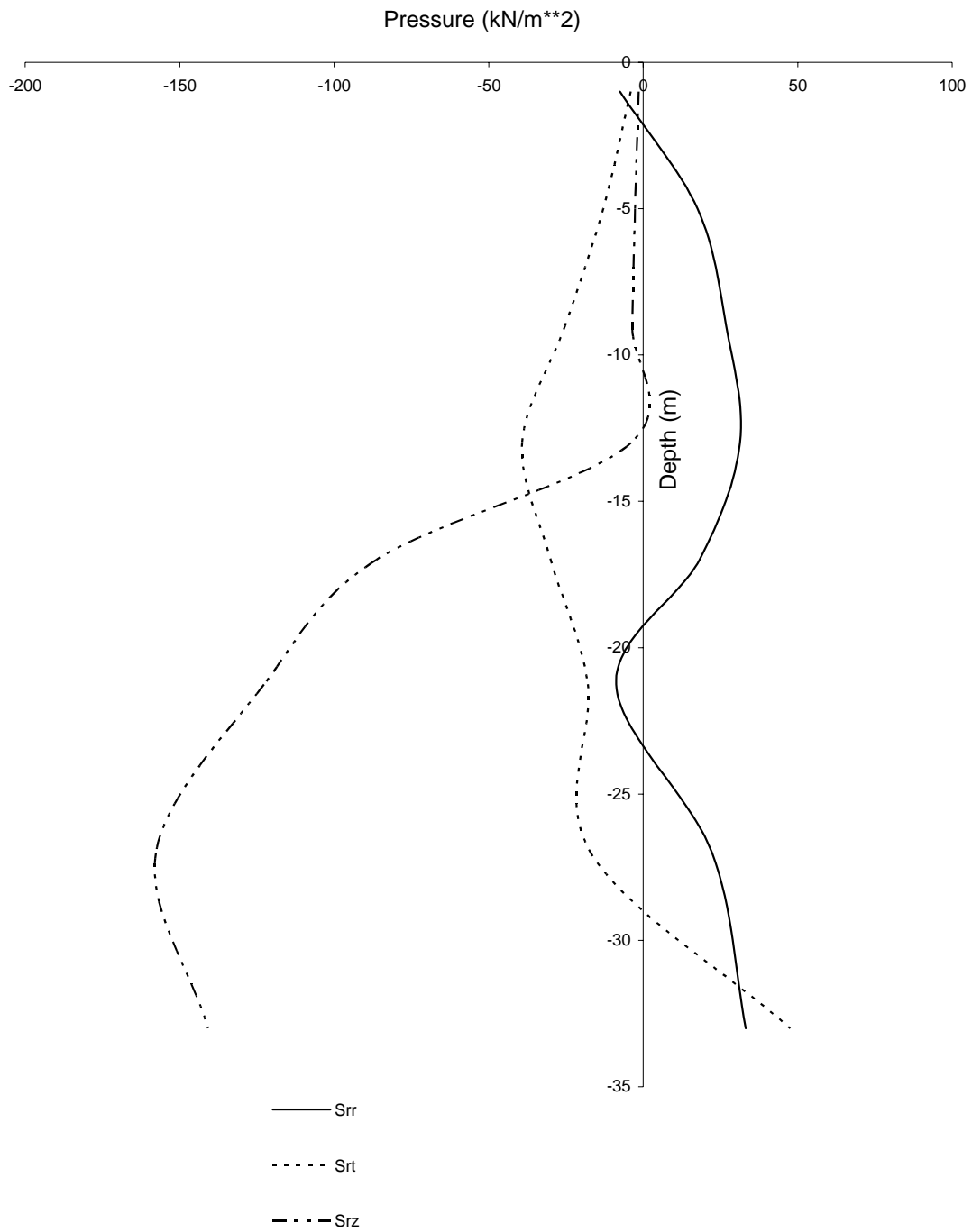


Figure 4.2.3-2 Vertical Distributions of Soil Pressure Computed from the 34.5 m DOB SASSI Model.

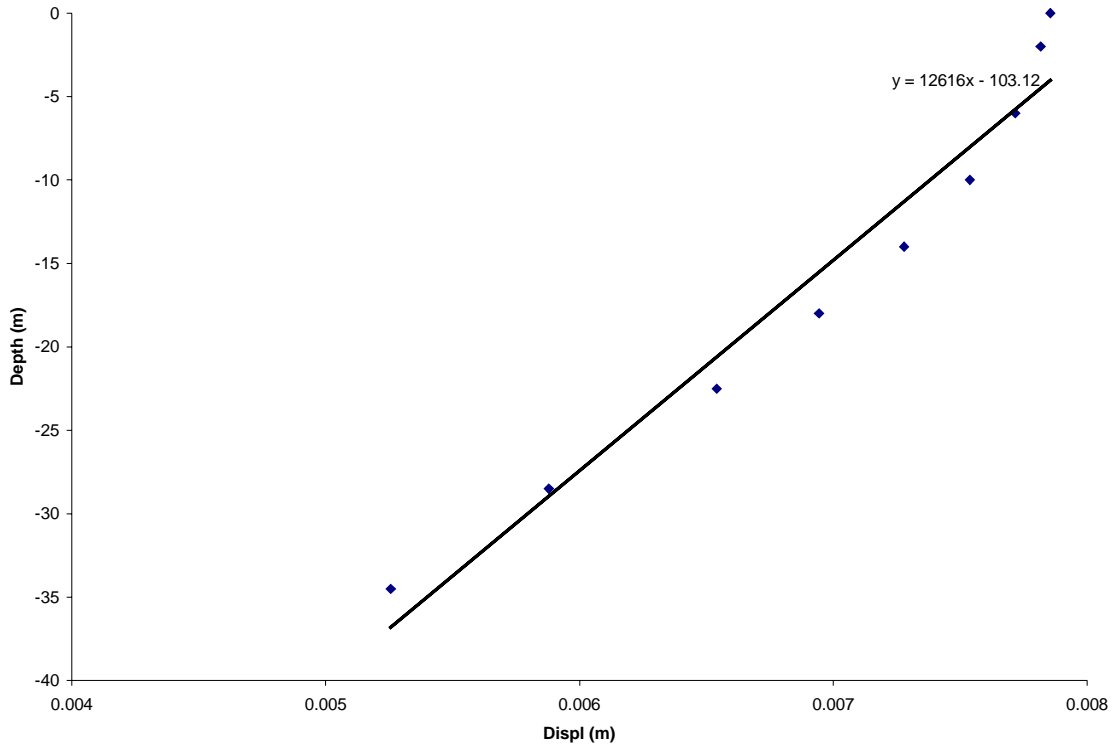


Figure 4.2.3-3 Lateral Wall Displacements Computed from the 34.5m DOB SASSI Model.

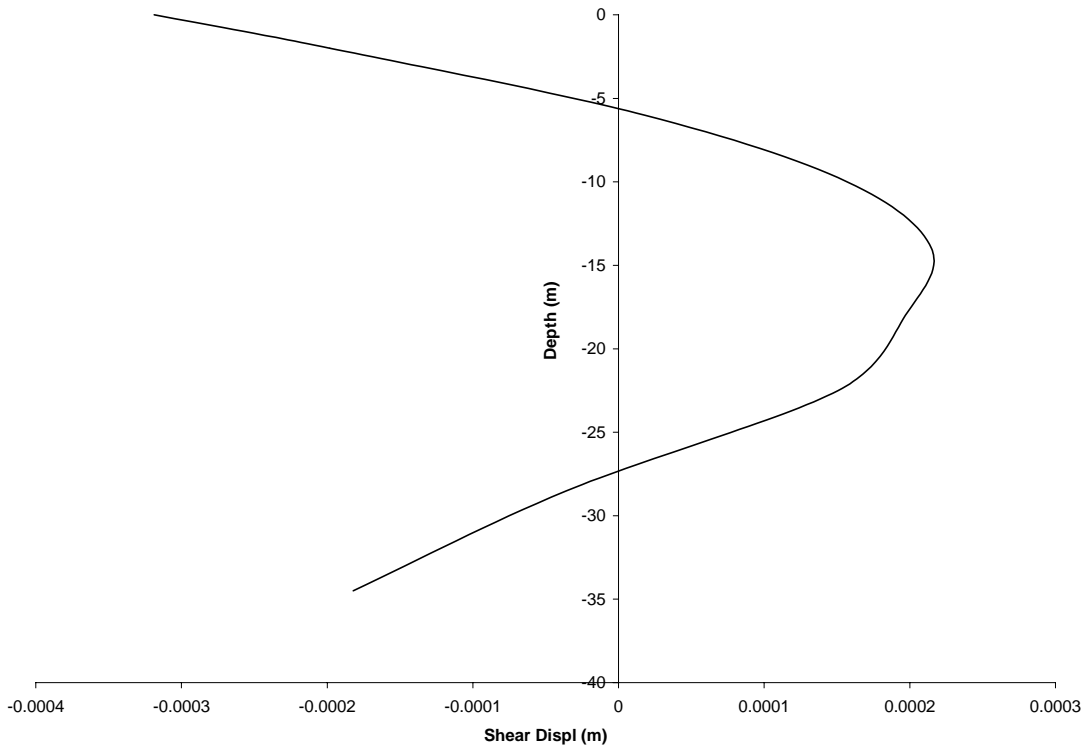


Figure 4.2.3-4 Lateral Wall Shear Displacements Computed from the 34.5 m DOB SASSI Model.

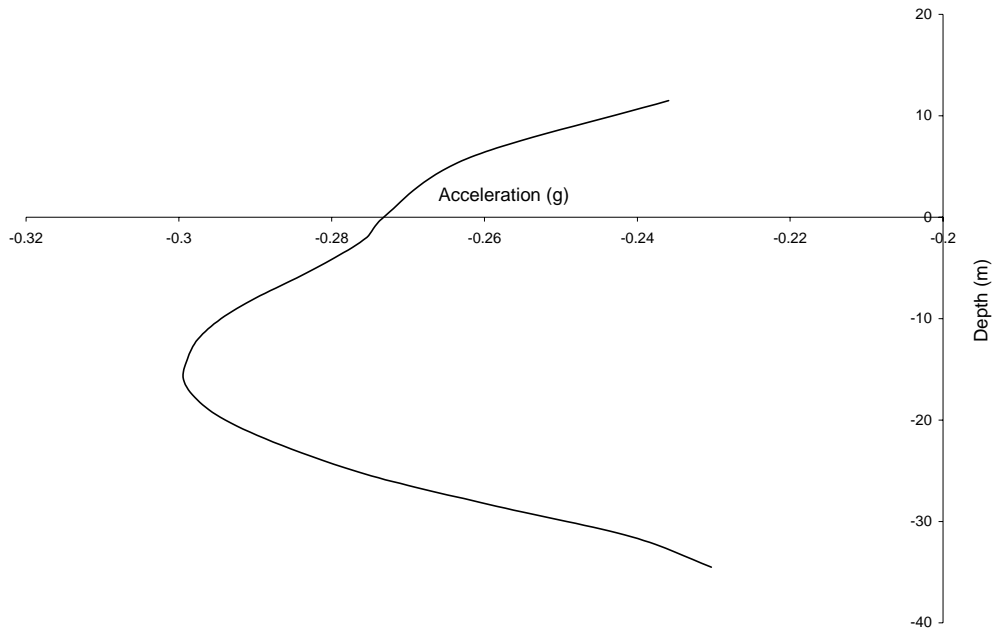


Figure 4.2.3-5 Structural Acceleration at 10.845 Seconds Computed from the 34.5 m DOB SASSI Model.

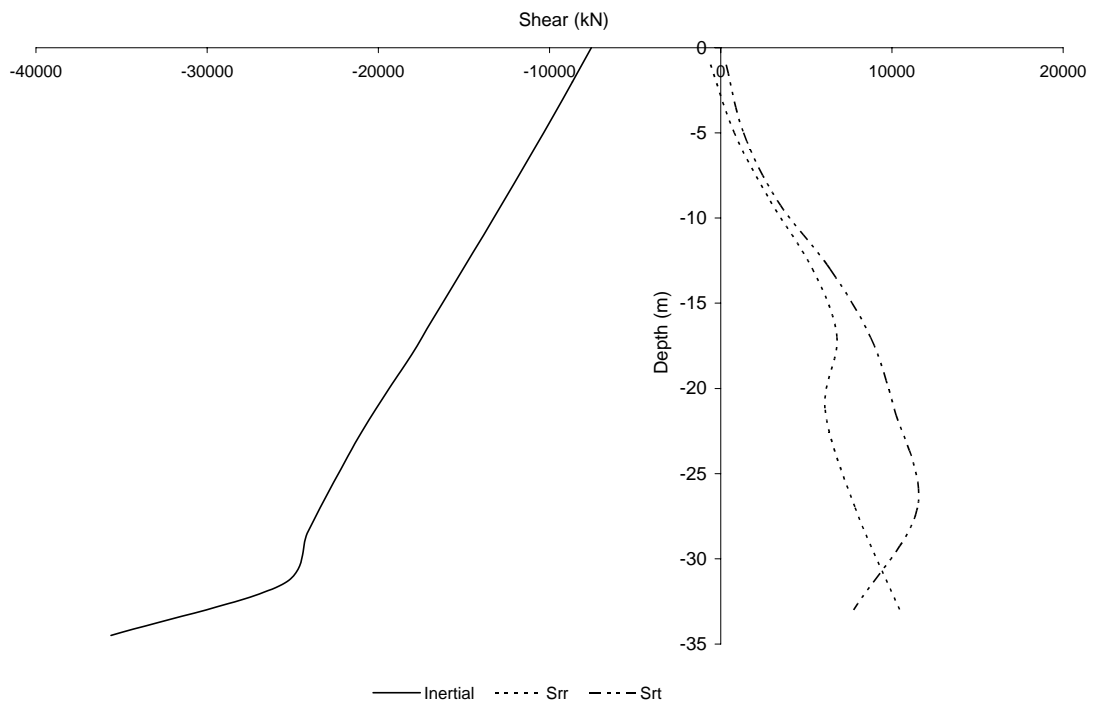


Figure 4.2.3-6 Variation of Shear over DOB at 10.845 Seconds Computed from the 34.5 m DOB SASSI Model.

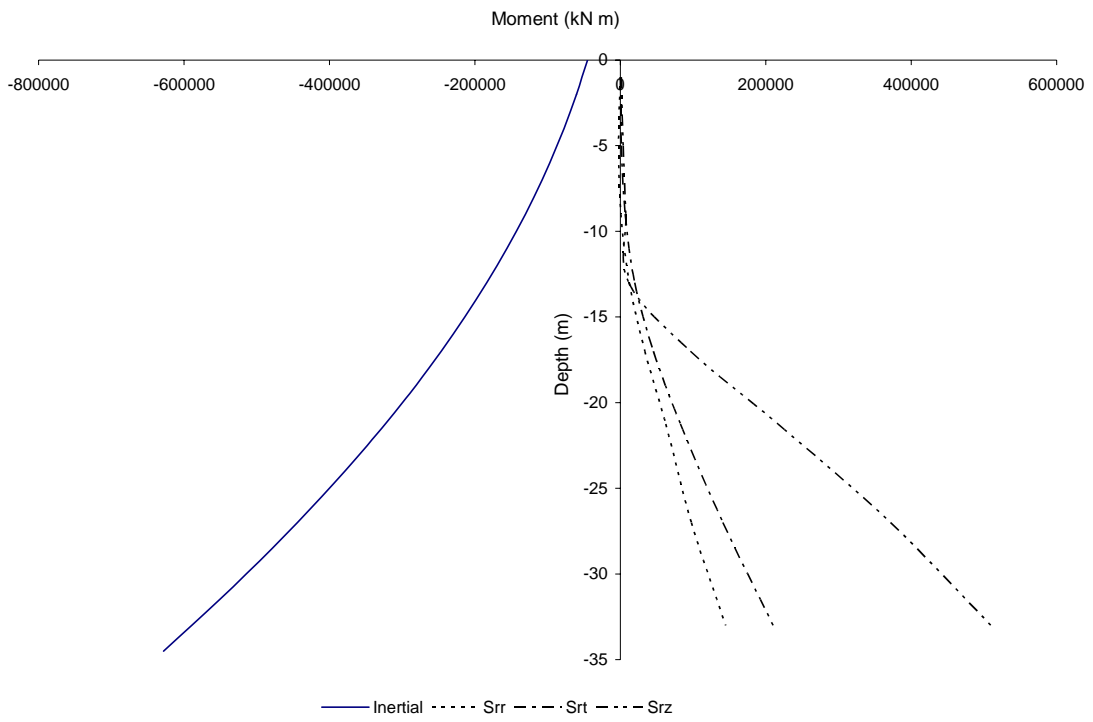


Figure 4.2.3-7 Variation of Moment over DOB at 10.845 Seconds Computed from the 34.5 m DOB SASSI Model.

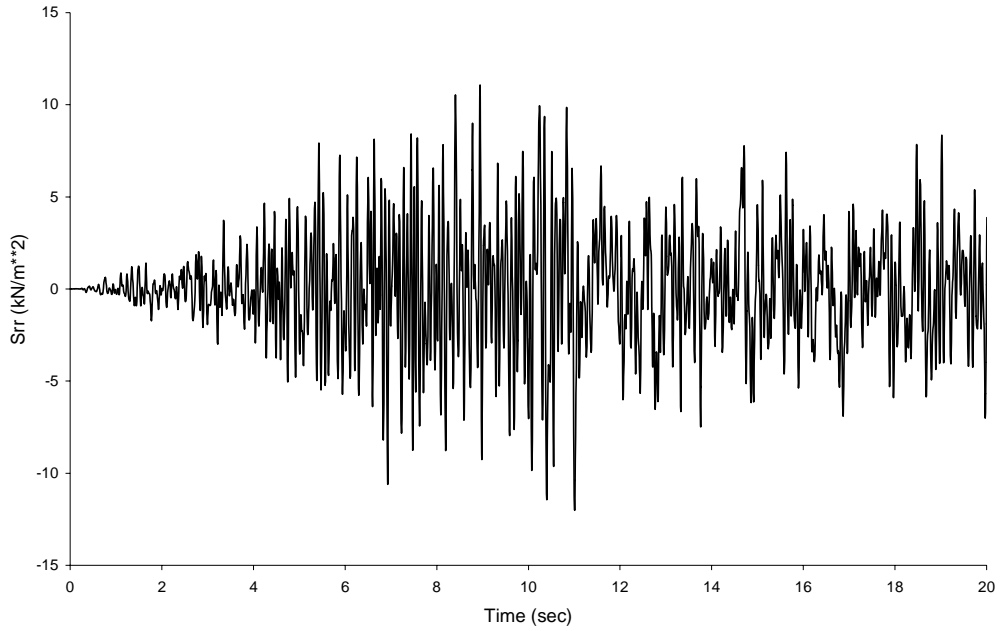


Figure 4.2.4-1 Normal Pressure on the Head-on Soil Element near the Mid-height of Structural Wall Computed from the 46 m DOB SASSI Model.

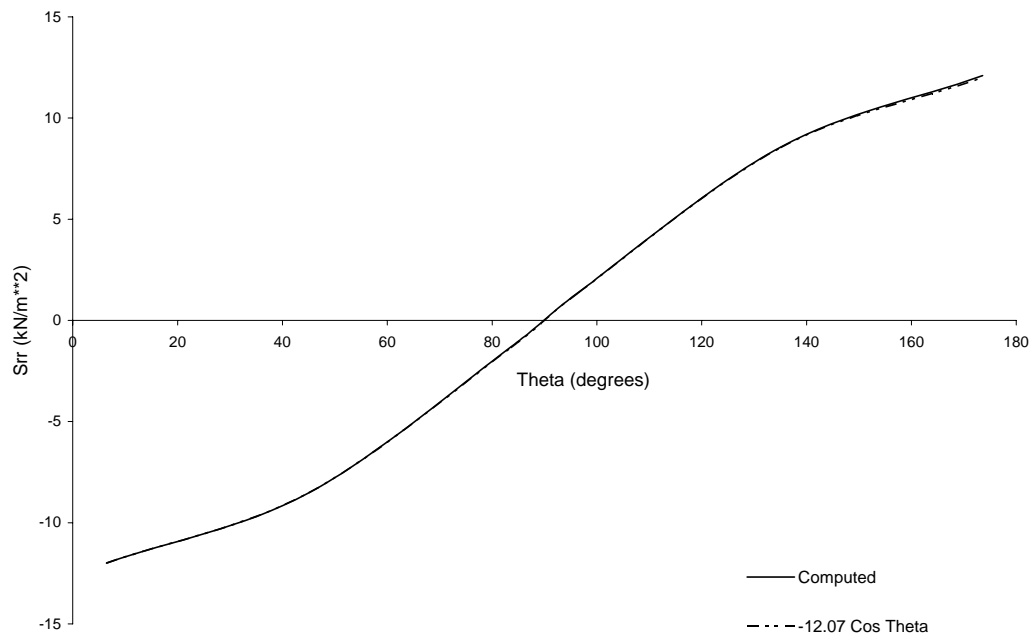


Figure 4.2.4-2 Circumferential Distribution of Normal Pressure Computed from the 46 m DOB SASSI Model.

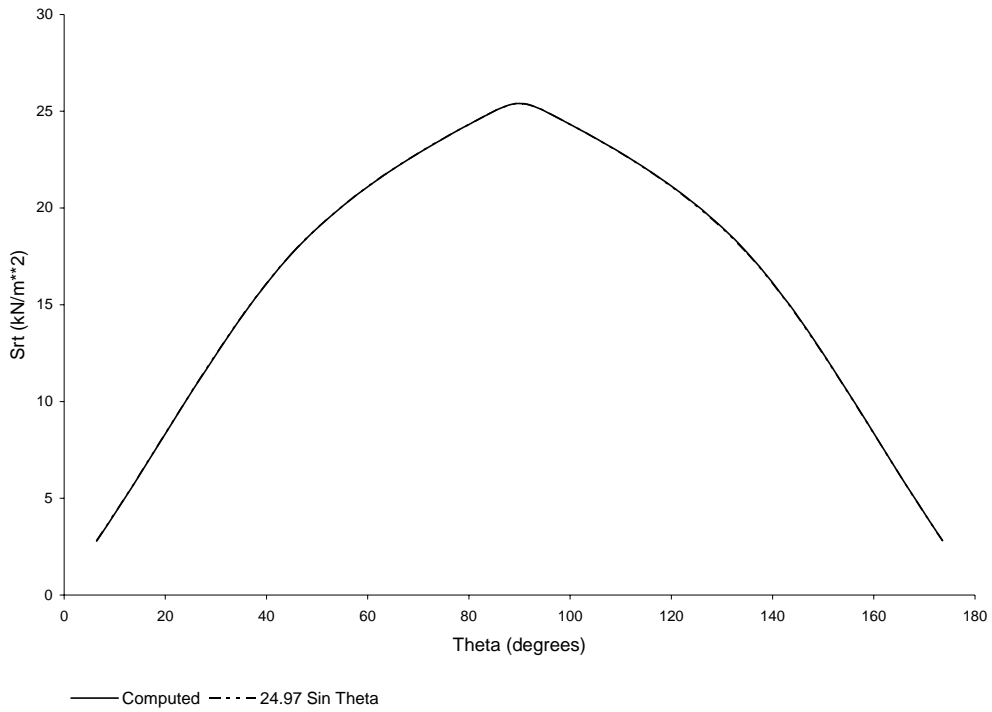


Figure 4.2.4-3 Circumferential Distribution of Tangential Shear Computed from the 46m DOB SASSI Model.

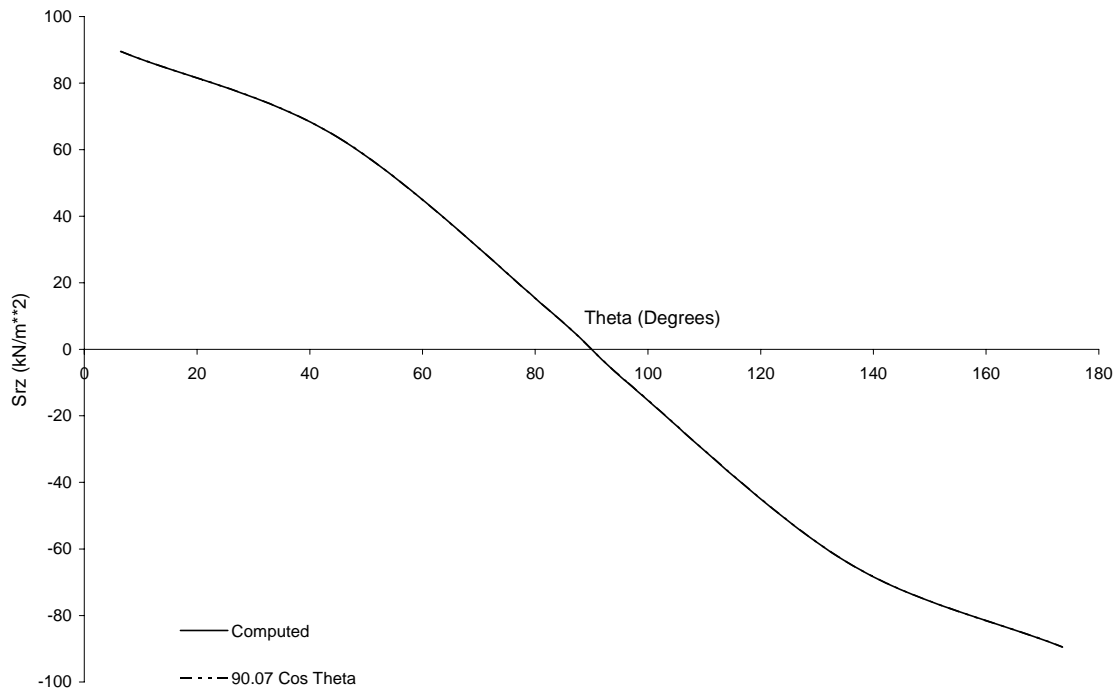


Figure 4.2.4-4 Circumferential Distribution of Vertical Shear Computed from the 46m DOB SASSI Model.

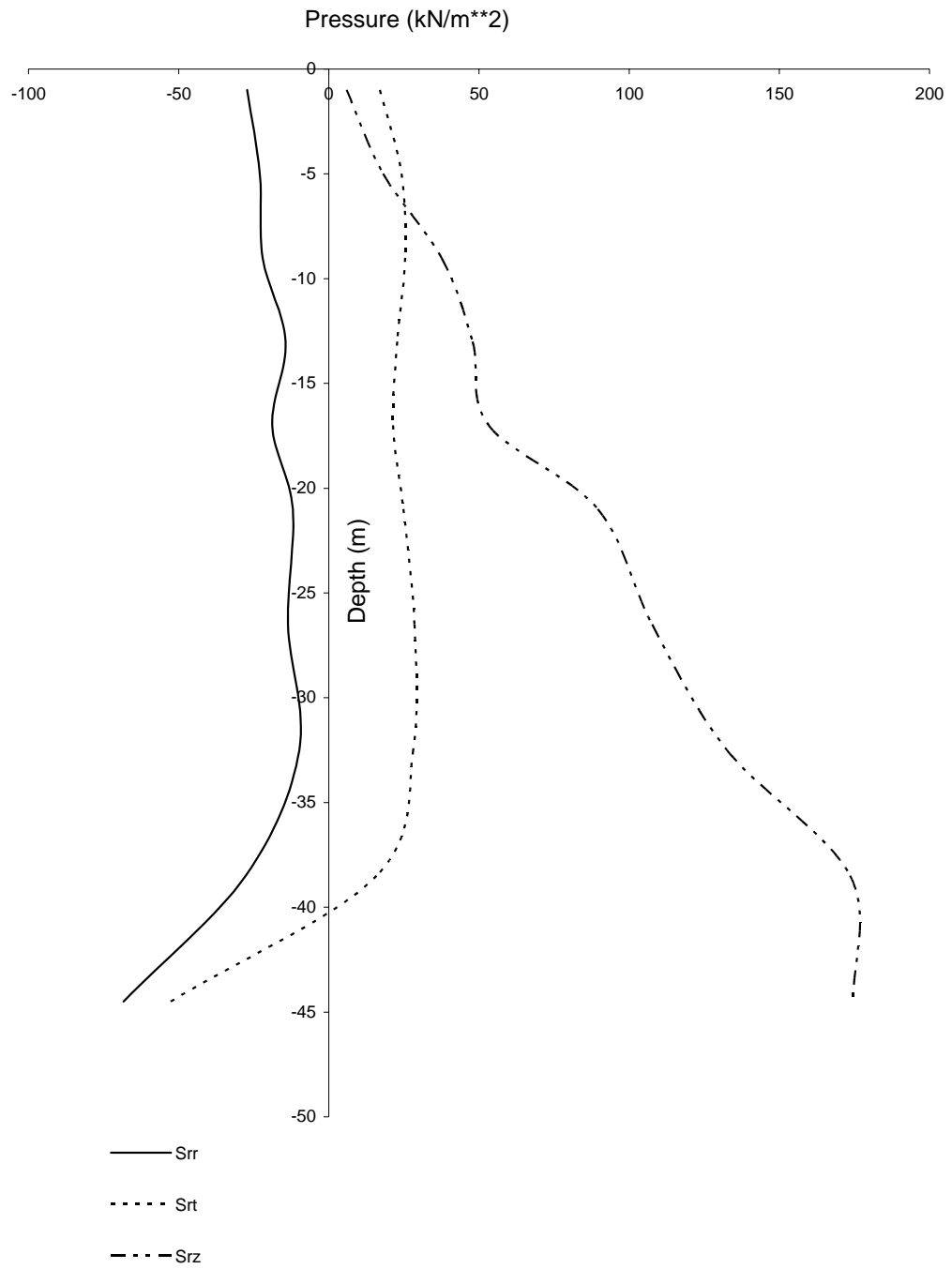


Figure 4.2.4-5 Vertical Distributions of Soil Pressure Computed from the 46 m DOB SASSI Model.

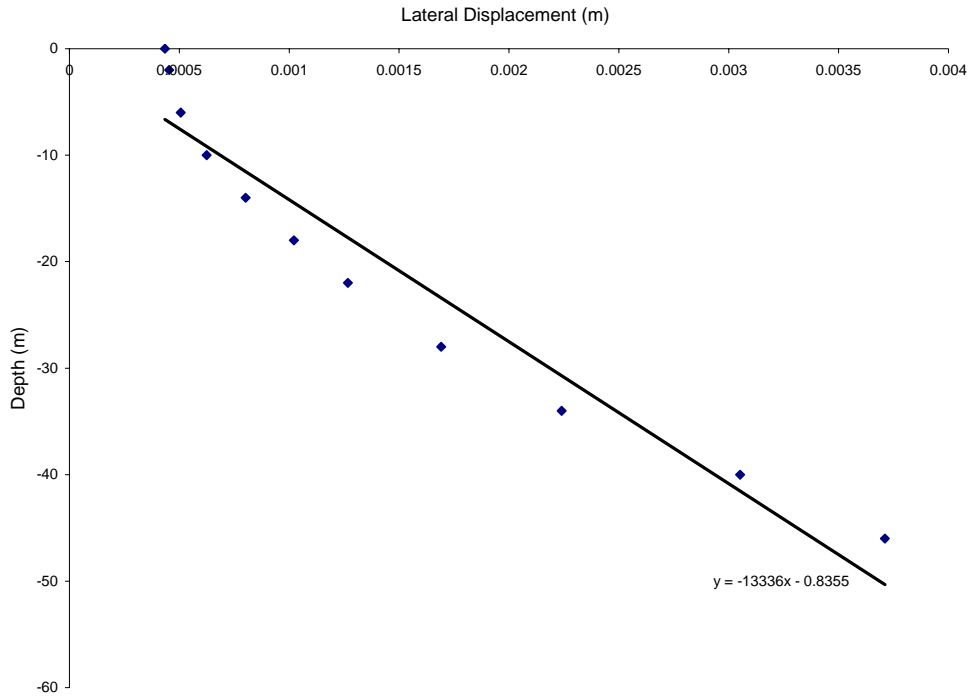


Figure 4.2.4-6 Lateral Wall Displacements Computed from the 46 m DOB SASSI Model.

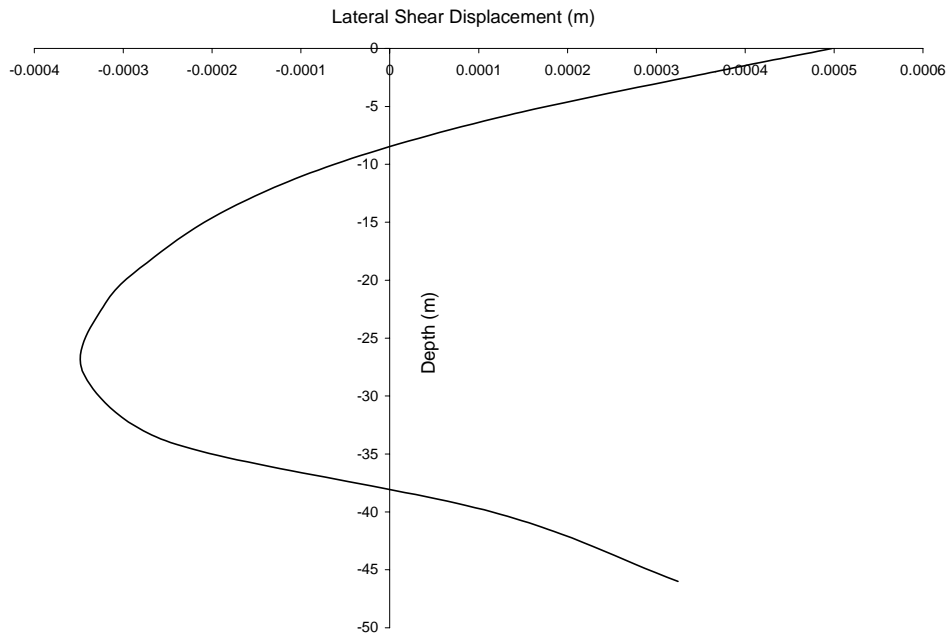


Figure 4.2.4-7 Lateral Wall Shear Displacements Computed from the 46 m DOB SASSI Model.

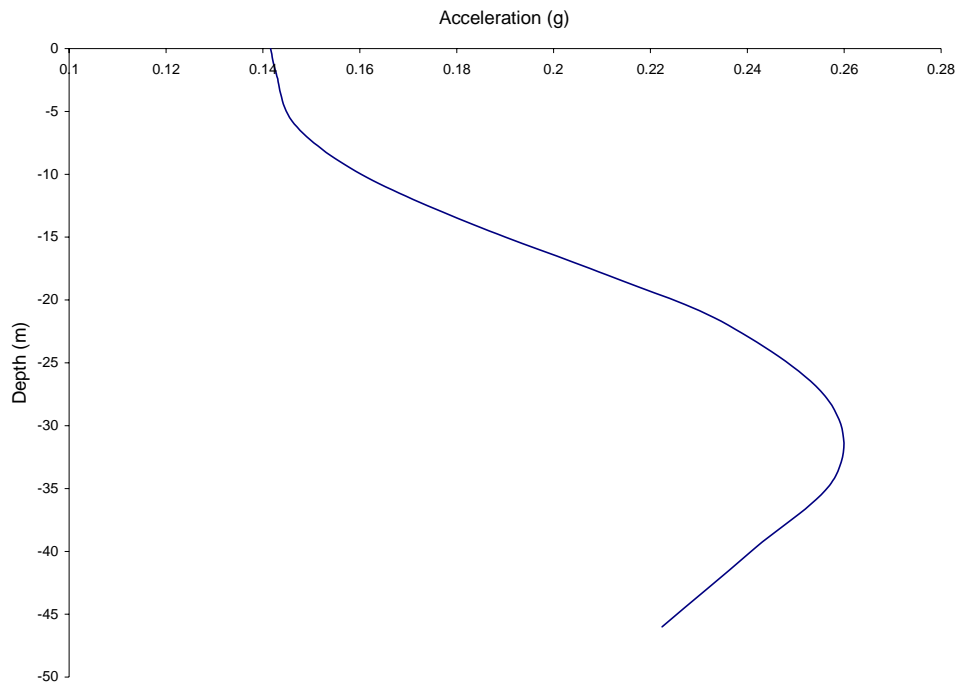


Figure 4.2.4-8 Structural Acceleration at 11.005 Seconds Computed from the 46 m DOB SASSI Model.

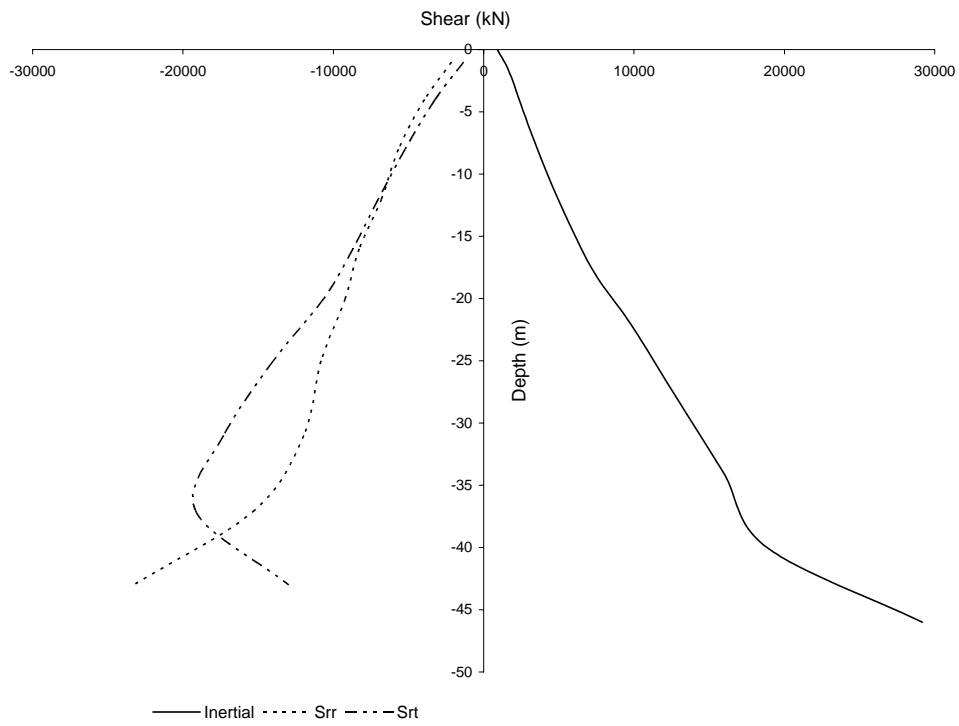


Figure 4.2.4-9 Variation of Shear over DOB at 11.005 Seconds Computed from the 46 m DOB SASSI Model.

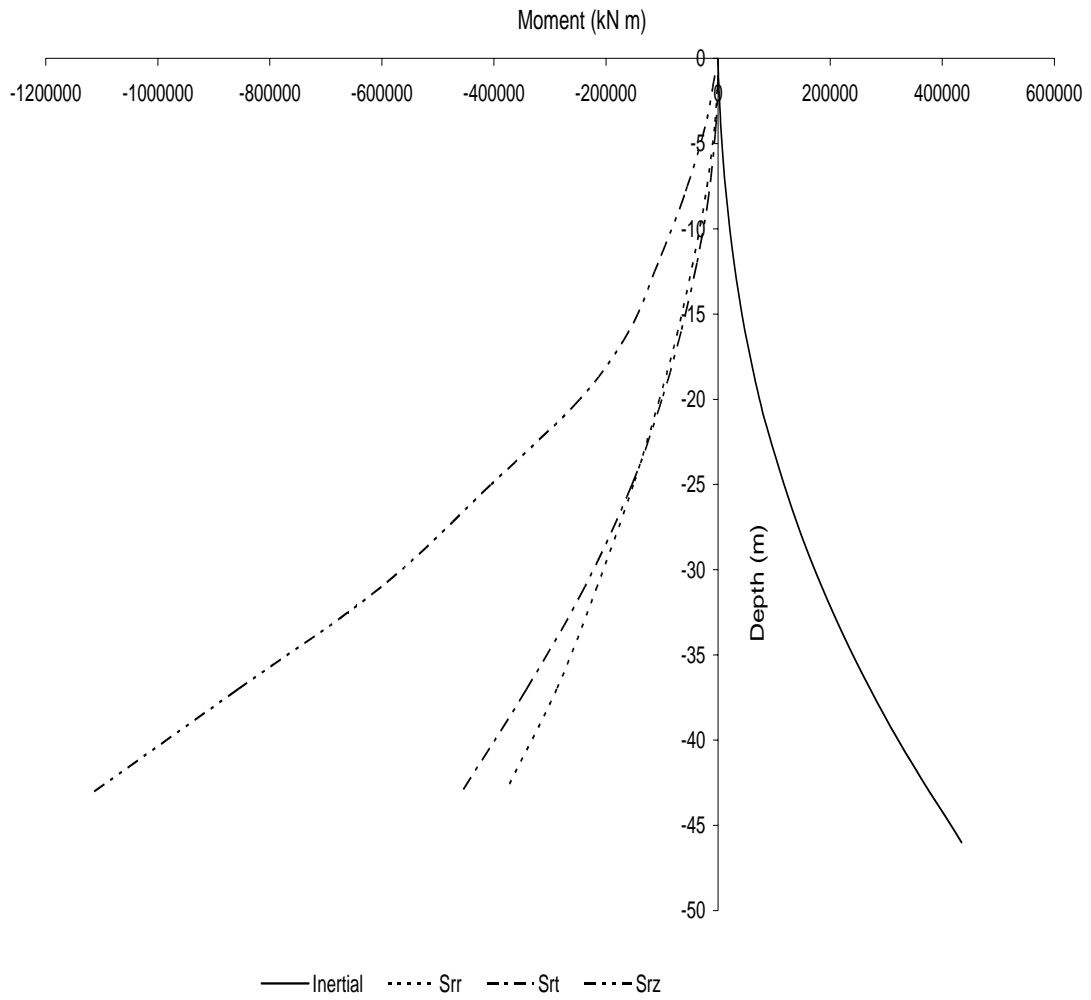


Figure 4.2.4-10 Variation of Moment over DOB at 11.005 Seconds Computed from the 46 m DOB SASSI Model.

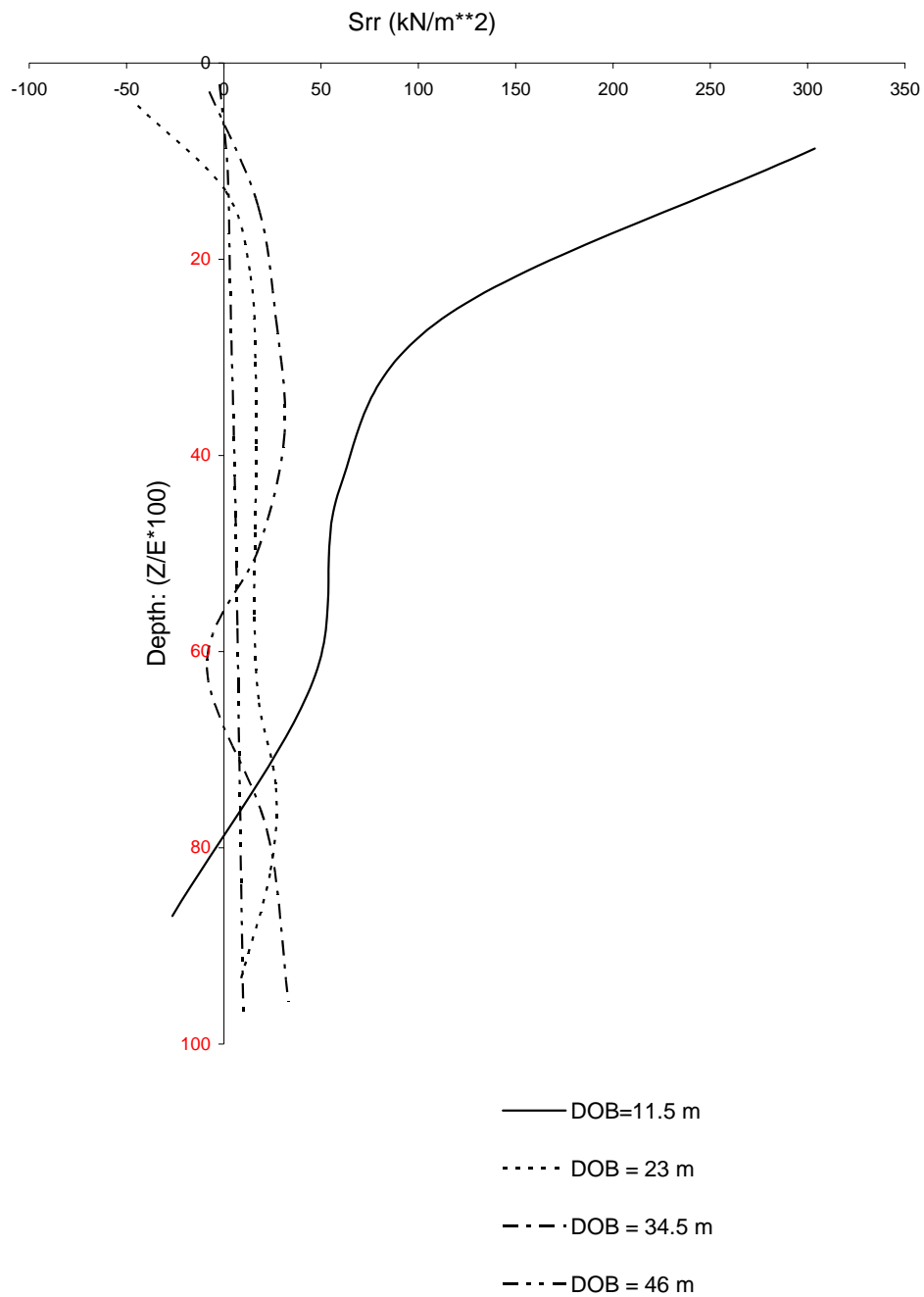


Figure 4.2.5-1 Comparison of Vertical Distributions of Normal Pressure Computed from the SASSI Models.

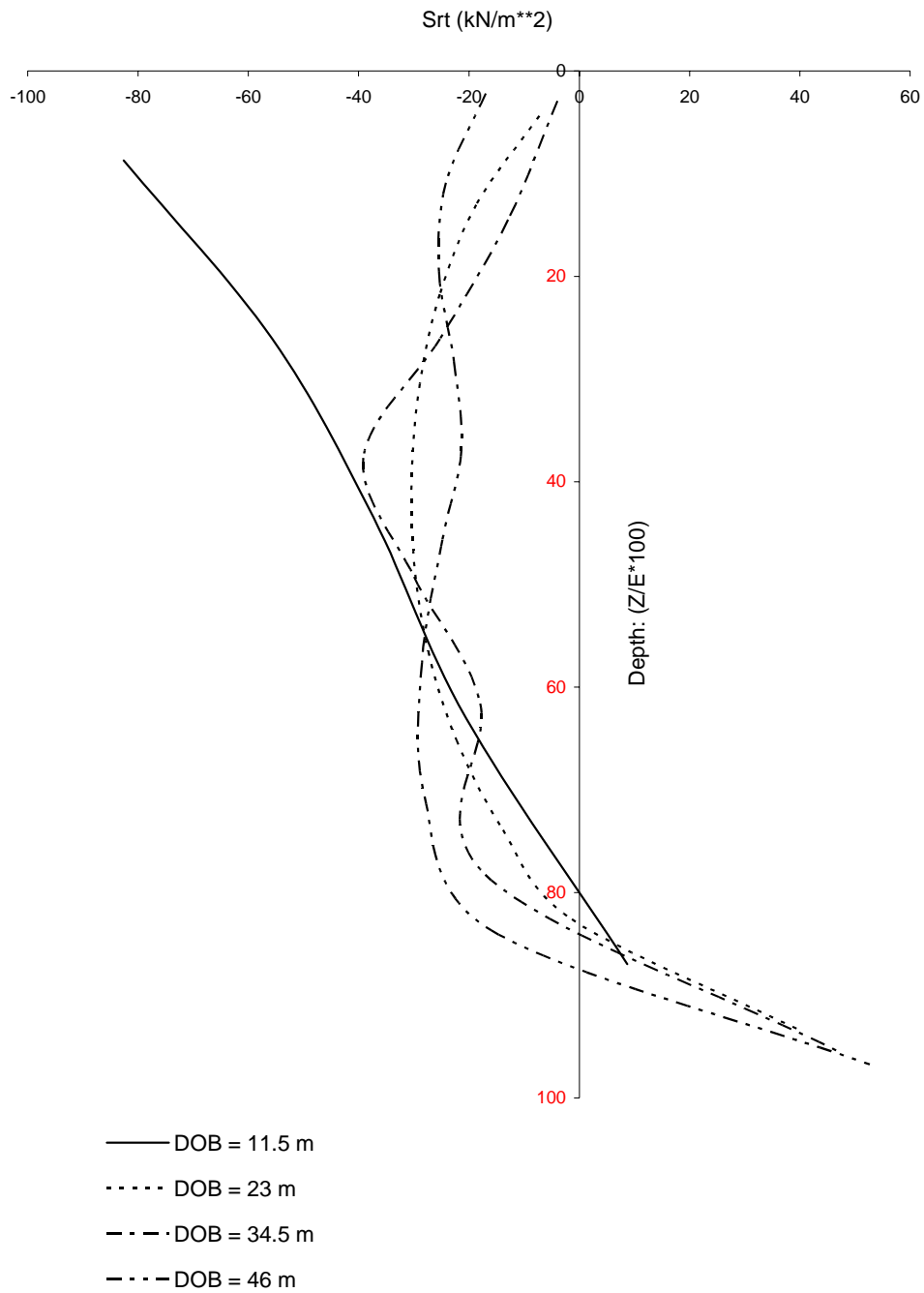


Figure 4.2.5-2 Comparison of Vertical Distributions of Tangential shears Computed from the SASSI Models.

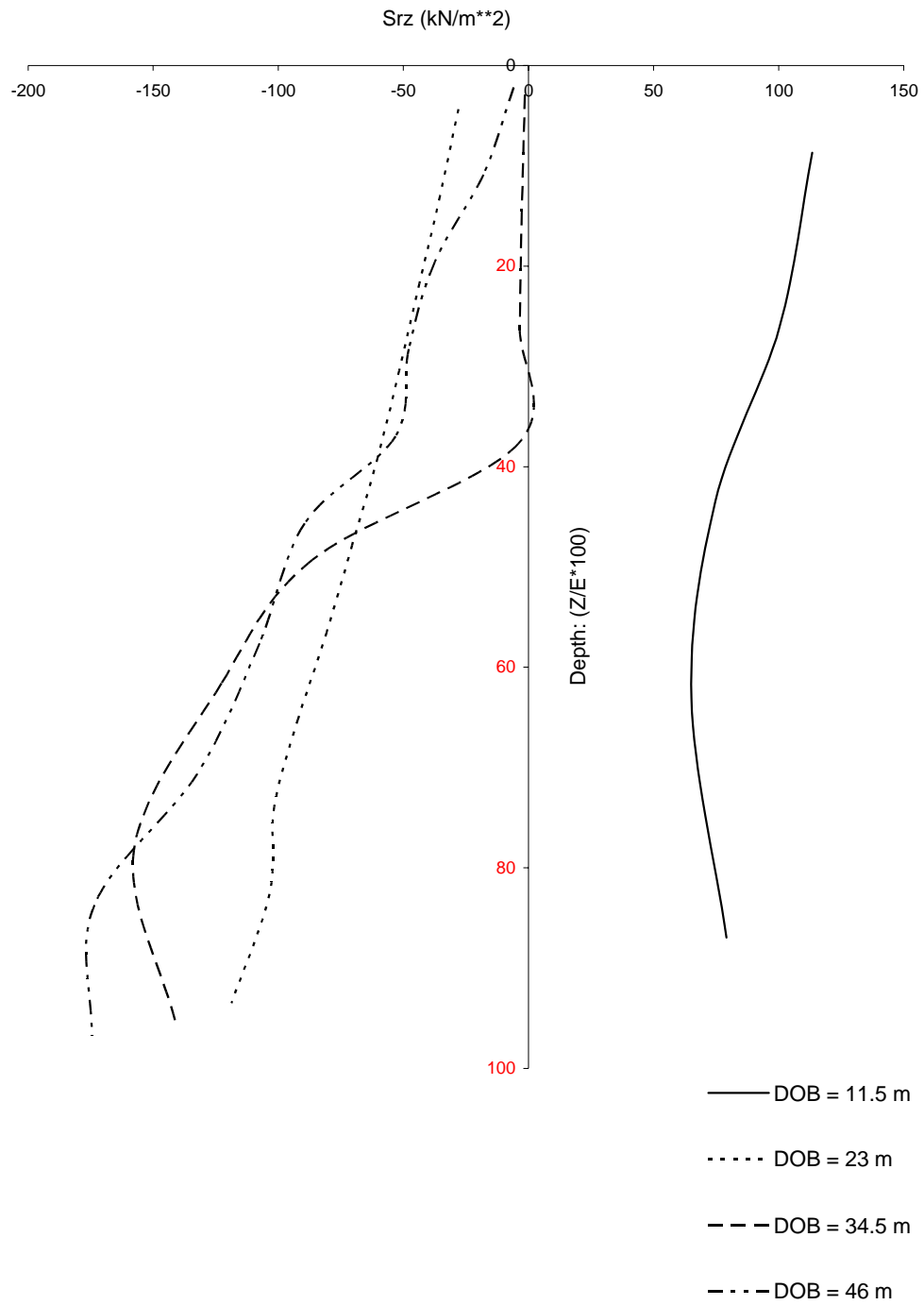


Figure 4.2.5-3 Comparison of Vertical Distributions of Vertical shears Computed from the SASSI Models.

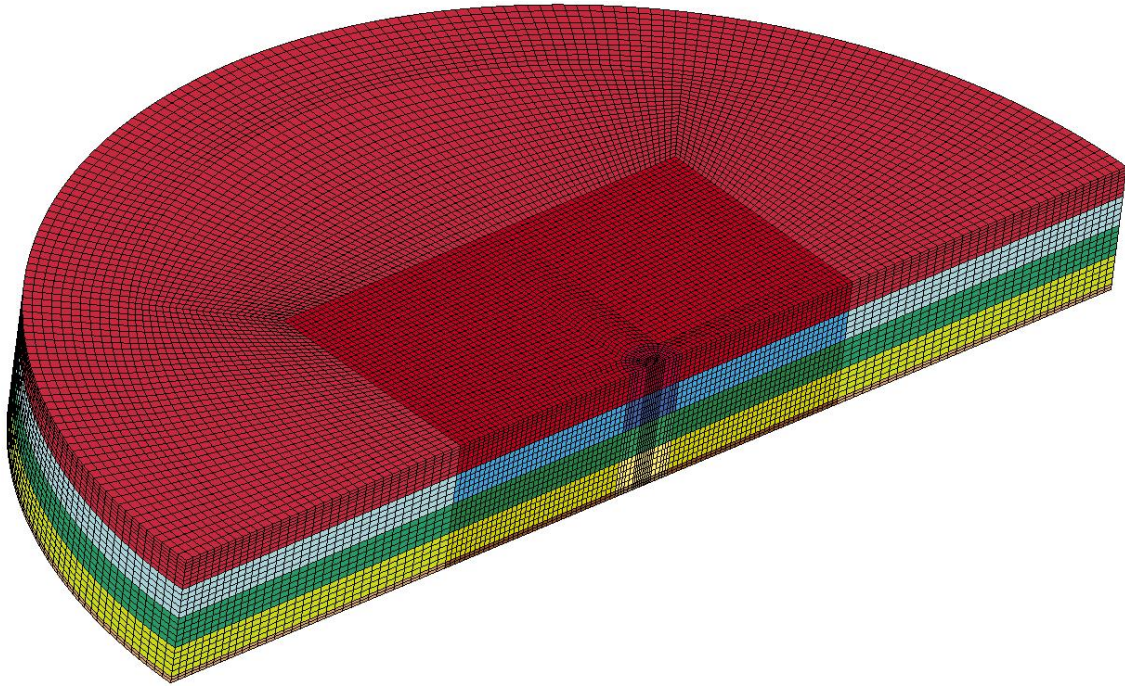


Figure 4.3.1-1 LS-DYNA Free Field Model.

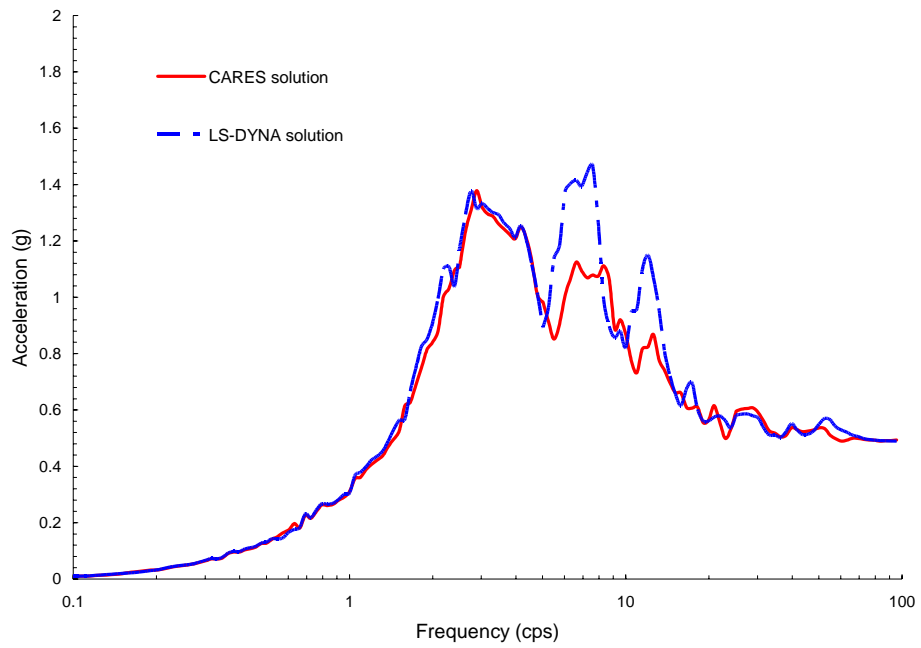


Figure 4.3.1-2 Comparison of Free Field Surface Spectra.

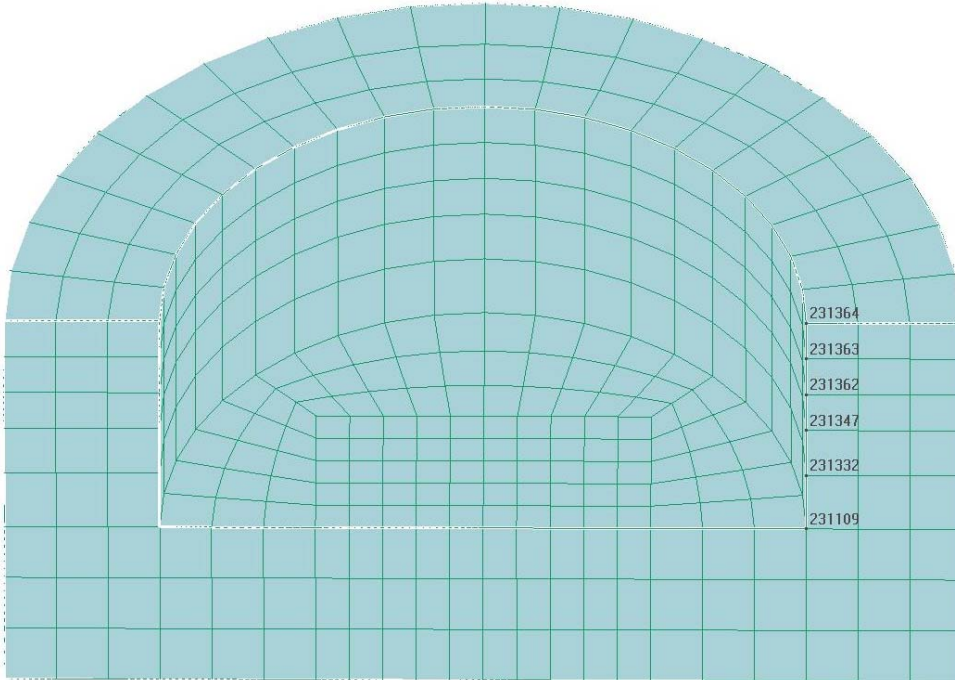


Figure 4.3.2-1 Nodes of Soil Elements on the Interface for the 11.5 m LS-DYNA Model.

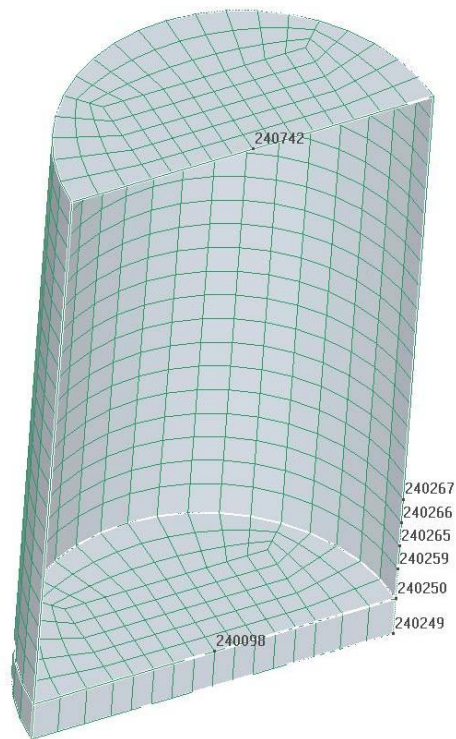


Figure 4.3.2-2 Nodes of the Structure on the Interface for the 11.5 m LS-DYNA Model.

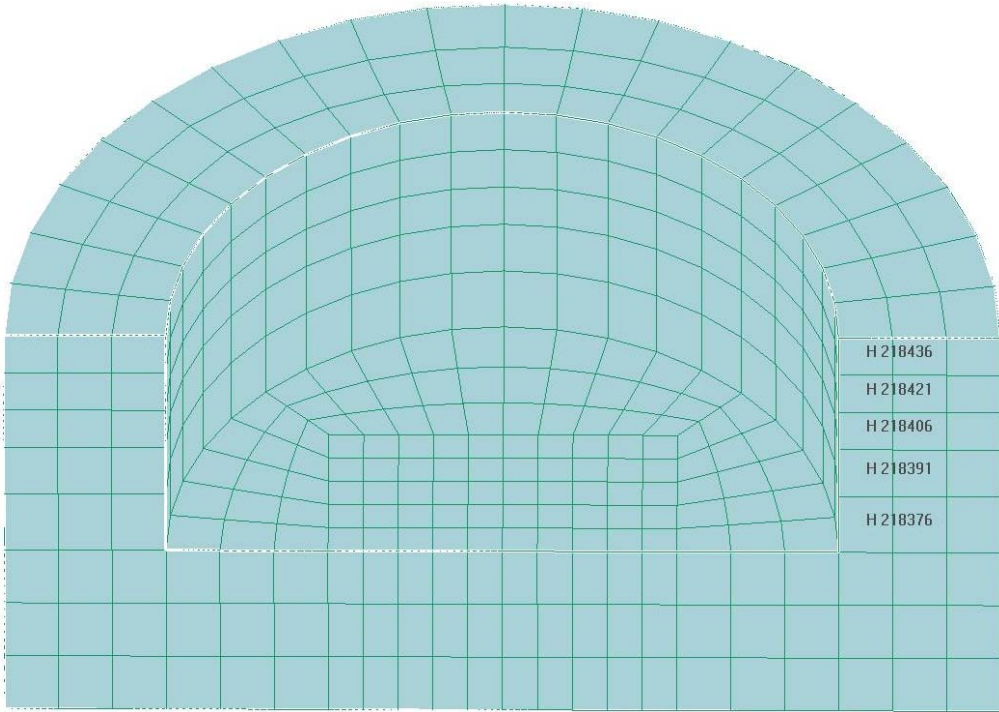


Figure 4.3.2-3 Soil Elements on the Interface for the 11.5 m LS-DYNA Model.

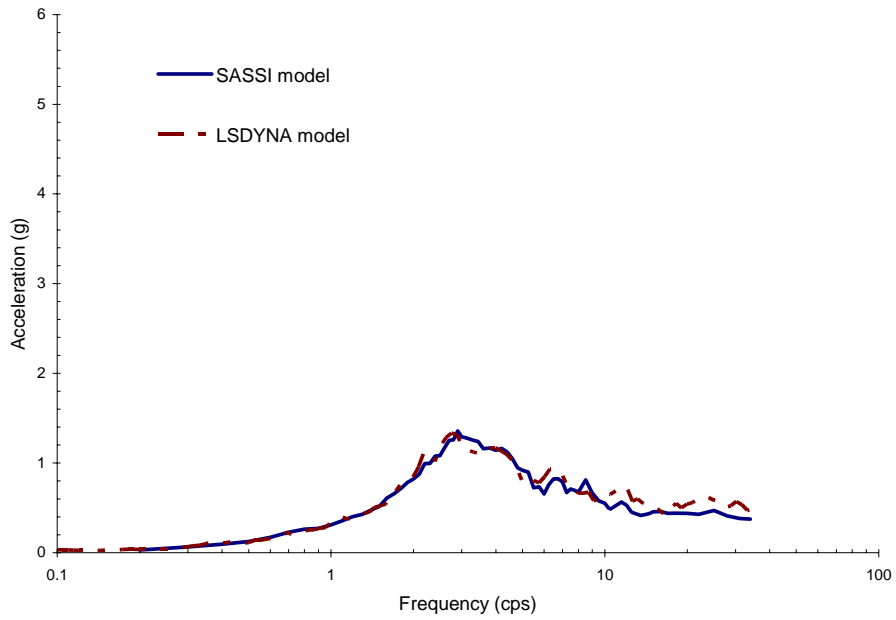


Figure 4.3.2-4 Comparison of Response Spectra at the Base for 11.5 m Embedment.

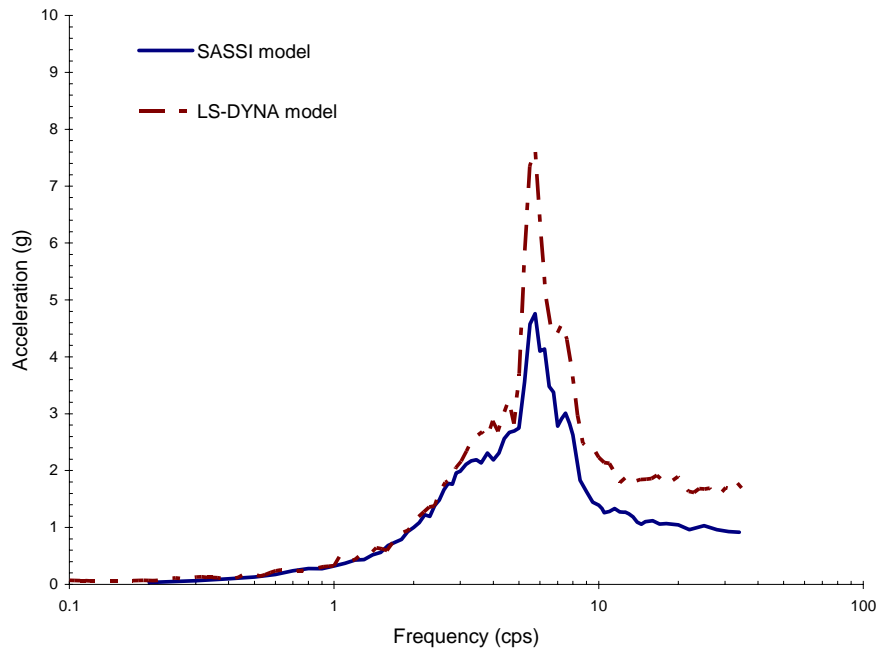


Figure 4.3.2-5 Comparison of Response Spectra at the Roof for the 11.5 m Embedment.

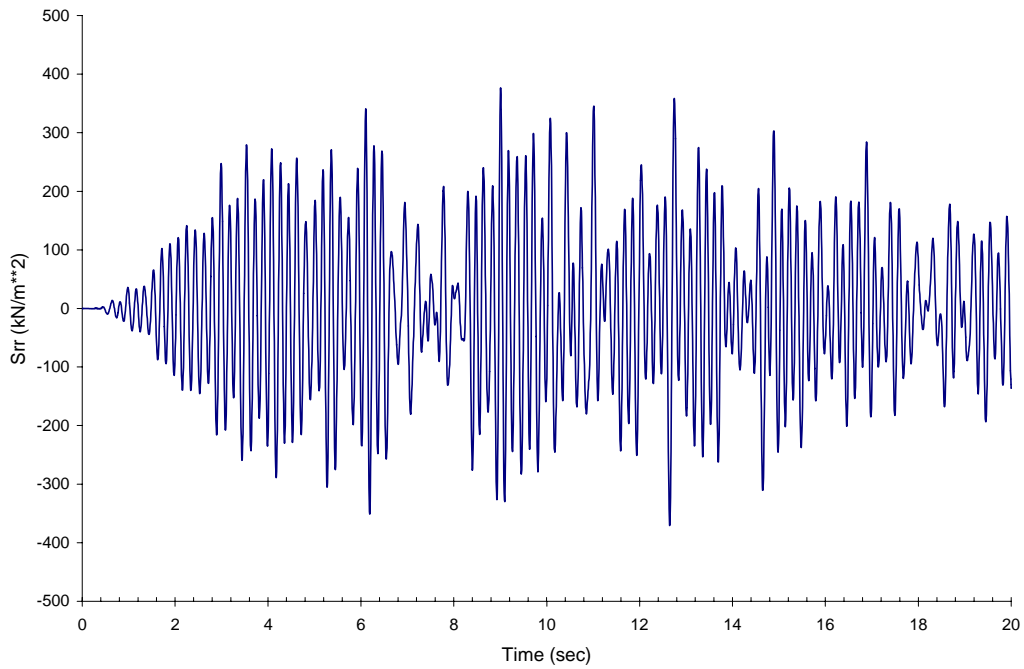


Figure 4.3.2-6 Soil Pressure in the Head-on Soil Element near the Ground Surface for the 11.5 m Embedment.

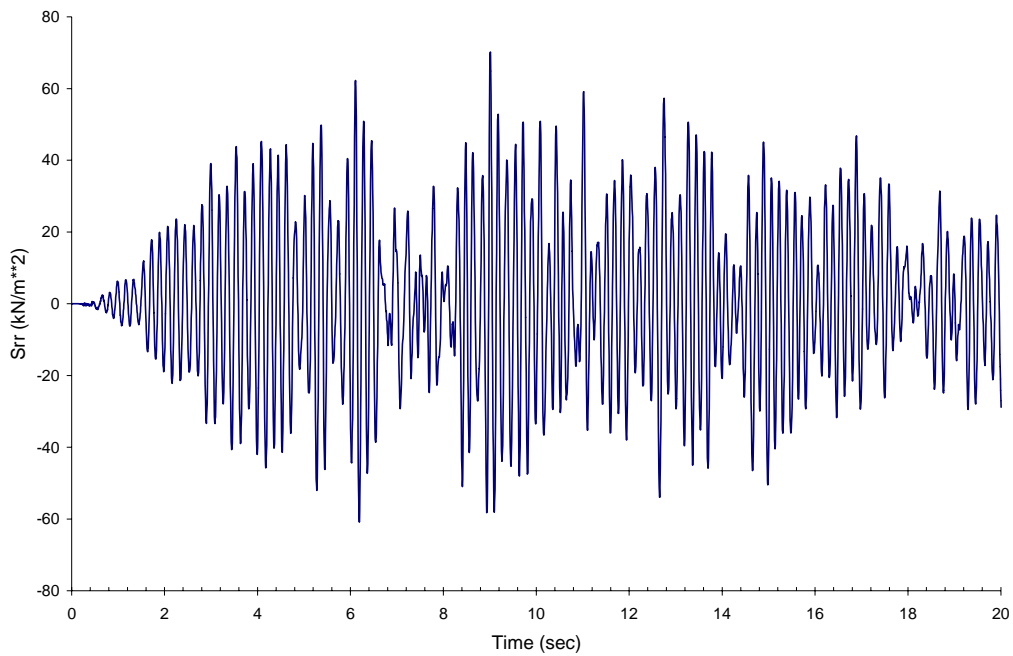


Figure 4.3.2-7 Soil Pressure in the Head-on Soil Element near the Mid-Height of Structure Wall for the 11.5 m Embedment.

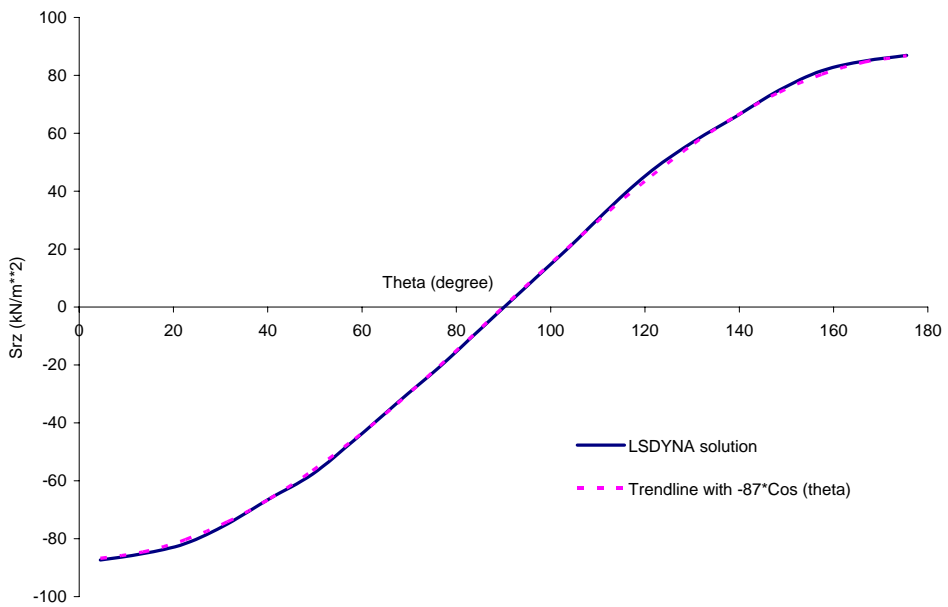


Figure 4.3.2-8 Circumferential Distribution of Vertical Shear Computed from Tied LS-DYNA Model without Gravity Load for the 11.5 m Embedment at 9 Seconds.

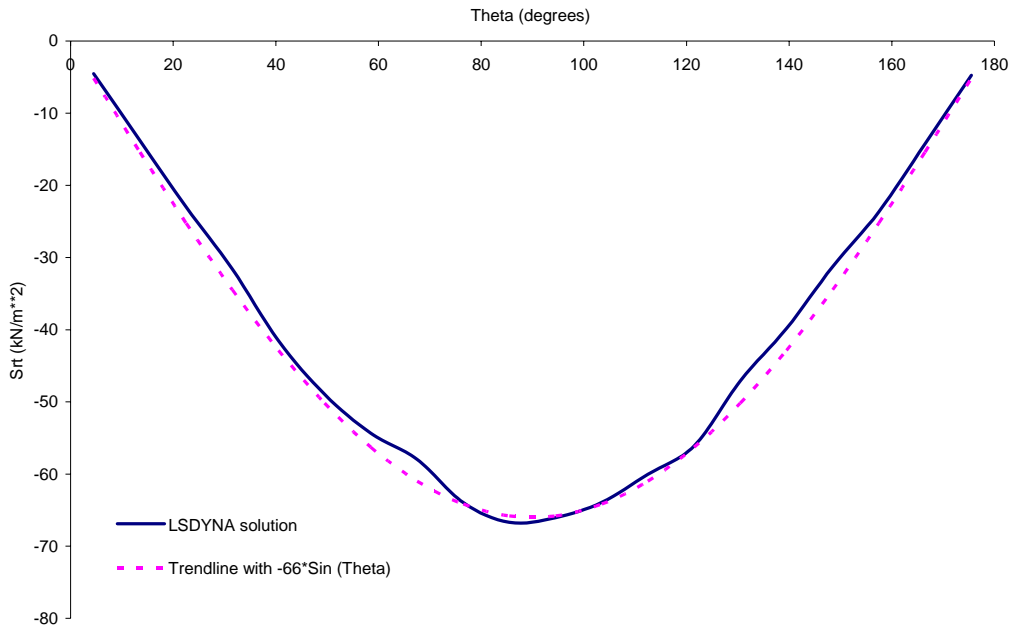


Figure 4.3.2-9 Circumferential Distribution of Tangential Shear Computed from Tied LS-DYNA Model without Gravity Load for the 11.5 m Embedment at 9 Seconds.

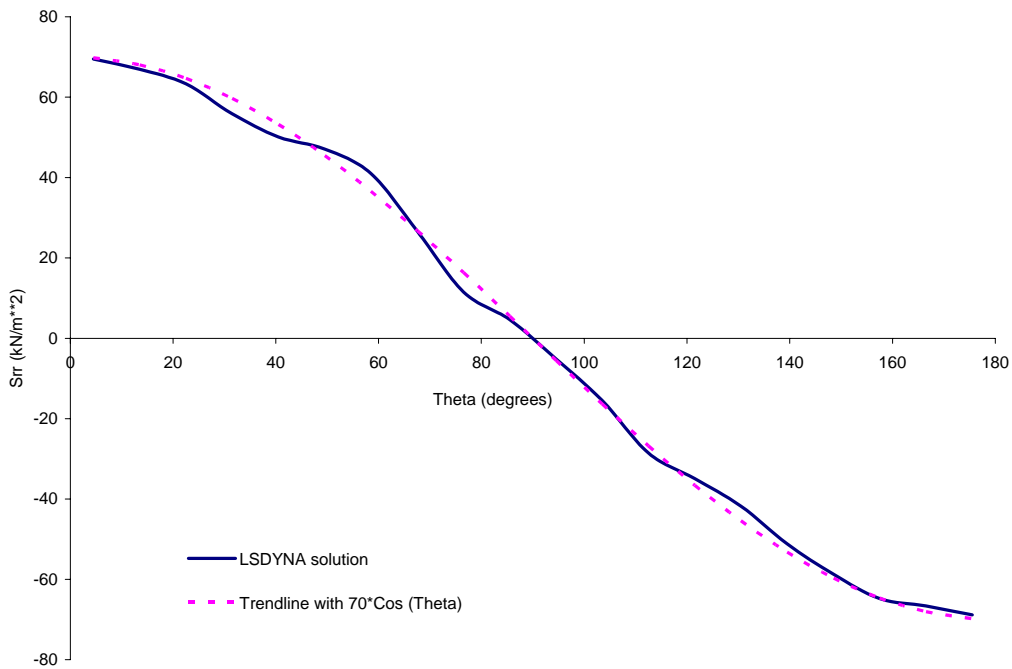


Figure 4.3.2-10 Circumferential Distribution of Normal Pressure Computed from Tied LS-DYNA Model without Gravity Load for the 11.5 m Embedment at 9 Seconds.

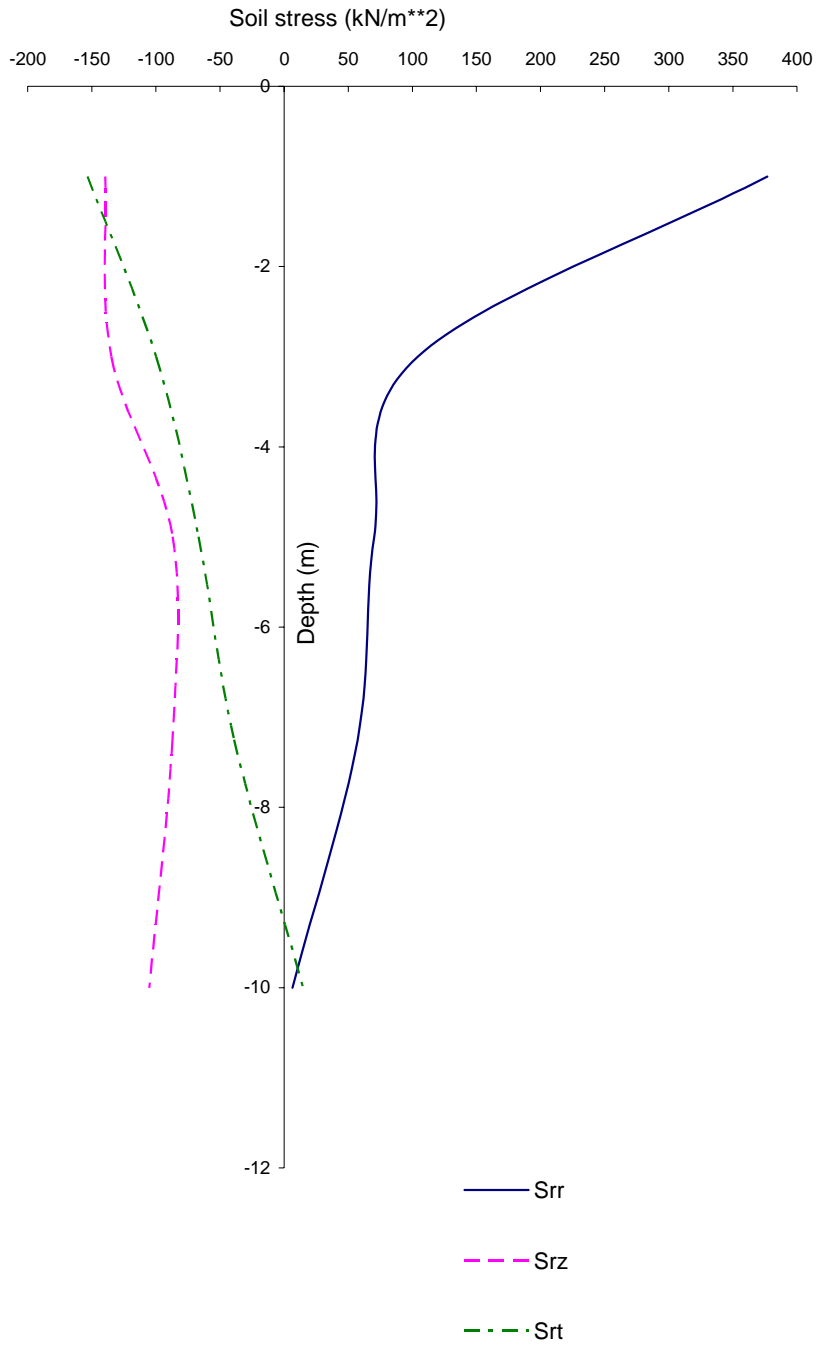


Figure 4.3.2-11 Vertical Distribution of Head-on Soil Stresses Computed from Tied LS-DYNA Model without Gravity Load for the 11.5 m Embedment at 9 Seconds.

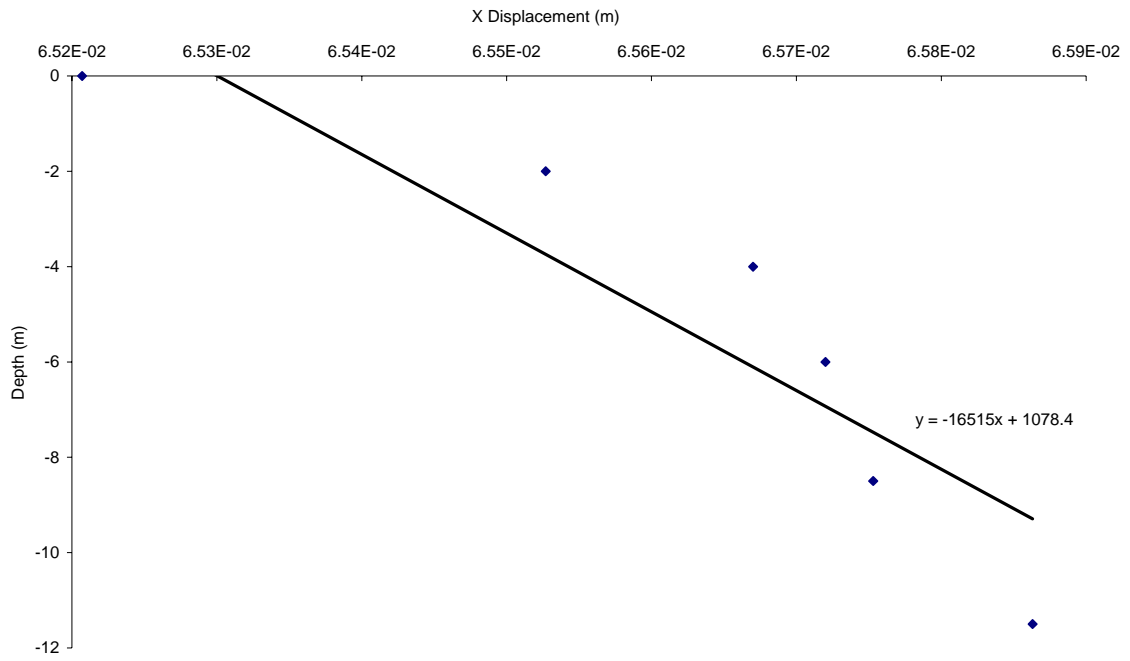


Figure 4.3.2-12 Lateral Embedded Wall Displacements Computed from Tied LS-DYNA Model without Gravity Load for the 11.5 m Embedment at 9 Seconds.

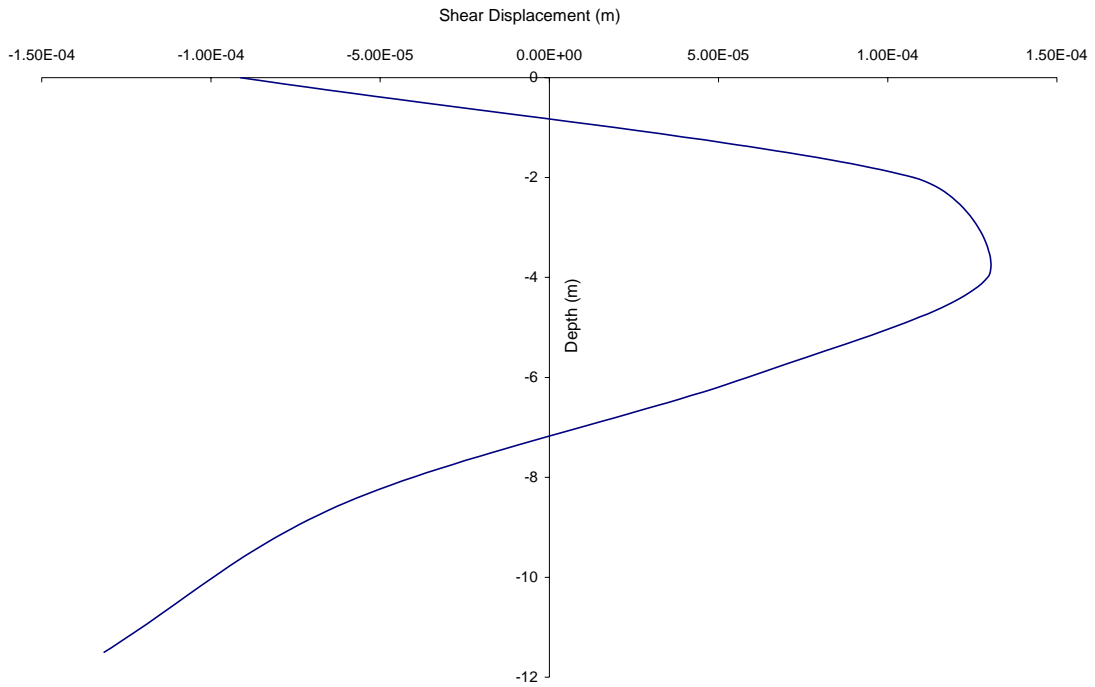


Figure 4.3.2-13 Lateral Wall Shear Displacements Computed from Tied LS-DYNA Model without Gravity Load for 11.5 m Embedment at 9 Seconds.

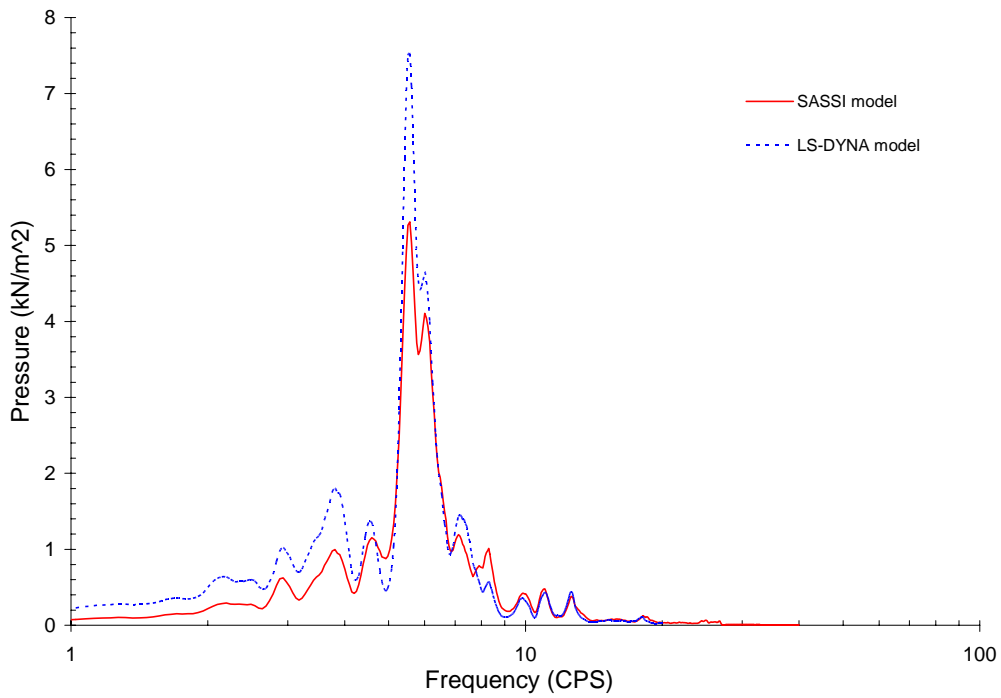


Figure 4.3.2-14 Fourier Spectra of Soil Pressure Computed at the Head-on Soil Element near Mid-Height Embedded Wall for 11.5 m DOB LD-DYNA model.

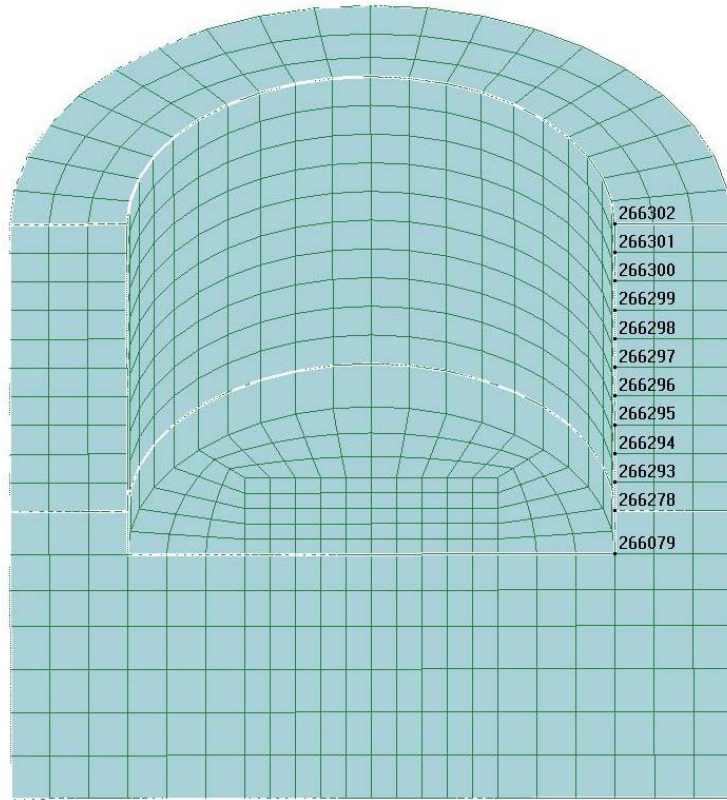


Figure 4.3.3-1 Nodes of Soil Elements on the Interface for the 23 m LS-DYNA Model.

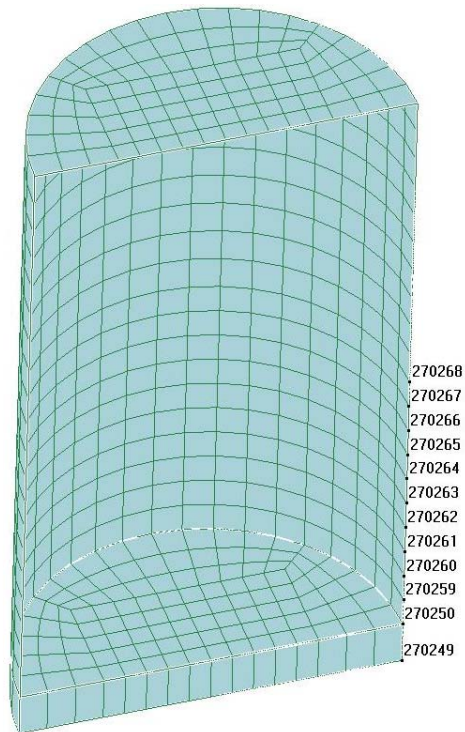


Figure 4.3.3-2 Nodes of the Structure on the Interface for the 23 m LS-DYNA Model.

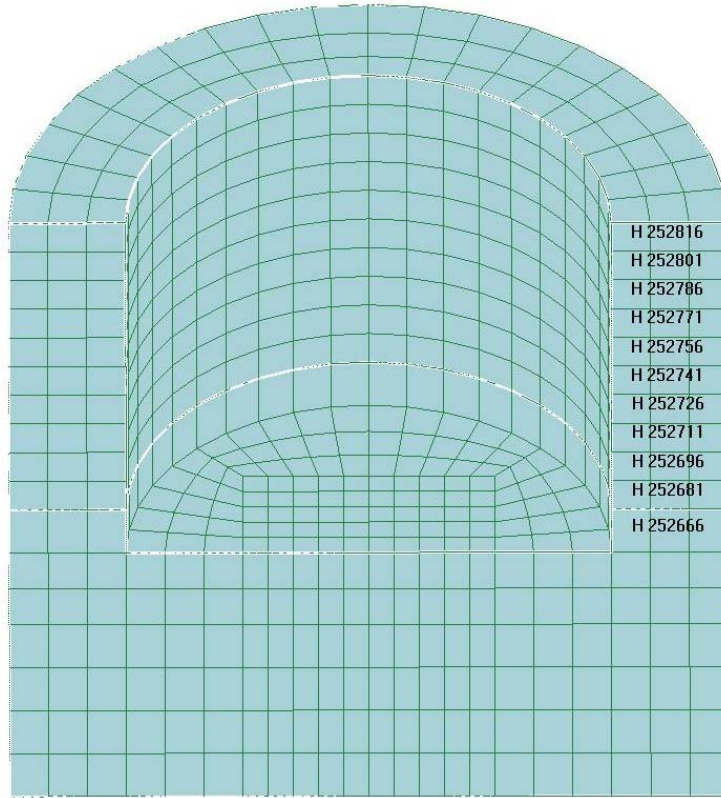


Figure 4.3.3-3 Soil Elements on the Interface for the 23 m LS-DYNA Model.

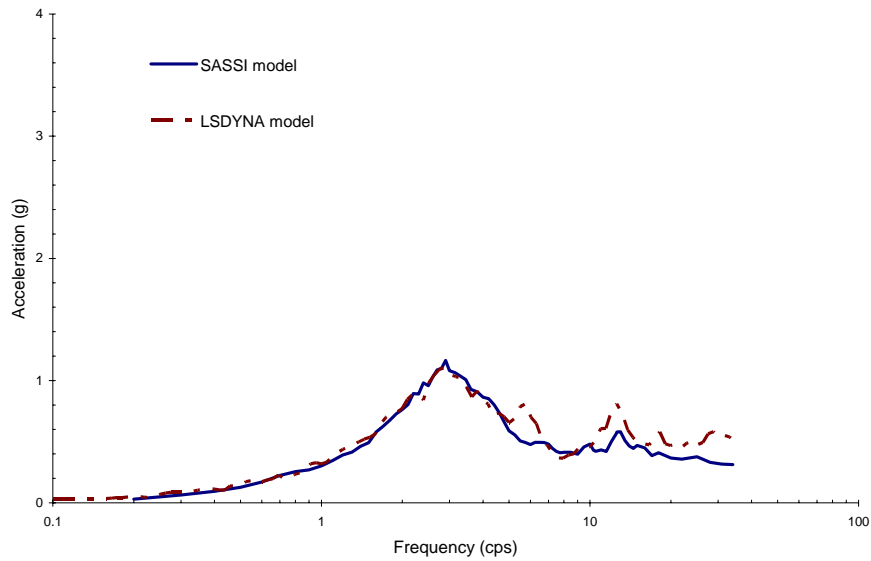


Figure 4.3.3-4 Comparison of Response Spectra at the Base for the 23 m Embedment.

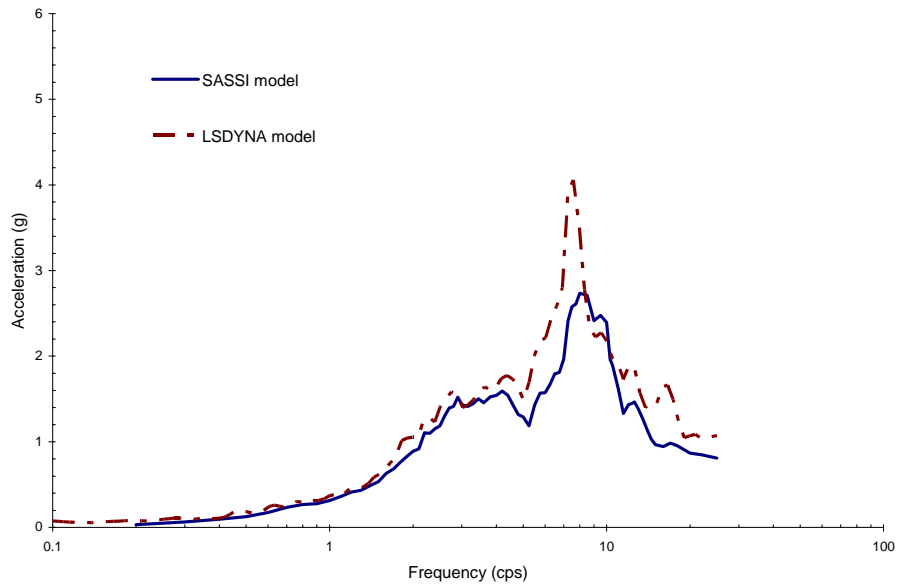


Figure 4.3.3-5 Comparison of Response Spectra at the Roof for the 23 m Embedment.

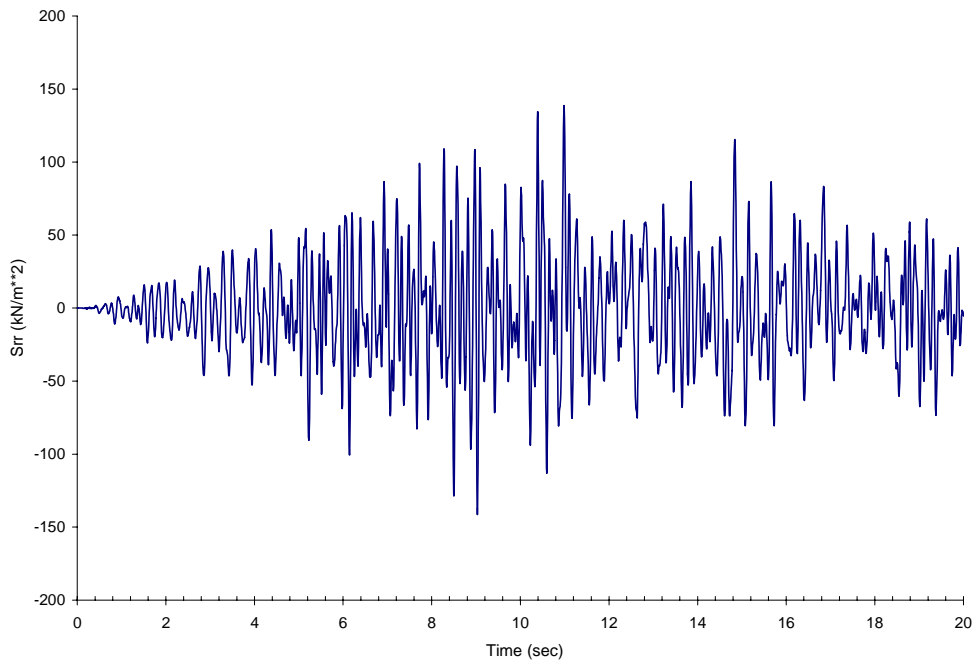


Figure 4.3.3-6 Soil Pressure in the Head-on Soil Element near the Ground Surface for the 23 m Embedment.

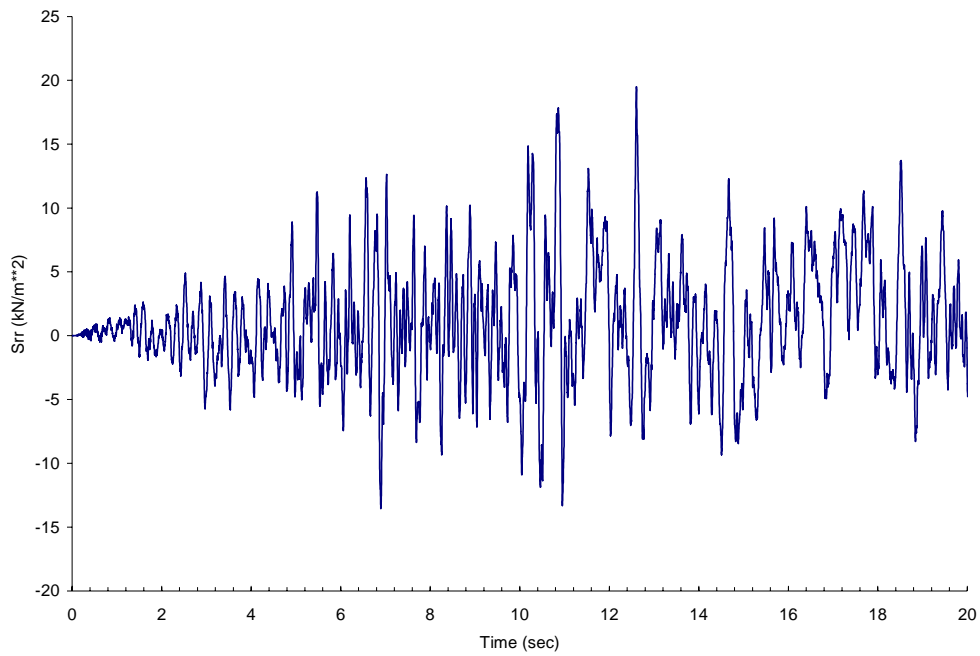


Figure 4.3.3-7 Soil Pressure in the Head-on Soil Element near the Mid-Height of Structure Wall for the 23 m Embedment.

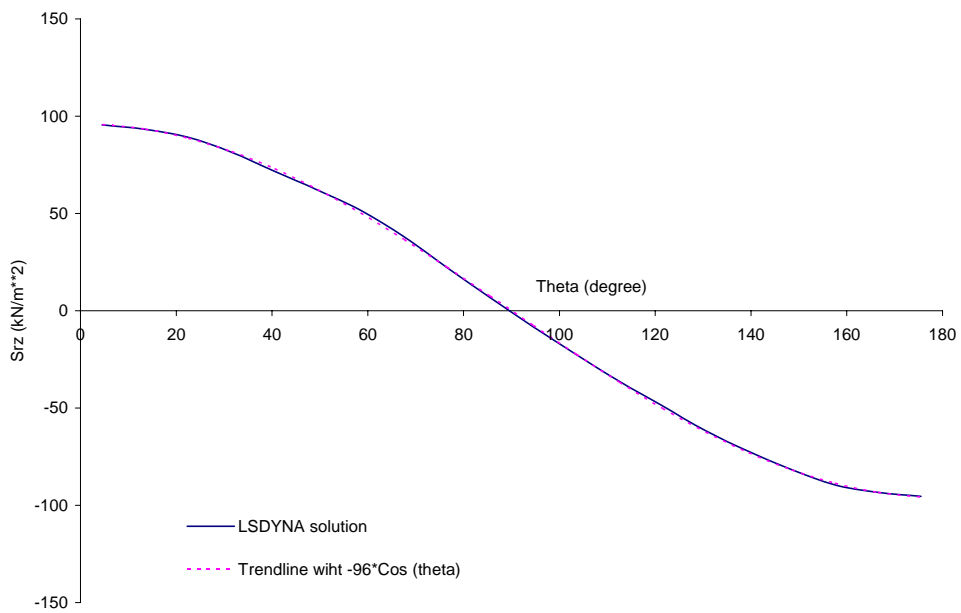


Figure 4.3.3-8 Circumferential Distribution of Vertical Shear Computed from Tied LS-DYNA Model without Gravity Load for the 23 m Embedment at 12.6 Seconds.

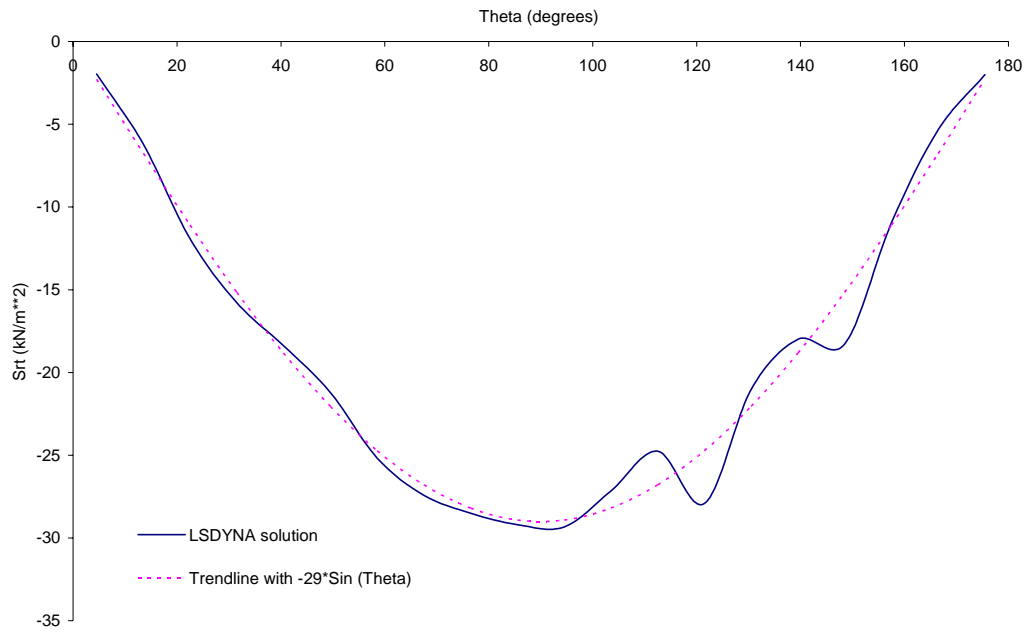


Figure 4.3.3-9 Circumferential Distribution of Tangential Shear Computed from Tied LS-DYNA Model without Gravity Load for the 23 m Embedment at 12.6 Seconds.

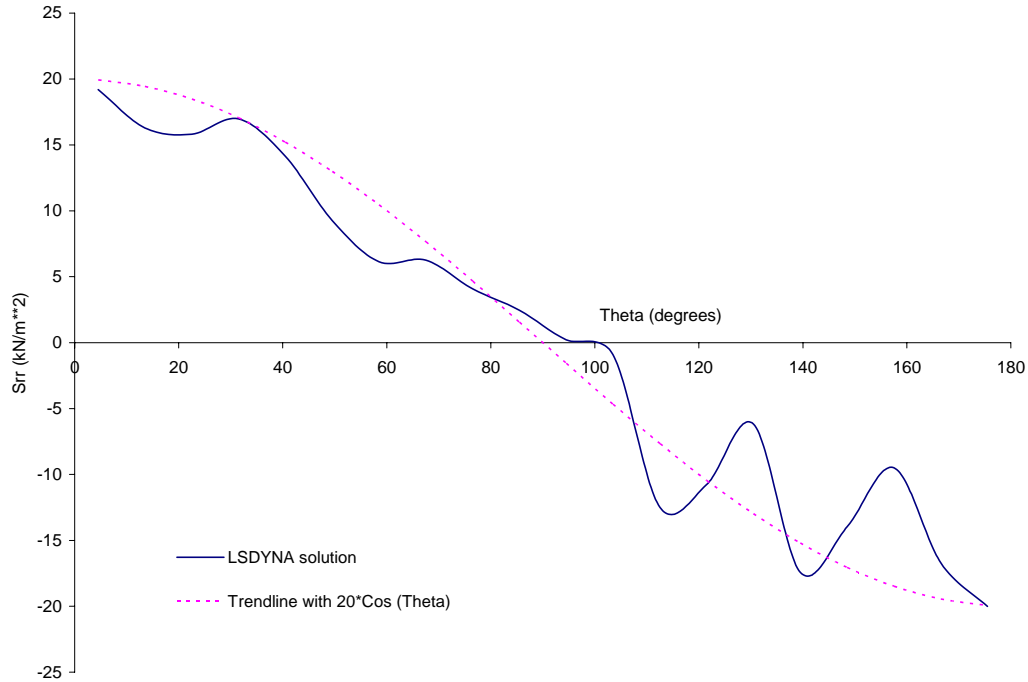


Figure 4.3.3-10 Circumferential Distribution of Normal Pressure Computed from Tied LS-DYNA Model without Gravity Load for the 23 m Embedment at 12.6 Seconds.

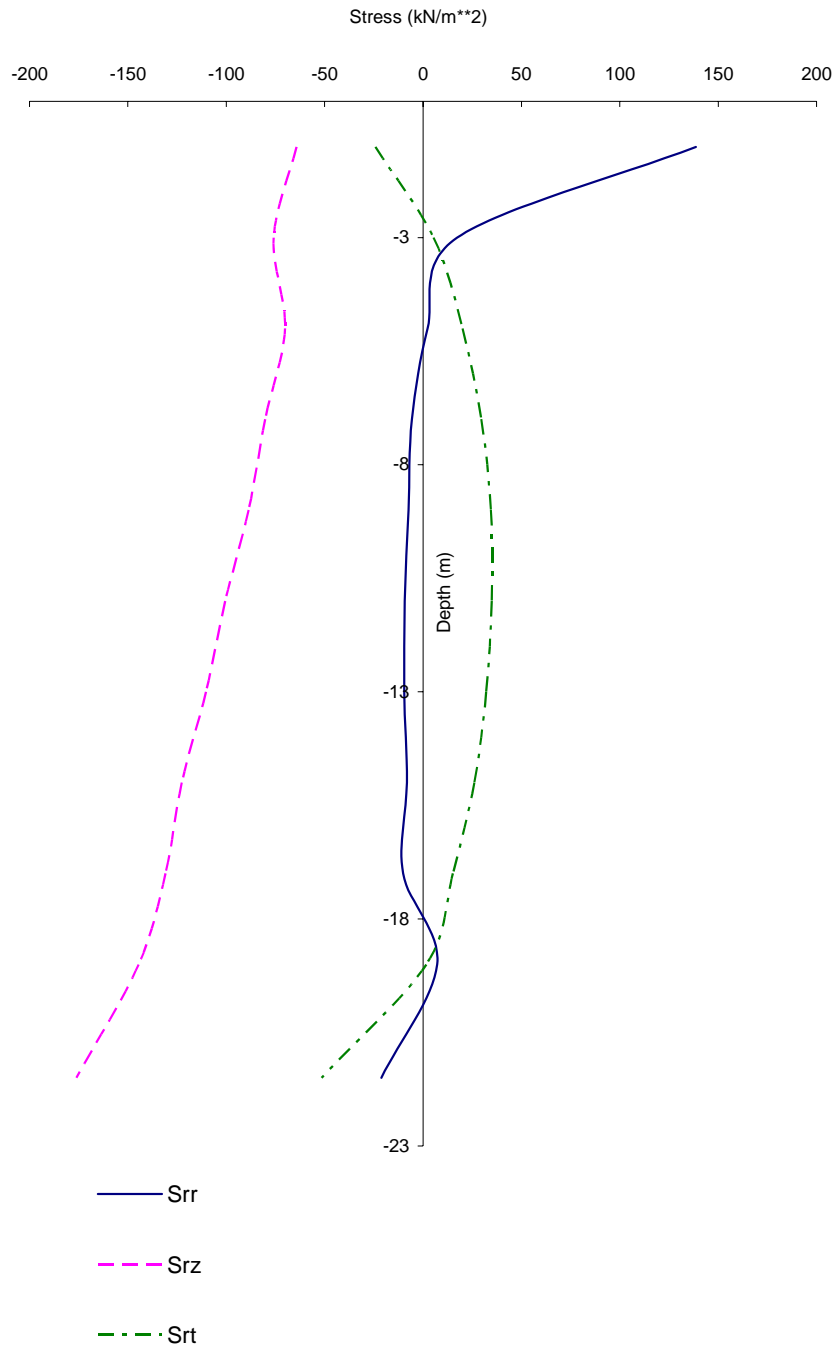


Figure 4.3.3-11 Vertical Distribution of Head-on Soil stress Computed from Tied LS-DYNA Model without Gravity Load for the 23 m Embedment at 11 Seconds.

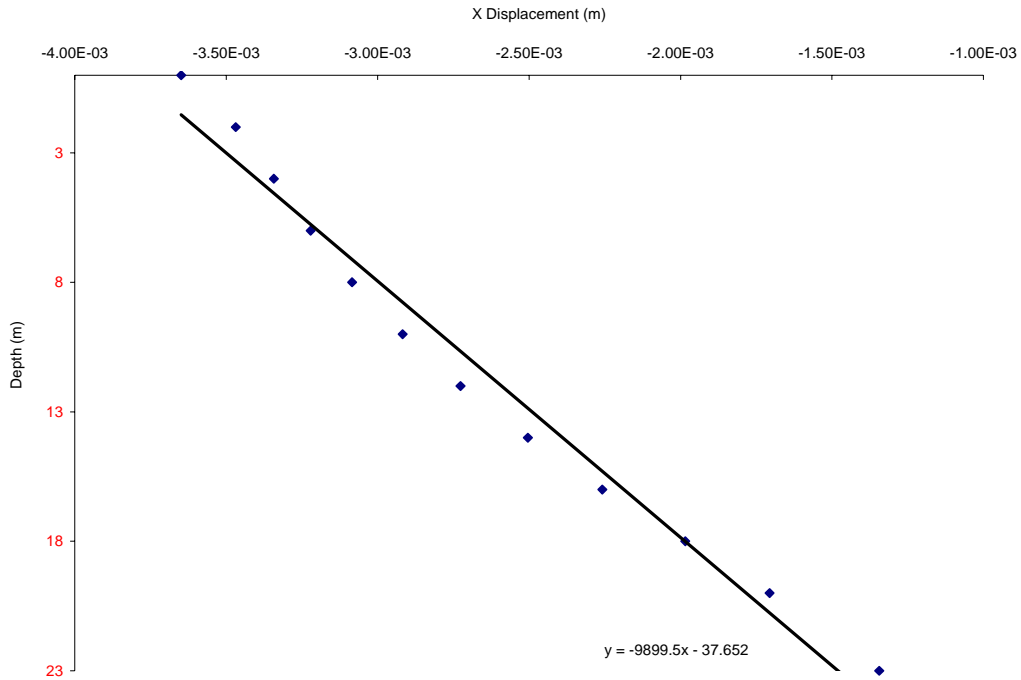


Figure 4.3.3-12 Lateral Embedded Wall Displacements Computed from Tied LS-DYNA Model without Gravity Load for the 23 m Embedment at 11 Seconds.

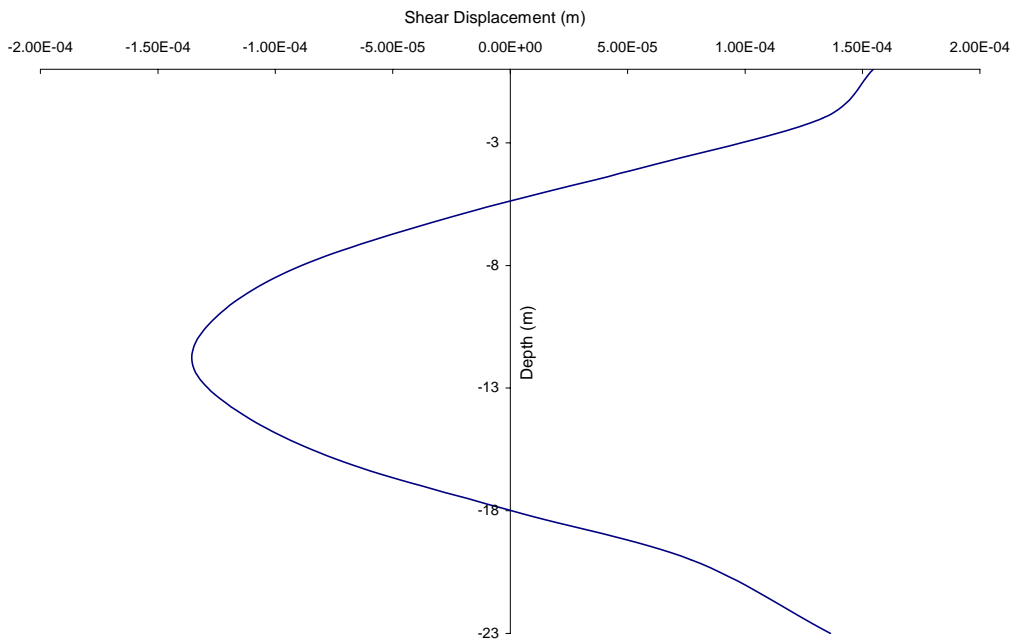


Figure 4.3.3-13 Lateral Wall Shear Displacements Computed from Tied LS-DYNA Model without Gravity Load for 23 m Embedment at 11 Seconds.

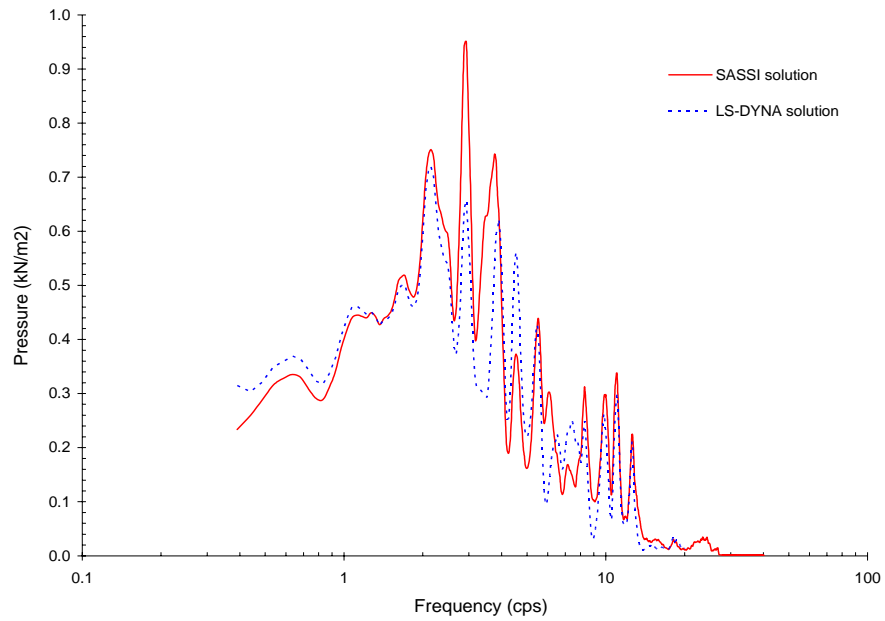


Figure 4.3.3-14 Fourier Spectra of Soil Pressure Computed at the Head-on Soil Element near Mid-Height Embedded Wall for 23 m DOB LD-DYNA model.

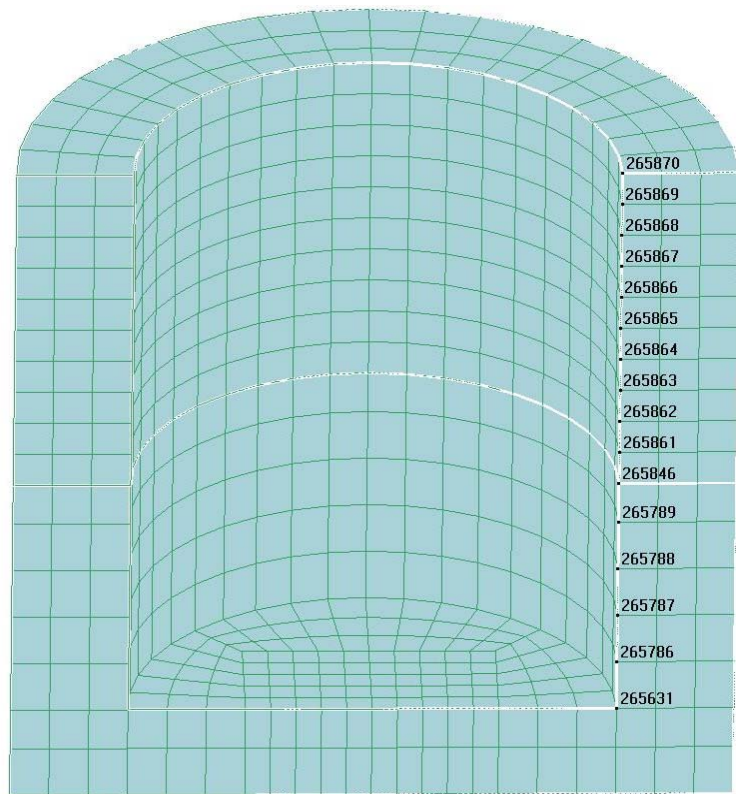


Figure 4.3.4-1 Nodes of Soil Elements on the Interface for the 34.5 m LS-DYNA Model.

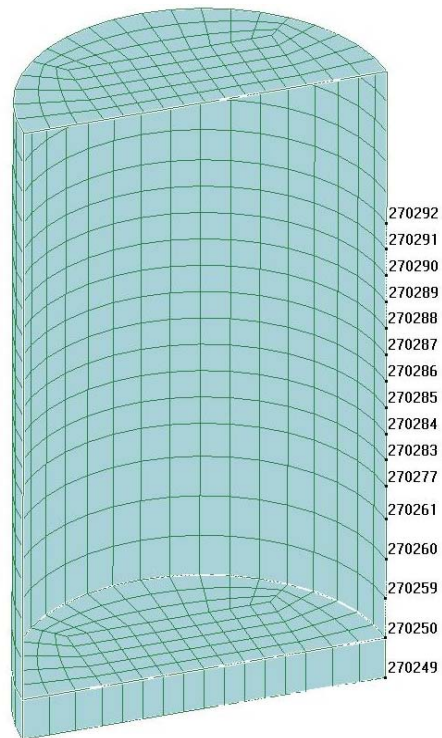


Figure 4.3.4-2 Nodes of the Structure on the Interface for the 34.5 m LS-DYNA Model.

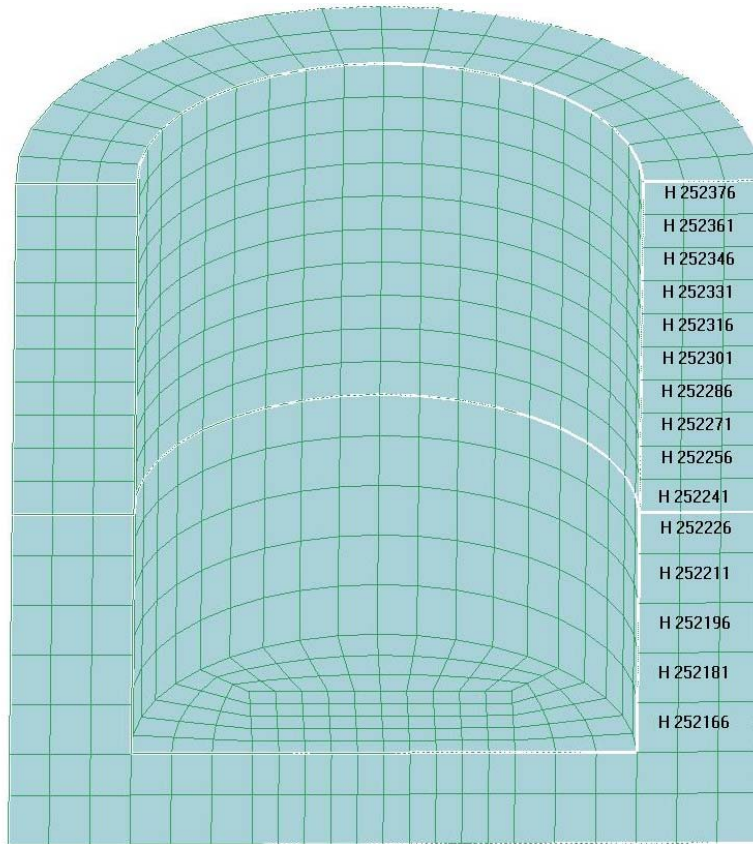


Figure 4.3.4-3 Soil Elements on the Interface for the 34.5 m LS-DYNA Model.

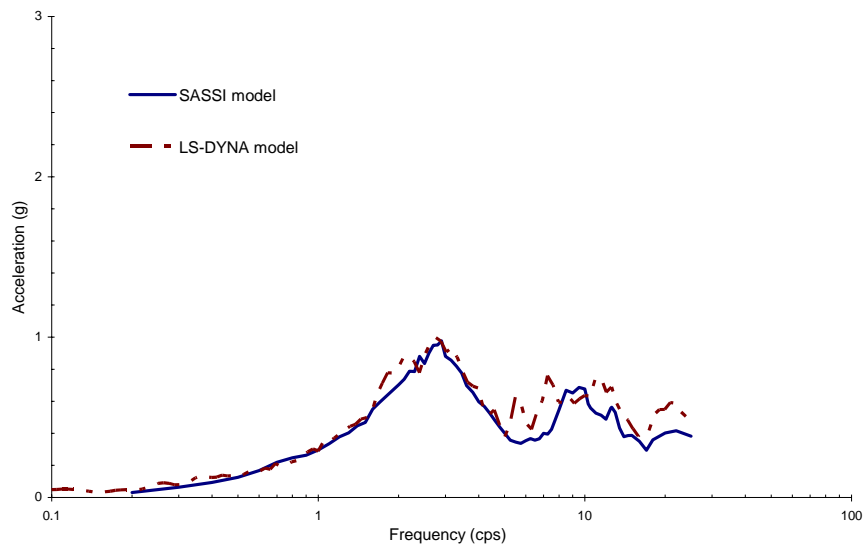


Figure 4.3.4-4 Comparison of Response Spectra at the Base for the 34.5 m Embedment.

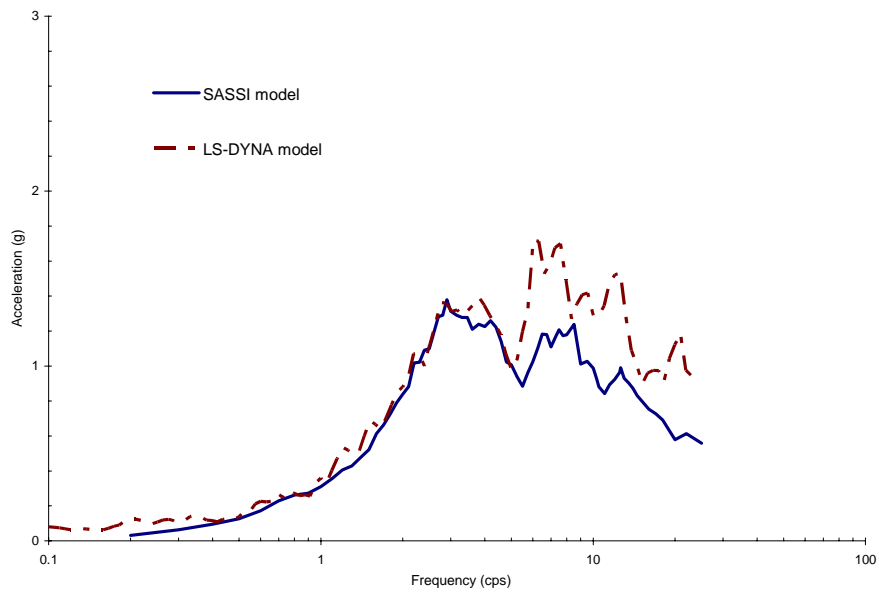


Figure 4.3.4-5 Comparison of Response Spectra at the Roof for the 34.5 m Embedment.

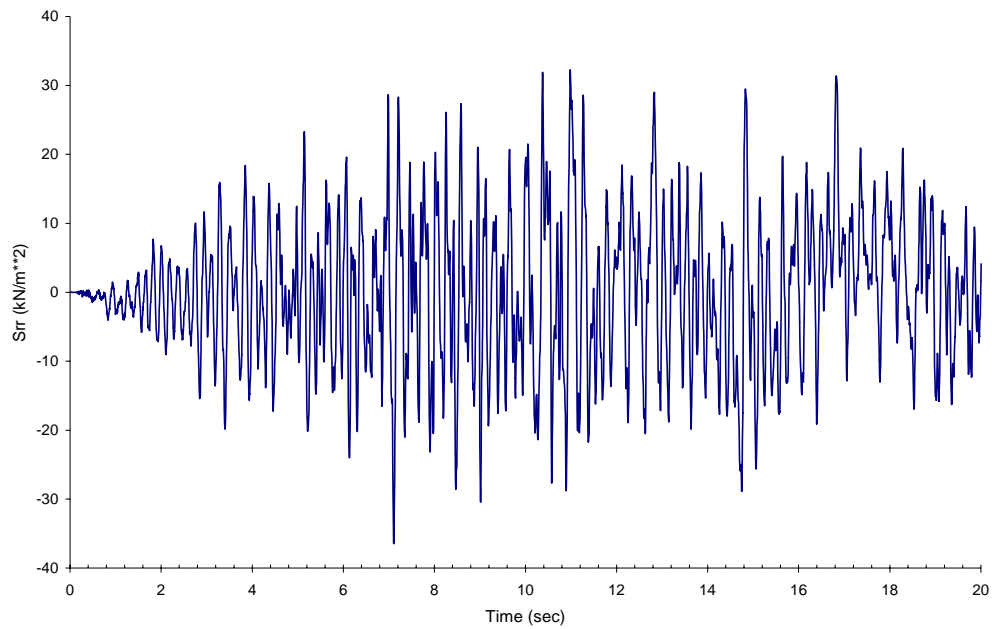


Figure 4.3.4-6 Soil Pressure in the Head-on Soil Element near the Ground Surface for the 34.5 m Embedment.

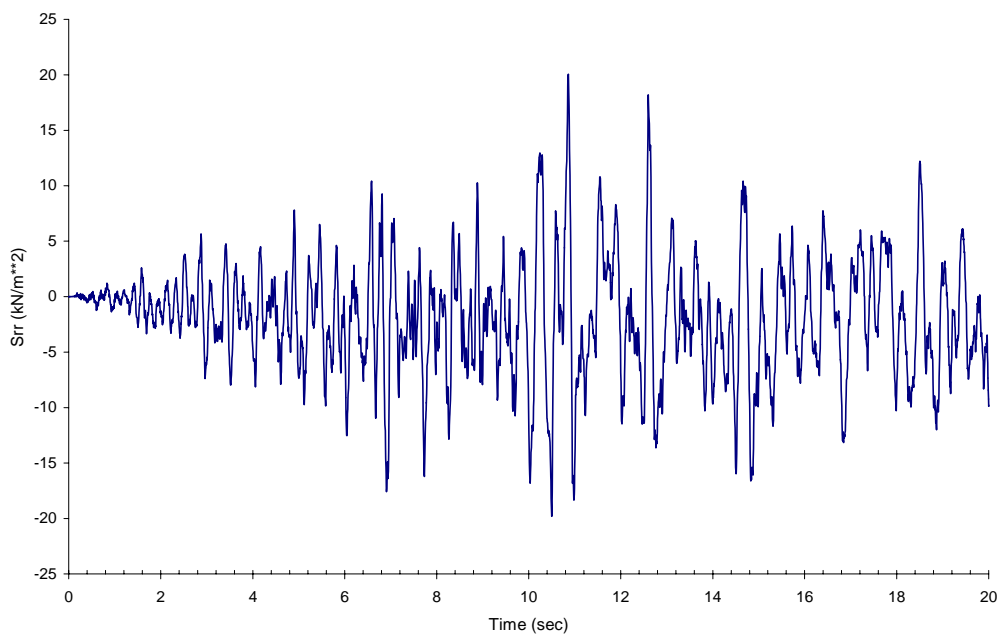


Figure 4.3.4-7 Soil Pressure in the Head-on Soil Element near the Mid-Height of Structure Wall for the 34.5 m Embedment.

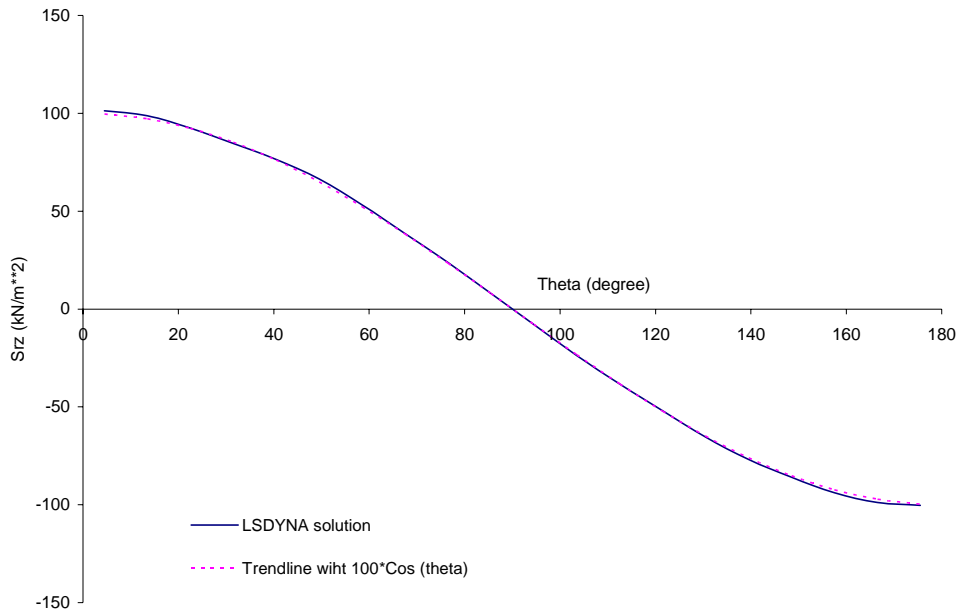


Figure 4.3.4-8 Circumferential Distribution of Vertical Shear Computed from Tied LS-DYNA Model without Gravity Load for the 34.5 m Embedment at 10.86 Seconds.

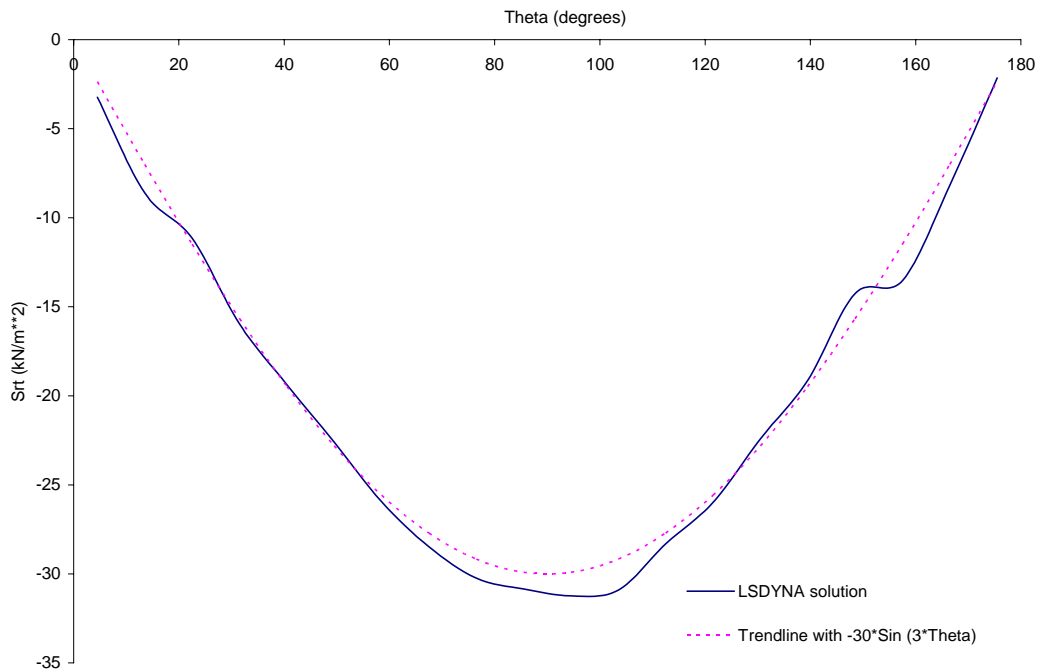


Figure 4.3.4-9 Circumferential Distribution of Tangential Shear Computed from Tied LS-DYNA Model without Gravity Load for the 34.5 m Embedment at 10.86 Seconds.

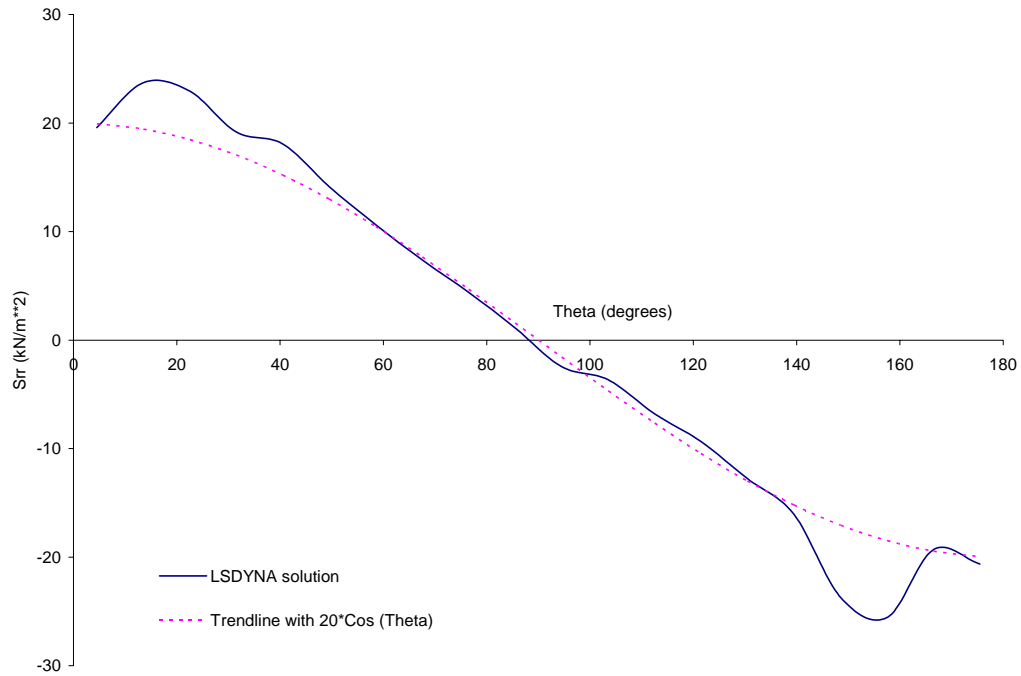


Figure 4.3.4-10 Circumferential Distribution of Normal Pressure Computed from Tied LS-DYNA Model without Gravity Load for the 34.5 m Embedment at 10.86 Seconds.

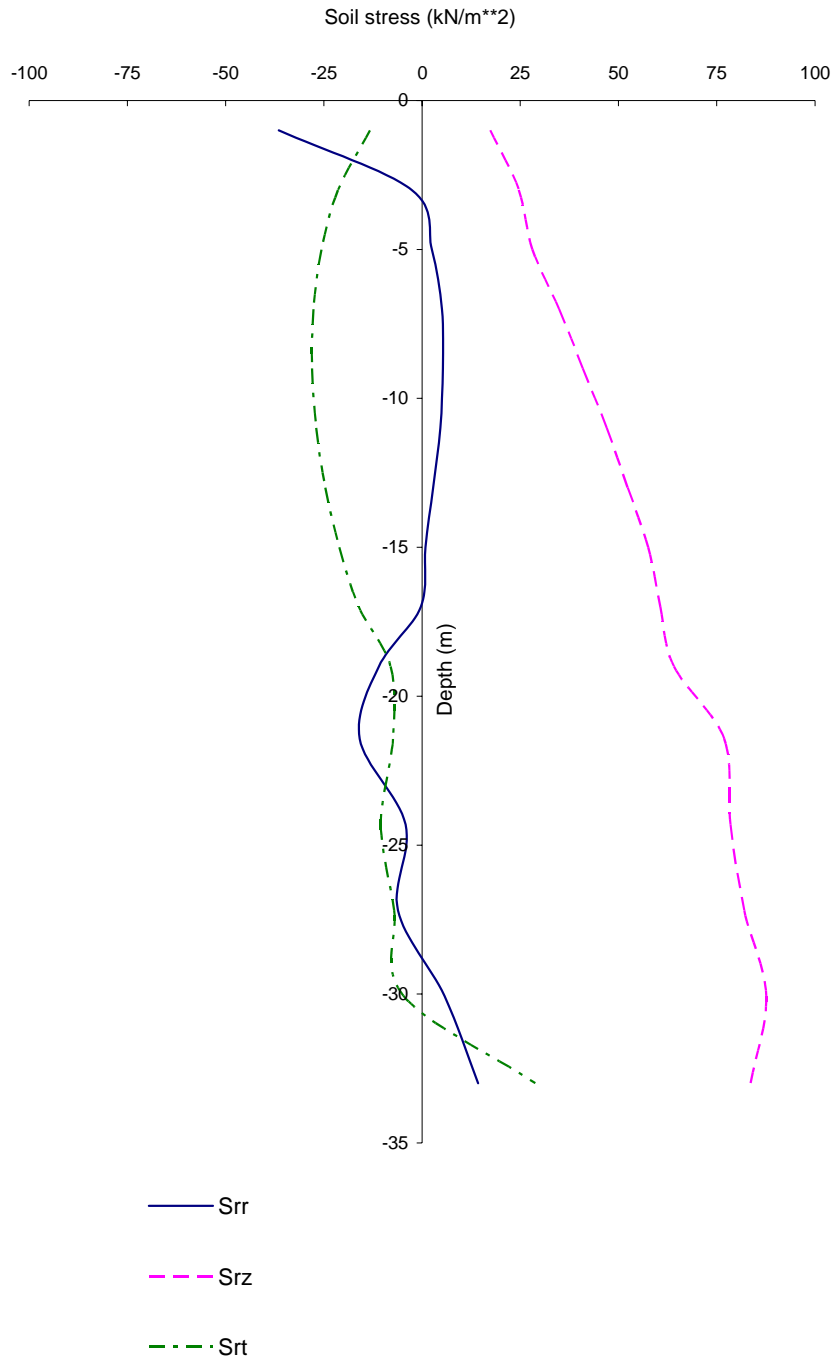


Figure 4.3.4-11 Vertical Distribution of Head-on Soil Stress Computed from Tied LS-DYNA Model without Gravity Load for the 34.5 m Embedment at 7.11 Seconds.

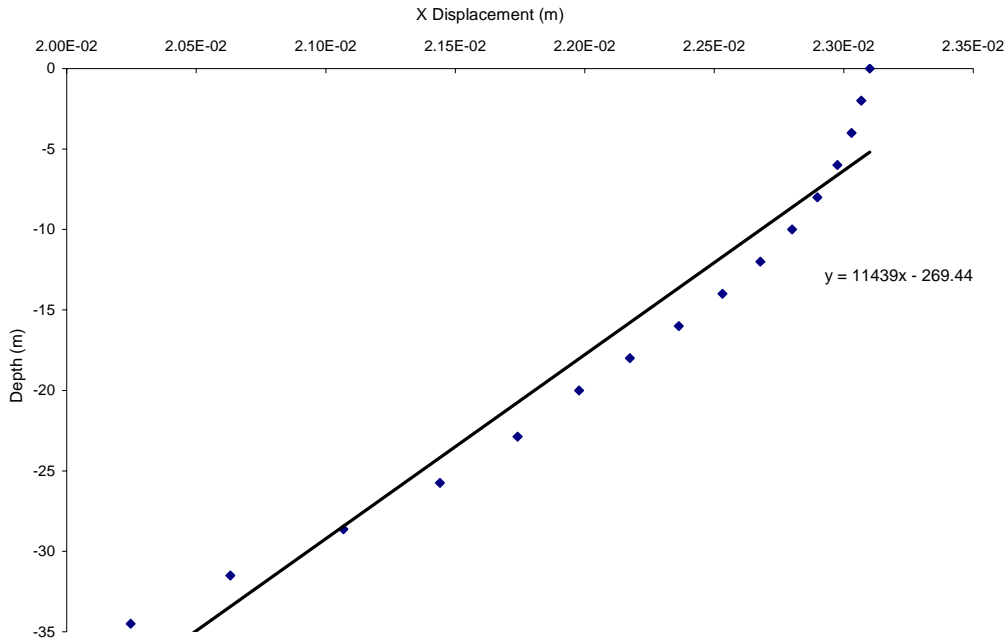


Figure 4.3.4-12 Lateral Embedded Wall Displacements Computed from Tied LS-DYNA Model without Gravity Load for the 34.5 m Embedment at 12.03 Seconds.

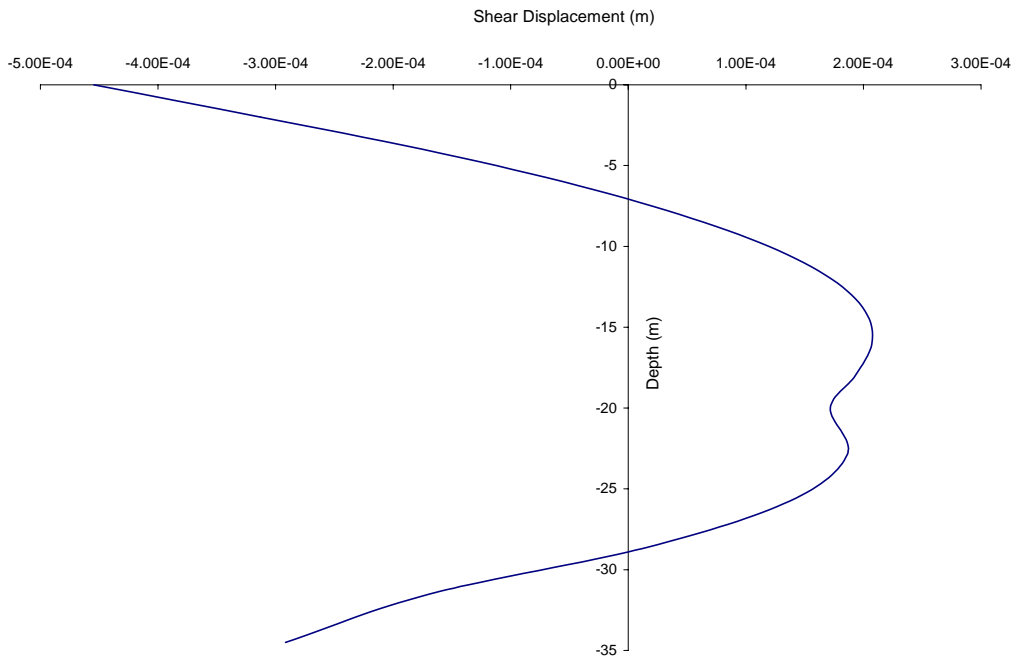


Figure 4.3.4-13 Lateral Wall Shear Displacements Computed from Tied LS-DYNA Model without Gravity Load for 34.5 m Embedment at 12.03 Seconds.

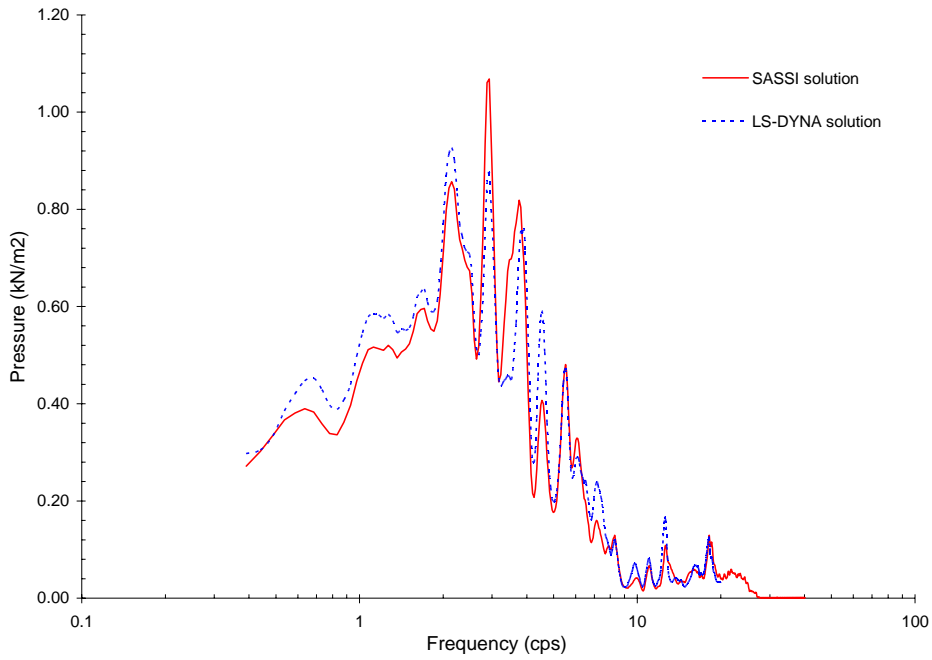


Figure 4.3.4-14 Fourier Spectra of Soil Pressure Computed at the Head-on Soil Element near Mid-Height Embedded Wall for 34.5 m DOB LD-DYNA model.

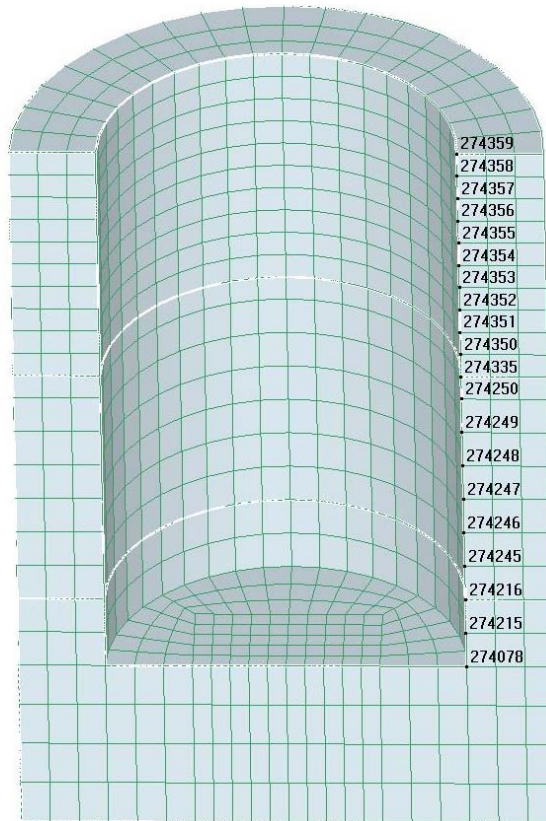


Figure 4.3.5-1 Nodes of Soil Elements on the Interface for the 46 m LS-DYNA Model.

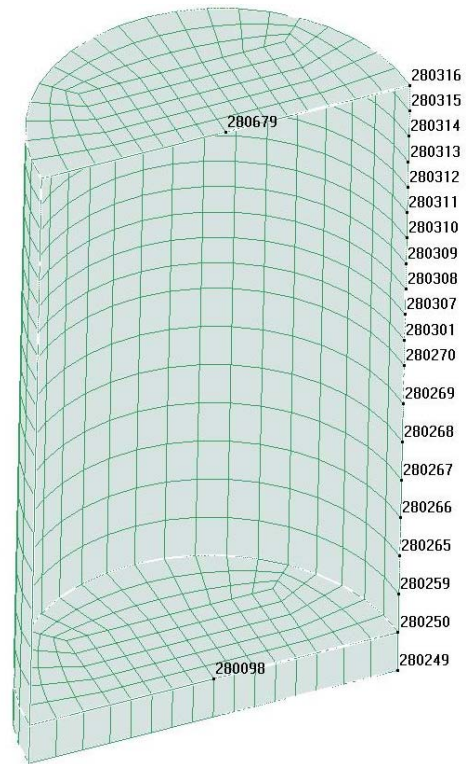


Figure 4.3.5-2 Nodes of the Structure on the Interface for the 46 m LS-DYNA Model.

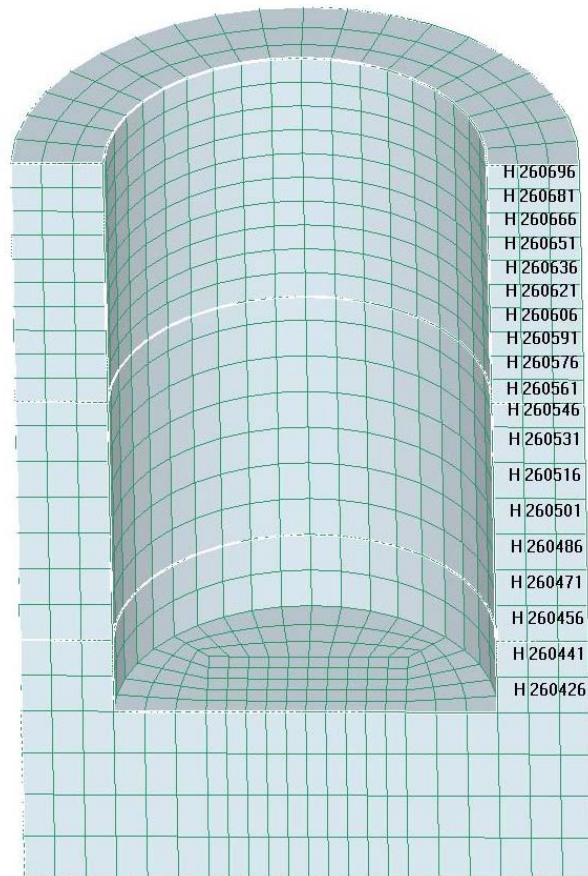


Figure 4.3.5-3 Soil Elements on the Interface for the 46 m LS-DYNA Model.

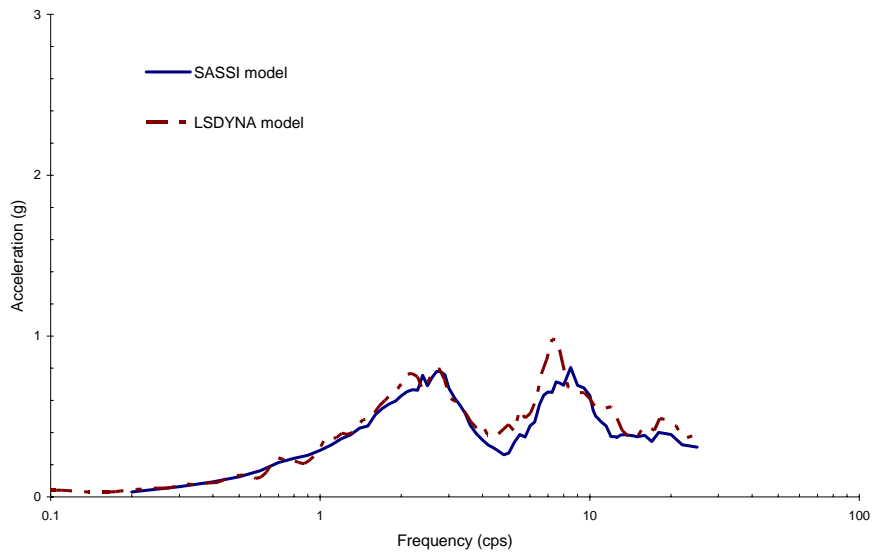


Figure 4.3.5-4 Comparison of Response Spectra at the Base for the 46 m Embedment.

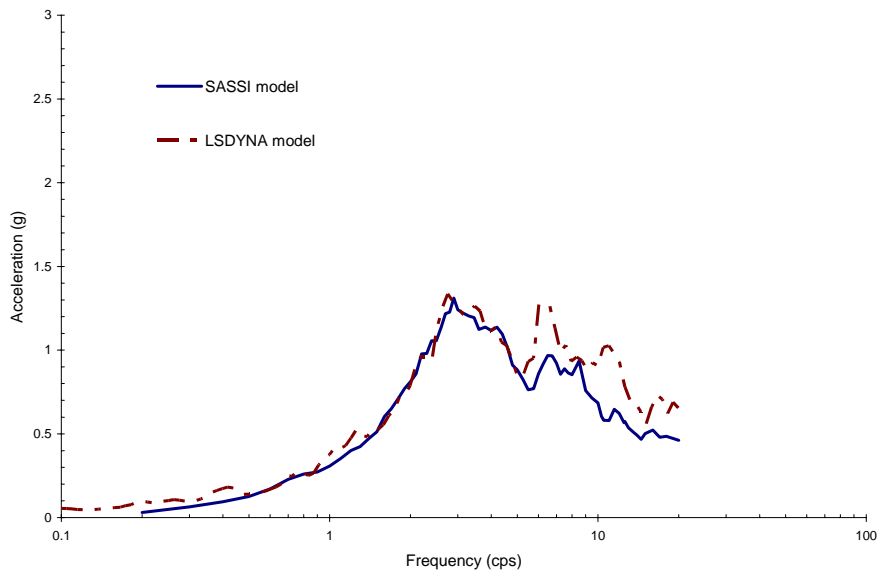


Figure 4.3.5-5 Comparison of Response Spectra at the Roof for the 46 m Embedment.

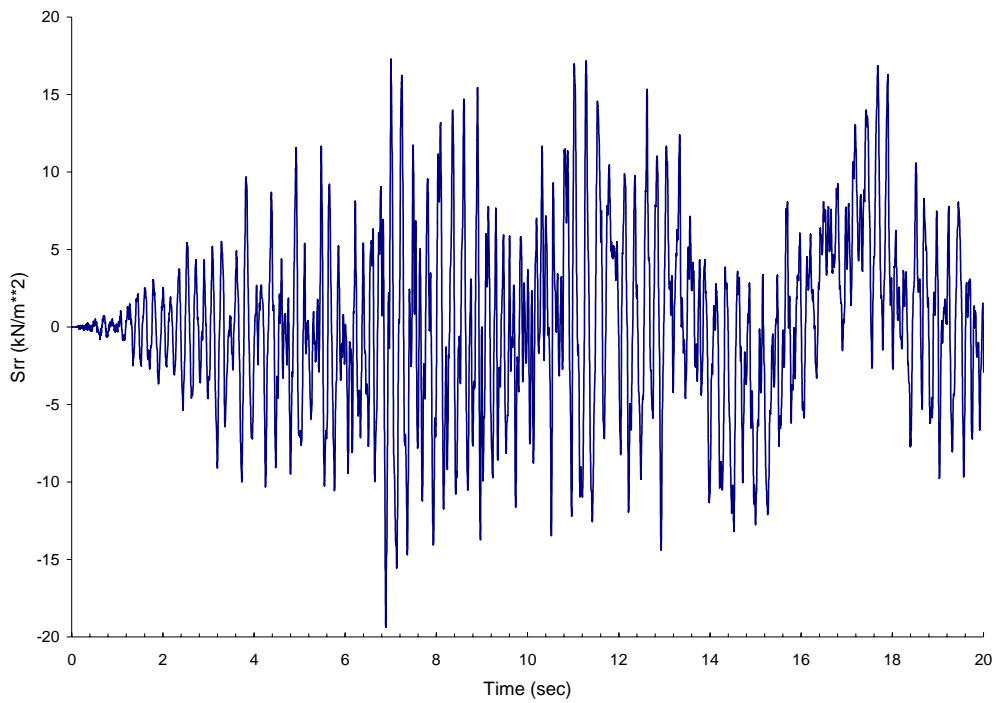


Figure 4.3.5-6 Normal Pressure in the Head-on Soil Element near the Ground Surface for the 46 m Embedment.

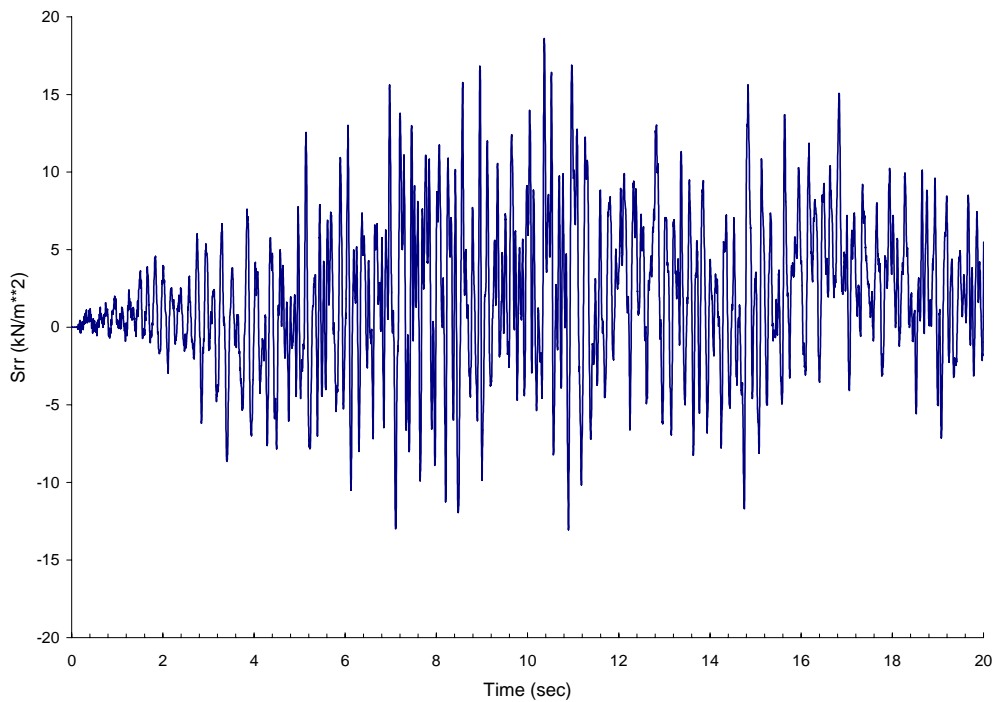


Figure 4.3.5-7 Normal Pressure in the Head-on Soil Element near the Mid-Height of Structure Wall for the 46 m Embedment.

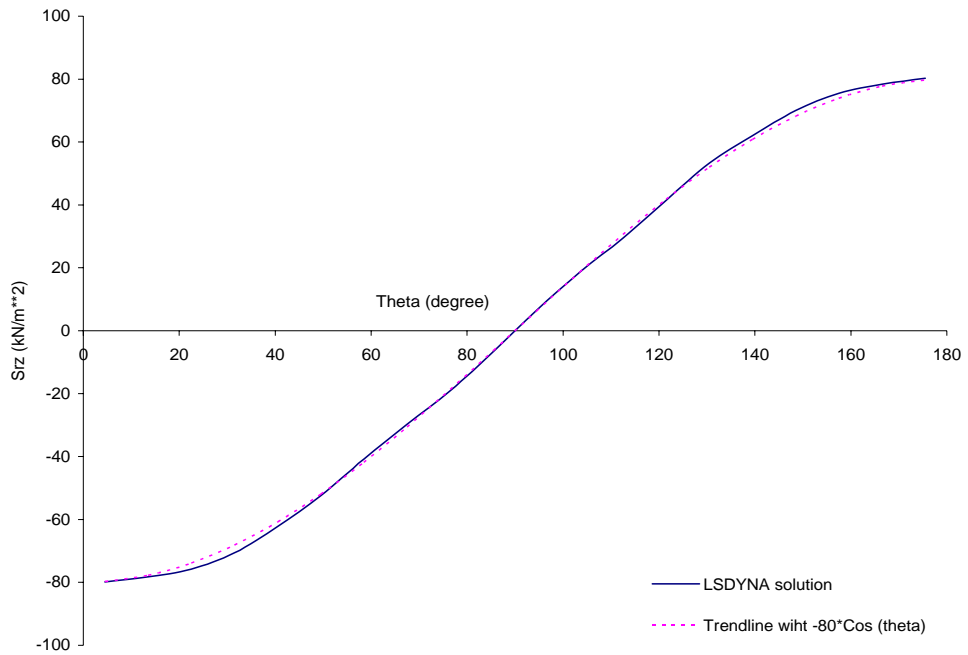


Figure 4.3.5-8 Circumferential Distribution of Vertical Shear at 10.3702 sec When Head-on Mid-Height S_{rr} Reaches Peak for Tied LS-DYNA Model without Gravity Load for the 46 m Embedment.

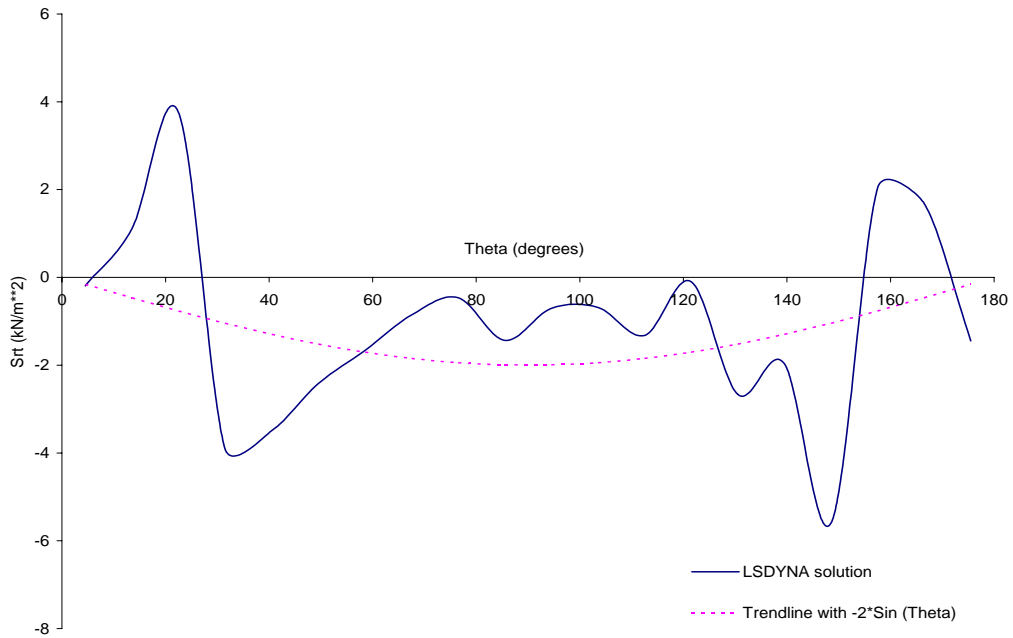


Figure 4.3.5-9 Circumferential Distribution of Tangential Shear at 10.3702 sec When Head-on Mid-Height S_{rr} Reaches Peak for Tied LS-DYNA Model without Gravity Load for the 46m Embedment.

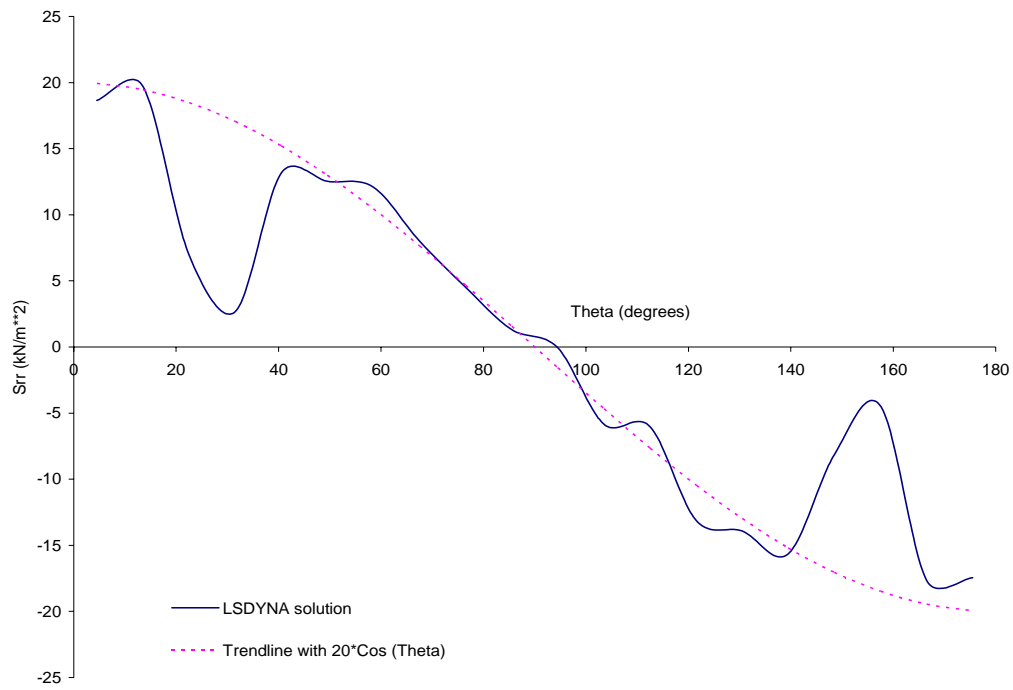


Figure 4.3.5-10 Circumferential Distribution of Normal Pressure at 10.3702 sec When Head-on Mid-Height S_{rr} Reaches Peak for Tied LS-DYNA Model without Gravity Load for the 46 m Embedment.

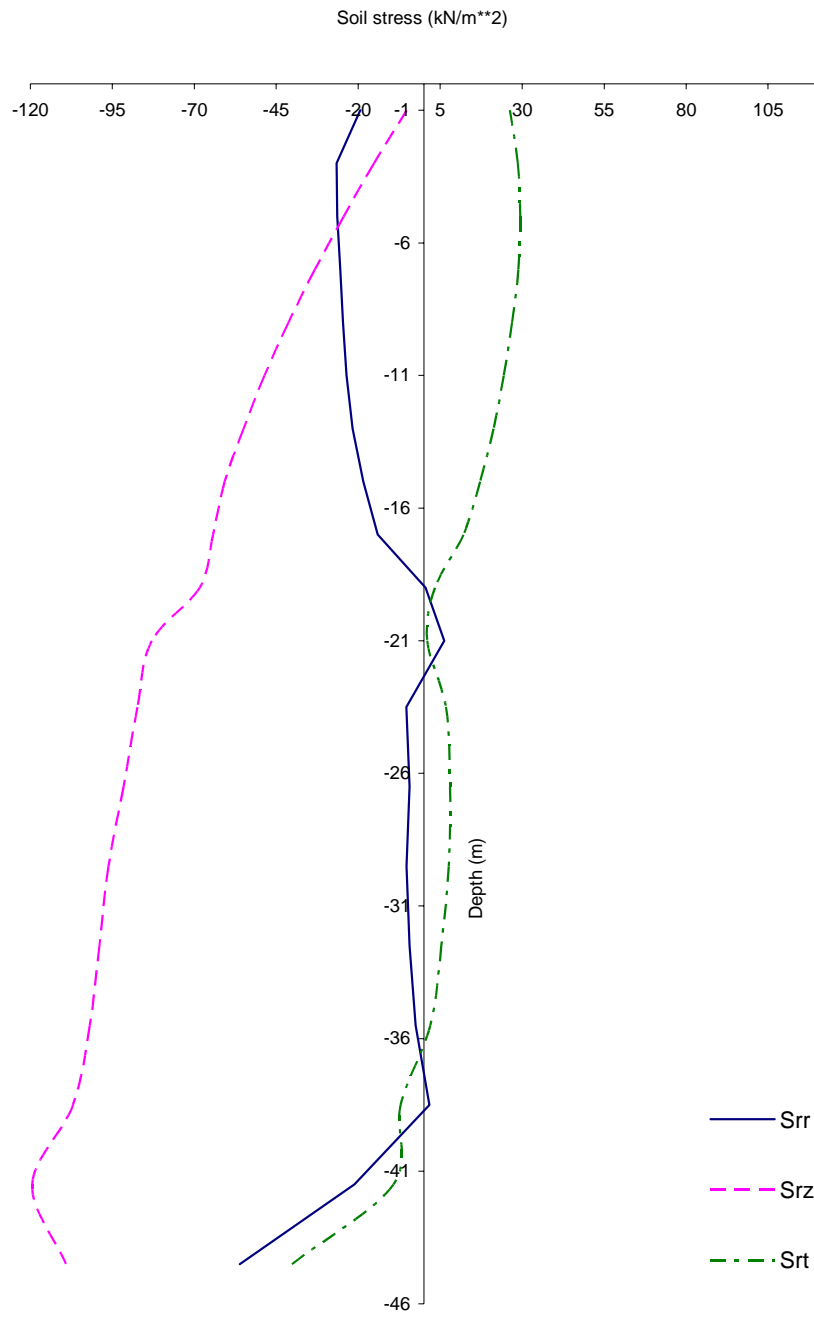


Figure 4.3.5-11 Vertical Distribution of Pressures When Head-on Surface S_{rr} Reaches Peak for Tied LS-DYNA Model without Gravity Load for the 46 m Embedment.

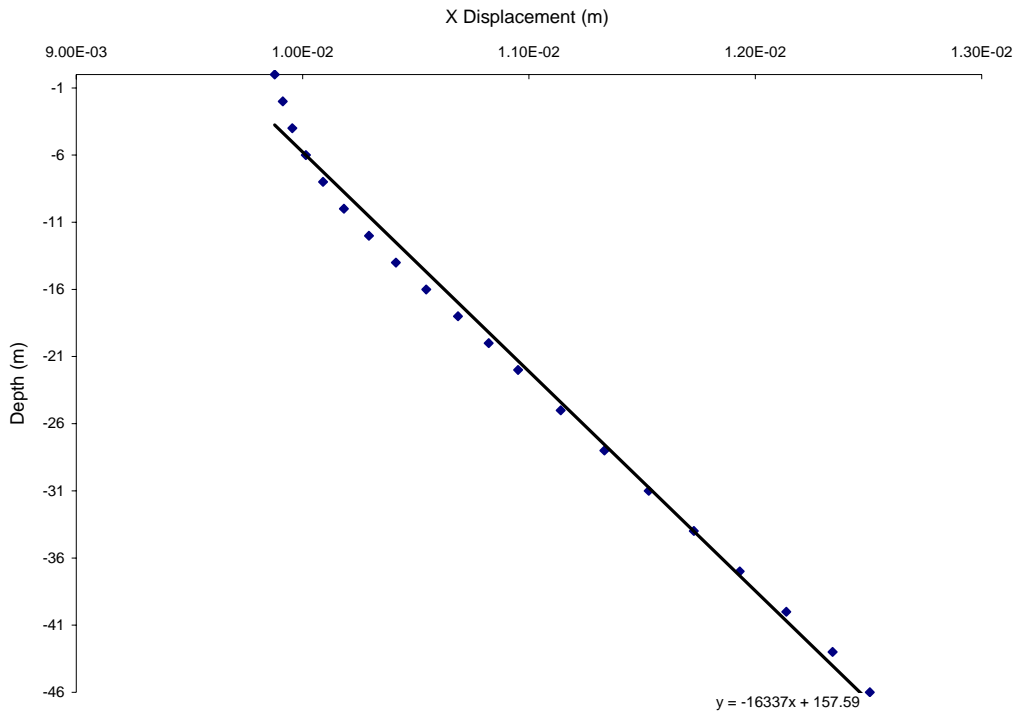


Figure 4.3.5-12 Lateral Embedded Wall Displacements Computed from Tied LS-DYNA Model without Gravity Load for the 46 m Embedment.

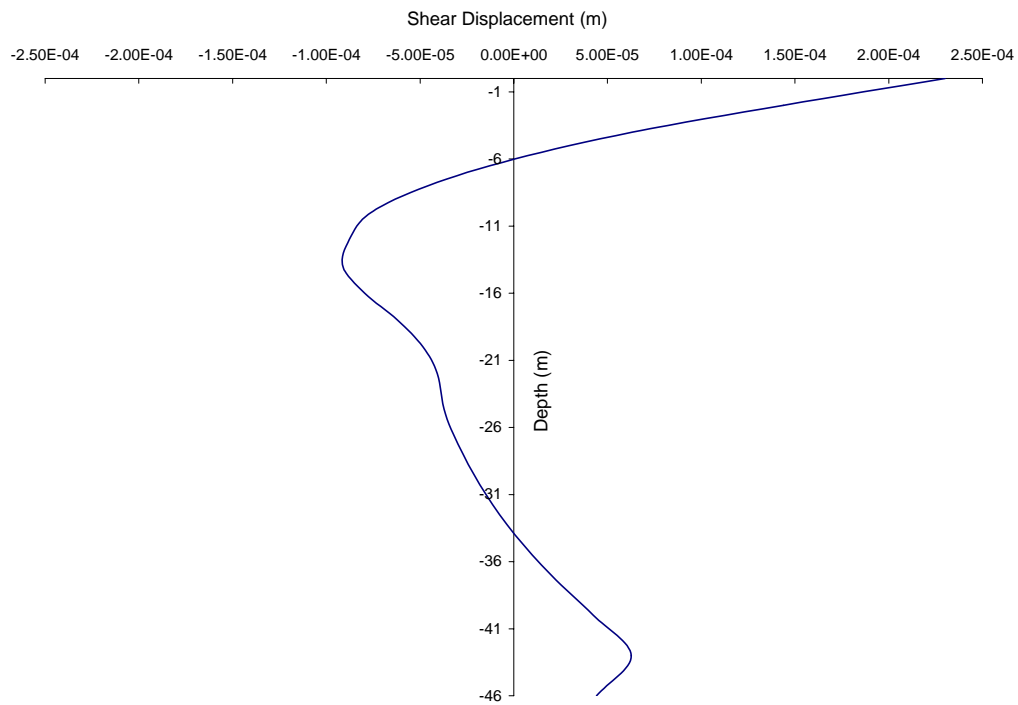


Figure 4.3.5-13 Lateral Wall Shear Displacements Computed from Tied LS-DYNA Model without Gravity Load for the 46m Embedment.

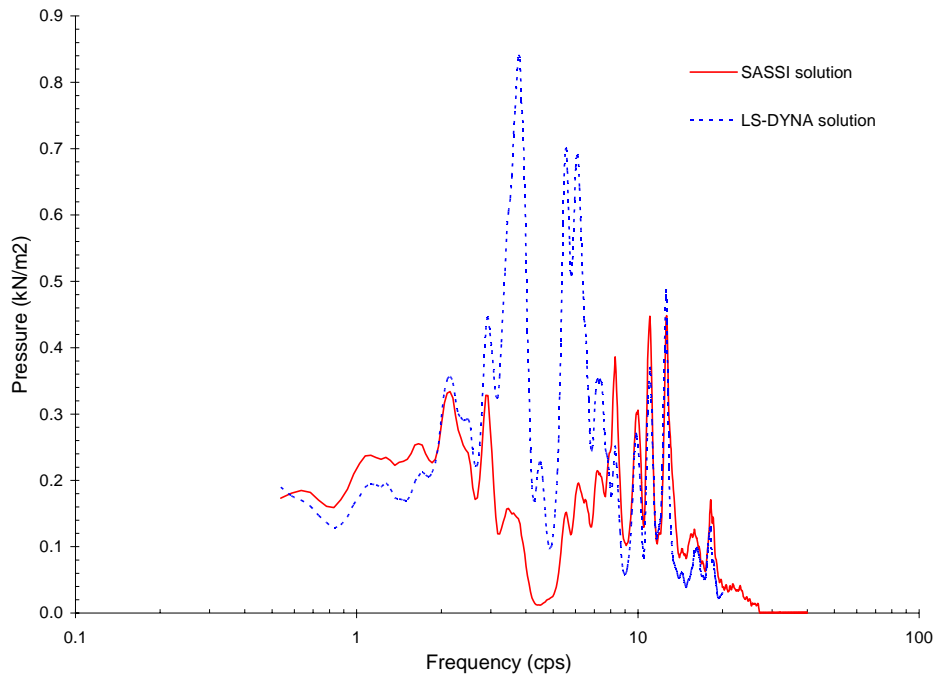


Figure 4.3.5-14 Fourier Spectra of Soil Pressure Computed at the Head-on Soil Element near Mid-Height Embedded Wall for the 46 m DOB LD-DYNA model.

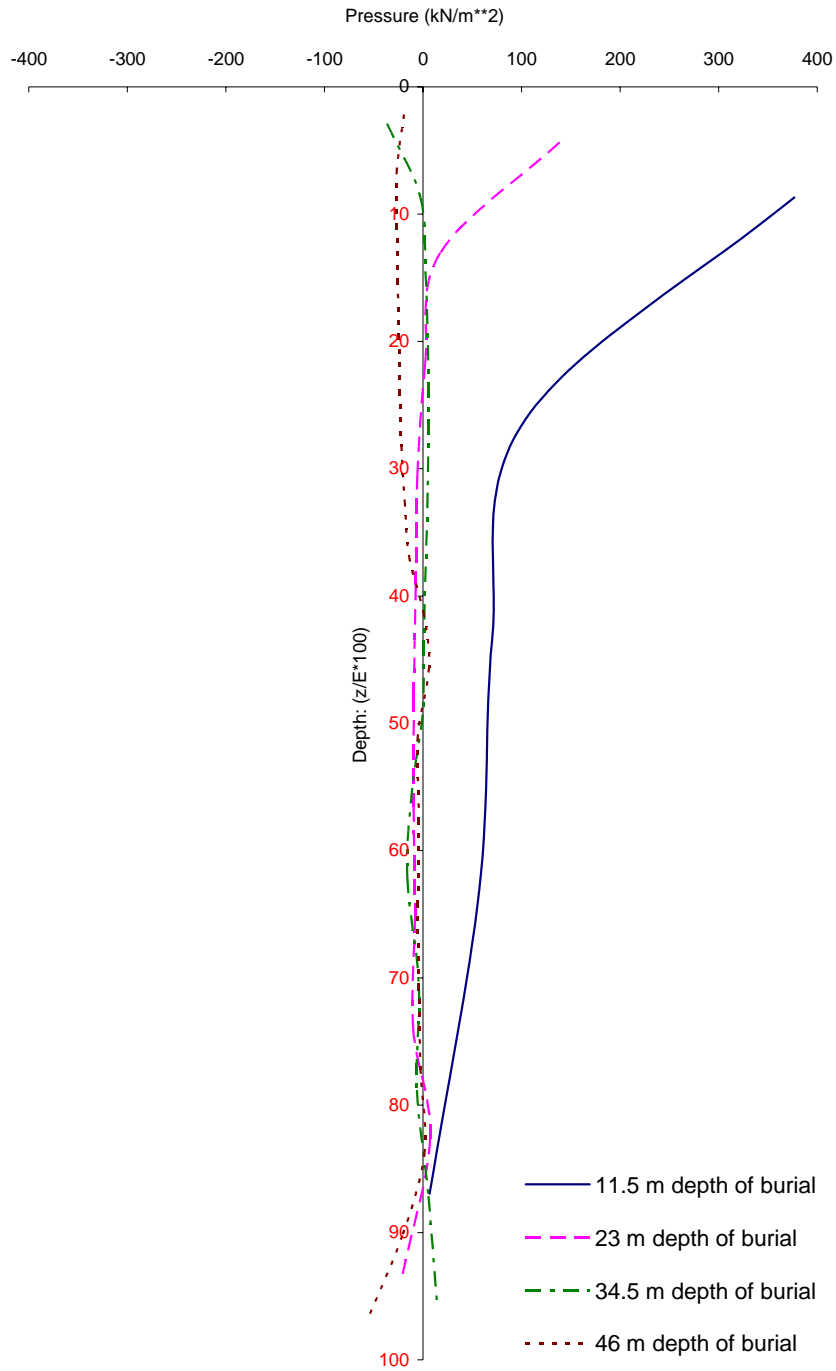


Figure 4.3.6-1 Comparison of Vertical Distributions of Normal Pressures Computed from Tied LS-DYNA Model for Various DOBs at Their Respective Surface Peak Times.

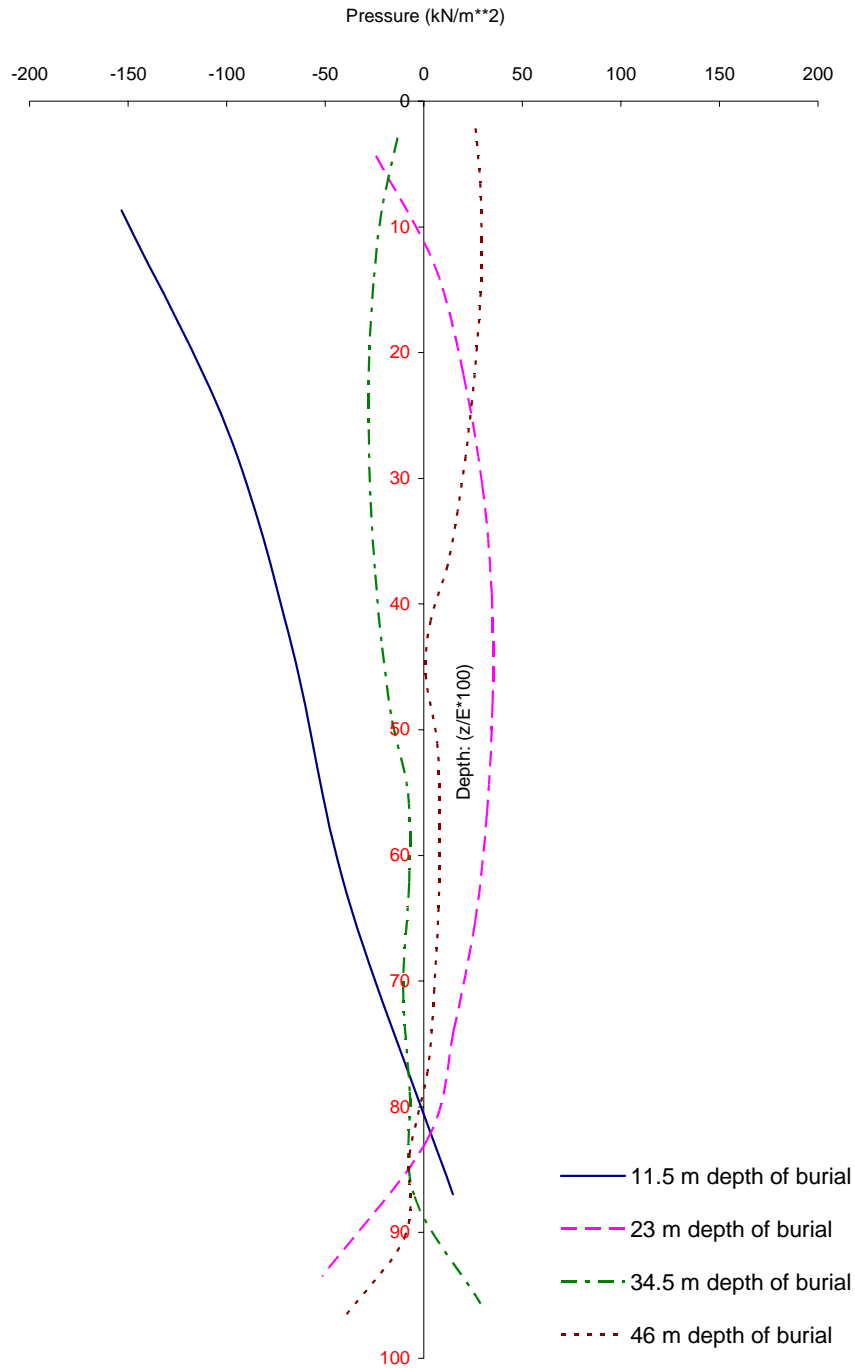


Figure 4.3.6-2 Comparison of Vertical Distributions of Tangential Shears Computed from Tied LS-DYNA Model for Various DOBs at Their Respective Surface Peak Times.

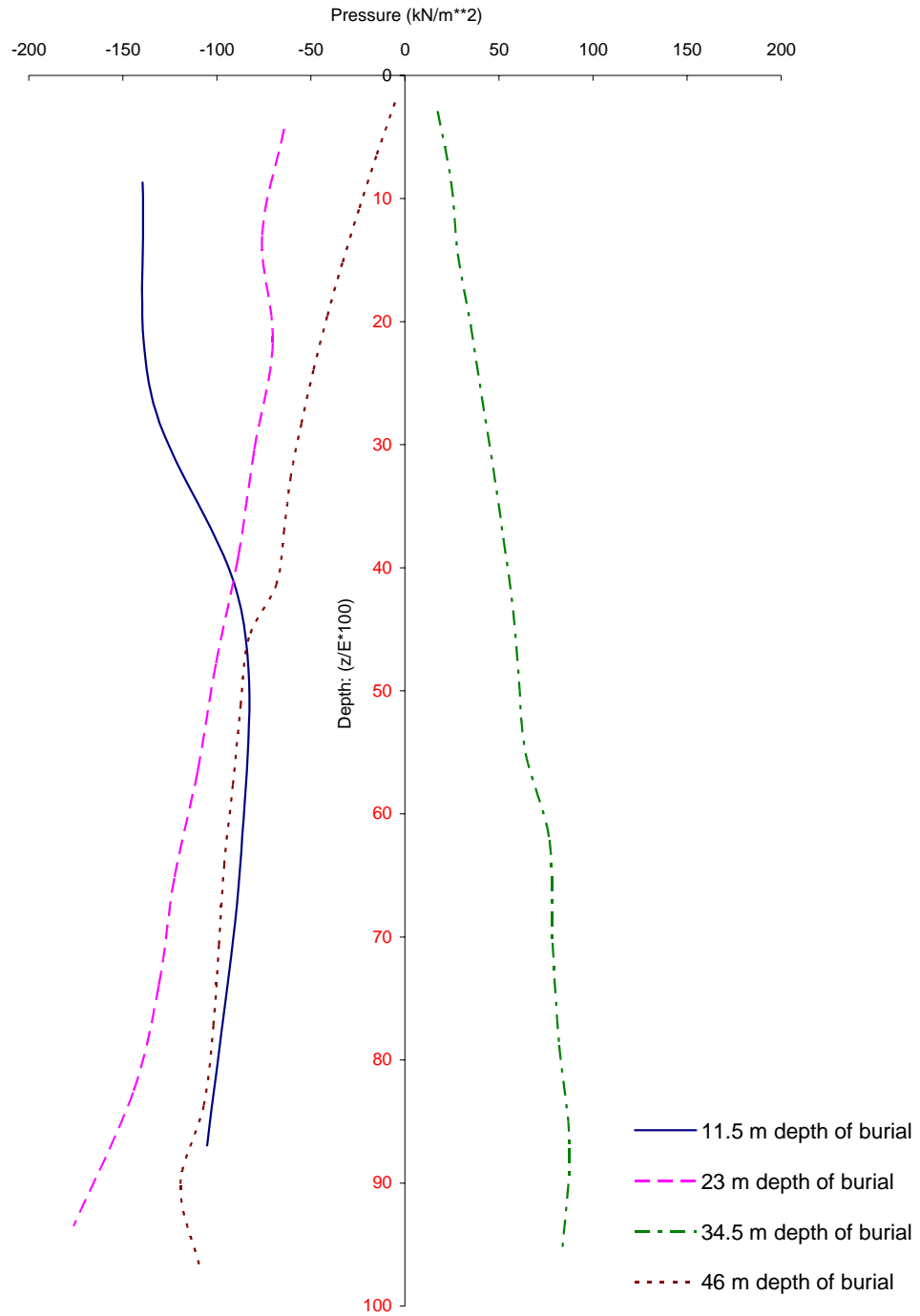


Figure 4.3.6-3 Comparison of Vertical Distributions of Vertical Shears Computed from Tied LS-DYNA Model for Various DOBs at Their Respective Surface Peak Times.

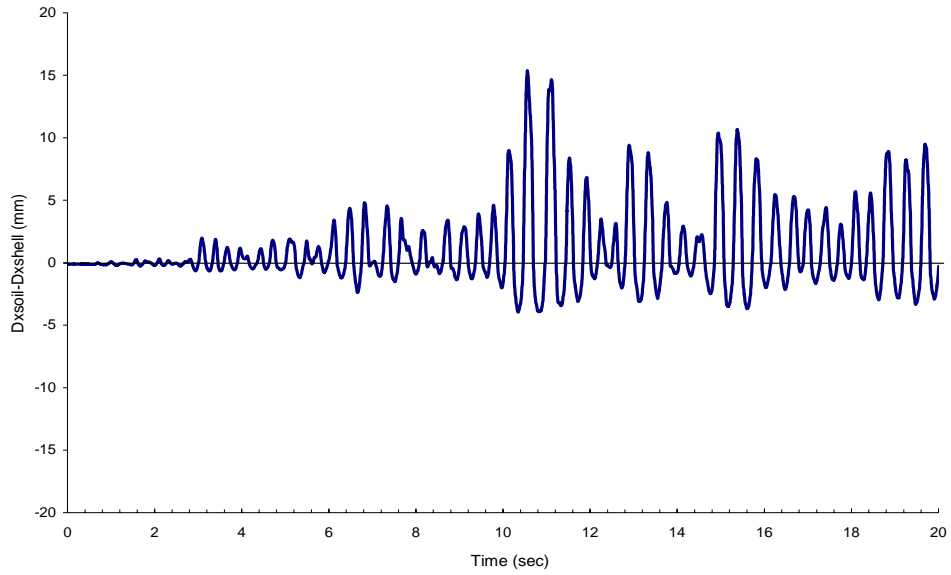


Figure 4.4.1-1 Relative Lateral Displacement of Structural Wall and Surrounding Soil at the Interface near ground Surface ($\theta=0$) from the 11.5 m DOB Contact Interface Model.

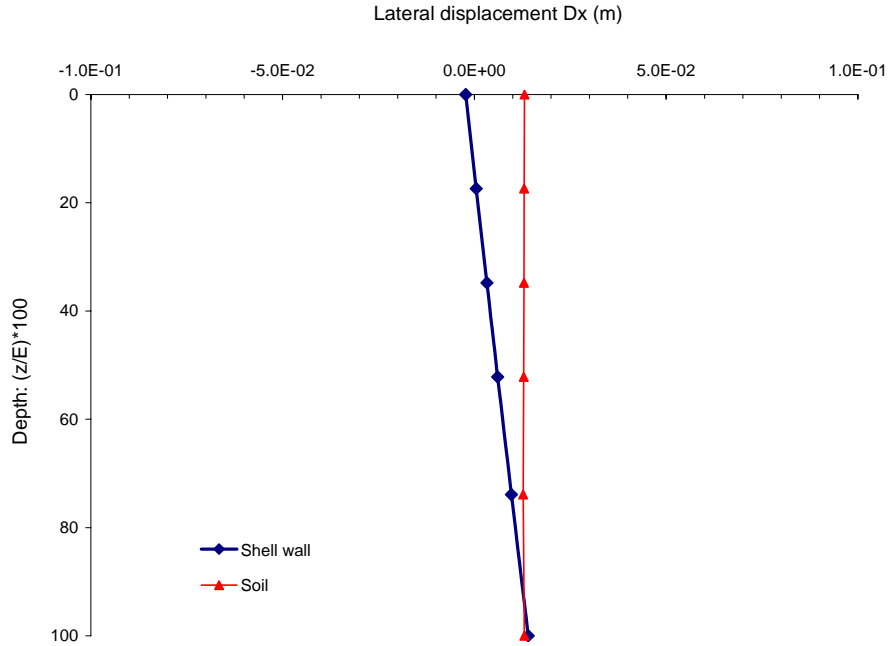


Figure 4.4.1-2 Vertical Distribution of Lateral Displacements of Structural Wall and Surrounding Soil at the Interface ($\theta=0$) from the 11.5 m DOB Contact Interface Model at 10.56 Seconds.

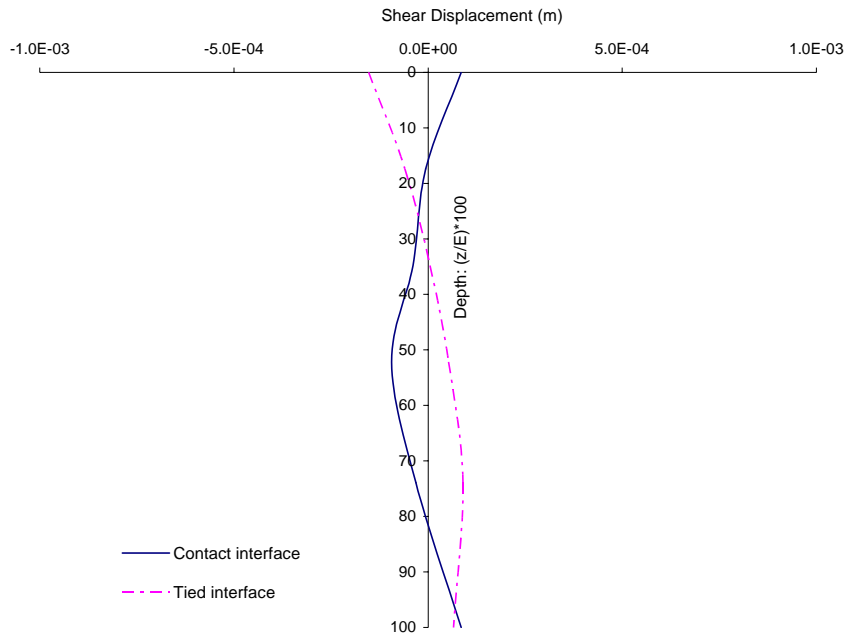


Figure 4.4.1-3 Comparison of Lateral Wall Shear Displacements Computed from the 11.5 m DOB Contact and Tied Interface Models at 10.56 Seconds.

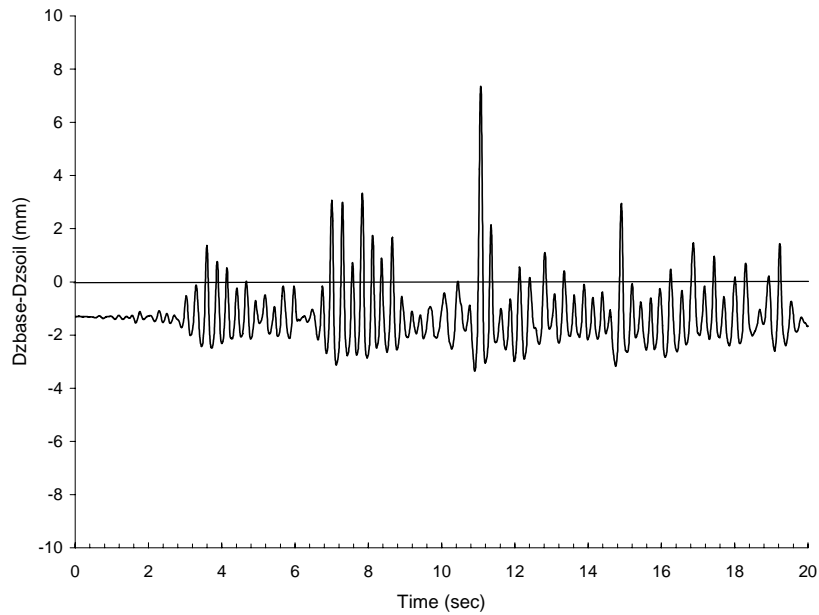


Figure 4.4.1-4 Vertical Displacements of Structural Foundation Relative to the Base Soil Computed from the 11.5 m DOB Contact Interface Model at Theta = 0.

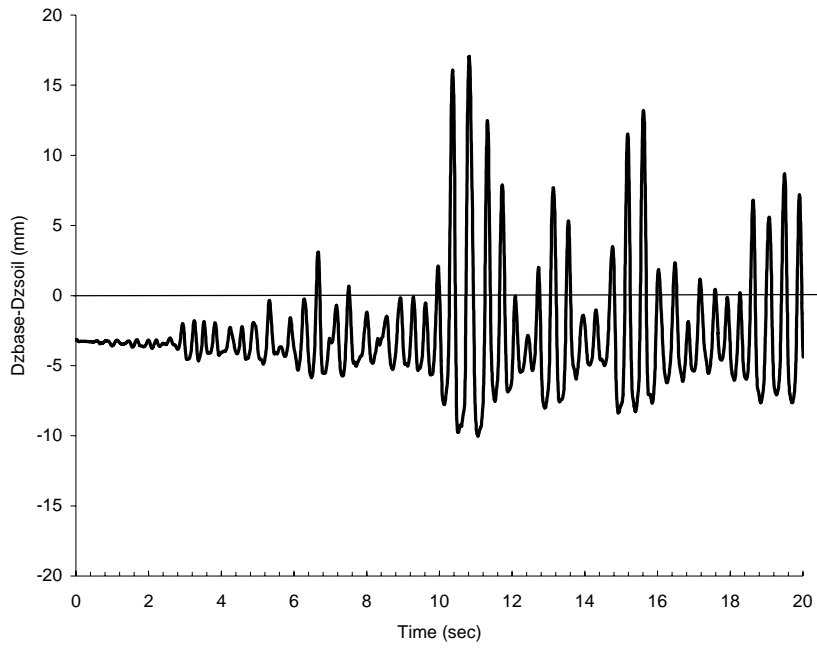


Figure 4.4.1-5 Vertical Displacements of Structural Foundation Relative to the Base Soil Computed from the 11.5 m DOB Contact Interface Model at Theta = 180.

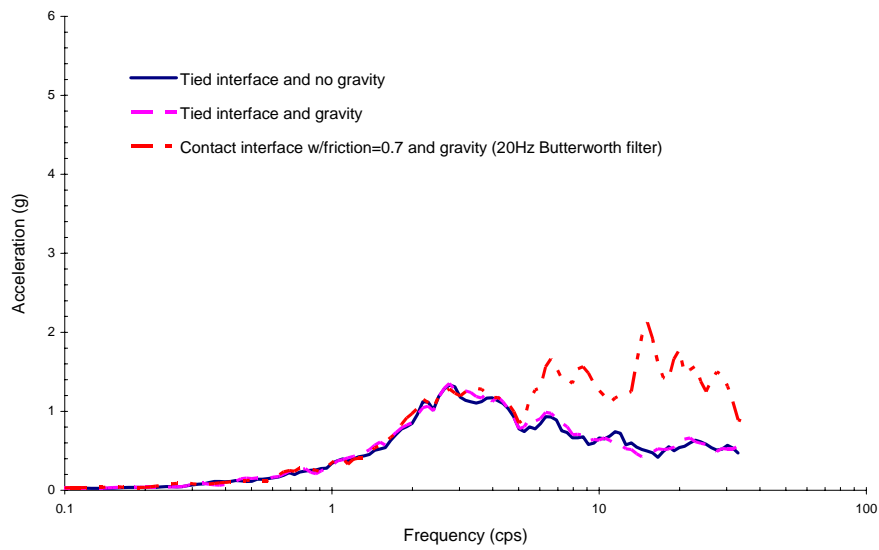
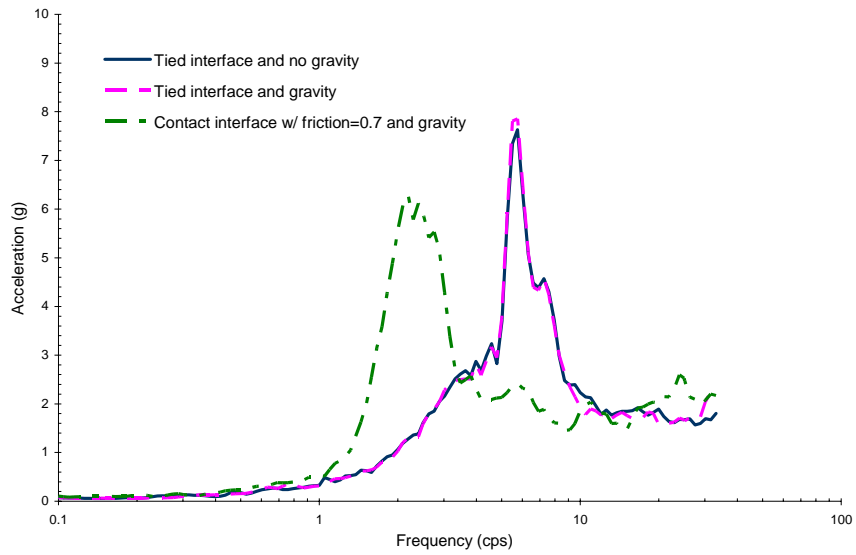


Figure 4.4.1-6 Comparison of Response Spectra at the Base for the 11.5 m DOB with various LS-DYNA models.



Effect of gravity and interface on LSDYNA SSI response at roof (11.5m embedment), Soil C.

Figure 4.4.1-7 Comparison of Response Spectra at the Roof for the 11.5 m DOB with various LS-DYNA models.

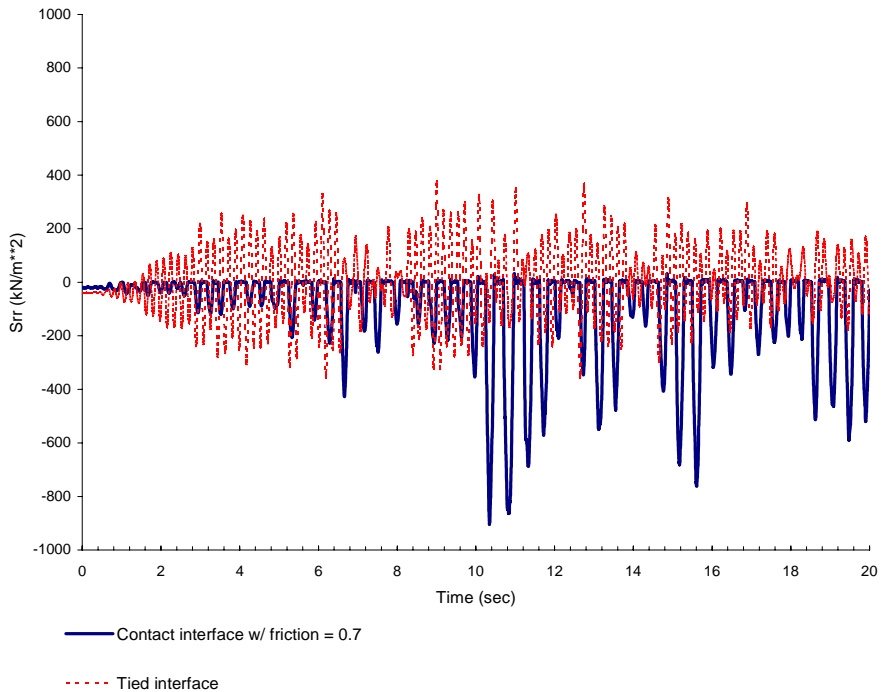


Figure 4.4.1-8 Comparison of Normal Pressure on the Head-on Soil Element near the Ground Surface Computed from the 11.5 m DOB Contact and Tied Interface Models.

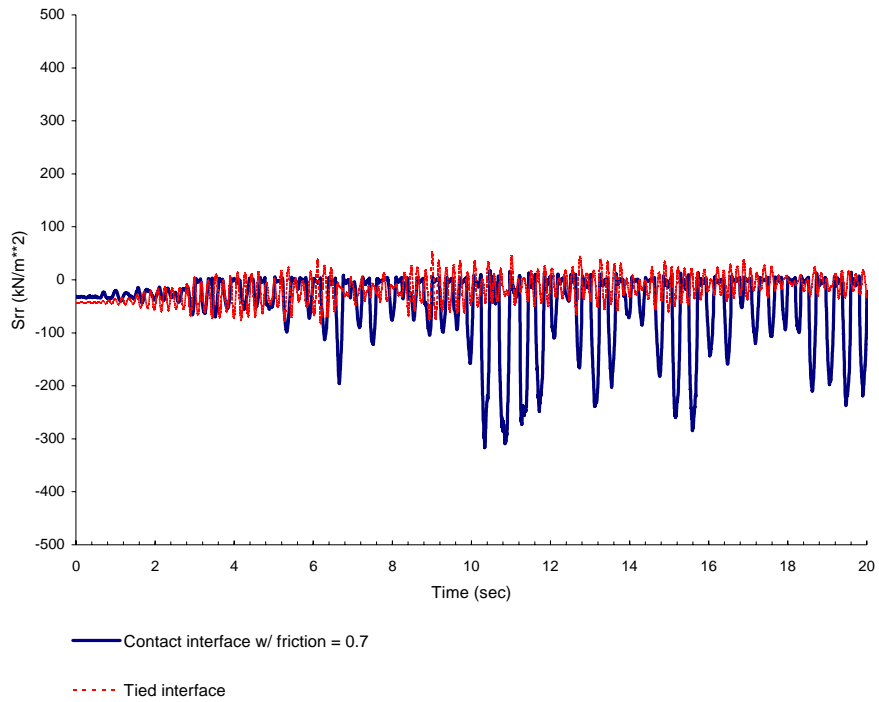


Figure 4.4.1-9 Comparison of Normal Pressure on the Head-on Soil Element near the Mid-height of Structural Wall Computed from the 11.5 m DOB Contact and Tied Interface Models.

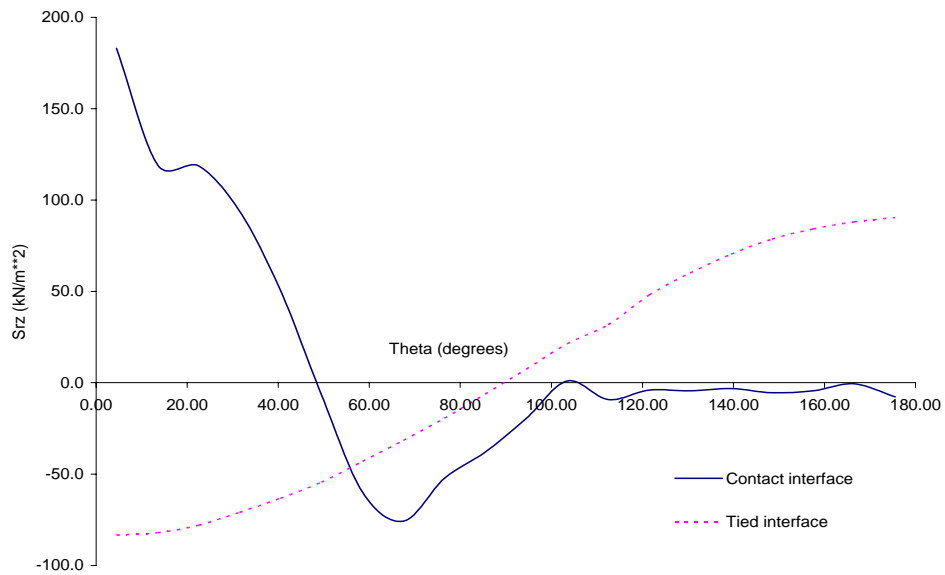


Figure 4.4.1-10 Comparison of Circumferential Distributions of Vertical Shear Computed from the 11.5 m DOB Contact and Tied Interface Models at Respective Mid-Height Peak S_{rr} Times.

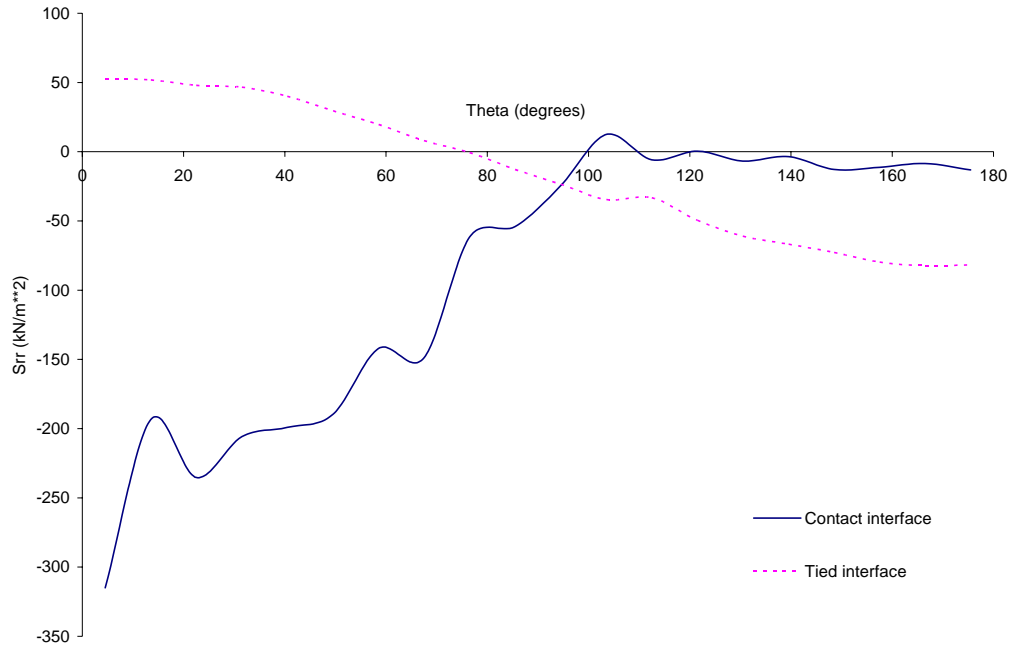


Figure 4.4.1-11 Comparison of Circumferential Distributions of Normal Pressures Computed from the 11.5 m DOB Contact and Tied Interface Models at Respective Mid-Height Peak S_{rr} Times.

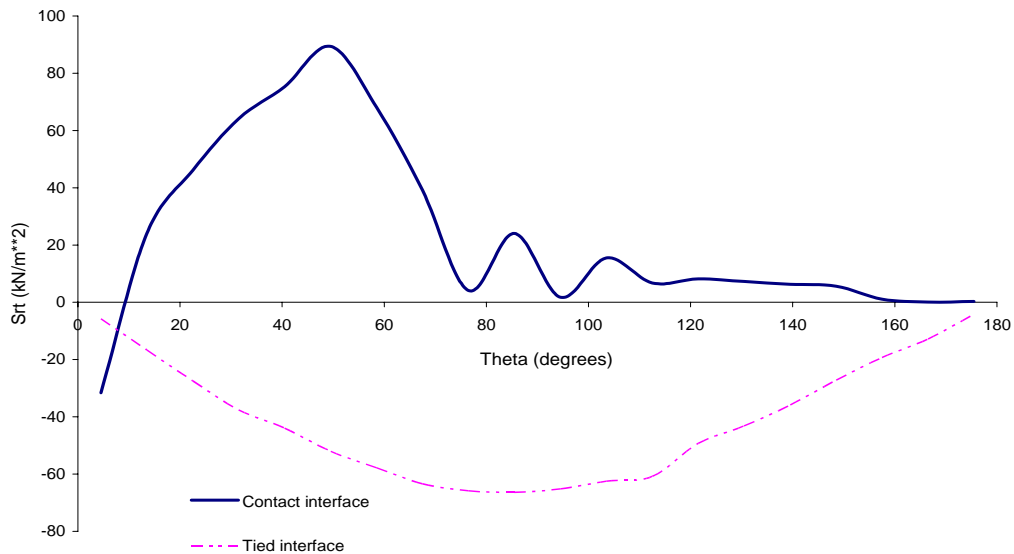


Figure 4.4.1-12 Comparison of Circumferential Distributions of Tangential Shear Pressures Computed from the 11.5 m DOB Contact and Tied Interface Models at Respective Mid-Height Peak S_{rt} Times.

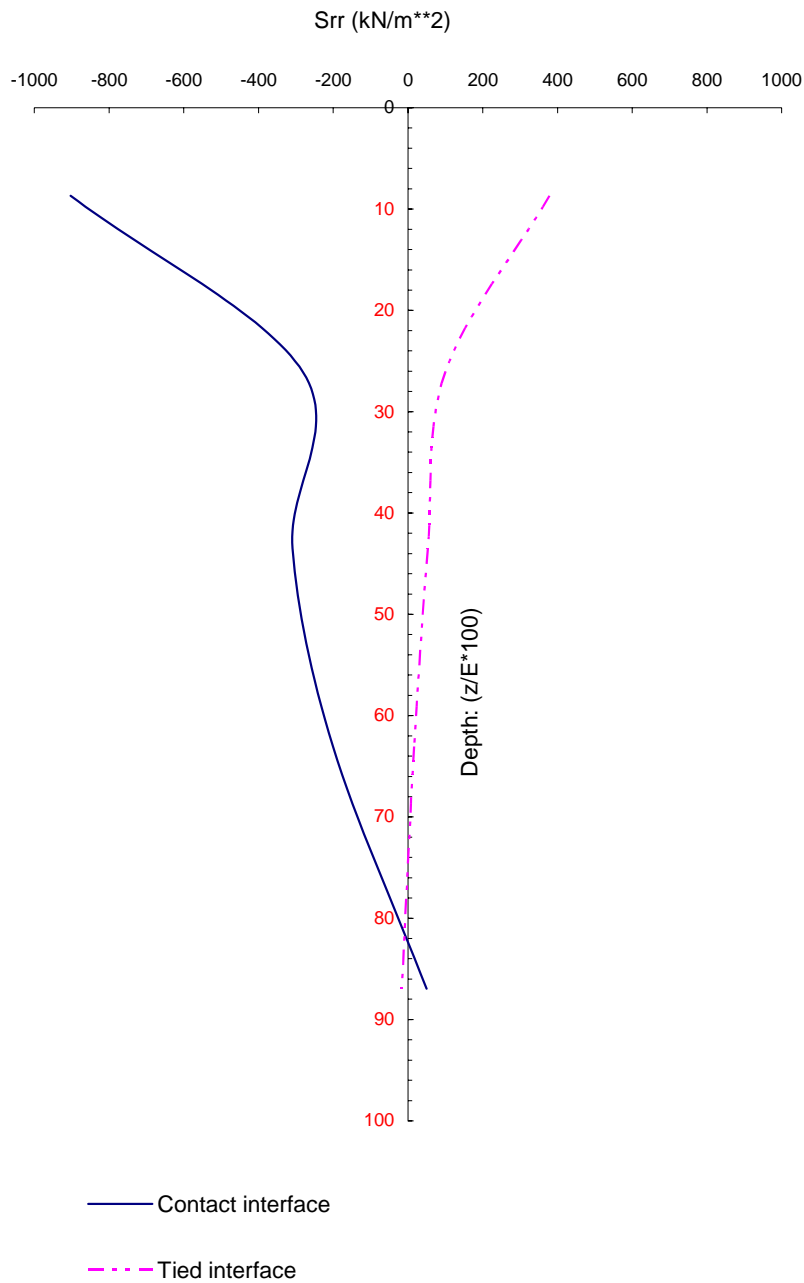


Figure 4.4.1-13 Comparison of Vertical Distributions of Normal Pressures Computed from the 11.5 m DOB Contact and Tied Interface Models at Respective Surface Peak S_{rr} Times.

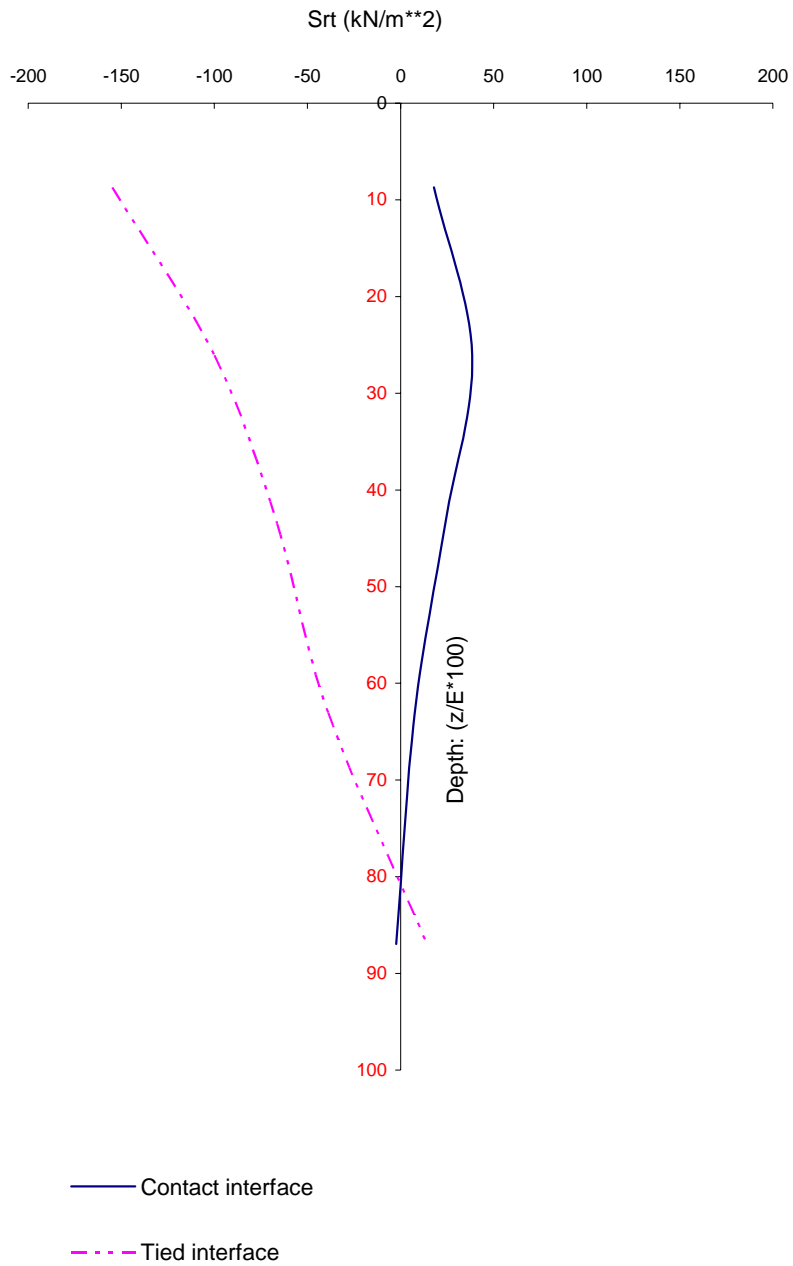


Figure 4.4.1-14 Comparison of Vertical Distributions of Tangential Computed from the 11.5 m DOB Contact and Tied Interface Models at Respective Surface Peak S_{rt} Times.

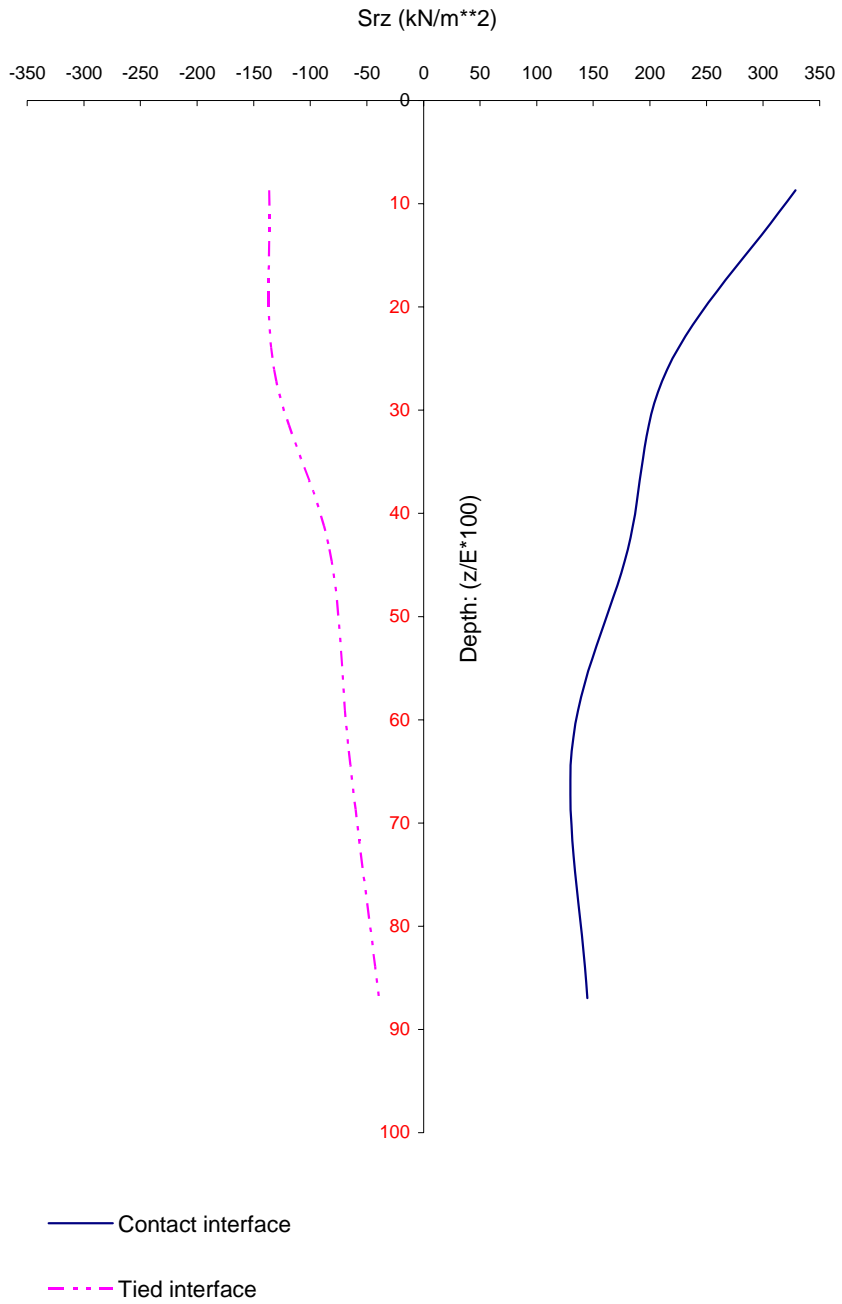


Figure 4.4.1-15 Comparison of Vertical Distributions of Vertical Shear Computed from the 11.5 m DOB Contact and Tied Interface Models at Respective Surface Peak S_{rr} Times.

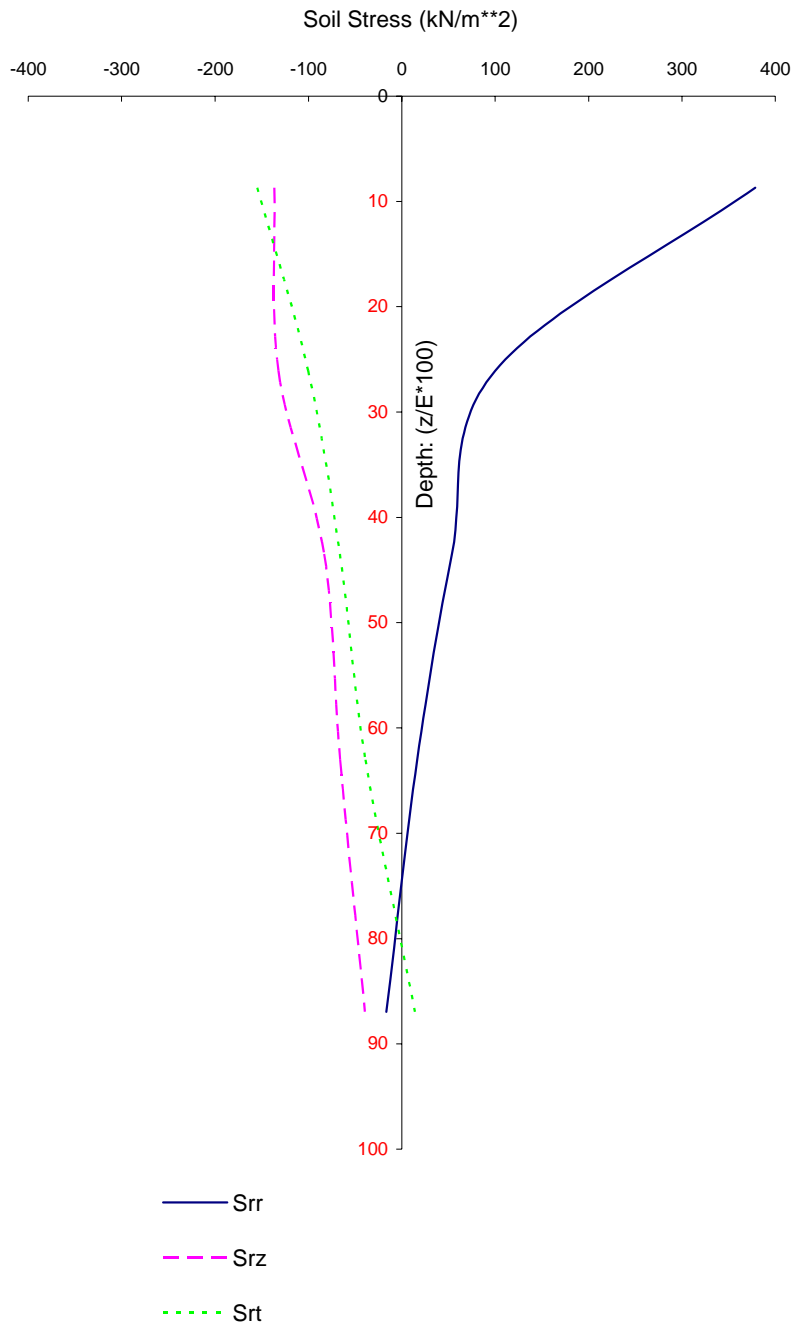


Figure 4.4.1-16 Vertical Distributions of Soil Stresses Computed from the 11.5 m DOB Tied Interface Model at Surface Peak S_{rr} Times.

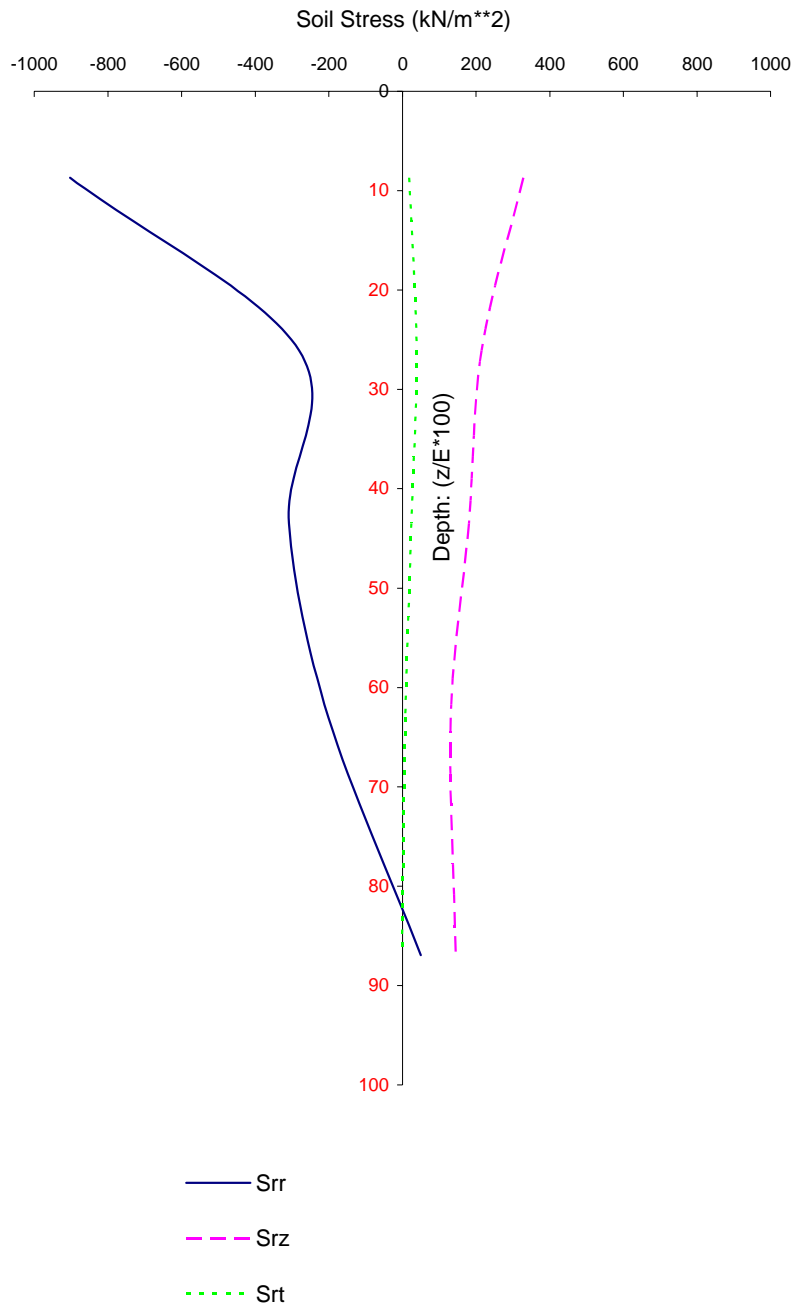


Figure 4.4.1-17 Vertical Distributions of Soil Stresses Computed from the 11.5 m DOB Contact Interface Model at Surface Peak S_{rr} Times.

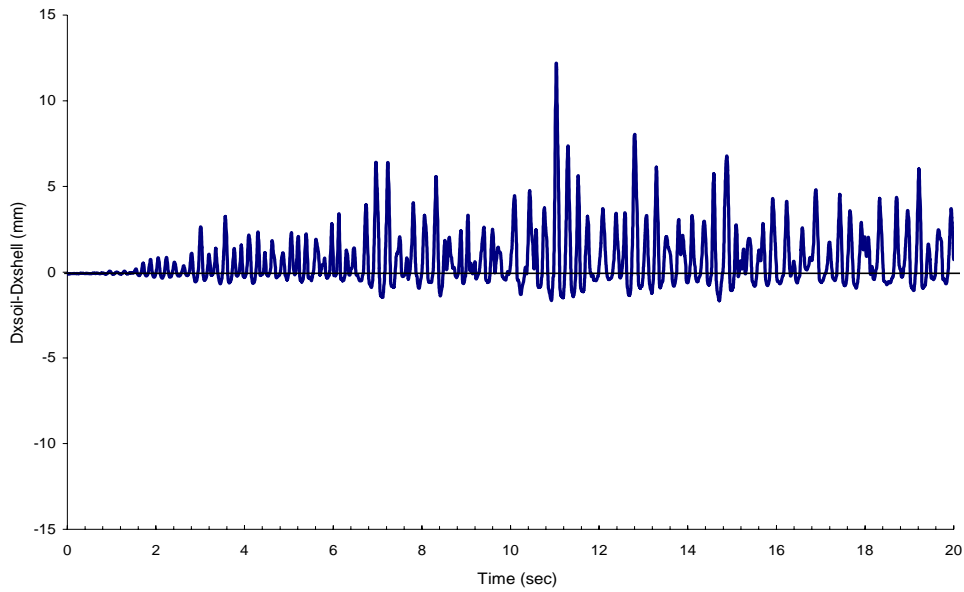


Figure 4.4.2-1 Relative Lateral Displacement of Structural Wall and Surrounding Soil at the Interface near ground Surface ($\theta=0$) from the 23 m DOB Contact Interface Model.

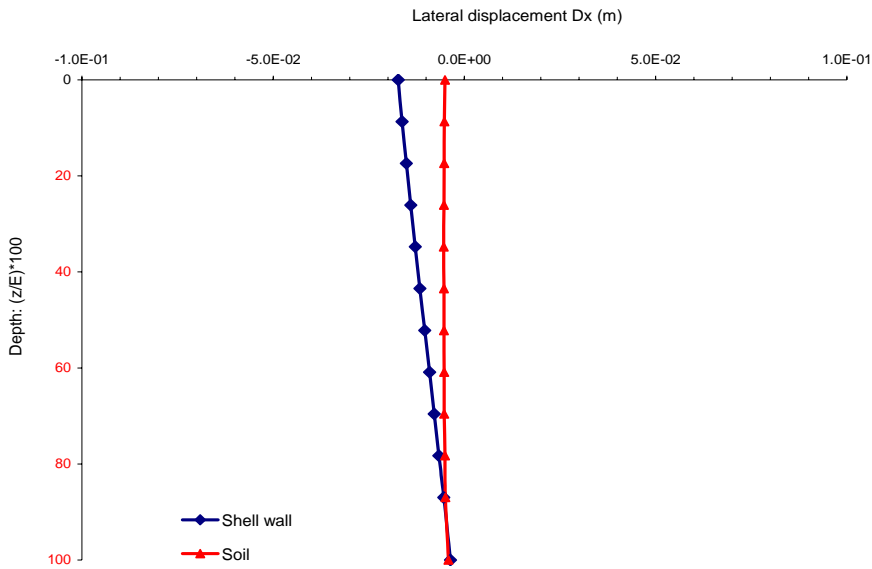


Figure 4.4.2-2 Vertical Distribution of Lateral Displacements of Structural Wall and Surrounding Soil at the Interface ($\theta=0$) from the 23 m DOB Contact Interface Model Computed at 11.03 Seconds.

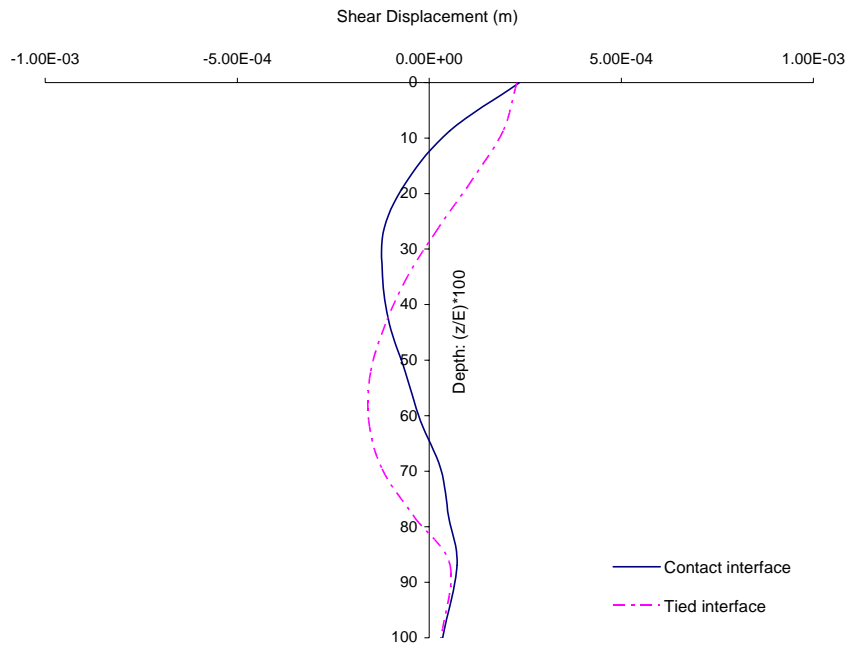


Figure 4.4.2-3 Comparison of Lateral Wall Shear Displacements Computed from the 23 m DOB Contact and Tied Interface Models Computed at 11.03 Seconds.

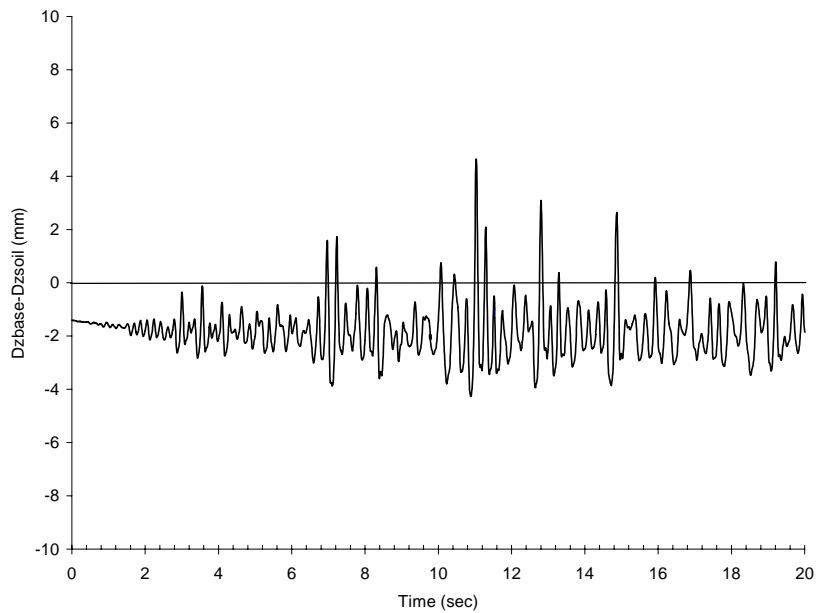


Figure 4.4.2-4 Vertical Displacements of Structural Foundation Relative to the Base Soil Computed from the 23 m DOB Contact Interface Models at Theta = 0.

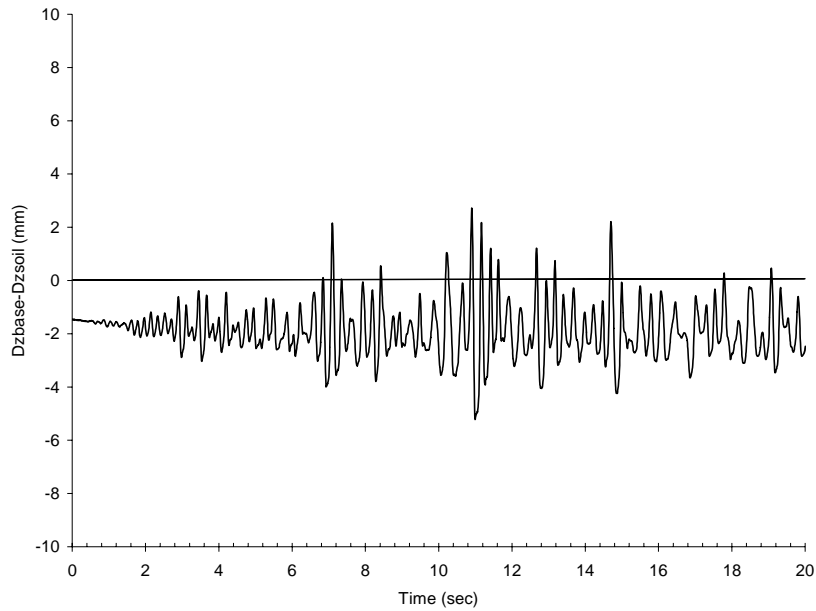


Figure 4.4.2-5 Vertical Displacements of Structural Foundation Relative to the Base Soil Computed from the 23 m DOB Contact Interface Models at Theta = 180.

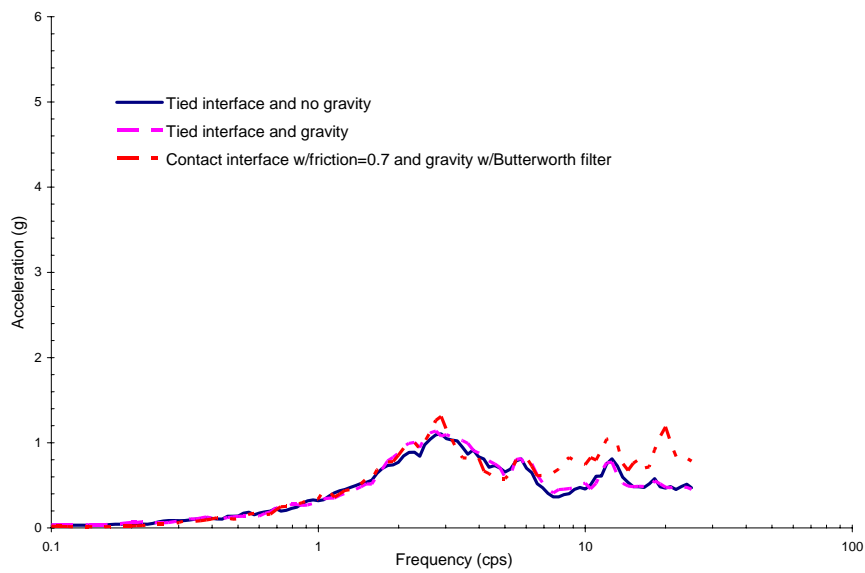


Figure 4.4.2-6 Comparison of Response Spectra at the Base for the 23 m DOB with Various LS-DYNA Models.

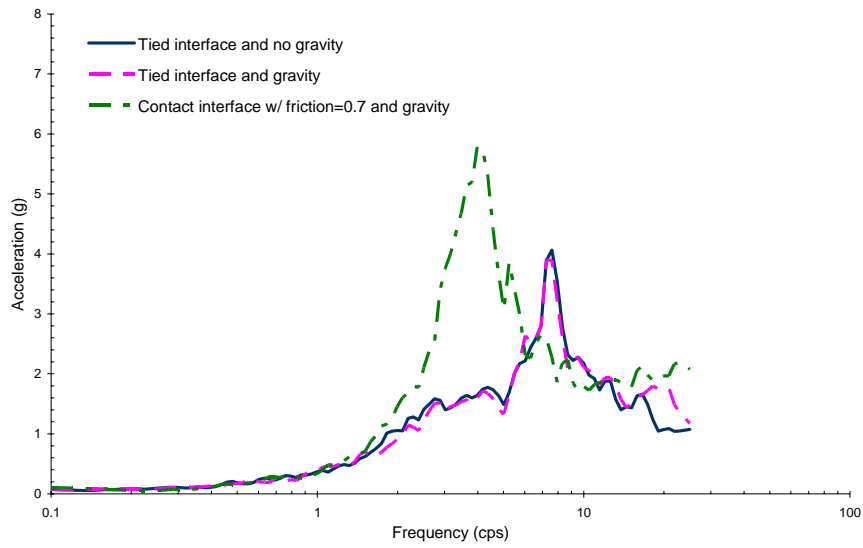


Figure 4.4.2-7 Comparison of Response Spectra at the Roof for the 23 m DOB with Various LS-DYNA Models.

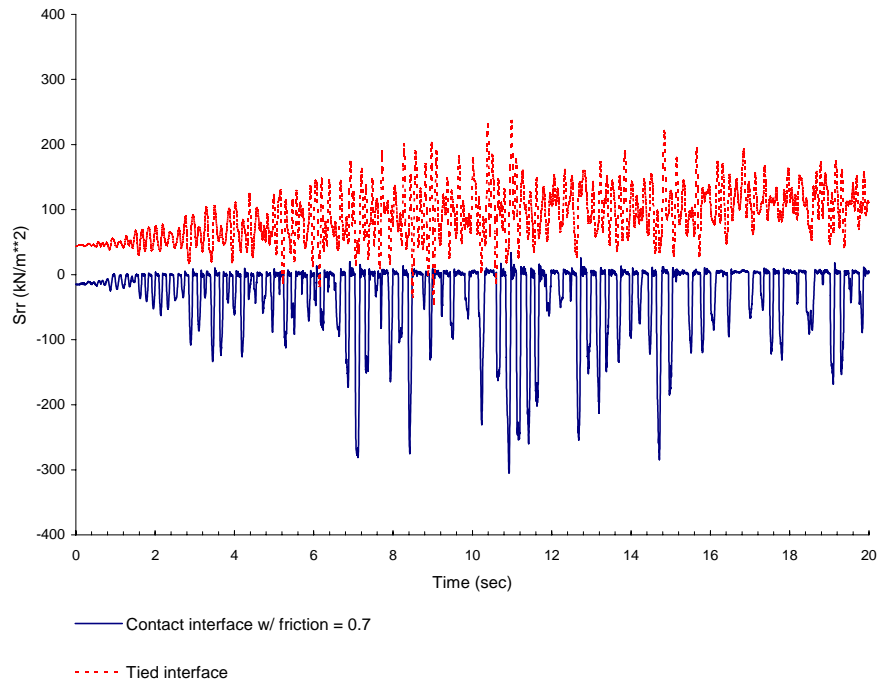


Figure 4.4.2-8 Comparison of Normal Pressure on the Head-on Soil Element near the Ground Surface Computed from the 23 m DOB Contact and Tied Interface Models.

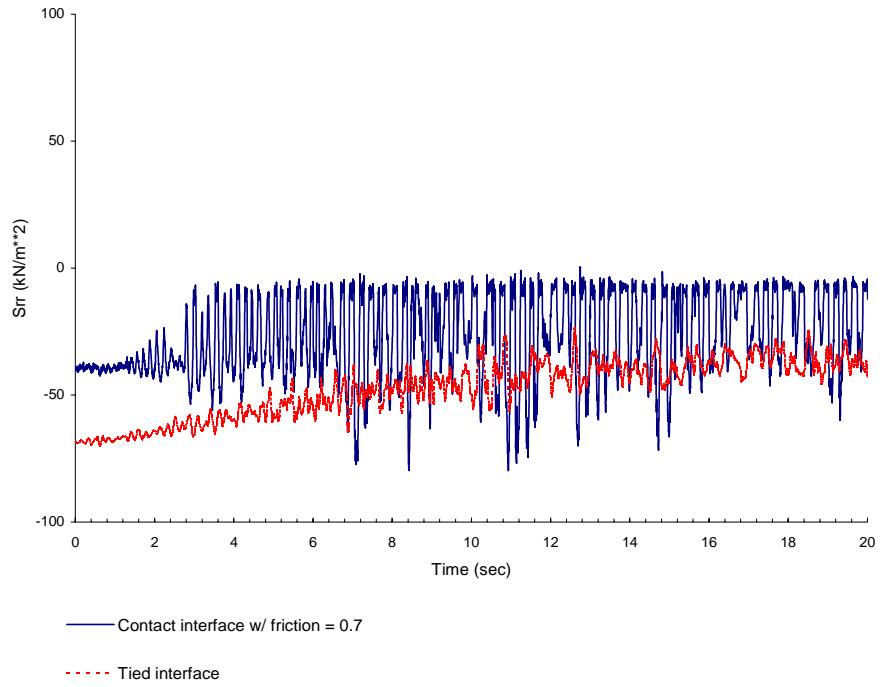


Figure 4.4.2-9 Comparison of Normal Pressure on the Head-on Soil Element near the Mid-height of Structural Wall Computed from the 23 m DOB Contact and Tied Interface Models.

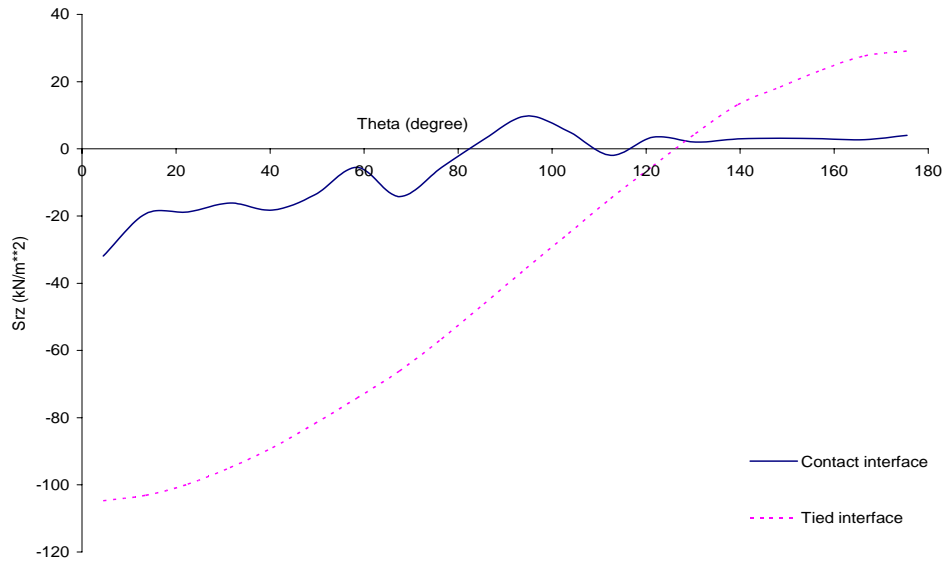


Figure 4.4.2-10 Comparison of Circumferential Distributions of Vertical Shear Computed from the 23 m DOB Contact and Tied Interface Models at Respective Mid-Height Peak S_{rr} Times.

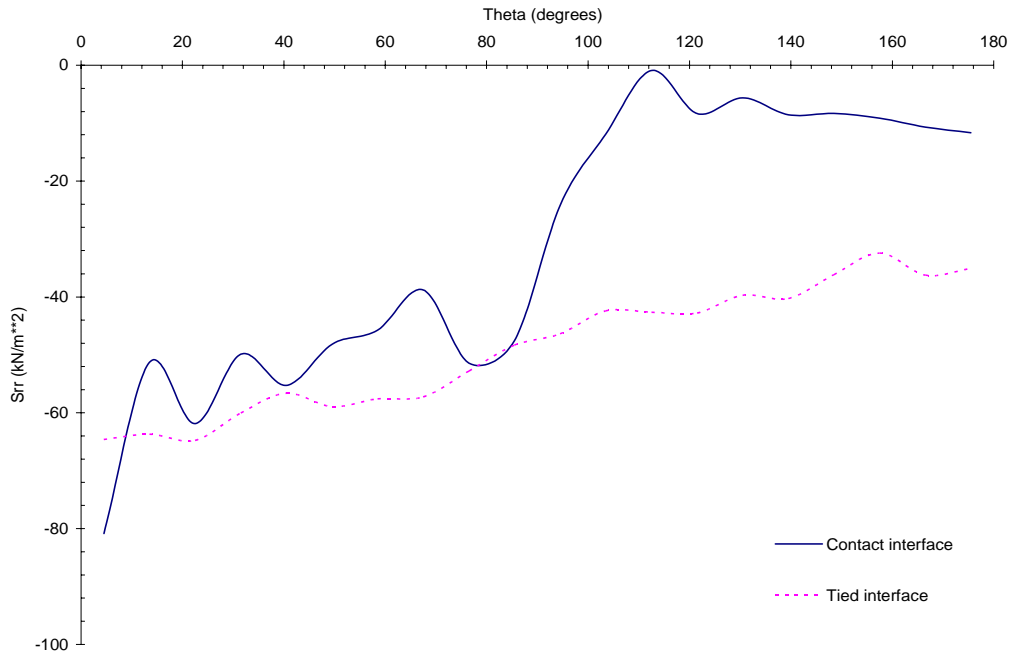


Figure 4.4.2-11 Comparison of Circumferential Distributions of Normal Pressures Computed from the 23 m DOB Contact and Tied Interface Models at Respective Mid-Height Peak S_{rr} Times.

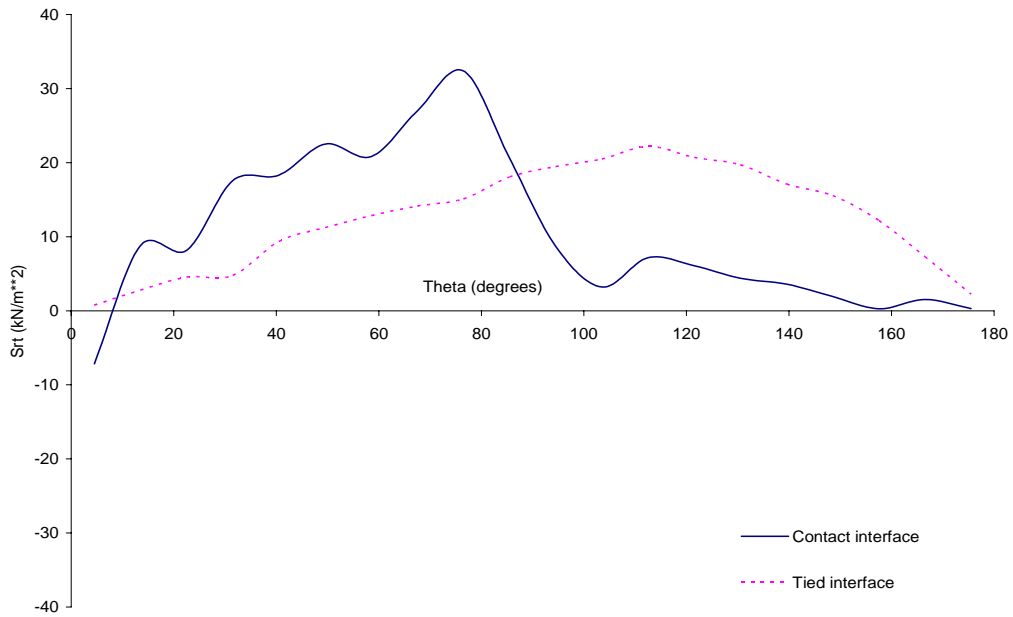


Figure 4.4.2-12 Comparison of Circumferential Distributions of Tangential Shear Computed from the 23 m DOB Contact and Tied Interface Models at Respective Mid-Height Peak S_{rr} Times.

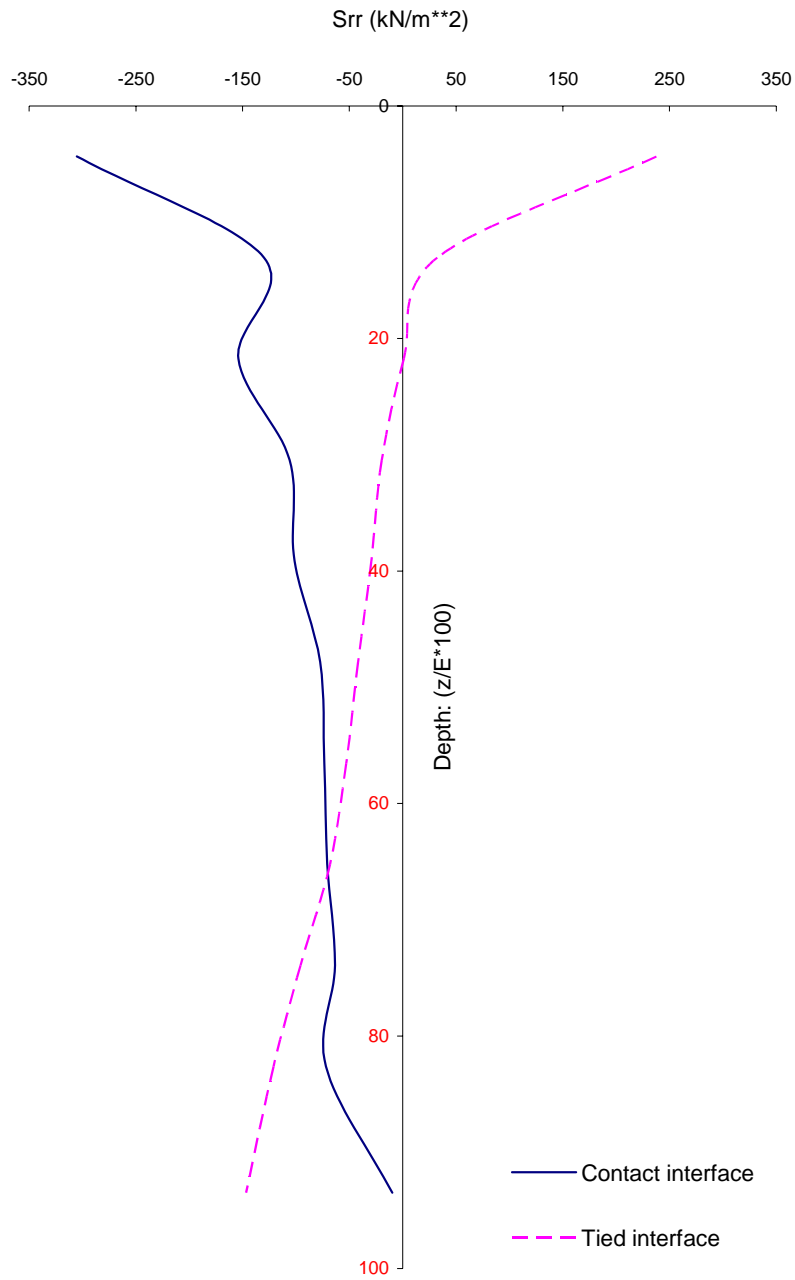


Figure 4.4.2-13 Comparison of Vertical Distributions of Normal Pressures Computed from the 23 m DOB Contact and Tied Interface Models at Respective Surface Peak S_{rr} Times.

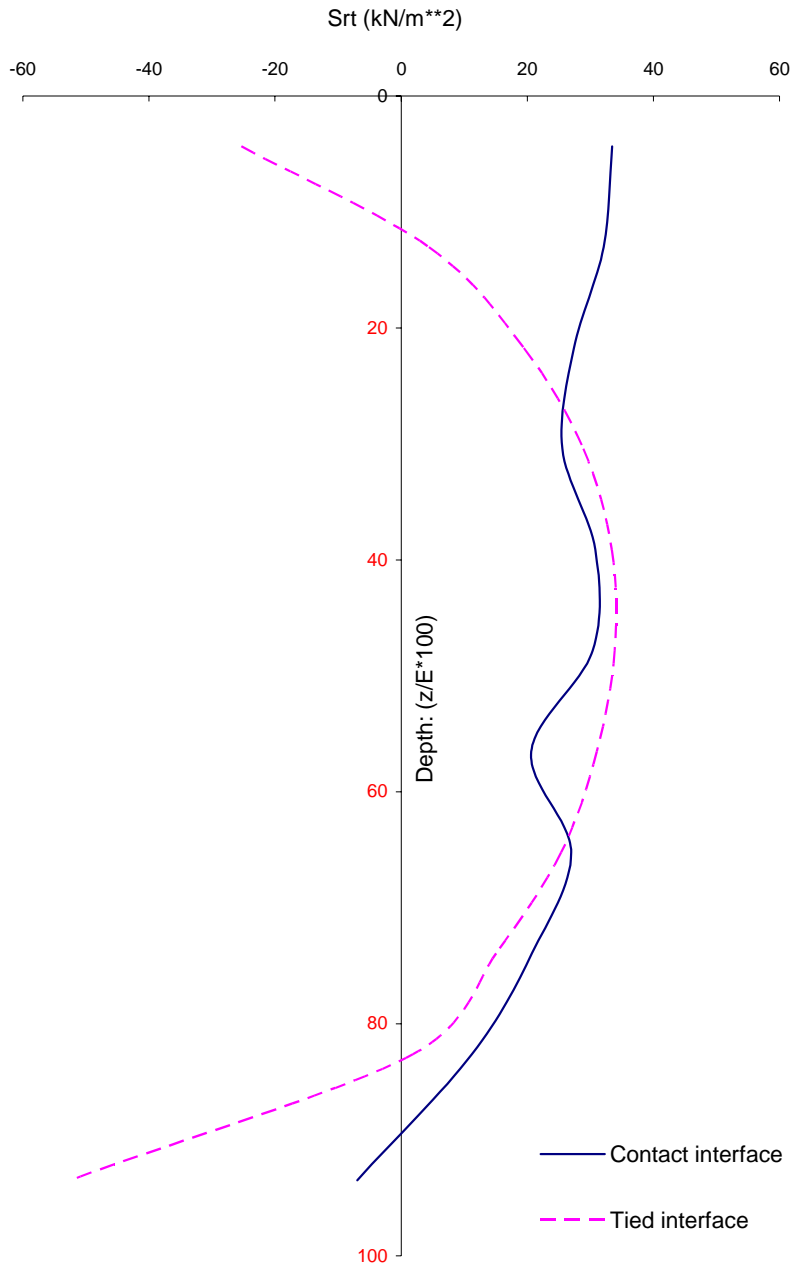


Figure 4.4.2-14 Comparison of Vertical Distributions of Tangential Shear Computed from the 23 m DOB Contact and Tied Interface Models at Respective Surface Peak S_{rt} Times.

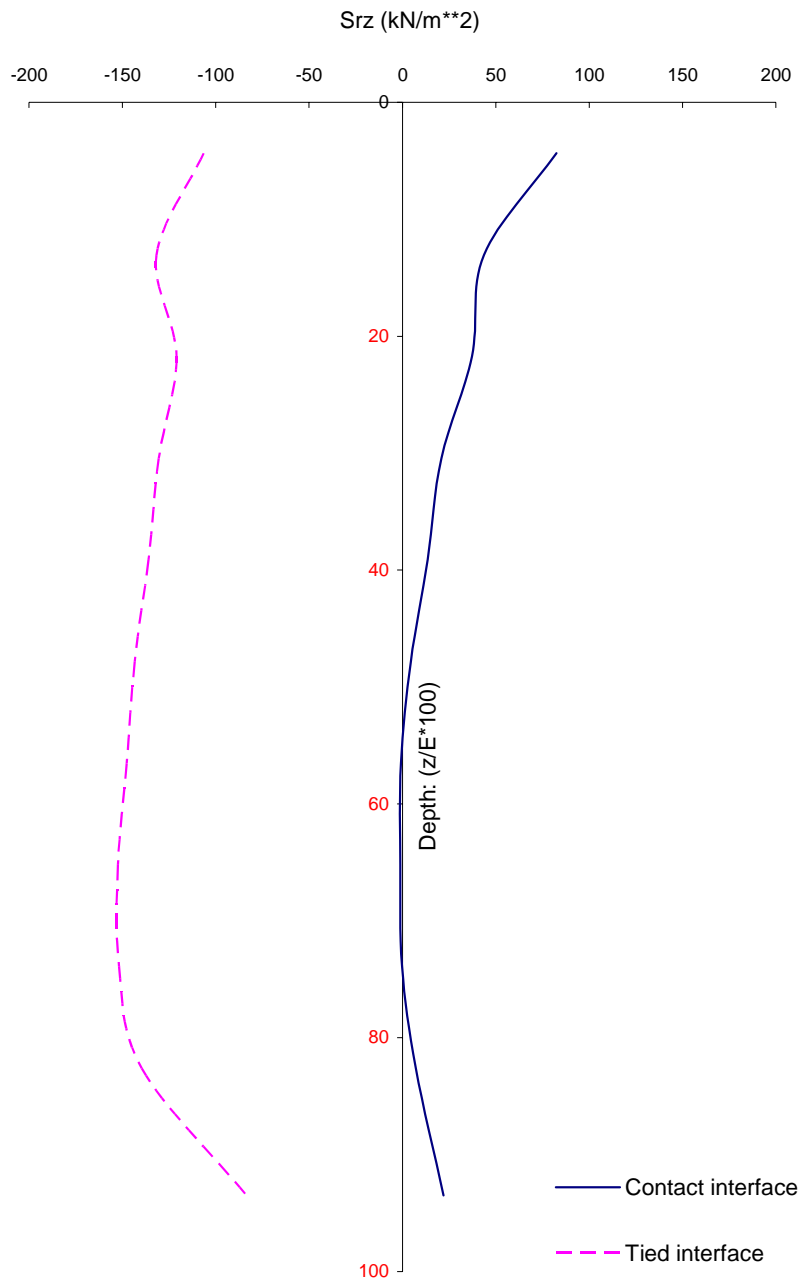


Figure 4.4.2-15 Comparison of Vertical Distributions of Vertical Shear Computed from the 23 m DOB Contact and Tied Interface Models at Respective Surface Peak S_{IT} Times.

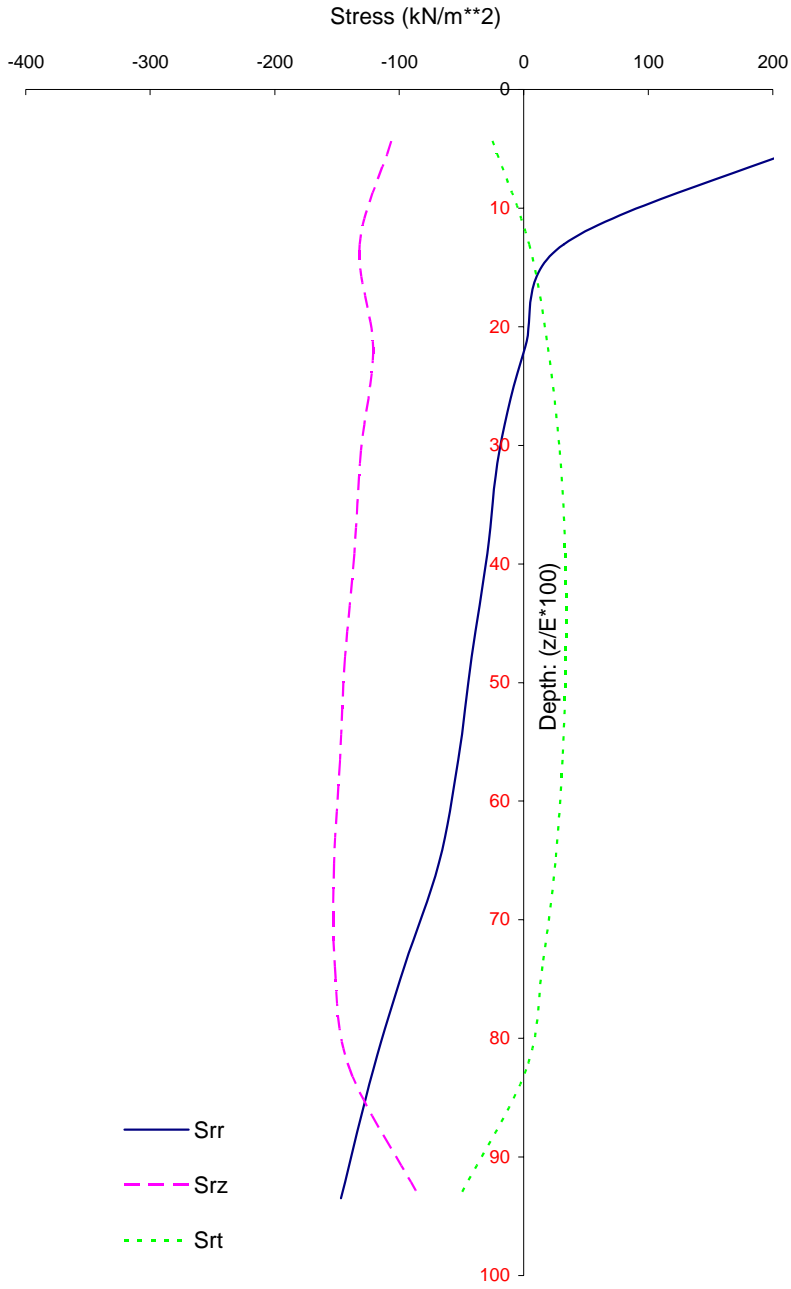


Figure 4.4.2-16 Vertical Distributions of Soil Stress Computed from the 23 m DOB Tied Interface Model at Surface Peak S_{rr} Time.

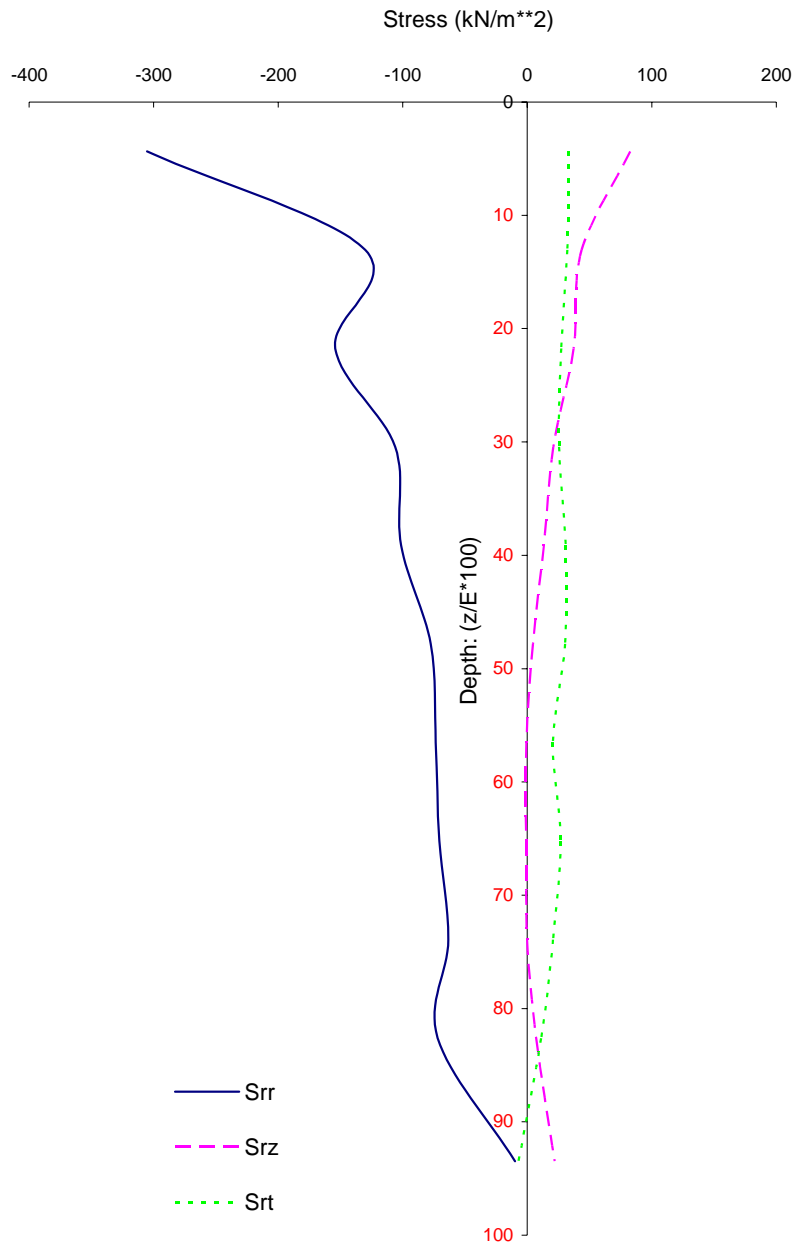


Figure 4.4.2-17 Vertical Distributions of Soil Stresses Computed from the 23 m DOB Contact Interface Model at Surface Peak S_{rr} Times.

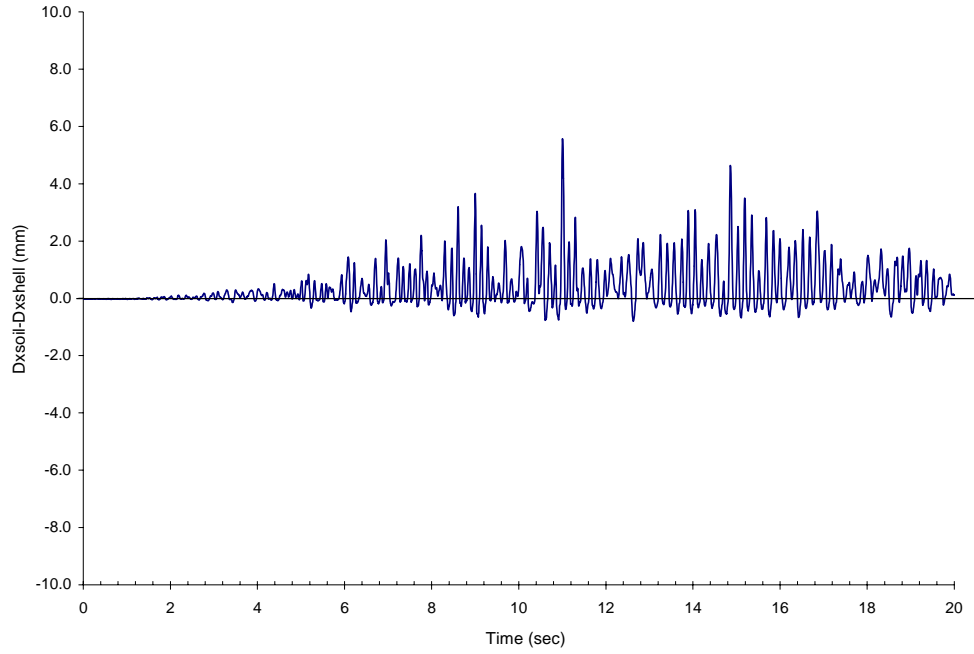


Figure 4.4.3-1 Relative Lateral Displacement of Structural Wall and Surrounding Soil at the Interface near ground Surface ($\theta=0$) from the 34.5 m DOB Contact Interface Model.

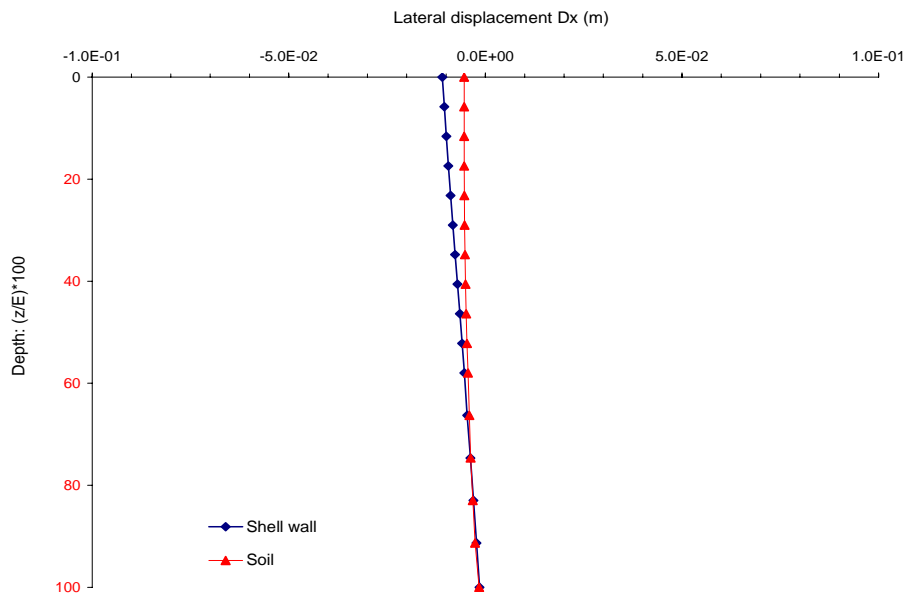


Figure 4.4.3-2 Vertical Distribution of Lateral Displacements of Structural Wall and Surrounding Soil at the Interface ($\theta=0$) from the 34.5 m DOB Contact Interface Model at 11 Seconds.

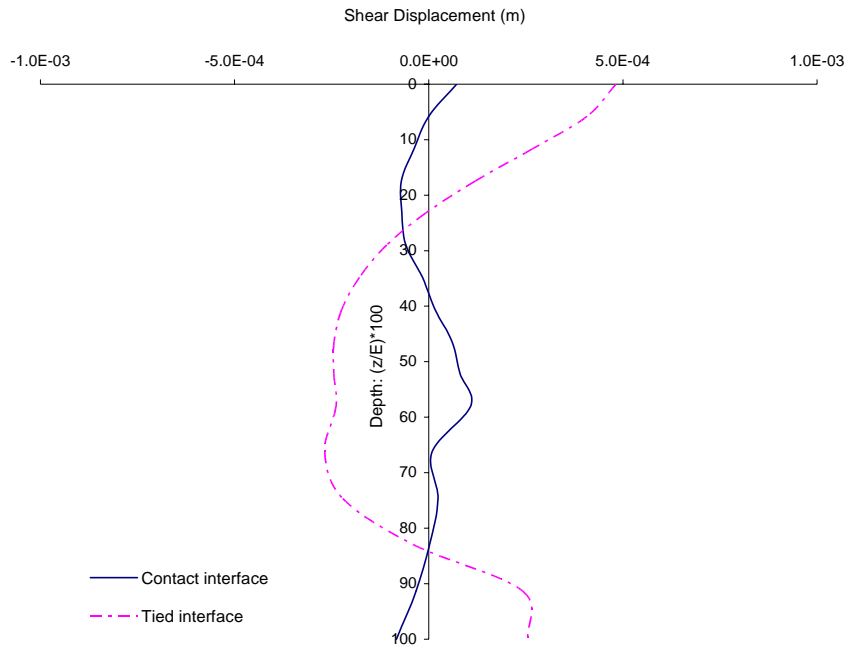


Figure 4.4.3-3 Comparison of Lateral Wall Shear Displacements Computed from the 34.5 m DOB Contact and Tied Interface Models at 11 Seconds.

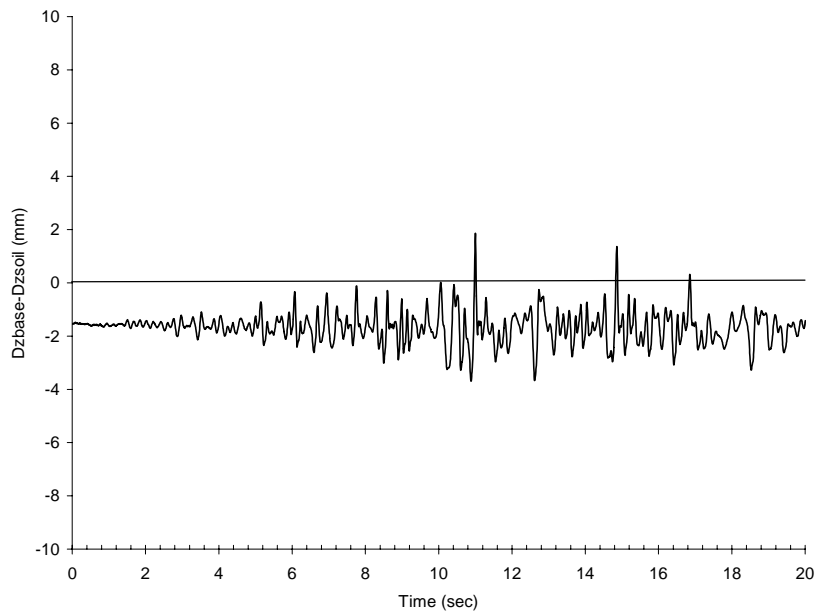


Figure 4.4.3-4 Vertical Displacements of Structural Foundation Relative to the Base Soil Computed from the 34.5 m DOB Contact Interface Models at Theta = 0.

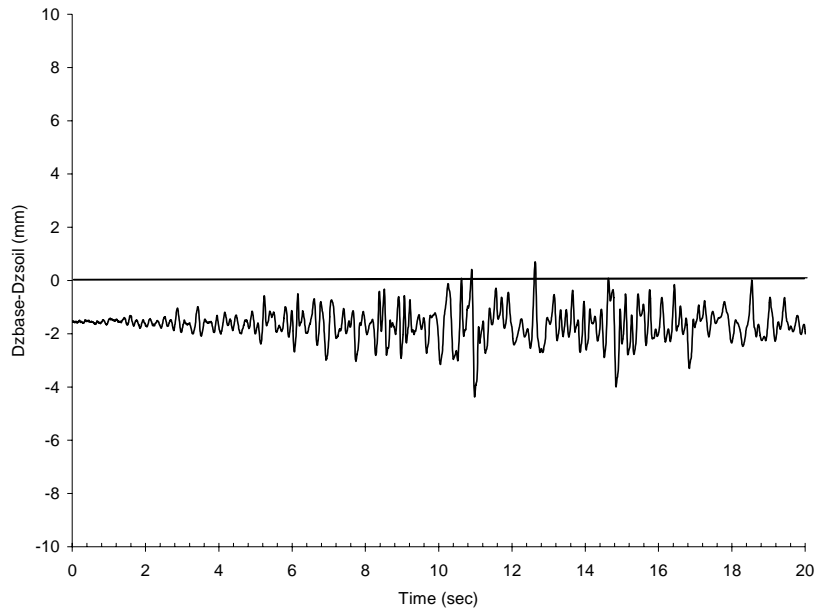


Figure 4.4.3-5 Vertical Displacements of Structural Foundation Relative to the Base Soil Computed from the 34.5 m DOB Contact Interface Models at Theta = 180.

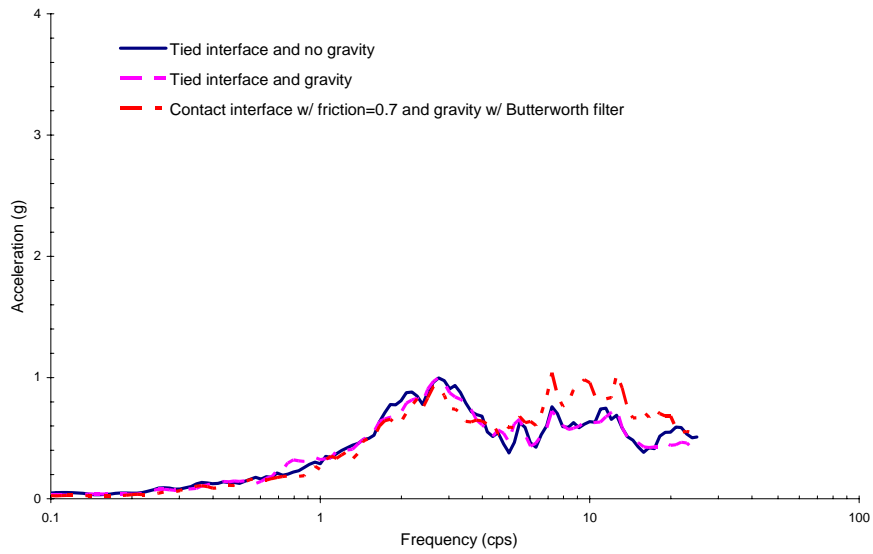


Figure 4.4.3-6 Comparison of Response Spectra at the Base for the 34.5 m DOB Computed with Various LS-DYNA Models.

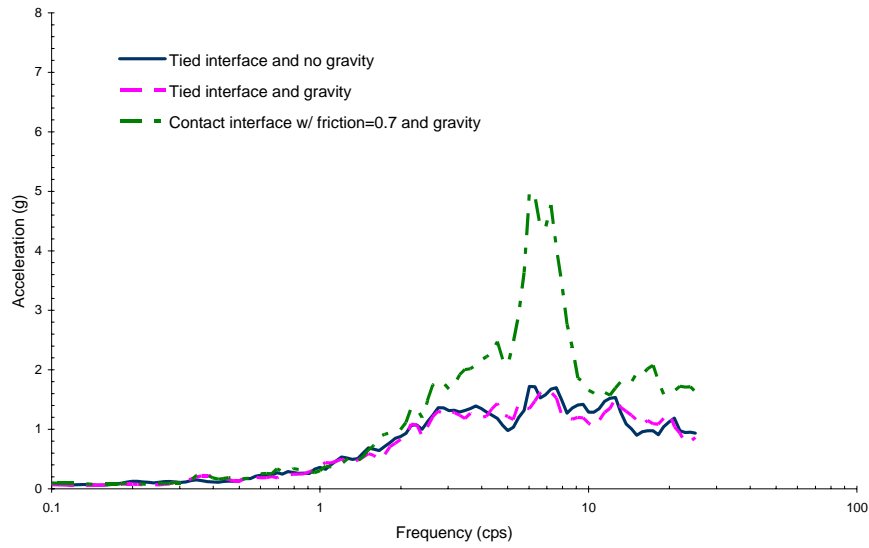


Figure 4.4.3-7 Comparison of Response Spectra at the Roof for the 34.5 m DOB Computed with Various LS-DYNA Models.

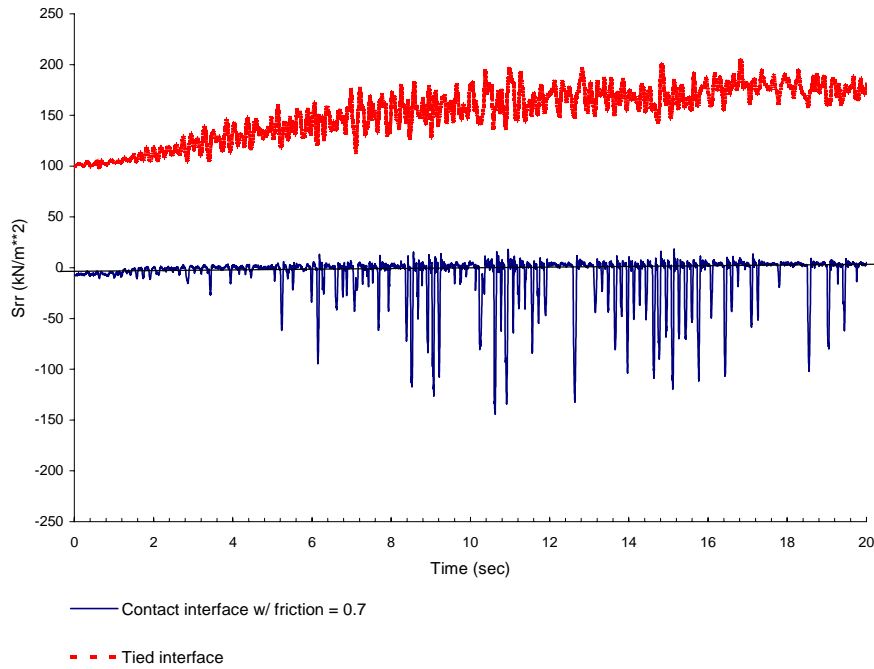


Figure 4.4.3-8 Comparison of Normal Pressure on the Head-on Soil Element near the Ground Surface Computed from the 34.5 m DOB Contact and Tied Interface Models.

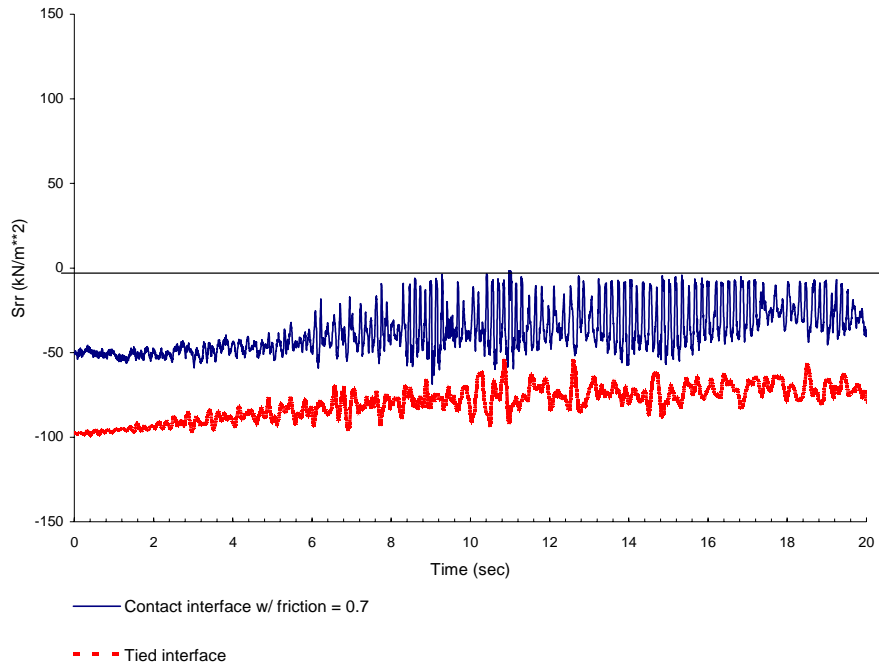


Figure 4.4.3-9 Comparison of Normal Pressure on the Head-on Soil Element near the Mid-height of Structural Wall Computed from the 34.5 m DOB Contact and Tied Interface Models.

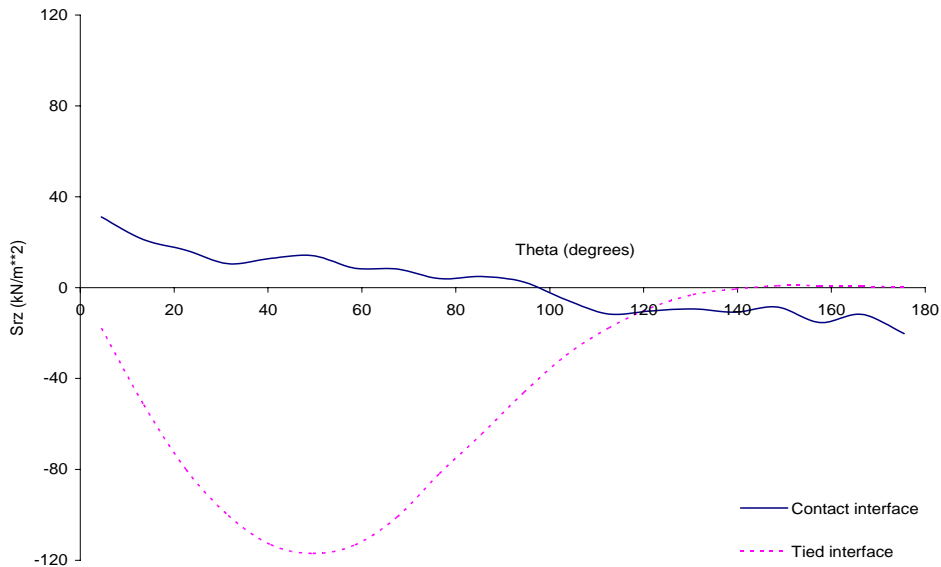


Figure 4.4.3-10 Comparison of Circumferential Distributions of Vertical Shear Computed from the 34.5 m DOB Contact and Tied Interface Models at Respective Mid-Height Peak S_{rr} Times.

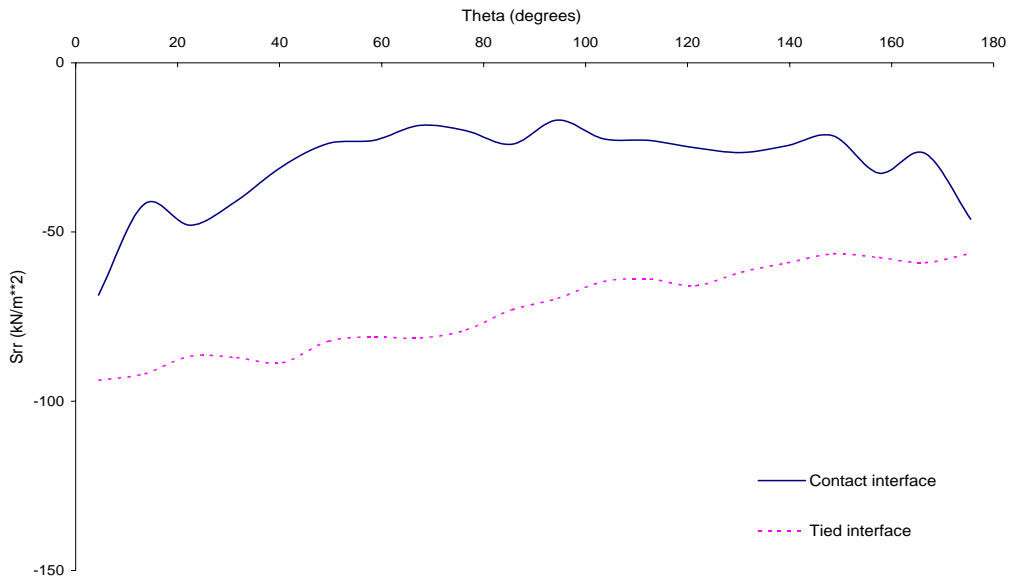


Figure 4.4.3-11 Comparison of Circumferential Distributions of Normal Pressures Computed from the 34.5 m DOB Contact and Tied Interface Models at Respective Mid-Height Peak S_{rr} Times.

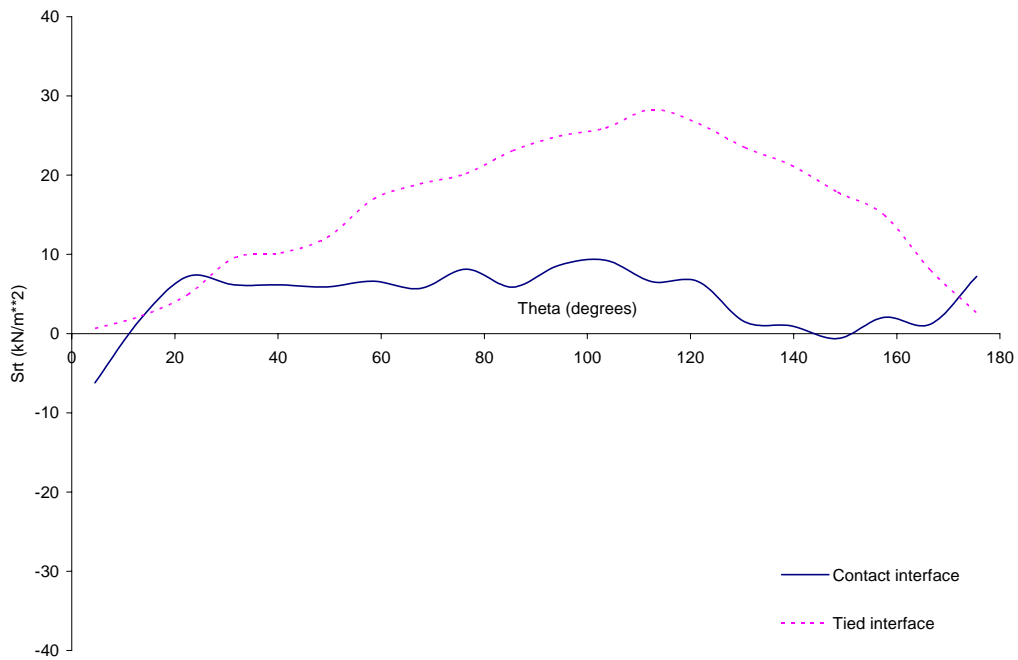


Figure 4.4.3-12 Comparison of Circumferential Distributions of Tangential Shear Computed from the 34.5 m DOB Contact and Tied Interface Models at Respective Mid-Height Peak S_{rt} Times.

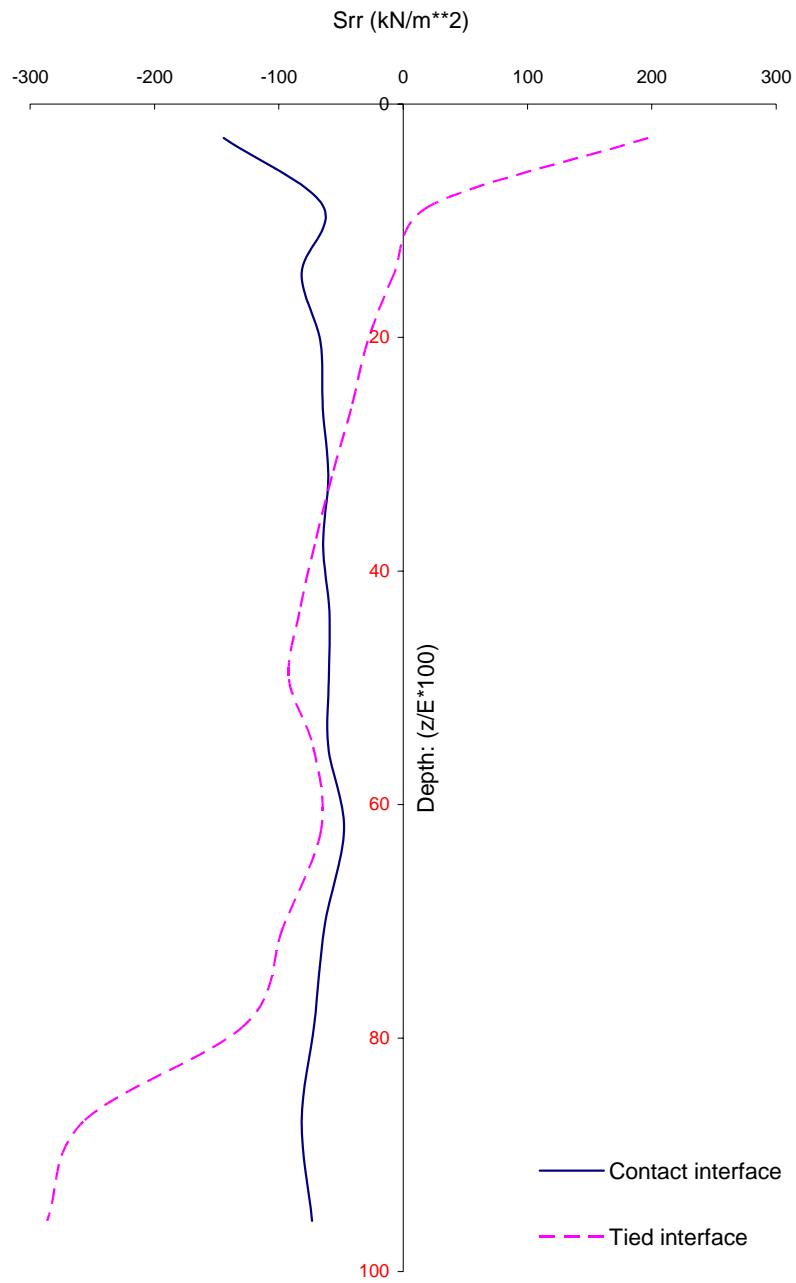


Figure 4.4.3-13 Comparison of Vertical Distributions of Normal Pressures Computed from the 34.5 m DOB Contact and Tied Interface Models at Respective Mid- Height Peak S_{rr} Times.

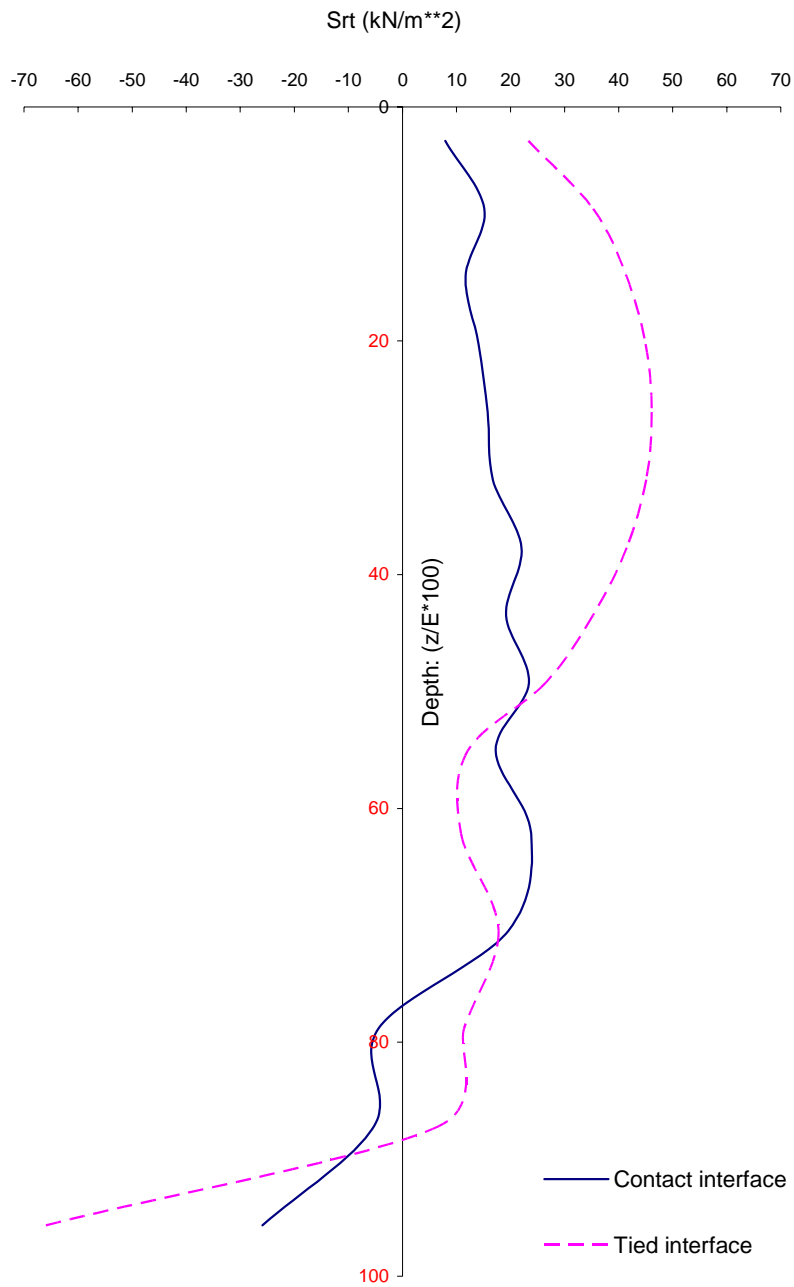


Figure 4.4.3-14 Comparison of Vertical Distributions of Tangential Shear Computed from the 34.5 m DOB Contact and Tied Interface Models at Respective Mid-Height Peak S_{rt} Times.



Figure 4.4.3-15 Comparison of Vertical Distributions of Vertical Shear Computed from the 34.5 m DOB Contact and Tied Interface Models at Respective Mid- Height Peak S_{rr} Times.

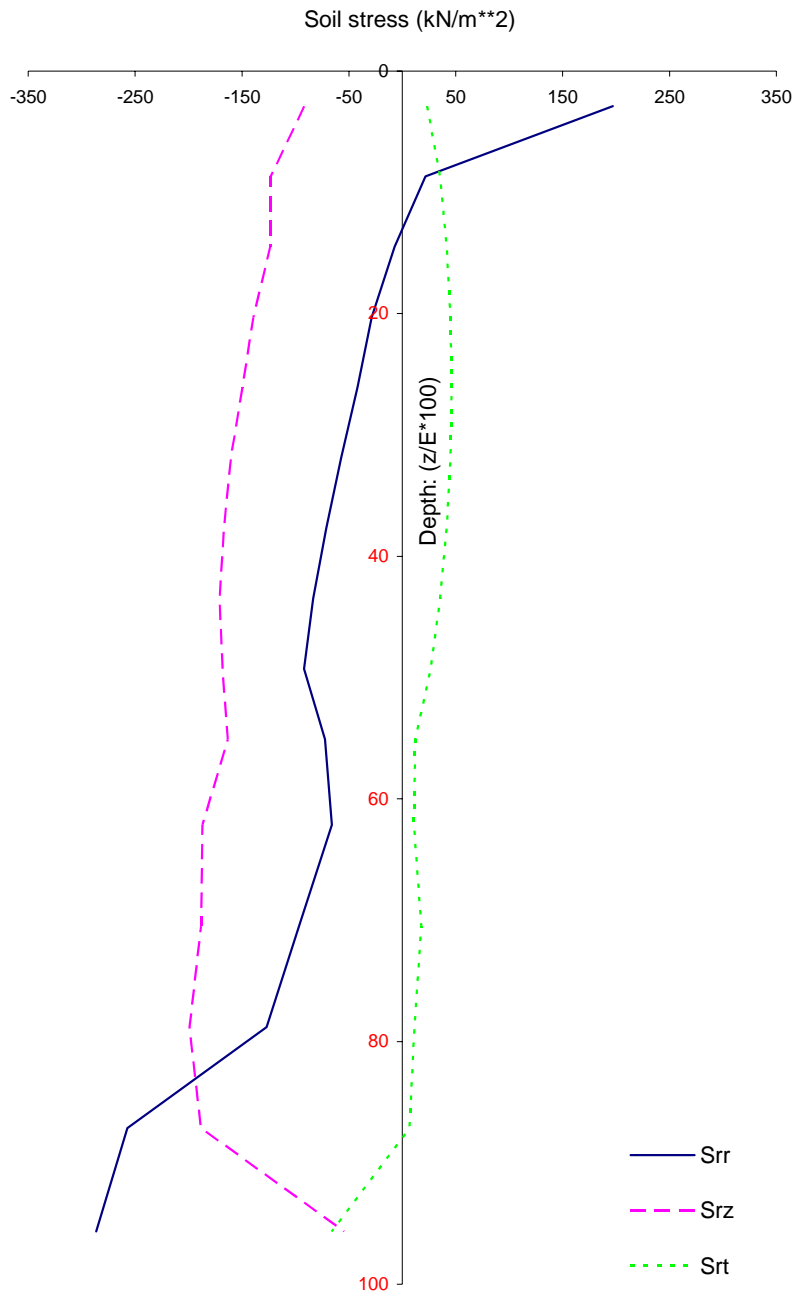


Figure 4.4.3-16 Vertical Distributions of Soil Stress Computed from the 34.5 m DOB Tied Interface Model at Surface Peak S_{rr} Times.

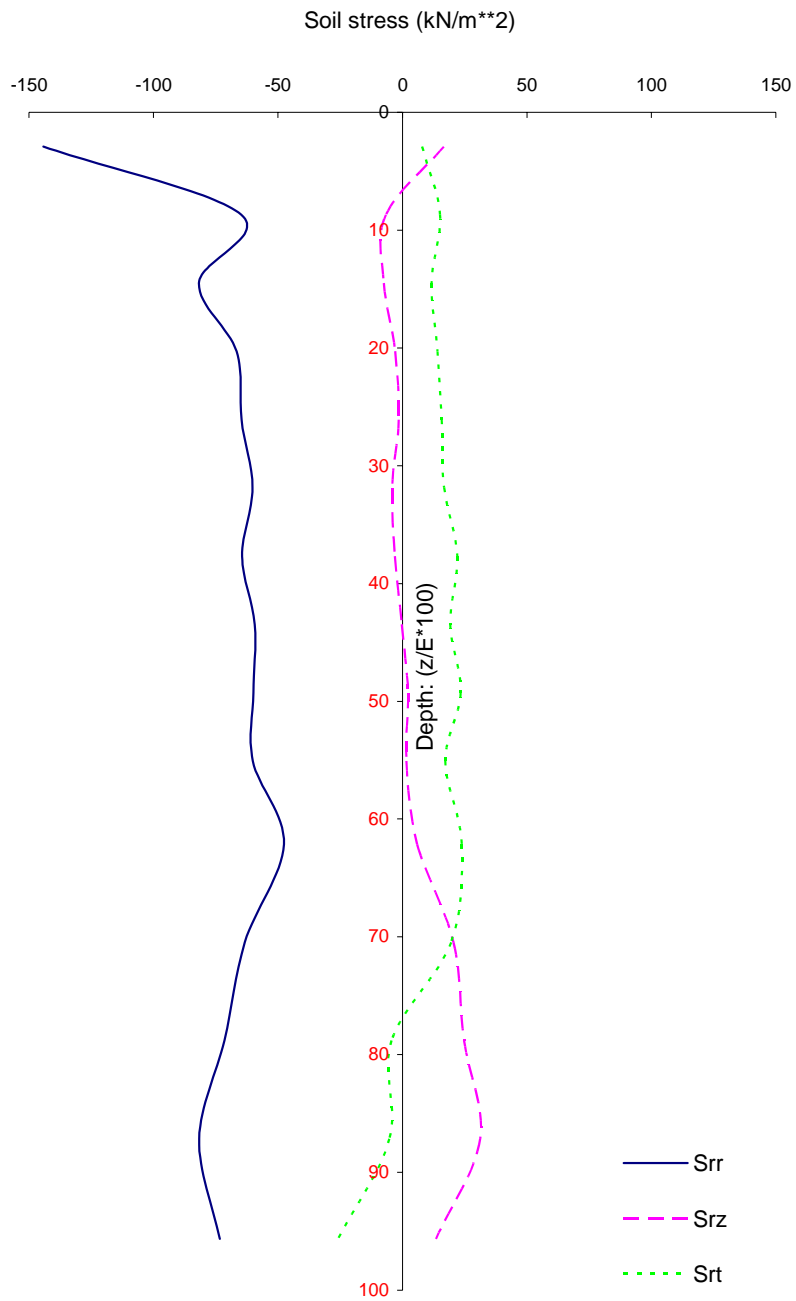


Figure 4.4.3-17 Vertical Distributions of Soil Stresses Computed from the 34.5 m DOB Contact Interface Model at Surface Peak S_{rr} Times.

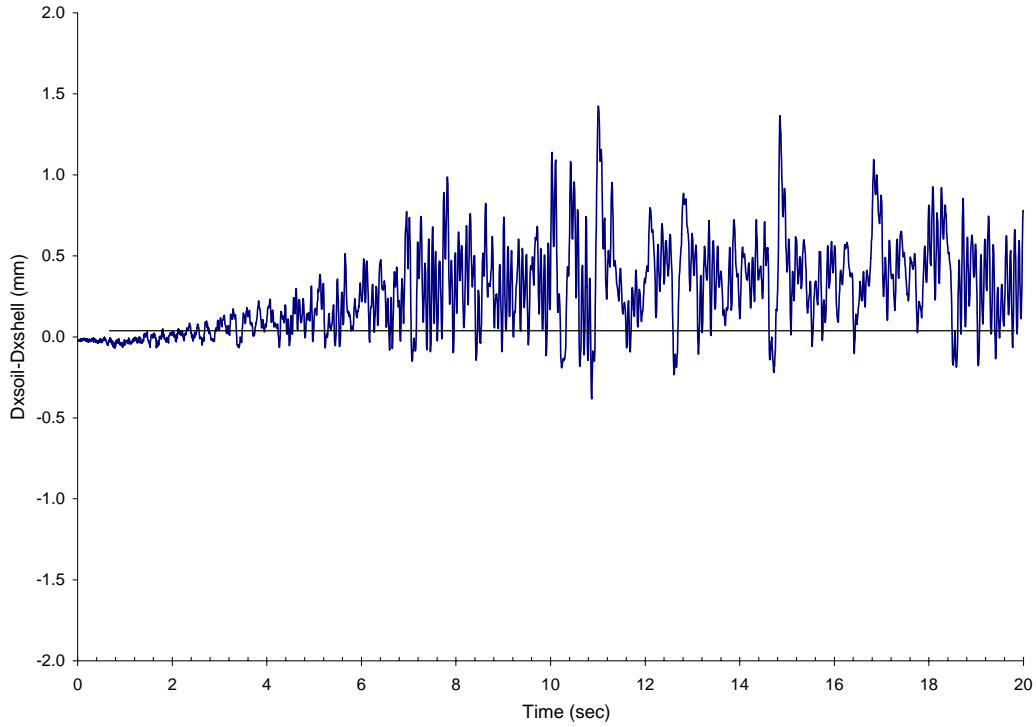


Figure 4.4.4-1 Relative Lateral Displacement of Structural Wall and Surrounding Soil at the Interface near ground Surface ($\theta=0$) from the 46 m DOB Contact Interface Model.

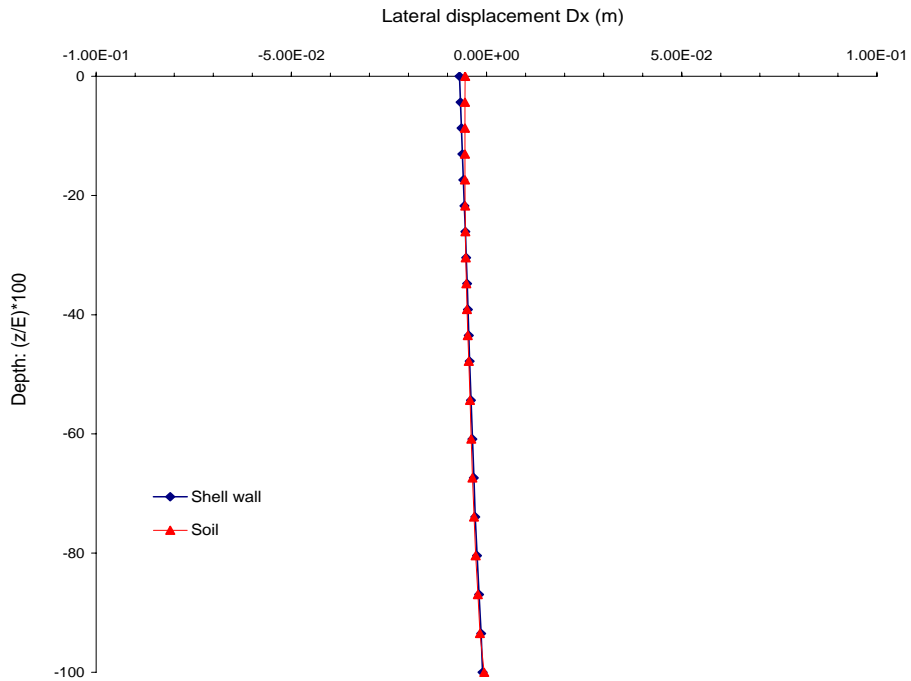


Figure 4.4.4-2 Vertical Distribution of Lateral Displacements of Structural Wall and Surrounding Soil at the Interface ($\theta=0$) from the 46 m DOB Contact Interface Model.

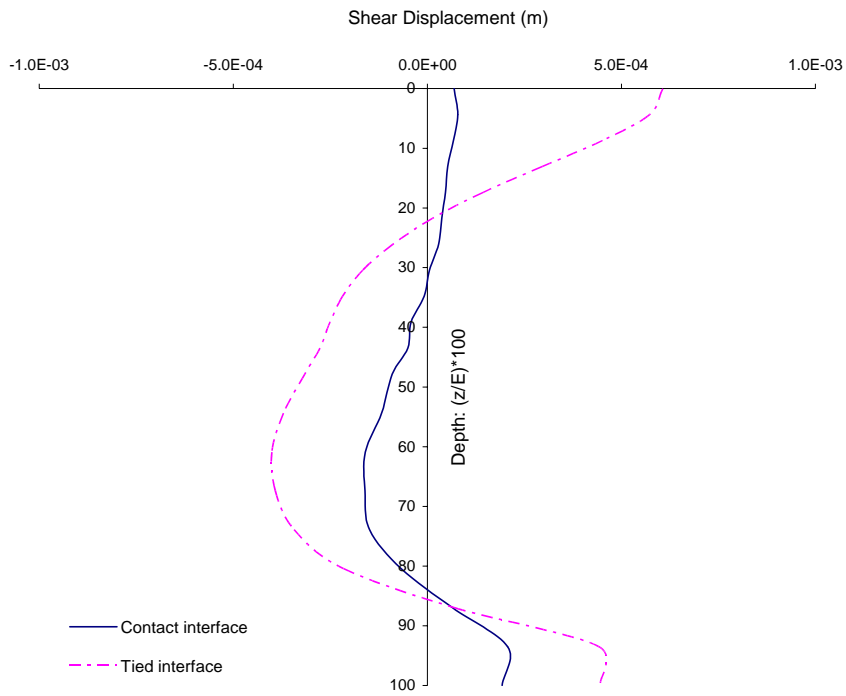


Figure 4.4.4-3 Comparison of Lateral Wall Shear Displacements Computed from the 46 m DOB Contact and Tied Interface Models.

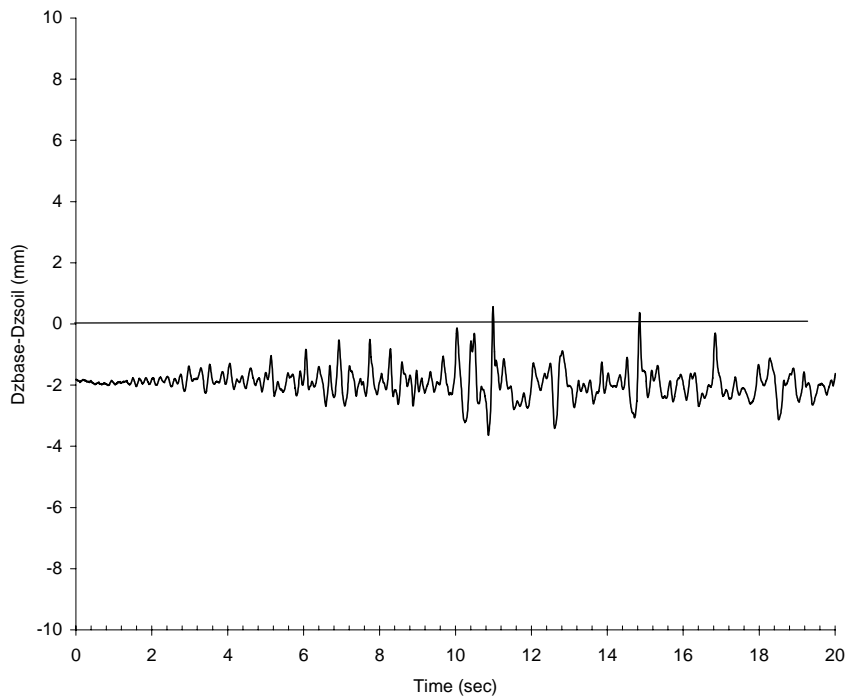


Figure 4.4.4-4 Vertical Displacements of Structural Foundation Relative to the Base Soil Computed from the 46 m DOB Contact Interface Models at Theta = 0.

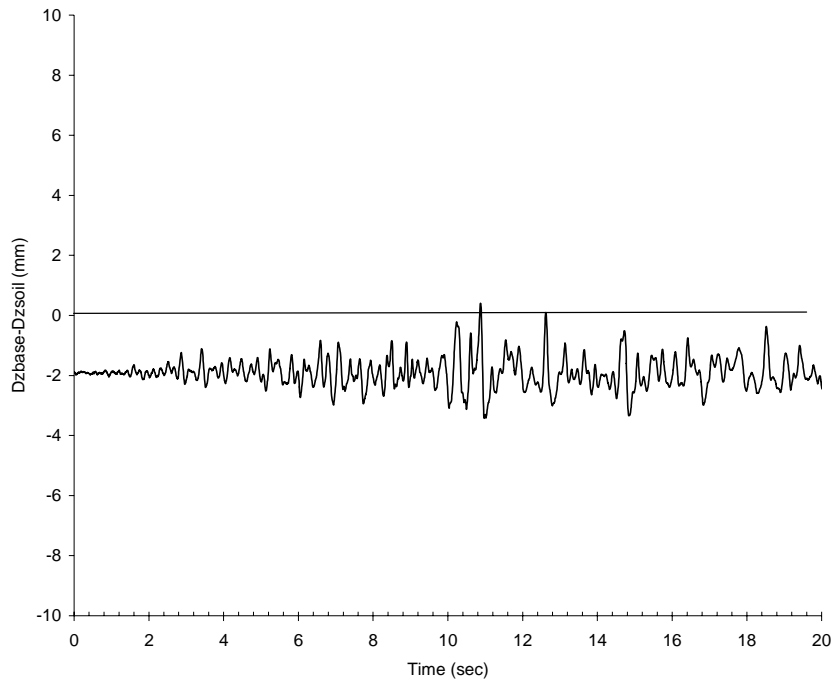


Figure 4.4.4-5 Vertical Displacements of Structural Foundation Relative to the Base Soil Computed from the 46 m DOB Contact Interface Models at Theta = 180.

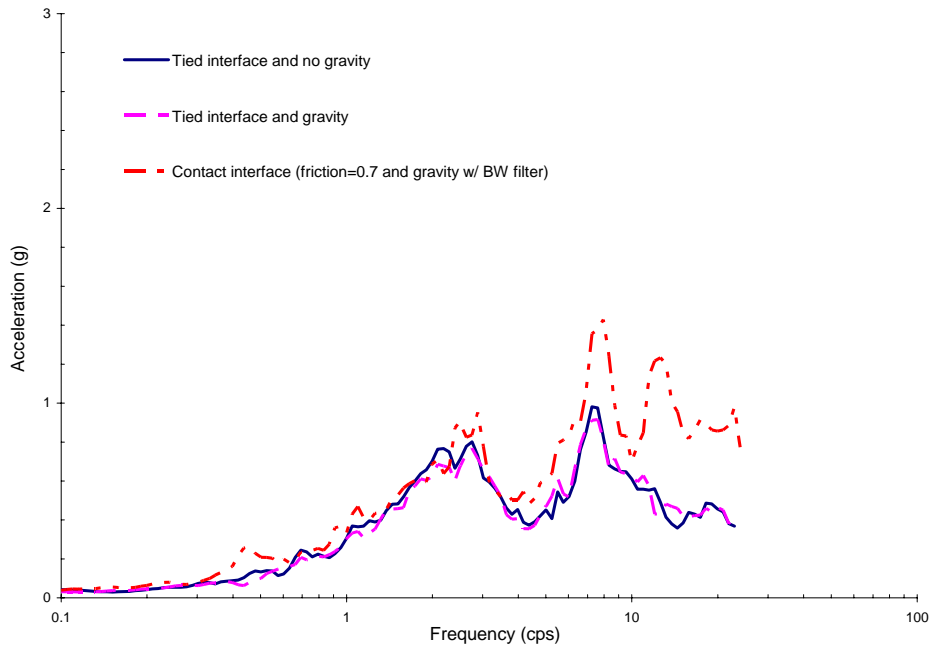


Figure 4.4.4-6 Comparison of Response Spectra at the Base for the 46 m DOB.

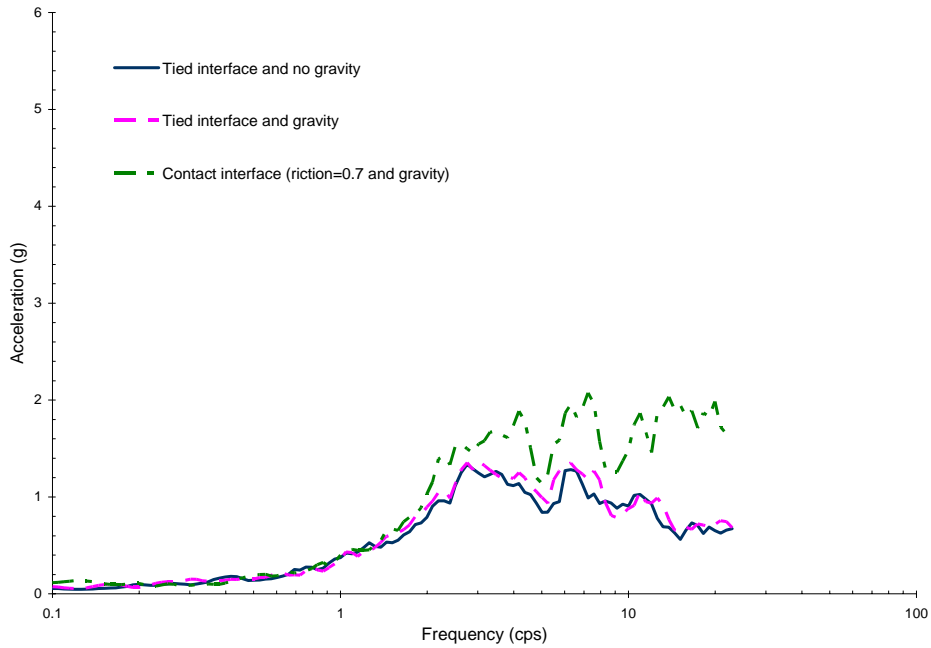


Figure 4.4.4-7 Comparison of Response Spectra at the Roof for the 46 m DOB.

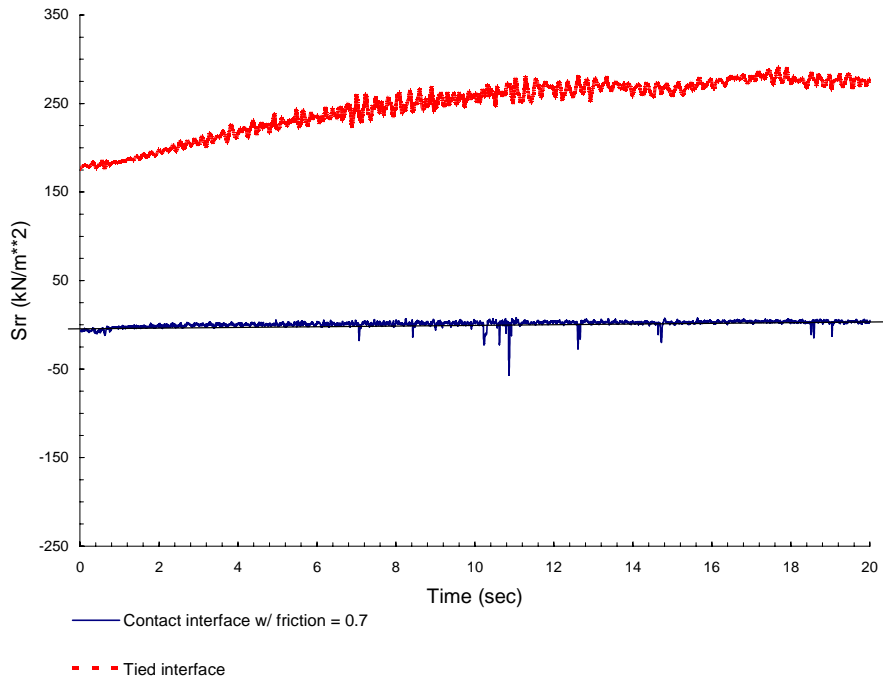


Figure 4.4.4-8 Comparison of Normal Pressure on the Head-on Soil Element near the Ground Surface Computed from the 46 m DOB Contact and Tied Interface Models.

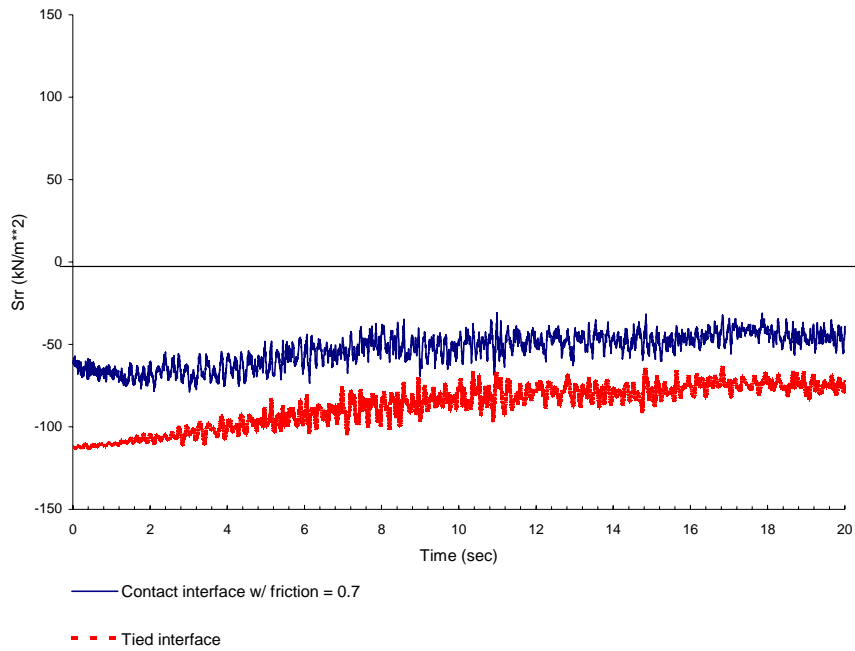


Figure 4.4.4-9 Comparison of Normal Pressure on the Head-on Soil Element near the Mid-height of Structural Wall Computed from the 46 m DOB Contact and Tied Interface Models.

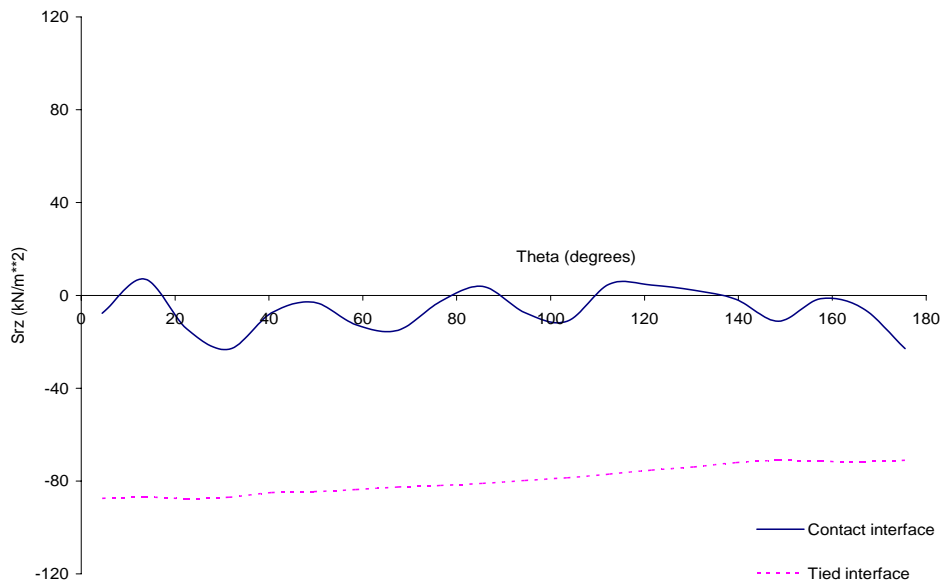


Figure 4.4.4-10 Comparison of Circumferential Distributions of Vertical Shear Computed from the 46 m DOB Contact and Tied Interface Models at Respective Mid-Height Peak S_{rr} Times .

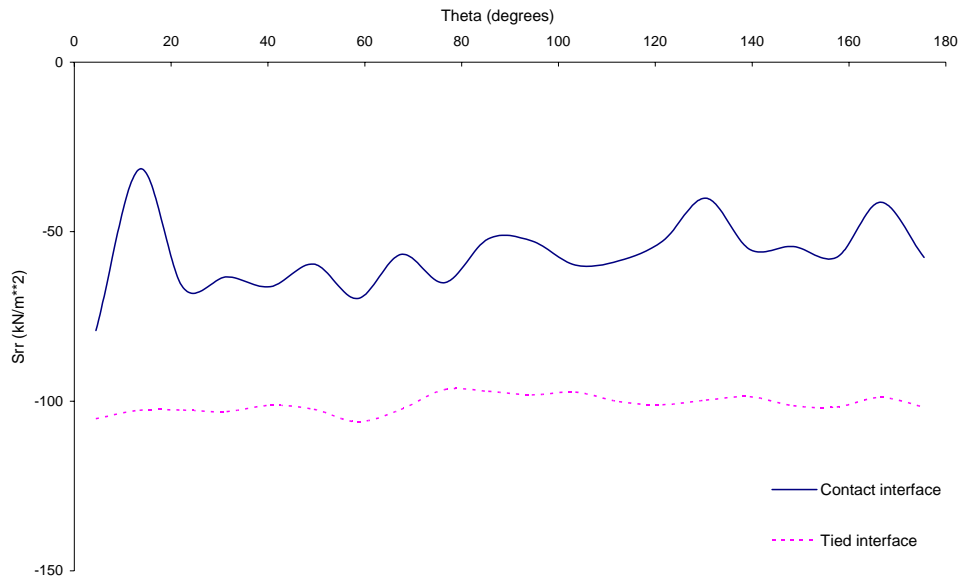


Figure 4.4.4-11 Comparison of Circumferential Distributions of Normal Pressures Computed from the 46 m DOB Contact and Tied Interface Models at Respective Mid-Height Peak S_{rr} Times

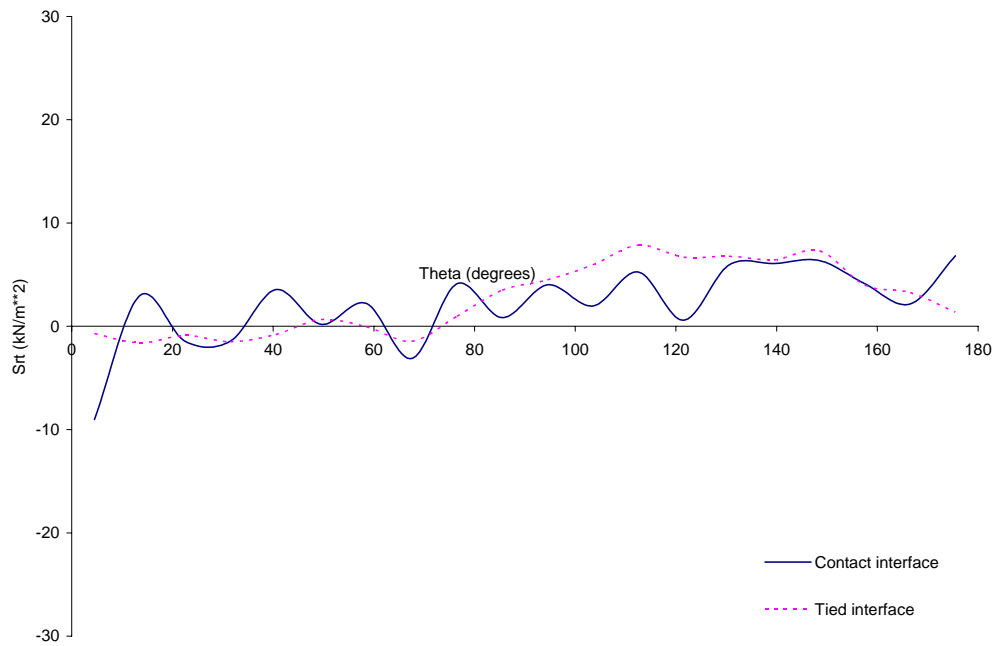


Figure 4.4.4-12 Comparison of Circumferential Distributions of Tangential Shear Computed from the 46 m DOB Contact and Tied Interface Models at Respective Mid-Height Peak S_{rr} Times.

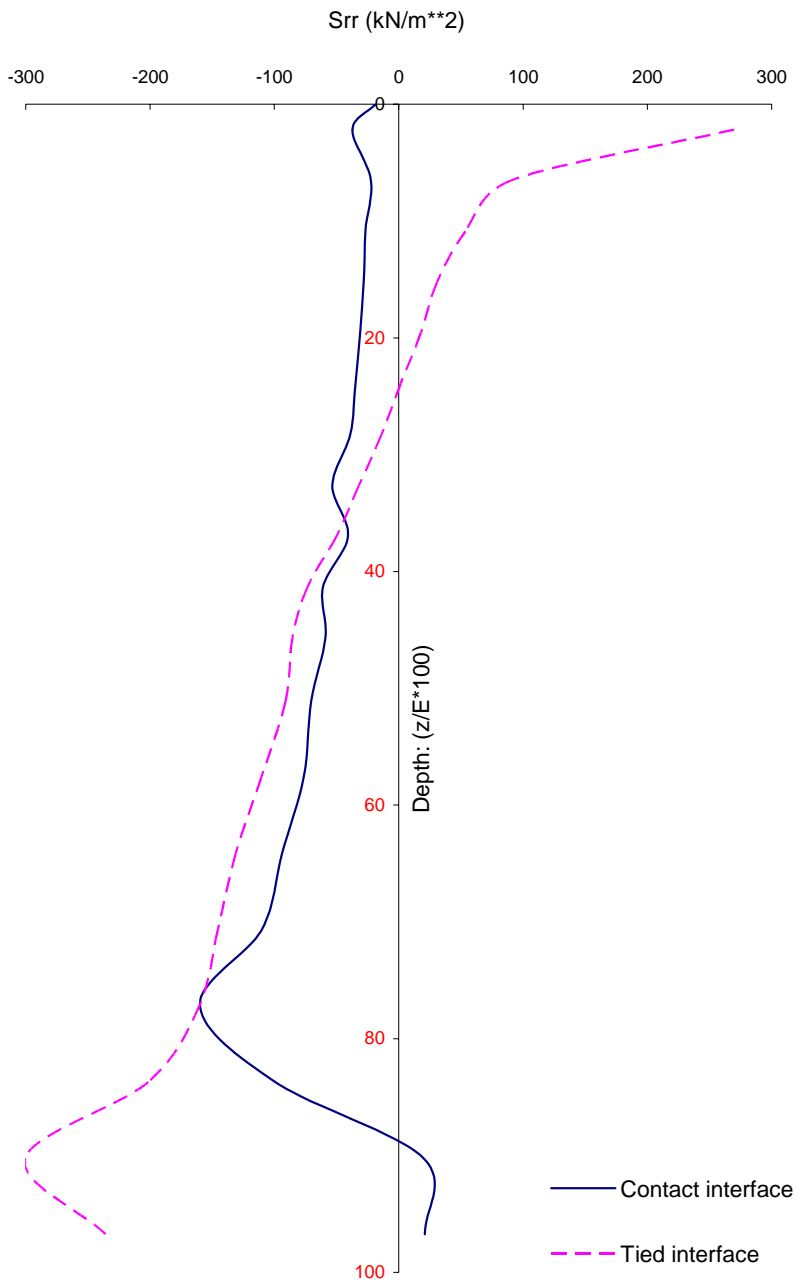


Figure 4.4.4-13 Comparison of Vertical Distributions of Normal Pressures Computed from the 46 m DOB Contact and Tied Interface Models at Respective Surface Peak S_{rr} Times.

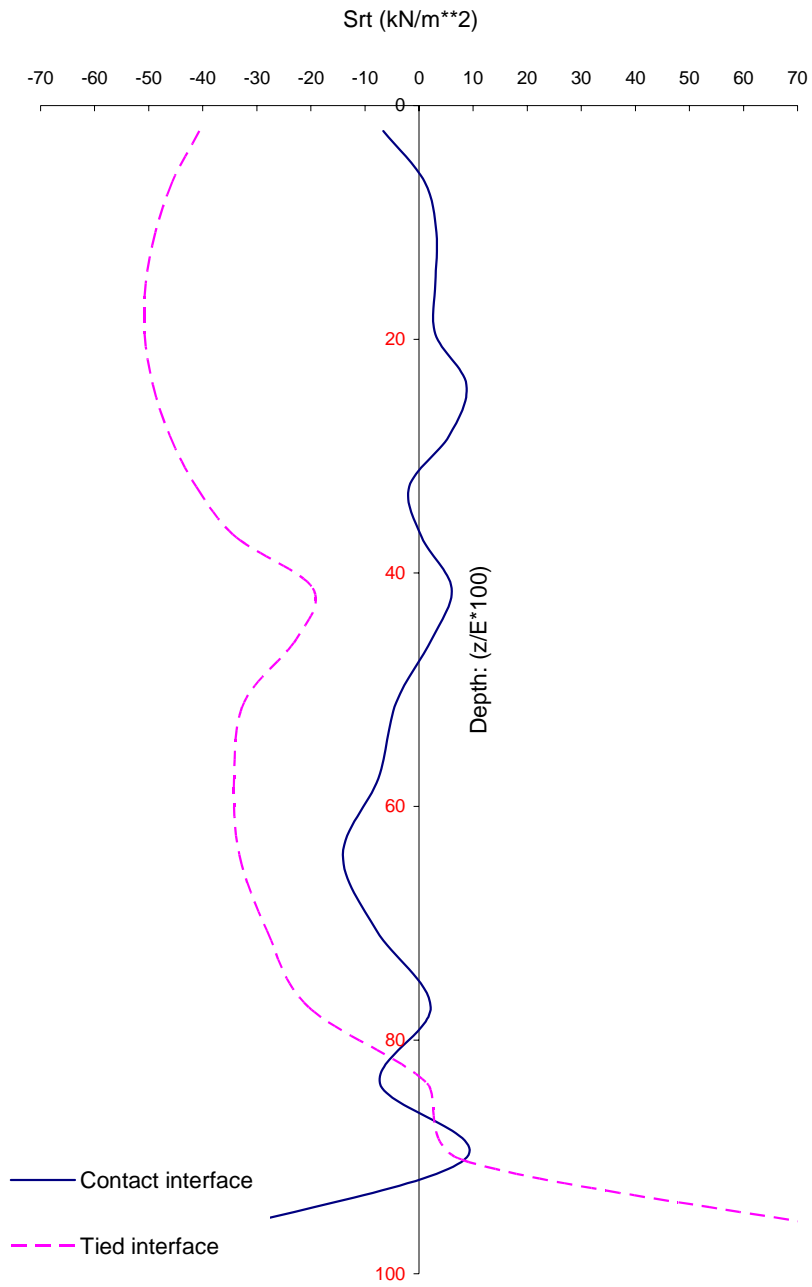


Figure 4.4.4-14 Comparison of Vertical Distribution of Tangential Shear Computed from the 46 m DOB Contact and Tied Interface Models at Respective Surface Peak S_{tr} Times.

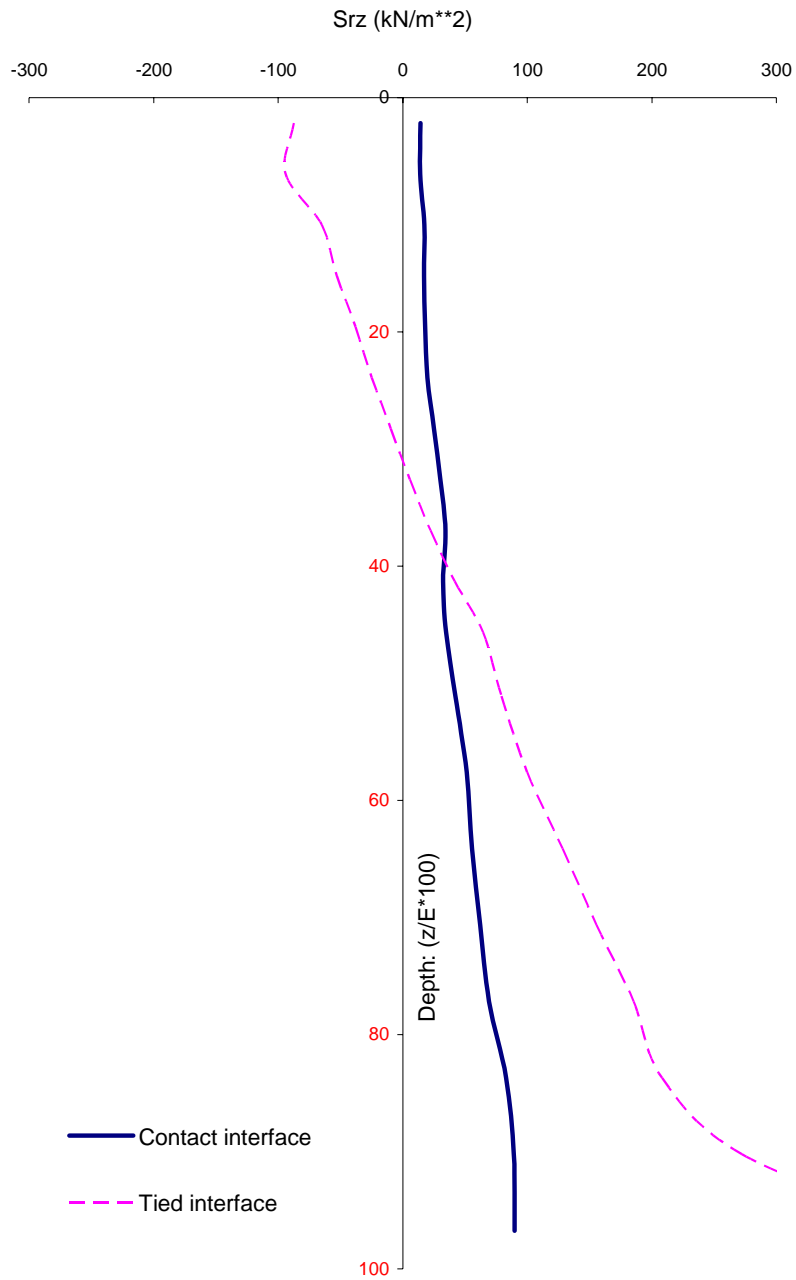


Figure 4.4.4-15 Comparison of Vertical Distributions of Vertical Shear Computed from the 46 m DOB Contact and Tied Interface Models at Respective Surface Peak S_{Tr} Times.

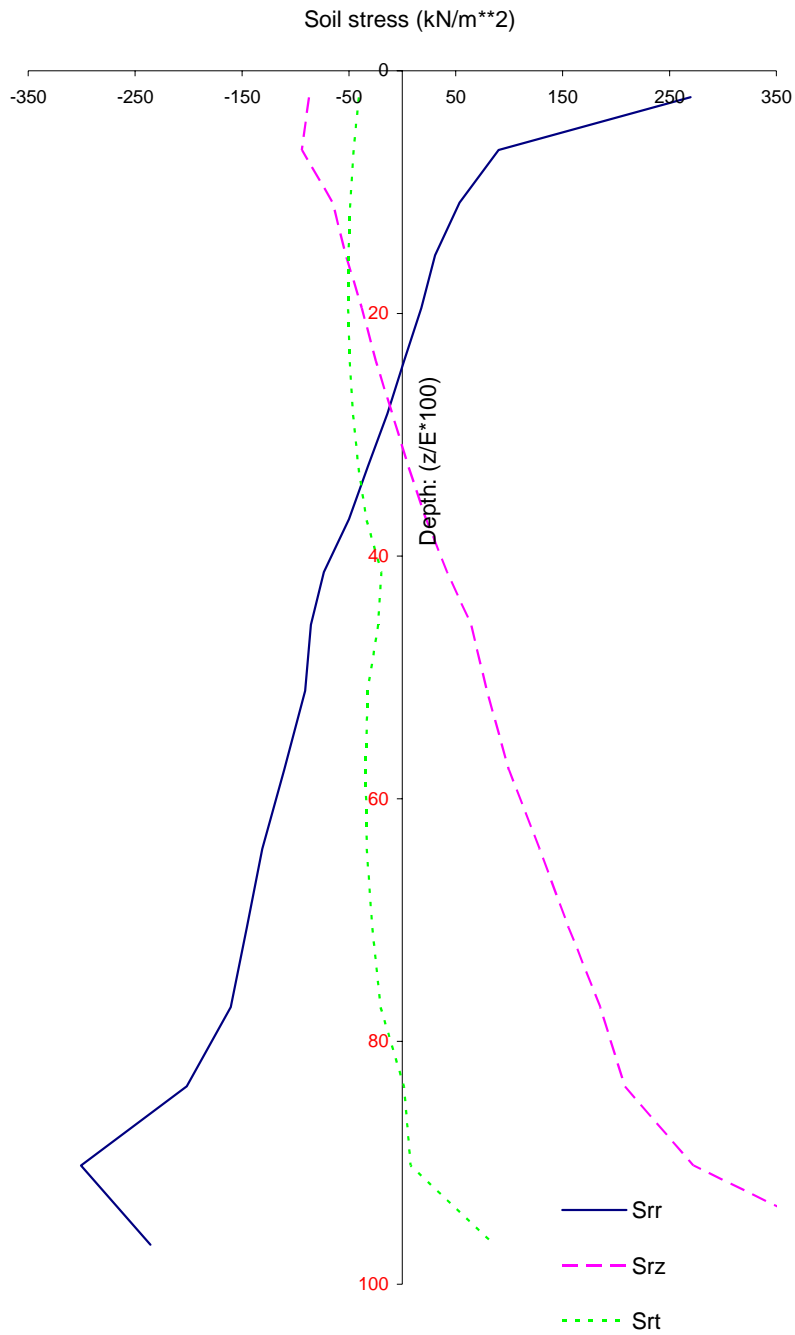


Figure 4.4.4-16 Comparison of Vertical Distributions of Soil Stresses Computed from the 46 m Tied Interface Models at Surface Peak S_{rr} Times.

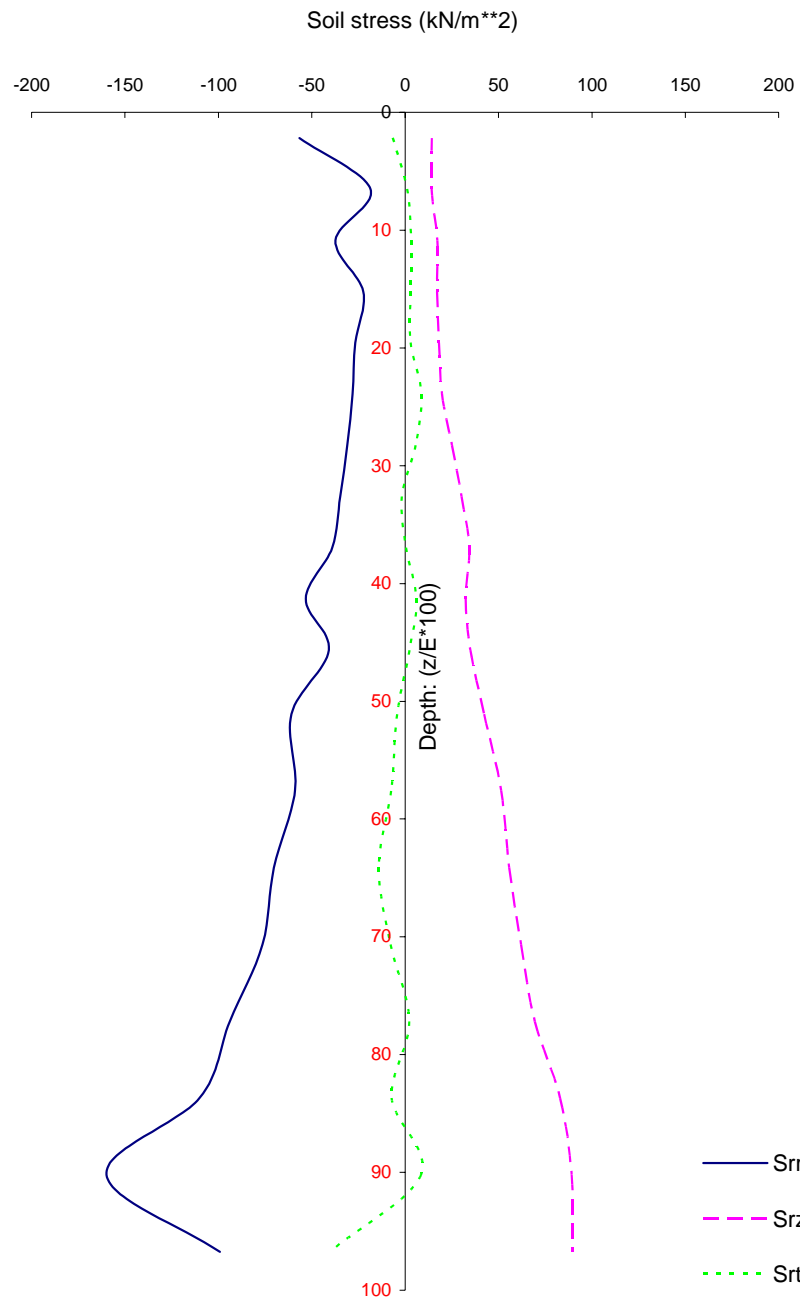


Figure 4.4.4-17 Comparison of Vertical Distributions of Soil Stresses Computed from the 46 m DOB Contact Interface Model at Surface Peak S_{rr} Times.

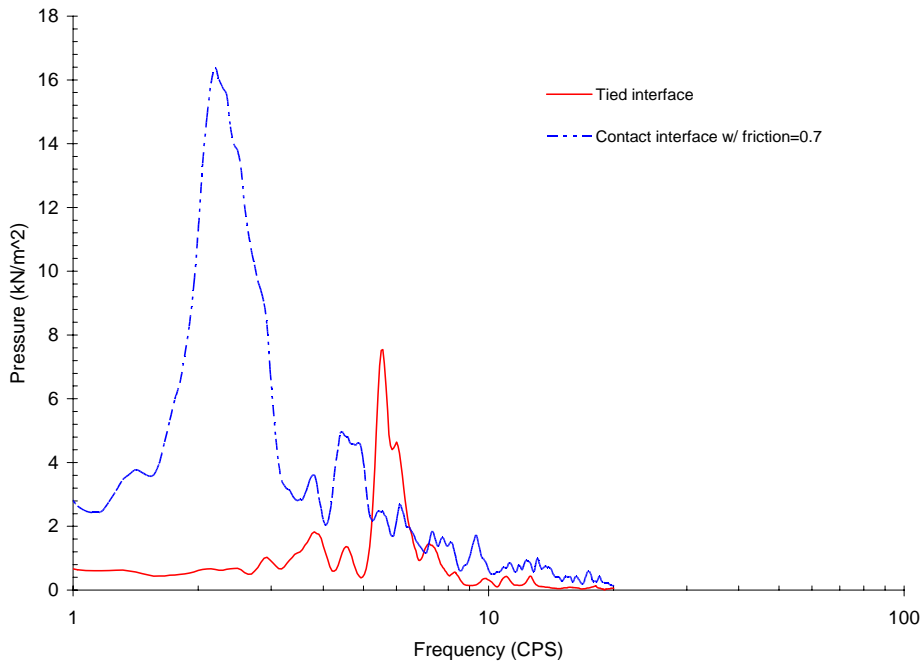


Figure 4.4.5-1 Smoothed Fourier Spectra of Soil Pressure in the Head-on Soil Element near the Mid-Height Wall Section for DOB = 11.5 m.

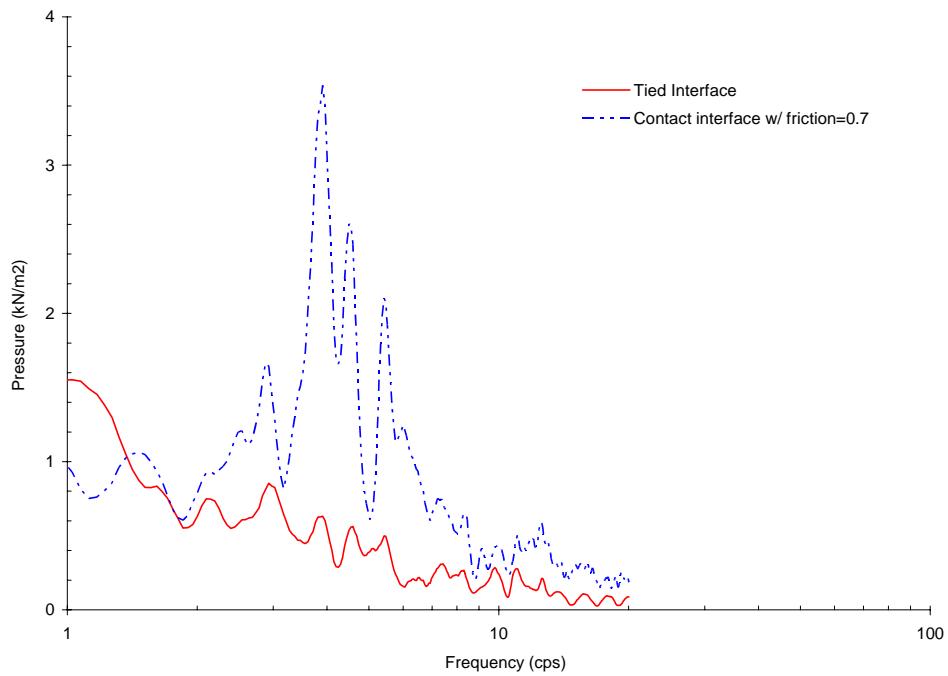


Figure 4.4.5-2 Smoothed Fourier Spectra of Soil Pressure in the Head-on Soil Element near the Mid-Height Wall Section for DOB = 23 m.

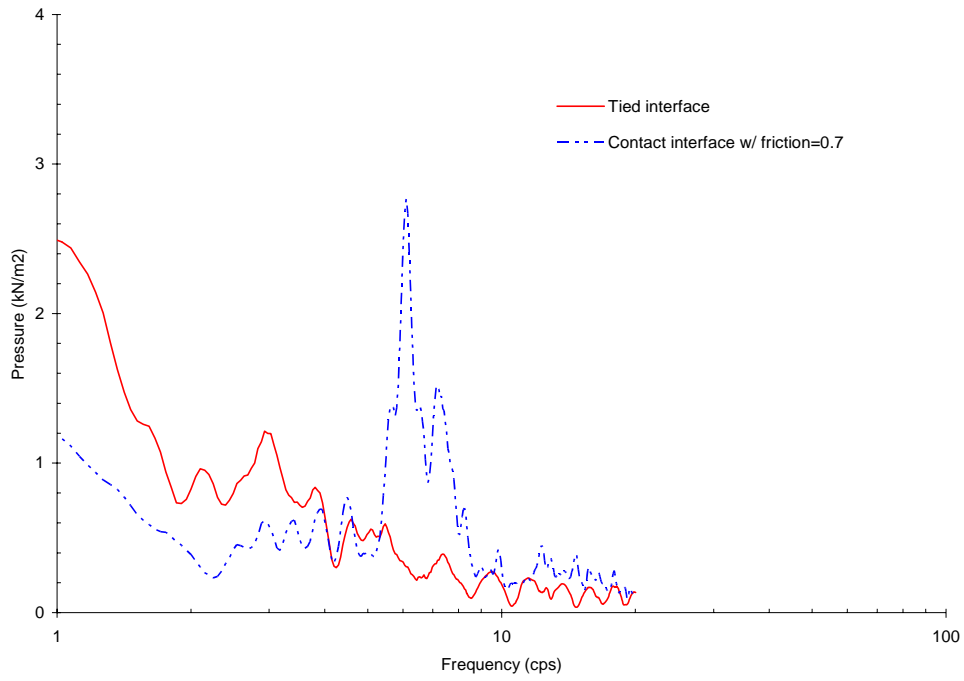


Figure 4.4.5-3 Smoothed Fourier Spectra of Soil Pressure in the Head-on Soil Element near the Mid-Height Wall Section for DOB = 34.5 m.

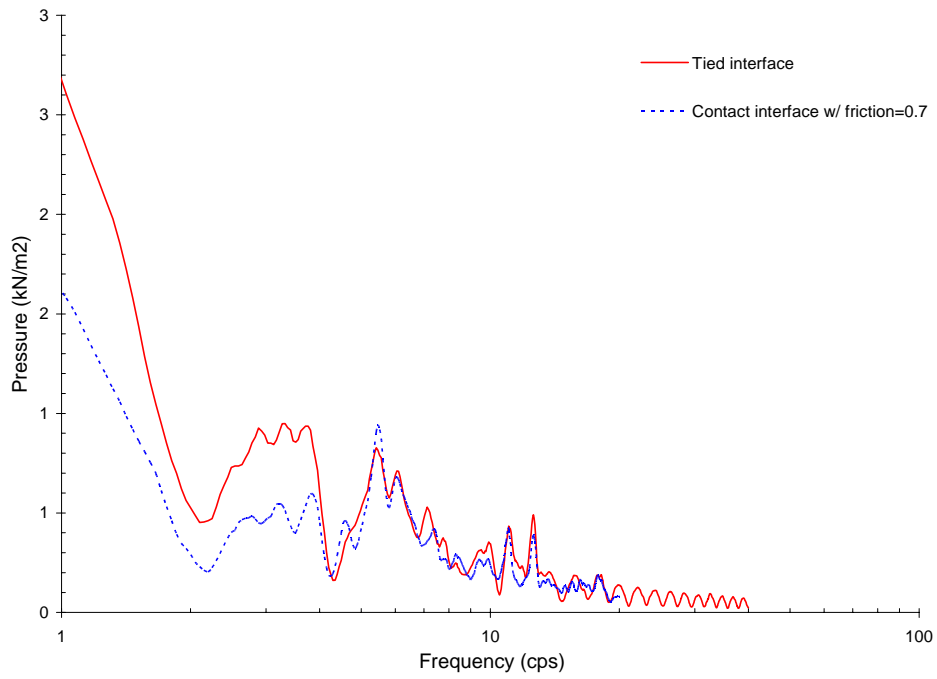


Figure 4.4.5-4 Smoothed Fourier Spectra of Soil Pressure in the Head-on Soil Element near the Mid-Height Wall Section for DOB = 46 m.

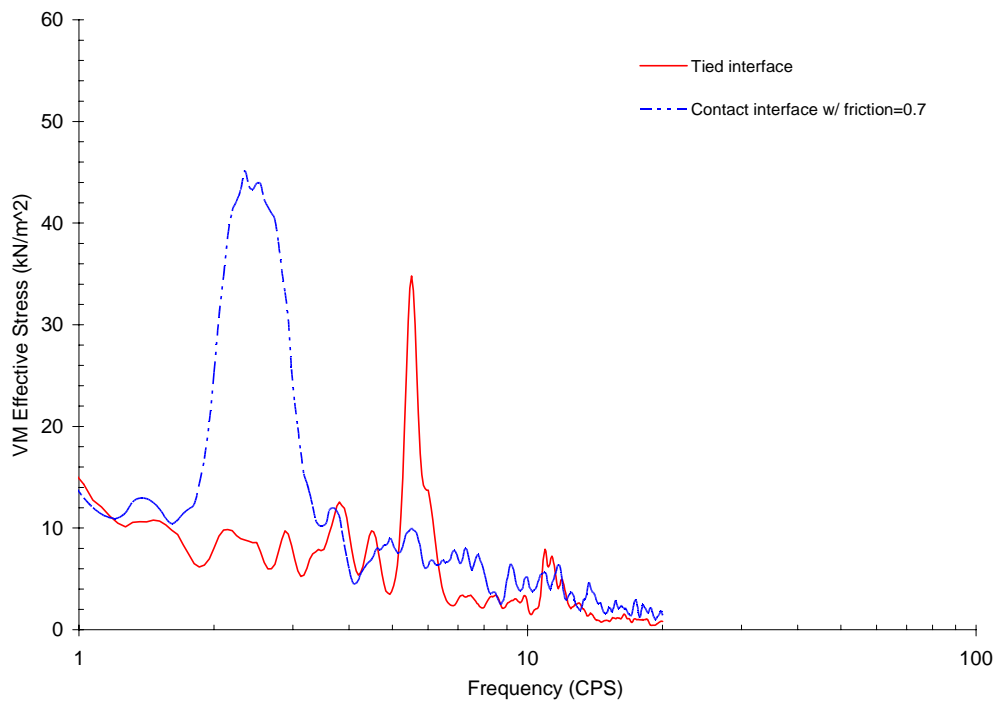


Figure 4.4.5-5 Smoothed Fourier Spectra of Von-Mises Effective Stress in the Head-on Structural Shell Element near the Ground Surface for DOB = 11.5 m.

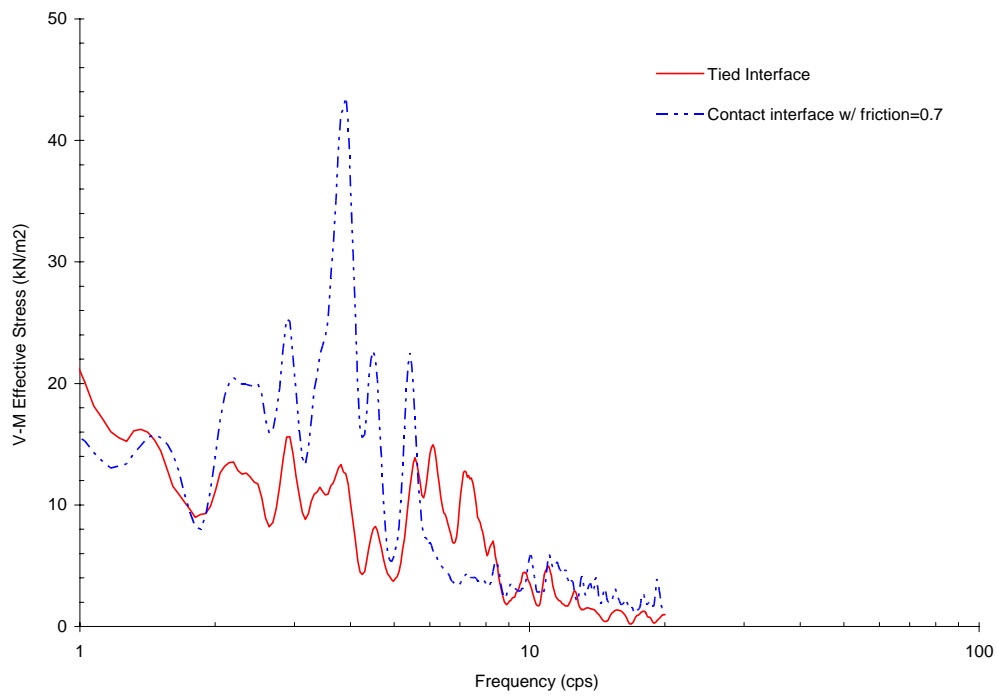


Figure 4.4.5-6 Smoothed Fourier Spectra of Von-Mises Effective Stress in the 5th Head-on Structural Shell Element from the Base for DOB = 23 m.

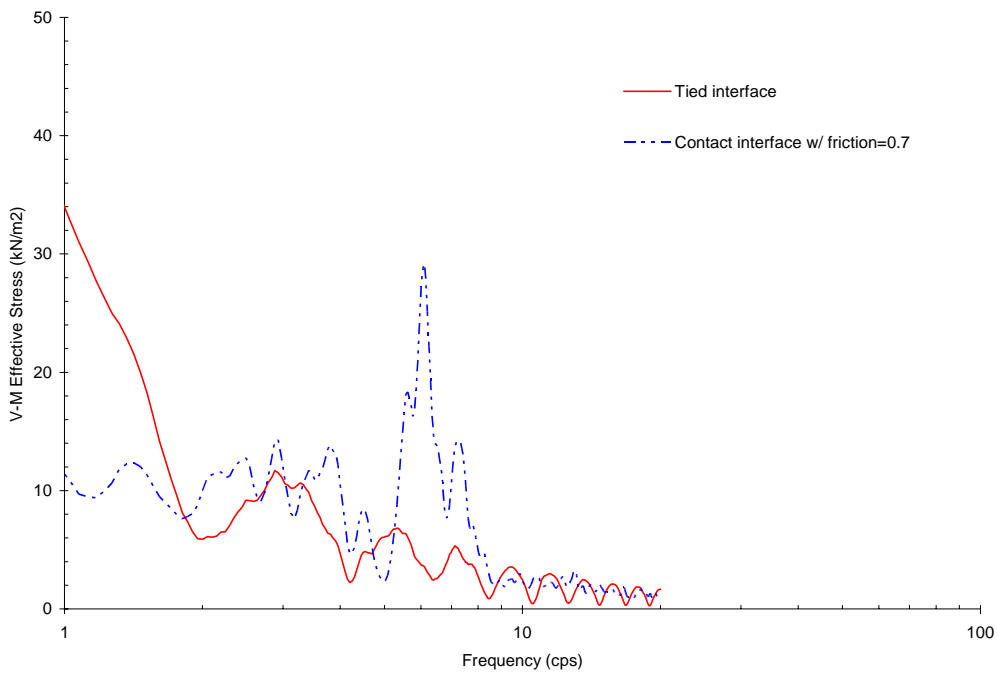


Figure 4.4.5-7 Smoothed Fourier Spectra of Von-Mises Effective Stress in the 5th Head-on Structural Shell Element from the Base for DOB = 34.5 m.

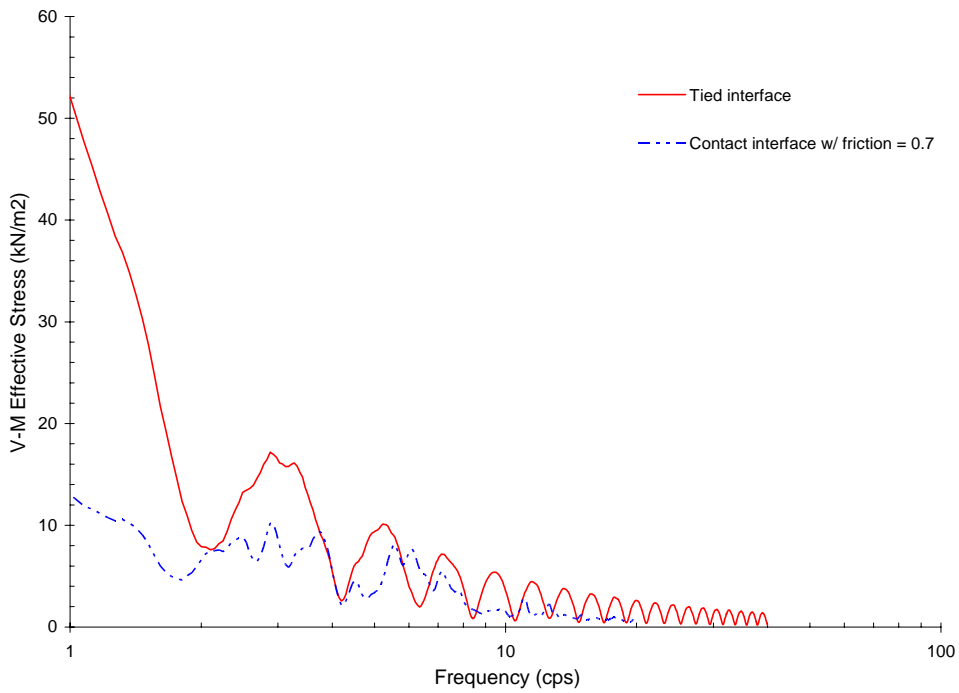


Figure 4.4.5-8 Smoothed Fourier Spectra of Von-Mises Effective Stress in the 5th Head-on Structural Shell Element from the Base for DOB = 46 m.

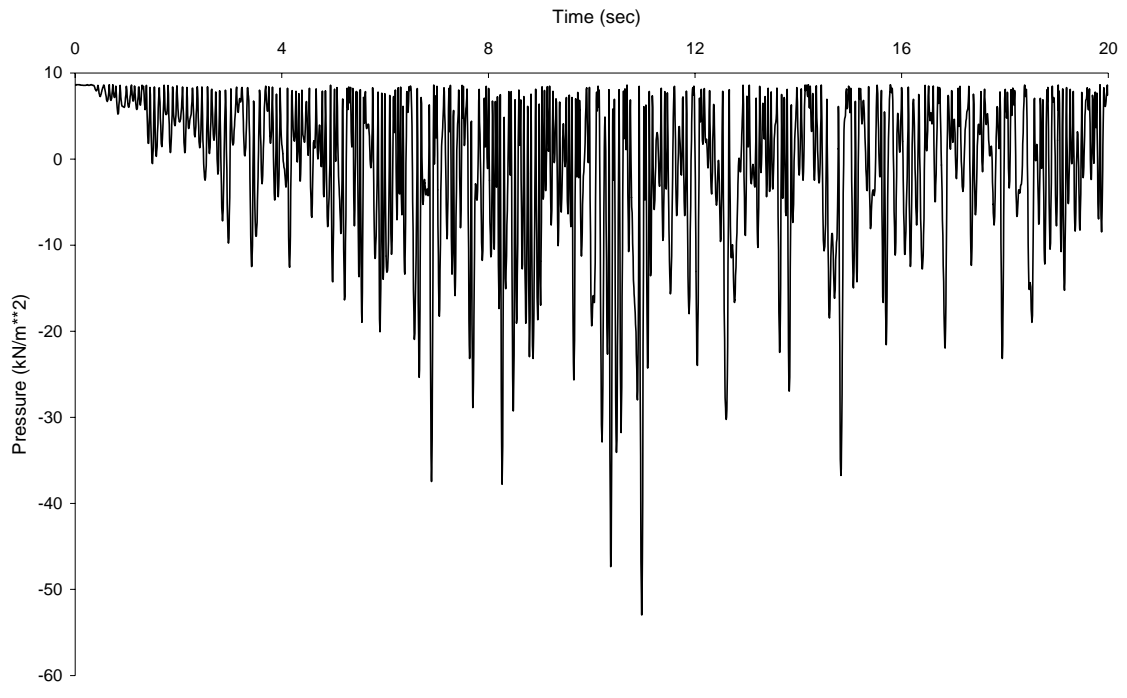


Figure 4.4.6-1 Normal Pressure (+Comp) for the 23 m DOB SASSI Model at Depth = 1 m.

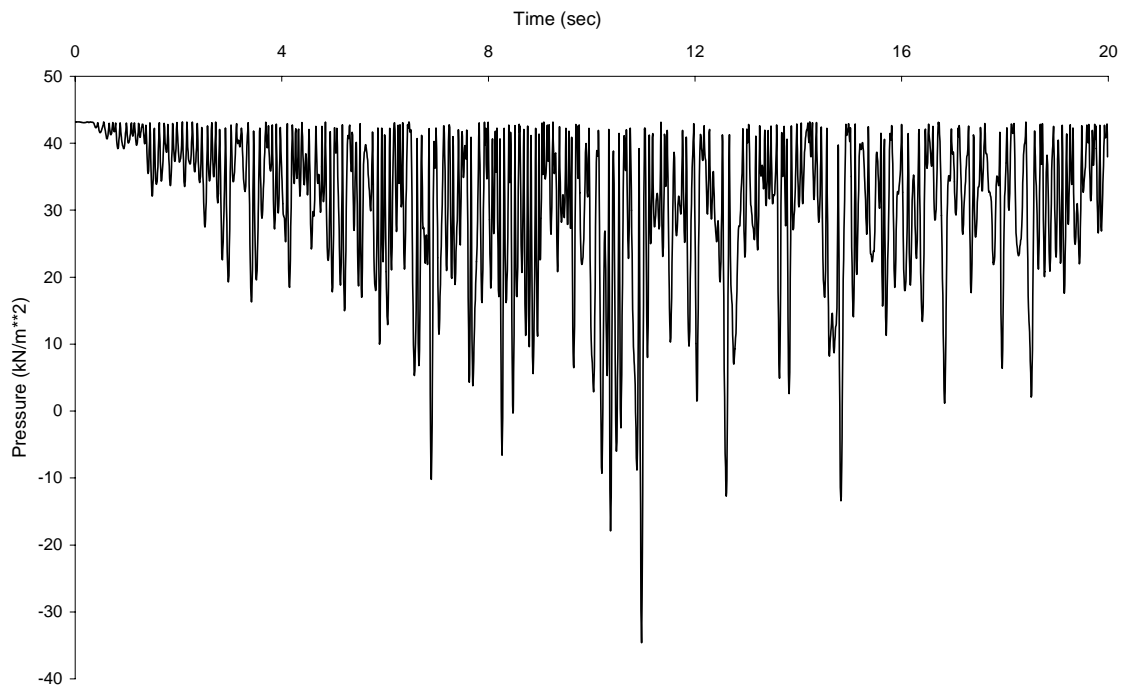


Figure 4.4.6-2 Normal Pressure (+Comp) for the 23 m DOB SASSI Model at Depth = 5 m.

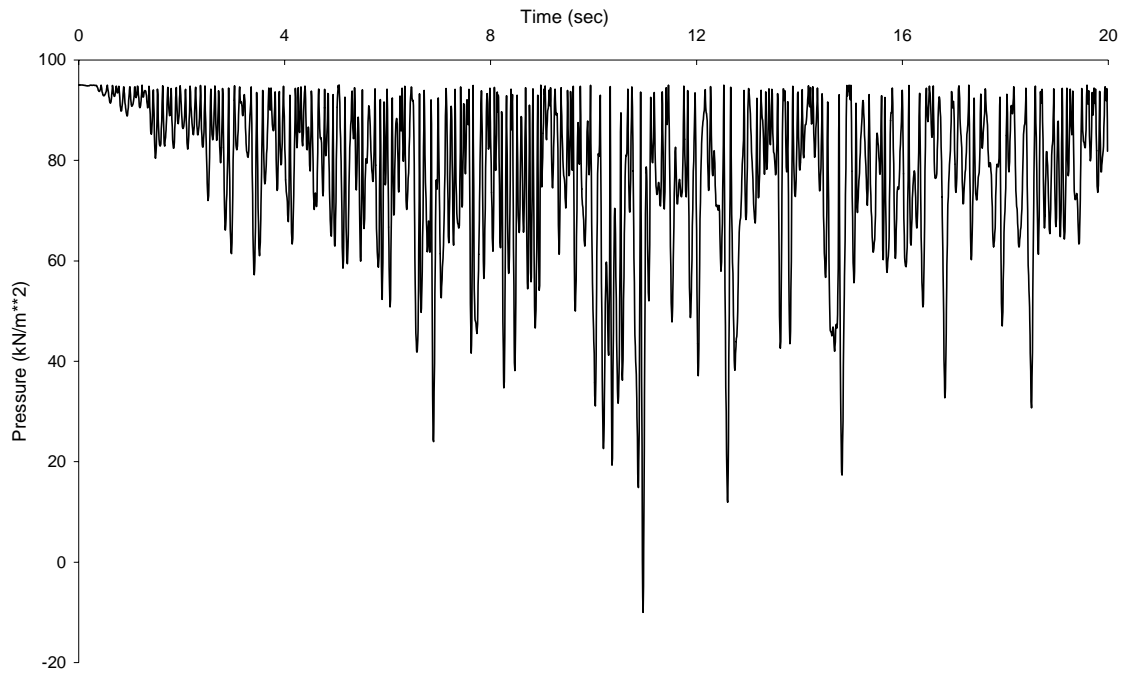


Figure 4.4.6-3 Normal Pressure (+Comp) for the 23 m DOB SASSI Model at Depth = 11 m.

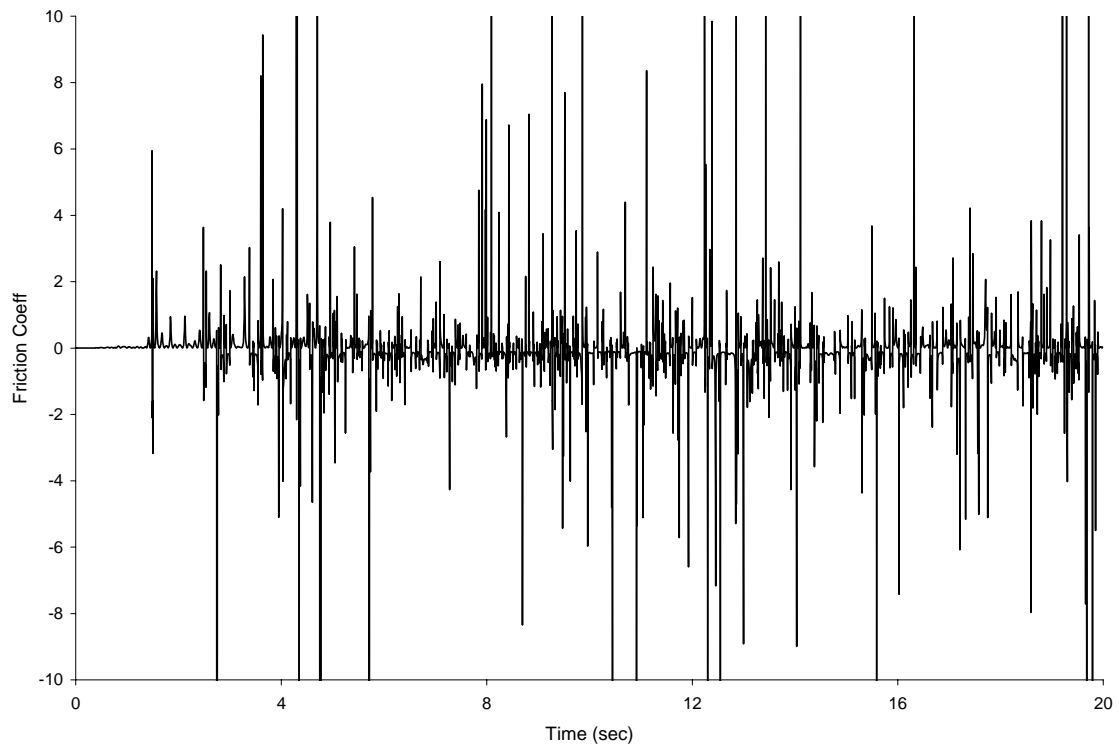


Figure 4.4.6-4 Head-on Friction Coefficient for the 23 m DOB SASSI Model at Depth = 1 m.

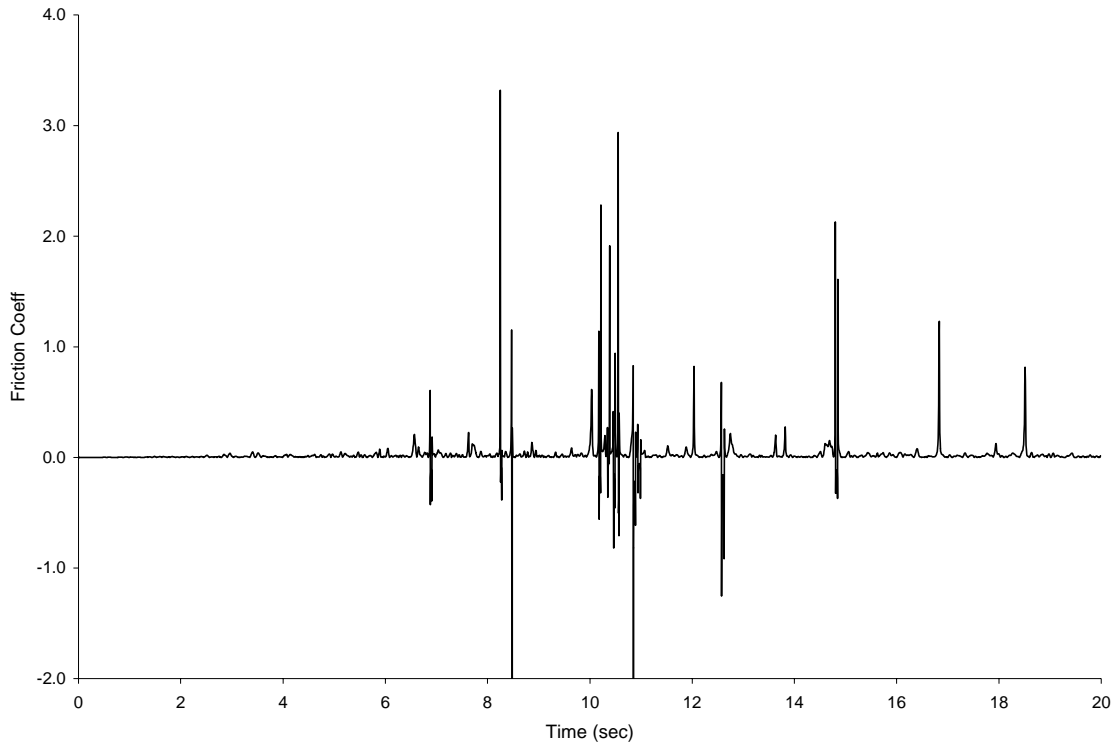


Figure 4.4.6-5 Head-on Friction Coefficient for the 23 m DOB SASSI Model at Depth = 5 m.

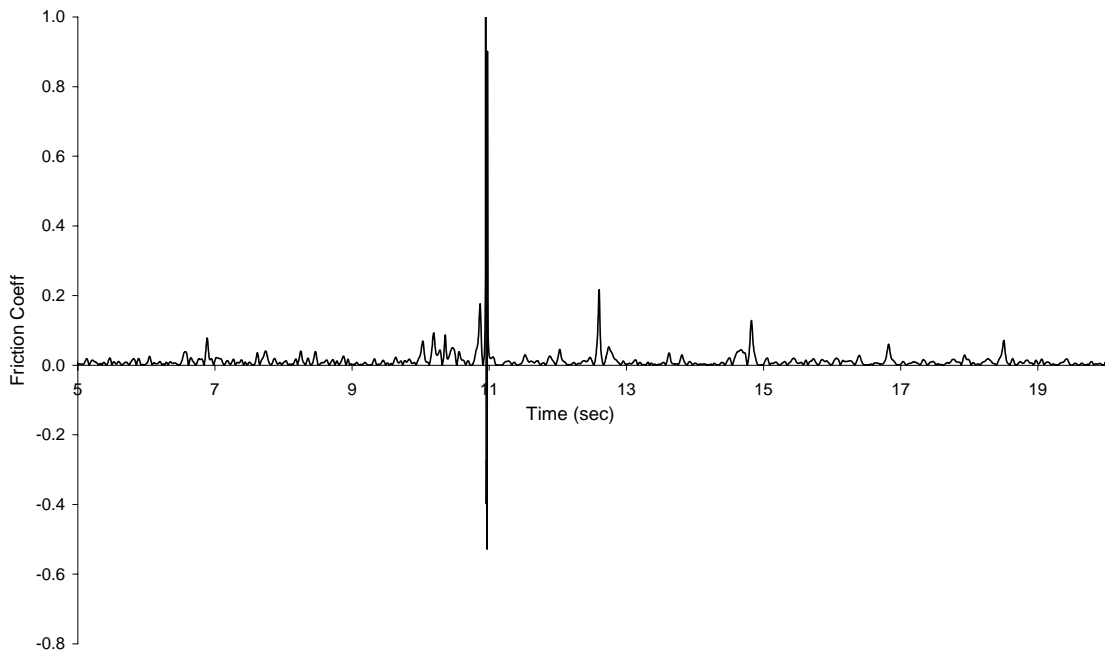


Figure 4.4.6-6 Head-on Friction Coefficient for the 23 m DOB SASSI Model at Depth = 11 m.

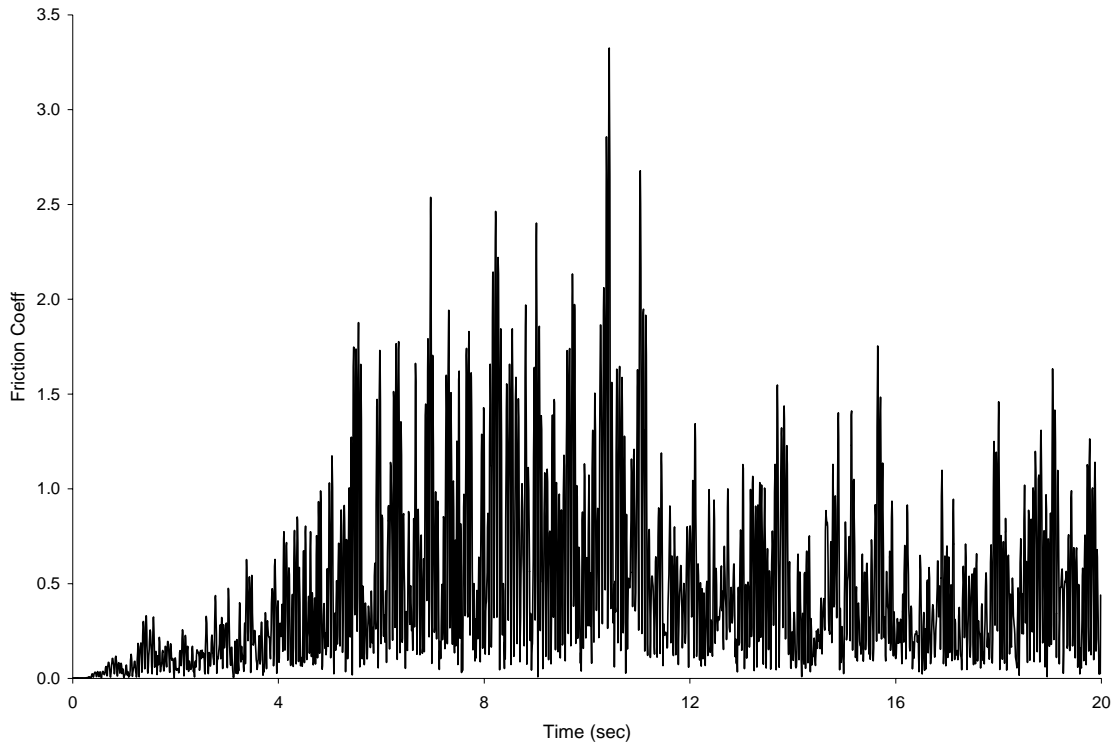


Figure 4.4.6-7 Side-on Friction Coefficient for the 23 m DOB SASSI Model at Depth = 1 m.

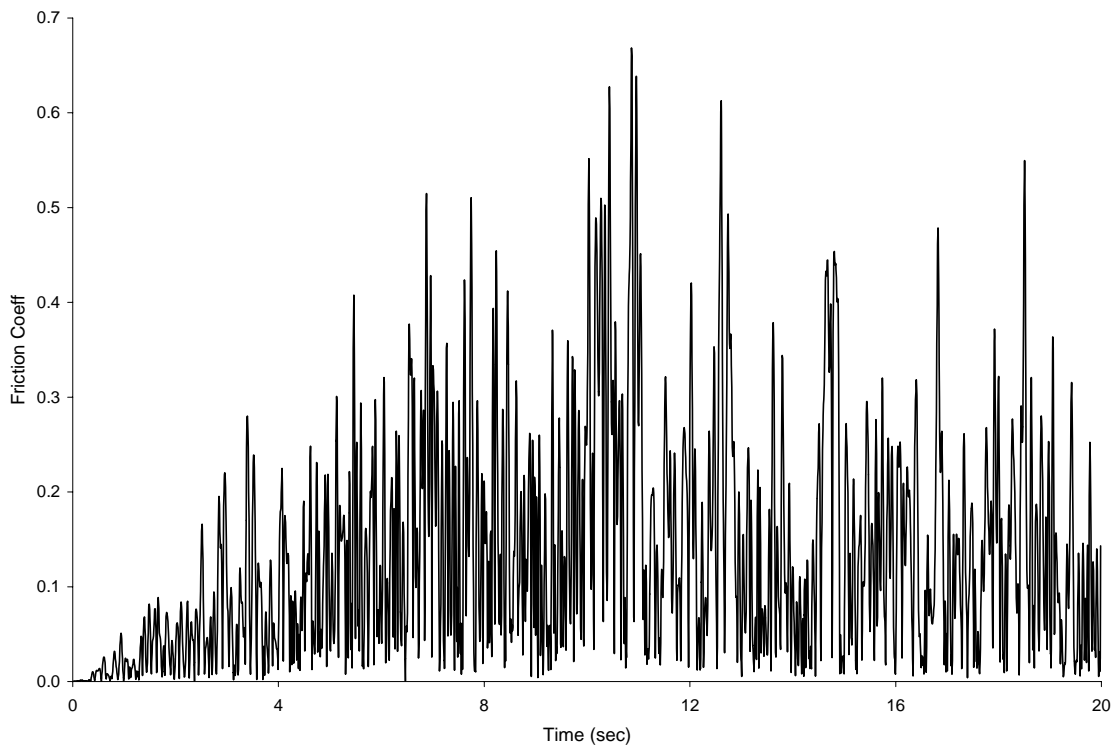


Figure 4.4.6-8 Side-on Friction Coefficient for the 23 m DOB SASSI Model at Depth = 5 m.

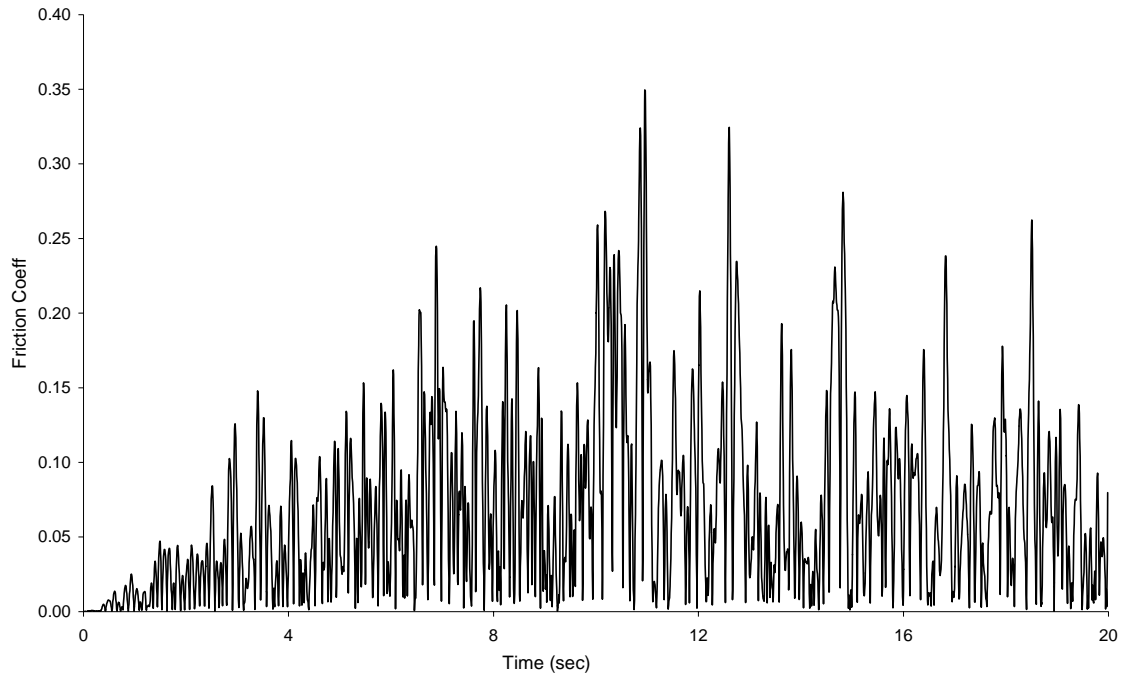


Figure 4.4.6-9 Side-on Friction Coefficient for the 23 m DOB SASSI Model at Depth = 11 m.

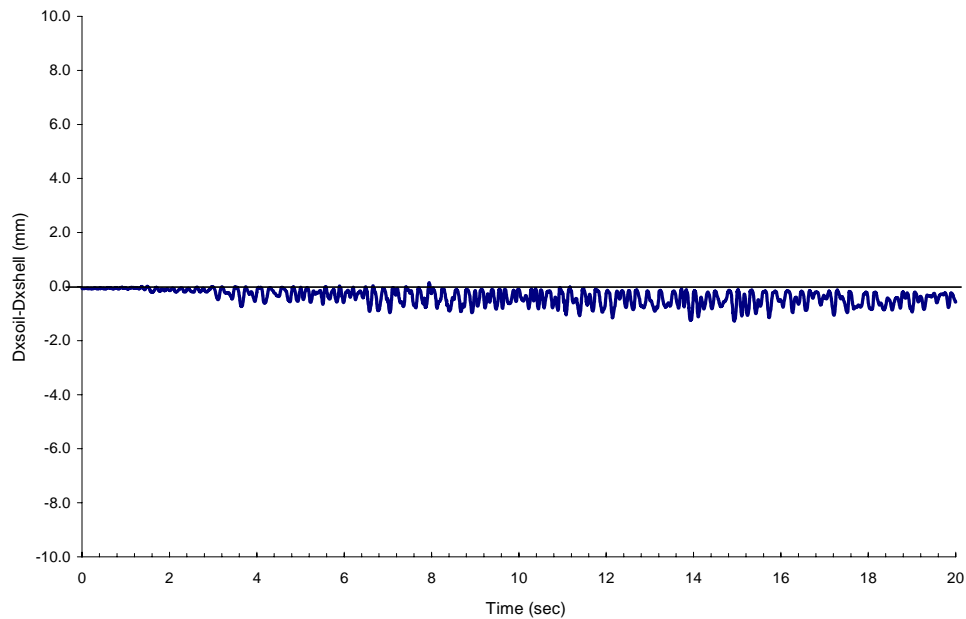


Figure 4.5-1 Relative Lateral Displacement of Structural Wall and Surrounding Soil at the Interface near ground Surface ($\theta=0$) from the 23 m DOB Contact Interface Model using Coulomb Soil.

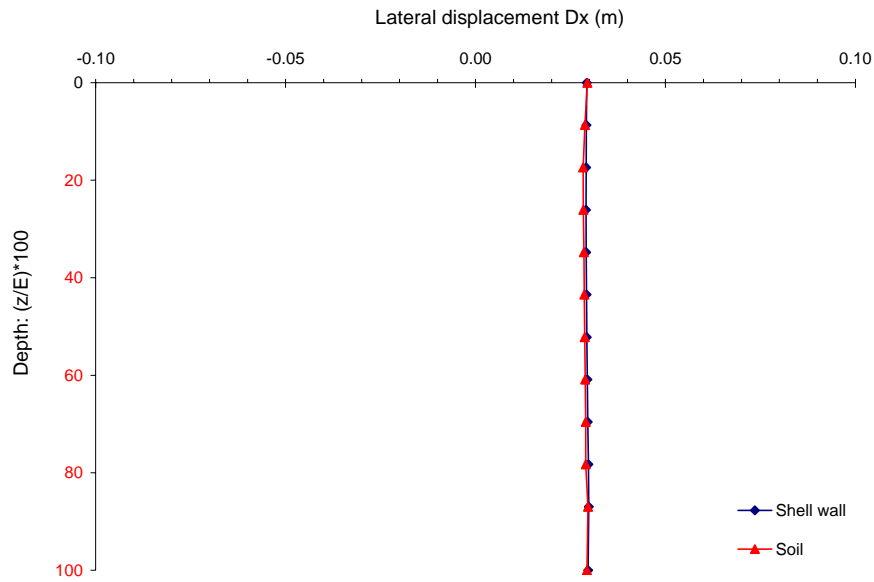


Figure 4.5-2 Vertical Distribution of Lateral Displacement of Structural Wall and Surrounding Soil at the Interface near ground Surface ($\theta=0$) from the 23 m DOB Contact Interface Model using Coulomb Soil at 7.95 Seconds.

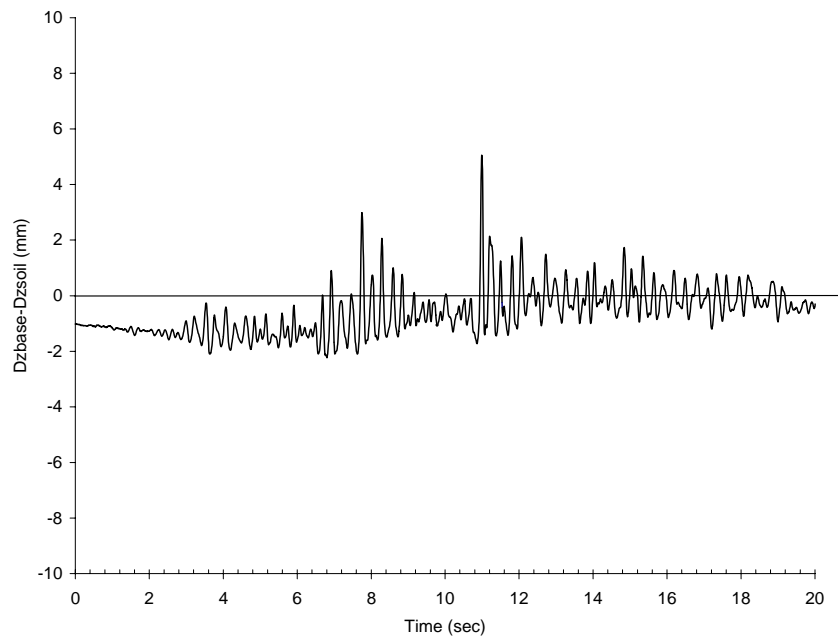


Figure 4.5-3 Vertical Displacement of Structural Foundation Relative to Base Soil Computed from the 23 m DOB Contact Interface Model using Coulomb Soil at $\theta = 0$.

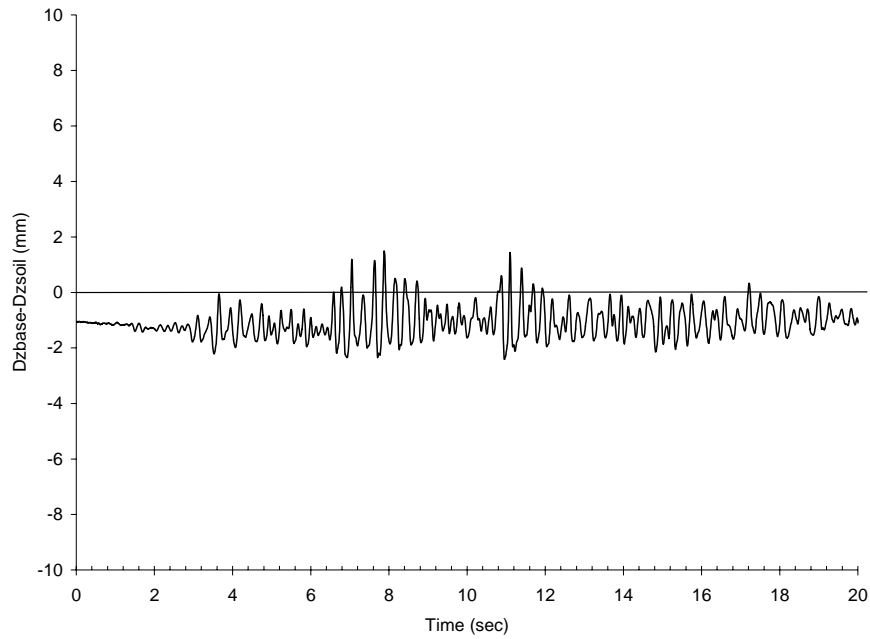


Figure 4.5-4 Vertical Displacement of Structural Foundation Relative to Base Soil Computed from the 23 m DOB Contact Interface Model using Coulomb Soil at Theta = 180.

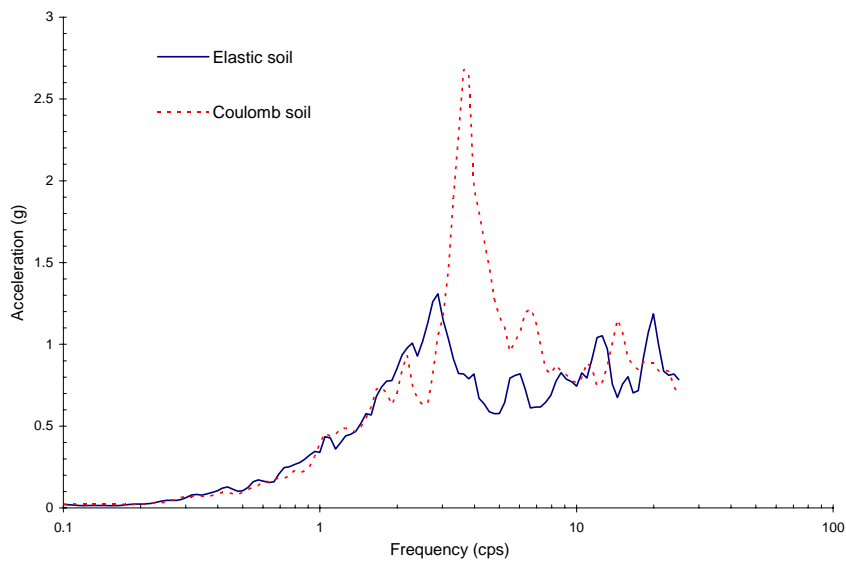


Figure 4.5-5 Effect of Soil Material Models on the Contact Interface LS-DYNA Response Spectra (5% Damping) at Structural Base with Butterworth Low-Pass High Cut Filter ($f_{\text{cutoff}} = 20$ Hz).

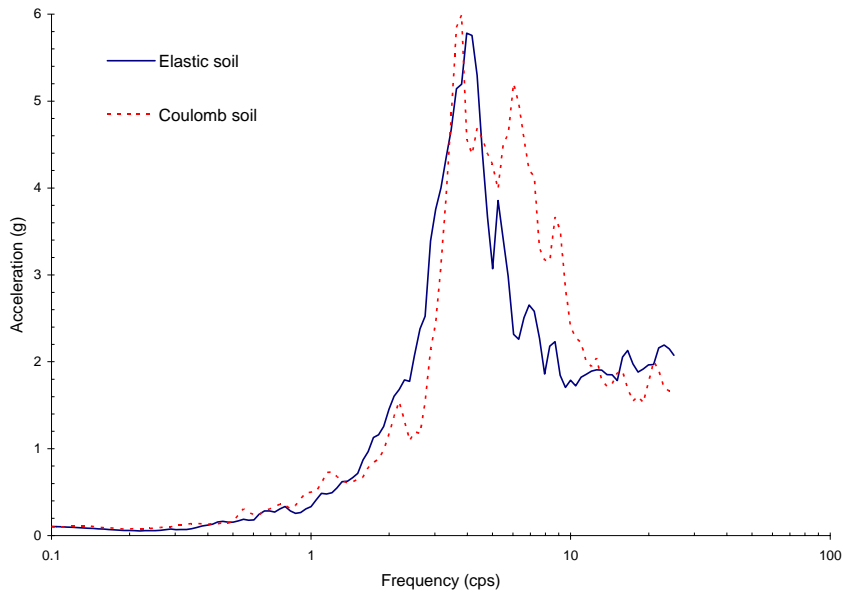


Figure 4.5-6 Effect of Soil Material Models on the Contact Interface LS-DYNA Response Spectra (5% Damping) at Structural Roof.

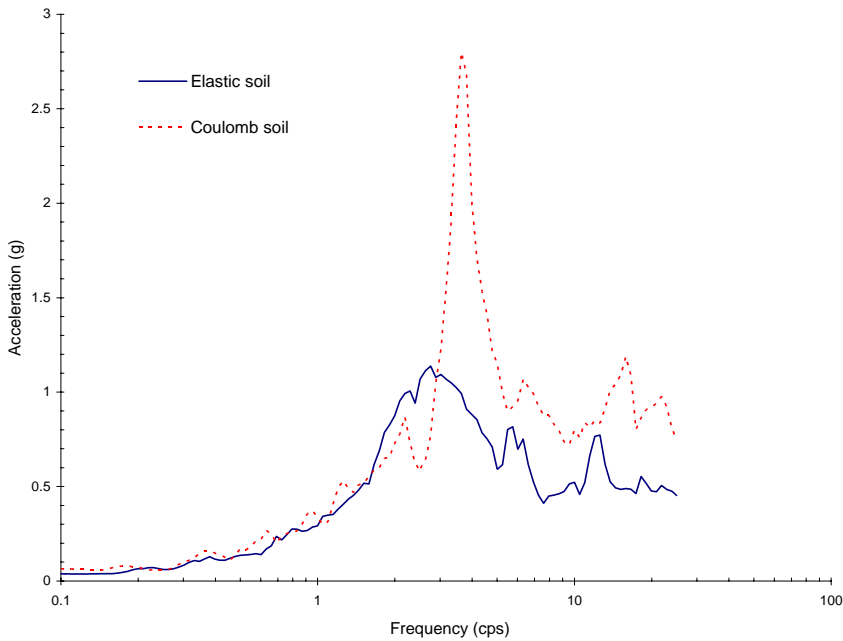


Figure 4.5-7 Effect of Soil Material Models on the Tied Interface LS-DYNA Response Spectra (5% Damping) at Structural Base with Butterworth Low-Pass High Cut Filter ($f_{\text{cutoff}} = 20$ Hz).

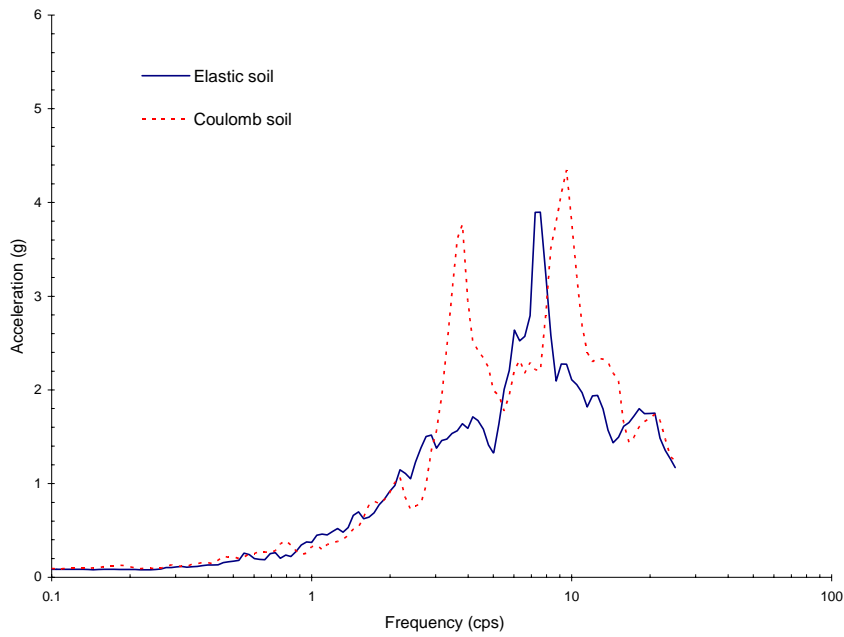


Figure 4.5-8 Effect of Soil Material Models on the Tied Interface LS-DYNA Response Spectra (5% Damping) at Structural Roof.

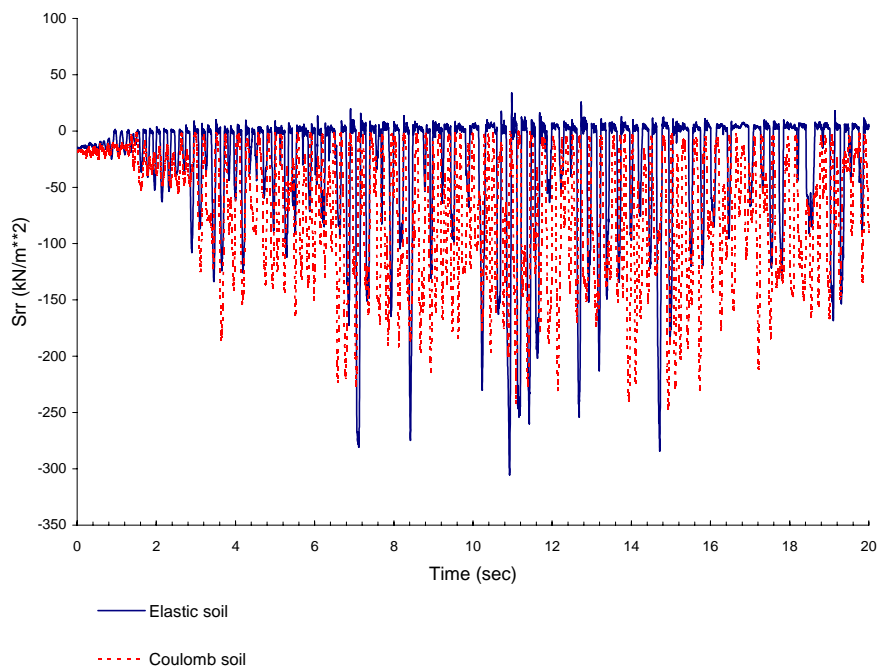


Figure 4.5-9 Effect of Soil Material Models on Normal Pressure in the Head-on Soil Element near Ground Surface Computed from 23 m DOB Contact Interface Model.

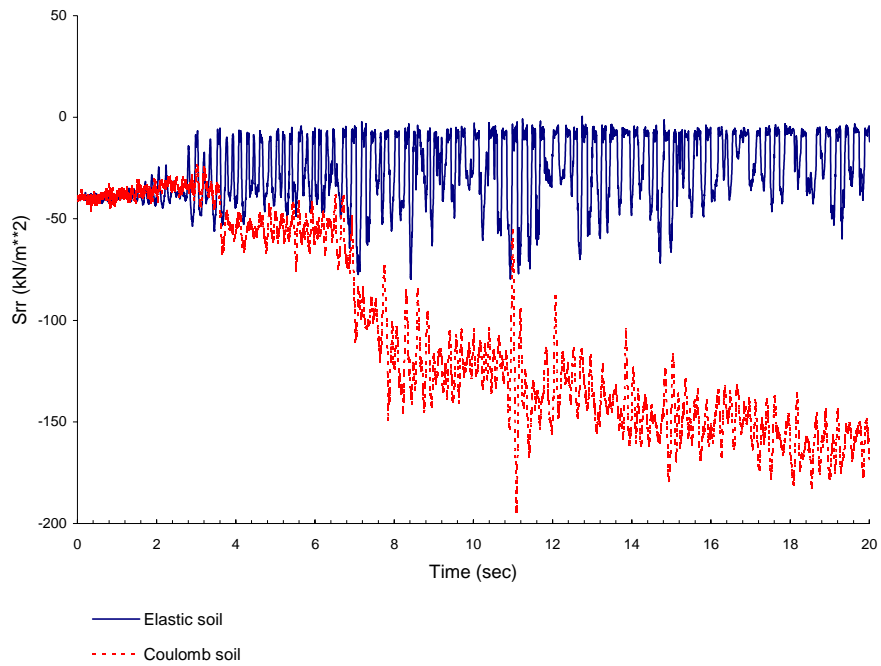


Figure 4.5-10 Effect of Soil Material Models on Normal Pressure in the Head-on Soil Element near Mid-Wall Height Computed from 23 m DOB Contact Interface Model.

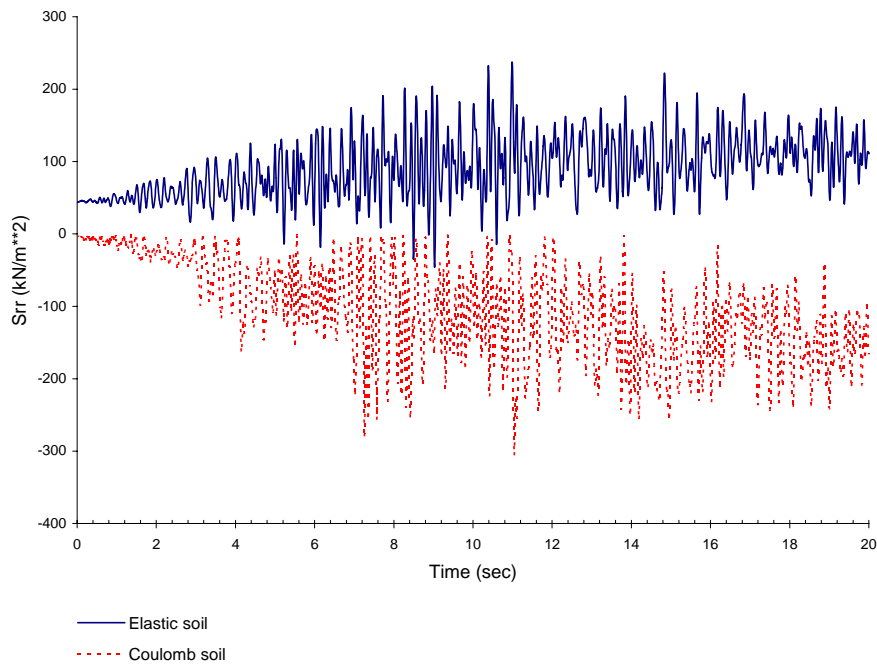


Figure 4.5-11 Effect of Soil Material Models on Normal Pressure in the Head-on Soil Element near Ground Surface Computed from 23 m DOB Tied Interface Model.

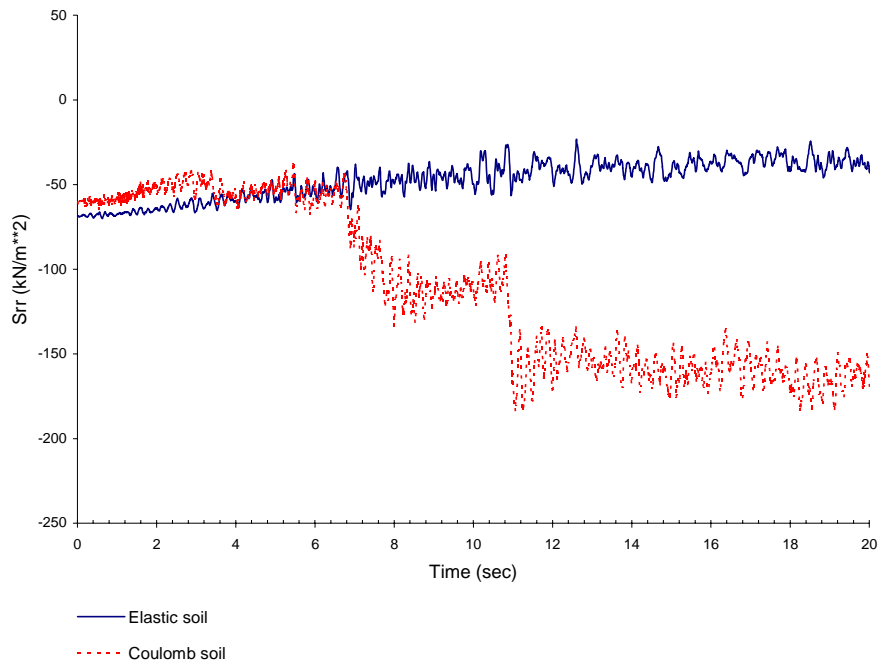


Figure 4.5-12 Effect of Soil Material Models on Normal Pressure in the Head-on Soil Element near Mid-Wall Height Computed from 23 m DOB Tied Interface Model.

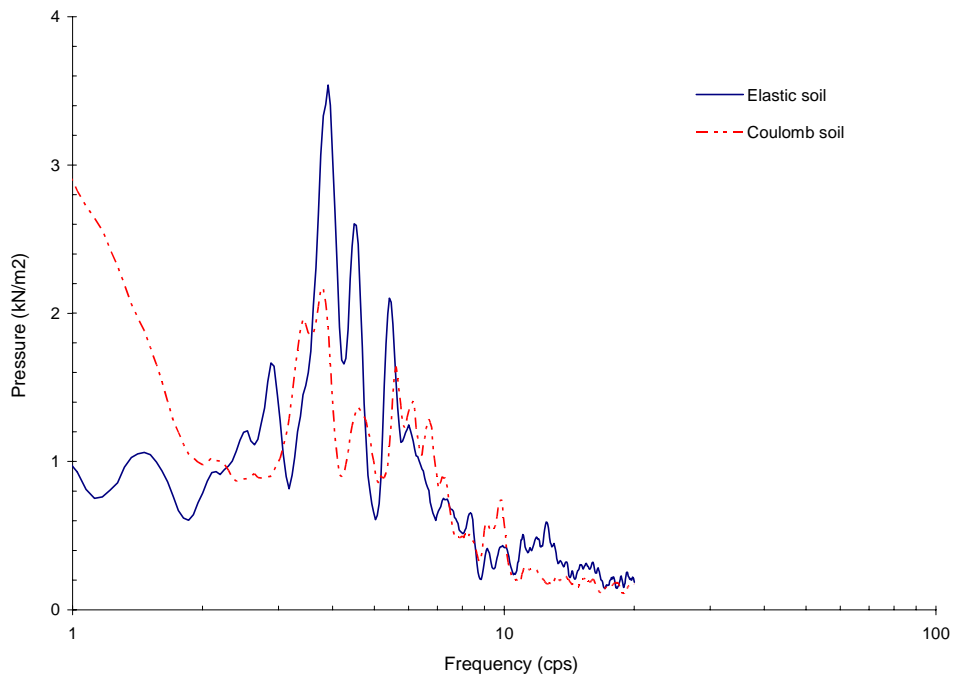


Figure 4.5-13 Fourier Spectra of Normal Pressure in the Head-on Soil Element near Mid-Wall Height Computed from 23 m DOB Contact Interface Model.

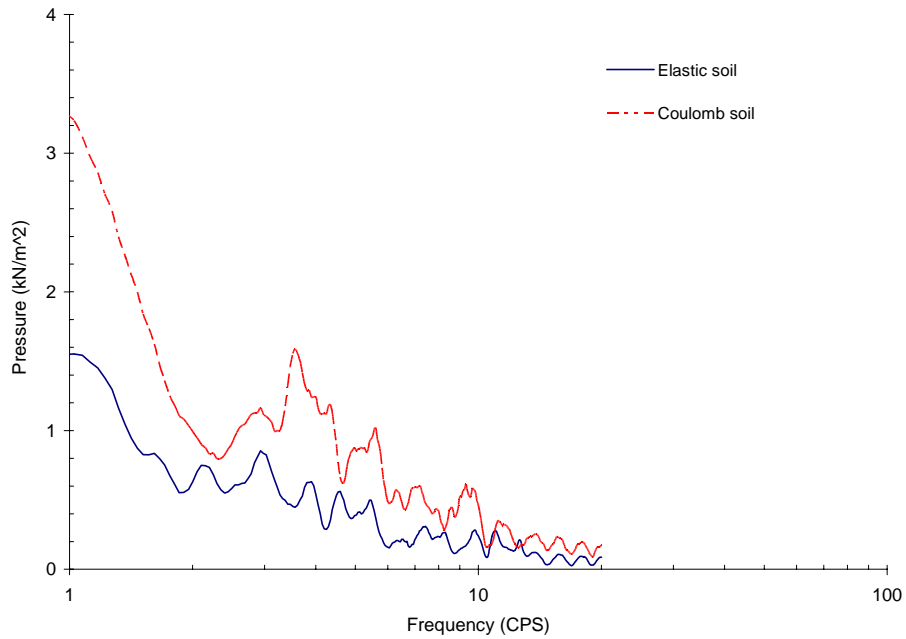


Figure 4.5-14 Fourier Spectra of Normal Pressure in the Head-on Soil Element near Mid-Wall Height Computed from 23 m DOB Tied Interface Model.

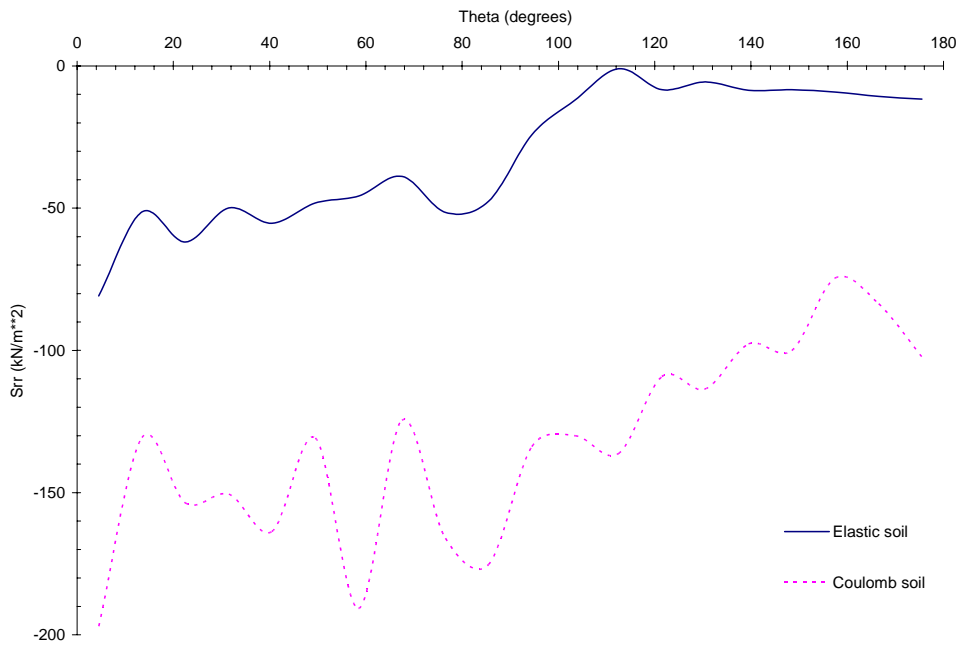


Figure 4.5-15 Effect of Soil Material Models on Circumferential Distribution of Normal Pressure Computed from the 23 m DOB Contact Interface LS-DYNA Model at Respective Mid-Height Peak S_{rr} Times.

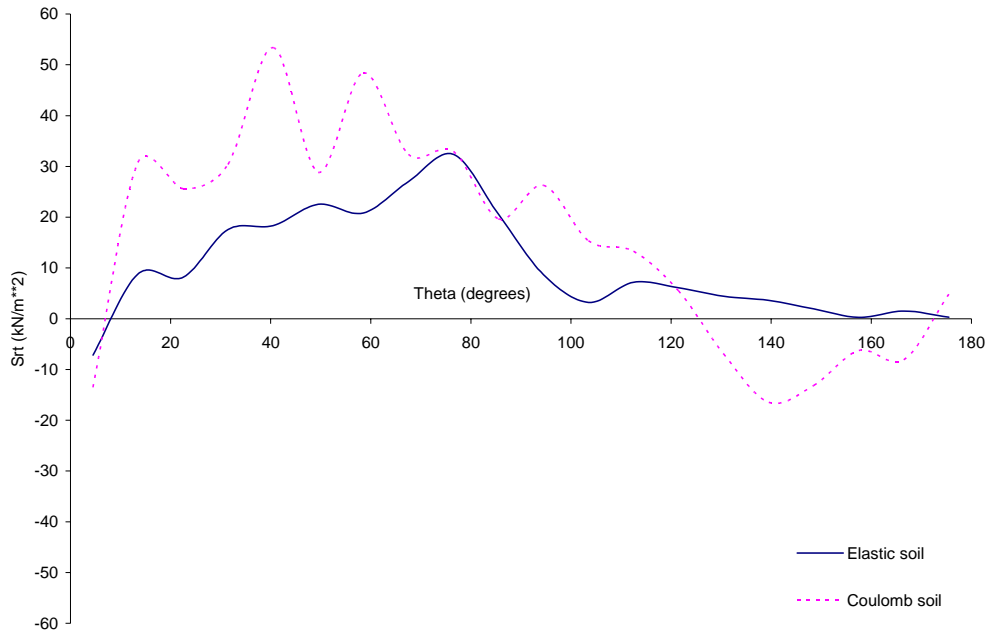


Figure 4.5-16 Effect of Soil Material Models on Circumferential Distribution of Tangential Shear Computed from the 23 m DOB Contact Interface LS-DYNA Model at Respective Mid-Height Peak S_{rt} Times.

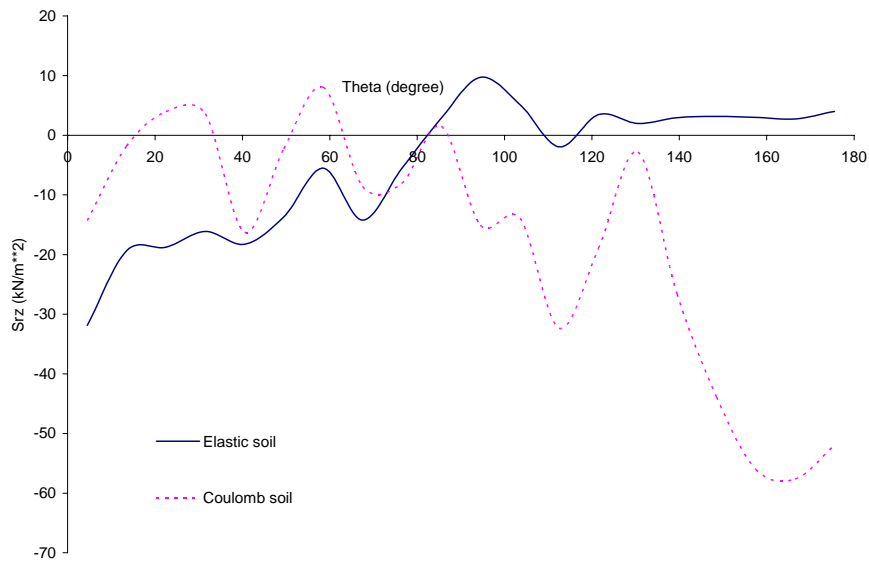


Figure 4.5-17 Effect of Soil Material Models on Circumferential Distribution of Vertical Shear Computed from the 23 m DOB Contact Interface LS-DYNA Model at Respective Mid-Height Peak S_{rt} Times.

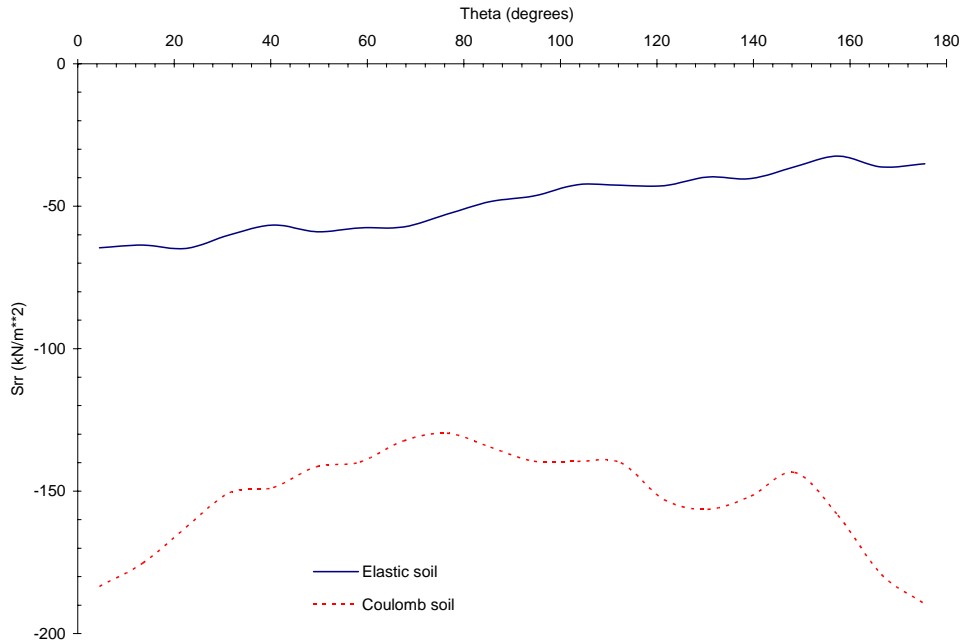


Figure 4.5-18 Effect of Soil Material Models on Circumferential Distribution of Normal Pressure Computed from the 23 m DOB Tied Interface LS-DYNA Model at Respective Mid-Height Peak S_{rr} Times.

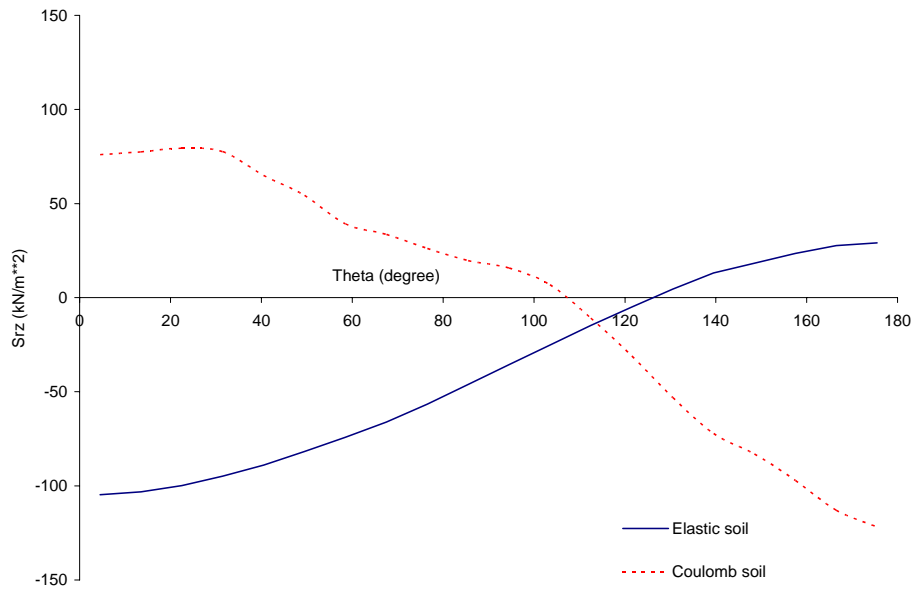


Figure 4.5-19 Effect of Soil Material Models on Circumferential Distribution of Vertical Shear Computed from the 23 m DOB Tied Interface LS-DYNA Model at Respective Mid-Height Peak S_{rr} Times.

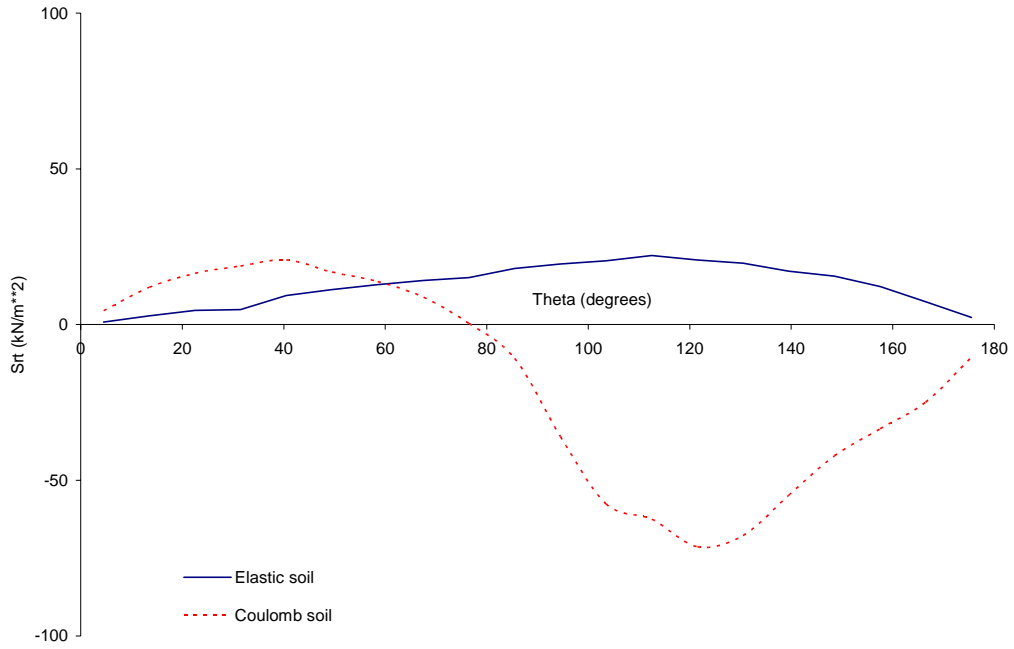


Figure 4.5-20 Effect of Soil Material Models on Circumferential Distribution of Tangential Shear Computed from the 23 m DOB Tied Interface LS-DYNA Model at Respective Mid-Height Peak S_{tr} Times.

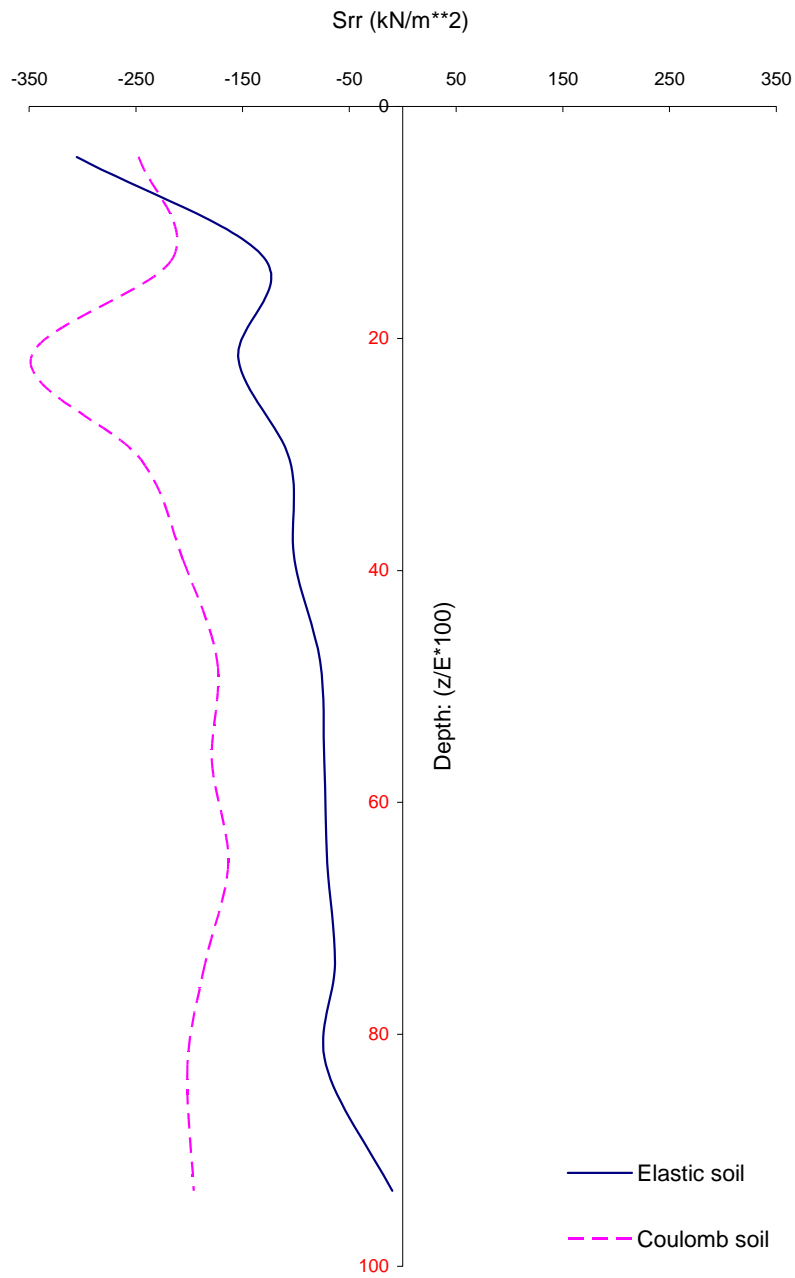


Figure 4.5-21 Effect of Soil Material Models on Vertical Distribution of Normal Pressure Computed from the 23 m DOB Contact Interface LS-DYNA Model at Respective Ground Surface Peak S_{rr} Times.

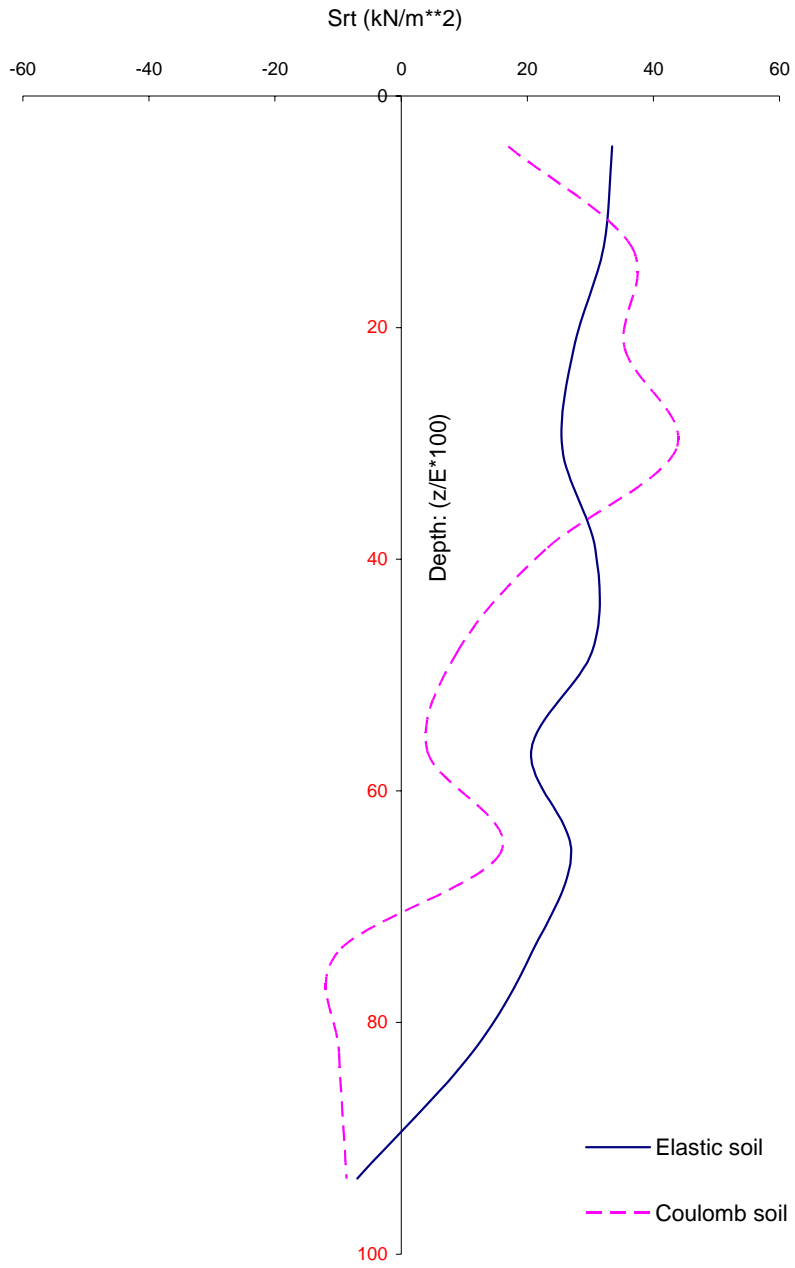


Figure 4.5-22 Effect of Soil Material Models on Vertical Distribution of Tangential Shear Computed from the 23 m DOB Contact Interface LS-DYNA Model at Respective Ground Surface Peak S_{rt} Times.



Figure 4.5-23 Effect of Soil Material Models on Vertical Distribution of Vertical Shear Computed from the 23 m DOB Contact Interface LS-DYNA Model at Respective Ground Surface Peak S_{rr} Times.

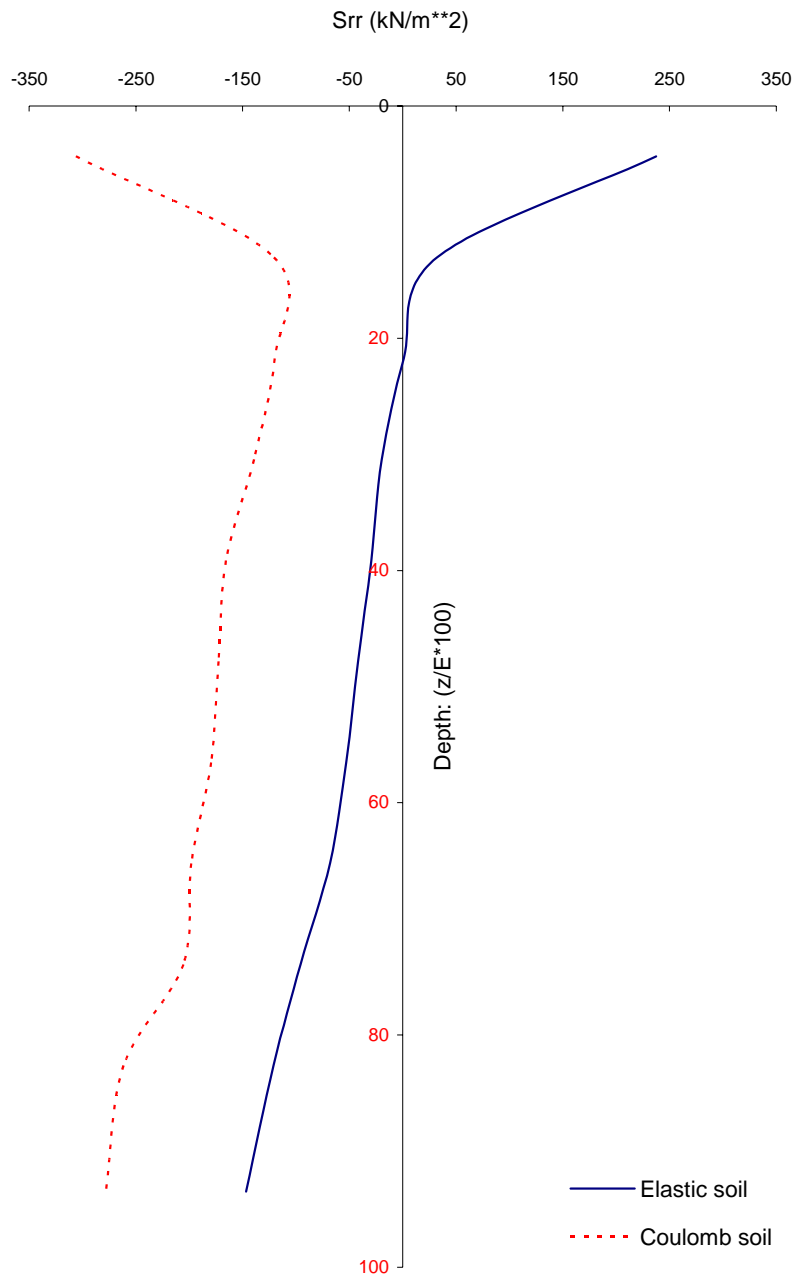


Figure 4.5-24 Effect of Soil Material Models on Vertical Distribution of Normal Pressure Computed from the 23 m DOB Tied Interface LS-DYNA Model at Respective Ground Surface Peak S_{rr} Times.

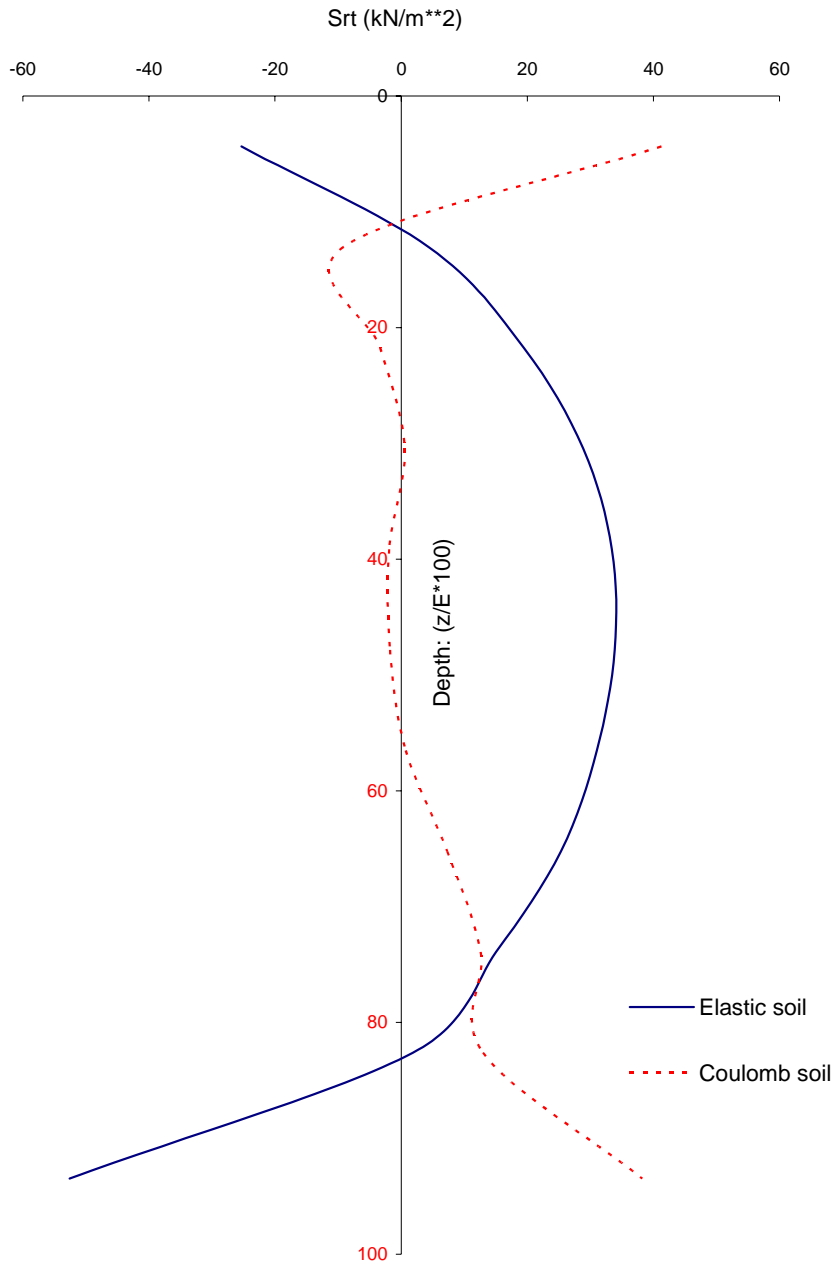


Figure 4.5-25 Effect of Soil Material Models on Vertical Distribution of Tangential Shear Computed from the 23 m DOB Tied Interface LS-DYNA Model at Respective Ground Surface Peak S_{rt} Times.

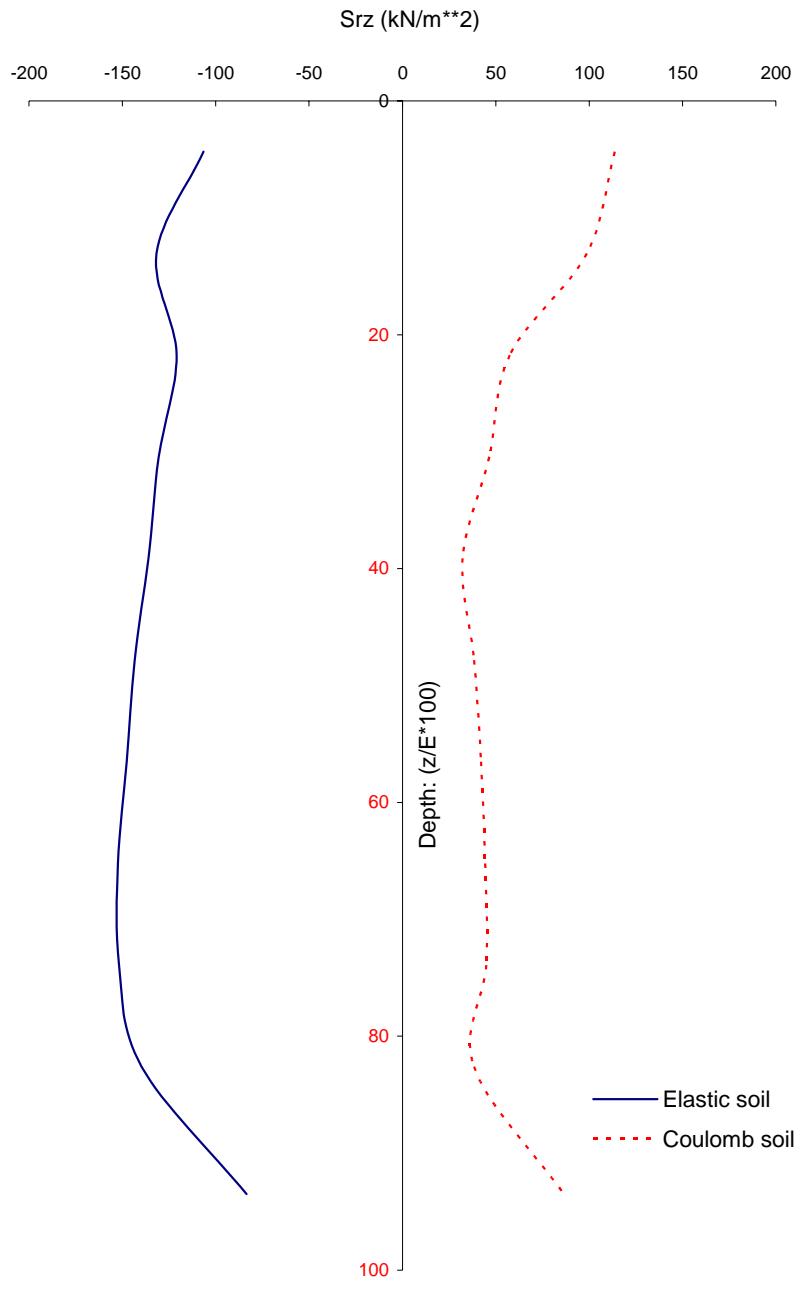


Figure 4.5-26 Effect of Soil Material Models on Vertical Distribution of Vertical Shear Computed from the 23 m DOB Tied Interface LS-DYNA Model at Respective Ground Surface Peak S_{rz} Times.

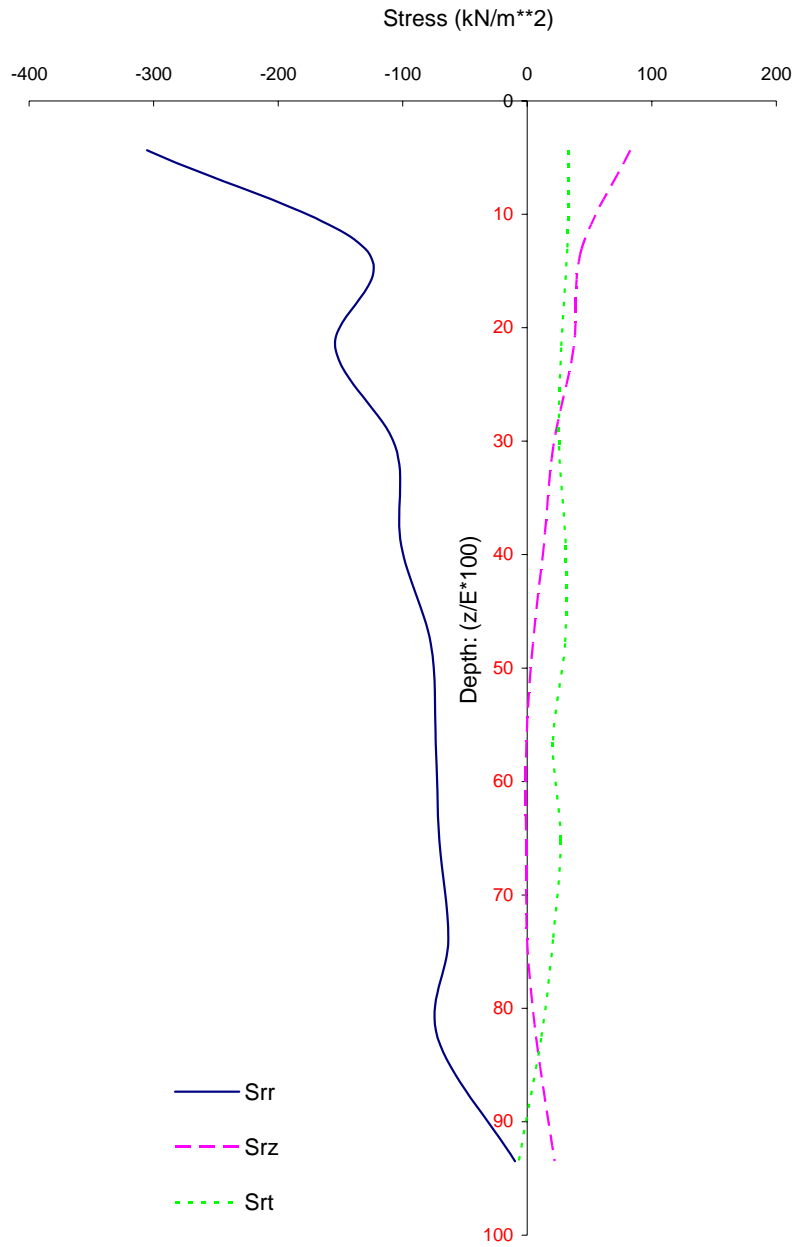


Figure 4.5-27 Vertical Distribution of Soil Stresses in the Head-on Soil Element near Ground Surface Computed using Elastic Soil Model from the 23 m DOB Contact Interface LS-DYNA Model at Respective Ground Surface Peak S_{rr} Times.

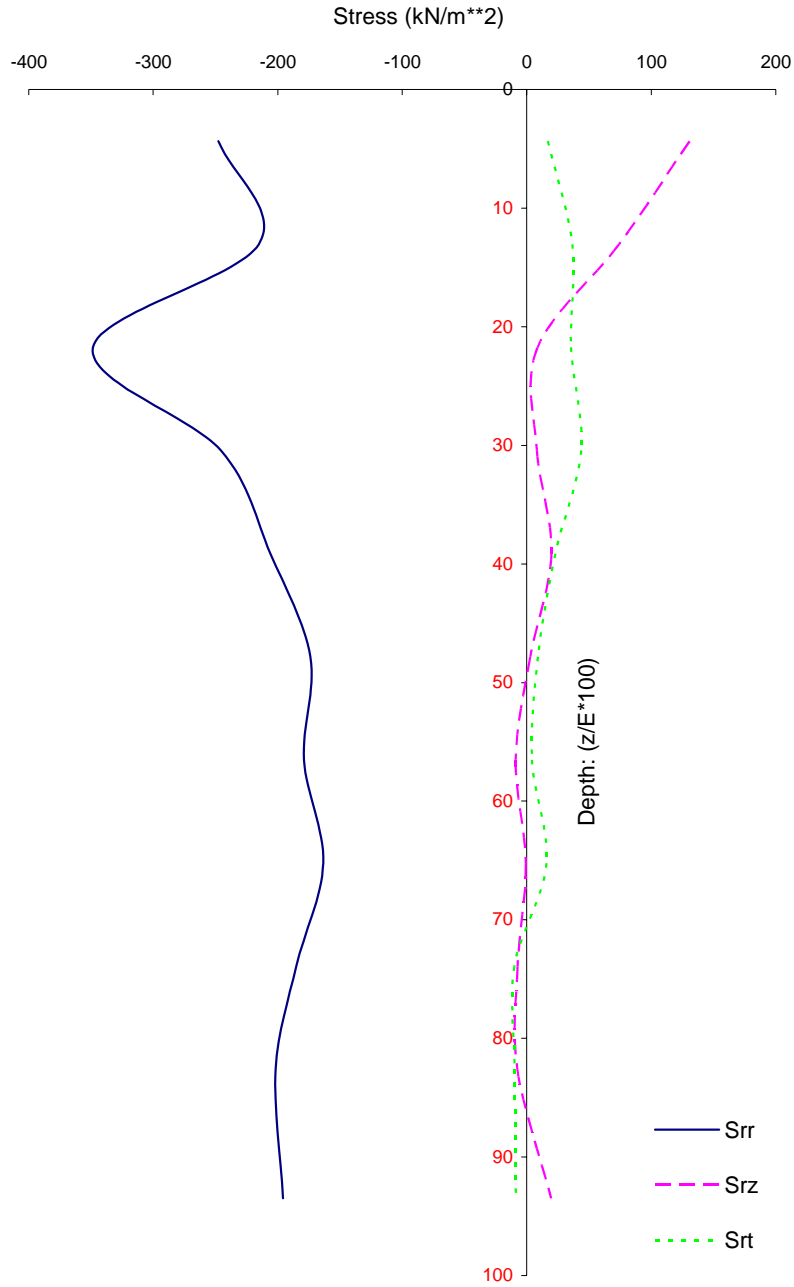


Figure 4.5-28 Vertical Distribution of Soil Stresses in the Head-on Soil Element near Ground Surface Computed using Coulomb Soil Model from the 23 m DOB Contact Interface LS-DYNA Model at Respective Ground Surface Peak S_{rr} Times.

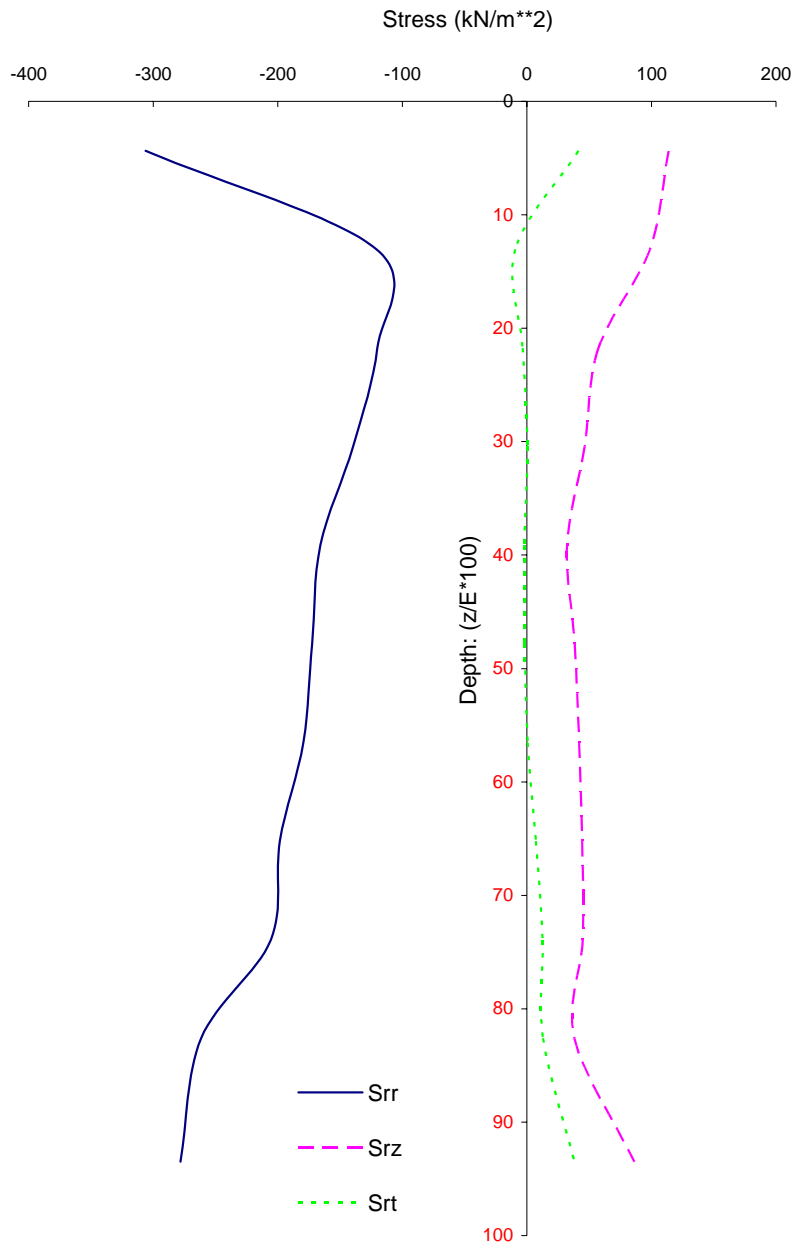


Figure 4.5-29 Vertical Distribution of Soil Stresses in the Head-on Soil Element near Ground Surface Computed using Coulomb Soil Model from the 23 m DOB Tied Interface LS-DYNA Model at Respective Ground Surface Peak S_{rr} Times.

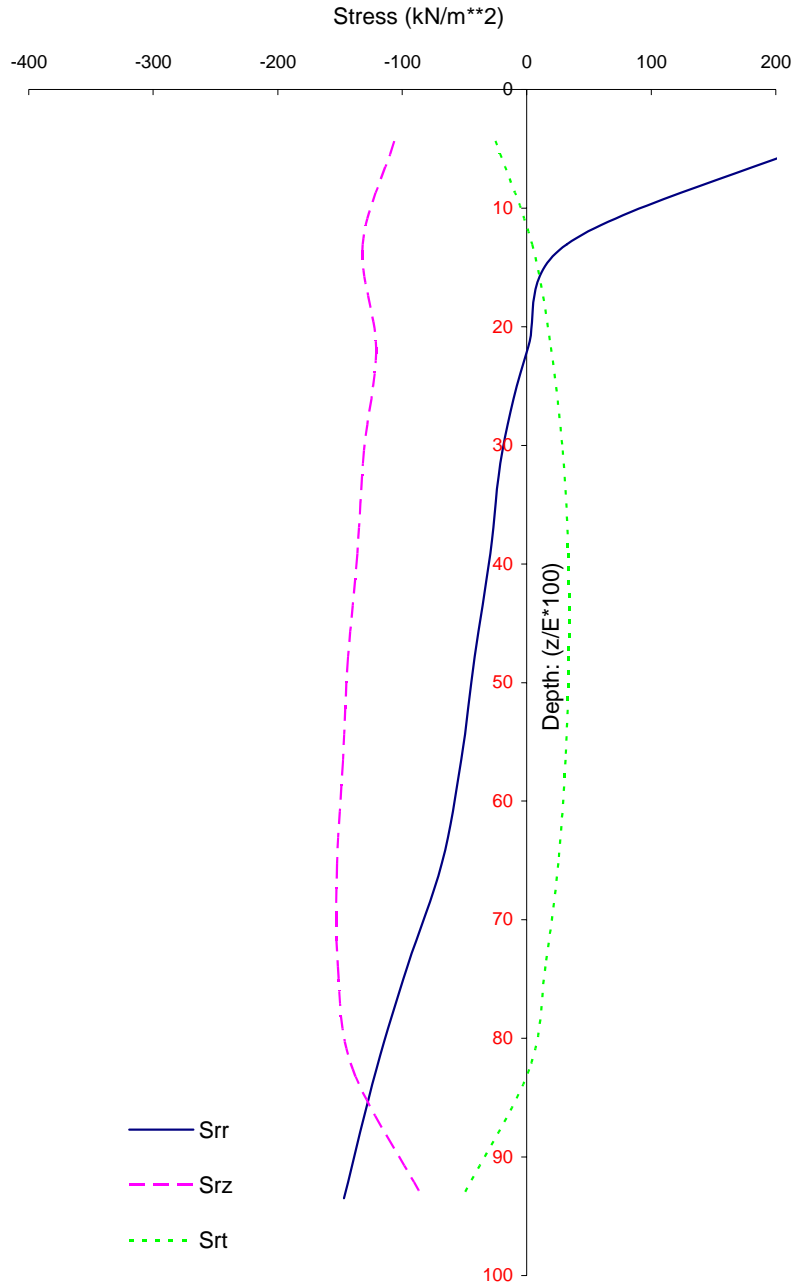


Figure 4.5-30 Vertical Distribution of Soil Stresses in the Head-on Soil Element near Ground Surface Computed using Elastic Soil Model from the 23 m DOB Tied Interface LS-DYNA Model at Respective Ground Surface Peak S_{rr} Times.

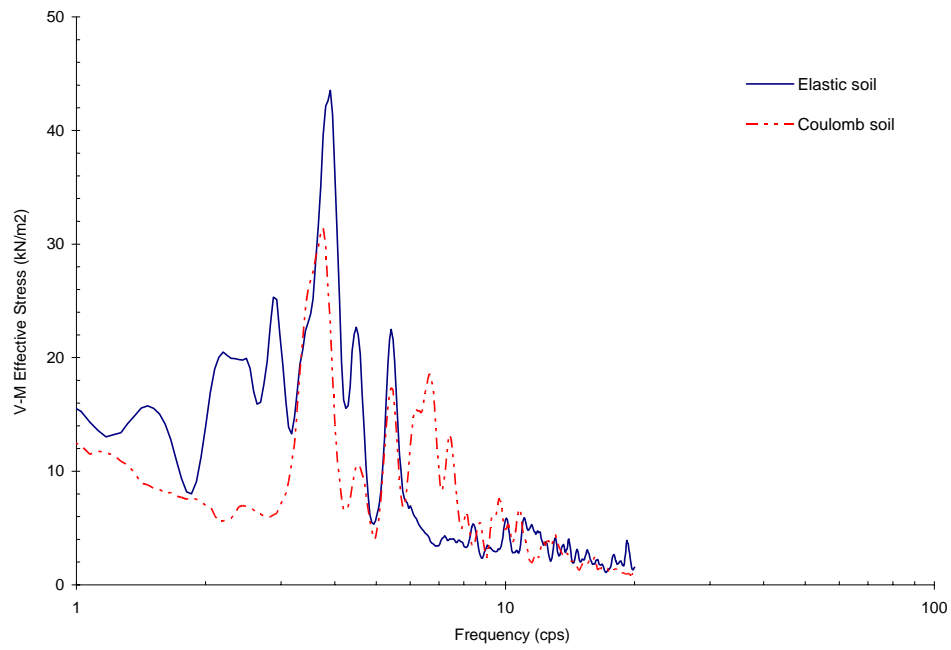


Figure 4.5-31 Fourier Spectra of Von-Mises Effective Stress in the 5th Head-on Structural Wall Shell Element Computed from 23 m DOB Contact Interface Model.

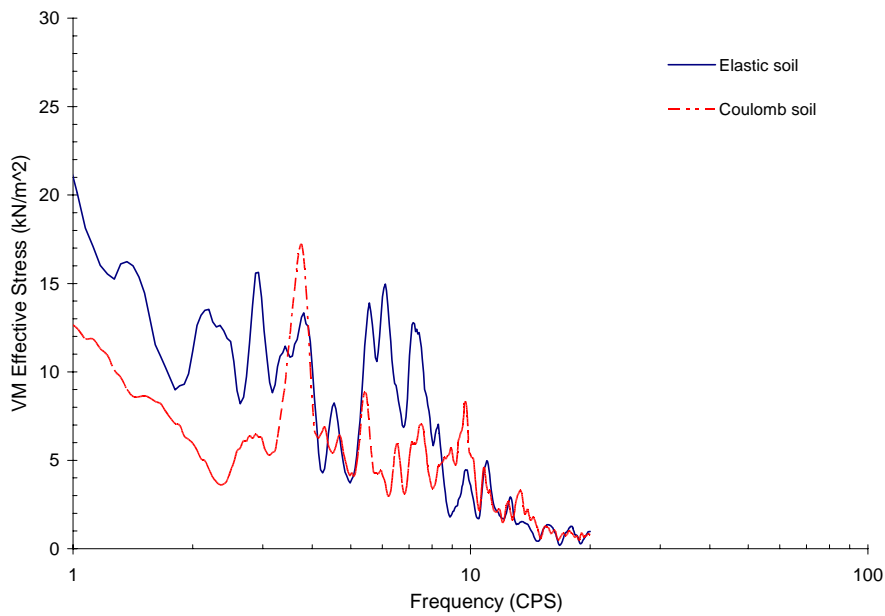


Figure 4.5-32 Fourier Spectra of Von-Mises Effective Stress in the 5th Head-on Structural Wall Shell Element Computed from 23 m DOB Tied Interface Model.

5.0 DEVELOPMENT OF BENCHMARK PROBLEMS

One objective of this study is to develop the characteristic parameters for a series of benchmark problems that can be used to verify whether any given computer code can adequately predict the seismic response of deeply embedded nuclear power plant facilities. To achieve this objective the benchmark problems should include a range of characteristics that are typical of the new generation power plants and most importantly include those parameters which significantly affect the seismic response of the facility. The characteristics of the selected problems are described in this section of the report.

The criteria used to develop the benchmark problems are discussed in the following section. This is followed with detailed descriptions of the problems.

5.1 Criteria Used to Select Benchmark Problems

The benchmark problems should be as simple as possible and still include the details that make them representative of the new generation of nuclear power plants and that contain a range of parameters that are important to their seismic response. The following selections are made to achieve these objectives:

- The structural model includes an exterior reinforced concrete structure that has vibration frequencies which interact with the soil-structure-interaction and free field column frequencies. The model interior includes some shear walls and floor diaphragms. A single structural model is used since the structural portion of most codes is not an issue of concern.
- Several depths of embedment are included ranging from shallow embedment to fully embedded. Underground facilities are not included.
- Several pieces of interior equipment are included in the models. A single set of characteristics for this equipment is used since this modeling is also not an issue of concern. These are major pieces of equipment having large masses and frequencies that interact with some of the other system frequencies. Piping runs are not included.
- Several soil models are included ranging from a very soft soil to a very hard soil. Uniform soil models and soils with properties varying with depth are included. Soil degradation effects are not included.
- The seismic input is specified at the rock outcrop. Since soil property degradation is not considered in the models the magnitude of the input is not important; seismic response scales directly with the level of the input for the linear models considered here.

The solutions for which comparisons can be made include: soil pressures acting on the outer walls; response spectra at various locations on the exterior and interior structures; and shear stresses in the outer walls, inner walls and floor diaphragms.

5.2 Problem Characteristics

Two sets of benchmark problems are considered. The characteristics of the first problem are derived from a cylindrical reinforced concrete structure representative of a typical conceptual design for advanced reactors. The second problem has a rectangular outer structure and is representative of an Advanced Boiling Water Reactor. The physical properties of each of these are discussed in the following sections.

5.2.1 Cylindrical Structure

The characteristics of this model are developed from those used for the sample problems considered for the variation of parameter studies described in Section 3 and 4 of this report. Details of these models are given in Section 3.1.1. The soil models and free field input used for the benchmark problems are the same as used for the sample problems and are not discussed further here.

The structural model is derived from the characteristics of a conceptual design for the advanced reactor as described in Section 3.1.1 and shown on Figure 3.1.1-1. The cylindrical portion of the facility containing the reactor and the power conversion vessel is selected as the structure to be used in this study. This cylinder is 46 m long and has an outer diameter of 26 m. The actual containment consists of a variable thickness outer shell and several major walls spanning across the containment providing both flexural rigidity and dividing the space into major compartments. This is modeled with a uniform thickness cylindrical shell having a wall thickness of 1 m. The basemat is modeled with a 3 m thick slab and the roof is modeled with a 1 m thick slab. The major interior walls are shown in the horizontal cross section on Figure 5.2-1(a). The power conversion vessel and the reactor vessel are located in the two spaces developed by the 2 m walls. A vertical section through the model is shown on Figure 5.2-1(b). The reactor vessel skirt sits on the floor 15 m above the foundation and lateral supports are 16 m higher. The power conversion vessel supports are located 21 m above the base. All of the structural elements (exterior and interior walls) are modeled with plate elements. The following properties are used for the concrete:

- Compressive strength = 27,580 kN/m²
- Poisson's ratio = 0.2
- Damping = 5 % of critical
- Density = 23.6 kN/m³

The structural weights of the cylindrical vessel with interior walls is (195,243 k N), the basemat weight is (150,116 kN), and the roof weight is (50,089 kN) giving a total weight of 395,450 kN. The cross sectional area of the cylinder (interior and exterior walls) is 197.3 m² and the moment of inertia of the cross section (about the weak axis) is 5906 m⁴.

A major parameter varied in the study is the depth of burial of this model. The model is buried to depths (E) equal to 25% (11.5 m), 50% (23 m), 75% (34.5 m), and 100 % (46 m) of the structural height. These depths of burial (DOB) correspond to DOB / radius ratios of 0.88, 1.77, 2.65, and 3.54 respectively. Current technology has been limited to DOB at the lowest end of this scale so that the primary objective of the study is to determine whether the application of this technology leads to uncertainties when the DOB increases beyond 25 % of the facility height or 85 % of the facility radius. The benchmark problem with a DOB closest to the design DOB should be used for verification of the computer code used for design.

The reactor and power conversion vessels are included in the model as discussed above. The reactor vessel is about 27 m long with a diameter of 7 m, and the power conversion vessel is 25 m long and 7m in diameter. Both are steel cylindrical shells. The reactor vessel wall thickness is 33 mm and the power conversion wall thickness is 24 mm. The weights of these two vessels are 8,229 kN and 13,520 kN respectively. Each of these vessels is modeled with a lumped mass beam and supported as discussed above. The total weight of the system becomes 417,199 kN when

these weights are added to the structural weight. An additional equipment weight of 88,960 kN is added to account for miscellaneous equipment and structure and brings the total weight to 506,159 kN.

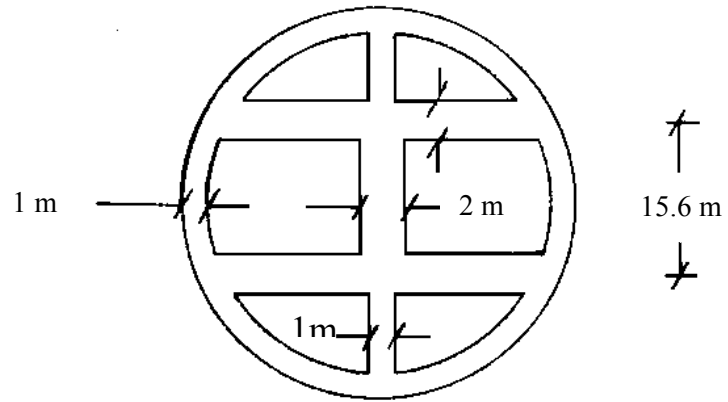
Assuming that the weight is uniformly distributed over the length (46 m) of the facility, the free – free frequency of the beam is found to be 19.3 cps. Other frequencies of interest are the frequency of the cantilever beam for the portion that protrudes above the ground surface. These frequencies are found to be 5.4 cps, 12.1 cps, and 48.4 cps for the lengths of beam above the ground equal to 34.5 m, 23 m, and 11.5 m respectively. Of course this frequency is of no interest for the case where the beam is totally buried.

It should be noted that solution for this benchmark model can be found in the results presented in Section 3 and 4 if the internal equipment is neglected. These include all of the variations in soil properties and depths of burial.

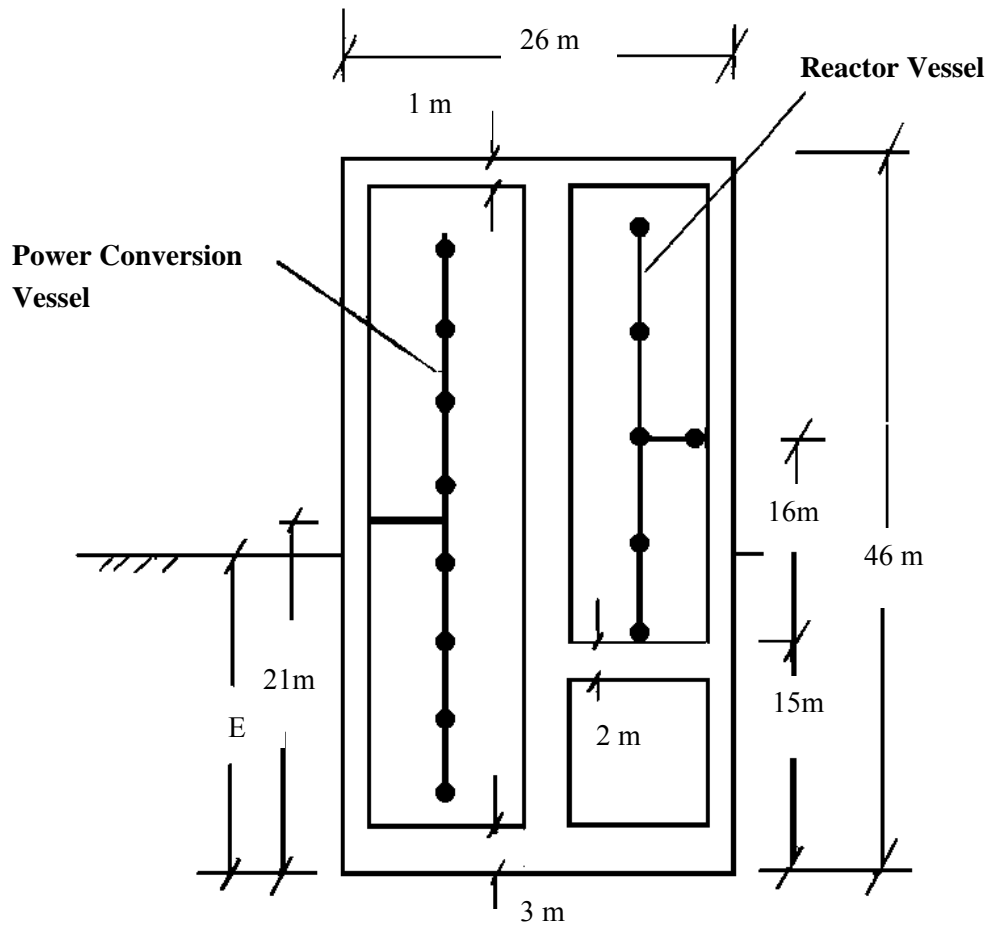
5.2.2 Square Box Type Structure

The structural characteristics of this model are derived from a test model structure for an ABWR reactor building. Dimensions are scaled up to be representative of the prototype. The reactor building is a square reinforced concrete structure 60 m by 60 m in plan, 83 m in height, and embedded to a depth of 33.75 m ($E/H = 0.41$). A sketch of a vertical section through the facility is shown on Figure 5.2-2 (a), and a typical horizontal cross section is shown on Figure 5.2-2 (b). Dimensions of all major structural elements are shown on these figures. The concrete properties are the same as those used for the example discussed in Section 5.2.1. The total structural weight is found to be about 1,270,000 kN. The moment of inertia of the structure is $1,100,000 \text{ m}^4$.

The same two internal pieces of equipment as for the first example problem are located as shown on Figure 5.2-2 (a) and supported in the same manner. The equipment weight is 21,750 kN. The total weight of the facility is therefore 1,121,750 kN resulting in a bearing pressure of 312 kN/m^2 . The free-free frequency of the structure is about 7.4 cps.

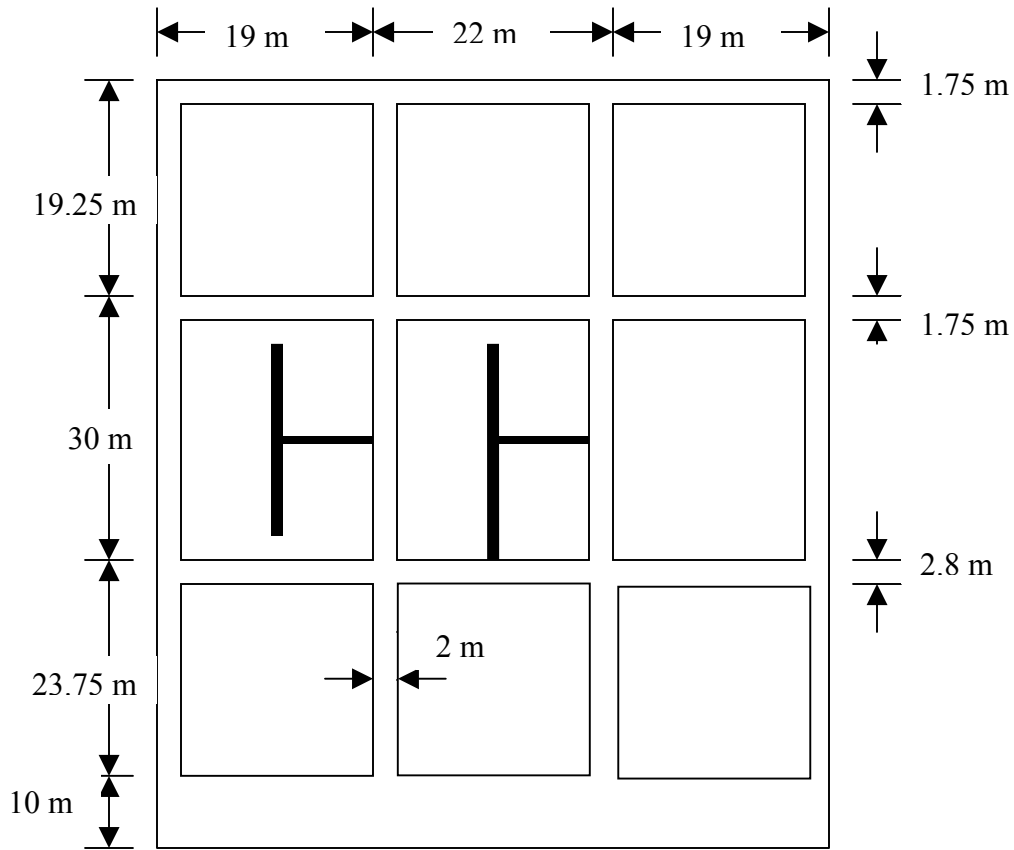


(a) Horizontal Cross Section

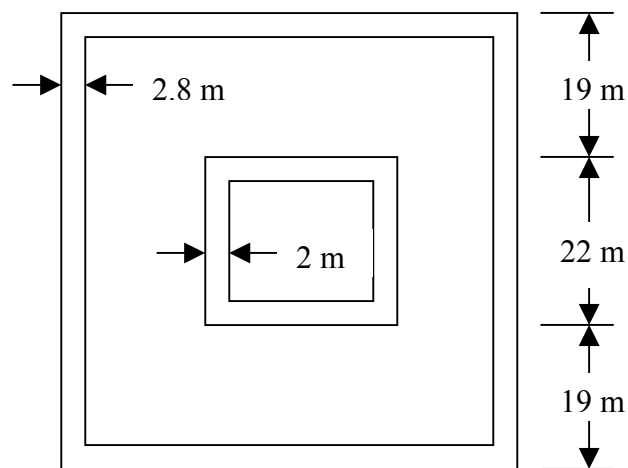


(b) Vertical Cross Section

Figure 5.2-1 Sketch of Cylindrical Benchmark Model



(a) Vertical Section



(b) Horizontal Section

Figure 5.2-2 Sketch of Square Benchmark Model

6.0 CONCLUSIONS AND RECOMMENDATIONS

The importance for understanding the SSI response characteristics of DEB structures is made clear by several proposed advanced reactor designs which include partial or completely buried containment and other NPP structures. It is important from a regulatory standpoint that practical aspects of existing SSI methods and computer programs be evaluated to determine their applicability and adequacy in capturing the seismic behavior of DEB NPP structures. Brookhaven National Laboratory (BNL) under JCN Y-6718 has performed this research program to address this issue. The overall objective of this research is to investigate the applicability of existing seismic design practice and SSI computer codes to DEB structures and to make recommendations for any modifications, if necessary. This report provides a detailed description of the program conducted at BNL to evaluate the extent to which current technology is adequate to address the seismic response of DEB structures.

This report consists of four major elements: 1) Review and evaluation of existing seismic design practice, 2) Assessment of simplified vs. detailed methodologies for SSI in-structure response spectrum analysis of DEB structures, 3) Assessment of methodologies for computing seismic induced earth pressures on DEB structures, and 4) Development of the criteria for benchmark problems which could be used for validating computer programs for computing seismic responses of DEB NPP structures.

During the review and evaluation phase of the program, a literature search was performed and over one hundred publications were identified pertaining to studies on the seismic response of partially to fully embedded structures. These studies reflect the state-of-the-art analysis methods, experimental tests and design guidelines that are currently available. A review of this information helps to identify gaps that may exist in knowledge and potential issues that may require better understanding when DEB NPP structures are considered. Several areas where uncertainties exist in the analytical methods used to evaluate the seismic response of deeply embedded facilities are identified and are discussed in the report. The major uncertainties found are:

- The effect of deep embedment on the relative significance of kinematic interaction;
- The extent to which non vertically propagating shear waves may be more important for deeply embedded structures than for those with shallow embedment depth;
- The impact of deep embedment on the accuracy of side wall impedance functions calculated with standard methods;
- The effect of nonlinear effects (separation of wall and soil, and soil material properties) on wall pressure calculations.

The term kinematic interaction refers to the modification of the free-field seismic waves by the geometry of the embedded portion of a structure and therefore is independent of the inertial properties of the structure. The term inertial interaction is associated with the dynamic response of the coupled structure-foundation system which is governed by the inertial properties of the structure and foundation impedance functions.

The above uncertainties provide the bases for the subjects of the study that is summarized in Sections 3 and 4 of this report. In Section 3, a containment structure for the conceptual design of a typical advanced reactor was considered. The CARES and SASSI programs were used which are representative of simplified and detailed analysis methods, respectively. Analyses were performed using both codes on the containment structure with various embedment conditions (25%, 50%, 75% and 100% of the structural height) to address the embedment effect on SSI characteristics

(both kinematic and inertial interaction) and the non-vertical wave propagation problem, as well as the methodologies to address them in terms of in-structure response spectrum calculations. Comparisons of basemat and roof response spectra are made to evaluate differences between the simplified and detailed analytical methods. Solutions are computed for three soil columns: a soft uniform column, a hard uniform column, and a variable stiffness column typical of a granular material. Based on the analyses performed for three soil profiles, the following conclusions are drawn with respect to the comparison of simplified vs. detailed methods for computing in-structure response spectra:

For Kinematic interaction:

The soft uniform soil column:

- Kinematic interaction effects are rather significant at the surface for frequencies greater than 2 cps.
- Kinematic interaction effects are much less significant at the basemat elevation and could probably be neglected.
- The CARES predictions are somewhat higher than the SASSI predictions at the surface and about the same at the basemat.

The hard uniform soil column:

- Kinematic interaction effects are not significant for the shallow depth of burial (DOB) but are significant for the deepest DOB.
- For the deepest DOB, the SASSI kinematic interaction predictions are higher than the CARES predictions, especially at frequencies greater than 3 cps.

The variable property soil column:

- The SASSI and CARES predictions are very close for the 11.5 m and 23 m DOBs.
- The CARES predictions at the surface are generally higher than the SASSI predictions for the 34.5 m and 46 m DOBs at frequencies greater than about 3 cps.
- The CARES and SASSI predictions are quite close at the basemat except for the region around 10 cps where the SASSI predictions exceed the CARES predictions.
- In general, kinematic interaction effects are significant for this soil column for all cases.

For all cases, the non-vertical incident wave effect was also studied using the SASSI program. The analysis assumes a constant input motion defined at the ground surface and the incident waves specified at the rock/soil interface. The SASSI analysis accounting for the non-vertical wave effect results in either a small reduction or virtually no changes in the SSI in-structure response spectra. The torsional effect due to the non-vertical waves on the translational response spectra results in less than 5% increase and could be neglected from a practical standpoint. However, had the input ground motion been defined at the base of the soil column consistent with the corresponding outcrop motion, the effect of the non-vertical incident waves on the SSI in-structure response spectra could have been considerably increased.

For SSI responses:

The soft uniform soil column:

- The SASSI and CARES predictions are similar for the 11.5 m embedment, except at the roof, where the SASSI prediction exceeds the CARES prediction at about 2 cps.
- The SASSI predictions generally exceed the CARES predictions at 46 m DOB.

The hard uniform soil column:

- The SASSI and CARES predictions are generally very close for both the shallow and deepest DOBs. The one exception occurs at the basemat level at about 10 cps, where the SASSI prediction exceeds the CARES prediction.

The variable property soil column:

- The SASSI and CARES predictions are generally very close for the 11.5 m and 23 m DOBs, except for the shallower DOB at the roof and at about 6 cps, where the SASSI prediction exceeds the CARES prediction.
- The SASSI and CARES predictions for the two deeper DOBs are somewhat different with the CARES predictions generally exceeding the SASSI predictions. The SASSI predictions exceed the CARES predictions at the basemat at about 10 cps.

To evaluate relative performance of the simplified vs. detailed analysis methods, two performance rating indexes were established. One index uses relative peak spectral acceleration and the other utilizes the frequency dependent relative spectral area differences. Both indexes were computed for the kinematic and SSI analyses results, and the following observations are made:

- When the peak rating indexes are used and assuming that a 10 % under prediction is considered to be acceptable, the CARES kinematic interaction results are acceptable for E/R ratios less than 2 and 3.5 for the soft and hard uniform soil columns, respectively. When SSI spectra are considered, the CARES results are never acceptable for the soft uniform soil column and are acceptable for E/R less than 2 for the hard uniform soil column. For the indexes with the variable soil column, CARES results are acceptable for E/R less than 2.5 for the kinematic spectra and for E/R less than 1.3 for the SSI spectra.
- When the rating indexes based on spectral areas are used, assuming again that the 10% difference is used as acceptance criteria, the CARES results are: not acceptable for the soft uniform soil column, acceptable for E/R less than 2.1 for the hard uniform column, and acceptable for E/R less than 2.2 for the variable soil column.

Another finding of the simplified method as implemented in CARES is that since the impedance functions are calculated based on averaged soil properties of both base and side, the radiation damping tends to be over-prescribed in CARES. As explained in Section 3.4, a cut-off frequency exists below which the radiation damping should be zero. A parametric analysis was performed in that the radiation damping was reduced to 70% of the nominal value in CARES and the resulting SSI response spectra are shown to be conservative compared to the SASSI results. However, addressing the over-prescribed radiation damping in CARES is problematic and further research would be necessary to develop a suitable model for handling the radiation damping within CARES.

The assessment of methodologies for computing seismic induced earth pressures on DEB structures is conducted using the SASSI and LS-DYNA codes. Due to the phenomenological change of SSI from primarily an inertial interaction effect for shallow embedded structures to predominantly a kinematic interaction effect for DEB structures, seismic induced wall pressures and their effects on the stresses induced in the embedded walls may become embedment dependent. In Section 4, the SASSI and LS-DYNA programs are first used for an assessment of the linear methodologies to investigate various important embedment effects on seismic induced pressures. An evaluation of the effect of the soil-structure interface models and soil material models on the seismic response characteristics is then performed using the LS-DYNA program with the contact interface and tied interface features.

For linear analysis based on the SASSI results for the four DOB (11.5 m, 23 m, 34.5 m, and 46 m), the characteristics of the seismic induced wall pressure are summarized below:

- The seismic induced wall pressure is primarily the result of the inertial interaction effect for DOB = 11.5 m and kinematic interaction for the three deeper DOBs;
- The variation of normal pressure and vertical shear follow a cosine variation around the cylinder and the tangential shear follows a sine variation. These are expected results based on the symmetry conditions of the problem;
- The distribution of the soil pressure with depth is also very different between the four DOB cases. For the 11.5 m case: the normal pressure varies from a peak value (300 kN/m^2) at the surface to almost zero at the basemat; the tangential shear also varies linearly from a peak value at the surface (80 kN/m^2) to almost zero at the basemat; and the vertical shear is fairly constant with depth at about 100 kN/m^2 . The pressure distributions are about the same for the other three cases and show: both the radial and tangential shears vary uniformly with depth at a value of about 25 kN/m^2 ; and the vertical shear varies linearly from near zero at the surface to a peak value at the basemat equal to about 150 kN/m^2 ;
- Having accounted for dead load, negative (tensile) normal pressure still is present for depths less than about 6 m for the 11.5 m DOB case. One might then expect that separation between the soil and wall would occur above 6 m and that this separation could significantly affect the results. This does not occur for the three deeper DOB cases;
- Since typical NPP containment structures are massive and very stiff structures, the major portion of the displacement is due to rigid body motion and the shear displacements are very small. The relatively small magnitude of the shear displacements as compared to the total displacements leads to questions of accuracy in the shear displacements (a result of taking the differences between two numbers which are large and close together). Small errors in the predictions of the total displacements may result in large errors in the predictions of the shear displacements. It may not be a good idea to use these predicted displacements to calculate shear loads in the structural walls.

The above observations based on the SASSI analysis were then confirmed by the LS-DYNA analysis using the tied structure/soil interface. The LS-DYNA analyses are performed with a detailed finite element mesh for both the structure and the near field surrounding soils, an approach usually referred to as the explicit SSI model (or direct approach). This is compared to the SASSI model which uses the sub-structuring approach.

Although considerable differences exist between the LS-DYNA models (approximate approach for the half-space, Rayleigh damping and time domain direct integration) and the SASSI models (analytical wave solution for the half-space, material damping, and frequency domain solution), the resulting SSI response parameters computed with both programs, such as in-

structure response spectra and soil induced wall pressure, are comparable within the linear analysis definition. In addition, the free field response is performed using the LS-DYNA model. The LS-DYNA free field surface response in terms of the 5% damped response spectrum is compared with the conventional 1-D convolution analysis performed using CARES. Reasonably good agreement of the free field response is found between the LS-DYNA and CARES analyses.

A summary of comparisons of the LS-DYNA and SASSI linear analyses are provided below:

- In general, LS-DYNA explicit linear analysis confirms the applicability of SASSI as a linear methodology for the seismic response of DEB structures;
- Reasonable correlations are found in the comparisons of the in-structure response spectra, especially at the roof location. The higher peak response seen in the LS-DYNA results may be attributed to the more refined model and the use of Rayleigh damping employed by LS-DYNA (as compared to the material damping used in CARES and SASSI);
- Similar circumferential distributions of the soil pressures are computed by LS-DYNA and SASSI, which track well with sinusoidal variations;
- Similar vertical distribution of the soil pressures are also established with both LS-DYNA and SASSI, although the pressure amplitudes may vary between the two analyses;
- Results of the shear displacements of the embedded structural wall are within the same order of magnitude computed with both LS-DYNA and SASSI. When compared with the total lateral displacements, the same conclusion with both LS-DYNA and SASSI can be reached regarding the large errors which could be produced in the prediction of the shear displacements;
- Fourier spectra of soil pressure computed at the head-on soil element for both the SASSI and LS-DYNA models result in remarkably close comparisons between the two programs.

For DEB structures, it is believed that the soil/structure interface modeling and the material models for the surrounding soil are the two most important factors which affect the quality of the seismic induced pressure calculations. To evaluate the effect of the soil-structure interface modeling on seismic response characteristics of DEB structures, seismic response analyses are performed using LS-DYNA models developed with contact interfaces. Traditional SSI analysis ignores the gravity effect when considering the SSI effect. However, in order to accurately establish the correct stress condition for the structure/soil interface, the LS-DYNA model considering the interface condition requires a preload of 1G gravity before commencing with the seismic transient analysis. This is done by statically ramping up the gravity load (dynamic relaxation phase) before performing the transient seismic analysis.

Two aspects of modeling are examined. One is associated with the wall/soil interface modeling effect. In this case the soil is modeled with linear elastic material, and two types of interface models are applied: contact interface and tied interface (Section 4.1.2). The second aspect is to assess the soil material modeling effect. The 23m DOB case is selected and the LS-DYNA analysis is performed for the soil, which is modeled as both linear elastic and Coulomb materials.

In order to develop insights into the interface modeling effect on the seismic response parameters, the analysis results of the LS-DYNA analysis with the contact wall/soil interface model are compared with a similar LS-DYNA analysis with the tied soil/structure interface model. The following conclusions are drawn based on the comparisons of the analysis results between the tied interface and the contact interface models which use the linear elastic model for soil:

- The separation effect at the structural wall and soil interface on the seismic response parameters is important. However, the largest amount of separation of the wall/soil interface is seen for the 11.5m DOB case (15.4 mm) and is gradually reduced as the DOB increases. For 23m DOB, the maximum wall/soil separation equals to 12.2 mm, for 34.5 mm, the maximum separation is reduced to 5.57 mm, and for the fully buried structure, the maximum separation becomes 1.42 mm, which is negligible compared to the dimension of the structure (27 m in diameter).
- The computed shear displacement is several magnitudes smaller than the computed total displacement, which implies that the structure mainly experiences rigid body movement. The shear displacement computed with the contact interface models appears to be reduced compared to that computed with the tied interface models.
- The structural base experiences up lifting from the supporting soil. However, the amount of base uplift reduces as DOB increases. For the fully buried configuration, no base uplift was observed.
- The in-structure response spectra are affected by the separation effect, including both peak amplification and peak shift to lower frequencies compared to the results computed with the tied interface model; the peak shift is more pronounced for shallow DOB cases.
- Circumferential variation of soil pressure no longer follows any sinusoidal functions and the peak pressure values are not always reduced compared with those computed with the tied interface model. Further, significant differences of the vertical distribution of soil pressure values are also observed between the contact and tied interface models.
- Vast differences were observed in both vertical and circumferential distributions of the soil pressures when computed using different interface models, and the contact interface tends to generate much higher pressure than that computed with the tied interface model.
- When the Fourier spectra of respective soil pressures are computed, the pressure peak computed with the tied interface condition tends to shift to lower frequencies as the depth of burial increases, while for the contact interface condition, the pressure peak tends to shift to higher frequencies as the depth of burial increases.
- The normal soil pressure is primarily induced by the inertial interaction effect. As DOB increases, the inertial effect reduces while the kinematic interaction becomes the primary mechanism for transmitting soil stresses to the structure; the normal soil pressure, therefore, is rapidly reduced. For the fully buried case, the calculated normal pressure is shown to be less than the initially imposed gravity load, suggesting that for large DOBs, the dynamic normal pressure load may not need to be considered.
- The structural stresses generally have frequency content similar to the respective soil pressures; however, the structural stresses induced by the soil pressures are not trivial, even though the structure may be fairly rigid.

In addition, when the gravity load is superimposed on the soil stresses computed using the SASSI linear analysis for the 23m DOB case (Section 4.4.6), negative (tensile) normal pressure still is present for depths less than about 11 m, which suggests that separation occurs at the interface between the wall and the soil from the ground surface to 11m in depth.

To assess the soil material modeling effect, the soil was modeled using both linear elastic and Coulomb models. The 23m DOB LS-DYNA model was used for assessing the soil material effect. The following conclusions are reached based on the comparisons of the results computed between the Coulomb soil model and elastic soil model:

- Separation effect at the structural wall and soil interface on the seismic response parameters is significantly reduced when the Coulomb soil model is used (maximum wall/soil gap of 0.15 mm computed with the Coulomb soil vs. 12.2 mm calculated with elastic soil model).
- The use of the Coulomb soil model modifies the in-structure response spectra, especially for the basemat, compared to the elastic solution.
- The Coulomb soil model results in noticeable changes in the soil pressure distributions in both circumferential and vertical directions. Fourier spectra of the normal pressure computed from the Coulomb soil model also contain low frequency upward drifts, which suggest that the impact of the Lysmer's transmitting boundary is more pronounced for the Coulomb soil model than the elastic soil.
- The Fourier spectra of the structural Von-Mises stresses generally indicate that even though the Coulomb soil model predicted higher normal pressure, the induced structural stresses are actually close to or lower than that computed with the elastic soil model.

Based on BNL's study, the criteria for a series of benchmark problems are defined. The purpose of the benchmark problems is that they can be used to verify whether any given computer code can adequately predict the seismic response of deeply embedded nuclear power plant facilities. To achieve this objective, a range of characteristics that are typical of the new generation power plants and most importantly their effects on the seismic response of the facility are identified. The following criteria are used to develop the benchmark problems:

- The structural model includes an exterior reinforced concrete structure that has vibration frequencies which interact with the soil-structure-interaction and free field column frequencies. The model interior includes some shear walls and floor diaphragms. A single structural model is used since the structural portion of most codes is not an issue of concern.
- Several depths of embedment are included ranging from shallow embedment to fully embedded. Underground facilities are not included.
- Several pieces of interior equipment are included in the models. A single set of characteristics for this equipment is used since this modeling is also not an issue of concern. These are major pieces of equipment having large masses and frequencies that interact with some of the other system frequencies. Piping runs are not included.
- Several soil models are included ranging from a very soft soil to a very hard soil. Uniform soil models and soils with properties varying with depth are included. Soil degradation effects are not included.
- The seismic input is specified at the rock outcrop. Since soil property degradation is not considered in the models, the magnitude of the input is not important; seismic response scales directly with the level of the input.
- The solutions for which comparisons can be made include: soil pressures acting on the outer walls; response spectra at various locations on the exterior and interior structures; and shear stresses in the outer walls, inner walls and floor diaphragms.

Based on the results documented in this report, it can be concluded that the linear SSI methodologies, including both simplified and detailed approaches, can be extended to DEB structures and produce acceptable SSI response calculations, provided that the SSI response induced by the ground motion is very much within the linear regime or the non-linear effect is not anticipated to control the SSI response parameters. Since there are as yet no general criteria that enable an analyst to predict a priori when nonlinear effects will become significant for a particular problem, the results of the linear calculations should be examined in enough detail to evaluate the potential for such effects. For example, peak stresses and stress ratios (shear/pressure) at critical locations along the building wall-soil interface can be determined from the linear calculation to

estimate if separation and/or shear sliding may potentially occur. Similarly, stresses under the toe of the foundation slabs can be examined to estimate if stress ratios are high enough to potentially lead to local failure levels.

For the case of strong ground motions, the non-linear effect is expected to have a strong impact on the SSI response calculations. For DEB structures, this study has shown significant uncertainties exist in the aspects of the interface modeling and soil material modeling. In this case, it was noted that the SSI response calculation is sensitive to the modeling assumptions made for the soil/structure interface and application of a particular material model for the soil. These modeling assumptions can only be validated through correlations with field or laboratory measured seismic response data, which are scarce, especially for moderate to strong earthquake events.

Additional strong ground motion response data are needed from tests and/or earthquake recordings to validate the pertinent modeling assumptions made for SSI response analysis of DEB NPP structures. Recognizing that it is difficult to obtain such data, additional analytic studies could be performed using the available nonlinear codes to try to determine which parameters of the structure-soil system are controlling SSI responses. For example, for the case of a linear structure and soil system, the parameters controlling separation and sliding along building-soil interfaces can be determined as a function of ground motion level. Once these controlling parameters are determined, the impact of nonlinear soil behavior on these relationships can be evaluated, using constitutive soil models considered appropriate for typical soil types. At least this process can lead to a scheme that a reviewer can use to ascertain when nonlinear behavior may be important.

7.0 REFERENCES

- ASCE Manual, "Design of Structures to Resist Nuclear Weapons Effects," Manual of Engineering Practice No. 42, ASCE, NY, 1961.
- ASCE 4-98, "ASCE Standard - Seismic Analysis of Safety Related Nuclear Structures and Commentary on Standard for Seismic Analysis of Safety Related Nuclear Structures," American Society of Civil Engineers, 1998.
- Abrahamson, N. A., Schneider, J. F., Stepp, J. C., "Empirical Spatial Coherency Functions for Application to Soil-Structure Interaction Analysis," Earthquake Spectra, Vol. 7, 1991.
- Abrahamson, N. A., "Spatial Variation Of Earthquake Ground Motion For Application To Soil-Structure Interaction," Report No. TR-100463, Electric Power Research Institute, March 1992.
- Agrawal, P. K., "Seismic Response of Underground Pipe and Structural Components," ASCE, New York, 1983.
- Aspel, R. J., et al., "Torsional Response of Rigid Embedded Foundations," Journal of the Eng. Mech. Div., ASCE, Vol. 102, No. EM6, pp 957-970, Dec. 1976.
- Aviles, J., et al., "Effects of Foundation Embedment During Building-Soil Interaction," Earthquake Engineering and Structural Dynamics, 27, 1523-1540, 1998.
- Beredugo, Y.O., and Novak,, M., "Coupled Horizontal and Rocking Vibration of Embedded Footings," Canadian Geotechnical Journal, Vol. 9.
- Baron, H., et al., "Theoretical Studies on the Ground Shock Phenomena," Report No. SR-19, The MITRE Corporation, 1960.
- BNL report, "Seismic Design and Evaluation Guidelines for The Department of Energy High-Level Waste Storage Tanks and Appurtenances," Prepared for the U.S. Department of Energy, BNL 52361 (Rev. 10/95), October 1995.
- Celebi, M., et al., "Inelastic Seismic Analysis of Deeply Embedded Reinforced Concrete Reactor Building," 5th Int. Conf. on Structural Mechanics in Reactor Technology, Amsterdam, Netherlands, 1979.
- Chen, P. C., et al., "Soil-Structure Interaction of Buried Structures," Structure Design of Nuclear Power Plant Facilities, Vol. 1-b, ASCE specialty conf., New Orleans, LA, pp.1032-1058, 1975.
- Day, S. M., "Finite Element Analysis of Seismic Scattering Problems, Ph.D Thesis, Univ. of California, San Diego, 1977.
- Dominguez, J., "Response of Embedded Foundations to Traveling Waves," Research Report R78-24, MIT, 1975.
- Dominguez, J., "Dynamic Stiffness of Rectangular Foundations," Report No. R78-20, MIT, Cambridge, Massachusetts, 1978.

EPRI NP-1728, "SIMQUAKE I – An Explosive test Series Designed to Simulate the Effects of Earthquake-Like Ground Motions on Nuclear Power Plant Models," vol. 1, Summary Report, February 1981.

Field, C. J., "Simulation of Full-Scale Seismic-Resistant Structural Frame Tests Using LS-DYNA," 4th European LA-DYNA User Conference, ULM, Germany, May 22-23, 2003. General Atomics, GT-MHR Conceptual Design Description Report, July 1996.

Hirota, M., "Study of Dynamic Earth Pressure through Observation," Tenth World Conf. on Earthquake Engineering, Balkema, Rotterdam, 1992.

Houston, T. W., et al., "Seismic Evaluation of A Fuel Facility in A Soil Layer over Rock," ASME Pressure vessel and piping conf., Boston, MA, July 1999.

Ichihara, M., et al., "Earth Pressure during Earthquake, Soil and Foundations," Japanese Soc. Soil and Found. Eng., pp. 75-86, 1973.

Ichihara, M., et al., "Earthquake Resistant Design of Quay Walls," Proc., 6th World Conf. On Earthquake Eng., 2. pp. 1969-1974, 1977.

Iguchi, M., "An Approximate Analysis of Input Motions for Rigid Embedded Foundations," Trans. of Architectural Inst. Of Japan, No. 315, pp. 61-75, May 1982.

Ishibashi, I., et al., "Dynamic Earth Pressure with Different Wall Movement Modes, Soils and Foundations," Japanese Soc. Of soil Mech. And Found. Eng., 27(4), pp. 11-22, 1987.

Japan Electric Association (JEA), "Technical Guidelines for Aseismic Design of Nuclear Power Plants," JEAG 4601-1991 Supplement (in Japanese).

Kato, M., "Review of Revised Japanese Seismic Guidelines for NPP Design," Nuclear Engineering and Design 114, pp 211-228, 1989.

Kausel, E., "Forced Vibrations of Circular Foundations on Layered Media," Report No. R74-11, MIT, Cambridge, Massachusetts, 1974.

Kausel, E., et al., "Dynamic Stiffness of Circular Foundations," Journal of Eng. Mech. Div, ASCE, vol. 101, No. EM6, pp.771-785, 1975.

Kausel, E., et al., "Vertical and Torsional Stiffness of Cylindrical Footings," Report No. R76-6, MIT, Cambridge Massachusetts, 1976.

Kausel, E., et al., "Dynamic Analysis of Embedded Structures," The 4th Int. Conf. on Structural Mechanics in Reactor Technology, K 2/6, 1977.

Kausel, E., "LAYSOL – A Program for the Dynamic Response Analysis of Layered Soils," version 3.1, Wellesley, MA 02181, 1992.

Kawamura, M., et al., "Effect of Interactions on Dynamic earth Pressures, Earth Pressures, Soil-Structure Interaction," A. S. Cakmak, ed., Elsevier, New York, pp. 103-110, 1987.

- Kiureghian, A., "A Response Spectrum Method for Random Vibration Analysis of MDF Systems," *Earthquake Eng. And Structural Dynamics*, vol. 9, pp.419-435, 1981.
- Konno, T., et al., "Site Response Based on the Borrego Valley Downhole Array Data," *Proceeding of the OECD/NEA Workshop on the Engineering Characterization of Seismic Input*, Brookhaven National Laboratory, Upton, New York, NEA/CSNI/R (2000) 2/Volume 2, 2001.
- Kuesel, T.R., "Earthquake Design Criteria for Subways," *J. Struct. Div. ASCE* 95, 1213-1231, 1969.
- Kuroda, T, et al., "Experimental and Analytical Studies on Seismic Qualification of 600Mwe CANDU Core," *The 6th Int. Conf. on Structural Mechanics in Reactor Technology*, K 9/3, 1981.
- LSTC, "LS-DYNA User's Manual," vols. 1 & 2, Version 960, March 2001.
- Luco, J. E., et al., "Dynamic response of Circular Footings," *Journal of Eng. Mech. Div., ASCE*, vol. 97, No. EM5, pp 1381-1395, 1971.
- Luco, J. E., et al., "Dynamic response of a Rigid Footing Bonded to an Elastic Half-space," *Journal of Applied Mech., ASME*, vol. 39, pp. 527-534, 1972.
- Luco, J. E., "Approximate External Boundaries for Truncated Models of Unbounded Media," *Proceedings, 3rd UJNR Workshop of Soil-Structure Interaction*, Menlo Park, CA, March 2004.
- Lysmer, J., et al., "LUSH, A Computer Program for Complex Response Analysis of Soil-Structure Systems," *Report No. EERC 74-4*, College of Engineering, University of California, 1974.
- Lysmer, J., et al., "SASSI – A System for Analysis of Soil-Structure Interaction," *Report No. UCB/GT/81-02*, Geotechnical Engineering, University of California, Berkeley, 1981.
- Lysmer, J., et al., 1999, "SASSI2000 – Theoretical Manual," Revision 1, Geotechnical Engineering, University of California, Berkeley.
- Masanori, H., "Study on Dynamic Earth Pressure through Observation," *10th World Conf. on Earthquake Engineering*, Balkema, Rotterdam, 1992.
- Masao, T., et al., "Earthquake Response of Nuclear Reactor Building Deeply Embedded in Soil," *5th Int. Conf. on Structural Mechanics in Reactor Technology*, Amsterdam, Netherlands, 1979.
- Miller, C., et al., "Soil-Structure Interaction Methods – SIM Code," *NUREG/CR-1717*, vol. III, September 1979.
- Miller, C., "Soil-Structure Interaction: vol. 2 – Influence of Lift-Off," *NUREG/CR-4588*, vol. 2, April 1986.
- Miller, C., et al., "Correlation of Fukushima Data with SSI Models," *The 8th Int. Conf. on Structural Mechanics in Reactor Technology*, k4, Brussels, Belgium, August 1985.
- Miller, C., et al., "CARES: Computer Analysis for Rapid Evaluation of Structures," Version 1.3, Earthquake Research Center at The City College of New York, prepared for U.S. Nuclear Regulatory Commission, May 2000.

- Miller, C., et al., "Degradation Effects on Soil Column and SSI Frequencies," The 16th Int. Conf. on Structural Mechanics in Reactor Technology, k4, Washington, D.C., August 2001.
- Mononobe, N, et al., "On the Determination of Earth Pressures during Earthquakes," Proc. World Eng. Conf., 9, 176, 1929.
- Morray, J. P., "Kinematic Interaction Problem of Embedded Circular Foundations," M. S. Thesis, Department of Civil Engineering, MIT, 1975.
- Mukherjee, S., "Non-Linear Analysis of an Embedded Structure under Transient Load," M.I.T. Report ADINA Conference August 1977, M.I.T., Cambridge, Massachusetts.
- Mukherjee, S., et al., "Non-Linear Analysis of a Deeply Embedded Power Plant Building Subjected to Earthquake Load," Brown Boveri Rev. 3-78, vol.65, no.3, pp 189-192, 1978.
- Murakami, H., et al., "Earthquake Response Analyses of Soil-Structure System Considering Kinematic Interaction," the 9th Int. Conf. on Structural Mechanics in Reactor Technology, 1987.
- Nadim, F., et al., "Seismically Induced Movement of Retaining Walls," J. Geotech. Eng. Conf., ASCE, 109(7), 915-931, 1983.
- Narikawa, M., et al., "Experimental and Analytical Study on Earth Pressure of an Embedded Building Model," 10th Int. Conf. on Structural Mechanics in Reactor Technology, k1, Anaheim, CA, 1989.
- Newmark, N.M., "Earthquake Design Response Analysis of Reactor Structures," Proc. 1st Int. Conf. on Structural Mechanics in Reactor Technology, Berlin, 1971.
- Novak, M., "Resistance of Soil to Horizontally Vibration Pile," EESD, Vol. 5, pp. 249-261, 1977.
- NRC RES Advanced Reactor Research Plan, Rev. 1 Draft report, ML021760135, June 2002.
- Nukui, Y., et al., "Fundamental Characteristics and Simplified Evaluation Method of Dynamic Earth Pressure," 10th Int. Conf. on Structural Mechanics in Reactor Technology, Anaheim, k1, CA, 1989.
- NUREG-0800, Revision 2, "Standard Review Plan," Office of Nuclear Reactor Regulation, U.S. Nuclear Regulatory Commission, 1989.
- Ohtomo, K, et al., "Research on Streamlining Seismic Safety Evaluation of Underground Reinforced Concrete Duct-Type Structures in Nuclear Power Stations - Part 2, Experimental Aspects of Laminar Shear Sand Box Excitation Tests with Embedded RC Models," 16th Int. Conf. on Structural Mechanics in Reactor Technology, k1, Washington, DC, 2001.
- Okabe, S., "General Theory of Earth Pressure," J. Japanese Soc. Of Civil Engrs., Tokyo, 12(1), 1926.
- Okamoto, S., "Earthquake Resistant Design Features of Submerged Tunnels in Japan," Earthquake Resistant design for civil eng struct., earth structures and foundations in Japan soc. Civil eng., Tokyo, pp 189-247, 1980.

Onimaru, S., et al., "Study of Dynamic Earth Pressure Acting on a Deeply Embedded Structure," 13th Int. Conf. on Structural Mechanics in Reactor Technology, k1, Porto Alegre, Brazil, 1995.

Ortigosa, P., et al., "Seismic Earth Pressures against Structures with Restrained Displacements," Proc., 2nd Int. Conf. On Recent Adv. In Geotech. Earthquake Eng. And Soil Dyn., 621-628, 1991.

Ostadan, F. and White, W. H., "Lateral Seismic Soil Pressure: An Updated Approach," 1st US-Japan SSI Workshop, Menlo Park, California, September 22-23, 1998.

Ostadan, F. and Penzien, J., "Seismic Design of Cut-and-Cover Sections of the Bay Area Rapid Extension to San Francisco Airport," 2nd US-Japan SSI Workshop, Tsukuba, Japan, March 6-8, 2001.

Pais, A., et al., "Stochastic response of foundations," Report No. R8506, MIT, Massachusetts, 1985.

Park, Y.J. and Hofmayer, C.H., "Technical Guidelines for Aseismic Design of Nuclear Power Plants - Translation of JEAG 4601-1987," NUREG/CR-6241, June 1994.

Pascal Pourcel, et al, "A Seismic Post Elastic Behavior of Spherical Tanks," 3rd European LS-DYNA User Conference, Paris, France, June 18-19, 2001.

Prato, C.A. et al., "Full Scale Dynamic Tests of Atucha II NPP," Nuclear Engineering and Design 179, pp. 225-243, 1998.

"Proceedings: EPRI/NRC/TPC Workshop on Seismic Soil-Structure Interaction Analysis Techniques Using Data from Lotung, Taiwan," vols. 1 and 2, EPRI NP-6154, March 1989.

Regulatory Guide 1.60, "Design Response Spectra for Seismic Design of Nuclear Power Plants," U.S. AEC, October 1973.

Richards, R., et al., "Seismic Earth Pressure on Retaining Structures," J. of Geotech. And Geoenv. Eng., ASCE, 771, 1999.

Roesset, J. M., "Perspectives on Soil Structure Interaction Analysis," Proceedings of EPRI/NRC/TPC Workshop on Seismic Soil-Structure Analysis, Lotung, Taiwan," Vol. 1, EPRI NP-6154, March 1989.

Roesset, J. M., "Seismic Response of Structures on Embedded Foundations," Advances in Earthquake Engineering, v2, Earthquake Resistant Engineering Structures, pp 19-34, Computational Mechanics Publisher, Southampton, Engl., 1995.

Romanel, C, et al., "Analysis of Deeply Embedded Structures in a Layered Half-Space," Proceedings of the 12th International Conf. On Offshore Mechanics and Arctic Engineering, ASME, Glasgow, Scotland, 1993.

Romanel, C., et al., "A Hybrid Modeling of Soil-Structure Interaction Problems for Deeply Embedded Structures in a Multilayered Medium," Earthquake Engineering and Structural Dynamics, vol. 22, 557-571 (1993).

- Schnabel, P.B., et al., "SHAKE, A Computer Program for Earthquake Response Analysis of Horizontally Layered Sites," Report No. EERC 72-12, College of Engineering, University of California, Berkeley, California, December 1972.
- Scott, R. F., "Earthquake-Induced Pressures on Retaining Walls," Proc., 5th World Conf. On Earthquake Eng., Int. Assn. of Earthquake Eng., Tokyo, 2, 1611-1620, 1973.
- Schneider, J. F., Abrahamson, N. A., Stepp, J. C., "The Spatial Variation of Earthquake Ground Motion and Effects of Local Site Conditions", Proceedings, Tenth World Conference on Earthquake Engineering, Madrid Spain, July 1992.
- Seed, H.B. and Idriss, I.M., "Soil Moduli and Damping Factors for Dynamic Response," Report No. EERC-70-10, College of Engineering, University of California, Berkeley, California, 1970.
- Seed, H. B., et al., 1984, "Soil Moduli and Damping Factors for Dynamic Response Analysis of Cohesionless Soils," Report No. UCB/EERC-8914, Earthq. Eng. Research Center, University of California, Berkeley, CA.
- Sherif, M. A., et al., "Earth Pressure against Rigid Retaining Walls," J. Geotech. Eng. Div., ASCE, 108(5), pp.679-695, 1982.
- Shibata, H., "Recent Development of Aseismic Design Practice of Equipment and Piping System in Japan," Transactions of the ASME, Journal of Pressure Vessel Technology, Vol. 115, pp 106-121, 1993.
- Siddharthan, R., et al., "On the Seismic Displacement Response of Rigid Retaining Walls," Soil and Foundations, 31(2), 51-64, 1991.
- Stamos, A. A., et al., "Dynamic Analysis of Large 3-D Underground Structures by the BEM," Earthquake Engineering and structural dynamics, vol. 24, 917-934, 1995.
- Steidl, J. H., et al, "Observations and Modeling of Ground Motion at the Garner Valley, California, Test Site," Proceeding of the OECD/NEA Workshop on the Engineering Characterization of Seismic Input, Brookhaven National Laboratory, Upton, New York, NEA/CSNI/R (2000) 2/Volume 2, 2001.
- Takada, T., et al., "Embedment Effect of Real Nuclear Power Reactor Building and Characteristics of Different Analytical Models," The 9th Int. Conf. on Structural Mechanics in Reactor Technology, k2, Lausanne, Switzerland, 1987.
- Tajimi, H, "Interaction of Building and Ground," Earthquake Engineering, Shokokusha Publishing Co., 1968.
- Tajimi, H., "Soil-Structure Dynamic Interaction," (in Japanese), 1985.
- Togashi, K., et al., "Preliminary assessment on the Influence of Distance between Nuclear Power Buildings," The 13th Intl. Conf. on Structural Mechanics in Reactor Technology, k3, Porto Alegre, Brazil, August 1995.
- Uldrich, E.D., et al., "Seismic Analysis of the ICPP High Level Liquid Waste Tanks and Vaults," Third DOE natural phenomena hazards mitigation conf., St. Louis, MO., Oct. 1991.

Valera, J. E., et al, "Seismic Soil-Structure Interaction Effects at Humbolt Bay Power Plant," J. of Geotechnical Eng. Div., ASCE, GT10, pp. 1143-1161, October 1977.

Vanmarcke, E. H., "On the Distribution of the First-Passage Time for Normal Stationary Random Processes," Journal of Applied Mech., vol.42, pp. 215-220, 1975.

Veletsos, A. S., et al., "Dynamic Soil Pressures on Rigid Vertical Walls," BNL Report, BNL-52357, December 1992.

Veletsos, A. S., et al., "Dynamic Soil Pressures on Rigid Cylindrical Vaults," BNL Report, BNL-52372, February 1993.

Veletsos, A. S., et al., "Dynamic Modeling and Response of Soil-Wall Systems," J. Geotech. Eng., ASCE, 120(12), 2155-2179, 1994.

Veletsos, A. S., et al., "Dynamic Modeling and Response of Rigid Embedded Cylinders," BNL Report, BNL-52444, October 1994.

Wang, L. R., et al, "State of the Art of Buried Lifeline Earthquake Engineering," Proc. Current state of lifeline earthquake engineering, ASCE, New York, pp. 252-266, 1977.

Wang, C. Y., "Structural and Seismic Analyses of Waste Facility Reinforced Concrete Storage Vaults," ASME Pressure vessel and piping conf., Honolulu, Hawaii, July 1995.

Weidlinger, P., et al., "Cavitations in Solid Medium," Journal of Engineering Mechanics, ASCE, vol.117, no.1, January 1991.

Wolf, J. P. , Dynamic Soil-Structure Interaction, Prentice-Hall, Inc., Englewood Cliffs, NJ 07632, 1985.

Wolf, J.P. and Song, C., Finite-Element Modelling of Unbounded Media, John Wiley & Sons, West Sussex, England, July 2000.

Wong, H. L. et al., "Interaction of a Shear Wall with the Soil for Incident Plane SH-waves: Elliptical Rigid Foundation," Bull. Seism. Soc. Amer., vol. 64, pp. 1825-1842, 1974.

Wong, H. L. et al., "Tables of Impedance functions and input Motions for Rectangular Foundations," Report No. CE78-15, Univ. of Southern California, 1978.

Wong, H. L., Luco, J. E., "Soil-Structure Interaction: A Linear Continuum Mechanical Approach (CLASSI)", Report CE, Department of Civil Engineering, University of Southern California, Los Angeles, CA, 1980.

Wood, J. H., "Earthquake Induced Pressures on a Rigid Wall Structure," Bull. Of New Zealand Nat. Soc. For Earthquake Eng., 8(3), 175-186, 1975.

Xu, J., et al., "Consideration of Kinematic Interaction in Determining Seismic Responses of Underground Structures," ASME-PVP Conf., Montreal, Canada, July 1996.

Xu, J., et al., "CARES (Computer Analysis for Rapid Evaluation of Structures), Seismic Module", Vol. 1, Theoretical Manual, Version 1.0, NUREG/CR-5588, 1990.

XYZ Scientific Applications, Inc., "Truegrid® Manual," version 2.1.0, September 2001.
Appendix – Solution to Benchmark Problems.

Yamamoto, S., et al., "Study of Dynamic Interaction between Turbine Building with Pile Foundation and Deeply Buried Reactor Building by Three-Dimensional Dynamic Analysis," The 15th Int. Conf. on Structural Mechanics in Reactor Technology, k3, Seoul, South Korea, August 1999.

Yamazaki, F., Turker, T., "Spatial Variation Study on Earthquake Ground Motion Observed by the Chiba Array", Proceedings, Tenth World Conference on Earthquake Engineering, Madrid Spain, July 1992.

Younan, A. H., et al., "Dynamic Response of Flexible Retaining Walls," BNL Report, BNL-52519, January 1997.